Appendix 11 - UN Fuel

Alternative Fabrication Routes for High Uranium Density Fuels

Final Report
Submitted: August 13, 2021

Prepared for:
Westinghouse Electric Company

Prepared by:
Adrian Gonzales and Dr. Elizabeth Sooby
The University of Texas at San Antonio

&

Dr. Michael A. Miller
Southwest Research Institute

THIS PAGE WAS INTENTIONALLY LEFT BLANK

SUMMARY

Thermo-Calc 2021b was used to fit experimental heat capacity data for the solid, liquid, and gaseous phases for UF_4 to obtain a Gibbs free energy equation. The phase transitions of UF_4 have been accurately modelled and fine tuning of the first two terms of each phases Gibbs functions can be done to further align with accepted thermochemistry data in the literature. Future efforts will be to implement the DFT calculations of UF_4, UN_2, and U-F-N-H intermediate phases, conducted at Southwest Research Institute and Los Alamos National Laboratory, into Thermo-Calc to find discover the equilibrium intermediate phases that form during the oxidative ammonolysis process.

THIS PAGE WAS INTENTIONALLY LEFT BLANK

CONTENTS

LIST OF FIGURES

Thermodynamic Modelling of scaled up production for high density fuel's

INTRODUCTION

Ideal synthesis methods for high density fuels (HDF) swill ideally have a starting material that is part of the current fuel cycle and can utilize existing conversion processes and infrastructures. Uranium nitride (UN) is conventionally synthesized using carbothermic reduction and nitridization (CTR-N) of the starting material UO_2. However, CTR-N method leaves carbon and oxygen impurities in the samples, in addition to requiring a constant flow of isotopically separated nitrogen gas. Another synthesis route involves hydriding-dehydriding-nitriding (HDN) elemental uranium, requiring a bulk uranium metal feedstock. The sol-gel method, a wet chemistry route, for producing UN microspheres has not displayed bulk UN production yet. Furthermore, UN has been researched for space reactors and liquid metal fast breeder reactors due to having a high melting temperature and its higher uranium density than UO_2 and other HDF of interests.

The U.S. Department of Energy, along with research institutes around the world, have become motivated by recent events to focus on creating more accident-tolerant fuel (ATF) forms. Research on the properties of high uranium density ATF compounds such as uranium nitride (UN) have been conducted, but the synthesis of UN from UF_6 and ammonia feedstocks remains elusive because the thermochemistry and plethora of intermediate compounds along favorable reaction pathways are poorly understood.

A synthesis route that starts with UF_6 would be ideal due to it being a part in the nuclear fuels' life cycle during uranium enrichment. UF_6 can be easily converted to UF_4 through dry and wet routes [1-3] and alternate routes starting with UF_4 are also of interest. Experiments reacting UF_4 with ammonia (oxidative ammonolysis) or nitrogen gas have been performed and resulted in higher uranium nitrides along with intermediate phases that could not be identified [4-7]. Thermodynamic modelling can provide insight into possible intermediate products forming during the oxidative ammonolysis process. Currently, there are no thermodynamic model for the U-F system and is to be addressed here.

RELEVANCE

The computational effort undertaken here is consistent with the DOE-NE strategic vision under Goal 1 Performance Indicators, seeking "By 2025, begin replacing existing fuel in U.S. commercial reactors with accident tolerant fuel." Commercial viability and widespread implementation of UN as an accident tolerant fuel form will depend largely on a scalable and cost-effective synthetic route for its production. Implementation and refinement of a first principles computational framework for deriving unknown thermochemical data, when coupled with phenomenological calculation tools, is aimed at accelerating the discovery of thermodynamically viable pathways leading to UN formation that otherwise are impractical and time consuming to test experimentally.

BACKGROUND

Computational methods combining first principles and data-driven phenomenological approaches are crucial to discovering and mapping the thermochemical landscape of possible reaction

pathways leading to the formation of UN. A primitive reaction scheme (Scheme I) for the synthesis of UN was considered as a sensible starting point for this effort :

$$UF_6\,(g) \longrightarrow UF_4\,(g) + F_2\,(g)$$
$$\downarrow$$
$$UF_4\,(s)$$

$$UF_4\,(s) + 6NH_3\,(g) \longrightarrow UN_2\,(s) + 4NH_4F\,(s) + H_2\,(g)$$

$$UN_2\,(s) \longrightarrow UN\,(s) + 1/2N_2\,(g)$$

Scheme I: Primitive reaction scheme for synthesis of UN.

This primitive scheme does not include the manifold of intermediate species that may potentially play a role in the reaction of UF_4 with ammonia at high temperatures. Most of these intermediate species have been tentatively identified and their solid structures predicted (Figure 1), but their thermochemical influence on Scheme I was beyond the scope of the present work.

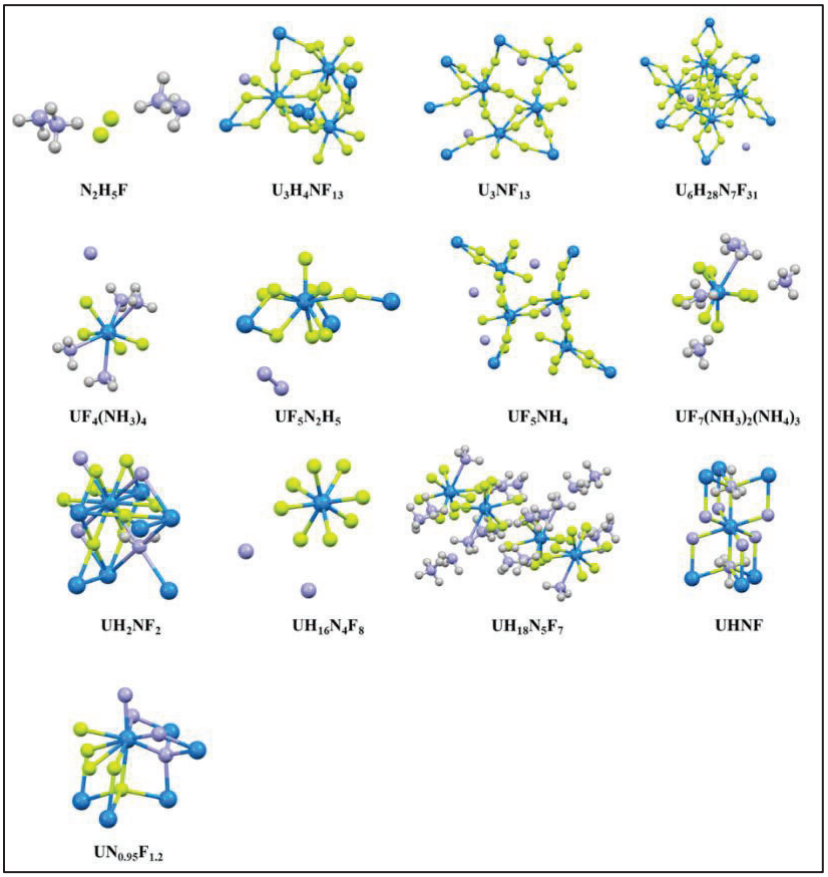

Figure 1. Intermediate compounds potentially involved in the primitive reaction scheme (Scheme I). The predicted crystalline structures are shown.

The thermodynamic model for the Gibbs free energy for a phase is described by the composition of different contributions[8, 9]:

$$G = G^{srf} + G^{phy} + G^{cnf} + G^{exs} \qquad \text{Equation 1}$$

Where the term G^{srf} is the surface of reference and describes the Gibbs energy for the unreacted mixture of the constituents of the phase. The G^{phy} term is the contribution of physical phenomena like magnetic transitions, Curie temperature, or Bohr magneton number. The G^{cnf} term is the configurational entropy of the phase and represents the number of possible arrangements (W) for the constituents in the phase and is given by the statistical thermodynamic equation for entropy, $S = kln(W)$. In practice, this term is used to describe the possible arrangements of constituents on each sublattice in the phase [9]. Finally, the G^{exs} term is the excess energy left over by the first three terms and in practice is only used for ternary, quaternary, and higher order interactions. All the terms except for the configurational term are a function dependent on temperature, pressure, and mole fraction of the constituents in the phase. A thermodynamic software like Thermo-Calc will model each of these terms separately for each phase. The temperature dependent function for the surface of reference and excess Gibb's energy for a phase is described by a power series in temperature:

$$G^{srf,exs} = a_0 + a_1T + a_2Tln(T) + \sum_n d_nT^n,\ T_1 < T < T_2 \qquad \text{Equation 2}$$

Thermodynamic quantities cannot be directly related to the coefficients in the above equation but using thermodynamic relations it can be shown that the term a_0 is related to the enthalpy of formation for the phase using $H = G - T\left(\frac{\partial G}{\partial T}\right)_{P,N}$. The a_1 term is related to the entropy of formation for the phase which can be derived using the relation, $S = -\left(\frac{\partial G}{\partial T}\right)_{P,N}$. The third and higher terms are all related to the heat capacity through the relation, $C_p = -T\left(\frac{\partial^2 G}{\partial^2 T^2}\right)_{P,N}$.

Thermodynamic

MATERIALS

Phenomenological

The Gibbs Energy System (GES) module in Thermo-Calc 2021b [11]was used to import the thermochemistry data found on the UF_4 phases by using a .POP file. A setup file was created and ran in the GES module to assign each phase to a model and to contain the Gibbs free energy equations, $Gsrf,exs = a_0 + a_1T + a_2Tln(T) + \sum_n d_nT^n,\ T_1 < T < T_2$ Equation 2, whose variables are to be determined. The PARROT module had been used to fit the model to the heat capacity data contained in the .POP file. The POLY module was utilized to run equilibrium calculation through the modelling process and the POST submodule was used to plot figures of the POLY calculations.

The UF_4 solid phase was model as a stoichiometric compound with the sublattice form of $(U)_1(F)_4$. The UF_4 liquid phase was modeled with using the ionic two sublattice liquid model and has the sublattice form $(U^{+4})_1(F^{-1})_4$. The liquid model was used due to its use in the

Thermodynamics of Advanced Fuels International Database (TAF-ID v12) [12] which is to be used for determining formations of nuclear fuels. There is only one gas phase in a database and TAF-ID already contained Gibbs functions for U gas but lacked information on the fluorine element and gas phases. The Gibbs function for the fluorine gas and element was taken from the PURE5 database, which contains the Scientific Groupe Thermodata Europe (SGTE) standardizations for all elements used in Thermo-Calc, and implemented into TAF-ID.

First Principles Computational Methods

First principles computational methods at the level of density functional theory (DFT) and Hartree-Fock (HF) were employed to compute the electronic structures and energies of reactant and product species for both the gas phase and some of the solid-state species (where applicable). Advanced basis sets for the exchange-correlation (XC) relativistic corrections were invoked for solid-state species by implementing the density-gradient expansion for XC functionals of Perdew, Burke, and Ernzerhof (PBEsol). In all species involving fluorine atoms, double zeta basis with polarization and diffuse functions (6-31 + G*) were used for fluorine atoms. To optimize accuracy, at least two basis sets were invoked for uranium atoms using the relativistic effective core potential (RECP) constraint in combination with DFT: Christiansen-Ross-Ermler-Nash-Bursten (CRENB) [13-16] and LANL2 [17].

Enthalpies were computed at 0 K (H_0) as the sum of electronic and zero-point energies (ZPE), along with the theoretical atomization energies (TAE) for gas-phase molecular species:

$$A_xB_y \rightarrow xA + yB$$

$$TAE_0 = xH_0(A) + yH_0(B) - H_0(A_xB_y)$$

The enthalpies of formation for each species at 0 K ($\Delta_f H_0$) were derived from the TAE and experimentally determined formation enthalpies of the elemental species.

$$\Delta H_{f0} = [x\Delta H_{f0}(A) + y\Delta H_{f0}(B)] - TAE_0$$

These energies were then extrapolated to standard conditions (298.15 K, 1 atm) by adding thermal enthalpy corrections to the zero Kelvin values to account for translational, rotational, and vibrational degrees of freedom. Band structures and density of states (DOS) were computed for UN_4 (cr) and UN_2 (cr) along the *k*-point pathways $\Gamma \rightarrow \chi \rightarrow W \rightarrow K \rightarrow L \rightarrow K$ in reciprocal space. Phonon modes for UN_2 (cr) were computed to derive the ZPE and the enthalpy corrections for standard conditions.

RESULTS AND DISCUSSION

Phenomenological Thermodynamic Results

The thermodynamic properties of crystalline, liquid, and gaseous UF_4 have been reported using various techniques [18, 19]. The heat capacity for this computational model used the selected values of the International Atomic Energy Agency [20] reviewed in Guillamont *et al. [19]* for the solid, liquid, and gaseous phases. The solid UF_4 heat capacity model was fitted to experimental

data values, Figure 1, which give the a_2 and higher variables in $G^{srf,exs} = a_0 + a_1T + a_2Tln(T) + \sum_n d_nT^n,\ T_1 < T < T_2$ Equation 2. A comparison of the model to the experiment values, Table 1, gave a maximum difference of 1.922 J/mol*K. The process was repeated for the gaseous heat capacity model, Figure 2, and a comparison to experimental data gave a maximum difference of 1.637 J/mol*K, Table 2. A single value was reported for the heat capacity of liquid UF_4 experimentally as 165 J/mol*K ±15 [19] and was used to model the liquid phase between the melting (1309K) and boiling point (1690K). The following equations display the temperature dependent heat capacity model obtained from the fittings and are used in the Gibbs free energy equation for each of the UF_4 phases.

$$Cp_{Solid}(T) = -5.65403715x10^2TLn(T) - 2.03785179x10^{-1}T^2 - 3.36012821x10^{-6}T^3 \quad \text{Equation 3}$$

$$Cp_{Gas}(T) = -4.82413702x10^2TLn(T) - 4.17722021x10^{-2}T^2 + 2.59705784x10^{-6}T^3 \quad \text{Equation 4}$$

$$Cp_{Liquid}(T) = -8.35x10^2TLn(T) \quad \text{Equation 5}$$

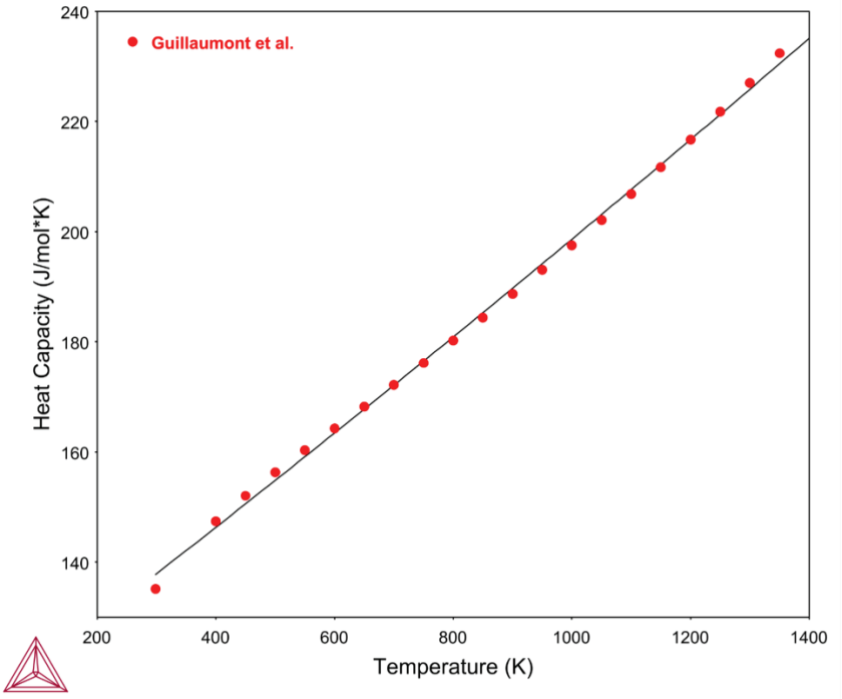

Figure

Experimental	Model	Experiment	ΔCp	Least-
135.14233	137.7	1.4	2.6	1.924
147.40778	146.3	1.5	-	-
152.03971	150.6	1.5	-	-
156.288	154.8	1.6	-	-

160.33406	159.1	1.6	-	-
164.28704	163.4	1.6	-	-
168.21579	167.8	1.7	-	-
172.1655	172.1	1.7	-	-
176.16681	176.5	1.8	0.3176	0.1803
180.2411	180.9	1.8	0.6315	0.3504
184.40365	185.3	1.8	0.8773	0.4757
188.66562	189.7	1.9	1.044	0.5533
193.03531	194.2	1.9	1.123	0.5817
197.519	198.6	2	1.108	0.5609
202.12151	203.1	2	0.9945	0.492
206.8466	207.6	2.1	0.7785	0.3764
211.69722	212.2	2.1	0.4572	0.216
216.67571	216.7	2.2	0.028222	0.013025
221.78397	221.3	2.2	-	-
227.02353	225.9	2.3	-	-
232.39566	230.5	2.3	-	-

Table

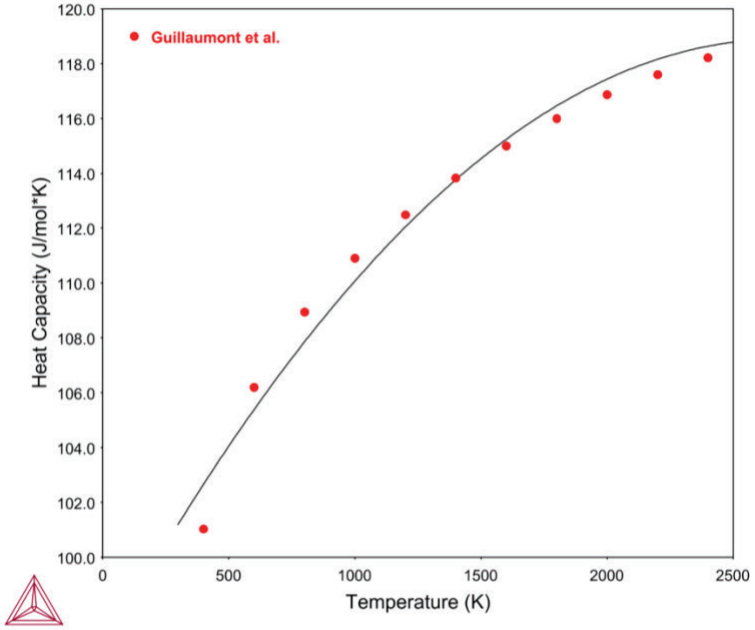

Figure

Experimental	Model	Experimental	ΔCp	Least-
101.03019	102.7	3	1.637	0.5403
106.19604	105.4	3.2	-	-

108.94075	107.9	3.3	-	-
110.90268	110.1	3.3	-	-
112.48611	112	3.4	-	-
113.82956	113.8	3.4	-	-
114.99089	115.2	3.4	0.2479	0.071861
115.99774	116.5	3.5	0.4636	0.1332
116.86467	117.4	3.5	0.57	0.1626
117.59994	118.2	3.5	0.5586	0.1583
118.20853	118.6	3.5	0.4247	0.1197
118.69356	118.9	3.6	0.1649	0.046321
119.05709	118.8	3.6	-	-
119.30052	118.6	3.6	-	-

Table

The first two terms in $Gsrf,exs = a_0 + a_1T + a_2Tln(T) + \sum_n d_nT^n,\ T_1 < T < T_2$ Equation 2 were optimized to align with experimental thermochemistry data and paired with the heat capacity models gave the Gibbs energy equation for each phase. $GSolid = -946541x10^6 + 3.15491x10^3T + Cp_{Solid}$ $298.15K < T < 1309K$ Equation 6-8 are the Gibbs free energy model obtained and implemented into the TAF-ID database. The experimental thermochemistry data for solid UF_4 can be obtained up to the melting point (1309K) therefore, the Gibbs free energy model needed to be sectioned into two parts to control the model after the melting point and was modeled after the liquid phase. The gas phase has an additional term in its Gibbs free energy equation, RTLnP, where R is the gas constant, T is temperature, and P is the ratio of the partial pressure of the gas phase to the standard atmospheric pressure of 101325 Pa.

$$G_{Solid} = -946541x10^6 + 3.15491x10^3T + Cp_{Solid} \quad 298.15K < T < 1309K$$
$$= -9.411564x10^6 + 4.773x10^3T + Cp_{liquid} \quad 1309 < T < 2500 \qquad \text{Equation 6}$$

$$G_{Gas} = -8.0259x10^6 + 1.3391x10^3T + Cp_{Gas} + RTLnP \quad 298.15 < T < 2500 \qquad \text{Equation 7}$$

$$G_{Liquid} = -9.061564x10^6 + 4.509x10^3T + Cp_{Liquid} \quad 298.15 < T < 2500 \qquad \text{Equation 8}$$

An equilibrium calculation of 1 mole of U and 4 moles of F at 1 atm pressure was performed, Figure 3, to find the phase transitions over a range of temperatures. The melting point was found to be at 1309 K and the boiling point at 1693K aligning up well to the experimental values of

1309K and 1690 K, respectively. The Gibbs energies, Figure 4, of the equilibrium were plotted and can be used to adjust the phase transitions and finally, the enthalpy was plotted to find the enthalpy of fusion, vaporization, and sublimation, Figure 5 .

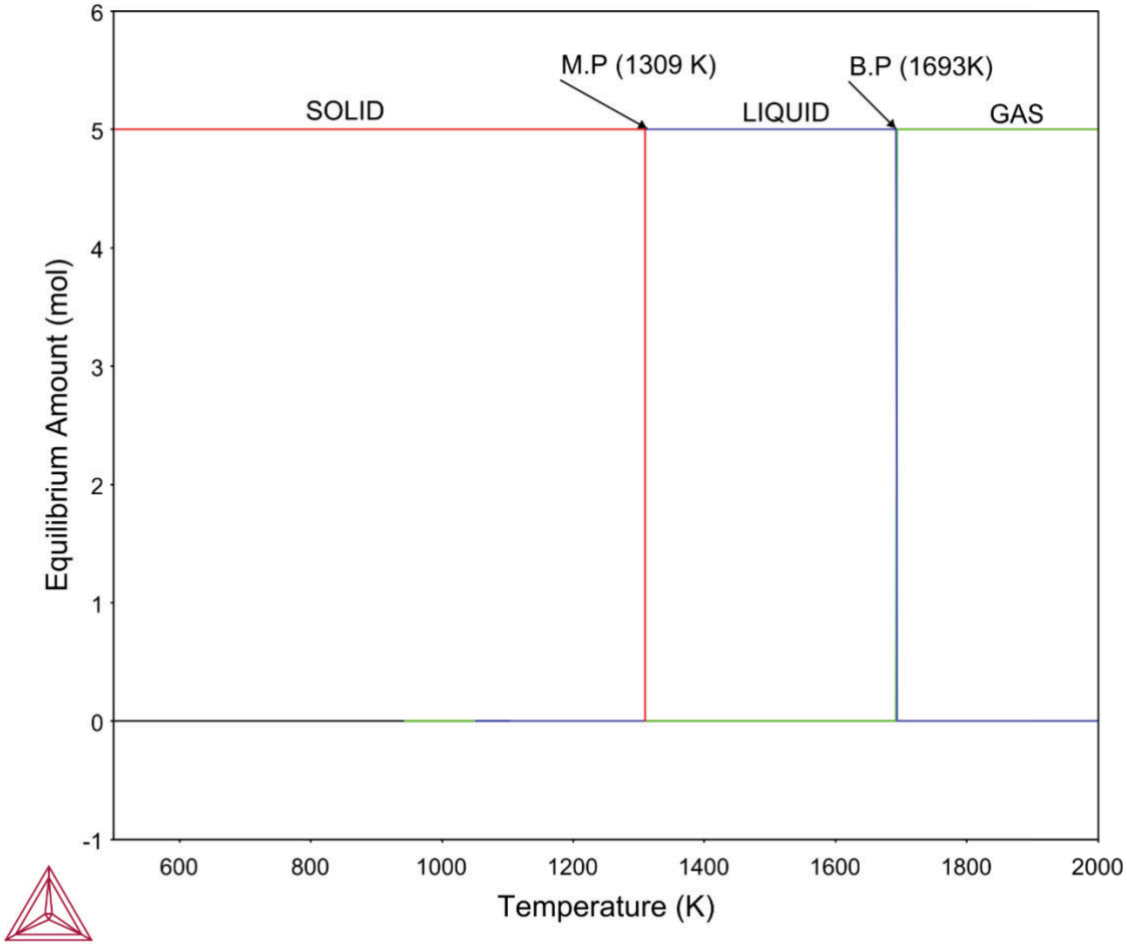

Figure 3. Equilibrium calculation performed in Thermo-Calc 2021b with the TAF-ID v12 database of UF_4 solid heat treated from 500-2000 K to display the phase transitions at 1 atm.

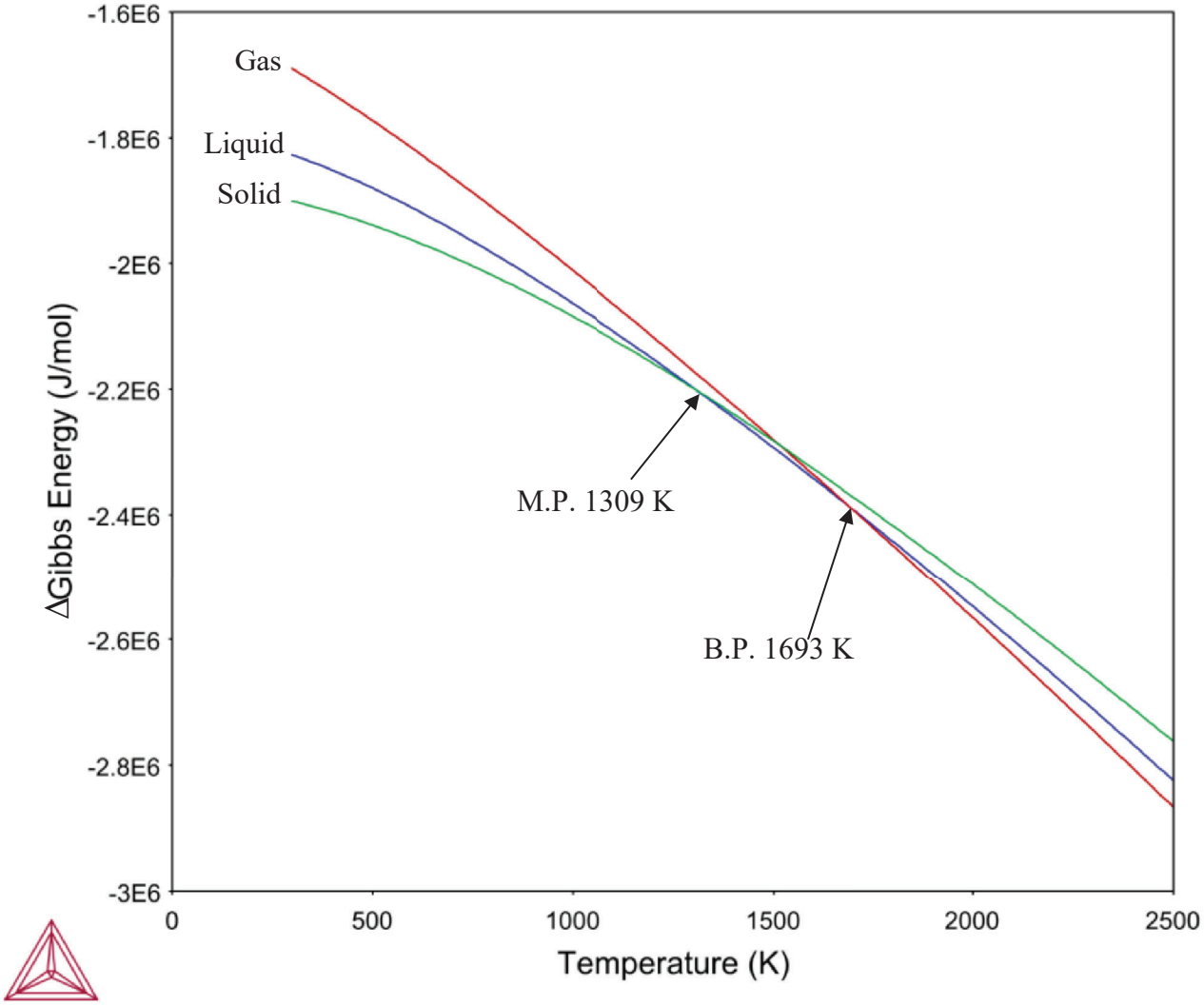

Figure 4. The ΔGibbs energy of formation for the UF_4 phases displaying the melting and boiling point.

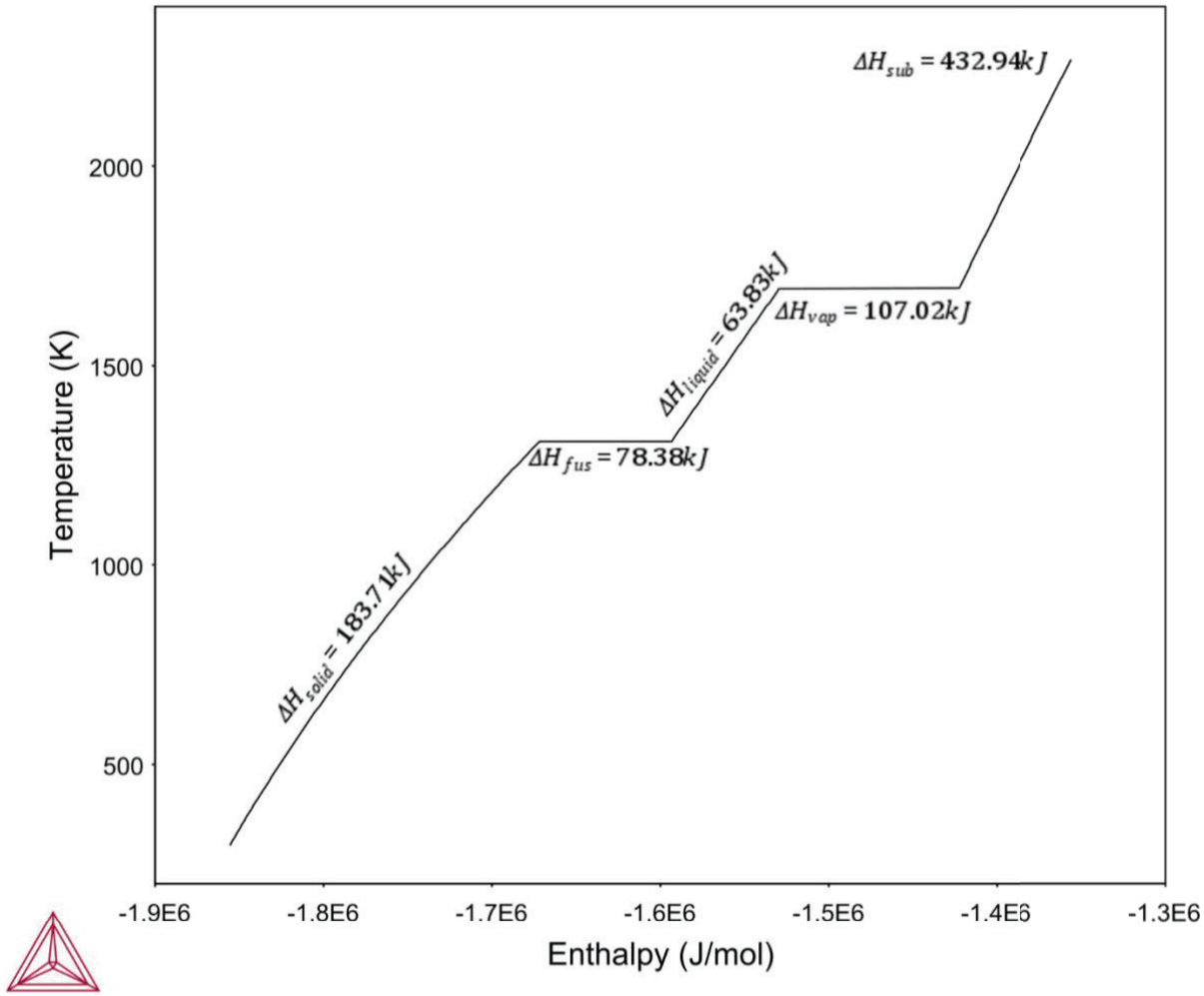

Figure 5. Enthalpy of the UF_4 modeled phases displaying the enthalpy of fusion, vaporization, and sublimation.

The thermodynamic models' calculations are summarized in Table 3, Table 4, and Table 5, that compare the experimental values to the models' value for each phase. The modelling started with fitting the model to the heat capacity data and deviations from the experimental values came from aligning to the ΔG_f values. All the deviations from the ΔG_f values came from aligning the model to the melting and boiling points. The enthalpy and entropy values were then obtained from the resulting model.

The experimental values for the solid enthalpy of formation varied from -1884.9 kJ/mol to -1921.3 kJ/mol depending on the type of experiment method. The selected value in Table 3 came from the IAEA review *[20]* which is a weighted average from Johnson *[21]* (using fluorine combustion calorimetry) and by Cordfunke et al. (using solution calorimetry) *[22]*. The models' enthalpy of formation value is lower than the range found in the literature and can be adjusted with the second term of its Gibbs free energy equation. This adjustment will change the melting and boiling points and cause for adjustments in the gas and liquid models as well. The other thermochemistry model values agree well with the literature values but since further adjustments are needed in the liquid

and gas models, the adjustments should start with the solid phases' enthalpy of formation value first.

UF_4 Solid		
Thermodynamic Property	Literature Values	Thermo-Calc Model
ΔH_f @298.15K (kJ/mol)	-1914.2 ±4.2 [18]	-1855.68
S @298.15K (J/mol*K)	151.67 ±0.2 [18]	151.51
Cp @298.15K (J/mol*K)	135.14 ±0.1 [19]	137.74
ΔG_f @298.15K (kJ/mol)	-1823.53 ±4.2 [19]	-1900.69
Melting Point (K)	1309 [19]	1309.24
Boiling Point (K)	1690 [19]	1693

Table 3. Solid UF_4 thermodynamic model compared to experimental values.

The literature value for the enthalpy of formation of the gaseous phase was calculated from the enthalpy of sublimation and the enthalpy of formation of the solid phase which was obtained from a third law analysis of the vapor pressure of the reaction UF_4 (s) = UF_4(g) [18]. Thermo-Calc produces the user with the enthalpy change of the product from its elements and resulted in a lower value than the literature value, Table 4. The ΔH_{sub} has a range of 306.8 - 363.85 kJ/mol found in the literature and the models' value is above this range and the second term in the Gibbs equation relates to the enthalpy values and can be used to adjust the models' values which will not affect the ΔG_f, Cp, or S values but will affect the boiling point. The ΔG_f value for the model is slightly lower than the literature value but can be adjusted using the first term in the Gibbs equation which will affect the enthalpy and entropy values as well.

UF_4 Gas		
Thermodynamic Property	Literature Values	Thermo-Calc Model
ΔH_f @298.15K (kJ/mol)	-1601.2 ± 6.5 [19]	-1575.64
S @298.15K (J/mol*K)	363.7 ± 5.0 [19]	383.22
Cp @298.15K (J/mol*K)	101.4 ± 3.0 [19]	101.1
ΔG_f @298.15K (kJ/mol)	-1712.74 ± 9.2 [19]	-1689.9
ΔH_{Sub} (kJ/mol)	313.0 ±8.0 [19]	432.94

Table 4. Gaseous UF_4 thermodynamic model compared to experimental values.

There was not a lot of literature found about the liquid phase and what has been reported are only approximations of the thermochemistry values, Table 5. It is difficult to determine the accuracy of the liquid phases' model and the focus was on aligning to the melting point values. No ΔH_{vap} was reported but from the reported ΔH_{sub} and ΔH_{fus} values, it was calculated using the equation $\Delta H_{sub} - \Delta H_{fus} = \Delta H_{vap}$.

UF_4 Liquid		
Thermodynamic Property	Literature Values	Thermo-Calc Model
ΔH_f @298.15K (kJ/mol)	-1936.8 ± 8.7 [19]	-1930.29
S @298.15K (J/mol*K)	476 ± 17 [19]	655.89
Cp (J/mol*K)	167 [19]	167
ΔG_f @298.15K (kJ/mol)	-1802.1 ±6.6 [19]	-1827.13
ΔH_{Fus} @1309 (kJ/mol)	46.98 ±5 [19]	78.38
ΔH_{vap} @1690K (kJ/mol)	262*	107.02

Table 5. Liquid UF4 thermodynamic model compared to experimental values. *Calculated value based on sublimation and fusion values.

First Principles Computational Results

The overall results of computed formation enthalpies and heats of reactions for Scheme I at 0 K and 298.15 K (1 atm) are shown in Tables 6 and 7, respectively. Formation enthalpies and heats of reactions involving crystalline solids are reported based on the energy per unit cell of each crystalline solid. Also included for the solids are the crystal phases and corresponding crystallographic parameters following DFT structural optimizations. In the case of UF_4 (cr), computation of phonon modes needed to derive formation enthalpies at standard conditions were not completed because the unit cell is defined by 30 atoms, which would have been computationally intractable using a 64 core computing machine.

We find from these results that, while the ammonolysis reaction for the formation of UN_2 (cr) from UF_4 (cr) is exothermic, the reaction enthalpies for conversion of UN_6 to UN_4 in the gas phase and the solid phase conversion of UN_2 to UN are both exothermic. The net thermodynamic balance for Scheme I is endothermic, $\Delta H_{net,rxn}$ = 604 kJ/mol at standard conditions.

The band structure and DOS computed for UN_2 (cr) are shown in Figure 6. A band gap of 0.682 eV at 0 K was calculated for this solid, which is similar to that of pure germanium. The phonon dispersion curves for this solid, which were computed along the same *k*-point pathways as the electronic band structure, are shown in Figure 7. These results indicate the occurrence of acoustic phonon modes between 0 and 300 cm^{-1} and optical phonons near 475 and 775 cm^{-1}.

Species / Reaction	Electronic Energy (kJ/mol) @ 0 K	Vibrational ZPE (kJ/mol) @ 0 K	Exp. Formation Enthalpy, ΔH_{f0} (kJ/mol) @ 0 K	Theoretical Atomization Energy (TAE) (kJ/mol) @ 0 K	Theoretical Formation / Rxn Enthalpy, ΔH_{f0} (kJ/mol) @ 0 K
U (g)	-134927.00	0.00	535.43		
F (g)	-63332.09	0.00	77.26		
UF_6 (g)	-518082.00	20.27		3142.17	-2143.19
UF_4 (g)	-390718.44	16.90		2446.16	-1601.70
F_2 (g)			0.00		
UF_6 (g) --> UF_4 (g) + F_2 (g)					**541.49**
UF_4 (cr) [Monoclinic, C2/c, a=12.73 Å b=10.75 Å c=8.43 Å; α=γ=90 β=126.333]	-22442.15			4337.16	-1919.41
U (g) PBE	-554.02	0.00	535.43		
N (g) PBE	-61.59	0.00	470.58		
NH_3 (g)			-38.65		
UN_2 (cr) [FCC, cF, a=b=c=7.0834; α=β=γ=60.00]	-2969.33	24.83		2267.30	-790.71
NH_4F (cr) [Hexagonal, $P6_3mc$, a=b=4.448 Å c=7.203 Å; α=β=90 γ=120]	-5831.59				-466.90
H_2 (g)			0.00		
UF_4 (cr) + 6NH_3 (g) --> UN_2 (cr) + 4NH_4F (cr) + H_2 (g)					**-506.97**
UN (cr) [Cubic, Fm3m, a=b=c=3.446 Å; α=β=γ=60.000]	-262356.54				-287.53
N_2 (g)			0.00		
UN_2 (cr) --> UN (cr) + 1/2N_2 (g)					**503.18**

Table 6. Theoretical formation enthalpies derived from first principles computations at 0 K (ZPE = Zero Point Energy; TAE = Theoretical Atomization Energy).

Species / Reaction	Enthalpy Correction (kJ/mol) @ 298.15 K	Electronic Energy (kJ/mol) @ 298.15 K	Exp. Formation Enthalpy, ΔH_{f0} (kJ/mol) @ 298.15 K	Theoretical Atomization Energy (TAE) (kJ/mol) @ 298.15 K	Theoretical Formation / Rxn Enthalpy, ΔH_{f0} (kJ/mol) @ 298.15 K
U (g)	2.48	-134924.52	533.00		
F (g)	2.48	-63329.62	79.04		
UF_6 (g)	44.75	-518037.25		3135.04	-2127.78
UF_4 (g)	37.89	-390680.55		2437.57	-1588.39
F_2 (g)			0.00		
UF_6 (g) --> UF_4 (g) + F_2 (g)					**539.39**
UF_4 (cr) [Monoclinic, C2/c, a=12.73 Å b=10.75 Å c=8.43 Å; α=γ=90 β=126.333]			-1936.80		-1914.20
U (g) PBE	2.48	-551.55	533.00		
N (g) PBE	2.48	-59.11	472.44		
NH_3 (g)			-45.56		
UN_2 (cr) [FCC, cF, a=b=c=7.0834; α=β=γ=60.00]	32.18	-2937.15		2267.39	-789.50
NH_4F (cr) [Hexagonal, $P6_3mc$, a=b=4.448 Å c=7.203 Å; a=b=90 γ=120]			-463.96		
H_2 (g)			0.00		
UF_4 (cr) + 6NH_3 (g) --> UN_2 (cr) + 4NH_4F (cr) + H_2 (g)					**-435.20**
UN (cr) [Cubic, Fm3m, a=b=c=3.446 Å; α=β=γ=60.000]			-290.00		
N_2 (g)			0.00		
UN_2 (cr) --> UN (cr) + 1/2N_2 (g)					**499.50**

Table 7. Theoretical formation enthalpies derived from first principles computations at 298.15 K and 1 atm (TAE = Theoretical Atomization Energy).

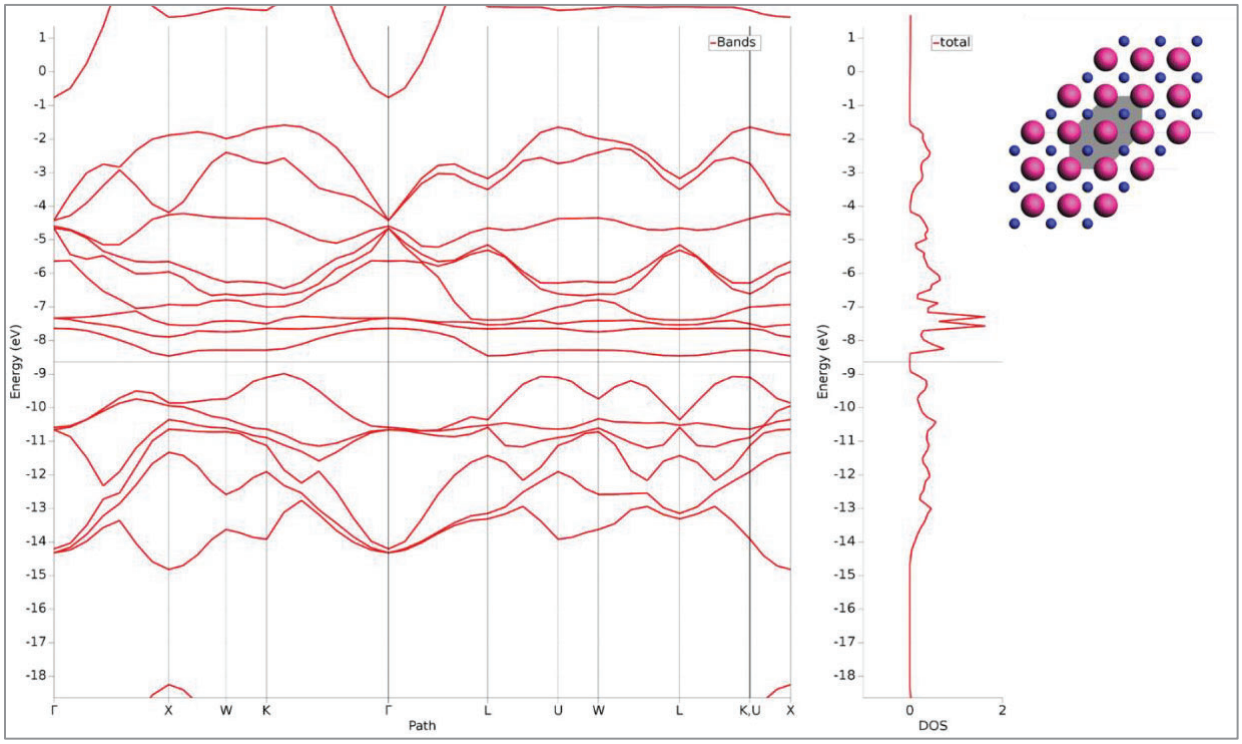

Figure 6. Solid-state electronic band structure and density of states (DOS) computed for UN2.

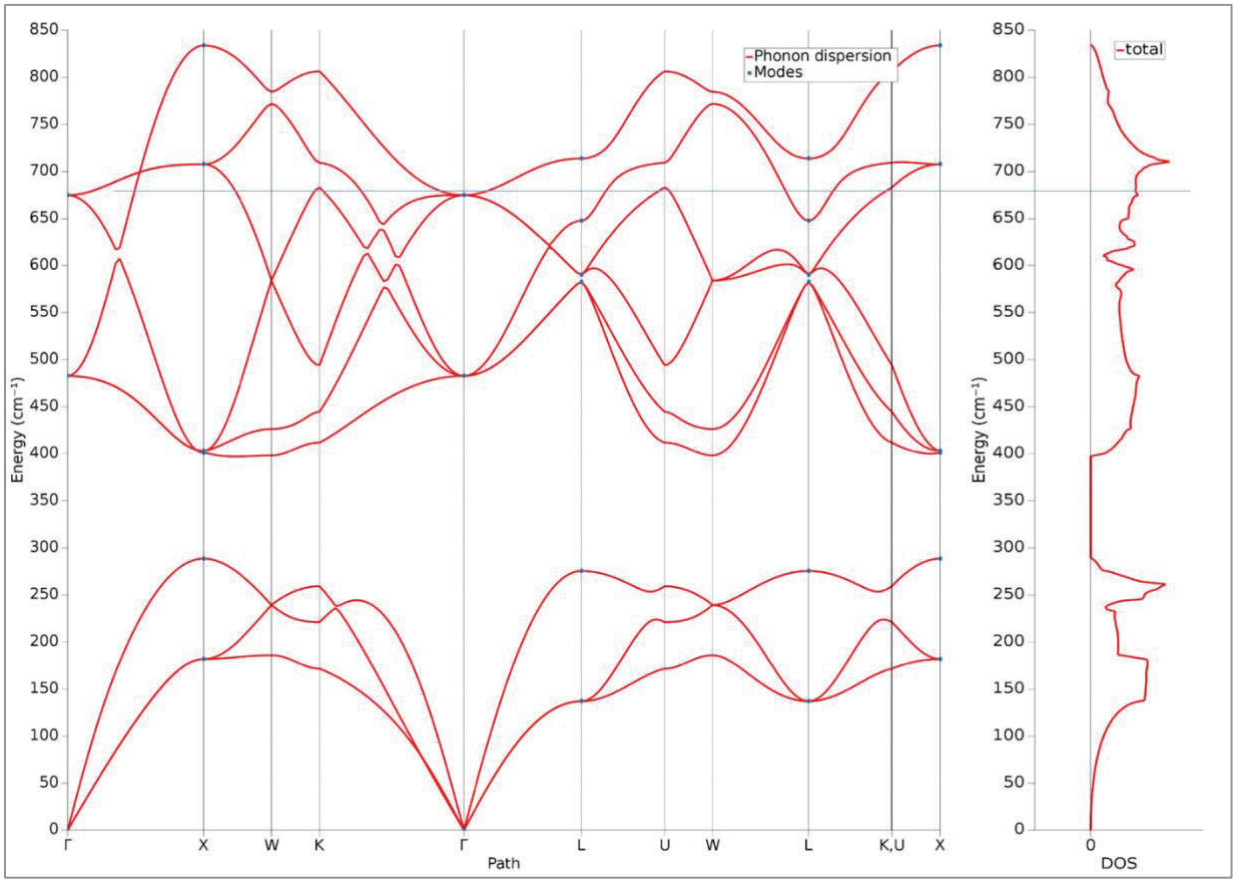

Figure 7. Phonon dispersion and density of states (DOS) computed for UN_2 at 0 K.

SUMMARY and FUTURE DIRECTIONS

Thermo-Calc 2021b was used to fit experimental heat capacity data for the solid, liquid, and gaseous phases for UF_4 to obtain a Gibbs free energy equation. The phase transitions of UF_4 have been accurately modelled and fine tuning of the first two terms of each phases Gibbs functions can be done to further align with accepted thermochemistry data in the literature. Future efforts will be to implement the DFT calculations of UF_4, UN_2, and U-F-N-H intermediate phases, conducted at Southwest Research Institute and Los Alamos National Laboratory, into Thermo-Calc to find discover the equilibrium intermediate phases that form during the oxidative ammonolysis process.

REFERENCES

1. Katz, J.J. and E. Rabinowitch, *Part 1-The elements, its binary and related compounds. The Chemistry of Uranium*. 1951, New York: McGraw-Hill.
2. Franca Junior, J.M., *Unidade piloto de tetrafluoreto de uranio pelo processo de'leito movel'em operacao no IEA.* 1975.
3. Frajndlich, E.U.C., A.M. Saliba-Silva, and M.A. Zorzetto. *Alternative route for UF6 conversion towards UF4 to produce metallic uranium*.
4. Wozniak, N., et al., *Report on Current Assessment of Fabrication Routes to Large-Scale UN Production*. 2019, Los Alamos National Lab.(LANL), Los Alamos, NM (United States).

5. Funk, H. and H. Böhland, *Zur Darstellung von Metallnitriden aus Ammoniumfluorometallaten und Ammoniak.* Zeitschrift für anorganische und allgemeine Chemie, 1964. **334**(3-4): p. 155-162.
6. Berthold, H.J. and H.G. Hein, *Über die hochtemperaturammonolyse von UF4.* Angewandte Chemie, 1969. **81**(22): p. 910-910.
7. Yoshihara, K., M. Kanno, and T. Mukaibo, *Preparation of uranium nitrides from uranium tetrafluoride.* Journal of Nuclear Science and Technology, 1968. **5**(12): p. 643-647.
8. Kattner, U.R., *The Calphad method and its role in material and process development.* Tecnologia em metalurgia, materiais e mineracao, 2016. **13**(1): p. 3.
9. Lukas, H.L., S.G. Fries, and B. Sundman, *Computational thermodynamics.* The CALPHAD method, 2007: p. 1-324.
10. Grimvall, G., *Thermophysical properties of materials*. 1999: Elsevier.
11. Andersson, J.-O., et al., *Thermo-Calc & DICTRA, computational tools for materials science.* Calphad, 2002. **26**(2): p. 273-312.
12. Massara, S. and C. Gueneau, *Thermodynamics of Advanced Fuels-International Database Project.* NEA News, 2014. **32**(1/2): p. 24.
13. Fernandez Pacios, L.; Christiansen, P. A. Ab Initio Relativistic Effective Potentials with Spin-Orbit Operators. I. Li through Ar. J. Chem. Phys. 1985, 82, 2664.
14. Hurley, M. M.; Pacios, L. F.; Christiansen, P. A.; Ross, R. B.; Ermler, W. C. Ab Initio Relativistic Effective Potentials with SpinOrbit Operators. II. K through Kr. J. Chem. Phys. 1986, 84, 6840.
15. LaJohn, L. A.; Christiansen, P. A.; Ross, R. B.; Atashroo, T.; Ermler, W. C. Ab Initio Relativistic Effective Potentials with Spin− orbit Operators. III. Rb through Xe. J. Chem. Phys. 1987, 87, 2812.
16. Ross, R. B.; Powers, J. M.; Atashroo, T.; Ermler, W. C.; LaJohn, L. A.; Christiansen, P. A. Ab Initio Relativistic Effective Potentials with Spin−orbit Operators. IV. Cs through Rn. J. Chem. Phys. 1990, 93, 6654.
17. Hay, P. J.; Wadt, W. R. *Ab Initio* Effective Core Potentials for Molecular Calculations. Potentials for K to Au Including the Outermost Core Orbitals. *The Journal of Chemical Physics* 1985, *82* (1), 299–310. https://doi.org/10.1063/1.448975.
18. Grenthe, I., et al., *Chemical thermodynamics of uranium*. Vol. 1. 1992: Elsevier Amsterdam.
19. Guillaumont, R., et al., *Update on the chemical thermodynamics of uranium, neptunium, plutonium, americium and technetium chemical thermodynamics.* Nuclear Energy Agency, Elsevier Science Publisher, 2003.
20. Fuger, J., et al., *Chemical thermodynamics of actinide elements and compounds. Pt. 8. The actinide halides.* 1983.
21. Johnson, G.K., *The enthalpy of formation of UF4 by fluorine bomb calorimetry*. Journal of Nuclear Materials, 1985. **130**: p. 102-108.
22. Cordfunke, E.H.P. and W. Ouweltjes, *Standard enthalpies of formation of uranium compounds VII. UF3 and UF4 (by solution calorimetry).* The Journal of Chemical Thermodynamics, 1981. **13**(2): p. 193-197.

Challenges and Opportunities to Alloyed and Composite Fuel Architectures to Mitigate High Uranium Density Fuel Oxidation: Uranium Mononitride

Jennifer K. Watkins[a,b], Adrian Gonzales[c], Adrian R. Wagner[a], Elizabeth S. Sooby[c], Brian J. Jaques[b,d]

[a] Idaho National Laboratory, Idaho Falls, ID, USA

[b] Micron School of Materials Science and Engineering, Boise State University, Boise, ID, USA

[c] Department of Physics and Astronomy, The University of Texas at San Antonio, San Antonio, TX, USA

[d] Center for Advanced Energy Studies, Idaho Falls, ID, USA

Author Contributions

Jennifer K. Watkins: Conceptualization, Investigation, Writing – Original Draft, Review and Editing

Adrian Gonzales: Investigation, Writing – Original Draft, Review and Editing

Adrian R. Wagner: Investigation, Resources, Supervision, Writing – Original Draft, Review and Editing

Elizabeth S. Sooby: Conceptualization, Resources, Supervision, Writing - Review and Editing

Brian J. Jaques: Conceptualization, Resources, Supervision, Writing - Review and Editing

Abstract

The challenges and opportunities to alloyed and composite fuel architectures designed and intended to mitigate oxidation of the fuel during a cladding breech of a water-cooled reactor are discussed in three review manuscripts developed in parallel, with the presented article focused on the oxidation performance of uranium mononitride. Several high uranium density fuels are under consideration for deployment as accident tolerant and/or advanced technology nuclear reactor fuels, including one on each: UN, U_3Si_2, UC and UB_2. Presented here is the research motivation for the incorporation of additives, dopants, or composite fuel architectures to improve the oxidation/corrosion behavior of high uranium density nuclear fuels for use in LWRs. Furthermore, this review covers the literature on the degradation modes, thermodynamics, and oxidation performance of pure UN and UN-compounds as well as reported alloyed and composite architectures.

Contents

1. Introduction

The 2011 earthquake and resulting tsunami that damaged the Fukushima Daiichi Nuclear Power Plant in Japan, prompted an increase in the development of fuels and claddings with enhanced accident tolerance [1]. Although decades of research have gone into the current benchmark uranium dioxide fuel/zirconium alloy cladding, continued deployment of advanced technologies to improve economic and safe operation have pushed the existing light water reactor (LWR) fuel technology near its inherent performance limits [1]. Investments in the current reactor fleet and new reactor technologies must include research and development into advanced nuclear fuels that can adapt to extreme conditions while remaining thermodynamically and mechanically stable. These advanced fuels need to maintain or improve fuel performance during normal operations, operational transients, as well as design-basis, and beyond design-basis events [1-5].

This review, presented in multiple related publications, focuses on the review of available literature on high uranium density nuclear fuels and their composites: Uranium mononitride (UN), triuranium disilicide (U_3Si_2), and other high density fuels including uranium monocarbide (UC) & uranium diboride (UB_2). Each of which are investigated in the United States (U.S.), and internationally, as alternatives to the benchmark uranium dioxide (UO_2) fuel. Industry and utility partners are motivated to advance high uranium density fuel technology, as the increase in fuel economy, in addition to the added safety margins enabled by the high thermal conductivity of these fuels, is attractive. However, for each of these fuel forms, there are two known challenges that must be addressed: First is fabrication as each of these are air sensitive fuel forms, and second is oxidation in water containing atmospheres. As fundamental research on these fuel forms has progressed over the last decade, it has been shown experimentally that these advanced technology fuels exhibit superior thermophysical properties compared to UO_2 [6-9]. Both U_3Si_2 and UN have also exhibited favorable irradiation performance, albeit at low temperatures (<250 °C) and low burnup for U_3Si_2 [6], while data on UN is limited to fast reactor applications [10, 11]. Accordingly, research interest has significantly increased for a drop-in replacement for UO_2. However, hand-in-hand with thermophysical and irradiation performance data, accident testing of these ATF (accident tolerant fuel) concepts has proven them, particularly UN and U_3Si_2 with less data available for UC and UB_2, to be highly susceptible to degradation and pulverization in simulated LWR off-normal conditions; namely, exposure to pressurized water and high temperature steam environments characteristic of a cladding breach during normal operation or loss of coolant accident [12-15].

This review will cover the research motivation (in this uranium mononitride review publication), and materials and techniques (in the uranium silicide review publication) for the incorporation of additives, dopants, or composite fuel architectures to improve the oxidation/corrosion behavior of high uranium density nuclear fuels for use in LWRs. It should be noted that while this review is intended to highlight the seminal literature on high uranium density nuclear fuels, it may not be fully exhaustive and it also does not specifically focus on synthesis and fabrication methods; although, they are briefly discussed due to their influence on fuel behavior and performance, particularly with respect to the impact of microstructure and presence of contaminant phases. The various methods for advanced fuel fabrication have been detailed in other recent publications [16, 17]. This review article also does not include literature discussing the use of

these fuel compounds, particularly UN and UC, in tristructural-isotropic particle (TRISO) fuels as direct exposure of the fuel to coolant and impurities is not an issue due to the inherent protection provided by fuel encapsulation.

2. Motivation for the implementation of high uranium density fuels

Compared to the benchmark, UO_2, each of the ATF candidates reviewed here, UN, UC, UB_2, and U_3Si_2 have higher uranium densities and higher thermal conductivities, as well as maintaining relatively high melting temperatures (see Table 1). In addition, the nitride and silicide fuels have shown acceptable performance under irradiation [7-9, 18-20]. The screening process for high density LWR fuel candidates includes those in which the uranium density exceeds that of UO_2 and includes a sufficiently high melting temperature which exceed the melting point of other core components [21].

Table 1: Material properties of ATF concept fuels

Material Properties	**UO_2**	**U_3Si_2**	**UB_2**	**UC**	**UN**
Uranium density (g-U/cm^3)[7, 22, 23]	9.7	11.3	11.7	13	13.5
Thermal conductivity (W/m·K at 300 °C)[24-28]	6.5 (95% TD)	14.7 (98% TD)	16.6 (80% TD)	20.4 (570°C, 99% TD)	16.6 (95% TD)
Melting temperature (°C)[7, 29-31]	2840	1665	2385	2525	2847

The United States Department of Energy defined accident tolerant fuels as those that can tolerate loss of active cooling in the reactor core for a considerably longer time period (increased coping time) than the benchmark UO_2-Zircaloy system [4]. The important considerations that need to be addressed for ATFs are highlighted in green and summarized in Figure 1. The ATF concepts discussed in this review do address the required improved fuel properties such as lower fuel center-line temperatures (due to their higher thermal conductivity) and an increased power to melt safety margin. The metrics for improved reaction kinetics with steam still need to be addressed and demonstrated by the ATF concepts discussed in this review; however, their use allows for the incorporation of advanced cladding structures which can provide additional safety margins with regards to steam reaction kinetics. Other considerations for these ATF concepts with regards to minimizing fuel-cladding interactions and retention of fission products also needs to be addressed.

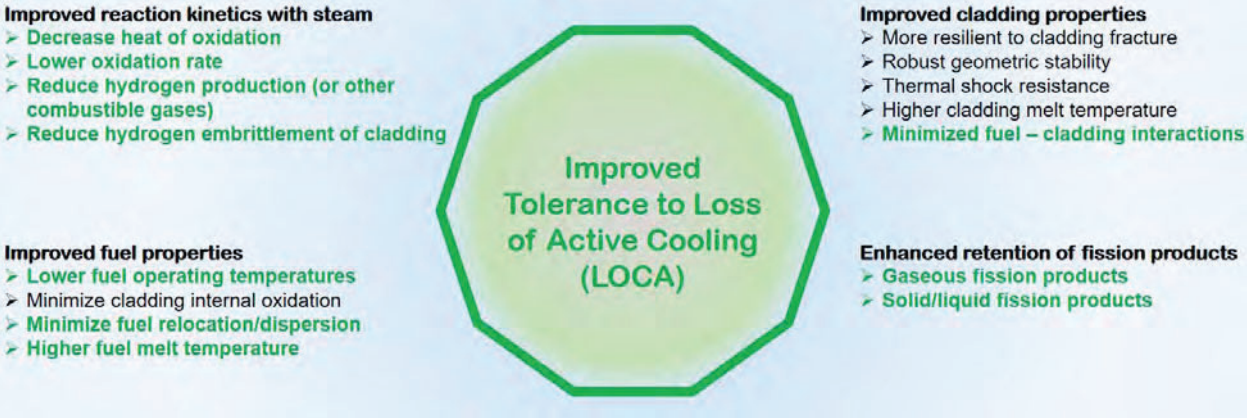

Figure 1: Primary attributes of accident tolerant fuels associated with fuel behavior and cladding at high temperatures. Modified from Carmack [32].

Implementation of UN, U_3Si_2, UC, or UB_2 will improve nuclear fuel performance by enabling higher burn-up, leading to lower waste volumes and longer cycle lengths [7, 15, 33]. Increased power up-rates are possible due to the increased power density these ATFs provide because of the increased uranium loading. These ATF materials can provide better performance in extreme temperatures due to their higher thermal conductivities, which reduce the stored energy in the core, mitigate high thermal gradients across fuel pellets, and increase the rate of heat transfer to the cladding during temperature transients. These thermal transport benefits result in reduced fuel failures and more efficient plant operation [7, 15, 33]. The four high uranium density candidates discussed in this review are grouped in the middle of Figure 2 as meeting these initial selection criteria.

The uranium mononitride part of this review (this publication) presents the background and motivation for the investigation of alloyed or composite high density fuel architectures. In addition, this review focuses on the performance of UN and UN-composites in oxygen and water containing atmospheres, whereas the uranium silicide part of the review introduces the various approaches to mitigating the water reaction and presents the current understanding of the performance of U_3Si_2 and the alloys and composites investigated to date. Lastly, the part of the review on UB_2 and UC will summarize the state of knowledge on alloyed and composite architectures and present the current literature on lesser studied fuels, UC and UB_2.

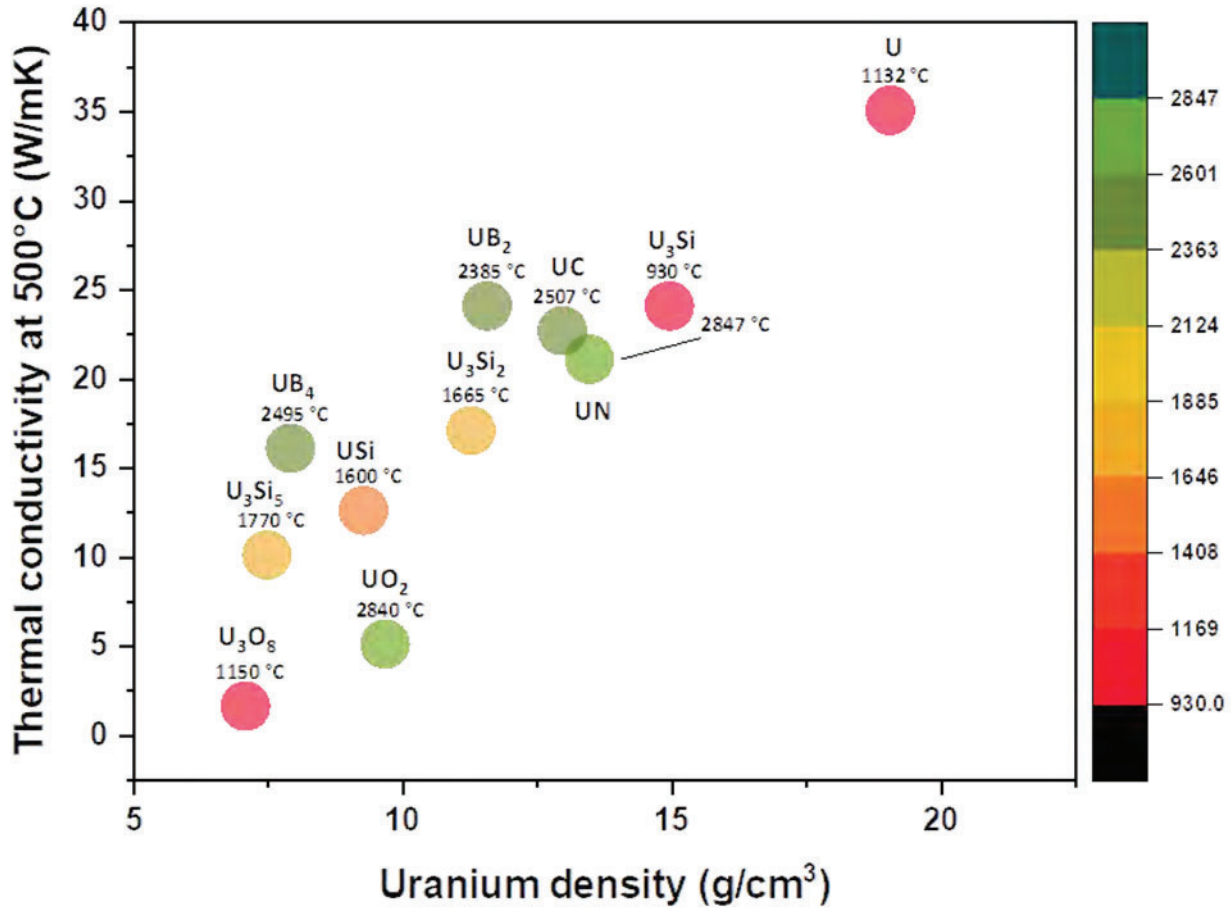

Figure 2: Thermal conductivity vs. uranium density and color mapped to melting temperature. The four high uranium density candidates discussed throughout these reviews (UN, U_3Si_2, and UB_2/UC) are grouped in the center of the plot.

3. Uranium Mononitride (UN)

Uranium mononitride fuels have been proposed, researched, and demonstrated for space power reactors and liquid metal fast breeder reactors because of their previously mentioned desirable properties [34, 35]. The following sections of the report present a review of publicly available literature on the current status of UN research; specifically related to the performance of UN and UN-composites in oxygen and water containing atmospheres. The low oxidation and corrosion resistance of the nitride fuel is a major concern for deployment into existing and advanced LWRs [36, 37]. The literature on UN's stability under oxidation and hydrothermal corrosion conditions is limited; moreover, it is evident that UN corrodes when exposed to oxygen, water, and steam environments Accordingly, the succeeding sections present a review of literature, which is organized into the common bulk UN synthesis methods, oxidation and corrosion testing of pure UN, reports on the introduction of additives and dopants into the UN matrix in attempts to mitigate corrosion behavior, and the effects of impurities and secondary phases in UN. It should be noted that in an attempt to include the applicable data on publicly available literature for UN, the following sections do include references to issued patents and graduate theses, which should

be viewed in light of the fact that they may not have undergone the same extensive peer-review processes as journal publications.

3.1 Synthesis Methods

Typically, UN feedstock is synthesized via two primary methods: metal hydride-dehydride-nitride (HDN) or carbothermic reduction and nitridization (CTR-N) [38]. The CTR-N method holds benefits over the HDN method in that it is easier to obtain, handle, and transport the UO_2 feedstock (starting materials) than that of the powdered elemental uranium feedstock necessary for HDN. In addition to safety and economic concerns associated with handling the finely divided UN powder achieved through the HDN route, CTR-N is the favored synthesis route due to the fact that it can utilize the existing conversion processes and infrastructure for current oxide fuel fabrication [38]. Bragg-Sitton *et al.* noted in design constraints for ATF concepts, that a new fuel concept must be backwards compatible with existing fuel handling equipment, fuel rod or assembly geometry, and coresident fuel in existing LWRs [39]. This constraint, along with the fact that CTR-N has been used and optimized for decades, makes the CTR-N method the most likely to be implemented for commercial scale-up production [16]. Although favored, the CTR-N method typically results in higher carbon and oxygen impurity levels in the starting powder, which must also be addressed prior to implementation. It is worth noting that the sol-gel method has also been successfully demonstrated for UN production, typically related to UN microspheres for fabrication of TRISO fuel [40], but it has not been commonly used for fabricating bulk UN and UN composites. To produce nuclear fuel relevant geometries, compact fabrication has been achieved by traditional cold pressing and sintering, hot isostatic pressing (HIP), and field assisted sintering, e.g. spark plasma sintering (SPS) methods. All these methods for synthesis and fabrication have been demonstrated in the literature [15, 16, 18, 34, 41-45].

The incorporation of dopants or secondary phases can be achieved through traditional powder metallurgy processes followed by any of the previously mentioned sintering methods; however, the sintering method and parameters must be tailored to each additive to avoid formation of unwanted phases or precipitates [14, 44]. Secondary phases and dissociation can be detrimental to fuel performance due to liquid phase formation and swelling, leading to fuel failure. Accordingly, it is important to understand that the activity of uranium is a function of partial pressure of nitrogen and oxygen as well as the presence of any alloying agent(s). As seen in the uranium-nitrogen binary phase diagram (Figure 3), stoichiometric UN has a narrow phase field and is known to be relatively unstable, either dissociating to form a liquid uranium phase or forming hyper-stoichiometric UN_2 and U_2N_3. Additionally, both Tennery and Matzke reported that UN is sensitive to decomposition at higher temperatures and low nitrogen partial pressures, and forms U_2N_3 at lower temperatures and higher N_2 partial pressures (see Figure 4) [46, 47]. This thermodynamic instability presents challenges for both synthesis and fabrication of UN and UN-composites. The phase field for stoichiometric UN can be widened above approximately 1200 °C if a sufficient nitrogen partial pressure is maintained, but at lower temperatures, only very low N_2 partial pressures will prevent formation of the U_2N_3 phase.

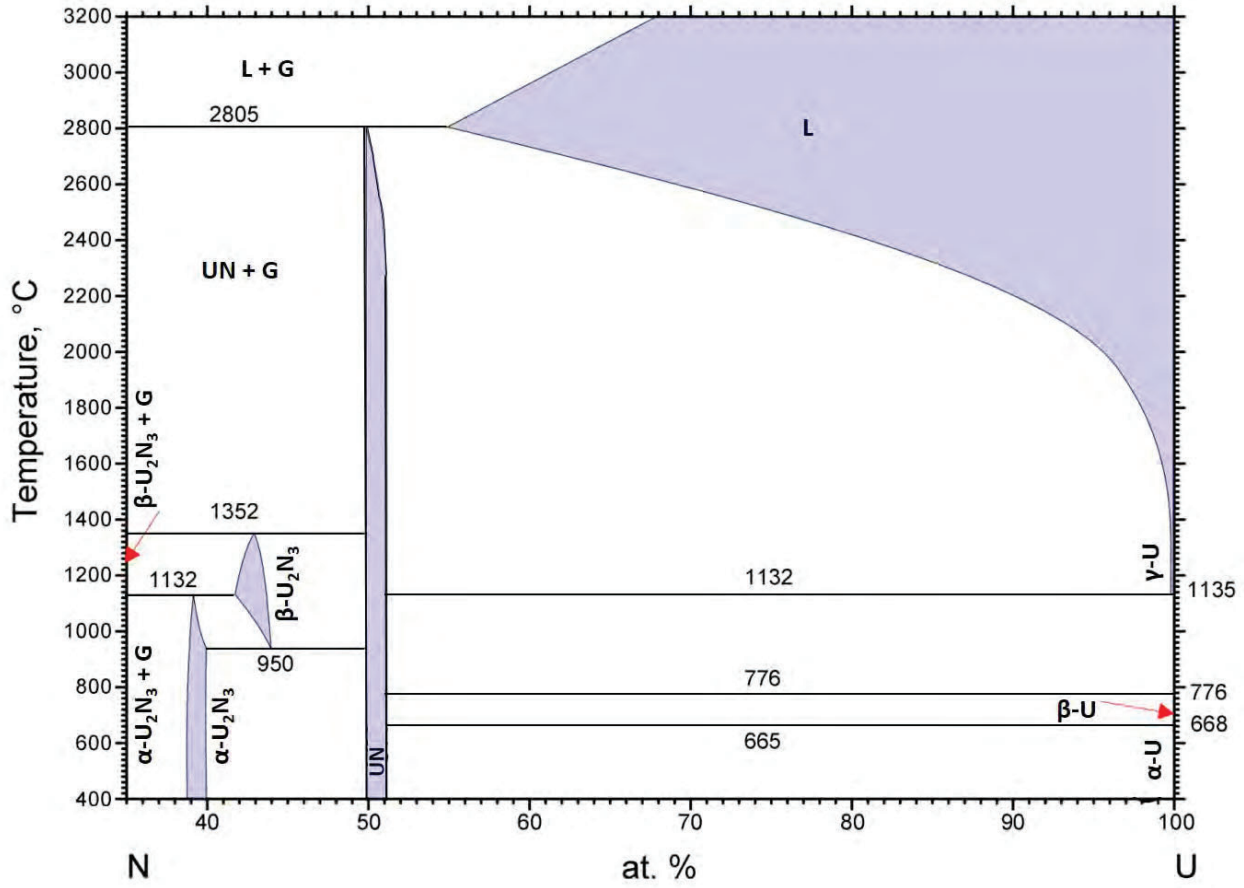

Figure 3: Uranium-nitrogen phase diagram (35-100 at% U, 400-3200 °C) Modified from Okamoto [48].

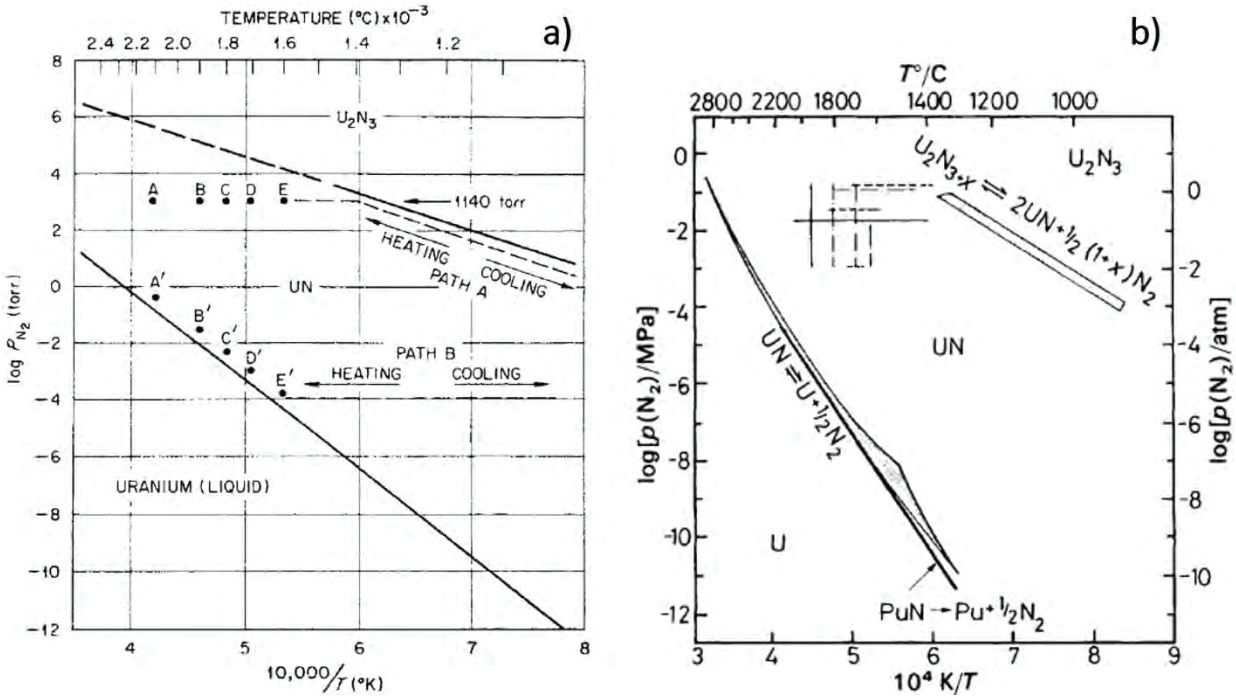

Figure 4: UN dissociation and U_2N_3 formation as a function of temperature and nitrogen partial pressures, a) From Tennery [46], and b) from Matzke [47].

It is important to note, however, that regardless of synthesis method or additives into the nuclear fuel forms, a fundamental challenge is presented when considering nitrogen in a nuclear reactor. It is understood that nitrogen in any fuel concept would need to be isotopically enriched from ^{14}N to ^{15}N to avoid significant ^{14}C production through the $^{14}N(n,p)^{14}C$ reaction (enrichment will lead to a 2 order of magnitude decrease in ^{14}C production [7]). Accordingly, Wallenius *et al.* investigated the influence of nitrogen enrichment on neutronics, cost, and ^{14}C production for different closed fuel cycle scenarios for fast reactors and accelerator driven systems [49]. It was determined a ^{15}N enrichment level of 99% was necessary to achieve the same amount of ^{14}C as with an oxide loaded core. The increased fuel fabrication cost was estimated at > 25%, albeit that increase dropped to 5-10% if reprocessing and a closed gas cycle was utilized [49]. As previously stated, nitrogen enrichment concerns must be considered regardless of the proposed UN synthesis method. However, some of the challenges are mitigated through the use of a closed gas cycle (e.g. when using CTR-N or HDN synthesis techniques) and recovery during UN synthesis, sintering, and reprocessing [49, 50]. Although not a specific focus of this review, the complications arising from the need for nitrogen enrichment in UN highlights an additional area of research in UN synthesis and reprocessing that must be pursued prior to deployment. An additional advantage to enriching the nitrogen in UN is the decrease in the thermal neutron cross section, as shown in Table 2.

Table 2: Thermal neutron cross-sections for ^{14}N and ^{15}N for the (n,p), (n, γ), and (n, e) reactions [51].

Isotope	(n,p) [b]	(n, γ) [b]	(n, e) [b]

^{14}N	1.86 ± 0.03	80.1E-3 ± 0.6E-3	10.02 ± 0.12
^{15}N	-	2.4E-5 ± 8E-6	4.59 0.05

3.2 Oxidation/corrosion testing of UN

3.2.1 Air oxidation of UN

Much of the literature that exists on the oxidation and corrosion behavior of UN was published in between the 1960's and 1990's as the fuel was being investigated for space power applications, radioisotope thermoelectric generators, LWRs, and HWRs. A summary of UN oxidation studies is presented in Table 3 and provides information (if provided within the reference) on synthesis and sintering methods, the type of sample oxidized (e.g. powder, compact, etc.), temperature testing range, test conditions, onset temperature, sample phase composition, grain size, and reaction products. Studies of the oxidation behavior of UN, including single crystal, polycrystalline, powder, and monolithic samples have been investigated in air, oxygen, CO_2, and NO_x atmospheres with varying results [36, 37, 52-59]. The onset of breakaway oxidation for UN has been reported from 200-340 °C with powder samples underperforming monolithic samples, which typically result in severe degradation or pulverization above 300 °C. Also, it has been observed that denser samples exhibit increased oxidation resistance, which is likely due to a lower surface area to volume ratio in higher density samples. Only general conclusions can be drawn as testing parameters for air oxidation of UN vary in the literature with regards to fabrication methods, sample configuration, partial pressures of oxygen (if reported) and temperatures. Results in the literature vary for the oxidation products identified under the various testing parameters, but generally included UO_2, U_2N_3, UO_3, and U_3O_8. In many cases, it was noted that either a U_2N_3 phase or an intermediate phase was "sandwiched" between the bulk UN and a surface UO_2 [36, 37, 52-61]. This was validated in a fundamental study by Sole *et al*. who observed oxidation products of U_2N_{3+x} and UO_2 via TEM diffraction patterns of UN foils heated for 2 minutes at 600 °C (O_2 partial pressure not given) [53]. The bulk of the publications on oxidation behavior of pure UN describe the oxidation behavior and provide kinetics data which indicate, as expected, increased reaction rate constants and mass gains with increased temperatures and durations.

The presence of images and micrographs of the evolution of UN oxidized in air or O_2 is limited in literature. However, a recent study has provided microstructural images of as-fabricated UN microspheres and SPS sintered UN microsphere samples oxidized in synthetic air up to 700 °C (Figure 5). The researchers stated the general behavior followed a successive oxidation path as denoted by Equations 1-2 (ΔH_{rxn} and ΔG_{rxn} values calculated using HSC Chemistry 9 [62]), resulting in a final oxidation product of U_3O_8. The ΔG_{rxn} is indicative of the thermodynamic likelihood the reaction will occur, but the ΔH_{rxn} is important to consider as the heat generated during the reaction can have a large impact on the reaction behavior, especially during an accident scenario. Adsorption of oxygen on the external surface, inside the open porosity as well as an external interface reaction allowed oxide diffusion towards the UN. Oxidation along grain boundaries also produced stresses causing intergranular cracking and spallation [63]. The intermediate step for formation of U_2N_3 and UO_2 is shown in Equation 3. Different results were

reported by Dell *et al*. for UN powders oxidized in 0.07 MPa oxygen, stating that the powders ignited at 290 °C and that the final product was UO_3, not UO_2 or U_3O_8 [37, 64]. Dell further studied these UN powders under oxidation at 260 °C, finding that after 1-2 days, both UO_2 and α-U_2N_3 were identified via X-ray diffraction. Another study oxidized UN microspheres at 6.6 kPa O_2 resulting in an oxidation onset of 217 °C and U_3O_8 containing dissolved nitrogen as the reaction product [56].

	ΔH_{rxn}	ΔG_{rxn}	
$\frac{3}{4}UN + O_2 \rightarrow \frac{1}{4}U_3O_8 + \frac{3}{8}N_2$	-673 kJ/mol$_{O_2}$	-643 kJ/mol$_{O_2}$	Eq(1)
$\frac{3}{8}U_2N_3 + O_2 \rightarrow \frac{1}{4}U_3O_8 + \frac{9}{16}N_2$	-608 kJ/mol$_{O_2}$	-588 kJ/ mol$_{O_2}$	Eq(2)
$3UN + O_2 \rightarrow U_2N_3 + UO_2$	-963 kJ/mol$_{O_2}$	-907 kJ/ mol$_{O_2}$	Eq(3)

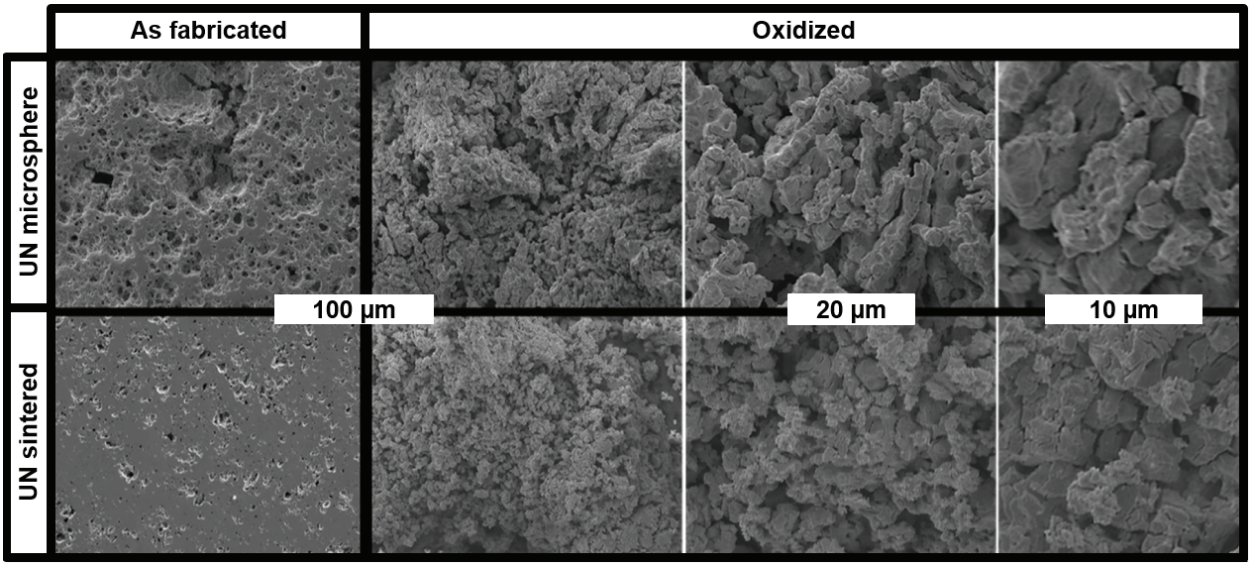

Figure 5: As-fabricated and SPS sintered UN microspheres (left column) and resulting microstructure (right columns) after oxidation in synthetic air up to 700 °C. Modified from Costa *et al*. [63].

In an attempt to better understand the mechanism of the oxidation of a UN surface, Dell *et al.* studied the oxidation of single crystal UN [37]. Accordingly, the (421) face of a UN crystal was oxidized in flowing oxygen at 400 °C for 10 and 30 minutes. The authors describe "track" formation in the early stages of oxidation and a general surface roughening; however, as the surface oxide thickened, a "blistering" was observed (Figure 6). This blistering effect can be attributed to nitrogen bubbles forming beneath the film. As the oxide thickened the surface detail was still retained leading the authors to postulate that the mechanism was oxygen diffusion inward rather than outward diffusion of uranium. Nitrogen atoms are released as gas through the

oxide layer, while other nitrogen atoms partially dissolve into the lattice at the nitride interface, resulting in the aforementioned "sandwich" structure [37].

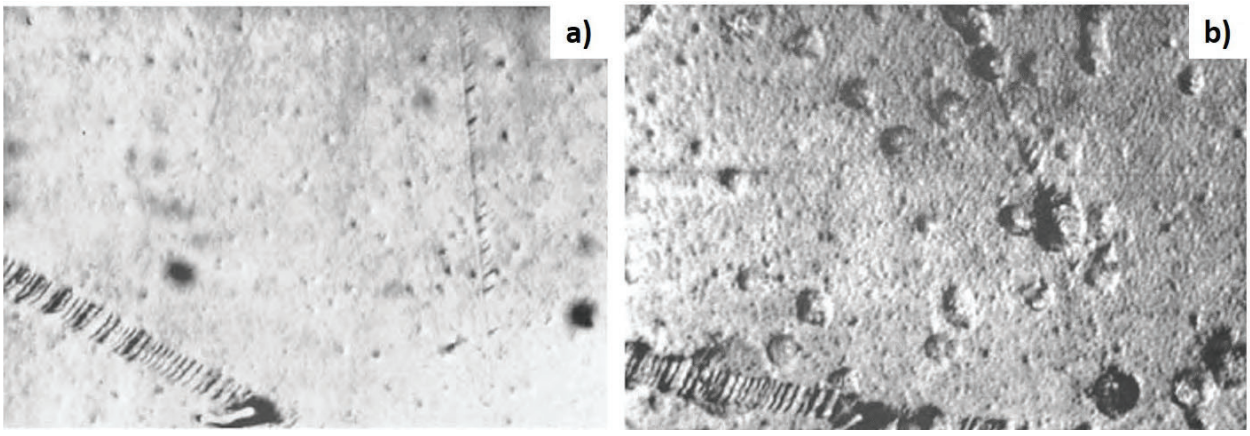

Figure 6: Images at 500X magnification of UN single crystal samples, (421) crystal faces, oxidized in flowing oxygen for a) 10 minutes, and b) 30 minutes. From Dell *et al*. [37].

While the above results for UN powders, microspheres, and single crystals do provide insight to the oxidation behavior of UN, oxidation studies on monolithic, polycrystalline samples are more relevant to samples in a LWR condition. Oxidation kinetics of UN polycrystalline samples (hypo-, stoichiometric, and hyper-), fabricated by powder metallurgy followed by hot isostatic pressing and by arc-melting were analyzed during oxidation in air and O_2 at 1 atm and 300-700 °C [36]. These oxidized samples ultimately formed U_3O_8 as the corrosion product and displayed linear reaction kinetics with the rate constant increasing with temperature, similar to other work by Ohmichi where the oxidation reaction activation energy of 124 kJ/mol was identified [36, 65]. Similar work oxidizing UN compacts (via HDN and conventionally sintered in 2.5 atm N_2) showed oxidation begins at 200 °C forming both U_2N_3 and an oxynitride. Rapid oxidation starts at 250 °C along with N_2 release and UO_3 is formed, ultimately forming U_3O_8 at 400 °C [52]. Other oxidation experiments on UN compacts (via HDN) in air and oxygen indicated the rate of oxidation in O_2 (onset 320 °C) was approximately 5x that in air (onset 348 °C) [55].

Despite the limited amount of literature available, UN powder synthesized via the HDN process and then subsequently arc-melted or conventionally sintered, or samples fabricated through arc-melting and SPS appear to provide an increased oxidation onset temperature [36, 37, 52, 53, 55, 58]. The increased resistance in these samples is attributed to a higher sintered density and reduced open porosity that is more easily achievable using SPS and arc melting. Samples fabricated through the sol-gel method (both microspheres and sintered compacts) reported the lowest onset temperatures in the available literature [56, 57]. The majority of samples tested in air were for pure UN, suggesting that air oxidation studies on UN-composites may be an area of research interest.

Table 3: Summary of air oxidation UN and UN with additives or composites.

	Ref.	Synthesis method	Sintering method	Type	Temp. test range [°C]	Test conditions	Onset temp. [°C]	Composition	Grain Size [μm]	Reaction products
Air/Oxygen	[36]	HDN/arc-melting	HIP	Single crystal, polycrystalline compacts	300-700	Isothermal	-	UN	n/a	U_3O_8
	[37, 64]	HDN	n/a	Powder	230-290	Isothermal	250 (powder ignited at 290)	UN	n/a	UO_3 with intermediates of UO_2, U_2N_3, and UO_3N_x
	[37]	Arc-melting	n/a	Single crystal	280-500	Isothermal	n/a	UN	n/a	U_2N_3, UO_2
	[52]	HDN	Conventional	Powder, compact	Up to 900	Ramped, 0.85°C/min and 0.4°C/min	250 (powder), 340 (compact)	UN	n/a	U_3O_8 with intermediates of U_2N_3, UO_2, and UO_3
	[53]	Arc-melting	n/a	Single crystal foil	Up to 800	Ramped	-	[a]UN	n/a	U_2N_{3+x}, UO_2
	[55]	HDN	n/a	Compact	325-450	Ramped, 2.5°C/min	320-348	UN	n/a	U_3O_8
	[56]	Sol-gel	n/a	Microspheres	Up to 927	Ramped, 4°C/min	217	UN	n/a	U_3O_8 with intermediates of U_2N_3, UO_2
	[56]	Sol-gel	n/a	Microspheres	Up to 927	Ramped, 4°C/min	212 (15mol%), [b]172 (30 mol%)	(U,Ce)N (15 and 30 mol% Ce)	n/a	U_2N_3 and MO_{2+x}(15 mol%); M_3O_8 and MO_{2+x} (30 mol%)
	[57]	Sol-gel	Conventional	Compact	25-767	Ramped, 3°C/min	202 (air), 232 (8% O_2), 257 (20% O_2)	UN	n/a	U_3O_8 with intermediates of U_2N_3, and UO_2
	[58]	HDN (UN), Arc-melting (U_3Si_2)	SPS	Compact fragments	Up to 800	Ramped, 5°C/min	320 (UN), 450 (UN+U_3Si_2)	UN, UN+10v% U_3Si_2	6-9.1 (UN), 80 (UN+ 10v% U_3Si_2)	U_3O_8 (UN)
	[59]	n/a	n/a	Pellet	Up to 452	Ramped, 10°C/min	307	[c]UN	n/a	U_3O_8 with intermediates of U_2N_3, and UO_2
	[63]	Sol-gel	SPS	UN microspheres and Pellet fragments	Up to 700	Ramped, 5°C/min	260 (UN microspheres), 283-320 (UO_2+UN)	UN microsphere, [d]UO_2+(10,30,50)UN	3.1-9.5	U_3O_8
	[65]	n/a	n/a	Crushed sintered pellet	Up to 315	Ramped (1,3, and 5°C/min, and Isothermal	Below 300°C	UN	n/a	U_3O_8

[a] Starting material had adherent U_2N_{3+x} layer at beginning of testing and heating parameters were not listed, sample had oxidized after diffraction pattern taken at 600 °C; [b]Ignited; [c]Samples had "detectable" amounts of UO_2 in starting material; [d] Composite samples had U_2N_3 phase present in varying amounts (3.7-16.3 wt%) and sample with highest oxidation onset temperature was calculated to be 95 wt% UO_2/1.3 wt% UN/3.7 wt% U_2N_3.

3.2.2 Water Corrosion of UN

Results like that from the oxidation testing have been found with UN corroded in water-saturated air, steam, nitric acid, H_2O_2, and for samples submerged in water. Various reaction products identified under an assortment of testing parameters generally included UO_2, UO_3, U_3O_7, U_3O_8, U_2N_3, $UN_{1.7}$, UN_2, as well as oxynitride phases (see Table 4) [13, 14, 36, 54, 57, 60, 61, 66-69].

In most cases, like seen in the air oxidation studies, it was noted that the U_2N_3 phase was "sandwiched" between the bulk UN and surface UO_2 or identified as an intermediate. An example of this "sandwich-like" structure of a non-protective surface layer of UO_2 followed by U_2N_3, which covers the UN grain is shown in Figure 7 [69]. Figure 7a shows an area of degradation for the UN steam exposure sample (9 MPa, 300 °C, 30 minutes). The chemical analysis of the higher magnification area (Figure 7b) shows region 1 as only UN, but regions 2 and 3 (at the grain boundary triple junctions) were identified as lower density with increased oxygen content. This oxide formation was correlated to the separation of the grains from the matrix due to the stress caused by the secondary phase formation at the grain boundaries [69].

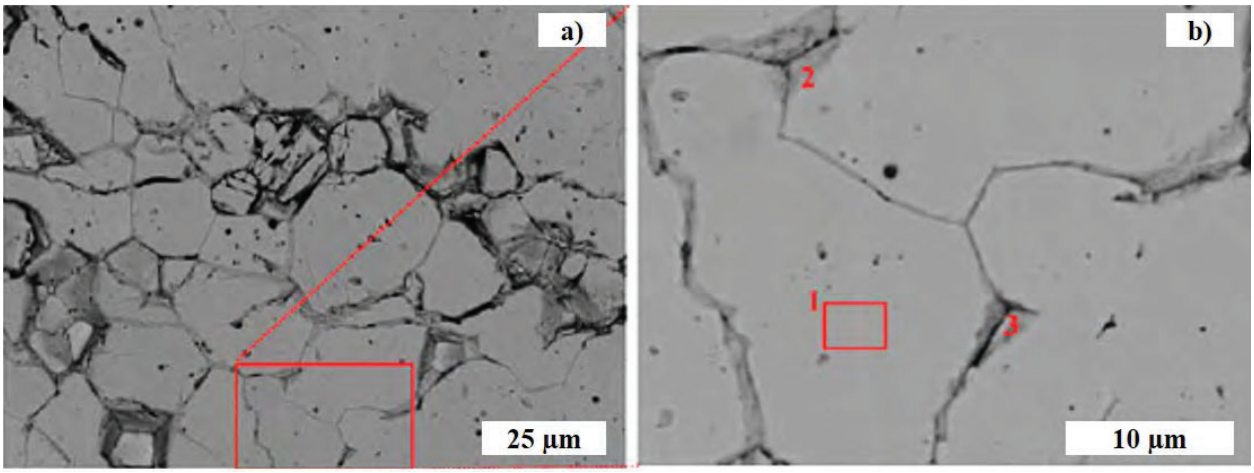

Figure 7: SEM micrographs of a) degraded microstructure of a UN pellet (98.25% TD) exposed to steam (9 MPa, 300 °C, 30 minutes) and b) higher magnification of the degraded region displaying "sandwich" structure of UO_2 with underlying nitride layer at the grain boundaries. Modified from Lopes *et al.* [69]

It is important to note that the formation of these intermediate phases creates a volume expansion and results in pulverization of monolithic samples. It is generally agreed that hydrolysis of UN occurs according to the following reactions [54, 61]:

	ΔH_{rxn}	ΔG_{rxn}	
$\frac{1}{2}UN + H_2O \rightarrow \frac{1}{2}UO_2 + \frac{1}{2}NH_3 + \frac{1}{4}H_2$	-132 kJ/mol$_{H_2O}$	-151 kJ/mol$_{H_2O}$	Eq(4)
$\frac{3}{2}UN + H_2O \rightarrow \frac{1}{2}UO_2 + \frac{1}{2}U_2N_3 + H_2$	-195 kJ/mol$_{H_2O}$	-215 kJ/ mol$_{H_2O}$	Eq(5)
$\frac{1}{4}U_2N_3 + H_2O \rightarrow \frac{1}{2}UO_2 + \frac{2}{3}NH_3 + \frac{1}{24}N_2$	-97.2 kJ/mol$_{H_2O}$	-117 kJ/ mol$_{H_2O}$	Eq(6)

The final oxidation product of UN under hydrolysis is UO_2, not the U_3O_8 seen during oxidation of UN. This is similar to the hydrothermal corrosion behavior of U_3Si_2 [70], UO_2 [71-74], and uranium metal [75].

The documentation of the microstructural evolution of UN in hydrothermal corrosion conditions is sparse in the open literature. Figure 8 is a compilation of available macro images for UN degradation under various hydrothermal corrosion conditions. Figure 8a (from UN feedstock via CTR-N) and b (from UN feedstock via HDN) show the degradation of conventionally sintered

UN pellets in static autoclave conditions at 300 °C for 48 hours and 30 minutes, respectively [13, 14]. Figure 8c and d show UN pellets sintered via SPS from HDN UN feedstock under steam corrosion at 340 °C for 105 minutes and 425 °C for 300 minutes [68]. Another high density UN sample (99.0% TD) sintered via SPS and subjected to static autoclave testing (time duration not listed) at 300 °C is shown in Figure 8e [76]. All samples show either complete pulverization to powder or fragments or cracking, spallation, and overall degradation of the monolithic samples.

Figure 8: UN degradation under hydrolysis; a) UN pellet following static autoclave testing in DI water at 300 °C/10 MPa for 48 hours (modified from Nelson *et al.*) [13], b) UN pellet after static auto testing at 300 °C/16 MPa for 30 minutes (modified from Watkins *et al.*) [14], c) UN after hydrolysis in steam at 340 °C for 105 minutes, d) UN after hydrolysis in steam at 425 °C for 300 minutes (modified from Jolkkonen *et al.*) [68], and e) UN after static autoclave corrosion at 300 °C, no time duration given (modified from Malkki) [76].

Examining the microstructural evolution of UN under corrosion conditions can help identify the reaction progression over various times and temperatures but to date, as previously stated, this information has been limited in literature. Figure 9, shows UN samples of approximately 92% TD (fabricated using HDN powder and conventional sintering) submerged in DI water for 30 minutes at ~16 MPa and temperatures of 250 °C, 275 °C, and 300 °C. UN sample degradation is noticeable at 250 °C with the edges of the right cylinders showing preferential attack. Grain boundary etching and eventual spallation increases with increasing time and temperature. While the post-corrosion results indicated the corroded samples were still primarily UN, the degradation behavior was attributed to the formation of secondary phases including hyper-stoichiometric UN, UO_2, and possibly an oxynitride phase. These results from Watkins *et al.* [14] correspond to the results reported by Jolkkonen *et al*. for UN samples of 96.6 and 97.7% TD fabricated via SPS with HDN powder [68].

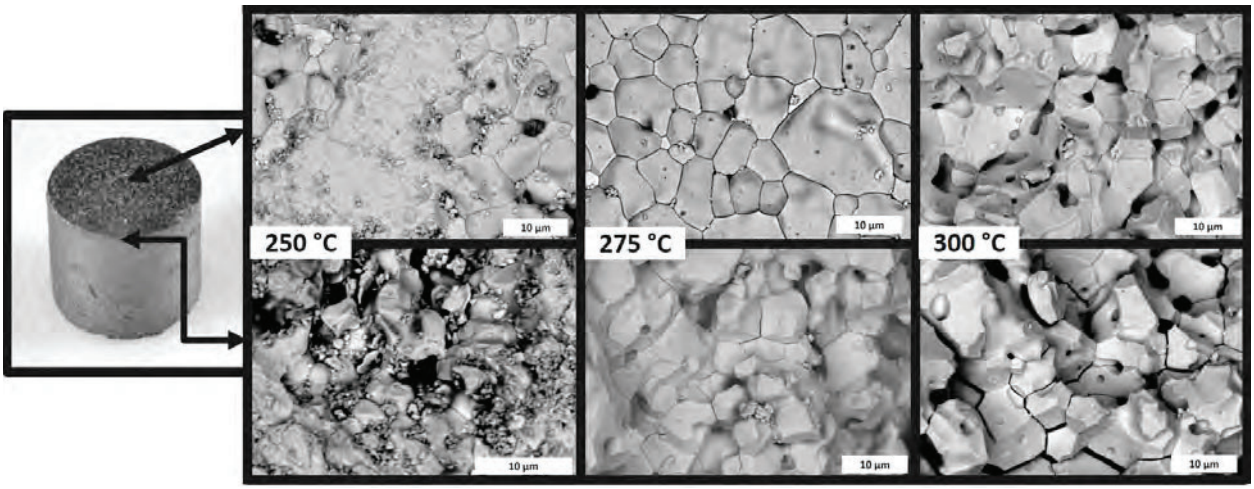

Figure 9: Backscattered electron micrographs of corroded UN pellets submerged in DI water for 30 minutes at 250 °C, 275 °C, and 300 °C and approximately 16 MPa. The top images were taken from the less corroded pellet surface while the bottom images show the preferential degradation from the pellet edges. Grain boundary etching and attack increases with temperature. From Watkins *et al.* [14].

Micrographs of UN microstructural degradation for 98.25% TD samples (fabricated with HDN powder and sintered via SPS) exposed to steam for 90 minutes at 300 °C and 9 MPa are seen in Figure 10 [69]. Similar to the above work seen in Figure 8b and Figure 9, some areas of the matrix are preserved but degraded regions display grain boundary etching causing weakening of the matrix.

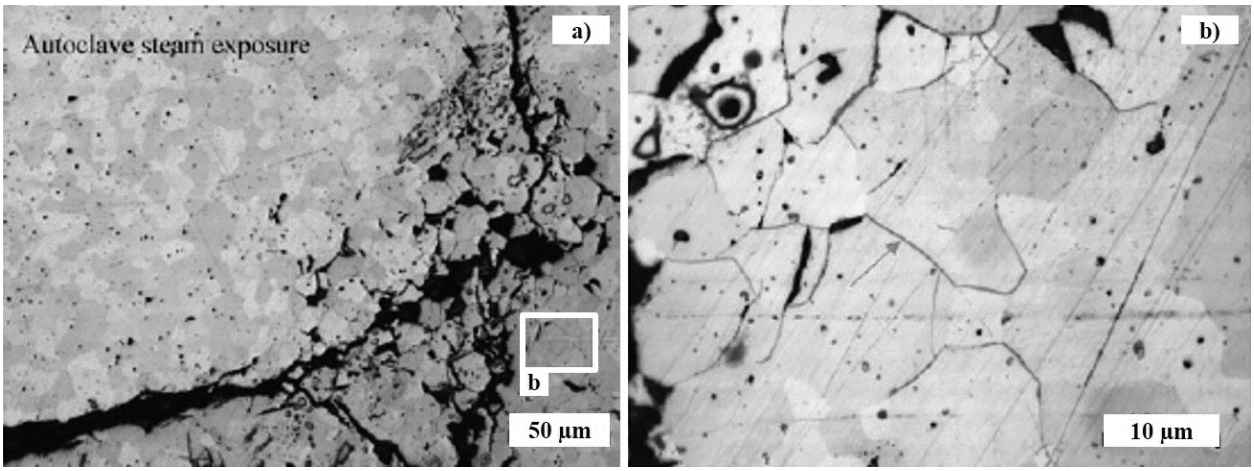

Figure 10: Optical micrographs of 98.25% TD UN exposed to steam at 9 MPa and 300 °C for 30 minutes. a) UN sample showing section where the matrix was preserved and other degraded regions and b) inset of a) displaying degraded region with grain boundary etching which causes weakening of the matrix. Modified from Lopes *et al*. [69].

No literature was found for monolithic UN samples subjected to corrosion in radiolysis conditions, such as would be expected for fuel exposed in a leaker/failed rod during reactor operation or during spent fuel storage. However, one study looked at the interaction of UN thin films exposed to 0.1 M H_2O_2 (a product of water radiolysis) at room temperature [77]. The results showed that a UN specimen (prepared via DC magnetron sputtering of a uranium target

and containing a small amount of U_2N_3 contamination) exposed to H_2O_2 for 50, 250, 1250, and 6000 seconds did oxidize to UO_2 and UO_{2+x}. The results also suggested UN had a lower corrosion rate in H_2O_2 as compared to a UO_2 sample tested under the same conditions [77]. These findings could suggest that UN may be more corrosion resistant in an accident scenario than previously believed and underscores the necessity for additional research for UN in radiolytic conditions.

While the differences in synthesis and sintering methods and variations in testing parameters make it difficult to provide definitive conclusions about UN in hydrolysis conditions, general observations can be made. Table 4 summarizes the available literature on UN and UN-composites under corrosion via water or steam. The summary includes (if available) the synthesis method for UN feedstock, sintering method, the physical form exposed to corrosion (i.e., powder, pellet, etc.), the temperature test range, test conditions, onset temperature, sample composition, grain size, and the resulting reaction products. Onset temperatures for UN and UN-composites tested in steam and water were generally < 200 °C for powder samples, between 200-300 °C for monolithic samples, and again, dense, high purity samples performed the best. Most of the available data is for pure UN samples, thus presenting a research opportunity for hydrothermal corrosion testing of UN-composites. Grain size was included in the table, even though most of the investigations did not report it. However, one of the studies which provided grain size data indicated samples having smaller grain size performed better due to increased mechanical stability and less susceptibility to intergranular cracking [69], highlighting that this is an important parameter to consider.

Table 4: Summary of water/steam corrosion of UN and UN with additives or composites.

	Ref.	Synthesis method	Sintering method	Type	Temp. test range [°C]	Test conditions	Onset temp. [°C]	Composition	Grain Size [μm]	Reaction products
Water/steam	[13]	CTR-N	Conventional	Pellet	300 (48 hr)	Static autoclave, ramped*	n/a	UN	15-25	UO_2
	[14]	HDN	Conventional	Pellet	250-350	Static autoclave, ramped, 1°C/min	250 (UN), 275-300 (UN-UO_2 composites)	UN, UN+5w% UO_2, UN+10w% UO_2	n/a	Hyper-stoichiometric UN, U-oxynitride, U_2N_3, and UO_2
	[36]	HDN/arc-melting	HIP	Single crystal, polycrystalline compacts	300-700	Isothermal	-	UN	n/a	U_3O_8 (H_2O sat. air), UO_2 (H_2O)
	[54]	n/a	n/a	Powder	100-400	Ramped, 5°C/min	250	UN	n/a	NH_3, H_2, U_2N_{3+x}, and UO_{2+y}
	[57]	Sol-gel	Conventional	Compact	25-767	Ramped, 3°C/min	~ 347	UN	n/a	UO_2 with U_2N_{3+x}
	[59]	n/a	n/a	Pellet	Up to 452, 30 min 13% water vapor	Ramped, 40°C/min	n/a	[a]UN	n/a	U_3O_8 with intermediates of U_2N_3, and UO_2
	[60]	n/a	Conventional	Compact	200-1000 (steam); 80-300 (water)	Ramped*	250	UN	n/a	UO_2, U_2N_3, NH_3

	[61]	Direct nitride of U metal	n/a	Powder	340-420	Isothermal	~ 300	UN	n/a	UO_2, U_2N_3, NH3, H_2,
	[61]	Direct nitride of U metal	Arc-melting	Single crystal	Up to 750	Ramped*	~ 400	UN	n/a	UO_2, U_2N_3
	[61]	Direct nitride of U metal	Arc-melting, Conventional	Powder, single crystal, pellet	210-300 (in high pressure, 80 atm)	Isothermal	180 (powder), 200 (pellet), 230 (single crystal)	UN	n/a	UO_2, U_2N_3
	[67]	n/a	n/a	Pellet	23 and 92	Static chamber, Ramped (for 92°C test*)	n/a	UN	n/a	UO_2 and NH_3
	[68]	HDN	SPS	Pellet	400-500	Isothermal	400	UN	n/a	UO_2, NH_3, H_2, U_2N_3, oxynitride
	[69]	HDN (UN), Arc-melting (U_3Si_2)	SPS	Pellet	300 (30-90 min)	Static autoclave, Ramped, 15°C/min	n/a	UN, UN+10w% U_3Si_2	6-24 (UN), 9 (UN+10w% U_3Si_2)	Oxide phase
	[76]	HDN	SPS	Pellet	150	Static autoclave, Ramped*	≤150	UN+30at%ZrN	n/a	n/a
	[78]	Sol-gel, CTR-N	Conventional	Pellet	Boiling water	n/a	[b]Intact after 5hr (UN-Cr), pulverized 10 min (UN-Ni), pulverized 5 min (UN-Al)	[b]UN+2.7w%Cr, UN+2.8w%Ni, UN+1.5w%Al	n/a	CrO_2, Cr_2O_3 (UN-Cr sample)
	[77]	DC magnetron sputtering	n/a	Thin film	0.1 M H_2O_2 at room temp	50, 250, 1250, 6000 seconds	n/a	[c]UN	10 nm	UO_2 and UO_{2+x}
	[*]no rate listed; [a] Samples had "detectable" amounts of UO_2 in starting material; [b] Material referred to as the UN-Cr sample noted as surviving 5 hours in boiling water was characterized prior to testing and identified as $UO_{2.11}$, with $UC_{0.18}N_{0.82}$ and CrO_2, material referred to as UN-Al sample was characterized prior to testing and identified as $UC_{0.5}N_{0.5}$, [c]Sample contained some U_2N_3 contamination									

4. Additives/Dopants to UN to mitigate oxidation behavior

A primary screening for suitable compounds or elements as a secondary addition to a UN fuel matrix includes oxidation resistance to LWR-relevant environments and temperatures. While many compounds could meet this challenge, the inclusion of a non-uranium bearing component to the UN fuel in excess of 28 vol% nullifies the advantages of UN over the benchmark UO_2 in terms of uranium density; this point is elaborated upon in the U_3Si_2 publication of this review series. Incorporation of a uranium-bearing compound to a UN matrix would ensure that the uranium density of the compound would always exceed that of UO_2. Research on combining UN with uranium silicide compounds, such as U_3Si_2, has been investigated, as until recently it was reported that U_3Si_2 was more resilient to oxidizing atmospheres [35, 79]. However, as reported by Wood *et al.*[12], U_3Si_2 is also susceptible to hydrothermal corrosion conditions resulting in an increase in research focusing on the addition of other compounds and alloying elements to UN that can hinder its corrosion behavior. The relevant literature related to UN alloys and composites is discussed, along with a thermodynamic assessment of the various systems. As previously mentioned, this review is not specifically focused on fabrication methods. The fabrication methods are discussed in terms of how synthesis and fabrication affect the

additive/dopant additions, resulting microstructures, subsequent phase compositions, and oxidation/corrosion performance. Few, if any of the studies discussed are fully optimized to explore the effects of time, temperature, and atmosphere on either fabrication or oxidation/corrosion conditions. This is a non-trivial issue and highlights the need for more robust, controlled experimentation conditions in both fabrication and corrosion testing.

As mentioned in Section 3.1 and shown in Figure 3, UN has a narrow phase field and is thermodynamically sensitive to decomposition, especially at higher temperatures and low partial pressures of nitrogen. To provide a better empirical observation of this phenomenon, the effect of sintering atmosphere on phase formation and microstructure was investigated by Jaques *et al.* with synthesis and sintering of UN-(5-10 wt%)UO_2 composites [44]. Pellets fabricated using UN feedstock (synthesized via the HDN method) were sintered in ultra-high purity Ar, Ar+1wt%N_2, and Ar+100 ppm N_2 to better understand how the nitrogen concentration affected secondary phase formation. Accordingly, sintering in pure argon at 1550 °C resulted in a "coring" effect, where UN dissociated, leading to an elemental liquid phase uranium along grain boundaries and an outer rim with enhanced densification (seen in Figure 11). The composites had UO_2 homogeneously distributed throughout, but with increased phase fractions of UO_2 and higher sintering temperatures, the structure coarsened and lowered the overall pellet density. This behavior is believed to be due to the favorable formation of oxygen stabilized nitrides or uranium oxynitrides [44].

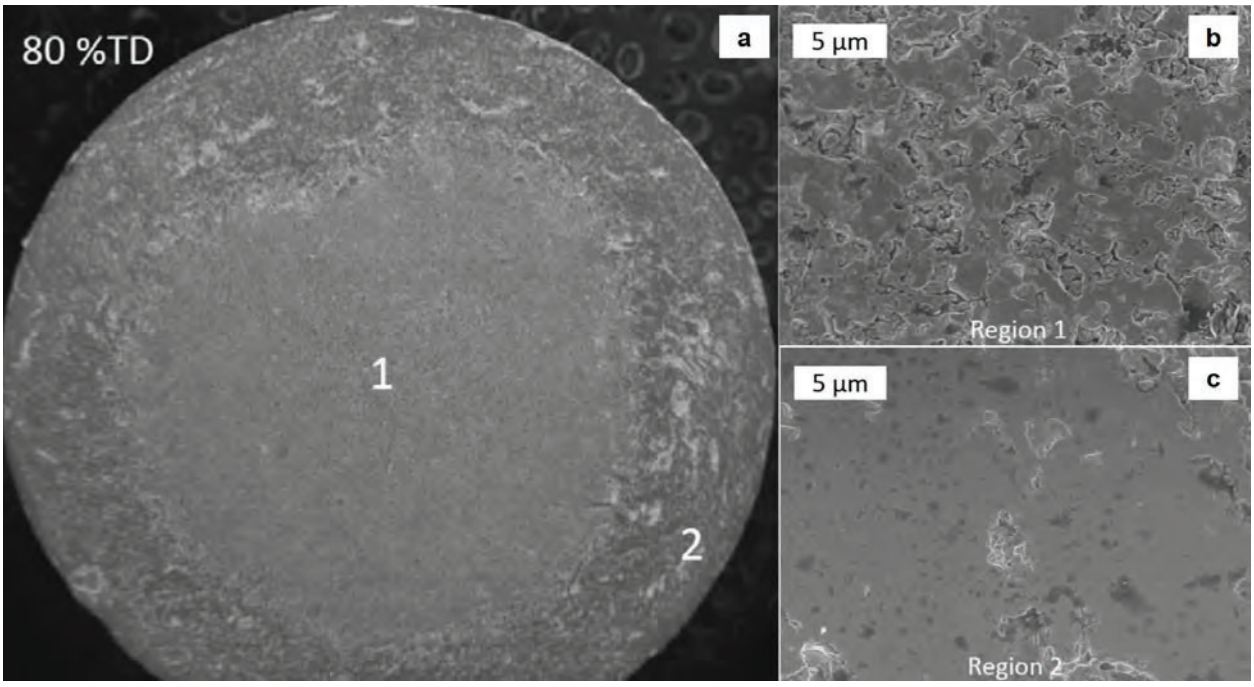

Figure 11: a) SEM micrograph of a UN pellet sintered in UHP-Ar at 1550 °C having an inner region of lower density and an outer rim with higher densification due to UN dissociation forming free elemental uranium resulting in liquid phase sintering, b) higher magnification of Region 1, and c) higher magnification of Region 2. Modified from Jaques *et al.* [44].

Work on another UN composite type to hinder UN dissociation was presented by Potter and Scott under a patent for a (U,Zr)N alloy consisting of single-phase UN containing dissolved Zr

(as ZrN) [80]. The invention describes nitriding uranium and < 10 wt% Zr to achieve a single-phase material, with 3-5 wt% being ideal for UN stabilization in preventing formation of higher uranium nitride phases, sintered in 1 atm of N_2 above 2200 °C. Potter and Scott compared the sintered pure UN samples and (U,Zr)N samples heated at 1600 °C under vacuum for 8 hours, followed by a 1700 °C dwell for an additional 8 hours. The results indicate UN dissociated and sintered to the tungsten plate used for sintering after only 1 hour at 1600 °C [80], a result which would be expected according to the above mentioned work of Tennery and Matzke (Figure 4) [46, 47]. The UN sample also showed extensive formation of free uranium, while the mass loss of the (U,Zr)N sample was 50% and 75% of the UN sample at 1600 °C and 1700 °C, respectively, and only had trace surface amounts of free uranium present [80]. These findings are similar to those of Watkins *et al.* who conventionally sintered UN (from CTR-N) composites of 10 wt% Zr in pure argon at 1500 °C [81]. In Figure 12, UN dissociation is evident in the highly porous structure having a phase identified as liquid uranium (region 1) and areas having U-N-Zr (region 2) and U-N-O-Zr (region 3). The inset in Figure 12a highlights a similar "coring" effect that was noted by Jaques *et al.*[44] due to UN dissociation, while Figure 12b and c show the extent and uniformity of the porosity and liquid uranium phase present in the monolithic pellet [81]. These results were confirmed in their XRD analysis showing shifted UN peaks (attributed to Zr incorporation in the UN lattice to form a ternary phase of unknown stoichiometry) and ZrO_2, as well as a small amount of U_2N_3. A similar result was seen in their fabrication of UN+10wt% Y samples sintered in argon [81].

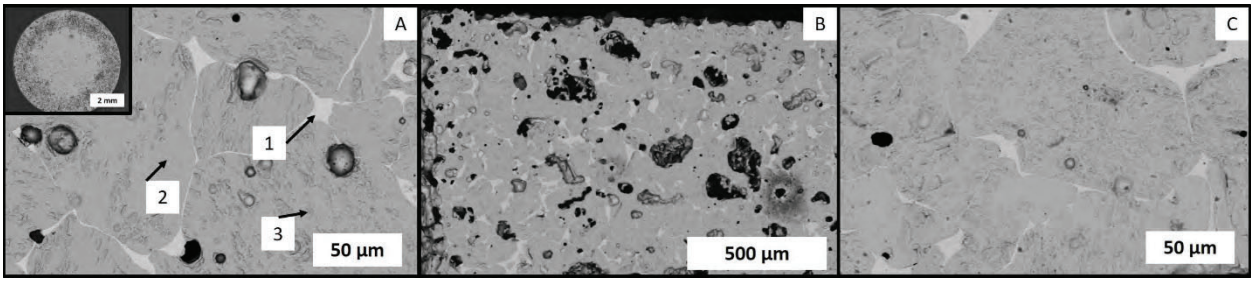

Figure 12: Backscatter electron micrographs of UN+10wt% Zr sintered in argon at 1500 °C. A) As-sintered microstructure showing formation of a liquid uranium phase at the grain boundaries indicating UN dissociation; inset is of the pellet surface showing the "coring" effect due to the UN dissociation, b) as-sintered microstructure highlighting the porous nature of the pellet and the uniformity of the liquid uranium phase, c) slightly higher magnification of the as-sintered microstructure showing the liquid uranium phase, and the phases identified as U-N-Zr and U-N-O-Zr. Modified from Watkins *et al*. [81].

This UN dissociation can be predicted through the use of an Ellingham diagram, which shows the relative thermodynamic stability of UN as compared to the nitride formation for potential additives (Figure 13) [82]. The importance of a diagram like this is that it provides a thermodynamic prediction of the most stable phases in relation to UN. Accordingly, if at any time during the processing of a fuel the free energy of formation (ΔG) of an additive nitride is lower than that of UN, it is thermodynamically favorable for the UN to dissociate (leaving elemental uranium) and form the nitride of the additive. Two examples of nitrides that are more favorable than UN are AlN below 600 °C and Si_3N_4 under approximately 800 °C (Figure 13).

This predicted thermodynamic stability of ZrN and TiN relative to UN was empirically validated by Potter and Watkins *et al.* [80, 81]

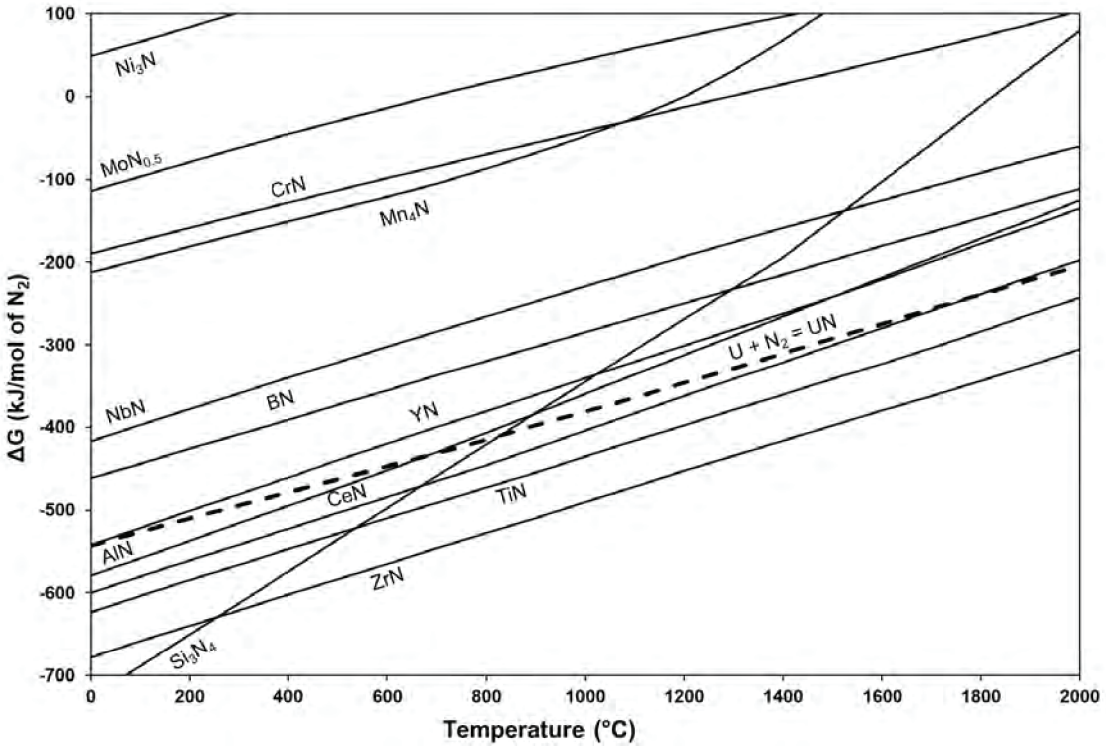

Figure 13: Ellingham-type diagram showing thermodynamic stability of nitride formation of various metallic elements considered for possible dopants into ATF concepts versus UN. Calculated using HSC Chemistry 9 [62].

In a follow-on study from that of Jaques *et al*. [44], UN-(5-10 wt%)UO_2 composites were examined for microstructural degradation under hydrothermal conditions [14]. Monolithic samples of approximately 92% TD were prepared using UN powder from a HDN method and commercially available UO_2. Green pellets were conventionally sintered in an Ar+100 ppm N_2 atmosphere. The sintered monoliths, along with pure UN and pure UO_2 samples as benchmarks, were submerged in DI water and heated to 250-350 °C and up to 16 MPa for 30 minutes [14]. As depicted in Figure 14a, the corrosion morphology of the pellets shows that reactions begin at the grain boundaries, resulting in grain boundary expansion and spallation. As the corrosion process advances with temperature, pellet degradation increases (as anticipated). The top surfaces of the composite pellets (top row of Figure 14) also exhibited an interesting phenomenon where an oxygen-rich phase (as identified with EDS) consumes the surface of the UN grains, suggesting that the oxide may be nucleating on the grains and propagating across the surface. This was not observed in the pure UN benchmark samples (Figure 9) [14]. The authors postulated that the UN reaction with water proceeds as a reaction layer and phase segregation occurs at the grain boundaries. The phase segregation results in the expansion of the intermediate layer leading to mechanical breakdown of the pellet. The researchers also noted in their batch study that the pellets fabricated with a higher starting oxygen impurity enhanced the degradation behavior [14]. Similar attempts at a solid solution of UN + (15,30at%) ZrN (~ 6.9,15.2 wt% ZrN) pellets was

attempted through SPS, but found both U-rich and Zr-rich regions post-sintering [76]. Figure 14b shows the fabricated microstructure of a UN+30at%ZrN pellet (approximately 91.3% TD) which had been heat treated in argon at 1400 °C for 4 hours after SPS. The brighter areas identified as the U-rich regions and the darker areas being Zr-rich. The sample was also subjected to autoclave testing in 3mL of DI water at 150 °C for 4 hours, and was already showing significant degradation as seen in Figure 14c. The authors postulated this degradation at 150 °C could have been enhanced by impurities introduced during the pre-corrosion heat treatment to improve the solid solution between the UN and ZrN. The corroded microstructure is shown in Figure 14d and the authors indicated there was possibly increased degradation due to carbon impurities (dark, pitted regions) that were introduced either from their uranium feedstock or through the SPS process from the graphite foil [76].

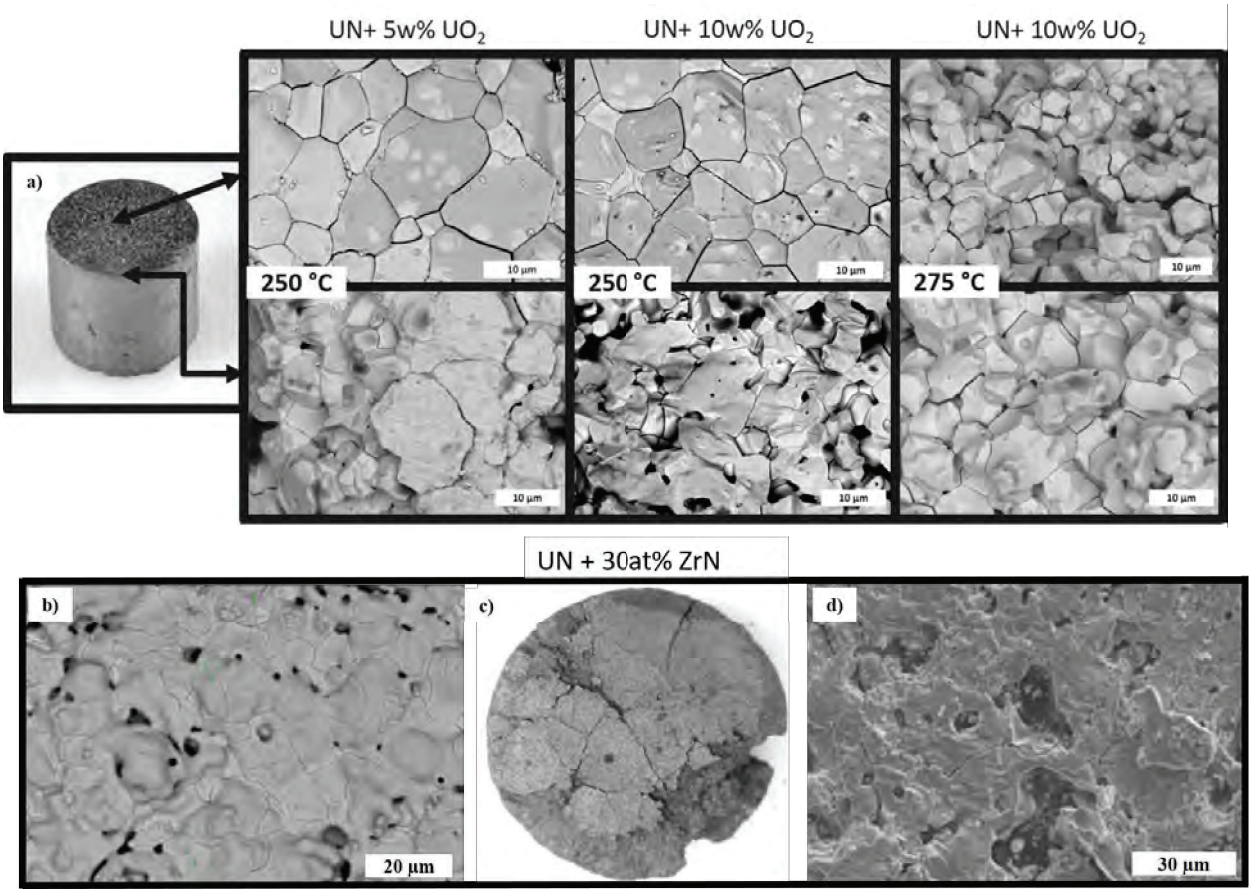

Figure 14: a) Representative optical image of UN+UO_2 pellet conventionally sintered and subjected to static autoclave testing, arrows point to the relevant areas where backscatter electron micrographs were taken of the corroded microstructure. The UN +(5-10 wt%) UO_2 samples corroded at 250 and 275 °C, show preferential edge and grain boundary attack. The pellets corroded at 250 °C also indicate clear light and dark phases present across the surface of the pellets, the dark phase being identified as an oxide phase via EDS (from Watkins *et al.*) [14]. b) SEM of sintered microstructure of a UN+30at% ZrN composite sintered via SPS and heat treated at 1400 °C for 4 hours in argon displaying U-rich (lighter) and Zr-rich (darker) regions, c) macro image of the sample subjected to autoclave testing in DI water for 4 hours at 150 °C, and d) corroded microstructure of the autoclave tested sample showing degradation and dark regions which were identified as carbon impurities (modified from Malkki) [76].

Discussed in more detail in the U_3Si_2 review publication, several methods and strategies for corrosion protection have been considered; one such strategy is to incorporate an additive or dopant which will preferentially oxidize, forming a protective/passivating barrier (oxide, nitride, or silicide) on the surface of the fuel element to protect it from corrosion [78, 81]. An Ellingham-type diagram, similar to Figure 13, for the thermodynamic stability of oxide formation for various proposed elemental additions to high uranium density fuels, is reported in the U_3Si_2 focused part of this review series. Using a similar strategy, Lahoda *et al*. have recently submitted a U.S. patent application on grain boundary enhanced UN and U_3Si_2 pellets for improved oxidation resistance [83]. The invention describes mixing UN or U_3Si_2 powders with an additive of selected passivating materials (<20 wt%) including Mo, Ti, Al, Cr, Th, Cu, Ni, Mn, W, Nb, Zr, Y, Ce, or Mg, or alloys containing at least 50 at% of the metal, MgN, $ZrSi_2$, $ZrSiO_4$, $CrSi_2$, BeO, UO_2, or glassy materials [83].

As previously stated, limited publications are available in the open literature that investigate the effects of adding dopants or components to the corrosion behavior of UN; however, there is more data on the addition of UN to other host matrices, including UO_2 and U_3Si_2. Accordingly, Yang *et al.* and Costa *et al.* investigated the oxidation resistance of UO_2/UN composite fuel compacts with up to 50 wt% UN [84, 85]. However, the synthesis techniques and observed behavior were significantly different. In the study by Yang *et al.*, hot-pressed composites of nearly 100%TD UO_2 along with (6-39 wt%)UN (synthesized from the HDN method) were fabricated for the purposes of improving the uranium density and thermal conductivity of UO_2. The authors indicated that approximately 7 wt% UO_2 impurity existed in the starting HDN UN powder along with approximately 3 wt% U_2N_3 (as determined by XRD via a relative intensity ratio, RIR, analysis). Although starting weight fractions for UN were listed as 19.4, 37.4, and 51.2, it was reported that the sintered composites had a marked decrease in the UN weight fraction (6-39 wt%), which was attributed to decomposition or the oxidation of the UN phase during sintering under vacuum. However, precise control of the sintering atmosphere was not detailed, and no elemental uranium phase was detected and so oxidation is probable and decomposition is unlikely. Backscatter electron images of the hot-pressed samples are shown in Figure 15 and show the UN (light phase) and UO_2 phase (dark contrast) comprising the microstructure. The authors suggest that the formation of a hypo-stoichiometric UO_2 is likely, which may be due to the low oxygen potential during hot-pressing in vacuum, resulting in the oxidation of UN. If the UN is oxidized, it is postulated that nitrogen dissolution into the UO_2 is possible, forming an oxynitride that decomposed upon cooling to UO_2 and U_2N_3. The authors also acknowledged that the RIR method for determining the final sintered compositions did not reflect the actual composition as the pattern was obtained from the sample surface and likely varied from the bulk [85].

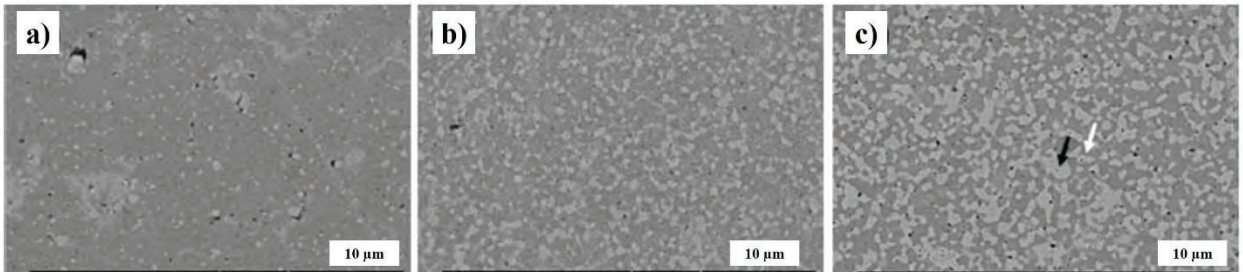

Figure 15: Backscatter electron images of the UO_2-UN samples hot-pressed at 1590 °C, a) 6.9 wt% UN, b) 26.4 wt% UN, and c) 39.3 wt% UN. Modified from Yang *et al.* [85].

More recently, Costa *et al.* also looked at composites of UO_2 with (10, 30, and 50wt%) UN (microspheres from the sol-gel process) sintered via SPS in vacuum. The following general behaviors were observed: Higher sintering temperatures and pressures resulted in a lower concentration of UN and a higher concentration of α-U_2N_3, and the cooling rate impacts the amount, size, and morphology of the U_2N_3 precipitates. Faster cooling resulted in less of the sesquinitride phase with a coarse grain structure and slow cooling rates produced a long range lamellar-type structure [84]. The sintered microstructure of the UN-UO_2 composites are shown in Figure 16a-d. The highly porous UN microspheres are well distributed throughout the UO_2 matrix but deviate from their original spherical shape to a more elongated oval, which is attributed to the induced compressive stresses applied during the SPS process. EDS chemical mapping was also used to identify α-U_2N_3 precipitates throughout the UO_2 matrix (identified by P3 in Figure 16d) [84]. As a follow-on study to this work, the authors oxidized their as fabricated UN microspheres, sintered UN microspheres, UO_2, and UO_2-(10,30, and 50 wt%) UN in a TGA in synthetic air up to 700 °C. The degradation of the as-fabricated and sintered UN microspheres oxidized in air was shown previously in Figure 5. The authors reported the highest oxidation onset temperature of 320 °C for their UO_2/10wt% UN sample, outperforming even the benchmark UO_2 sample. It should be noted that the authors indicated the actual phase composition of their UO_2/10wt% UN sample after sintering was 95 wt% UO_2/1.7 wt% UN/3.7 wt% U_2N_3 via XRD RIR method. This composite also had a higher maximum reaction temperature and lower oxidation rate at its maximum than their benchmark UO_2 sample. The as fabricated UN microspheres (52% TD) and sintered UN microspheres (83.8% TD) had the lowest oxidation onset temperatures (276 and 260 °C, respectively).

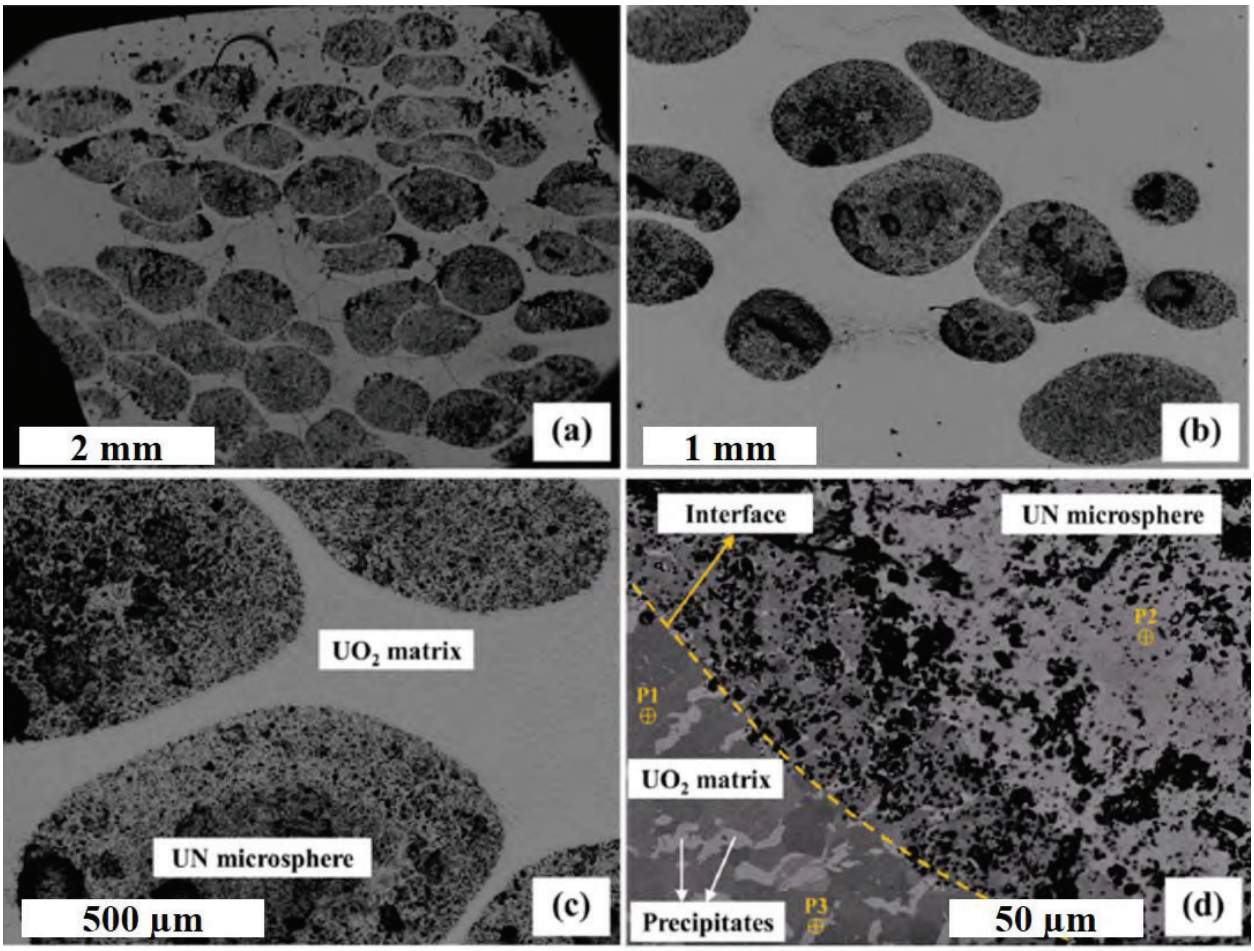

Figure 16: Backscatter electron micrographs of UN microspheres embedded in a UO_2 matrix. a) showing UN microspheres relatively well dispersed throughout the UO_2 matrix but elongated from their original spherical shape, b) higher magnification of the UN microspheres, c) higher magnification image showing the more porous UN microsphere as compared to the denser UO_2 matrix, and d) highlighting the UO_2-UN microsphere interface. Modified from Costa *et al.* [84].

Other work using UN microspheres investigated dopants of Cr, Ni, or Al (2.7, 2.8, and 1.5 wt% respectively) to achieve a passivation via preferentially formed oxide layers of the metallic additives during water exposure [78]. The desired additives were dissolved into the feed solution to make spheres which then underwent carbothermic reduction. The authors indicate as-fabricated microspheres were all highly porous (< 80% TD for their proposed compositions). Due to the use of carbon nano-powder during the internal sol-gel process, significant washout of carbon into the solution occurred making control of carbon contaminates in the final product difficult. Considerable contamination of the microsphere's surfaces with silicon oil was found which likely affected the sintering process. X-ray diffraction of the nitride microspheres indicated the UN/Cr samples contained UN, UO_2, Cr_2O_3, and CrN, the UN/Ni samples only indicated UN, while the UN/Al samples corresponded to UN, AlN, and Al_2O_3 [78]. Figure 17a and c show SEM micrographs of the UN-Cr and UN-Ni doped microspheres after nitridation and prior to sintering, Figure 17e is the air-dried UN-Al microsphere prior to nitridation, while b, d,

and f are the SEM micrographs and chemical maps showing elemental distribution on the sphere surfaces.

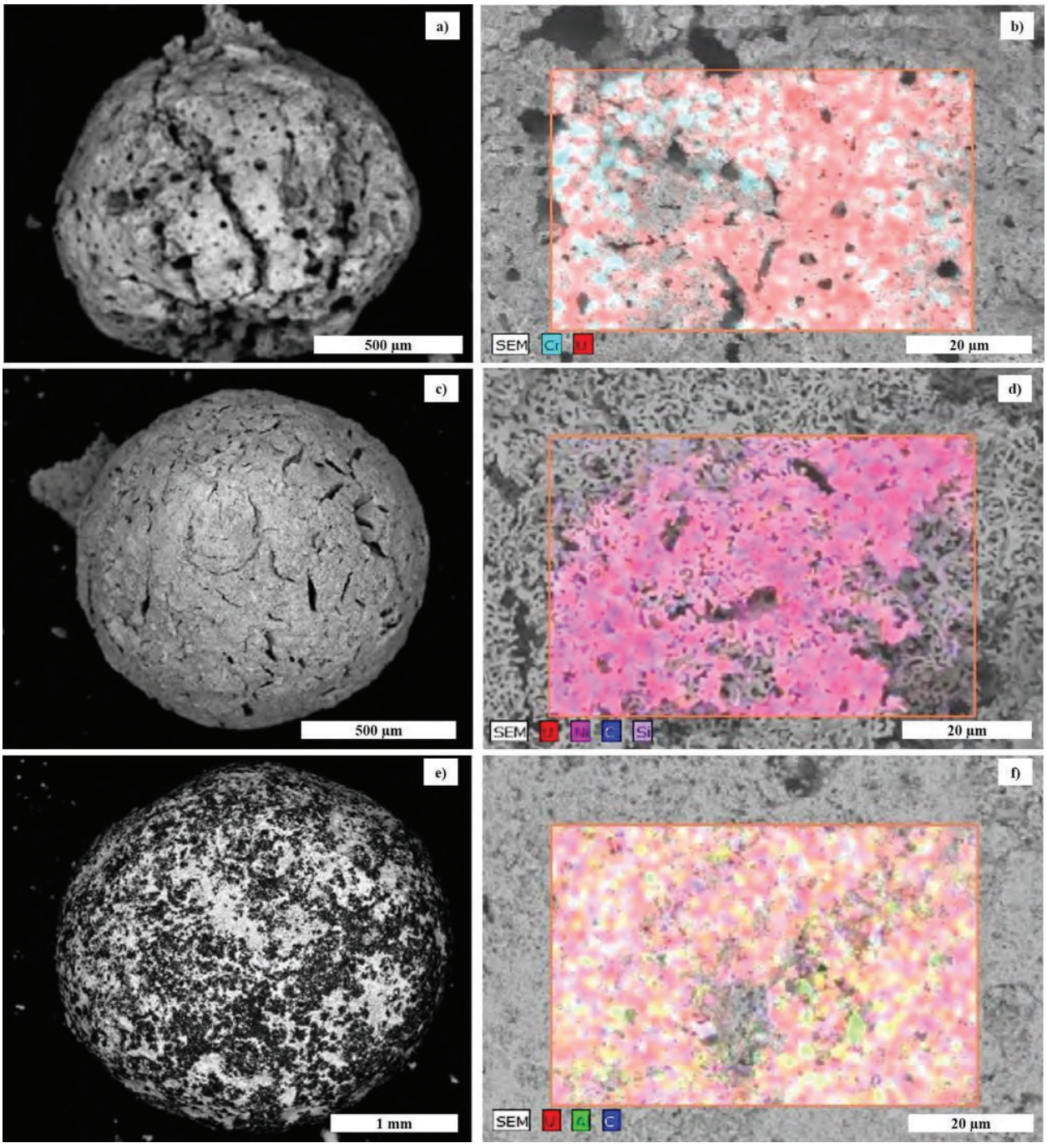

Figure 17: SEM micrograph compilation of UN-doped microspheres before sintering. a) UN-Cr microsphere after nitridation and b) EDS mapping of surface of the nitrided microsphere showing U and Cr distribution although XRD analysis identified UN, UO_2, Cr_2O_3, and CrN; c) UN-Ni microsphere after nitridation and d) EDS mapping of the UN-Ni nitrided microsphere showing U, Ni, C, and Si distribution, XRD only identified UN; e) UN-Al air-dried

microsphere before nitridation and f) EDS mapping of the UN-Al microsphere after nitridation showing U, Al, and Cr distribution, XRD identified UN, AlN, and Al_2O_3. Modified from Herman and Ekberg [78].

The microspheres were compacted and conventionally sintered inside a graphite element furnace. The UN/Cr pellet had varying porosity across the pellet (calculated to be 40% TD of UN) and showed indication of chromium migration away from the surface and an interaction between the W-setter plate using during sintering and the pellet bottom. XRD patterns from the surface identified UO_2, CrO_2 and a uranium carbonitride. The UN/Ni samples showed nickel segregation to the grain boundaries and formation of what the authors identified as UNi_5 (calculated 57% TD of UN). The UN/Al samples showed Al segregated to the edge of the pellet and the surface was cracked and extremely porous, while XRD only identified a uranium carbonitride phase (calculated 50% TD of UN). All the as-sintered samples were subsequently placed into boiling DI water, with the authors stating the UN/Cr sample survived 5 hours without disintegrating. Although the pH of the final solution containing the UN-Cr sample was neutral, bubble formation was seen at the pellet surface. These bubbles were postulated to be from ammonia formation which could be correlated back to the UN corrosion Eqn. 4. [78]. As seen in Figure 18a-b, the microstructure appeared unchanged (per SEM) after the corrosion experiment. The authors indicated the peak intensity of the XRD analysis of the nitride phase was smaller after corrosion, while the intensity of the detected oxide phases (CrO_2 and Cr_2O_3) were larger. The UN/Ni pellet disintegrated after 10 minutes in the boiling water and the UN/Al pellet was lost after 5 minutes and both solutions measured pH were neutral [78]. Another reference to UN composite formation using a sol-gel method was part of the oxidation study performed by Dehadraya *et al.* which included samples of (U,Ce)N microspheres having 15 and 30 mol% cerium [56]. The final oxidation product of the composites containing 15 mol% Ce were MO_{2+x} (M = metal) with a sesquinitride as an intermediate. The authors reported the 30 mol% Ce sample ignited during the reaction forming a mix of M_3O_8 and MO_{2+x} [56].

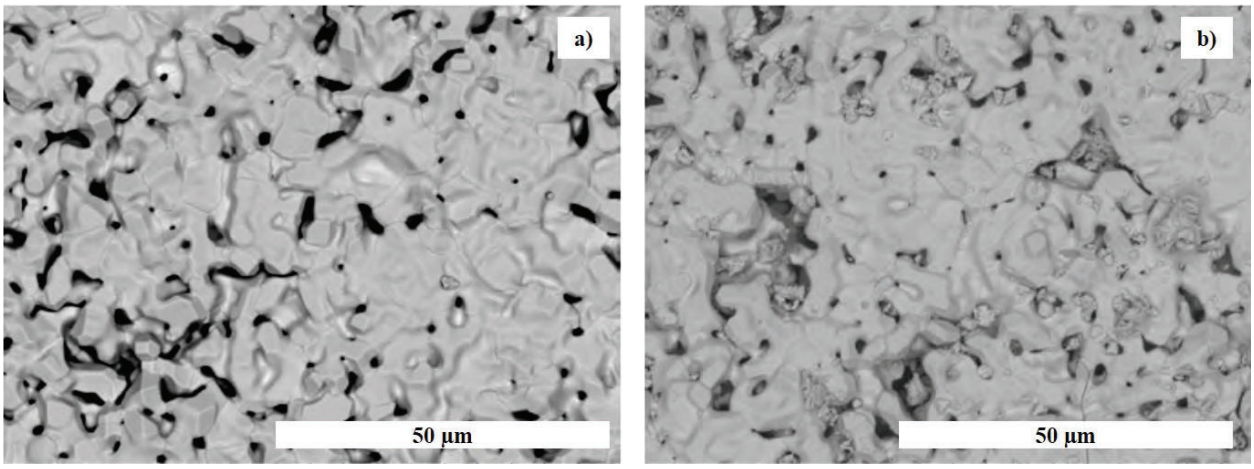

Figure 18: SEM micrographs of the UN-Cr microsphere microstructure prior to submersion in boiling water and b) UN-Cr microsphere after 5 hours in boiling water. Modified from Herman and Ekberg [78].

Several researchers have investigated the use of another ATF concept, U_3Si_2, as a secondary phase in UN for increased accident tolerance. The microstructure of UN-U_3Si_2 compacts of various compositions (10, 20, and 25 wt% silicide) fabricated via SPS using HDN UN powder

and arc-melted U_3Si_2 are seen in Figure 19a-c [86]. The formation of a ternary U-N-Si phase was identified as the dark phase in the figures. In Figure 19a the lighter phase inside the large silicon-rich inclusion (seen in all the compositions due to the UN and silicide powders being manually mixed) was said to most closely match the original U_3Si_2 phase. In the 20 wt% and 25 wt% silicide samples (Figure 19b-c) this phase was seen primarily at the grain boundaries. The authors proposed that this intergranular phase led to liquid phase sintering during the SPS process as they also found evidence of a liquid phase melt on their graphite dies [86]. This same work was also documented by Johnson *et al.* who stated that the resulting pellets had high homogeneity with well dispersed U_3Si_2 confined to the grain boundaries, although complete saturation of the UN grain boundaries was not achieved [87].

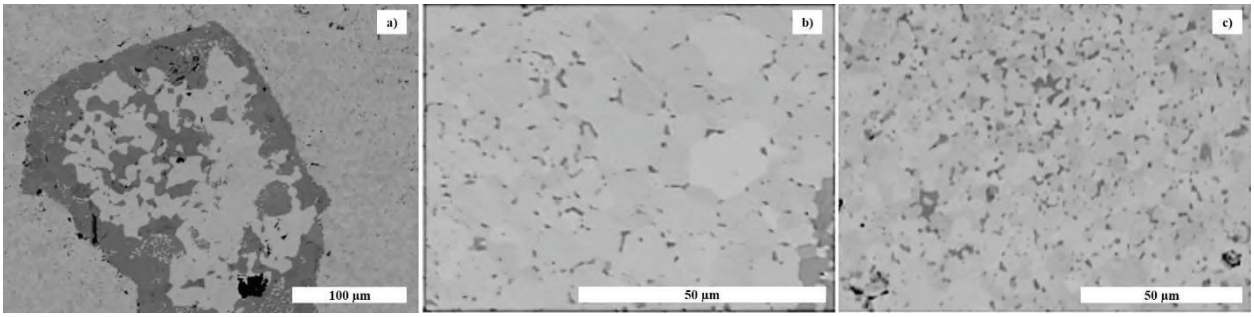

Figure 19: SEM micrographs of the SPS sintered microstructure of UN-U_3Si_2 composites a) 10 wt% U_3Si_2, b) 20 wt% U_3Si_2, and c) 25 wt% U_3Si_2. Modified from Raftery [86].

A separate study using UN powder from CTR-N and UN microspheres prepared from a sol-gel process combined with (25-35 wt%) arc-melted U_3Si_2 powder and then conventionally sintered resulted in different behavior [8]. Higher temperature sintering resulted in increased interactions with the crucible material, pellet slumping, and evidence of a separate silicide phase formation. The phase morphology of the samples fabricated with conventional sintering methods (<95% TD) indicated a relatively continuous U_3Si_2 phase with UN existing as separate regions within it (see Figure 20) [8].

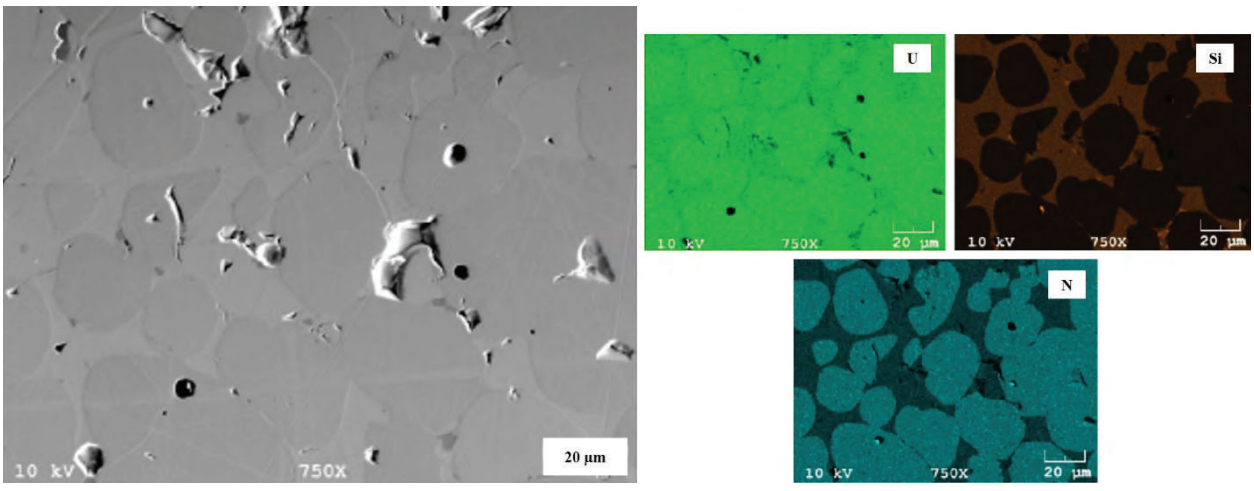

Figure 20: Backscatter electron image of UN+30 wt% U_3Si_2 sample sintered at 1700 °C for 3 hours using HDN UN powder and arc-melted U_3Si_2 exhibiting a fairly continuous U_3Si_2 phase around the larger UN

grains and the accompanying EDS chemical maps showing small areas of silicon-rich regions. Modified from Ortega *et al.* [8]

Only a couple of studies have examined the oxidation and corrosion behavior of UN/U_3Si_2 composites. A UN-10 wt% U_3Si_2 crushed powder sample oxidized in air up to 800 °C (along with pure UN as noted earlier, see Table 3) generally followed the same reaction behavior of UN [58]. Although the oxidation onset was slightly delayed, given the more rapid kinetics like they observed with pure U_3Si_2 the oxidation reaction completed at the same point as the typically more poor performing UN [58]. A follow-on study examined the degradation behavior of a UN-10wt%U_3Si_2 composite in a steam environment (along with pure UN samples as noted previously) using pellets sintered as outlined in Johnson *et al.* [87]. A UN-10wt%U_3Si_2 sample was subjected to steam exposure at 300 °C and 9 MPa for 90 minutes [69, 88]. The corrosion mechanism in the composite was identified as intragranular cracking, as opposed to the intergranular cracking (seen in their pure UN samples resulting in matrix degradation and pesting). The exposure of less fresh surfaces to oxidation in the composite delayed the attack on the UN grains resulting in a 5x lower mass increase during steam exposure as compared to the pure UN sample of the same porosity [69]. Figure 21a shows the mass increase for UN as a function of porosity as well as for the UN-U_3Si_2 sample, b) the as-fabricated microstructure of the composite, and c) and d) exhibiting the corroded microstructure and intragranular cracking of the composite pellet [69]. The UN matrix appeared to have no chemical variation at the cracks, but the U_3Si_2 exhibited regions having increased oxygen content. This suggests that it is not the silicide which has an increased resistance to corrosion but that the presence of the silicide provides mechanical stability by reducing or eliminating intergranular cracking and grain relief in the UN matrix [69].

Although noted above with regards to the specific experiments, the differences in synthesis and fabrication methods, along with the inclusion of the various additive components many times result in samples that are not of the nominal composition as intended and reported by the researchers. While this review has attempted to bring to light those experimental conditions and the actual phase compositions of the samples tested, readers are cautioned to examine the literature carefully for specific experimental details regarding fabrication.

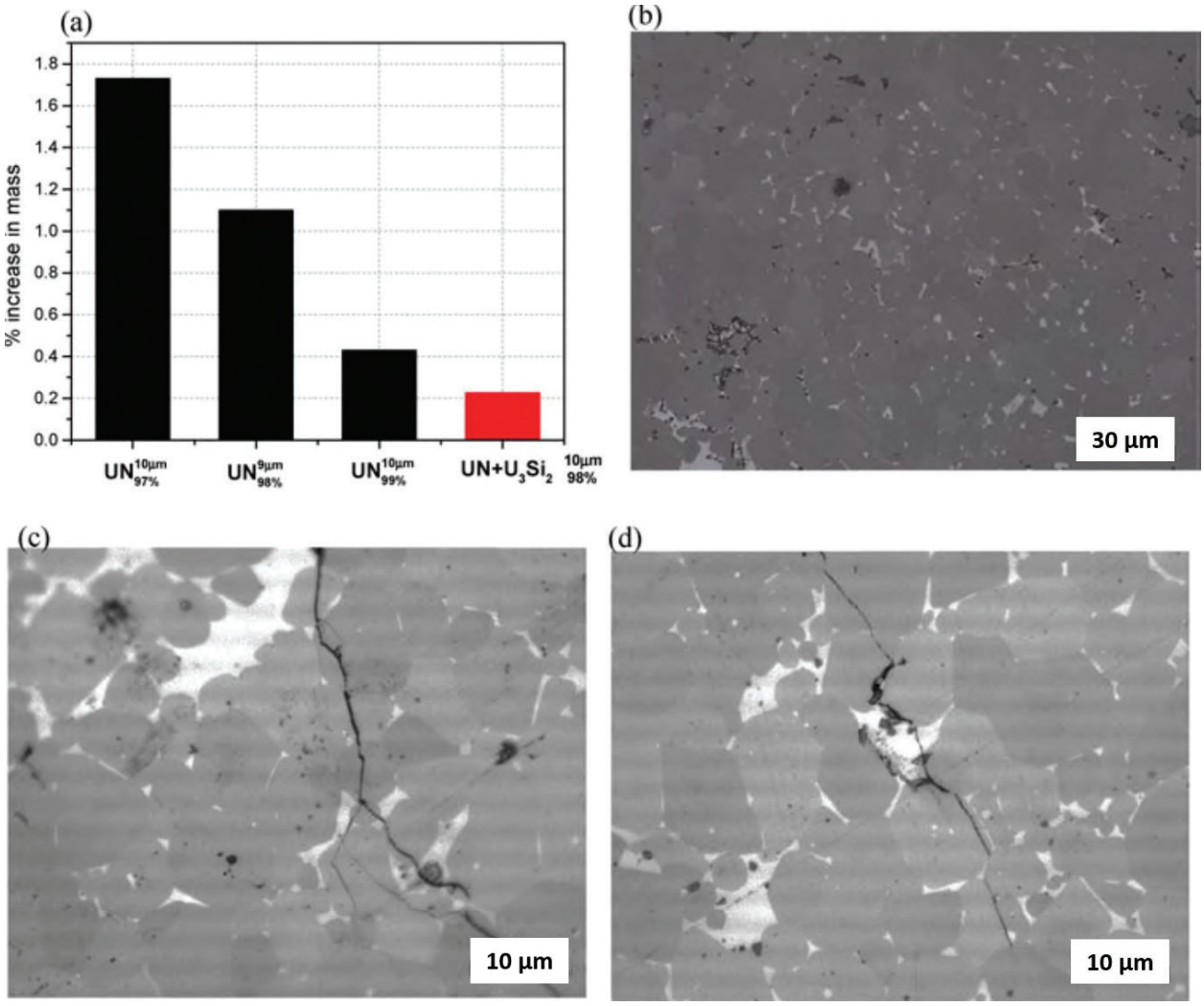

Figure 21: Modified from Lopes *et al.* [69] showing a) the % mass increase during steam corrosion for UN pellets with varying porosity and a UN-10 wt% U_3Si_2 composite, b) the as-fabricated microstructure of the composite, and c) and d) showing the corroded microstructure with intragranular cracking present.

5. Effects of impurities and secondary phases in UN

5.1 Impurities in UN

This section briefly discusses the role impurities have on the performance of UN under corrosion. More information has been published about how impurities affect UN's in-pile behavior. The role that impurities play in the degradation behavior of UN in oxidation and corrosion conditions has not been well studied. Only a couple of the previously mentioned corrosion studies postulated that increased oxygen content in the UN resulted in more severe oxidation and corrosion behavior [14, 57]. Incorporation of C and O impurities on the N, U, and interstitial lattice sites of UN via DFT theory found that C and O are energetically favorable in the N site and that O is stable in the interstitial position [89]. Carbon and oxygen strongly interact with vacancies and cluster at grain boundaries, dislocations, or surfaces. Oxygen also has a lower energy barrier for diffusion as compared to N or C and O will form a psuedo UO_2

coordination, while C has very directional and inflexible bonding with U, requiring much more energy [89]. Carbon direct interstitial diffusion was found to have a low energy barrier and can rapidly diffuse to a N vacancy position, while O has a 0.15 eV lower energy barrier than N self-diffusion, all of which can be significant in UN fuel [89]. Concentration of residual carbon in UN should also be held to a minimum as formation of UC can result in even less desirable corrosion behavior, which is elaborated upon in the UB_2/UC publication of this review series [90].

The effects of carbon and oxygen impurities in UN are also important to note due to the effects their presence can have on formation and separation of phases within the fuel (with fission products and uranium) during the course of irradiation [91]. Experimental results show the maximum oxygen solubility in UN is 3-7 mol% (1.5-3.5 at% O) in the temperature range 1527-1900 °C and an increase in oxygen concentration likely leads to formation of separate phases of UO_2, U, and U_2N_3 [91]. Oxygen and carbon content within the mononitride fuel can affect creep, radiation swelling, emission of gaseous fission products, and thermal conductivity [92]. UN fuel with mass fractions of 0.4-0.5% oxygen and 0.35-0.45% carbon were tested in two zones in a BR-10 reactor. Gaseous emissions from the fuel was approximately 25% of the total amount of gaseous fission products formed. Fuel having mass fractions of 0.1% for oxygen and carbon had gaseous emissions of 20-22% of the total gaseous fission products formed [92]. UN's compatibility with EI847 steel cladding in the BR-10 was affected by increased oxygen and carbon content in the fuel [92]. Carbonization of the cladding inner surface was three times greater in fuel that had O and C mass fractions of 0.3-0.45% versus fuel having mass fractions below 0.15% [92]. The importance of oxygen and carbon impurities on in-pile performance is still not well understood, likely due to other parameters which prevent absolute determination of impurity effects on irradiation behavior [93]. It has been observed that carbon and oxygen content does have a strong correlation to fission product behavior due to the stability of the carbide, nitride and oxide phases of the major fission products [93]. Irradiation tests on UN with various cladding materials (Nb-1% Zr and Nb-1%Zr-0.1% C) were conducted as part of the SNAP-50 reactor development program [10, 94, 95]. Overall irradiation performance was deemed satisfactory, but the data on the swelling results exhibited substantial scatter for fuel burnup <1.12 at% [10]. Testing parameters varied — from 10-93% ^{235}U enrichment, burnups from 0.3-4.58 (at%) and centerline temperatures from 912-1565 °C — however tests for both cladding materials indicated carbon impurities of 300-600 ppm C, and 1000-2000 ppm O. It was proposed that the oxide was present as a fine precipitate and was considered an advantageous nucleating field for fission gases, suspected to have aided in the superior irradiation performance of UN as compared to UC [94]. As part of the SP-100 research, other irradiation tests on UN with cladding materials of W-26% Re showed significant scatter in the swelling data as well cladding failures which did not allow for definitive analysis, while cladding of Ta-111 was similar to that of the Nb-1% Zr and Nb-1%Zr-0.1% C [10].

The effects of C and O impurities on the thermal conductivity of UN fuel has also been studied [96]. Carbon impurities up to 0.5 wt% resulted in a slight increase in thermal conductivity, but above that concentration the thermal conductivity showed a marked decrease. The effects on UN thermal conductivity as a function of oxygen concentration in argon and helium atmospheres from 293-1273 K was also studied [96]. The thermal conductivity of UN for O_2 concentrations of

0.2-2.25 wt% was decreased by approximately 41% at 600 °C and by almost 53% at 100 °C (see Figure 22). UN samples having 0.13 wt% oxygen content (and 12.4% porosity) had the highest thermal conductivity values [96].

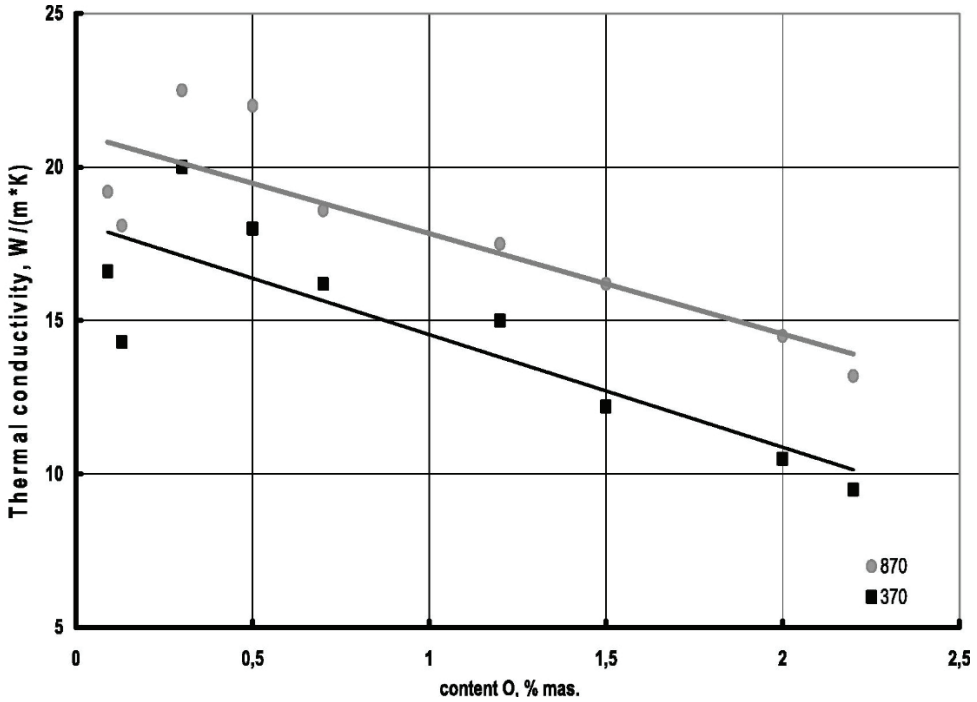

Figure 22: Dependence of thermal conductivity in UN as a function of oxygen content. From Solntceva *et al*. [96].

5.2 Secondary phases in UN

In addition to the role secondary phases play on oxidation and corrosion behavior, the impact these phases can have on other properties (e.g. thermophysical and neutronic) and irradiation effects needs to be considered. Early work, from the 1960's to the 1980's, on additives to a UN fuel matrix included additions of other nitrides and elements such as AlN, ThN, ZrN, O, C, Mo, Th, Ti, and Y. One of the earlier investigations reported on the addition of refractory AlN to UN via cold compacting and sintering and hot isostatic pressing [97]. The results suggest that the thermal conductivity is slightly decreased with the addition of 10-30 vol% AlN over pure UN (even though AlN has a higher thermal conductivity than UN under ~600 °C). The authors attributed these lower thermal conductivity values to intra- and inter-granular cracking due to differences in the thermal expansion of the two materials [97]. These UN/AlN compacts (having 75-85% TDs) were oxidized at 500 °C in dry CO_2 and results showed initial mass gain was very rapid but that a protective oxide formed after about 1 hour. Significant mass gain was seen after ~14 hours (although no samples disintegrated) and UO_2 was identified as the final oxidation product [97]. Other work for UN/metal nitride composites was proposed in a patent referencing a solid solution of (U,Th,Pu)N and a metal nitride, with the preferred fuel comprised of UN and TiN or YN [98]. It is stated that both TiN and YN will result in a loss of thermal conductivity of the composite fuel but are not dissimilar to that of a (U,Pu)N fuel. Addition of Gd_2O_3 and GdN

as a burnable absorber to a UN matrix has also been reported to lower the thermal conductivity of UN [99]. The impact of UN addition to a UO_2 matrix (39 wt% UN) has been shown to provide a 2x increase in thermal conductivity as compared to reference UO_2 [85]. A UN-Mo cermet was also fabricated from binder-jet printed Mo and UN microspheres sintered via SPS showing an increase in thermal conductivity when compared to pure UN [100]. Alexander addresses an important challenge with fabrication of UN and UN-composites, indicating that additives, such as TiN or YN (5-10-20 mol%) can stabilize the UN, decreasing the thermodynamic activity of the uranium, and preventing the formation of a molten uranium phase [98].

Other efforts related to in-pile performance investigated incorporating additions of O, C, Mo, and Th to the UN structure based on findings that fine precipitates in uranium metal reduce fission-induced swelling [101]. The authors state Mo is slightly soluble at approximately 0.10 wt% at 2600 °C, precipitating as submicroscopic particles upon rapid cooling. Thorium, dissolved as ThN into UN, can be oxidized to UO_2 forming $(U,Th)O_2$ precipitates within UN grains [101]. It has also been reported that ThN is more reactive towards water than UN [102]. Potter *et al.* indicate that oxygen quantities can be controlled by adding carbon to samples [101], although as previously mentioned, carbon and oxygen impurities in UN can be detrimental to fuel performance. More recently, a UN-5 wt% UO_2 composite system (via HDN and conventionally sintered) under proton irradiation (2 MeV up to $4*10^{18}$ and $8*10^{18}$ ions/cm^2 at 400 °C and 700 °C and $<10^{-6}$ torr) was studied for phase and defect evolution [103]. High angle annular dark field (HAADF) and bright field (BF) scanning transmission electron microscopy images of the UN-5wt%UO_2 composite irradiated at 710 °C and up to $8*10^{18}$ ions/cm^2 along with EDS chemical maps show the aforementioned sandwich structure of $UN/U_2N_3/UO_2$ as previously mentioned in the oxidation literature (see Figure 23). The authors concluded that the irradiation accelerated the oxidation and phase transformation in the composite sample. The study also found that in the nitride phases the dislocation loops grew (3x that of UO_2) and with increasing temperature and dose the number density of the loops also increased [103].

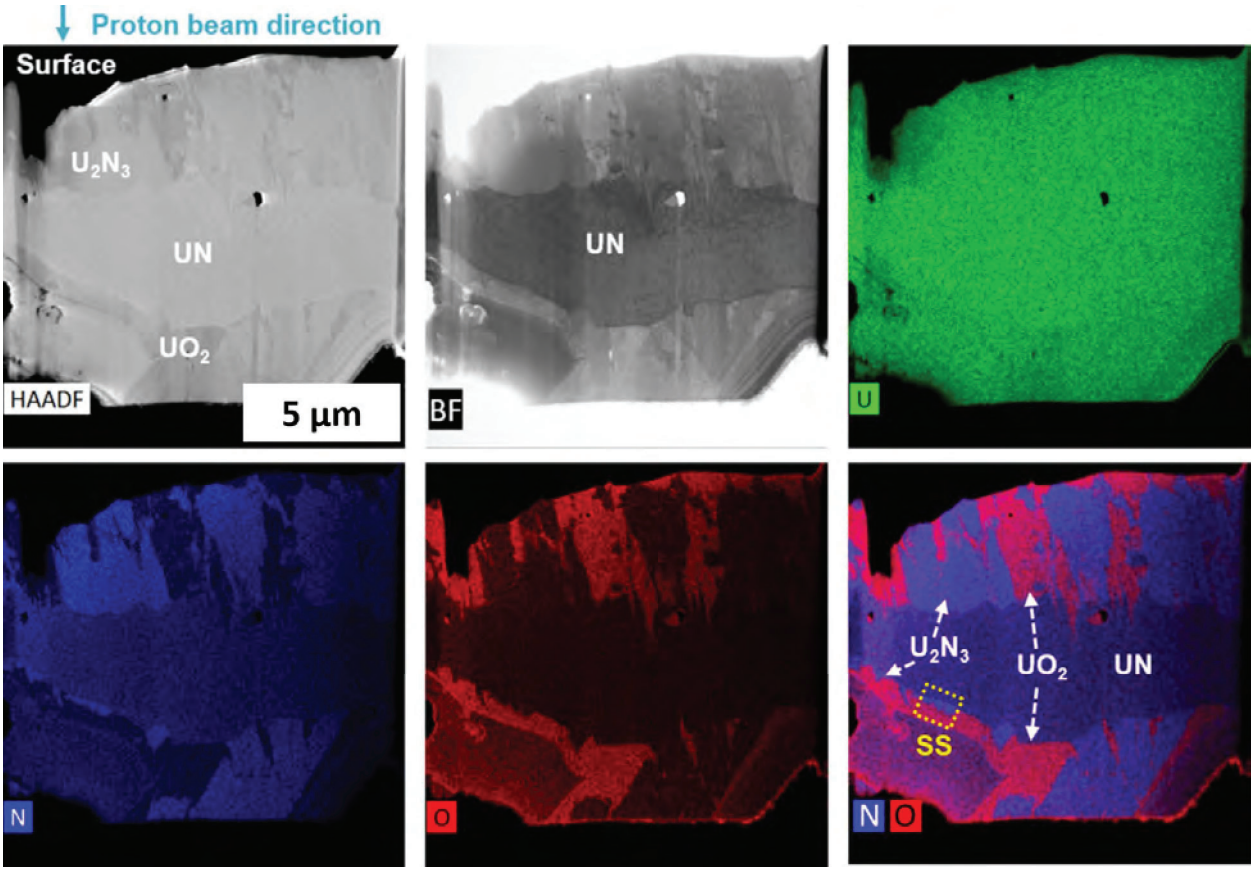

Figure 23: High angle annular dark field (HAADF) and bright field (BF) STEM images with EDS chemical maps of a UN-5wt% UO_2 composite after proton irradiation at 710 °C and up to a fluence of $8*10^{18}$ ions/cm^2 indicating the presence of UN, U_2N_3, and UO_2. The "sandwich structure" of the three phases is denoted by the yellow dashed rectangle in the bottom right image; the proton irradiation beam direction is marked by an arrow in the upper left. Modified from He *et al*. [103].

The effects of secondary constituents in UN on neutronic performance of UN fuel has also been studied through modeling [19, 104]. A neutronics simulation was performed on UN and UN-(Al, Cr, Nb, Ni) metal composites with Zr-clad fuel pins [104]. The cycle length on undoped UN increased by 25% compared to UO_2, while dopant addition to the UN lattice only slightly affected the increased cycle length. The changes to the increased cycle length were smallest in the following order: Al > Cr > Ni > Nb [104]. Another neutronic assessment was performed for UN with secondary candidate materials of U_3Si_5, U_3Si_2, UB_4, and ZrO_2 in nominal conditions in a reference pressurized water reactor with Zr cladding [19]. Small volume fractions (<10%) have a relatively small influence on the neutronic behavior of the these UN-based composite fuels [19]. A further study examined a UN-U_3Si_5 composite fuel concept with advanced cladding materials (FeCrAl alloys) finding that the reactor physics and fuel performance were similar to that of the benchmark UO_2-Zr cladding [105].

Given the impact impurities have on UN's performance, it is essential that the synthesis and sintering conditions are controlled to limit impurity concentrations, especially oxygen and carbon. The impact that these impurities play on corrosion behavior is also clearly not well-studied, leaving open the opportunity for research in this area. The authors postulate that delaying the onset of reaction of UN in oxidizing atmospheres can be achieved by enhancing the

purity and density of UN, though mitigation strategies are necessary to facilitate oxidation performance similar to benchmark UO_2. Examining the results presented in the above literature synthesis of UN via the HDN method may be the best choice for achieving high-purity UN feedstock with limited C and O impurities, followed by CTR-N. The sol-gel method for UN microspheres used to make monolithic pellets appears to result in much higher carbon impurities and unwanted secondary phase formation during sintering than the other two more traditional synthesis routes. The SPS method provides for obtaining high-density samples at lower temperatures and shorter sintering times. However, the opportunity for introduction of impurities (from the dies or barrier materials used during sintering) is much greater, as is the potential for metastable phases which can impact the microstructure and fuel performance. The influence that secondary additions have not only to oxidation and corrosion behavior, but to thermophysical, neutronic, and fission product interaction/behavior must also be considered. As mentioned above, specific research into how oxygen and carbon impurities affect UN's performance in hydrothermal corrosion conditions is warranted. Additionally, the effects that irradiation may have on the corrosion behavior of UN must also be considered. Moreover, little data exists on the effects that microstructural evolution and the presence of fission products may have on oxidation and corrosion of UN, which is important not only for in-pile performance but for storage and transportation of spent fuel. As future work is explored on UN, including irradiation, opportunities exist for research in this area.

6. Summary

If UN is to be considered as a replacement for UO_2 for use in existing and future LWRs, a modification of the fuel matrix to mitigate its undesirable corrosion behavior is required. The literature on UN corrosion, while somewhat varied due to differences in synthesis, fabrication, and testing parameters, agrees that the onset of oxidation occurs at temperatures too low for use in LWRs. Research suggests that samples with high densities and low oxygen and carbon impurities perform better, therefore benchmarking leaker-rod tests of high purity, high density UN would indicate the extent to which hydrothermal corrosion will limit deployment. As the literature is limited and varied for synthesis and fabrication, it would be presumptive to conclude that one method is superior over another; however, it has been shown that the hydride-dehydride-nitride method for UN synthesis generally results in less C and O impurities and SPS or HIP can provide higher density samples. Fewer impurities and higher density can contribute to higher onset oxidation temperatures and improved performance. However, the CTR-N method is backwards compatible with current UO_2 fabrication facilities and has been demonstrated in the fabrication of large quantities of fuel quality UN. The issue of isotopically enriching UN with ^{15}N to avoid formation of ^{14}C and limit neutron absorption, remains an opportunity for research, whether through implementation of a closed gas cycle during synthesis, or recovery of nitrogen during synthesis, sintering, and reprocessing.

Oxidation experiments of UN in air, although not relevant to LWR conditions, can provide a comparison to the oxidation behavior of other fuel forms. This behavior in air is also applicable to off-normal transportation and storage scenarios. A summary of the onset temperatures from the UN air oxidation experiments in Table 3 is shown in Figure 23 compared to the reported

ramp testing air onset oxidation of 455 °C for UO_2 from Wood *et al.* [106]. The values range from 202 °C to 450 °C, with this range due to a variety of factors related to UN synthesis and sintering methods, as well as the addition of a secondary phase. The lowest onset temperature was for UN compacts fabricated from the sol-gel method, and the highest onset temperature was for a UN+10vol% U_3Si_2 compact fabricated from HDN powder and sintered via SPS, close to that of UO_2. U_3Si_2 is further reviewed in the U_3Si_2 publication of this review series. The highest onset for a pure UN sample (fabricated from HDN powder and conventionally sintered) was 340 °C.

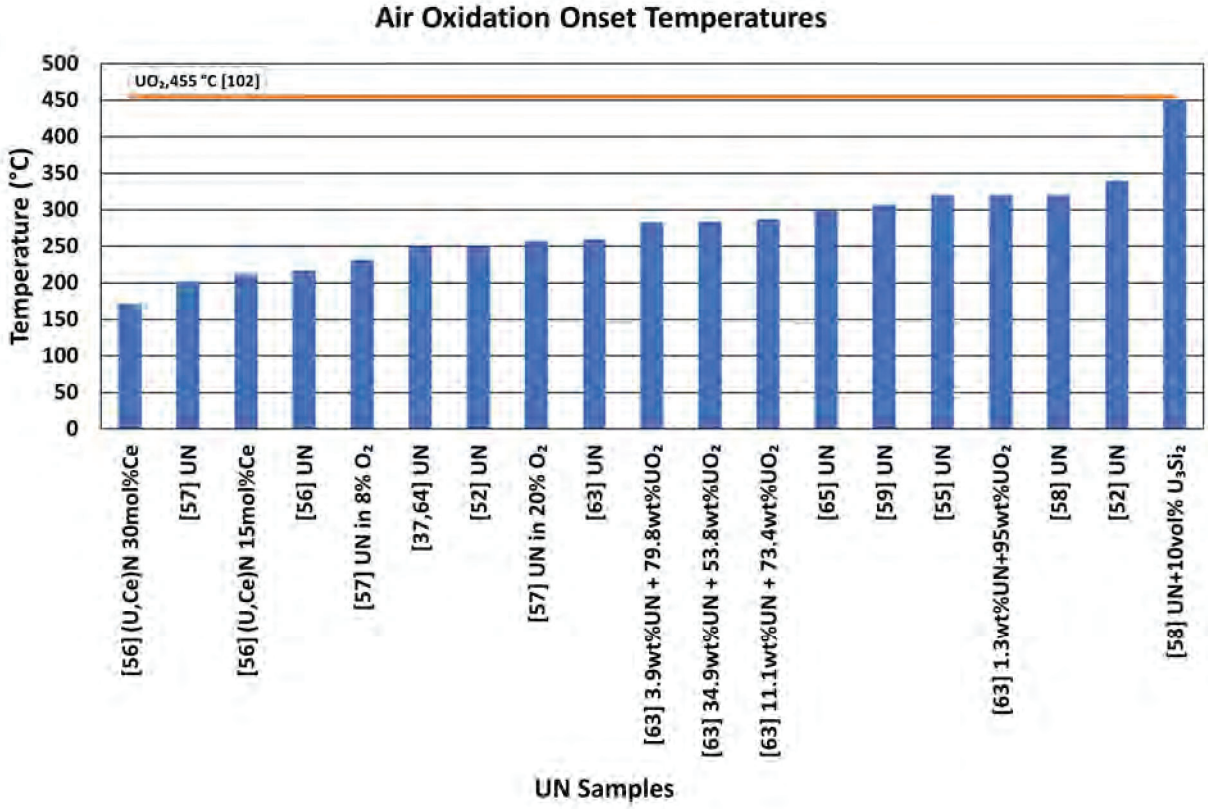

Figure 24: Plot of the air oxidation onset temperatures from Table 3 compared to reference data for air onset oxidation of UO_2 from Wood *et al.* [106].

Data from water and/or steam corrosion experiments is considered here to be the most relevant for screening conditions when evaluating possible ATF fuel forms. Onset temperatures for UN or UN-composite samples tested in water or steam are summarized in Figure 24. The lowest reported onset temperature in water/steam (~150 °C) was for a UN+30at%ZrN sample (via HDN and SPS) and 180 °C for UN powder. The highest onset was at 400 °C for a pure UN pellet fabricated via HDN and SPS. Only one reported study looked at UN thin film corrosion in radiolytic conditions at room temperature. While the results suggested improved corrosion resistance in conditions similar to what would be seen in a leaker/failure rod scenario, more extensive research is required in this area.

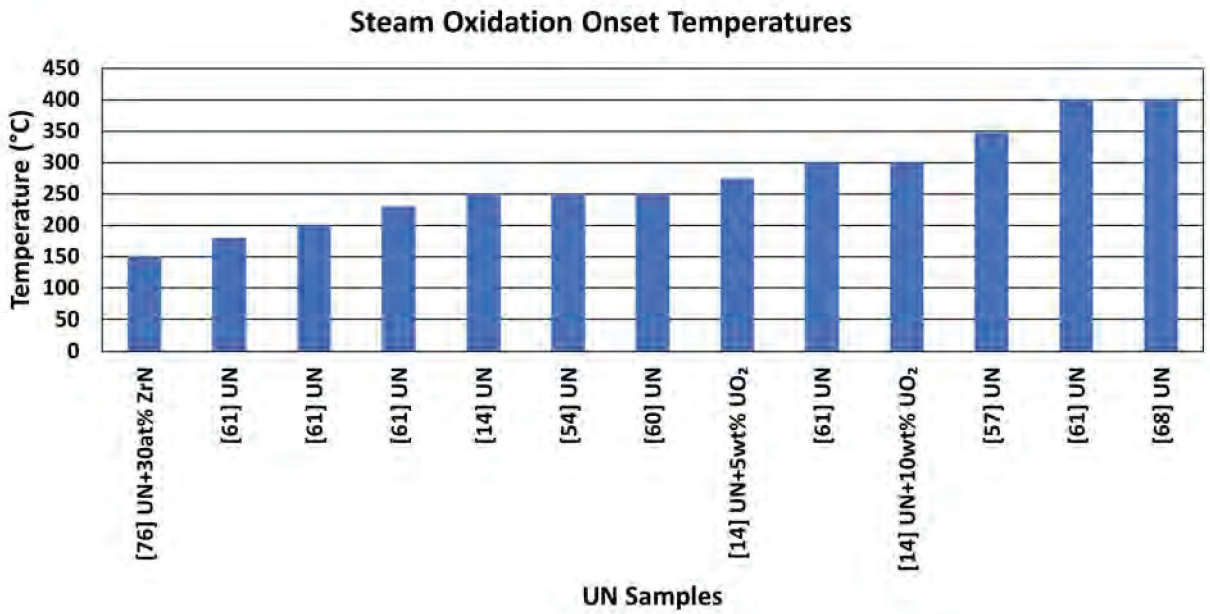

Figure 25: Plot of the water/steam onset temperatures from Table 4.

Regardless of synthesis technique, UN pulverization during corrosion is due to the formation of a reaction product at grain boundaries. The reaction product is generally a progressive formation of sesquinitride and oxynitride phases (with an associated volume expansion) leading to instability in monolithic samples. The U_3Si_2 focused publication of this review series will explore protection strategies in more depth. However, current research on UN protection is primarily directed at the addition of a suitable additive that will act as a protective barrier. This is envisaged to be through either the preferential oxidation of the dopant over UN and subsequent formation of another corrosion resistant phase during oxidation/corrosion or microstructural refinement in which the UN grains are protected by the additive; some combination of these degradation mitigating phenomena could also be expected. The literature that includes incorporation of an additive or secondary phase to UN favors more traditional synthesis techniques, such as HDN and CTR-N for UN synthesis followed by conventional powder metallurgy and sintering. The challenges remain in identifying a scalable process for synthesis and fabrication which limits impurities (namely O and C), and one in which additives can be easily incorporated without formation of unwanted secondary phases, or dissociation of the UN. Research opportunities also remain in identifying the specific effects that O and C impurities play in hydrothermal corrosion of monolithic UN.

While still limited and somewhat varied, the available literature on oxidation and corrosion of UN and UN with various additions demonstrates the continued need to identify a pathway for improving UN's corrosion resistance. To date, none of the literature has successfully demonstrated significant improvements to the corrosion resistance of pure UN or UN with an additive/secondary phase. Additionally, a proven method to fabricate and sinter high density UN with an additive that can improve corrosion performance, which is scalable, economical, and does not result in unwanted phases or undesirable impurity levels remains elusive. Further

investigation into suitable additives for UN as well as more relevant water and steam testing for such systems remains an opportunity in fuels research.

Acknowledgements

Work at the collaborating institutions, including Westinghouse Electric Company, was supported by the U.S. Department of Energy, Office of Nuclear Energy under DOE Idaho Operations Office Contract DE-NE0008824 funding opportunity. Accordingly, the U.S. Government retains and the publisher, by accepting the article for publication, acknowledges that the U.S. Government retains a nonexclusive, paid-up, irrevocable, worldwide license to publish or reproduce the published form of this manuscript or allow others to do so, for U.S. Government purposes.

References

[1] P. Lyons, B. Crowell, Development of light water reactor fuels with enhanced accident tolerance, Report to Congress, United States Department of Energy, Washington, DC, 2015.
[2] S. Bragg-Sitton, Development of advanced accident-tolerant fuels for commercial LWRs, Nuclear News 57(3) (2014) 83.
[3] S.J. Zinkle, K.A. Terrani, J.C. Gehin, L.J. Ott, L.L. Snead, Accident tolerant fuels for LWRs: A perspective, Journal of Nuclear Materials 448(1) (2014) 374-379.
[4] F. Goldner, Development strategy for advanced LWR fuels with enhanced accident tolerance, Enhanced Accident Tolerant LWR Fuels National Metrics Workshop, Germantown, MD, 2012.
[5] D. Wachs, N. Woolstenhulme, Advanced fuel cycle technology: Special session in honor of Dr. Michael Lineberry, Transactions of the American Nuclear Society 110(INL/JOU-14-33095) (2014).
[6] F. Cappia, J.M. Harp, Postirradiation examinations of low burnup U_3Si_2 fuel for light water reactor applications, Journal of Nuclear Materials 518 (2019) 62-79.
[7] G.J. Youinou, R.S. Sen, Impact of accident-tolerant fuels and claddings on the overall fuel cycle: A preliminary systems analysis, Nuclear Technology 188(2) (2014) 123-138.
[8] L.H. Ortega, B.J. Blamer, J.A. Evans, S.M. McDeavitt, Development of an accident-tolerant fuel composite from uranium mononitride (UN) and uranium sesquisilicide (U_3Si_2) with increased uranium loading, Journal of Nuclear Materials 471 (2016) 116-121.
[9] R.B. Matthews, Irradiation performance of nitride fuels, Los Alamos National Lab., NM (United States), 1993.
[10] S.B. Ross, M.S. El-Genk, R.B. Matthews, Uranium nitride fuel swelling correlation, Journal of Nuclear Materials 170(2) (1990) 169-177.
[11] S.S. Voss, Space Fission Power: Historical Review, Reference Module in Earth Systems and Environmental Sciences, Elsevier2021.
[12] E.S. Wood, J.T. White, C.J. Grote, A.T. Nelson, U_3Si_2 behavior in H_2O: Part I, flowing steam and the effect of hydrogen, Journal of Nuclear Materials 501 (2018) 404-412.
[13] A.T. Nelson, A. Migdisov, E.S. Wood, C.J. Grote, U_3Si_2 behavior in H_2O environments: Part II, pressurized water with controlled redox chemistry, Journal of Nuclear Materials 500 (2018) 81-91.
[14] J.K. Watkins, D.P. Butt, B.J. Jaques, Microstructural degradation of UN and UN-UO_2 composites in hydrothermal oxidation conditions, Journal of Nuclear Materials 518 (2019) 30-40.
[15] H. Matzke, Science of advanced LMFBR fuels, (1986).
[16] E.S. Wood, J.T. White, B. Jaques, D. Burkes, P. Demkowicz, Advances in fuel fabrication, Advances in Nuclear Fuel Chemistry, Elsevier2020, pp. 371-418.

[17] M. Kato, Fuel Design and Fabrication: Pellet-Type Fuel, Reference Module in Earth Systems and Environmental Sciences, Elsevier2021.
[18] S.L. Hayes, J.K. Thomas, K.L. Peddicord, Material property correlations for uranium mononitride: 1. physical properties, Journal of Nuclear Materials 171(2-3) (1990) 262-270.
[19] N.R. Brown, A. Aronson, M. Todosow, R. Brito, K.J. McClellan, Neutronic performance of uranium nitride composite fuels in a PWR, Nuclear Engineering and Design 275 (2014) 393-407.
[20] J. Zakova, J. Wallenius, Fuel residence time in BWRs with nitride fuels, Annals of Nuclear Energy 47 (2012) 182-191.
[21] A.T. Nelson, Property and performance assessment to support candidacy of U_3Si_2 as LWR fuel, Los Alamos National Lab, Los Alamos, NM, 2018.
[22] K.J. Mcclellan, FY2014 Ceramic Fuels Development Annual Highlights, Los Alamos National Lab.(LANL), Los Alamos, NM (United States), 2014.
[23] Y.S. Kim, 3.14 - Uranium Intermetallic Fuels (U–Al, U–Si, U–Mo), in: R.J.M. Konings (Ed.), Comprehensive Nuclear Materials, Elsevier, Oxford, 2012, pp. 391-422.
[24] J.T. White, D.D. Byler, Report on the basic chemistry, microstructure and physical properties of high uranium density boride compounds, Los Alamos National Laboratory, Los Alamos, NM, 2015.
[25] J.K. Fink, Thermophysical properties of uranium dioxide, Journal of Nuclear Materials 279(1) (2000) 1-18.
[26] S.L. Hayes, J.K. Thomas, K.L. Peddicord, Material property correlations for uranium mononitride: III. Transport properties, Journal of Nuclear Materials 171(2) (1990) 289-299.
[27] R. De Coninck, W. Van Lierde, A. Gijs, Uranium carbide: Thermal diffusivity, thermal conductivity and spectral emissivity at high temperatures, Journal of Nuclear Materials 57(1) (1975) 69-76.
[28] J.T. White, A.T. Nelson, J.T. Dunwoody, D.D. Byler, D.J. Safarik, K.J. McClellan, Thermophysical properties of U_3Si_2 to 1773K, Journal of Nuclear materials 464 (2015) 275-280.
[29] H. Okamoto, B-U (Boron-Uranium), Binary Alloy Phase Diagrams II Edition 1 (1990) 551-552.
[30] D. Burns, S. Johnson, Nuclear Thermal Propulsion Reactor Materials, Nuclear Materials, IntechOpen2020.
[31] U.C. Nunez, D. Prieur, R. Bohler, D. Manara, Melting point determination of uranium nitride and uranium plutonium nitride: A laser heating study, Journal of Nuclear Materials 449(1-3) (2014) 1-8.
[32] J. Carmack, Update on U.S. Accident Tolerant Fuel Program Nuclear Regulatory Commission Briefing, 2016.
[33] G. Pastore, A. Toptan, Fresh Fuel Properties: Ceramic Compounds, Reference Module in Earth Systems and Environmental Sciences, Elsevier2021.
[34] R. Matthews, K. Chidester, C. Hoth, R. Mason, R. Petty, Fabrication and testing of uranium nitride fuel for space power reactors, Journal of Nuclear Materials 151(3) (1988) 345.
[35] P.A. Lessing, Oxidation protection of uranium nitride fuel using liquid phase sintering, Idaho National Laboratory (INL), 2012.
[36] J. Bugl, A.A. Bauer, Corrosion and oxidation characteristics of uranium mononitride, Battelle Memorial Institute, Columbus, OH, 1964.
[37] R. Dell, V. Wheeler, E. McIver, Oxidation of uranium mononitride and uranium monocarbide, Transactions of the Faraday Society 62 (1966) 3591-3606.
[38] S. Voit, K. McClellan, R. Margevicius, C. Stanek, H. Hawkins, The design and production of actinide nitride fuels at the Los Alamos National Laboratory for the Advanced Fuel Cycle Initiative program, LANL, 2006.
[39] S.M. Bragg-Sitton, M. Todosow, R. Montgomery, C.R. Stanek, R. Montgomery, W.J. Carmack, Metrics for the Technical Performance Evaluation of Light Water Reactor Accident-Tolerant Fuel, Nuclear Technology 195(2) (2016) 111-123.

[40] K.A. Terrani, B.C. Jolly, J.M. Harp, Uranium nitride tristructural-isotropic fuel particle, Journal of Nuclear Materials 531 (2020) 152034.
[41] R.R. Metroka, Fabrication of uranium mononitride compacts, National Aeronautics and Space Administration1970.
[42] H. Muta, K. Kurosaki, M. Uno, S. Yamanaka, Thermal and mechanical properties of uranium nitride prepared by SPS technique, Journal of Materials Science 43(19) (2008) 6429-6434.
[43] K.D. Johnson, J. Wallenius, M. Jolkkonen, A. Claisse, Spark plasma sintering and porosity studies of uranium nitride, Journal of Nuclear Materials 473 (2016) 13-17.
[44] B.J. Jaques, J. Watkins, J.R. Croteau, G.A. Alanko, B. Tyburska-Pueschel, M. Meyer, P. Xu, E.J. Lahoda, D.P. Butt, Synthesis and sintering of UN-UO_2 fuel composites, Journal of Nuclear Materials 466 (2015) 745-754.
[45] G. Kim, J. Ahn, S. Ahn, Grain growth and densification of uranium mononitride during spark plasma sintering, Ceramics International 47(5) (2021) 7258-7262.
[46] V. Tennery, T. Godfrey, R. Potter, Sintering of UN as a function of temperature and N_2 pressure, Journal of the American Ceramic Society 54(7) (1971) 327-331.
[47] H. Matzke, Atomic mechanisms of mass transport in ceramic nuclear fuel materials, Journal of the Chemical Society, Faraday Transactions 86(8) (1990) 1243-1256.
[48] H. Okamoto, NU (nitrogen-uranium), Journal of Phase Equilibria 18(1) (1997).
[49] J. Wallenius, Y. Arai, K. Minato, Influence of N-15 enrichment on neutronics, costs and C-14 production in nitride fuel cycle scenarios, 2004.
[50] K. Johnson, D.A. Lopes, Fabrication of High Density UN with Enriched N-15 for Test Irradiation, 2017 Water Reactor Fuel Performance Meeting, Jeju Island, Korea, 2017.
[51] I.A.E.A.N.D. Section, LiveChart of Nuclides, Vienna, Austria.
[52] M. Paljević, Z. Despotović, Oxidation of uranium mononitride, Journal of Nuclear Materials 57(3) (1975) 253-257.
[53] M.J. Sole, C. Van der Walt, Oxidation and deformation studies of uranium nitride by electron microscopy, Acta Metallurgica 16(4) (1968) 501-510.
[54] S. Sugihara, S. Imoto, Hydrolysis of uranium nitrides, Journal of Nuclear Science and Technology 6(5) (1969) 237-242.
[55] G. Novoselov, V. Kushnikov, V. Baronov, V. Serebryakov, N. Stepennova, Oxidation of uranium and plutonium mononitride and monocarbide briquettes, Soviet Atomic Energy 53(2) (1982) 528-532.
[56] J. Dehadraya, S. Mukerjee, G.R. Rao, V. Vaidya, V. Venugopal, D. Sood, The oxidation of uranium-cerium mononitride microspheres, Journal of Alloys and Compounds 257(1-2) (1997) 313-321.
[57] G.R. Rao, S. Mukerjee, V. Vaidya, V. Venugopal, D. Sood, Oxidation and hydrolysis kinetic studies on UN, Journal of Nuclear Materials 185(2) (1991) 231-241.
[58] K. Johnson, V. Ström, J. Wallenius, D.A. Lopes, Oxidation of accident tolerant fuel candidates, Journal of Nuclear Science and Technology 54(3) (2017) 280-286.
[59] S.A. Kulyukhin, Y.M. Nevolin, A.V. Gordeev, A.A. Bessonov, Gas-phase volume oxidation of uranium mononitride, Radiochemistry 61(2) (2019) 146-155.
[60] J. Antill, B. Myatt, Kinetics of the oxidation of UN and U(CO) in carbon dioxide, steam and water at elevated temperatures, Corrosion Science 6(1) (1966) 17-23.
[61] R.M. Dell, V.J. Wheeler, N.J. Bridger, Hydrolysis of uranium mononitride, Transactions of the Faraday Society 63 (1967) 1286-1294.
[62] A. Roine, HSC Chemistry, Outotec, Pori, 2019.
[63] D.R. Costa, M. Hedberg, S.C. Middleburgh, J. Wallenius, P. Olsson, D.A. Lopes, Oxidation of UN/U_2N_3-UO_2 composites: an evaluation of UO_2 as an oxidation barrier for the nitride phases, Journal of Nuclear Materials 544 (2020) 152700.

[64] R. Dell, V. Wheeler, The ignition of uranium mononitride and uranium monocarbide in oxygen, Journal of Nuclear Materials 21(3) (1967) 328-336.
[65] T. Ohmichi, T. Honda, The oxidation of UC and UN powder in air, Journal of Nuclear Science and Technology 5(11) (1968) 600-602.
[66] L.M. Ferris, Reactions of uranium mononitride thorium monocarbide and uranium monocarbide with nitric acid and other aqueous reagents, Journal of Inorganic & Nuclear Chemistry 30(10) (1968) 2661.
[67] S. Sunder, N. Miller, XPS and XRD studies of corrosion of uranium nitride by water, Journal of Alloys and Compounds 271 (1998) 568-572.
[68] M. Jolkkonen, P. Malkki, K. Johnson, J. Wallenius, Uranium nitride fuels in superheated steam, Journal of Nuclear Science and Technology 54(5) (2017) 513-519.
[69] D.A. Lopes, S. Uygur, K. Johnson, Degradation of UN and UN–U_3Si_2 pellets in steam environment, Journal of Nuclear Science and Technology 54(4) (2017) 405-413.
[70] E.S. Wood, C. Moczygemba, G. Robles, Z. Acosta, B.A. Brigham, C.J. Grote, K.E. Metzger, L. Cai, High temperature steam oxidation dynamics of U_3Si_2 with alloying additions: Al, Cr, and Y, Journal of Nuclear Materials 533 (2020) 11.
[71] J. Abrefah, A.d. Aguiar Braid, W. Wang, Y. Khalil, D.R. Olander, High temperature oxidation of UO_2 in steam-hydrogen mixtures, Journal of Nuclear Materials 208(1) (1994) 98-110.
[72] D.R. Olander, Oxidation of UO_2 by High-Pressure Steam, Nuclear Technology 74(2) (1986) 215-217.
[73] D. Olander, Mechanistic interpretations of UO_2 oxidation, Journal of nuclear materials 252(1-2) (1998) 121-130.
[74] B. Dobrov, V. Likhanskii, V. Ozrin, A. Solodov, M. Kissane, H. Manenc, Kinetics of UO_2 oxidation in steam atmosphere, Journal of nuclear materials 255(1) (1998) 59-66.
[75] J.M. Haschke, Corrosion of uranium in air and water vapor: consequences for environmental dispersal, Journal of Alloys and Compounds 278(1) (1998) 149-160.
[76] P. Malkki, The manufacturing of uranium nitride for possible use in light water reactors, KTH Royal Institute of Technology, 2015.
[77] E.L. Bright, S. Rennie, A. Siberry, K. Samani, K. Clarke, D. Goddard, R. Springell, Comparing the corrosion of uranium nitride and uranium dioxide surfaces with H_2O_2, Journal of Nuclear Materials (2019).
[78] A. Herman, C. Ekberg, A Uranium Nitride Doped with Chromium, Nickel or Aluminum as an Accident Tolerant Fuel, Res. Rev. J. Mater. Sci 5(4) (2017) 83.
[79] J.T. White, A.W. Travis, J.T. Dunwoody, A.T. Nelson, Fabrication and thermophysical property characterization of UN/U_3Si_2 composite fuel forms, Journal of Nuclear Materials 495 (2017) 463-474.
[80] R.A. Potter, J.L. Scott, (U, Zr) N alloy having enhanced thermal stability, Google Patents, 1977.
[81] J.K. Watkins, E. Sikorski, L. Li, B.J. Jaques, Improved hydrothermal corrosion resistance of UN fuel forms via addition of metallic constituents, TopFuel 2019, American Nuclear Society, Seattle, WA, 2019, pp. 1147-1156.
[82] H.J.T. Ellingham, Reducibility of oxides and sulfides in metallurgical processes, Journal of the Society of Chemical Industry Transactions and Communications 63 (1944).
[83] E.J. Lahoda, P. Xu, R.L. Oelrich, H. Shah, J. Wright, C. Lu, Grain boundary enhanced UN and U_3Si_2 pellets with improved oxidation resistance, Google Patents, 2019.
[84] D.R. Costa, M. Hedberg, S.C. Middleburgh, J. Wallenius, P. Olsson, D.A. Lopes, UN microspheres embedded in UO_2 matrix: An innovative accident tolerant fuel, Journal of Nuclear Materials (2020) 152355.
[85] J.H. Yang, D.J. Kim, K.S. Kim, Y.H. Koo, UO_2–UN composites with enhanced uranium density and thermal conductivity, Journal of Nuclear Materials 465 (2015) 509-515.
[86] A.M. Raftery, Fabrication and characterization of UN-USi_x nuclear fuel, 2015.

[87] K.D. Johnson, A.M. Raftery, D.A. Lopes, J. Wallenius, Fabrication and microstructural analysis of UN-U_3Si_2 composites for accident tolerant fuel applications, Journal of Nuclear Materials 477 (2016) 18-23.
[88] S. Uygur, Degradation mechanisms of UN and UN–10U_3Si_2 pellets of varying microstructure by comparative steam oxidation experiments, TRITA-FYS, 2016, p. 48.
[89] D.A. Lopes, A. Claisse, P. Olsson, Ab-initio study of C and O impurities in uranium nitride, Journal of Nuclear Materials 478 (2016) 112-118.
[90] P. Xu, J. Yan, E. Lahoda, S. Ray, Uranium mononitride as a potential commercial LWR fuel, Proceedings of the 2012 International Congress on Advances in Nuclear Power Plants-ICAPP'12, 2012.
[91] D.Y. Lyubimov, A. Androsov, G. Bulatov, K. Gedgovd, Thermodynamic modeling of oxygen dissolution in uranium mononitride at 900–1400 K, Radiochemistry 56(5) (2014) 496-500.
[92] B. Rogozkin, N. Stepennova, A. Proshkin, Mononitride fuel for fast reactors, Atomic Energy 95(3) (2003) 624-636.
[93] A.T. Nelson, P. Demkowicz, Other power reactor fuels, Advances in Nuclear Fuel Chemistry, Elsevier2020, pp. 215-247.
[94] M. DeCrescente, M. Freed, S. Caplow, Uranium nitride fuel development, SNAP-50, Pratt and Whitney Aircraft, Middletown, Conn.(USA). Connecticut Advanced Nuclear Engineering Lab., 1965.
[95] S. Weaver, J. Scott, R. Senn, B. Montgomery, Effects of irradiation on uranium nitride under space-reactor conditions, 1969.
[96] E.S. Solntceva, M.L. Taubin, V.I. Vybyvanets, I.E. Galyov, V.G. Baranov, O.V. Homyakov, A.V. Tenishev, Thermal conductivity of perspective fuel based on uranium nitride, Ann. Nucl. Energy 87, Part 2 (2016) 799-802.
[97] T. Davies, P. Evans, The preparation and examination of mixtures of aluminium nitride (AlN) and uranium mononitride (UN), Journal of Nuclear Materials 13(2) (1964) 152-168.
[98] C.A. Alexander, Metal-actinide nitride nuclear fuel, Google Patents, 1986.
[99] G. Kim, S. Ahn, Thermal conductivity of gadolinium added uranium mononitride fuel pellets sintered by spark plasma sintering, Journal of Nuclear Materials 546 (2021).
[100] A. Raftery, R. Seibert, D. Brown, M. Trammell, A. Nelson, K. Terrani, Fabrication of UN-Mo CERMET nuclear fuel using advanced manufacturing techniques, Oak Ridge National Lab.(ORNL), Oak Ridge, TN (United States), 2020.
[101] R. Potter, T. Godfrey, J. Leitnake, Precipitates in Uranium Nitride, American Ceramic Society Bulletin, Amer Ceramic Soc 735 Ceramic Place, P.O. Box 6136, Westerville, OH 43081-6136, 1966, pp. 822-823.
[102] S. Peterson, R. Adams, D. Douglas Jr, Properties of thorium, its alloys, and its compounds, Oak Ridge National Lab., Tenn., 1965.
[103] L. He, M. Khafizov, C. Jiang, B. Tyburska-Püschel, B.J. Jaques, P. Xiu, P. Xu, M.K. Meyer, K. Sridharan, D.P. Butt, J. Gan, Phase and defect evolution in uranium-nitrogen-oxygen system under irradiation, Acta Materialia 208 (2021) 116778.
[104] K. Insulander Björk, A. Herman, M. Hedberg, C. Ekberg, Scoping Studies of Dopants for Stabilization of Uranium Nitride Fuel, Nuclear Science and Engineering 193(11) (2019) 1255-1264.
[105] N.R. Brown, M. Todosow, A. Cuadra, Screening of advanced cladding materials and UN–U_3Si_5 fuel, Journal of Nuclear Materials 462 (2015) 26-42.
[106] E.S. Wood, J. White, A. Nelson, Oxidation behavior of U-Si compounds in air from 25 to 1000 C, Journal of Nuclear Materials 484 (2017) 245-257.

Cr-doped uranium nitride composite fuels with enhanced mechanical performance and oxidation resistance

Kun Yang[1], Erofili Kardoulaki,[2] Dong Zhao,[1] Bowen Gong,[1] Andre Broussard,[1] Kathryn Metzger,[3] Joshua T. White,[2] Michael R. Sivack,[3] Kenneth J. Mcclellan,[2] Edward J. Lahoda[3] and Jie Lian[1]

[1]Department of Mechanical, Aerospace and Nuclear Engineering, Rensselaer Polytechnic Institute
[2]Los Alamos National Laboratory
[3]Westinghouse Electric Company

* Corresponding author, Email: lianj@rpi.edu; Office: 518-276-6081; Fax: 518-276-6025

Abstract

Cr-doped UN composite fuels with different doping amounts up to 10 wt% are fabricated by spark plasma sintering, and their microstructure and phase heterogeneity are analyzed. Highly densified microstructure and homogeneous Cr distribution are identified for the Cr-doped UN pellets, demonstrating a liquid sintering characteristic with a Cr enriched phase on the UN grain boundary. A ternary phase U_2CrN_3 forms in the Cr-doped UN matrix with doping amounts of 5 wt% and 10 wt%. The SPS densified Cr-doped UN composite pellets display ~~greatly improved~~greatly improved thermal conductivity and simultaneously high hardness and fracture toughness. Of particular significance, the fracture toughness of the Cr-doped UN pellet is ~5.5 MPa-$m^{1/2}$, representing almost 130% enhancement in the fracture toughness of as compared with that of monolithic UN. The incorporation of the Cr doping also increases the onset temperature for oxidation and reduce the maximum oxidation rate. These results highlight that Cr doping and the formation of a ternary phase can be useful to design advanced UN fuels with enhanced thermal-mechanical properties, oxidation resistance, and maintained high fissile element density.

1. Introduction

Accident tolerant fuel (ATF) became a primary focus after the Fukushima accident to replace the current uranium dioxide and zircaloy fuel system to improve accident tolerance of light water reactors (LWRs) [1]. Triuranium disilicide (U_3Si_2), uranium nitride (UN) and uranium carbide (UC) are the favorable candidate fuel materials for LWRs [2]. These compounds exhibit superior thermal conductivity and higher fission element density compared to UO_2. Thus, AFTs can significantly improve the fuel safety margin and prolong the fuel life ~~cycle, and~~cycle and can potentially increase burnups reducing the fuel exchange frequency [3-5]. Among these fuel candidates, mono-uranium nitride fuel (UN) possesses distinct advantages of high thermal conductivity, an extremely high melting point, high fuel density and good chemical compatibility with fuel cladding [6]. In addition, uranium nitride fuel also represents an attractive high-performance nuclear fuel form. It is possible to operate it at high temperatures [7], and UN displays excellent irradiation stability up to 2 at% burnup at temperature up to 1500 ºC [8]. Despite excellent thermal conductivity and high fissile element density, uranium nitride suffers intrinsic problems including low oxidation resistance and it is energetically favorable for UN to react with water vapor. UN fuel can hydrolyze and convert into oxide (in a solid form), constraining its application in LWRs [9,10]. Previous research indicated that the oxidation of UN occurred at an onset temperature around 320 ºC [11], significantly lower than that of other ATFs, such as U_3Si_2, which is typically around 384 ºC in the air [12].

A detailed oxidation study reported that UN reacted with water vapor at ~250 ºC and formed ammonia and hydrogen [13]. A protective layer of UO_2 can then form on the surface of UN, spiking up the onset temperature in moist air up to 270 ºC [13]. However, O_2 diffuses through this UO_2 layer and reacts on the interface with UO_2/U_2N_3 by releasing nitrogen. Oxidation products such as U_3O_8 or UO_3 formed during oxidation [14]. By further

consolidating a highly densified pellet by sparking plasma sintering (SPS), the onset temperature for oxidation can be spiked up to 380-400 ºC as denoted by previous research [15,16]. Further oxidation test under superheated steam/argon mixture at an atmospheric pressure indicated that a complete degradation of UN pellets was obtained within 1 hour in 0.5 bar steam at 500 ºC, and the final products were identified as uranium dioxide, ammonia, and hydrogen gas without detection of nitrogen oxides [16]. Therefore, the key challenges yet to be overcome include: (1) how to increase the onset temperature of oxidation and (2) how to reduce oxidation and corrosion rates to design oxidation and corrosion-resistant uranium nitride fuels.

Extensive efforts are carried out to optimize the UN fuel performance, for instance, by designing UO_2-UN composite fuels showing enhanced uranium density and thermal conductivity [17]. Ortega (2016) successfully densified the UN-U_3Si_2 through liquid phase sintering, which has 30% higher uranium density compare to UO_2, and the composite fuels are highly resistant to steam oxidation and chemical corrosion [18]. In addition, alloying with different additives incorporated into UN matrix has also been proposed to form protective oxide scales and thus improve oxidation resistance. The possibility of doping UN matrix with a suitable protective component, for example, chromium oxide, aluminum oxide, or nickel oxide in a concentration less than 10 vol% was proposed ~~in order to~~to maintain the economic benefit of ATFs and meanwhile not significantly sacrifice the uranium density in the fuel [19]. Lessing (2012) investigated alloying of UN with CrN and Al and reported the formation of a Cr_2O_3 protective surface film under steam or air oxidation analogous to these formed by steam oxidation of Cr-alloyed stainless steels [19]. Herman (2017) demonstrated a uranium nitride fuel doped with chromium (Cr 2.7 wt%), nickel (2.8 wt%), or aluminum (Al 1.5 wt%) prepared by internal sol-gel and carbothermal reduction, and materials show extraordinary stability without degradation post 5 hours of water boiling [20]. Therefore, a uniform protective layer

or multiple layers of Cr_2O_3 would prevent UN from corrosion under operating conditions in the core.

Although the incorporation of Cr or Al in UN matrix can significantly enhance the UN anti-oxidation property, the successful incorporation of Cr or Al strongly depends on the sintering condition according to the phase diagram. Several binary or ternary phases might be produced by tailoring the sintering condition, which can significantly influence fuel performance. For example, high aluminum addition into U_3Si_2 led to the formation of a ternary phase $U_3Al_2Si_2$, reducing the fissile element density below that of UO_2 and defying the purpose of utilizing the high-density silicide fuel as an ATF candidate [21]. ~~Similar to~~Like U_3Si_2, Cr incorporation into UN can form ~~an~~a U-Cr-N ternary phase, which can be stable at a temperature between 1200 ºC to 1600 ºC based on the first ~~principle~~principal calculation by Holleck (1968) [22]. The latest research conducted by Mishichenko (2021) supported the theoretical calculation by observing the existence of U_2CrN_3 during the Cr incorporation into UN fuel matrix consolidated by SPS under 1500 ºC [23]. The presence of the ternary compounds can be significant for the performance of the UN composite fuel. However, whether this effect is beneficial or detrimental to the fuel performance still require further study.

In the present study, we report promising results of significantly improved oxidation resistance of nitride fuels by synergizing Cr-doping and post thermal annealing to form the ternary phase of U_2CrN_3 and chromium oxide protective scales. The highly densified Cr-UN composite fuel with various weight ratios were sintered through powder metallurgy combining high energy ball milling (HEBM) and SPS consolidation. Their key properties and characteristics relevant to ATF applications were characterized. We demonstrate that a small amount of Cr addition (5 wt%) is sufficient to create a protective layer upon thermal annealing in the air to increase the onset oxidation temperature of the UN pellets above 450 ºC, meanwhile significantly increasing the thermal conductivity and mechanical properties. These

results highlight an effective strategy of using a minimal amount of alloying elements to maximize doping effects and design oxidation and corrosion resistant UN fuels. SPS as an advanced fuel sintering technology holds immerse potentials in manufacturing high-quality UN fuels with well-controlled property.

2. Materials and Methods

2.1 Powder preparation and sparking plasma sintering

The original powders of high purity UN were produced through the powder metallurgy in Los Alamos National Lab (LANL) following the identical procedure to our previous publication [15]. The as-received UN powders were subsequently refined into smaller particle sizes ~~in order to~~to enhance their sinterability with HEBM. The high purity chromium powders were purchased from Alfa Alsea with a powder size of 40 μm. The UN and Cr starting powder particle sizes can be controlled by tailoring the ball milling cycles. Several different UN and Cr starting powder combinations were chosen to fabricate the Cr-doped UN pellets (see Table I). The UN and Cr powder were then mixed homogeneously through ball milling for 4 cycles at a similar ball milling condition with the identical ball milling speed and idle time.

The consolidation of the dense UN pellets was conducted inside an environmentally controlled glovebox interfaced with a Fuji 211x SPS (Fuji, Dr. Sinter SPS 211-LX, Saitama, Japan). The graphite die with an inner diameter of 10-mm was loaded with 1.2 grams of ball milled-UN powders. The sample loading procedure and sintering conditions were previously tested [15]. The SPS sintering was conducted with a heating rate of 200 ºC/min until reaching the maximum target temperature of 1550 ºC and held isothermally at 1550 ºC for 10 min. Axial pressure was increased simultaneously to 50 MPa from 10 MPa and holding for 10 min as well, followed by free cooling in argon atmosphere down to room temperature. During SPS sintering and cooling, the SPS chamber was purged with high purity argon with a flow rate of 1 L/min. After sintering, the dense pellet was safe to be removed from the chamber, following

mechanically polishing by silicon carbide papers and diamond paste. The physical density was measured using an Archimedes method with anhydrous ethanol acted as measuring media. The as-measured theoretical density indicated in Table 1 was estimated based on the 100% density UN-Cr pellet.

2.2 Microstructural characterization of the sintered pellet

~~Cyrstalline~~Crystalline phase characterization of each Cr-UN pellets ~~were~~was carried out through X-ray diffraction (XRD) patterns with a Panalytical X'Pert XRD system (Westborough, MA, USA) assembled with a Cu Kα irradiation target, the wavelength of which is 1.5406 Å. The scanning range is 10° to 90° with a scanning step of 0.05°, with a scanning rate of 2 s/step. The microstructure and elemental analysis of the as-sintered Cr-UN pellets were determined through scanning electron microscopy (SEM) and energy dispersion X-ray spectroscopy (EDS) a Versa Dual-beam system. The average grain size was characterized using a rectangular intercept method according to the American society for testing and materials (ASTM) E112-196 standard (1992) [26].

2.3 Thermal mechanical properties measurements and dynamic oxidation testing

The thermal diffusivity of the as-sintered Cr-UN pellets was measured with a laser flash apparatus (LFA-457, NETZCH, Bavaria, Germany). The Cr-UN pellets were pre-coated with sprayed graphite paste on both sides before the measurement. After loading the sample, the chamber of the LFA was vacuumed three times and ultra-high purity Argon was purged in the chamber with a flow rate of 100 ml/min throughout the measurement. The heating rate is kept to 5 °C/min during the measurement and the thermal diffusivity was evaluated with a Cape-Lehman pulse correction model that uses non-linear regression. Thermal diffusivity was measured three times in the range of 300 K-800 K with an interval of 100 K. Corresponding thermal conductivity κ (w • (m • k)$^{-1}$), was calculated based on the correlation $\kappa = \alpha \rho c_p$, where

ρ is the density of the sample pellet, α is the measured thermal diffusivity ($mm^2 \cdot s^{-1}$), and c_p is the specific heat capacity [27]. The sample density corresponding to the temperature applied herein to calculate the thermal conductivity was previously corrected by the following Equation (1), where ρ_0 is the density determined at the reference temperature T_0, and the calculated mean value of α_p stands for the coefficient of thermal expansion of UN [28]

$$\rho = \frac{\rho_0}{[1+\alpha_p(T-T_0)]^3} \quad (1)$$

The specific heat capacity c_p was corrected based on each temperature by taking consideration of the Cr and UN phases through a Neumann-Kopp rule by the rule of mixtures of the constituent compounds [29]. The thermal conductivity was further normalized according to 100% TD based on the following equation (2) [30], where P is the measured porosity, the k and $k_{measured}$ stands for the corrected thermal conductivity for a full-dense specimen and the measured thermal conductivity of the specimen, respectively.

$$k_{measured} = k(1-P)^{1.5} \quad (2)$$

The mechanical properties of the as-sintered samples were characterized by micro-hardness through a LECO M-400 Microhardness Tester to create a micro sized diamond-shaped indentation on the polished sample surfaces. Each indentation was generated at room temperature (25 °C) with a load of 1 kgF (~9.8 N) and holding for 15 seconds. More than 10 indentations were generated for every specimen and following by taking average of the indentation size according to the standard ASTM C1327 [31]. Hardness and fracture toughness were derived by evaluating the SEM images taken at each indentation. Specifically, hardness

(GPa) was calculated using Eq. (3), where P is the load applied and α is the mean of the indentation's diagonal lengths (μm).

$$H = 1.854\frac{P}{\alpha^2} \quad (3)$$

Fracture toughness was subsequently derived using Eq. (4), where σ is a parameter associated with indenter geometry, E is Young's modulus based on the previous report [32], H is the hardness derived from Eq. (3), P is the applied load, and C is the mean of crack lengths measured from the top of the diamond-shaped indentation to the end of the cracking line.

$$K_{IC} = \sigma(\frac{E}{H})^{0.5}(\frac{P}{C^{1.5}}) \quad (4)$$

The dynamic oxidation testing was conducted using a simultaneous DSC/TGA system (SDT650, TA instrument, DE, USA) that measures the mass change and heat flow with the elevation of the temperature at a weight sensitivity of 0.1 μg. In the current work, thermogravimetric analysis (TGA) analysis was applied to monitor the oxidation behavior of the Cr-doped UN pellets ~~in order to~~to determine the onset temperature and weight gain during oxidation following the same testing protocol reported in our previous publications [12,15]. The onset temperature of the oxidation was taken as the transition point of the heat flow curve, as described in Ref. (33) [33]. Time to complete oxidation was defined as the time from oxidation onset to the full oxidation of the pellet until weight did not change during dynamic oxidation testing.

3. Results and Discussion

3.1 Crystalline phase stability of the SPS densified UN pellets

Dense UN pellets of various Cr doping amounts of 3, 5, and 10 wt% were prepared by HEBM, followed by SPS consolidation. The as-received UN powders were first ball milled for 80 cycles to reduce the particle size, while the purchased Cr powder was ball milled for 40 cycles, respectively. The mixture of the Cr and UN powders was further ball milled for an additional 4 cycles ~~in order to~~to mix them homogeneously before SPS consolidation. ~~All of~~All the SPS-densified pellets achieve a physical density above 90 TD% as shown in Table 1. The theoretical density gradually increases from 91% to 94.5% with the increasing Cr doping amount from 3 wt% to 10 wt% for UN ball milled under 80 cycles. This is consistent with the liquid sintering effect and microstructure showing the Cr encapsulated UN phase and dense grain boundaries, which will be discussed later.

The crystalline phases of the as-sintered Cr-UN were studied and their corresponding XRD profiles and semi-quantitative analysis were shown in Figure 1. Despite the secondary phase of UO_2, a ternary crystalline phase containing Cr (U_2CrN_3) formed by the interaction between UN and Cr. In addition, metallic Cr also remained in the Cr-UN pellets, which can be attributed to the non-fully reacted Cr metal additives. The phase content was obtained by refining the XRD profile by Rietwald peak refinement as indicated in Figure 1. The ternary phase of U_2CrN_3 gradually increases up to 39.6 wt% with increasing Cr additives from 3 wt% to 10 wt%. Meanwhile, the UO_2 phase is around 8 wt% among three different Cr doping ratios but the original UN phase significantly reduced from 3 wt% to 10 wt% Cr doping, as evidenced by the phase degradation of UN upon reaction with Cr. Therefore, the formation of the uranium oxide secondary phase can only be impacted by the sintering temperature while increasing the Cr doping amount can significantly promote the formation of ternary phase U_2CrN_3. In addition, the lattice constant decreases by increasing the Cr doping (see Figure 1c), which can be attributed to the incorporation of Cr with smaller ionic radius compare to UN. Similar lattice

contraction by incorporating Cr can be found for the Cr-U_3Si_2 composite fuel as denoted by Gong (2020) [34].

3.2 **Elemental distribution of the SPS densified Cr-UN pellets**

Figure 2 demonstrates the SEM images (in a BSE mode) of the polished surface of the Cr-doped UN with different Cr amounts from 3 wt% to 10 wt% and different starting UN powder sizes. The grain sizes are approximately similar among ~~all of~~all the Cr-doped UN pellets, and the average grain sizes are between 3-6 μm as shown in Figure 2a-c. The Cr additives were embedded uniformly in the dense UN matrix due to the liquid sintering effect, especially on the grain boundary of the fuel matrix and no significant pores can be identified in the sintered pellets. The distinct dual-crystalline phase structure can be clearly identified with the dark region belongs to a Cr-enriched area (lighter element) while the lighter region can be attributed to the UN phase (heavy element). An uniform distribution of Cr additives on the grain boundaries and junctions of UN particles can also be observed in the 10 wt% Cr-doped UN pellets sintered from 4 cycle-ball milled powders ~~(Figure~~(Figure 2d). EDS elemental mappings, as shown in Figure 3, are obtained by scanning the selected area on the 5 wt% Cr-doped UN pellet showing distinct phase compositions. The UN phase is encapsulated by the Cr-enriched phase marked as green color. In addition, tiny amount of oxygen seems to be enriched in the region with strong Cr signals as demonstrated in Figure 3b, suggesting a co-existence of minor chromium oxide with U_2CrN_3. However, the amount of the minor chromium oxide phase might be too ~~low, and~~low and cannot be detected by XRD. The elemental analysis of UN with 10 wt% of Cr doping can be seen in Figure 4. Semi-quantitative elemental analysis from an EDS spectrum 1 as shown in Figure 4 clearly demonstrates that the Cr-additives (obvious Cr enriched zones) are embedded on the grain boundaries or junctions of UN particles. The UN grains surrounded nearby also contain a large amount of Cr as denoted by the spot analysis and the atomic ratio is approximately equal to the secondary phase of U_2CrN_3 (spectrum 2). For

comparison, the grain on the external of the secondary phase U_2CrN_3 clearly demonstrates a UN enriched feature as the atomic ratio is approximate to 1.0 (spectrum 3). According to the previous research by Holleck (1975), the ternary phase of U_2CrN_3 is predicted to form in the temperature range between 1200 to 1600 ^oC, which is consistent with the SPS sintering temperature herein (1550 ^oC) [22]. This ternary phase, although described with a different crystallographic space group, can be viewed as a distorted version of UN, as demonstrated by the research conducted by Mishchenko (2021) [23]. Therefore, an elemental~~ly~~ gradient distribution of Cr can be observed at the grain boundaries and junctions ~~as a result of~~because of the Cr diffusion and reaction pathway.

To investigate the impact of the oxide layer on its oxidation resistance, thermal annealing under 250 ^oC for 30 mins in air are performed for some of the Cr-UN pellets. The microstructure and elemental analysis of the 5 wt% Cr-doped UN pellet post thermal annealing are demonstrated in Figure 5. Compared to the Cr-UN pellet prior to the thermal annealing, a large amount of oxidized region can be observed around the Cr phase as denoted in the spot analysis in region 4. The corresponding semi-quantitative analysis suggests that chromium oxide and the ternary phase of U_2CrN_3 are the major phases in region 4. Therefore, thermal annealing in atmosphere significantly propagates the Cr oxidation into chromium oxide, which might act as a potential passive layer on the UN. The light color showed on the back scattering image in Figure 5 (region 1) demonstrates the coexistence of both UN and uranium oxides, which can be attributed to the slow oxidation of UN pellet during thermal annealing. The elemental mapping of Cr in Figure 5 also confirms the large area of coexistence of Cr with U surrounding the single phase of Cr. Instead of forming uranium oxide, which has higher corrosion resistance compared to single-phase Cr, the Cr tends to distribute at the grain boundaries as both metallic chromium or oxides supported by the elemental analysis in Figure

5 for thermally annealed samples in air. The metallic chromium will gradually be oxidized to chromium oxide by prolonging the thermal annealing time.

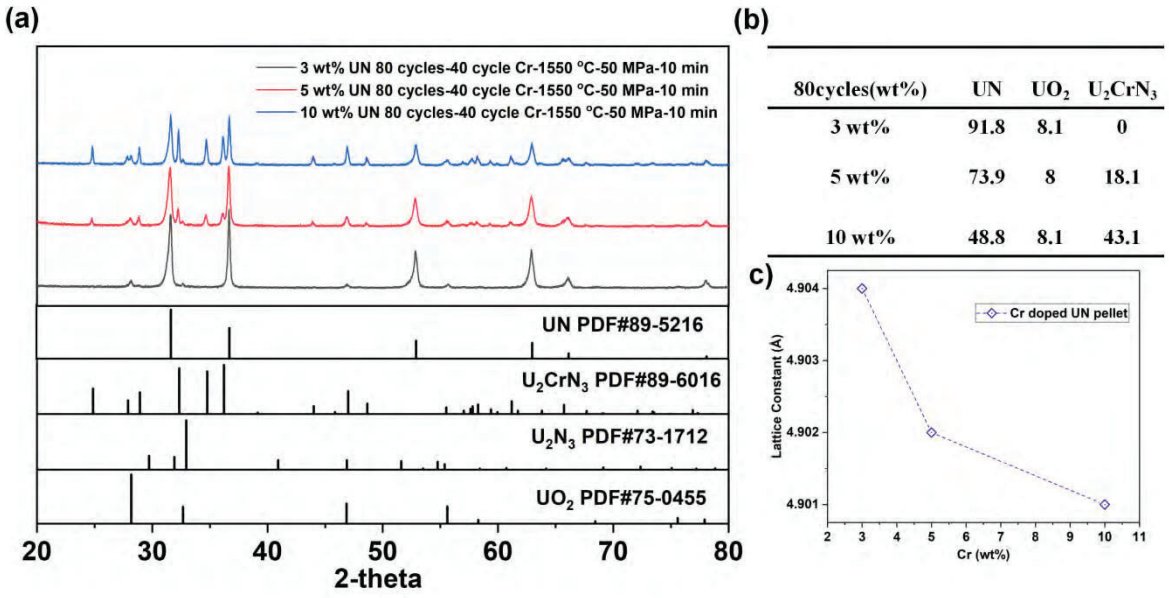

Figure 1. XRD diffraction patterns (a), phase contents (b) and corresponding lattice constants of the as-sintered Cr-UN pellets with different Cr-doping amounts.

Table 1 Summary of Cr-doped UN sample pellets densified by SPS

Sintering conditions	Composition	Relative density (%)
3 wt% Cr-UN 80 cycles 1550 °C-50 MPa-10 min	80 cycles UN+40 cycles Cr	91.1
5 wt% Cr-UN 80 cycles 1550 °C-50 MPa-10 min	80 cycles UN+40 cycles Cr	92.2
10 wt% Cr-UN 80 cycles 1550 °C-50 MPa-10 min	80 cycles UN+40 cycles Cr	94.5
10 wt% Cr-UN 4 cycles 1550 °C-50 MPa-10 min	4 cycles UN+40 cycles Cr	94.2

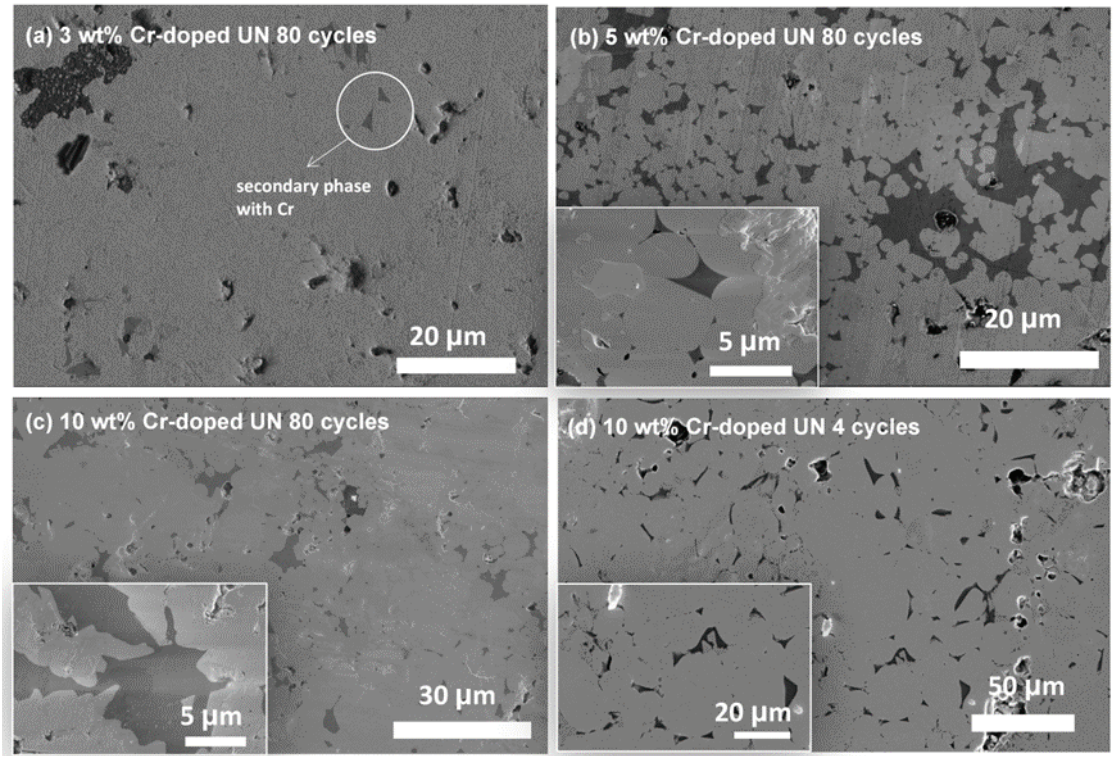

Figure 2. SEM images of the polished surfaces of the Cr-UN pellets with different Cr-dopings sintered at 1550 ºC under 50 MPa.

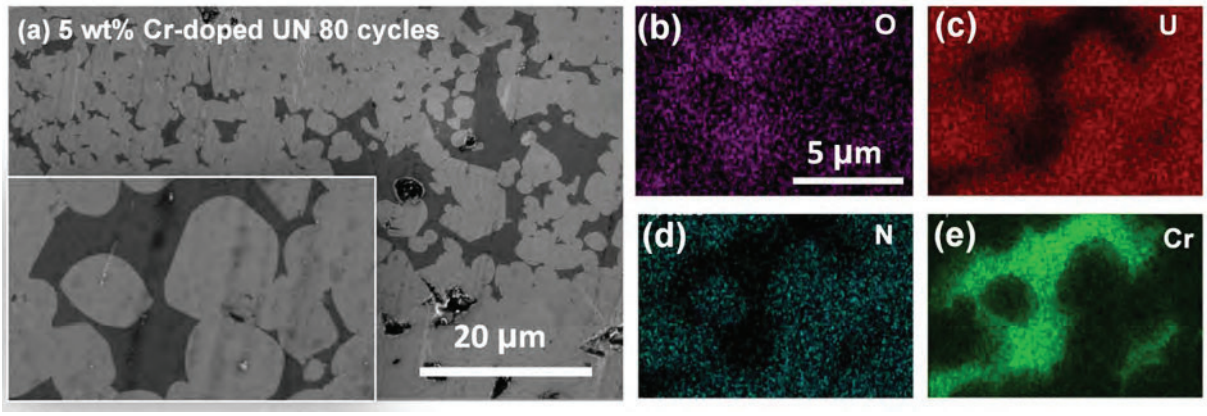

Figure 3. SEM images of the polished surface and elemental analysis of the corresponding area for the 5 wt% Cr-doped UN pellet sintered at 1550 ºC under 50 MPa.

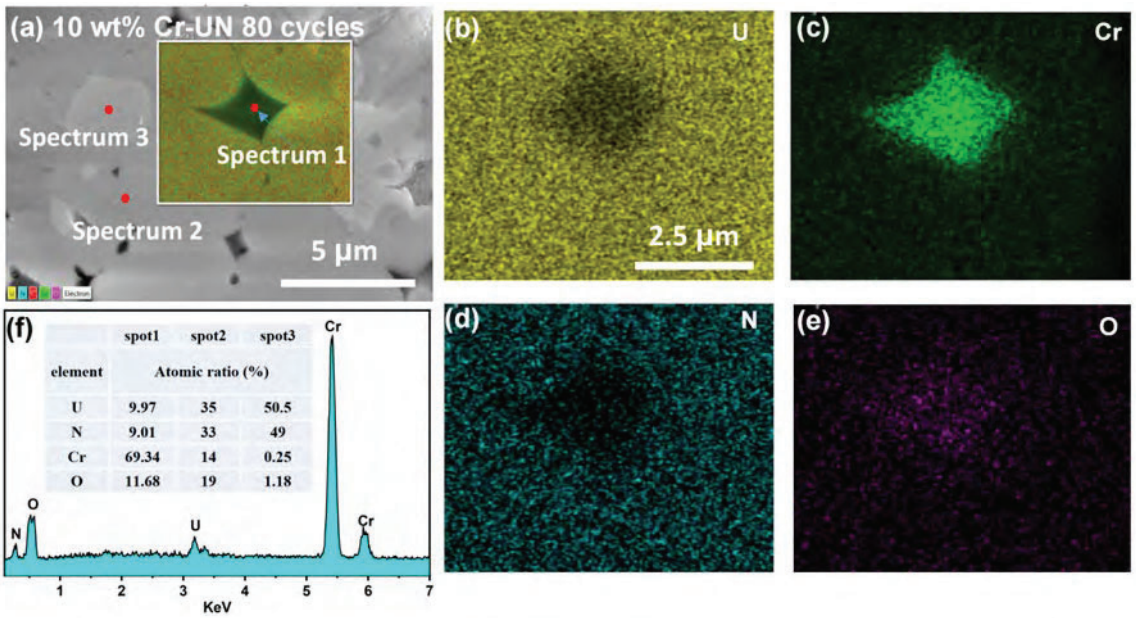

Figure 4. SEM images of the polished surface and elemental analysis of the corresponding area for the 10 wt% Cr-doped UN pellet sintered at 1550 ºC under 50 MPa.

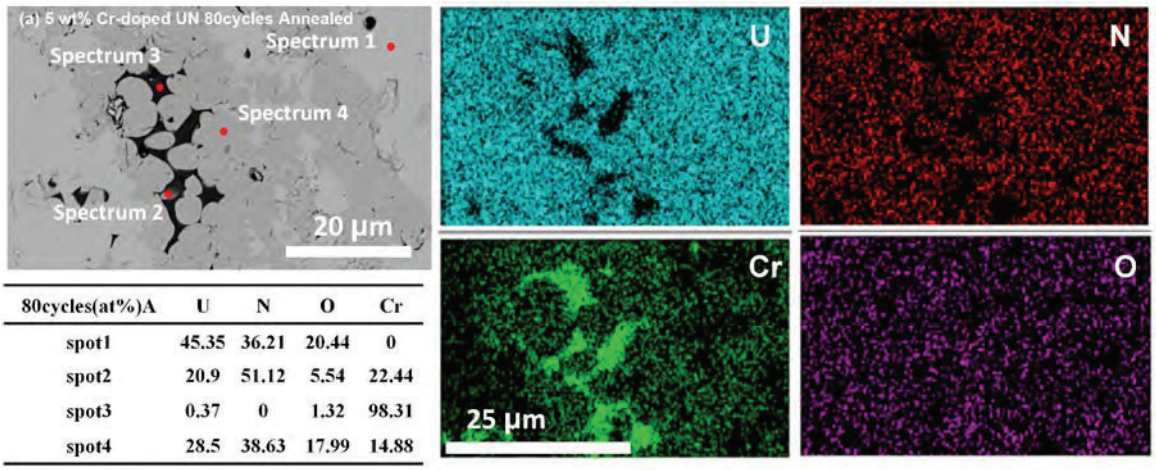

80cycles(at%)A	U	N	O	Cr
spot1	45.35	36.21	20.44	0
spot2	20.9	51.12	5.54	22.44
spot3	0.37	0	1.32	98.31
spot4	28.5	38.63	17.99	14.88

Figure 5. SEM images of the polished surface and elemental analysis of the corresponding area for the 5 wt% Cr-doped UN pellet post thermal annealing at 250 ºC for 30 mins in air.

3.3 Mechanical and thermal properties of the UN pellets and microstructure impact

In the section, mechanical properties including micro hardness and fracture toughness of the as-sintered Cr-UN pellets are analyzed by based on the Vicker Hardness testing (Figure 6). Figures 6a-b show SEM images of the micro-indentations generated on the surfaces of the 3

wt% and 10 wt% Cr-doped UN pellets. In general, the hardness of the Cr-doped UN is within the range of 6.0 – 7.5 GPa, much higher than that of the monolithic UN synthesized under the same condition (-5.7 GPa), but lower than that of submicron grain-sized UN pellet consolidated with 100 cycle ball milled UN powders [15]. This can be explained by the Hall-Petch effect in ~~which~~which hardness is negatively correlated to the grain size. The increased grain boundaries through grain refinement ~~lead~~led to the misalignment and the pile-up of dislocations at grain boundaries to impede the movement of dislocations [36]. The addition of Cr additives increases the hardness of the composite pellets, consistent with a previous observation of Cr doped Fe_2B [37]. The elevation of the micron hardness by Cr doping can probably be attributed to a solution strengthening effect previously confirmed by the Al-doped U_3Si_2 [39]. The highest hardness can be found for the UN doped with 5 wt% of Cr, followed by the 10 wt% Cr doped UN and the 3 wt% Cr-UN pellet. The results strongly support the idea that Cr addition strengthens the UN grain boundaries by cross-linking the UN grains through liquid sintering. The as-sintered Cr-doped UN composites also display significantly higher hardness than UO_2 (in general 5 MPa) and comparable to the U_3Si_2 sintered by Gong (2020) [12,38]. Although the monolithic UN pellet consolidated with 100 cycles of UN powder demonstrates higher hardness, the fracture toughness is lower than the Cr doped UN pellets.

The fracture toughness of the monolithic UN generally lies within the range of 2.5 – 3.5 MPa-$m^{1/2}$ [15], lower than the UN pellets doped with 3 wt%, 5 wt% and 10 wt% Cr. The fracture toughness (5.5 MPa-$m^{1/2}$) of the Cr-doped UN composites is significantly higher as compared with that of monolithic UN (~2.4 MPa-$m^{1/2}$) with 80 cycle-ball milling powders, representing almost 130% enhancement in the fracture toughness. The higher fracture toughness of the Cr-doped UN pellet than the undoped UN counterpart could be attributed to the mismatch of lattice thermal expansion between UN ($7.5x10^{-6}$/°C at 200 °C) [28] and Cr ($5.7x10^{-6}$/°C at 200 °C) [39]. During cooling of the SPS consolidation process, the less volume

contraction of Cr additives may apply compressive stress on UN matrix, enhancing the capability against crack formation and propagation. Crack propagation as shown in the SEM images in Figure 6a-b demonstrates an intra-granular fracture feature with crack propagating through the UN grains as well as the Cr enriched phase. The cracks are likely to propagate on the Cr-enriched phase as shown in the 10 wt% Cr-doped UN pellet (Fig. 6b), which can be used to explain the enhancement of fracture toughness with the doping of Cr. Although it is obvious that Cr-doped UN demonstrates higher toughness, the effect of the ternary phase formation (U_2CrN_3), particularly in the higher Cr-doped pellets, on the mechanical properties is unclear. Nevertheless, ~~all of~~all the Cr-doped UN pellets have significantly higher fracture toughness than uranium oxides, beneficial to mitigate fuel cladding mechanical interaction during reactor operation. The high mechanical properties, particularly fracture toughness, might be useful to increase the oxidation and corrosion resistance due to the improved resistance against crack propagation, which is demonstrated by the results of the dynamic oxidation test later.

Thermal diffusivity measured by the LFA and thermal conductivity of the Cr-doped Un pellets calculated from the thermal diffusivity are summarized in Figure 7a-b and compared with these of monolithic UN pellets, UO_2 and U_3Si_2. The thermal conductivities of the Cr-doped UN pellets increase typically with temperature, ~~similar to~~like metallic materials, facilitating the thermal transportation and enhancing the fuel safety margin compared to UO_2. This behavior is consistent with the reported thermal conductivity of U_3Si_2 [12]. The 80 cycle-ball milled UN pellet with 5 wt% Cr incorporation demonstrates 10% increasing in the thermal conductivity for the same sintering condition. However, the enhancement in thermal conductivity for the 10 wt% Cr doping and 80 cycle-ball milled UN pellet at the same sintering conditions is not significant. This might be attributed to the formation of a large amount of U_2CrN_3 instead of metallic Cr, as the metallic Cr generally exhibit higher thermal conductivity

than UN. On the other hand, the large grain size of UN (4 cycles UN) exhibits superior high thermal conductivity with 40% enhancement as compared to the other UN sample pellets, highlighting the important impact of microstructure on thermal transport behavior. The incorporation of highly thermally conductive Cr additive into UN pellet can improve thermal conductivity of the composite fuels, particularly at elevated temperatures.

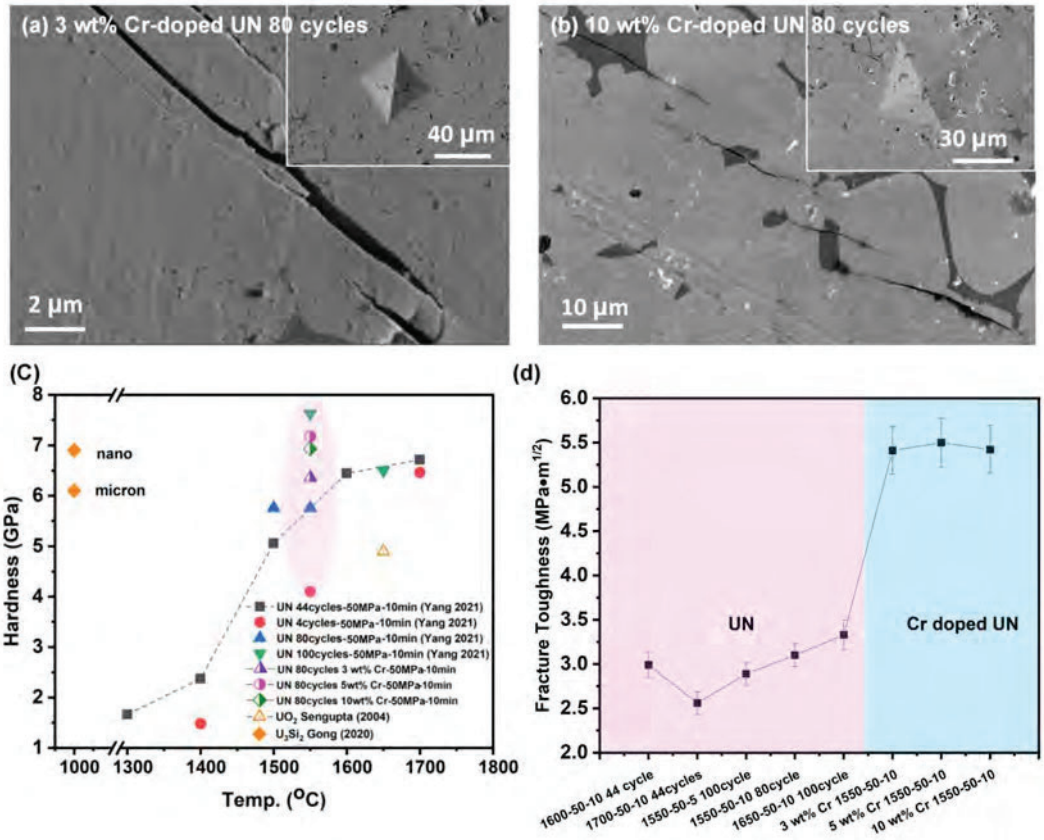

Figure 6. SEM images of the micro-indentation of the 5 wt% (a) and 10 wt% (b) Cr-doped UN pellets, and the determined hardness (c) and fracture toughness (d).

Table 2 Summary of the Vicker hardness and fracture toughness of the Cr-doped UN pellets

Sintering conditions	Hardness (GPa)	Toughness (MPa $m^{1/2}$)
3 wt% Cr-UN 80 cycles 1550 °C-50 MPa-10 min	6.4	5.6
5 wt% Cr-UN 80 cycles 1550 °C-50 MPa-10 min	7.3	5.7
10 wt% Cr-UN 80 cycles 1550 °C-50 MPa-10 min	7.0	5.6
80 cycle 1550 °C-50 MPa-10 min	5.9	3.1
100 cycle 1550 °C-50 MPa-10 min	7.7	2.9
44 cycle 1600 °C-50 MPa-10 min	6.5	3.0

44 cycle 1700 °C-50 MPa-10 min	6.7	2.6

3.4 Dynamic oxidation behavior of the SPS consolidated Cr-doped UN pellets

The dynamic oxidation behavior of the SPS densified Cr-doped UN pellets is tested by a thermogravimetric analyzer, and the results are shown in Figure 7c-d. Compared to the monolithic UN pellet, the Cr-doped UN pellets exhibit improved oxidation resistance as demonstrated by the increase in the on-set temperature for oxidation with increased Cr-doping amount. For comparison, the on-set oxidation temperature for the 5 wt% Cr doped UN is around 419.5 °C, higher than the monolithic UN fabricated under the same condition (401.3 °C). Further increasing Cr addition to 10 wt% does not enhance the oxidation resistance significantly and the onset temperature is slightly higher for the 10 wt% Cr-UN (425.7 °C) than the materials synthesized at the same conditions. Therefore, an optimized Cr doping could be identified around 5 wt% based on a combination of the enhanced thermal-mechanical properties, oxidation resistance and meanwhile maintained high fissile element density.

To study the impact of post thermal annealing on the oxidation resistance, the 5 wt% Cr-UN pellets are thermally annealed in the atmosphere at a low temperature of 250 °C for 30 mins ~~in order to~~to form a ternary phase or a protective oxide scale. The on-set oxidation temperature increases to 452.5 °C for the 5 wt% Cr-doped UN pellet post thermal annealing, 25% higher than the monolithic UN previously reported [15]. The formation of a possible passive oxidation protective layer after thermal annealing in the 5 wt% Cr-doped samples, might be beneficial to improve the oxidation resistance of the composite fuels. This is consistent with the SEM-EDS analysis showing the gradually enriched zone of chromium oxide which slow down the oxygen diffusion and passivate the matrix against further oxidation.

The addition of Cr into the UN composite fuels reduces the maximum weight gain, and the lowest oxidation weight gain among the three Cr doping ratios belongs to the 3 wt% Cr-UN, which is below 10 wt% as compared to the undoped UN (13 wt%). The reduction in the

oxidation weight gain can be attributed to the formation of the chromium oxides as well as the slight oxidation of UN during the SPS consolidation and the post thermal annealing as confirmed by the SEM-EDS in Figure 5. Furthermore, the oxidation weight gain is lower for the Cr-doped UN post thermal annealing, corresponding to the gradual formation of the uranium oxides. Oxidation rates (summarized in Table 3) for each sample are also derived based on the TGA testing as evaluated by the weight gain percentage over the duration for oxidation. No significance differences can be observed in the oxidation rate among the undoped and doped Cr-UN, although the Cr doping can significantly delay the onset temperature for oxidation and improve the oxidation resistance of the composite fuel. Therefore, the incorporation of Cr into UN pellet can offer better oxidation resistance compared to the monolithic UN.

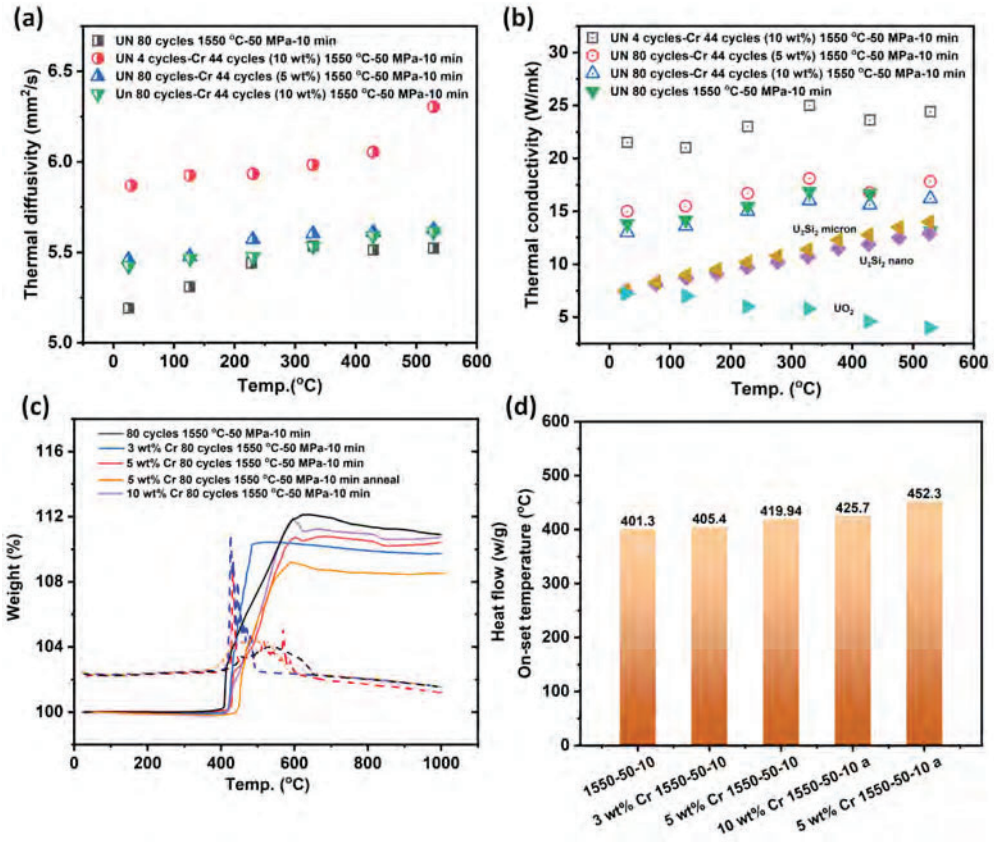

Figure 7. Thermal diffusivity (a), thermal conductivity (b), and dynamic oxidation behavior (c) of the Cr-doped UN pellets with different Cr amount; (d) summary of the onset oxidation temperature of the Cr-doped UN composite fuels as compared with monolithic UN.

Table 3 Summary of the dynamic oxidation tests of the SPS densified pellets sintered at different conditions as measured by a TGA-DSC thermal analyzer. The ramping rate is 10 °C/min.

Onset temperature (°C)	Onset oxidation Temperature	Completion point (°C)	Oxidation rate (wt%/min)	Weight gain (%)
1550 °C-50 mpa-10 min 80 cycles	401.3	705.1	0.40	10.70
3 wt% 1550 °C-50 mpa-10 min 80 cycles	405.4	513.2	0.93	9.99
5 wt% 1550 °C-50 mpa-10 min 80 cycles	419.5	600.9	0.59	10.55
10 wt% 1550 °C-50 mpa-10 min 80 cycles	425.7	600.5	0.67	11.79
5 wt% 1550 °C-50 mpa-10 min 80 cycles annealed	452.3	606.5	0.62	9.58

4. Summary

In summary, dense Cr-doped UN pellets with different doping amounts of 3, 5 and 10 wt% are fabricated by SPS, and their physical, thermal-mechanical and oxidation properties of the SPS densified Cr-doped UN pellets are investigated systematically. The microstructure and elemental analysis indicate a multiphase feature of a ternary phase U_2CrN_3 and a Cr-enriched oxide distributed at grain boundaries and junctions of UN grains. The Cr doped UN demonstrates superior thermal conductivity for UN pellets with larger grain size to monolithic UN. The SPS-densified Cr-UN pellets possess simultaneously high hardness (6.4-7.3 GPa) and ~~significantly improved~~significantly improved fracture toughness about 5.7 MPa $m^{1/2}$ than monolithic UN. The addition of Cr and post-thermal annealing can generally enhance oxidation

resistance of the UN pellets as evidenced by the increase in the onset temperature for oxidation and reduced maximum oxidation rates. The addition of minimum Cr doping into the UN fuel matrix could be beneficial to design advanced UN fuels with simultaneously enhanced thermal-mechanical properties, oxidation resistance and thus improved fuel performance.

Acknowledgment

This work was supported by the US Department of Energy's (DOE's) Office of Nuclear Energy under a Nuclear Engineer University Program (award number: DE-NE0008947) and by Westinghouse Electric Company under the DOE ATF program supported by the Department of Energy under Award Number DE-NE0008824. This report was prepared as an account of work sponsored by an agency of the United States Government. Neither the United States Government nor any agency thereof, nor any of their employees, makes any warranty, express or implied, or assumes any legal liability or responsibility for the accuracy, completeness, or usefulness of any information, apparatus, product, or process disclosed, or represents that its use would not infringe privately owned rights. Reference herein to any specific commercial product, process, or service by trade name, trademark, manufacturer, or otherwise does not necessarily constitute or imply its endorsement, recommendation, or favoring by the United States Government or any agency thereof. The views and opinions of authors expressed herein do not necessarily state or reflect those of the United States Government or any agency thereof.

Reference

[1] Sitton S.M.B., Braase L., Montgomery R., Stanek C.R., Montgomery R.H. Enhanced accident tolerant LWR fuels: metrics development. LWR Fuel Perform Meeting Top Fuel, 2013.

[2]Ortega L.H., Blamer B.J., Evans J.A., McDeavitt S.M. Development of an accident-tolerant fuel composite from uranium mononitride (UN) and uranium sesquisilicide (U_3Si_2) with

increased uranium loading. Journal of Nuclear Materials, 471(2016)116-121.

[3]Uno M., Nishi T., Takano M. Thermodynamic and thermophysical properties of the actinide nitrides. Comprehensive Nuclear Materials, Oxford, 61-85 (2012).

[4]Szpunar B., Szpunar J.A. Thermal conductivity of uranium nitride and carbide. International Journal of Nuclear Energy, 178360(2014)1-7.

[5]Ross S.B., El-genk M.S. Thermal conductivity correlation for uranium nitride fuel between 10 and 1923K. Journal of Nuclear Materials, 151(1988)313-317.

[6]Metroka R.R. Fabrication of uranium mononitride compacts. Lewis Research Center, NASA TN D-5876.

[7] Alexander C.A. Metal actinide nitride nuclear fuel (patent number 4624828). ~~Retrived~~Retrieved from Grove city 1986.

[8] Potter R.A., Scott J.L. Continuation of development of nitrides for space nuclear reactors (NASA CR-134498, ORNL-TM-4496). 1974

[9]Malkki P. The manufacturing of uranium nitride for possible use in light water reactors. Royal Institute of Technology, Swiss. Thesis. (2015)

[10]Jolkkonen M., Malkki P., Johnson K., Wallenius J. Uranium nitride fuels in superheated steam. Journal of Nuclear Science and technology, 54(2017)513-519.

[11] Paljevic M., Despotovic Z. Oxidation of uranium mononitride. Journal of Nuclear Materials, 57(1975)253-257.

[12]Gong B.W., Yao T.K., Lei P.H., Harp J., Nelson A.T., Lian J. Spark plasma sintering (SPS) densified U_3Si_2 pellets: microstructure control and enhanced mechanical and oxidation properties. Journal of Alloys and Compounds, 825(2020)1-10.

[13]Costa D.R., Hedberg M., Middleburgh S.C., Wallenius J., Olsson P., Lopes D.A. Oxidation of UN/U_2N_3-UO_2 composites: an evaluation of UO_2 as ~~a~~an oxidation barrier for the nitride phases. Journal of Nuclear Materials, 544(2021)1-10.

[14]Dell R.M., Wheeler V.J., Mciver E.J. Oxidation of uranium mononitride and uranium monocarbide.

[15] Yang K., Kardoulaki E., Zhao D., Gong B.W., Broussard A., Metzger K., White J.T., Sivack M.R., ~~Mcclellan~~McClellan K.J., Lahoda E.J., Lian J. Uranium nitride (UN) pellets with controllable microstructure and phases fabrication by spark plasma sintering and fuel properties. Journal of Nuclear Materials (under review)

[16] Johnson K., Strom V., Wallenius J., Lopes D.A. Oxidation of accident tolerant fuel candidates. Journal of Nuclear Science and Technology, 54(2017)280-286.

[17] Jolkkonen M., Malkki P., Johnson K., Wallenius J. Uranium nitride fuels in superheated steam. Journal of Nuclear Science and technology, 54(2017)513-519.

[18] Yang J.H., Kim D.J., Kim K.S., Koo Y.H. UO_2-UN composites with enhanced uranium density and thermal conductivity. Journal of Nuclear Materials, 465(2015)509-515.

[19] Ortega L.H., Blamer B.J., Evans J.A., McDeavitt S.M. Development of an accident-tolerant fuel composite from uranium mononitride (UN) and uranium sesquisilicide (U_3Si_2) with increased uranium loading. Journal of Nuclear Materials, 471(2016)116-121.

[20] Lessing P. Oxidation Protection of uranium nitride fuel using liquid phase sintering. Idaho Falls, ID: Idaho National Lab, (INL/EXT-12-24974) (2012).

[21] Herman A., Ekberg C. A uranium nitride doped with chromium, nickel or aluminum as an accident tolerant fuel. Research and Reviews: Journal of material sciences, 5(2017)83-99.

[22] Wood E.S., Moczygemba C., Robles G., Acosta Z., Brigham B.A., Grote C.J., Metzger K.E., Cai L. High temperature steam oxidation dynamics of U3Si2 with alloying additions: Al, Cr and Y. Journal of Nuclear Materials, 533(2020)152072.

[23] Holleck H. Ternary phase ~~equilibra~~equilibria in the systems actinide transition metal carbon and actinide transition metal nitrogen. Int. Atomic Energy Agency (1975) Vienna. CONF-741030-P2.

[24] Mishchenko Y., Johnson K.D., Wallenius J., Lopes D.A. ~~Design~~Design, and fabrication of UN composites: from first principles to pellet production. Journal of Nuclear Materials, 553(2021)153047.

[25]Malkki P. The manufacturing of uranium nitride for possible use in light water reactors. Royal Institute of Technology, Swiss. Thesis. (2015)

[26]Metroka R.R. Fabrication of uranium mononitride compacts. Lewis Research Center, NASA TN D-5876.

[27]ASTM E112-E196. Standard test methods for determining average grain size. ASM International, West Conshohocken, (2004).

[28] Cape, J. and Lehman, G. (1963) Temperature and Finite Pulse-Time Effects in the Flash Method for Measuring Thermal Diffusivity. Journal of Applied Physics, 34, 1909-1913.

[29] Hayes S.L., Thomas J.K., Peddicord K.L. Material property correlations for uranium mononitride I. Physical properties. Journal of Nuclear Materials, 171(1990)262-270.

[30] Barin I. Thermochemical data of pure substance. VCH, Weinheim, 1995.

[31] Rice R.W. Porosity of ceramics: properties and applications, CRC press, Boca Raton, FL., 1998.

[32] ASTM C1327. Standard test method for Vickers indentation hardness of advanced ceramics. 2019

[33]Muta H., Kurosaki K., Uno M., Yamanaka S. Thermal and mechanical properties of uranium nitride prepared by SPS technique. Proceedings of the symposium on spark plasma synthesis and sintering. 43(2008)6429-6434.

[34] Wood E.S., White J., Nelson A. Oxidation behavior of U-Si compounds in air from 25 to 1000 ^{o}C. Journal of Nuclear Materials, 484(2017)245-257.

[35] Gong B.W., Cai L., Lei P.H., Metzger K.E., Lahoda E.J., Boylan F.A., Yang K., Fay J., Harp J., Lian J. Cr-doped U3Si2 composite fuel under steam corrosion. Corrosion Science, 177(2020)109001.

[36] Gong B.W., Yao T.K., Lei P.H., Cai L., Metzger K.E., Lahoda E.J., Boylan F.A., Mohamad A., Harp J., Nelson A.T., Lian J. U_3Si_2 and UO_2 composites densified by spark plasma sintering for accident tolerant fuel. Journal of Nuclear Materials, 534(2020)1-8.

[37] Scattergood R., Koch C. A modified model for Hall-Petch behavior in nano-crystalline materials. Scripta Metallurgy Material, 27(1992)1195-1200.

[38] Wei X., Chen Z.G., Zhong J., Wang L., Wang Y.P., Shu Z.L. First principles investigation of Cr doped Fe2B: structural, mechanical, electronic and magnetic properties. Journal of Magnetism and Magnetic Materials, 456(2018)150-159.

[39] Sengupta A.K., Basak C.B., Jarvis T., Bhagat R.K., Pandey V.D., Majumdar S. Effect of titania addition on hot hardness of UO_2. Journal of Nuclear Materials, 325(2004)141-147.

[40] Dubrovinskaia N.A., Dubrovinsky D.A., Saxena S.K. Thermal expansion of chromium (Cr) to melting temperature. Calphad, 21(1997)497-508.

Design and fabrication of UN composites: from first principles to pellet production

Yulia Mishchenko[a], Kyle D. Johnson[b], Antoine Claisse[c], Janne Wallenius[a], Denise Adorno Lopes[a,c]

[a]*KTH-Royal Institute of Technology, Stockholm, Sweden, yuliam@kth.se*

[b]*Studsvik Nuclear AB, Nyköping, Sweden*

[c]*Westinghouse Electric Sweden AB, Västerås, Sweden*

Abstract

In this study the composite UN-AlN, UN-Cr, UN-CrN and UN-AlN-CrN pellets were fabricated, and the advanced microstructure with different modes of interaction between the phases was obtained. The dopants for this study were selected based on the results of the ab-initio modeling calculations, that identified the AlN phase as insoluble and CrN and Cr as soluble in the UN matrix. This method allowed to investigate the possibility of improving the corrosion resistance of UN by protecting the grain boundaries with insoluble AlN and by hindering the diffusion of oxygen through the bulk by adding soluble CrN and Cr.
The UN powder was produced by hydriding-nitriding method and mixed with the AlN, CrN and Cr powders. High density (>90 %TD) composite pellets were sintered by Spark Plasma Sintering (SPS). The microstructure of the pellets was analysed using SEM coupled with EDS. The phase purity was determined by XRD. For the first time the presence on the ternary U_2CrN_3 phase was observed in the composite pellets containing Cr and CrN dopants. The results obtained in this study allowed to assess the methodology for fabrication of the UN composites with controlled microstructure.

1. Introduction

Uranium nitride (UN) is a potential candidate for the nuclear fuel alternatives being considered as part of the Accident Tolerant Fuel (ATF) initiative. UN is known for its high thermal conductivity, high melting temperature, high fissile density and good fission product retention [1], [2] . These positive qualities of the UN fuel will allow to improve the safety of the system during the reactor operation, as well as to bring the economic benefits by increasing the length of the fuel cycle [3]. In addition to that, the high fissile density of the UN fuel will provide the neutronic margins, which will allow the use of cladding materials with high oxidation resistance and low hydrogen production (such as FeCrAl) [4], [5], [6]. However, the oxidation resistance of UN is significantly inferior to the UO_2 fuel, violating the ATF concept itself [2], [7], [8], which drives the motivation for development of techniques for improving the oxidation resistance properties of UN.

In order to improve the oxidation resistance of UN different number of alloying systems such as ceramics (cercer) and metals (cermet) have been considered [9]. In previous studies potential additives were identified based on their thermophysical and oxidation resistance properties. Composite pellets containing UN and such materials as U_3Si_2, UO_2, Cr, Ni, Al have been manufactured and analysed [10], [11], [12], [13], [14]. Different experimental methods have been applied to produce such composites including powder metallurgical methods and sol-gel method, as in the case of UN pellets doped with Cr, Ni and Al that were produced by Herman et al. [13]. In some cases, the complexity of the fabrication process creates difficulty in understanding the interaction between the alloying elements and the fuel matrix. As an example, in the sol-gel method the high temperatures applied during the carbothermic reduction and pelletising resulted in a significant amount of Cr being lost due to evaporation [13]. Another issue in the design of these composites was the absence of information on how the additives would interact with the UN matrix, as observed for UN-UO_2 composites where significant reaction under sintering occurred favouring an equilibrium of UO_2-U_2N_3 [15], [16], [11]. In some studies, the attempt has been made to predict the possible formation of the solid solution between the UN matrix and the additive using the Hume-Rothery Rules, as in the case with Herman et al. However, the comparison of the atomic radii, electronegativities and the valences of the uranium atoms and the additive atoms predicted that no solid solution could be formed between CrN or AlN and the matrix of UN [13]. However, this type of assessment does not provide information about the existence of possible ternary compounds, that can be found in the phase diagrams, as in the case with U-Cr-N, where the formation of the ternary U_2CrN_3 was predicted by Holleck [17]. The presence of the ternary compounds can be important for the performance of the composite materials. The information about all possible interactions between the additives and the UN is needed in order to eliminate the candidates that will be completely unsuitable for these purposes.

The interaction behaviour between UN and such materials as TiN, YN, CeN, NbN has been previously investigated experimentally by Holleck [18], [19], [20]. Composite materials containing the above-mentioned nitrides and UN were prepared by such methods as arc melting followed by homogenisation and long-term annealing of powder mixtures. The results obtained in those studies identified such systems as UN-CeN, UN-NbN, UN-YN to be completely miscible in each other, whereas TiN was shown to be soluble in UN from about 1 mol% at 1700°C to 4 mol% at 2400°C. However, investigating the possible interaction between a wide range of available materials and the UN experimentally could be a very expensive and time-consuming process. Therefore, a preselecting tool for identifying the potential candidates and predicting their behaviour is highly desirable.

In this study a methodology of using atomistic modeling to predict the interaction behaviour between various metallic and nitrogenous additives with UN is described. The goal is to use this as a preselecting tool for the fabrication of UN compounds in order to help determine if a given material and phase will be soluble in the base UN matrix. Elements from different electronic configuration groups being 3*p* (Al, Si, P), 3*d* (V, Ti, Cr), 4*d* (Y, Zr, Nb, Mo), and 4*f* (La, Ce) were analysed using the proposed method. From the calculated systems Al and Cr were selected to demonstrate the interaction trends predicted by the modeling. Advanced fabrication using materials as AlN-nano, Cr-nano metal, CrN-micro and sintering by Spark Plasma Sintering (SPS) technique with temperatures not exceeding 1650°C was applied to produce selected composite pellets. High purity UN powders were synthesised using the hydriding-nitriding method from metallic uranium for obtaining high purity materials. A further intention of this work is to provide a fabrication routine, i.e. selection of powder morphology and chemical form, sintering parameters, etc., which can be used as guidelines for

producing UN composites with a tailored microstructure. The results of the experiments confirmed the predictions of the atomistic modeling, making it a valuable tool to be used in future research into composite fuels design.

2. Methodology

2.1 First-principles calculations

DFT calculations were performed with the Vienna Ab initio Simulation Package (VASP) [21], [22]. The electron exchange correlation was modeled using the generalized gradient approximation (GGA) of Perdew, Burke and Ernzernhof (PBE) [23] and projector augmented wave (PAW) potentials [24], [25]. To better describe the correlated nature of the U 5*f* electrons, GGA + *U* method with Dudarev's rotationally invariant approach [26] and an effective U, U_{eff}= 1.9 eV (U_{eff} = U – J) was used. The unit cells for UN were fully relaxed using a cut-off energy of 520 eV. Convergence criteria of 0.02 eV/Å^{-1} and 10^{-5} eV were adopted for the forces and total energy, respectively. A 2 × 2 × 2 supercell of UN was used for calculating the defect formation energies. A γ-centered Monkhorst-pack k-point spacing of <0.25 Å^{-1} was applied for sampling the Brillouin zone for each structure. No methods to avoid the metastable states were used, as the symmetry was heavily broken by the incorporation of foreign atoms and the energetics of point defects in UN are one order of magnitude larger than the ones of metastable states.

The general trend for incorporation of elements from electronic configuration groups 3*p* (Al, Si, P), 3*d* (V, Ti, Cr), 4*d* (Y, Zr, Nb, Mo) and 4*f* (La, Ce) in the UN matrix was evaluated by calculating the formation energies of point defects. The incorporation was modeled considering the uranium site for all elements in addition to the nitrogen site for the 3*p* elements. The formation energy was calculated using Eq. (1), where E^0_{tot} and E^D_{tot}, are the total energies of the supercell without and with a defect, respectively, and μ^0_i is the standard state chemical potential (DFT calculated energy per atom) of the element *i*. The standard states used for each element are listed in **Table 1**. ΔN^D_i is the number of atoms of type *i* added ($\Delta N^D_i > 0$) or removed ($\Delta N^D_i < 0$) from the perfect supercell to create the defect, and the sum is over all added and removed elements. Additionally, incorporation energy analysis can be extended to evaluate another phase as the source of the incorporated atom. This can be done by adding a correction term $\Delta\mu_i$ (in Eq. (1)) as the change in the chemical potential of element *i* resulting from an N-phase equilibrium (i.e., from the local environment), which can be calculated by solving the set of linear equations (Eq. (2)), where c_{ik} is the coefficient representing the concentration of each atom considering the phase equilibria. On the scopes of this work the equilibrium of UN-(Nitride Phase)-N_2 was also considered and the nitride phases evaluated are also listed in **Table 1** with their respective calculated $\Delta\mu$.

$$\Delta E_f^D = E_{tot}^D - E_{tot}^0 - \sum_{i=1}^{N} \Delta N_i^D \left(\mu_i^0 + \Delta\mu_i\right) \quad (1)$$

$$\Delta H_{f,k} = \sum_{i=1}^{N} c_{ik} \Delta\mu_i \quad (2)$$

It is important to mention that the applications of GGA + *U* results in inconsistency for direct comparison with reference state α-Uranium, more appropriately modeled by GGA framework. Therefore, the methodology that predicts formation enthalpies by mixing GGA and GGA+*U* results proposed by Jain *et al*. [27] was applied, where the experimentally reported formation energy of U_2N_3 [28] were used for correction.

Table 1: Standard states and their respective μ_o (eV/atom), and the nitride phases with the calculated $\Delta\mu$ (eV/atom).

Standard state	**Space group**	**μ_o (eV/at)**	**Nitride phases**	**Space group**	**Calculated Δμ**
Al	Fm-3m [225]	-3.7481	AlN	P63mc [186]	-3.192
Si	Fd3m [227]	-5.4234	Si_3N_4	P63/m [176]	-3.066
P		-8.1781	P_3N_5	C2/c [15]	-1.435
Ti	P6/mmm [191]	-7.8899	TiN	Fm3m [225]	-3.816
V	Im3m [229]	-9.0866	VN	Fm3m [225]	-2.328
			V_8N	P42/mnm [136]	-0.421
Cr	Im3m [229]	-9.6367	CrN	Fm3m [225]	-1.31
			Cr_2N	P31m [162]	-0.771
Y	P63/mmc [194]	-6.4674	YN	Fm3m [225]	-3.758
Zr	P63/mmc [194]	-8.5475	ZrN	Fm3m [225]	-3.74
Nb	Im3m [229]	-10.1131	NbN	P6m2 [187]	-2.52
Mo	Im3m [229]	-10.4345	MoN	P63mc [186]	-1.118
			Mo_2N	I41/amd [141]	-0.552
Pd	Fm3m [225]	-5.1765			
La	Fm3m [225]	-4.9353	LaN		-2.998
Ce	Fm3m [225]	-5.9315	CeN		-3.38

This analysis creates a way to evaluate the trend of the materials to react with the UN fuel matrix not only from the metal state but the nitride forms. **Figure 1** offers the summary of the modeling method.

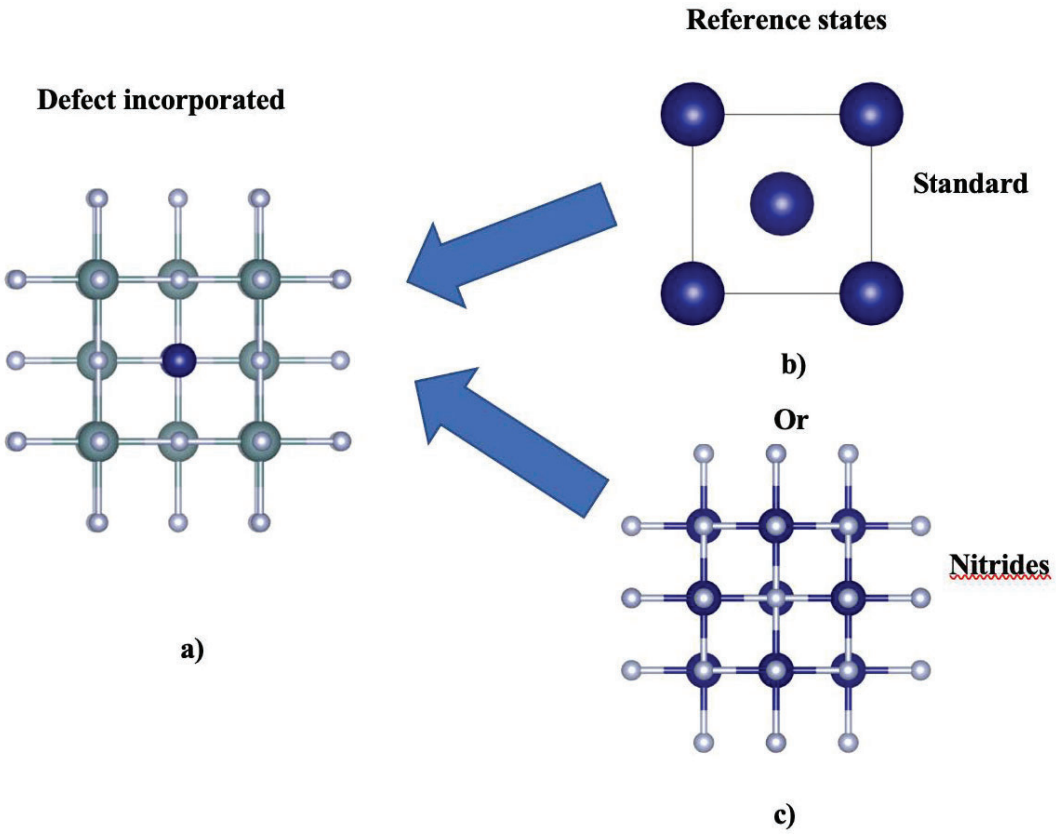

Fig. 1. (a) UN with an incorporated impurity; (b) standard reference state and (c) nitride phase both considered as the source for the impurity in the reaction with UN.

The obtained results for incorporation energies are shown in **Figure 2**. In this notation negative incorporation energies are thermodynamically favourable to occur.

From the results it is possible to observe that in general the elements at 3*p* configuration presented limited solubility in the UN matrix, independently of the site considered. One exception is P in the nitrogen site that seems to be energetically favourable. This may reflect the existence of the phases U_3P_4, UP and UP_2 [29], [30] and point out for the trend of P to strongly interact with uranium atoms. Another way to evaluate the incorporation energies is to correct the chemical potential for the impurity considering the origin as other phases. To understand the trends of solution here we also evaluated the incorporation considering stable nitride phases reported in literature. For the 3*p* group the AlN, Si_3N_4 and P_3N_5 phases were considered in this analysis. The result is also presented in **Figure 2** (orange). With this result it is possible to observe limited solubility for the 3*p* materials, from both pure and nitride states. It is possible to notice that when the nitrides are considered the reaction with UN becomes even less likely. Therefore, these elements and mainly their respective nitride phases can be used as additive to UN to produce, for example, coated grain.

The 3*d* transition metals present a different trend from the previous group. For these elements considerable solubility is observed considering the pure metal state as a reference. As the incorporation of the impurities required a U_{vac}, the amount of solution formed may be limited by the number of this defect created with temperature over the sintering process. A way to

extend the solubility is to provide at the same time nitrogen and keep the ratio metal/nitrogen close to 1:1. Therefore, it once again becomes of interest to re-evaluate the trend by correcting the chemical potential using the nitride phases as reference state. For this purpose, the TiN, CrN, Cr_2N, VN and V_8N were considered. The results can be seen in **Figure 2** (orange and grey). From this analysis it can be noticed that the incorporation of Cr in UN is still favourable even when the Cr-nitride phases (CrN and Cr_2N) are considered as the source for the incorporation impurity. This behaviour permits preservation of the metal/nitrogen ratios which can promote significant solubility. On the other hand, Ti and V nitride phases seem not very likely to react with UN. These pure metals will form solution with UN but with the solubility limited by the fraction of U_{vac}. The obtained results for Ti are in agreement with the outcomes of the experimental investigations performed on the U-N-Ti system by Holleck [18]. Therefore, Ti and V metal and nitrides can be used to combine doped grain with partially coated grain by using a combination of metal and nitride phases.

The elements of 4*d* transition metals also demonstrated a considerable degree of solubility in UN matrix when considered reaction with the pure metal state. The trend for the solubility decreases progressively from Y to Mo, demonstrating that the increase in the electronic configuration plays significant role in the solubility in UN matrix. The reaction from the nitride phases still seems very likely, being negative for Y and Zr while relatively small for the Nb and Mo, which could be overcome by entropy terms, i.e., increase in temperature. The solubility of of NbN, ZrN and YN in the matrix of UN has been investigated by Holleck et al. in a number of experimental studies. It was found that at 2000°C the system UN-ZrN demonstrate complete solid solubility [18]. The solid solution between NbN and UN was obtained by annealing the composite pellets made from the constituent nitrides in the temperature range between 1800°C and 1900°C for a long time. The X-ray analysis of the obtained product confirmed that the system UN-NbN is completely miscible [19]. The same results were obtained for UN-YN samples prepared by Holleck et al. The metallographic studies of the samples concluded that the system UN-YN shows complete solid solubility [20]. In the light of these results, these elements and their respective nitride phases can mainly be used to produce UN composite with doped grains.

The 4*f* elements demonstrated solubility in the UN matrix. This is in agreement with the experimental results obtained for the LaN-UN and CeN-UN systems [20], [19]. However, the equilibrium solid solution between CeN and UN was difficult to achieve experimentally and required long-term annealing at high temperatures [19]. This observation indicates that kinetics play significant role for these systems that might be influenced by slow diffusion of heavy elements. Although the described here methodology based on the modeling cannot predict how fast or slow the equilibrium in the system could be reached, it can still be used as a preselecting tool for experimental studies.

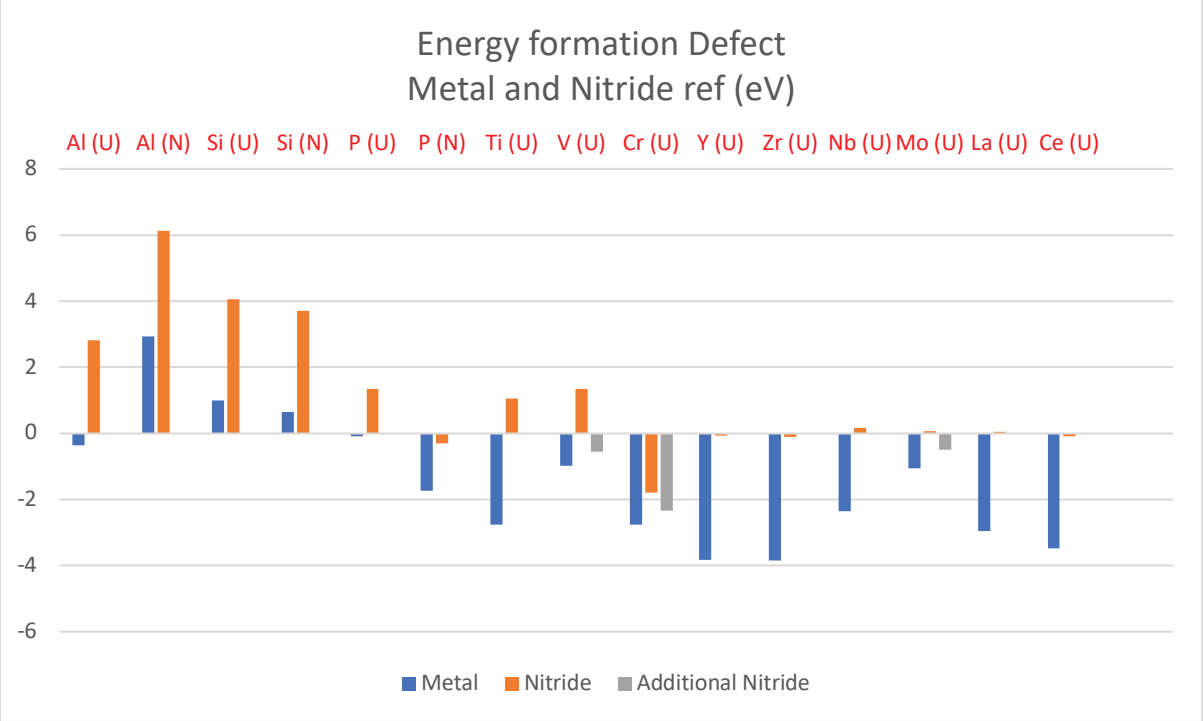

Fig. 2. Incorporation energy formation as reference from metals and nitrides

Considering the obtained results, it is possible to design composite materials with engineered microstructure by combining the insoluble in UN materials to protect the grains and soluble compounds to increase the corrosion resistance of the bulk. This concept is explained by **Figure 3.**

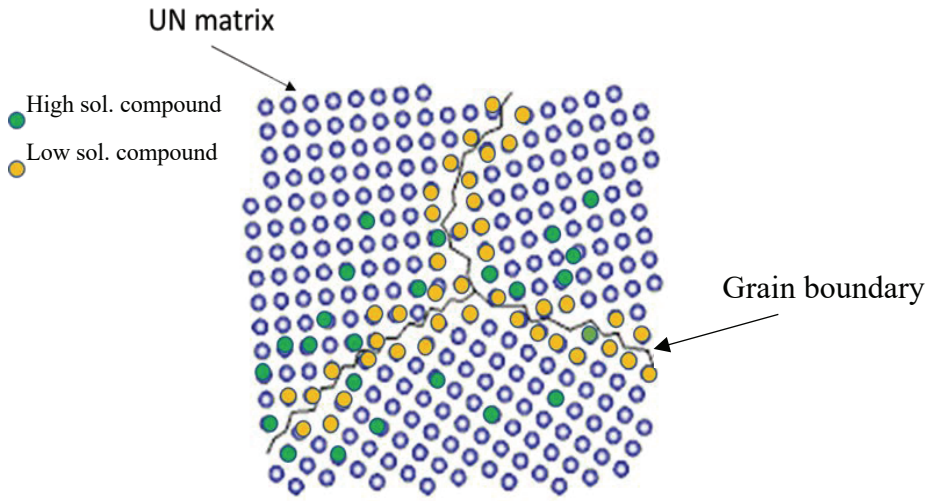

Fig. 3. Illustration of the microstructure resulting from the use of low and high solubility phases in UN matrix.

From **Figure 2** it is evident that chromium metal as well as chromium nitrides (CrN and Cr_2N) have negative values for the defect incorporation energies and, therefore, are good candidates for testing the concept of doped grains experimentally. The value for the defect incorporation energy of AlN, on the other hand, is positive, suggesting that no interaction should take place

between UN and AlN. For that reason, AlN, Cr and CrN were selected as dopants for experimental investigation. In the next section the fabrication of UN composites is presented, taking in consideration the interaction trends presented in this section. Four different systems were sintered being (i) low solubility, addition of AlN; (ii) high solubility from metal Cr and (iii) nitride CrN phase and a (iv) compound containing both low (AlN) and high (CrN) solubility to demonstrate the capability to produce a highly tailored microstructure by combining different incorporation trends.

2.2 Pellet fabrication and characterization

Composite samples were manufactured to validate the design proposed by the modeling calculations. The additives were chosen to demonstrate different modeling trends for interaction behaviour between the additives and the fuel UN matrix, namely: insolubility, limited solubility, and considerable solubility. The additive phases that were predicted to be insoluble in the UN matrix were added in the form of nanopowder (< 100nm). The purpose was to test the capability of the insoluble phase to coat the grains of UN and to work functionally to prevent it from coming into contact with the oxidising agent. Introducing the additive in the form of nanopowder would allow the material to easier distribute itself along the grain boundaries. Matrix-soluble additives were added in the form of micropowders (< 5μm). These materials were expected to form the solid solution with the UN matrix. The solid solution can operate to protect the bulk of the material from oxidation by self-passivation.

The UN powder used in this study was synthesised by the hydriding-nitriding method from natural uranium metal (acquired from the Institutt for Energiteknikk, Norway) following the procedure and the heating profile described in previously published work [31]. The resulting UN powders were transferred into an argon filled glovebox for handling. The XRD analysis on the as fabricated powder was performed using a Siemens D5000 diffractometer with Cu k-alpha target at 40 mA current and 35 kV voltage using an air-tight sample holder (Bruker, A100B138). The Rietveld refinement of the X-ray diffraction pattern on the produced UN powder was performed using Maud software [32] and the Crystallography Open Database [33]. The measured value of the lattice parameter is 4.8889 ± 0.0003 Å, corresponding to a face-centered cubic uranium mononitride [34]. Based on the obtained value of the lattice parameter the concentration of carbon impurities could be estimated to be around 300 ppm using the results of the study performed by Muromura and Tagawa [35]. Elemental analysis was performed to determine the powder oxygen and nitrogen concentrations by the inert gas fusion method using a LECO TC-136. Nitrogen and oxygen were measured to 5.4 wt% and 1600 ppm, respectively. Theoretical value for nitrogen concentration in UN is 5.56 wt% [36].

The AlN nanopowder was obtained from Sigma-Aldrich Sweden AB (98% purity), CrN (99.99% purity) and Cr (99.95% purity) powders were provided by Nanografi. The XRD analysis of the as received CrN powder confirmed the additional presence of a Cr_2N phase, with Rietveld analysis indicating a composition of 75 wt% Cr_2N and 25 wt% CrN. For simplicity, this powder will still be referred to as CrN for the remainder of the text.

The powders were mixed to obtain the following compositions in the produced pellets: UN-10AlN, UN-20AlN, UN-10Cr, UN-20Cr, UN-10CrN, UN-20CrN, UN-5AlN-5CrN, UN-10AlN-10CrN, where the numeric indicator refers to the volume percent of the secondary phase(s). The composite pellets were produced using different mixing techniques. For the first batch of pellets the composite powders were mixed mechanically inside of a glass vial with

small grinding balls. Subsequent batches were ground together in a mortar and pestle. For the pellets containing both AlN and CrN, these powders were premixed together before adding UN powder and continuing to mix. This second routine was identified as more suitable to produce a homogenous microstructure and subsequent samples were therefore produced using this route. The composite powders were transferred into graphite (9.3 mm inner diameter) sintering dies lined on the inside with graphite paper. The composite pellets were sintered using the SPS technique (Dr. Sinter, 530-ET, Stockholm University, Department of Materials and Environmental chemistry), located inside of an Ar-filled glovebox (maintained with less than 0.1 ppm O_2 and less than 0.1 ppm H_2O). Approximately 3 g of composite powders were used for each pellet. Sintering was performed in vacuum (the sintering chamber was depressurised to 2 Pa). The sintering parameters including the applied uniaxial pressure, maximum sintering temperature, holding time at the maximum temperature, as well as the densities of the sintered pellets and final oxygen composition of the sintered pellets are presented in **Table 2**. The composition of the pellets in the table is given in volume percent. The pellets that have been sintered from the premixed powders are identified by the superscript.

Table 2: Sintering parameters used to produce composite pellets.

Pellet	***Sintering temperature °C***	***Holding time, min***	***Uniaxial pressure, MPa***	***Pellet density, %TD***	***O_2, wt%***
UN	1650	3	45	97	0.3
UN-10AlN	1650	3	45	97	1.02
UN-10AlN^{premix}	1650	3	45	97	0.66
UN-20AlN^{premix}	1650	3	45	98	1.57
UN-10Cr^{premix}	1450	5	70	93	0.39
UN-20Cr^{premix}	1450	5	70	96	0.43
UN-10CrN	1450	5	70	96	0.38
UN-20CrN^{premix}	1550	5	70	99	0.22
UN-5AlN-5CrN	1550	5	70	96	0.66
UN-5AlN-5CrN^{premix}	1550	5	70	98	0.43
UN-10AlN- 10CrN^{premix}	1550	5	70	99	1.01

The density of the sintered composite pellets was measured by the Archimedes method in chloroform at the ambient temperature (T=22°C). The density of chloroform at this temperature is 1.48 g/cm^3. The amount of open porosity was measured by submerging the pellet in chloroform and pulling high vacuum (0.05 bar, just above the chloroform vapor pressure).

Phase volume fractions of the composite pellets were calculated by performing the quantitative image analysis of the micrographs using ImageJ software [37]. For each pellet composition 5 micrographs of varying magnification were analysed using the software. The area occupied by each phase on the micrograph was selected and the average value for the area fraction was obtained. The volume fraction of the corresponding phase was taken to be the measured area fraction. From the volume fraction of each phase and the theoretical densities of the individual phases (14.33 g/cm^3 for UN [34], 3.26 g/cm^3 for AlN [38], 7.19 g/cm^3 for Cr [39] and 12.7 g/cm^3 for U_2CrN_3 [40]) the density of the composite pellets was obtained by the rule of mixtures. Sintered composite pellets were cut into small pieces using a diamond saw to provide small amounts of sintered material for elemental analysis. Concentrations of oxygen and nitrogen in the sintered pellets were measured by inert fusion using a LECO TC-136, with three replicates for each material.

Transversal sections of pellets were mounted in bakelite, ground using silicon carbide paper, and polished with diamond suspension and cloth sheets. Microstructural characterization was performed by scanning electron microscopy (SEM) and energy-dispersive x-ray spectrometry (EDS) using Philips XL-30 ESEM microscope (KTH, Department of Chemistry) and JEOL JSM-7000F microscopes (Department of Materials and Environmental Chemistry, Stockholm University). Larger pieces of the sintered pellets were crushed into powder and the XRD analysis was performed on the sintered material at Studsvik Nuclear AB using a Panalytical, X-Pert^3 Power diffractometer and the Bruker sample holder. The phase composition of each pellet was determined by Rietveld analysis of the corresponding XRD pattern using a HighScore Plus software.

3. Results and discussion

3.1 UN-AlN

The resulting microstructure of the composite UN-AlN pellet is presented in **Figure 4**. It can be observed that the AlN phase (dark contrast in backscattering mode) is fairly evenly distributed over the entire sample. As was suggested by the modeling, the AlN phase demonstrated itself insoluble in the UN matrix. The EDS analysis indicated the segregation of an unreacted AlN phase being dispersed principally along the grain boundaries of the UN matrix. **Figure 5** presents high magnification images of samples produced by different mixing techniques. It is apparent that the mixture of powders prior to sintering had a significant effect on the resulting microstructure. Nanopowder, for example, has a strong tendency to cluster forming large agglomerates (**Figure 5a**). Despite this trend the results demonstrate that these agglomerates are easily broken apart by mechanical premixing of the powders (**Figure 5b** and **5c)**. Elemental analysis performed on the sintered UN-AlN pellets demonstrated a higher level of oxygen (~8000 ppm). This was not observed for pure UN pellets sintered from the same batch and same condition as a base line. This points out that the main source of O_2 is in the AlN nanopowder: a considerable amount of O_2 may have been physiosorbed in the surface. This increased level of oxygen is reflected in the XRD analysis that identified the presence of UN, AlN as well as UO_2 phase as shown in **Figure 6**. The oxygen in the system could be present in the form of uranium oxide. Small amounts of oxygen can be dissolved in the UN matrix. The solubility of oxygen in the UN has been reported to be around 5 at% [11]. The XRD analysis of the sintered composite UN-AlN pellets identified the presence of UO_2 phase in the amount of 9 wt%.

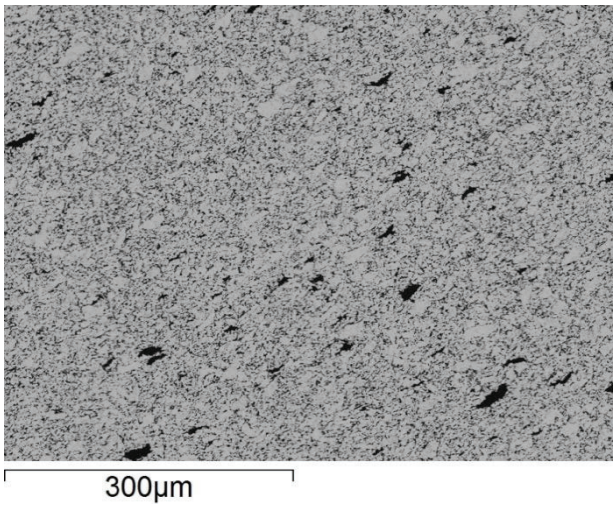

Fig. 4. Scanning electron image of the sintered composite pellet UN-20AlN^{premix}.

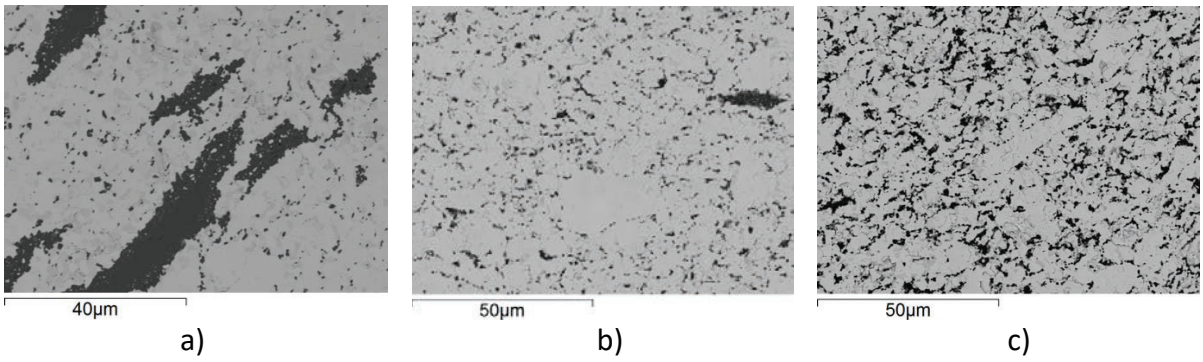

Fig. 5. Scanning electron images of sintered pellets: a) UN-10AlN, b) UN-10AlN^{premix}, c) UN-20AlN^{premix}.

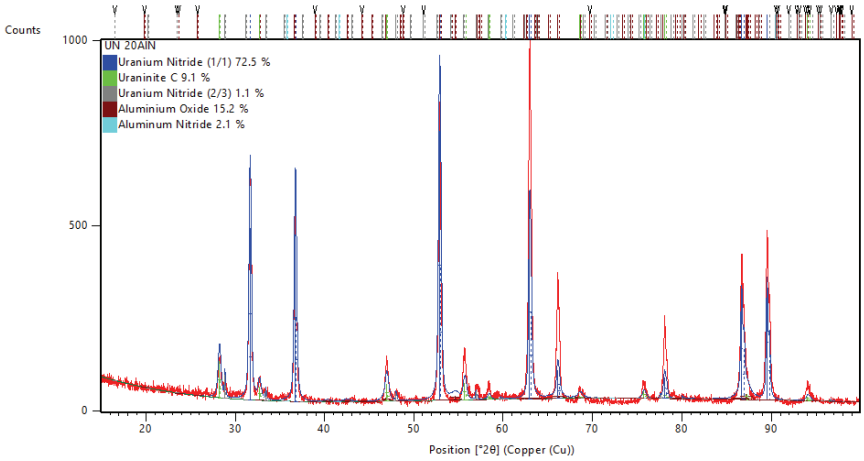

Fig. 6. XRD pattern of the as-sintered UN-20AlN^{premix} composite pellet

The absence of interaction between the AlN phase and the UN matrix is highlighted in the high magnification SEM image shown in **Figure 7**. On this image it can be seen that small particles of UN powder are dispersed within the AlN agglomerate, which demonstrates thorough mixing

of raw powders and is evidence of the absence of solubility, as neither phase is able to dissolve even such small particle sizes. On this scale it is also clear that the AlN inclusions are located along the grain boundaries of UN and a fine dispersion of the nanopowder can produce significant grain coating, thereby permitting the creation of a potentially protective layer without the need for significant addition of material.

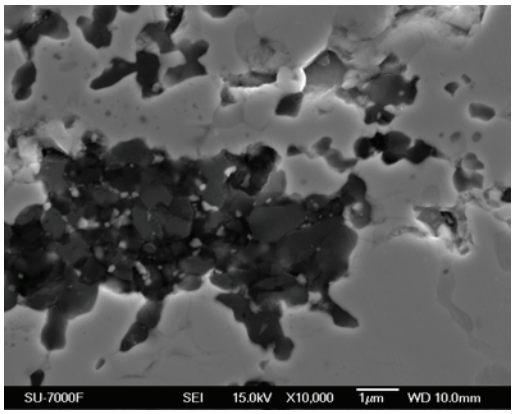

Fig. 7. Scanning electron image of sintered composite pellet UN-20AlN^{premix}

3.2 UN-Cr

The resulting microstructure for the UN composite with Cr-metal is presented in **Figure 8** for UN-10Cr^{premix} mixture. To guide the phase identification EDS was performed and a summary is presented in **Figure 9**. On the backscatter electron analysis, three distinct phases become distinguishable. The matrix, brighter in contrast, is composed of uranium and nitrogen elements. The black phase, always localized at grain boundaries, presents the composition of Cr-metal. The intermediate grey phase is observed to be occurring in the interface of Cr-metal and the matrix, and demonstrates a composition of uranium, chromium and nitrogen.

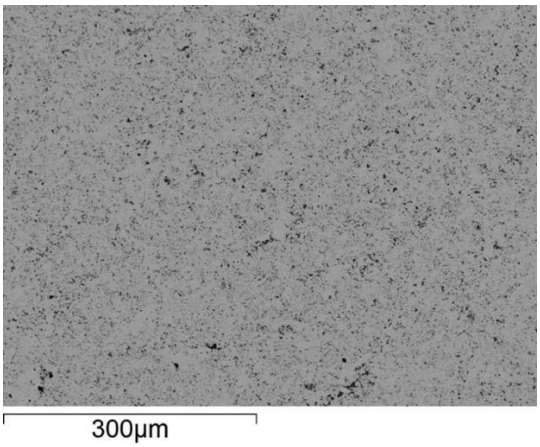

Fig. 8. Scanning electron images of the sintered UN-10Cr^{premix} pellet

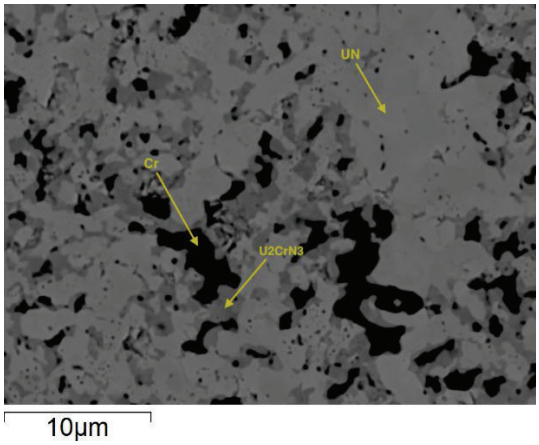

Phase	*N*	*Cr*	*U*
UN	79.05		20.95
U_2CrN_3	76.22	7.76	16.02
Cr		100	

Fig. 9. Micrograph and corresponding EDS analysis of the UN-10Cr^{premix} pellet (in atomic percent)

The proportion of uranium to chromium atoms in this intermediate grey phase was determined to be approximately 2:1 respectively. This proportion is in agreement with the ternary phase U_2CrN_3 [40]. In previous work by Herman et al., when the fabrication process of the compounds was performed through the sol-gel method, the formation of this phase was not observed [13]. However, based on the existing ternary phase diagram of the uranium-chromium-nitrogen system it is predicted to form in the temperature range between 1200°C and 1600°C [17]. This ternary phase, although described with a different crystallographic space group, can be viewed as a distorted version of UN, as can be demonstrated in **Figure 10**. The ternary U_2CrN_3 phase was previously investigated by Zachariasen et al. [41]. This phase has an orthorhombic crystal structure and belongs to space group Immm [40]. If compared with the crystal structure of UN, the similarities between the two could be detected. The unit cell of the U_2CrN_3 phase consists of two UN unit cells in *c*-direction. The U-N and Cr-N bond lengths in the ternary phase are almost the same as the bond lengths in UN and CrN. When a chromium atom replaces the uranium atom in the lattice of the face-centered cubic UN, the bond length decreases from 2.45 Å for UN to 2.07 Å for CrN causing the distortion in the original lattice [41]. The distortion in the lattice caused by Cr replacement in uranium site seems to limit the amount of solution to 33 at%, forcing the Cr to only occupy the 2nd nearest neighbours (NN). The orthorhombic structure is generally formed in the same way from a cubic lattice by stretching the bonds. The density of the ternary phase is reported to be 12.7 g/cc [40]. The uranium density of this compound is 10.61 g/cc, which is higher than the uranium density of UO_2 (9.66 g/cc), making the ternary phase a potential candidate for the ATF concept. The occurrence of this phase, being basically a solid solution with limited solution up to 33 at% demonstrated again agreement with the modeling result for the incorporation of Cr in UN. It is worth to mention that on the EDS analysis level of nitrogen is high, both for UN and U_2CrN_3 phases. That could be due to fluorescence in nitrogen caused by very energetic X-rays from uranium atoms [42]. The XRD pattern of the sintered composite pellet is shown in **Figure 11**. The amount of the phases was quantified using Rietveld analysis. Based on the results of the analysis the majority of the composite pellet consists of the unreacted UN, followed by the ternary U_2CrN_3 phase. The presence of metallic chromium could not be detected with the XRD analysis probably due to the low scattering factor this metal has in comparison with the phase containing uranium.

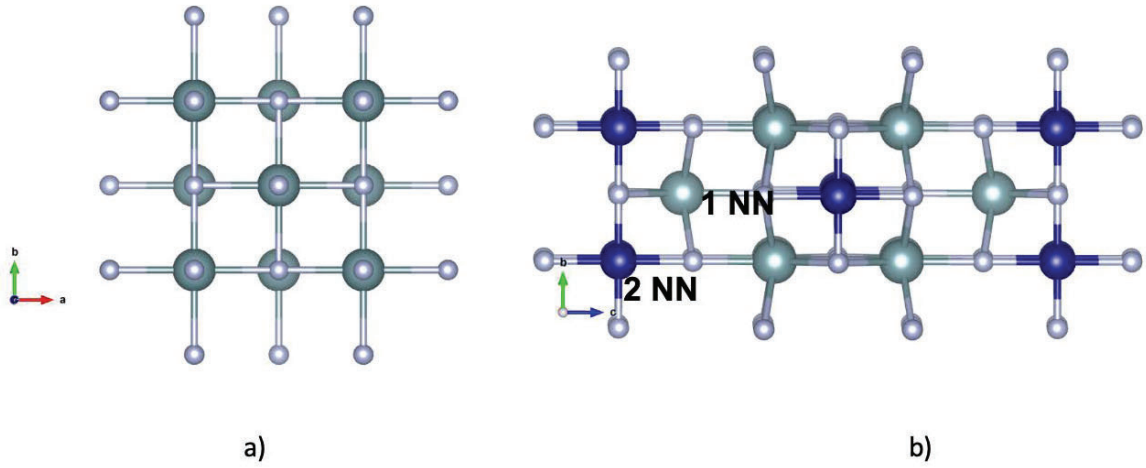

Fig. 10. Demonstration of the unit cell (a) UN and (b) U_2CrN_3

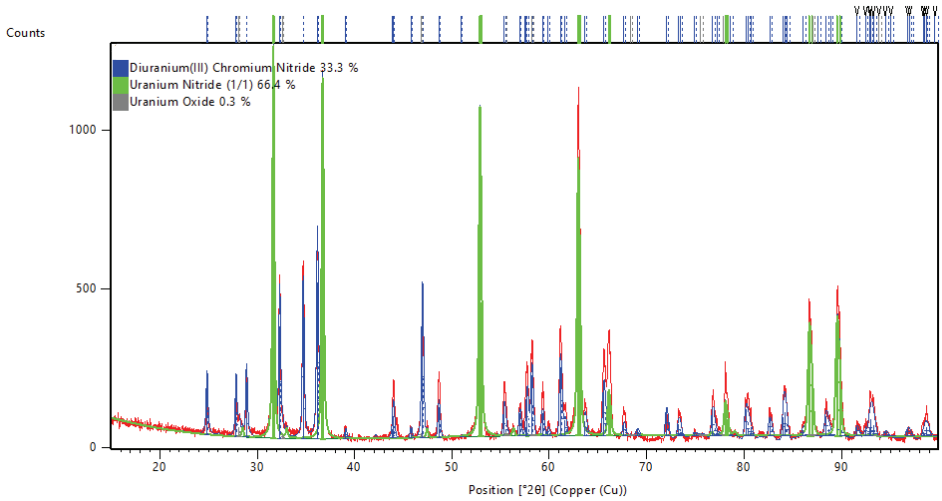

Fig. 11. XRD pattern of the as-sintered UN-20Cr^{premix} composite pellet

Theoretical densities of the UN-Cr composite pellets were calculated by quantitative image analysis using ImageJ software, as described in the methodology section. In **Figure 12**, one of the micrographs used in this calculation is shown, demonstrating how the phase selection by threshold was performed in this study.

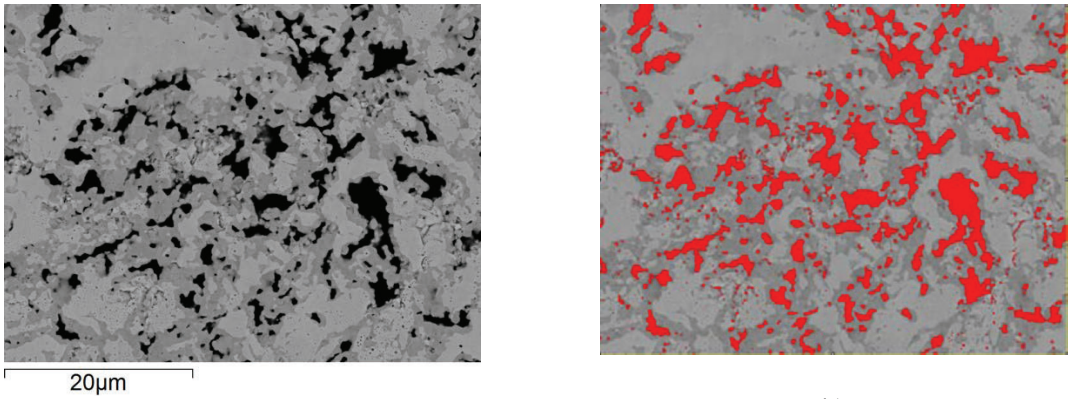

Fig. 12. Scanning electron images of UN-20Cr^{premix}: a) original, b) being analysed by ImageJ.

The actual densities of the pellets (measured by the Archimedes method) were compared to the theoretical densities, calculated by the image analysis method. Even though the sintering parameters for both pellets were identical, the densities of them were slightly different. The UN-10Cr^{premix} composite pellet exhibited lower density, 93%TD with 3.64 % open porosity. The density of the UN-20Cr^{premix} was measured to be 96%TD with 0.48% open porosity. This difference could be due to metallic chromium softening during sintering and assisting with densification.

The image analysis of the micrographs was also used to calculate the total solubility of Cr-metal in the matrix of UN. The volume fraction of the ternary phase (U_2CrN_3) in the pellets containing 10 and 20 vol % of Cr is 30% and 42% respectively. These results correspond to the amount of chromium that formed the ternary U_2CrN_3 phase in the UN matrix being 33% by weight in both pellets. This number indicates that the solubility of chromium in UN is limited. The majority of the chromium added remained in the separate phase. From the micrograph shown in **Figure 12** it could be observed that the ternary phase formed around the chromium inclusions. This indicates that chromium atoms diffused from the chromium rich regions into the uranium nitride. As was shown in the modeling calculation section the incorporation of Cr-metal into the matrix of UN is facilitated by the formation of uranium vacancies. The number of vacancies in the UN is increased dramatically during sintering. Chromium atoms move into the vacant positions in the UN lattice forming the ternary U_2CrN_3 phase. The amount of this phase is limited to the number of uranium vacancies.

3.3 UN-CrN

The microstructure of the composite UN-CrN pellet is shown in **Figure 13**. The EDS analysis and the XRD confirmed the presence of the ternary U_2CrN_3 phase similar to what has been observed for Cr-metal addition. As was suggested by the modeling calculations the formation of the solid solution between UN and CrN is also energetically favourable.

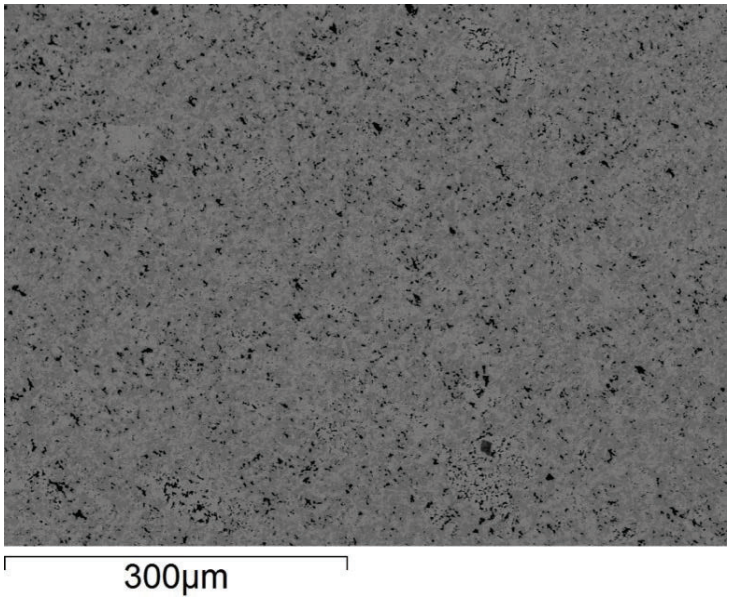

Fig. 13. Scanning electron images of UN-20CrN^{premix} composite pellet

The same qualitative image analysis of the pellet microstructure was performed providing the volume fraction of the ternary phase within the pellets, being around 52 vol% and 36 vol% for the UN-20CrN^{premix} and UN-10CrN respectively. The calculated weight fraction of Cr being present in the ternary phase is approximately 50 wt% in the UN-20CrN^{premix} and 40 wt% in the UN-10CrN. The difference in the amounts of chromium being present in the metallic form and in the ternary phase could be attributed to different mixing techniques but also to different sintering temperatures.

If compared to the composite pellets with Cr-metal as a starting material, it is evident that the doped fraction formed in the UN matrix increases if chromium enters the system in the form of the nitride, as demonstrated in **Figure 14**. The presence of nitrogen in the CrN phase changes the mechanism of formation of the ternary compound. The solubility of Cr in the UN for the UN-Cr composites was limited by the number of uranium vacancies in the UN lattice. In the UN-CrN system the formation of the solid solution is favoured thermodynamically, accompanied by the reduction in the total Gibbs energy of the system. Thermodynamically, the reactions between Cr_2N, CrN and UN are suggested to be as follows [40]:

$$0.667\ UN + 0.333\ Cr_2N \rightarrow 0.333\ U_2CrN_3 + 0.333\ Cr, \quad E_{rxn} = -21.06\ kJ/mol \qquad (3)$$

$$0.667\ UN + 0.333\ CrN \rightarrow 0.333\ U_2CrN_3, \quad E_{rxn} = -25.42\ kJ/mol \qquad (4)$$

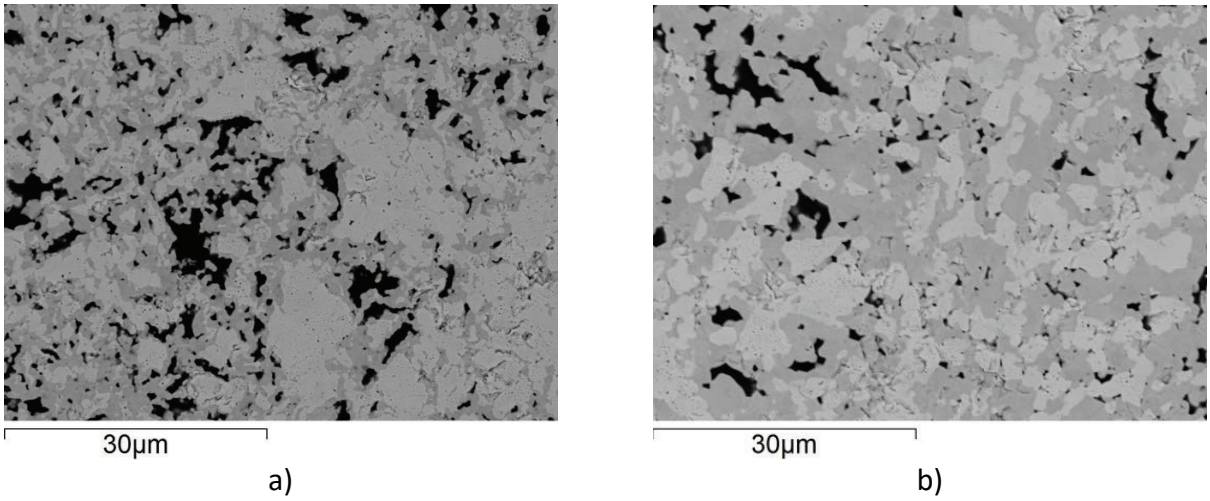

Fig. 14. Scanning electron images of sintered composite pellets: a) UN-20Cr^{premix}, b) UN-20CrN^{premix}.

The presence of the Cr_2N in the starting material resulted in the inclusions of Cr-metal. The shape of the metallic chromium phase in **Figure 15** suggests that the phase softened during sintering similar to what was observed for Cr-metal addition.

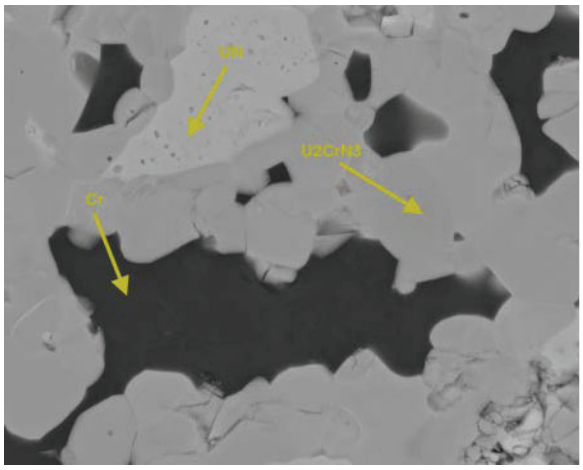

Fig. 15. Scanning electron images of sintered composite pellet UN-20CrN^{premix}.

In agreement with the modeling results these nitride composites can be used to obtain extensive solution in the UN matrix providing a high fraction of produced doped grains.

3.4 UN-CrN-AlN

The microstructure of the composite pellet containing AlN and CrN with UN is shown in **Figure 16**. Similar to the composite pellets containing only CrN or only AlN, the microstructure of the composite pellet UN-10AlN-10CrN^{premix} demonstrates the presence of the metallic chromium phase, the ternary U_2CrN_3, as well as the unreacted AlN and UN (**Figure 17**). The contrast of the image in **Figure 17** allows to differentiate between the AlN and the

metallic Cr, the AlN being slightly darker in colour than chromium. This microstructure demonstrates two trends predicted by modeling: the solubility of CrN in UN and the complete insolubility of the AlN and highlights the possibility to combine both to produce composite with a tailored microstructure.

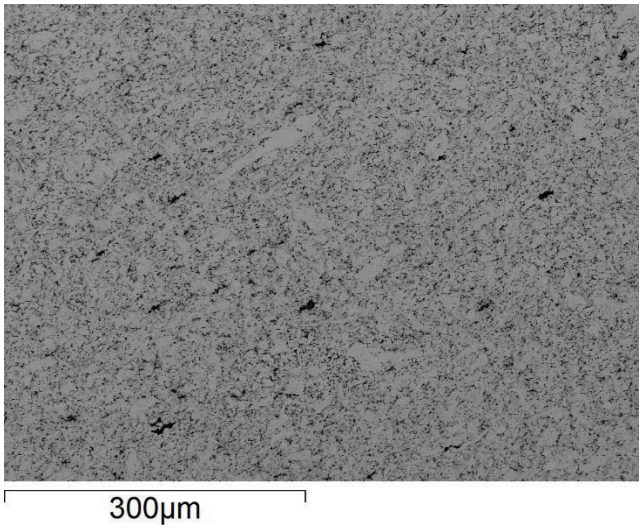

Fig. 16. Scanning electron images of sintered composite pellet UN-10AlN-10CrN^{premix}.

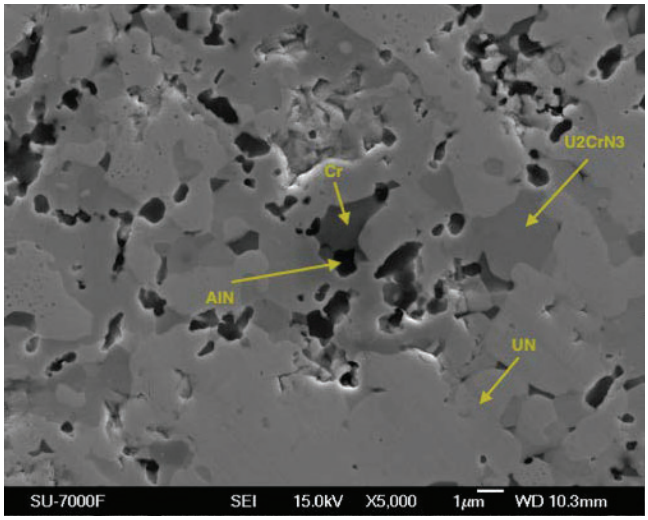

Fig. 17. Scanning electron images of sintered composite pellet UN-10AlN-10CrN^{premix}

The element mapping presented in **Figure 18** assisted further with the identification of the phases. The yellow map shows the distribution of chromium. Two trends are visible on the map. The bright yellow areas correspond to Cr-metal, formed in the reaction between Cr_2N and UN (Eq. 3). The less saturated parts of the map correspond to the ternary U_2CrN_3 phase.

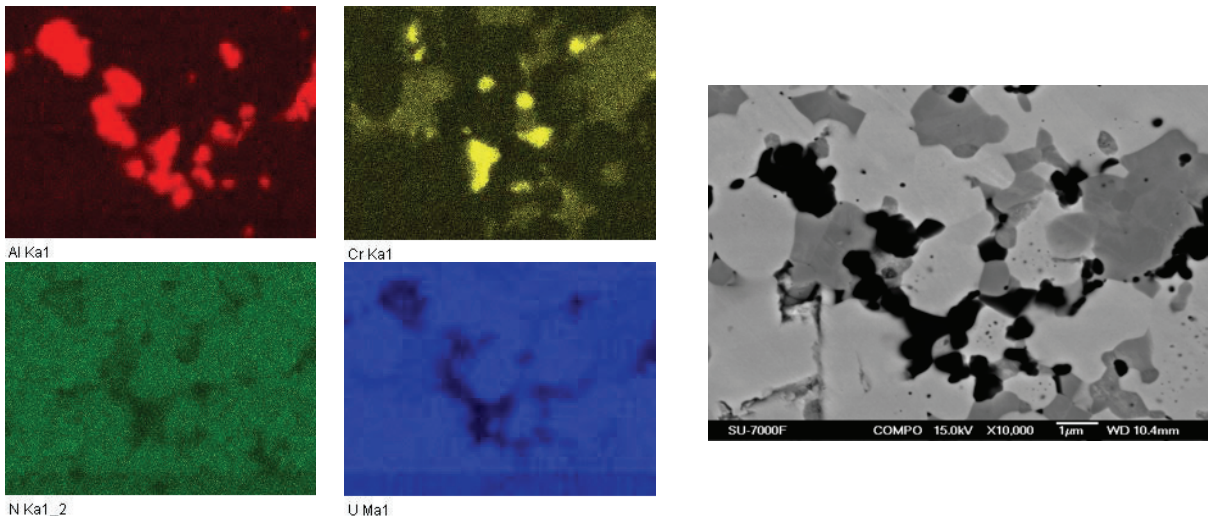

Fig. 18. Element mapping of the composite pellet UN-10AlN-10CrN^{premix}

The XRD pattern of the composite pellet UN-5AlN-5CrN is presented in **Figure 19**. The main phase after sintering is uranium nitride. The AlN phase in the sintered pellet is unchanged, further confirming the lack of interaction between this phase and the UN matrix. The presence of the diuranium(III) chromium nitride (U_2CrN_3) in the amount of 10.5 wt% confirms the solubility of chromium in the UN matrix. The oxide phase is present in the amount of 2.9 wt%, similar to the UN-AlN composites suggesting that the nanopowder surface is the main source of oxygen.

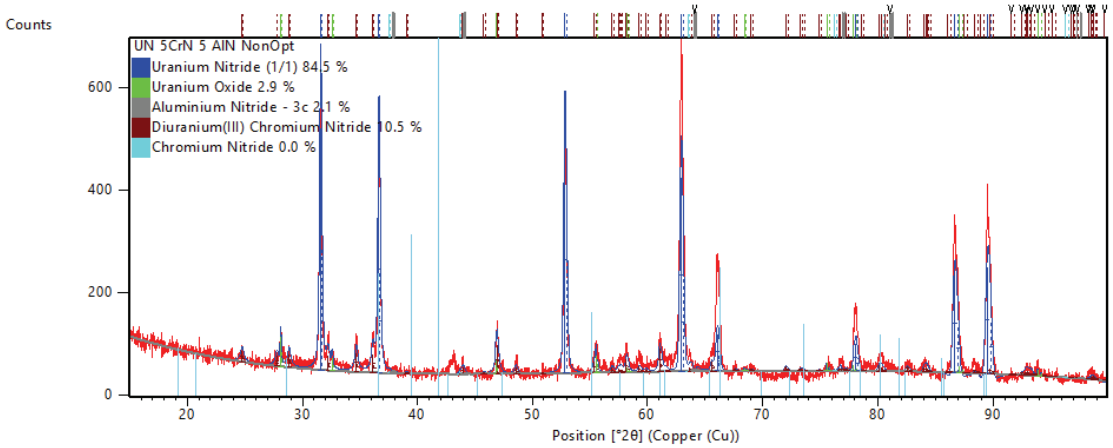

Fig. 19. XRD pattern of the as-sintered UN-5AlN-5CrN composite pellet

The interaction between the phases in the composite pellet UN-10AlN-10CrN^{premix} is shown in **Figure 20**. The interface between the UN matrix and the ternary U_2CrN_3 is smooth. The morphology of both phases appears similar. AlN exhibits different behaviour. The phase is brittle and is easily removed during sample preparation, as shown in **Figure 20 b**. It appears

that AlN introduces stress to UN matrix, where in some areas of the sample intragranular cracking in the UN matrix was observed.

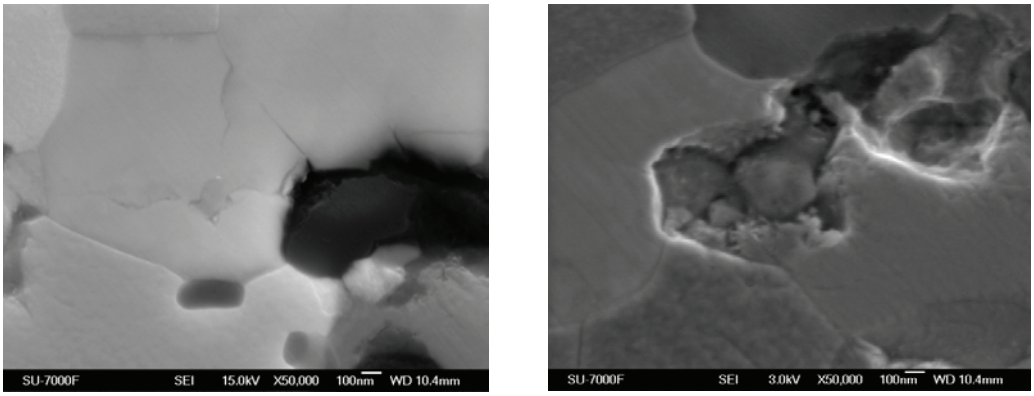

a) b)

Fig. 20. Scanning electron images of sintered composite pellet UN-10AlN-10CrN^{premix}

The resulting microstructure observed for the UN-CrN-AlN composites showed consistency with the design microstructure proposed in **Figure 3**. This highlights the efficiency of using modeling results to guide composite fabrication and reinforces the fact that the fabrication route adopted in this work is suitable to produce such tailored microstructure.

4. Conclusions

In this study we presented a methodology of fabrication of UN composites with engineered microstructure. The dopants were added into the UN matrix in order to improve the corrosion resistance of UN fuel by interacting with the UN matrix in two ways: to shield the grains of UN from coming into contact with the oxidising agent (coated grains) and to lower the rate of oxygen diffusion through the bulk (doped grains). The modeling calculations were conducted to screen the potential additive candidates and to predict the possible interactions between these additives and the UN matrix. The results based on first principles calculation predicted that elements from the electronic configuration group 3*p* (e.g., Al, Si, P) will demonstrate limited solubility in U site when added to the UN, when entered either in the form of nitride or the pure compound. The elements from the 3*d* group (e.g., Cr, V, Ti), on the other hand, were predicted to demonstrate considerable solubility with UN. From this group Cr was the only one identified as the material that will interact with the UN matrix to form solid solution, if added as metal and as a nitride phase. However, it was possible to conclude that the amount of solid solution formed when Cr-metal was added is limited by the number of uranium vacancies present in the lattice of UN. If Cr entered the system in the form of CrN or Cr_2N, the amount of the solid solution formed was predicted to be higher.

In order to evaluate the results of the modeling calculation Al and Cr were selected for the experimental investigation. Composite pellets containing AlN, CrN and Cr were sintered using the Spark Plasma Sintering. The metallographic analysis of the composite pellets confirmed the possibility to obtain an engineered microstructure. No interaction between the AlN and the UN was observed in the UN-AlN composite pellets. The unreacted AlN phase was distributed along the grain boundaries of UN, creating the coated grain effect. This experimental result

confirmed that it would be possible to produce a protective coating around the grains of UN by adding small amounts of the corrosion resistant additive. The presence of the ternary U_2CrN_3 phase was encountered in the composite pellets containing chromium, which confirms the modeling prediction of the interaction between Cr and UN. The ternary phase is a distorted version of UN formed by chromium atoms replacing the uranium atoms in the UN lattice and can be considered a solid solution (maximum Cr solubility 33 at%). This phase has not been observed experimentally in previous studies where chromium was added into the UN fuel matrix, although the existence of this phase has been predicted by the phase diagram. It is evident that the manufacturing parameters used for the fabrication of the composite materials play an important role in the resulting microstructure of the composite pellets. The amount of solid solution in the samples differed depending on whether the additive material was introduced into the system in the form of CrN or Cr-metal. The amount of the solid solution in the samples produced from Cr-metal was limited by the number of uranium vacancies formed in UN at elevated temperature. The fraction of the doped grains increased in the composite pellets produced from CrN. The formation of the ternary phase in the UN-CrN system is favoured thermodynamically. Different mechanisms of formation of the solid solution in the two systems allow to have a combination of doped grains of UN (with CrN as additive) and partially doped grains (with Cr-metal as additive). The U_2CrN_3 phase has a higher uranium density than UO_2, which makes it an interesting ATF fuel candidate. Therefore, more studies need to be done to investigate the properties and characteristics of the ternary U_2CrN_3 compound, as well as its oxidation behaviour under various oxidising environments.

Experimental results obtained in this study demonstrate that design microstructures of UN composite materials could be fabricated to create coated grains by addition of insoluble compounds as well as doped and partially doped grains by addition of soluble elements. The modeling calculations presented here can be successfully applied for screening of the potential candidates for composite materials and for predicting their interaction with the UN matrix. Using this tool prior to experimental research will allow to better design and perform experiments, choosing only the best additive candidates considering the main goal to be achieved.

REFERENCES

[1] E. O. Speidel and D. L. Keller, ‘FABRICATION AND PROPERTIES OF HOT-PRESSED URANIUM MONONITRIDE’, Battelle Memorial Inst., Columbus, Ohio, BMI-1633; EURAEC-706, May 1963. doi: https://doi.org/10.2172/4674236.

[2] G. J. Youinou and R. S. Sen, ‘Impact of Accident-Tolerant Fuels and Claddings on the Overall Fuel Cycle: A Preliminary Systems Analysis’, *Nucl. Technol.*, vol. 188, no. 2, pp. 123–138, Nov. 2014, doi: 10.13182/NT14-22.

[3] J. Zakova and J. Wallenius, ‘Fuel residence time in BWRs with nitride fuels’, *Ann. Nucl. Energy Oxf.*, vol. 47, pp. 182–191, 2012, doi: 10.1016/j.anucene.2012.03.033.

[4] S. J. Zinkle, K. A. Terrani, J. C. Gehin, L. J. Ott, and L. L. Snead, ‘Accident tolerant fuels for LWRs: A perspective’, *J. Nucl. Mater.*, vol. 448, no. 1, pp. 374–379, May 2014, doi: 10.1016/j.jnucmat.2013.12.005.

[5] Y. Yamamoto, B. A. Pint, K. A. Terrani, K. G. Field, Y. Yang, and L. L. Snead, ‘Development and property evaluation of nuclear grade wrought FeCrAl fuel cladding for light water reactors’, *J. Nucl. Mater.*, vol. 467, pp. 703–716, Dec. 2015, doi: 10.1016/j.jnucmat.2015.10.019.

[6] S. Dryepondt, K. A. Unocic, D. T. Hoelzer, C. P. Massey, and B. A. Pint, ‘Development of low-Cr ODS FeCrAl alloys for accident-tolerant fuel cladding’, *J. Nucl. Mater.*, vol. 501, pp. 59–71, Apr. 2018, doi: 10.1016/j.jnucmat.2017.12.035.

[7] J. E. Antill and B. L. Mya, ‘KINETICS OF THE OXIDATION OF UN AND U(C0) IN CARBON DIOXIDE, STEAM AND WATER AT. ELEVATED TEMPERATURES’, p. 7.

[8] K. Johnson, V. Ström, J. Wallenius, and D. A. Lopes, ‘Oxidation of accident tolerant fuel candidates’, *J. Nucl. Sci. Technol.*, vol. 54, no. 3, pp. 280–286, Mar. 2017, doi: 10.1080/00223131.2016.1262297.

[9] A. P. Shivprasad, A. C. Telles, and J. T. White, ‘Report on waterproofing of UN studies’, LA-UR-19-28422, 1565797, Sep. 2019. doi: 10.2172/1565797.

[10] D. A. Lopes, S. Uygur, and K. Johnson, ‘Degradation of UN and UN–U3Si2 pellets in steam environment’, *J. Nucl. Sci. Technol.*, vol. 54, no. 4, pp. 405–413, Apr. 2017, doi: 10.1080/00223131.2016.1274689.

[11] B. J. Jaques *et al.*, ‘Synthesis and sintering of UN-UO2 fuel composites’, *J. Nucl. Mater.*, vol. 466, pp. 745–754, Nov. 2015, doi: 10.1016/j.jnucmat.2015.06.029.

[12] J. K. Watkins, D. P. Butt, and B. J. Jaques, ‘Microstructural degradation of UN and UN-UO2 composites in hydrothermal oxidation conditions’, *J. Nucl. Mater.*, vol. 518, pp. 30–40, May 2019, doi: 10.1016/j.jnucmat.2019.02.027.

[13] A. Herman and C. Ekberg, ‘A Uranium Nitride Doped with Chromium, Nickel or Aluminum as an Accident Tolerant Fuel’, *Res. Rev. J. Mater. Sci.*, vol. 05, Jan. 2017, doi: 10.4172/2321-6212.1000196.

[14] T. J. Davies and P. E. Evans, ‘The preparation and examination of mixtures of aluminium nitride (AlN) and uranium mononitride (UN)’, *J. Nucl. Mater.*, vol. 13, no. 2, pp. 152–168, Jan. 1964, doi: 10.1016/0022-3115(64)90037-6.
[15] Y. Mishchenko, *Composite UN-UO2 fuels*. 2018.
[16] D. Costa, M. Hedberg, S. Middleburgh, J. Wallenius, P. Olsson, and D. Lopes, ‘UN microspheres embedded in UO2 matrix: An innovative accident tolerant fuel’, *J. Nucl. Mater.*, vol. 540C, Jul. 2020, doi: 10.1016/j.jnucmat.2020.152355.
[17] H. Holleck, ‘Ternary phase equilibria in the systems actinide--transition metal--carbon and actinide--transition metal--nitrogen’, International Atomic Energy Agency, Vienna, CONF-741030-P2, Jan. 1975. Accessed: Nov. 02, 2020. [Online]. Available: https://www.osti.gov/biblio/4177518.
[18] H. Holleck, E. Smallos, and F. Thümmler, ‘Zur Mischkristallbildung in den quasibinären Systemen von UN und den Mononitriden der IV A-Gruppe TiN, ZrN und HfN’, *Monatshefte Für Chem. Chem. Mon.*, vol. 99, no. 3, pp. 985–989, May 1968, doi: 10.1007/BF00913744.
[19] H. Holleck, E. Smailos, and F. Thümmler, ‘Zur mischkristallbildung von un mit den nitriden der seltenen erden CeN und NdN’, *J. Nucl. Mater.*, vol. 28, no. 1, pp. 105–109, Oct. 1968, doi: 10.1016/0022-3115(68)90061-5.
[20] H. Holleck, E. Smailos, and F. Thümmler, ‘Zur mischphasenbildung der mononitride in den systemen U- (Y, La, Pr)-N’, *J. Nucl. Mater.*, vol. 32, no. 2, pp. 281–289, Sep. 1969, doi: 10.1016/0022-3115(69)90077-4.
[21] G. Kresse and J. Furthmüller, ‘Efficiency of ab-initio total energy calculations for metals and semiconductors using a plane-wave basis set’, *Comput. Mater. Sci.*, vol. 6, no. 1, pp. 15–50, Jul. 1996, doi: 10.1016/0927-0256(96)00008-0.
[22] G. Kresse and J. Furthmüller, ‘Efficient iterative schemes for ab initio total-energy calculations using a plane-wave basis set’, *Phys. Rev. B*, vol. 54, no. 16, pp. 11169–11186, Oct. 1996, doi: 10.1103/PhysRevB.54.11169.
[23] J. P. Perdew, K. Burke, and M. Ernzerhof, ‘Generalized Gradient Approximation Made Simple’, *Phys. Rev. Lett.*, vol. 77, no. 18, pp. 3865–3868, Oct. 1996, doi: 10.1103/PhysRevLett.77.3865.
[24] P. E. Blöchl, ‘Projector augmented-wave method’, *Phys. Rev. B*, vol. 50, no. 24, pp. 17953–17979, Dec. 1994, doi: 10.1103/PhysRevB.50.17953.
[25] G. Kresse and D. Joubert, ‘From ultrasoft pseudopotentials to the projector augmented-wave method’, *Phys. Rev. B*, vol. 59, no. 3, pp. 1758–1775, Jan. 1999, doi: 10.1103/PhysRevB.59.1758.
[26] S. L. Dudarev, G. A. Botton, S. Y. Savrasov, C. J. Humphreys, and A. P. Sutton, ‘Electron-energy-loss spectra and the structural stability of nickel oxide: An LSDA+U study’, *Phys. Rev. B*, vol. 57, no. 3, pp. 1505–1509, Jan. 1998, doi: 10.1103/PhysRevB.57.1505.
[27] A. Jain *et al.*, ‘Formation enthalpies by mixing GGA and GGA $+$ U calculations’, *Phys. Rev. B*, vol. 84, no. 4, p. 045115, Jul. 2011, doi: 10.1103/PhysRevB.84.045115.
[28] O. Kubaschewski, C. B. Alcock, P. J. Spencer, and O. Kubaschewski, *Materials thermochemistry*. Oxford; New York: Pergamon Press, 1993.
[29] P. Burlet, J. Rossat-Mignod, R. Troć, and Z. Henkie, ‘Non-colinear magnetic structure of U3P4 and U3As4’, *Solid State Commun.*, vol. 39, no. 6, pp. 745–749, Aug. 1981, doi: 10.1016/0038-1098(81)90449-X.
[30] J. S. Olsen, L. Gerward, U. Benedict, S. Dabos, and O. Vogt, ‘High-pressure phases of uranium monophosphide studied by synchrotron x-ray diffraction’, *Phys. Rev. B*, vol. 37, no. 15, pp. 8713–8718, 1988, doi: 10.1103/PhysRevB.37.8713.

[31] P. Malkki, M. Jolkkonen, T. Hollmer, and J. Wallenius, ‘Manufacture of fully dense uranium nitride pellets using hydride derived powders with spark plasma sintering’, *J. Nucl. Mater.*, vol. 452, no. 1, pp. 548–551, Sep. 2014, doi: 10.1016/j.jnucmat.2014.06.012.
[32] L. Lutterotti, M. Bortolotti, G. Ischia, I. Lonardelli, and H.-R. Wenk, ‘Rietveld Texture Analysis from Diffraction Images’, *Z. Krist. Suppl.*, vol. 2007, Nov. 2007, doi: 10.1524/zksu.2007.2007.suppl_26.125.
[33] ‘Crystallography Open Database’. http://www.crystallography.net/cod/ (accessed Jul. 09, 2020).
[34] R. E. Rundle, N. C. Baenziger, A. S. Wilson, and R. A. McDonald, ‘The Structures of the Carbides, Nitrides and Oxides of Uranium [1]’, *J. Am. Chem. Soc.*, vol. 70, no. 1, pp. 99–105, Jan. 1948, doi: 10.1021/ja01181a029.
[35] T. Muromura and H. Tagawa, ‘Lattice parameter of uranium mononitride’, *J. Nucl. Mater.*, vol. 79, no. 1, pp. 264–266, 1979.
[36] R. M. Dell, V. J. Wheeler, and E. J. McIver, ‘Oxidation of uranium mononitride and uranium monocarbide’, *Trans. Faraday Soc.*, vol. 62, no. 0, pp. 3591–3606, 1966, doi: 10.1039/TF9666203591.
[37] S. M. Hartig, ‘Basic Image Analysis and Manipulation in ImageJ’, *Curr. Protoc. Mol. Biol.*, vol. 102, no. 1, p. 14.15.1-14.15.12, 2013, doi: https://doi.org/10.1002/0471142727.mb1415s102.
[38] K. M. Taylor and C. Lenie, ‘Some Properties of Aluminum Nitride’, *J. Electrochem. Soc.*, vol. 107, no. 4, p. 308, 1960, doi: 10.1149/1.2427686.
[39] H.-J. Lunk, ‘Discovery, properties and applications of chromium and its compounds’, *ChemTexts*, vol. 1, Mar. 2015, doi: 10.1007/s40828-015-0007-z.
[40] ‘Materials Project’. https://materialsproject.org/#apps/interfacereactions (accessed Aug. 19, 2020).
[41] R. Benz and W. H. Zachariasen, ‘Crystal structures of Th2CrN3, Th2MnN3, U2CrN3 and U2MnN3’, *J. Nucl. Mater.*, vol. 37, no. 1, pp. 109–113, Oct. 1970, doi: 10.1016/0022-3115(70)90187-X.
[42] D. E. Newbury* and N. W. M. Ritchie, ‘Is Scanning Electron Microscopy/Energy Dispersive X-ray Spectrometry (SEM/EDS) Quantitative?’, *Scanning*, vol. 35, no. 3, pp. 141–168, 2013, doi: https://doi.org/10.1002/sca.21041.
26/01/2021 12:22:00

Design and fabrication of UN composites: from first principles to pellet production

Yulia Mishchenko[a], Kyle D. Johnson[b], Antoine Claisse[c], Janne Wallenius[a], Denise Adorno Lopes[a,c]

[a]*KTH-Royal Institute of Technology, Stockholm, Sweden, yuliam@kth.se*

[b]*Studsvik Nuclear AB, Nyköping, Sweden*

[c]*Westinghouse Electric Sweden AB, Västerås, Sweden*

Abstract

In this study the composite UN-AlN, UN-Cr, UN-CrN and UN-AlN-CrN pellets were fabricated, and the advanced microstructure with different modes of interaction between the phases was obtained. The dopants for this study were selected based on the results of the ab-initio modeling calculations, that identified the AlN phase as insoluble and CrN and Cr as soluble in the UN matrix. This method allowed to investigate the possibility of improving the corrosion resistance of UN by protecting the grain boundaries with insoluble AlN and by hindering the diffusion of oxygen through the bulk by adding soluble CrN and Cr.
The UN powder was produced by hydriding-nitriding method and mixed with the AlN, CrN and Cr powders. High density (>90 %TD) composite pellets were sintered by Spark Plasma Sintering (SPS). The microstructure of the pellets was analysed using SEM coupled with EDS. The phase purity was determined by XRD. For the first time the presence on the ternary U_2CrN_3 phase was observed in the composite pellets containing Cr and CrN dopants. The results obtained in this study allowed to assess the methodology for fabrication of the UN composites with controlled microstructure.

1. Introduction

Uranium nitride (UN) is a potential candidate for the nuclear fuel alternatives being considered as part of the Accident Tolerant Fuel (ATF) initiative. UN is known for its high thermal conductivity, high melting temperature, high fissile density and good fission product retention [1], [2] . These positive qualities of the UN fuel will allow to improve the safety of the system during the reactor operation, as well as to bring the economic benefits by increasing the length of the fuel cycle [3]. In addition to that, the high fissile density of the UN fuel will provide the neutronic margins, which will allow the use of cladding materials with high oxidation resistance and low hydrogen production (such as FeCrAl) [4], [5], [6]. However, the oxidation resistance of UN is significantly inferior to the UO_2 fuel, violating the ATF concept itself [2], [7], [8], which drives the motivation for development of techniques for improving the oxidation resistance properties of UN.

In order to improve the oxidation resistance of UN different number of alloying systems such as ceramics (cercer) and metals (cermet) have been considered [9]. In previous studies potential additives were identified based on their thermophysical and oxidation resistance properties. Composite pellets containing UN and such materials as U_3Si_2, UO_2, Cr, Ni, Al have been manufactured and analysed [10], [11], [12], [13], [14]. Different experimental methods have been applied to produce such composites including powder metallurgical methods and sol-gel method, as in the case of UN pellets doped with Cr, Ni and Al that were produced by Herman et al. [13]. In some cases, the complexity of the fabrication process creates difficulty in understanding the interaction between the alloying elements and the fuel matrix. As an example, in the sol-gel method the high temperatures applied during the carbothermic reduction and pelletising resulted in a significant amount of Cr being lost due to evaporation [13]. Another issue in the design of these composites was the absence of information on how the additives would interact with the UN matrix, as observed for UN-UO_2 composites where significant reaction under sintering occurred favouring an equilibrium of UO_2-U_2N_3 [15], [16], [11]. In some studies, the attempt has been made to predict the possible formation of the solid solution between the UN matrix and the additive using the Hume-Rothery Rules, as in the case with Herman et al. However, the comparison of the atomic radii, electronegativities and the valences of the uranium atoms and the additive atoms predicted that no solid solution could be formed between CrN or AlN and the matrix of UN [13]. However, this type of assessment does not provide information about the existence of possible ternary compounds, that can be found in the phase diagrams, as in the case with U-Cr-N, where the formation of the ternary U_2CrN_3 was predicted by Holleck [17]. The presence of the ternary compounds can be important for the performance of the composite materials. The information about all possible interactions between the additives and the UN is needed in order to eliminate the candidates that will be completely unsuitable for these purposes.

The interaction behaviour between UN and such materials as TiN, YN, CeN, NbN has been previously investigated experimentally by Holleck [18], [19], [20]. Composite materials containing the above-mentioned nitrides and UN were prepared by such methods as arc melting followed by homogenisation and long-term annealing of powder mixtures. The results obtained in those studies identified such systems as UN-CeN, UN-NbN, UN-YN to be completely miscible in each other, whereas TiN was shown to be soluble in UN from about 1 mol% at 1700°C to 4 mol% at 2400°C. However, investigating the possible interaction between a wide range of available materials and the UN experimentally could be a very expensive and time-consuming process. Therefore, a preselecting tool for identifying the potential candidates and predicting their behaviour is highly desirable.

In this study a methodology of using atomistic modeling to predict the interaction behaviour between various metallic and nitrogenous additives with UN is described. The goal is to use this as a preselecting tool for the fabrication of UN compounds in order to help determine if a given material and phase will be soluble in the base UN matrix. Elements from different electronic configuration groups being 3*p* (Al, Si, P), 3*d* (V, Ti, Cr), 4*d* (Y, Zr, Nb, Mo), and 4*f* (La, Ce) were analysed using the proposed method. From the calculated systems Al and Cr were selected to demonstrate the interaction trends predicted by the modeling. Advanced fabrication using materials as AlN-nano, Cr-nano metal, CrN-micro and sintering by Spark Plasma Sintering (SPS) technique with temperatures not exceeding 1650°C was applied to produce selected composite pellets. High purity UN powders were synthesised using the hydriding-nitriding method from metallic uranium for obtaining high purity materials. A further intention of this work is to provide a fabrication routine, i.e. selection of powder morphology and chemical form, sintering parameters, etc., which can be used as guidelines for

producing UN composites with a tailored microstructure. The results of the experiments confirmed the predictions of the atomistic modeling, making it a valuable tool to be used in future research into composite fuels design.

2. Methodology

2.1 First-principles calculations

DFT calculations were performed with the Vienna Ab initio Simulation Package (VASP) [21], [22]. The electron exchange correlation was modeled using the generalized gradient approximation (GGA) of Perdew, Burke and Ernzernhof (PBE) [23] and projector augmented wave (PAW) potentials [24], [25]. To better describe the correlated nature of the U 5*f* electrons, GGA + *U* method with Dudarev's rotationally invariant approach [26] and an effective U, U_{eff}= 1.9 eV (U_{eff} = U – J) was used. The unit cells for UN were fully relaxed using a cut-off energy of 520 eV. Convergence criteria of 0.02 eV/Å^{-1} and 10^{-5} eV were adopted for the forces and total energy, respectively. A 2 × 2 × 2 supercell of UN was used for calculating the defect formation energies. A γ-centered Monkhorst-pack k-point spacing of <0.25 Å^{-1} was applied for sampling the Brillouin zone for each structure. No methods to avoid the metastable states were used, as the symmetry was heavily broken by the incorporation of foreign atoms and the energetics of point defects in UN are one order of magnitude larger than the ones of metastable states.

The general trend for incorporation of elements from electronic configuration groups 3*p* (Al, Si, P), 3*d* (V, Ti, Cr), 4*d* (Y, Zr, Nb, Mo) and 4*f* (La, Ce) in the UN matrix was evaluated by calculating the formation energies of point defects. The incorporation was modeled considering the uranium site for all elements in addition to the nitrogen site for the 3*p* elements. The formation energy was calculated using Eq. (1), where E^0_{tot} and E^D_{tot}, are the total energies of the supercell without and with a defect, respectively, and μ^0_i is the standard state chemical potential (DFT calculated energy per atom) of the element *i*. The standard states used for each element are listed in **Table 1**. ΔN^D_i is the number of atoms of type *i* added ($\Delta N^D_i > 0$) or removed ($\Delta N^D_i < 0$) from the perfect supercell to create the defect, and the sum is over all added and removed elements. Additionally, incorporation energy analysis can be extended to evaluate another phase as the source of the incorporated atom. This can be done by adding a correction term $\Delta\mu_i$ (in Eq. (1)) as the change in the chemical potential of element *i* resulting from an N-phase equilibrium (i.e., from the local environment), which can be calculated by solving the set of linear equations (Eq. (2)), where c_{ik} is the coefficient representing the concentration of each atom considering the phase equilibria. On the scopes of this work the equilibrium of UN-(Nitride Phase)-N_2 was also considered and the nitride phases evaluated are also listed in **Table 1** with their respective calculated $\Delta\mu$.

$$\Delta E_f^D = E_{tot}^D - E_{tot}^0 - \sum_{i=1}^{N} \Delta N_i^D \left(\mu_i^0 + \Delta\mu_i\right) \quad (1)$$

$$\Delta H_{f,k} = \sum_{i=1}^{N} c_{ik} \Delta\mu_i \quad (2)$$

It is important to mention that the applications of GGA + *U* results in inconsistency for direct comparison with reference state α-Uranium, more appropriately modeled by GGA framework. Therefore, the methodology that predicts formation enthalpies by mixing GGA and GGA+*U* results proposed by Jain *et al*. [27] was applied, where the experimentally reported formation energy of U_2N_3 [28] were used for correction.

Table 1: Standard states and their respective μ_o (eV/atom), and the nitride phases with the calculated $\Delta\mu$ (eV/atom).

Standard state	**Space group**	**μ_o (eV/at)**	**Nitride phases**	**Space group**	**Calculated Δμ**
Al	Fm-3m [225]	-3.7481	AlN	P63mc [186]	-3.192
Si	Fd3m [227]	-5.4234	Si_3N_4	P63/m [176]	-3.066
P		-8.1781	P_3N_5	C2/c [15]	-1.435
Ti	P6/mmm [191]	-7.8899	TiN	Fm3m [225]	-3.816
V	Im3m [229]	-9.0866	VN	Fm3m [225]	-2.328
			V_8N	P42/mnm [136]	-0.421
Cr	Im3m [229]	-9.6367	CrN	Fm3m [225]	-1.31
			Cr_2N	P31m [162]	-0.771
Y	P63/mmc [194]	-6.4674	YN	Fm3m [225]	-3.758
Zr	P63/mmc [194]	-8.5475	ZrN	Fm3m [225]	-3.74
Nb	Im3m [229]	-10.1131	NbN	P6m2 [187]	-2.52
Mo	Im3m [229]	-10.4345	MoN	P63mc [186]	-1.118
			Mo_2N	I41/amd [141]	-0.552
Pd	Fm3m [225]	-5.1765			
La	Fm3m [225]	-4.9353	LaN		-2.998
Ce	Fm3m [225]	-5.9315	CeN		-3.38

This analysis creates a way to evaluate the trend of the materials to react with the UN fuel matrix not only from the metal state but the nitride forms. **Figure 1** offers the summary of the modeling method.

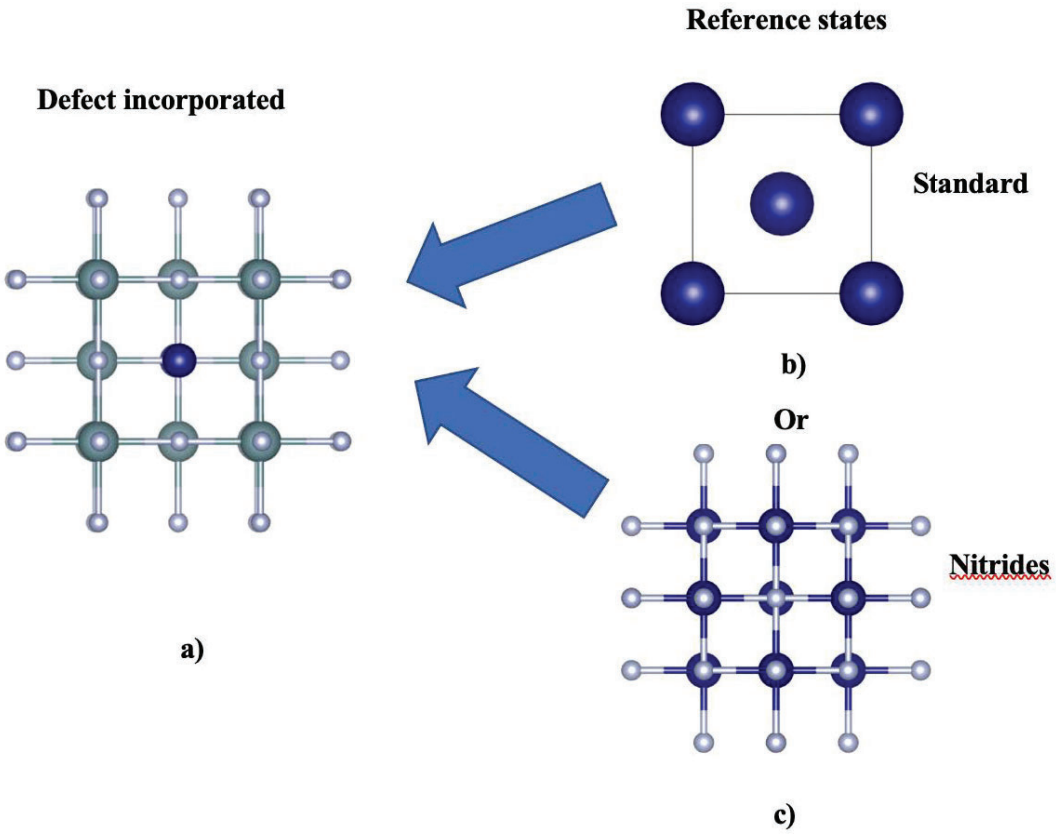

Fig. 1. (a) UN with an incorporated impurity; (b) standard reference state and (c) nitride phase both considered as the source for the impurity in the reaction with UN.

The obtained results for incorporation energies are shown in **Figure 2**. In this notation negative incorporation energies are thermodynamically favourable to occur.

From the results it is possible to observe that in general the elements at 3*p* configuration presented limited solubility in the UN matrix, independently of the site considered. One exception is P in the nitrogen site that seems to be energetically favourable. This may reflect the existence of the phases U_3P_4, UP and UP_2 [29], [30] and point out for the trend of P to strongly interact with uranium atoms. Another way to evaluate the incorporation energies is to correct the chemical potential for the impurity considering the origin as other phases. To understand the trends of solution here we also evaluated the incorporation considering stable nitride phases reported in literature. For the 3*p* group the AlN, Si_3N_4 and P_3N_5 phases were considered in this analysis. The result is also presented in **Figure 2** (orange). With this result it is possible to observe limited solubility for the 3*p* materials, from both pure and nitride states. It is possible to notice that when the nitrides are considered the reaction with UN becomes even less likely. Therefore, these elements and mainly their respective nitride phases can be used as additive to UN to produce, for example, coated grain.

The 3*d* transition metals present a different trend from the previous group. For these elements considerable solubility is observed considering the pure metal state as a reference. As the incorporation of the impurities required a U_{vac}, the amount of solution formed may be limited by the number of this defect created with temperature over the sintering process. A way to

extend the solubility is to provide at the same time nitrogen and keep the ratio metal/nitrogen close to 1:1. Therefore, it once again becomes of interest to re-evaluate the trend by correcting the chemical potential using the nitride phases as reference state. For this purpose, the TiN, CrN, Cr_2N, VN and V_8N were considered. The results can be seen in **Figure 2** (orange and grey). From this analysis it can be noticed that the incorporation of Cr in UN is still favourable even when the Cr-nitride phases (CrN and Cr_2N) are considered as the source for the incorporation impurity. This behaviour permits preservation of the metal/nitrogen ratios which can promote significant solubility. On the other hand, Ti and V nitride phases seem not very likely to react with UN. These pure metals will form solution with UN but with the solubility limited by the fraction of U_{vac}. The obtained results for Ti are in agreement with the outcomes of the experimental investigations performed on the U-N-Ti system by Holleck [18]. Therefore, Ti and V metal and nitrides can be used to combine doped grain with partially coated grain by using a combination of metal and nitride phases.

The elements of 4*d* transition metals also demonstrated a considerable degree of solubility in UN matrix when considered reaction with the pure metal state. The trend for the solubility decreases progressively from Y to Mo, demonstrating that the increase in the electronic configuration plays significant role in the solubility in UN matrix. The reaction from the nitride phases still seems very likely, being negative for Y and Zr while relatively small for the Nb and Mo, which could be overcome by entropy terms, i.e., increase in temperature. The solubility of of NbN, ZrN and YN in the matrix of UN has been investigated by Holleck et al. in a number of experimental studies. It was found that at 2000°C the system UN-ZrN demonstrate complete solid solubility [18]. The solid solution between NbN and UN was obtained by annealing the composite pellets made from the constituent nitrides in the temperature range between 1800°C and 1900°C for a long time. The X-ray analysis of the obtained product confirmed that the system UN-NbN is completely miscible [19]. The same results were obtained for UN-YN samples prepared by Holleck et al. The metallographic studies of the samples concluded that the system UN-YN shows complete solid solubility [20]. In the light of these results, these elements and their respective nitride phases can mainly be used to produce UN composite with doped grains.

The 4*f* elements demonstrated solubility in the UN matrix. This is in agreement with the experimental results obtained for the LaN-UN and CeN-UN systems [20], [19]. However, the equilibrium solid solution between CeN and UN was difficult to achieve experimentally and required long-term annealing at high temperatures [19]. This observation indicates that kinetics play significant role for these systems that might be influenced by slow diffusion of heavy elements. Although the described here methodology based on the modeling cannot predict how fast or slow the equilibrium in the system could be reached, it can still be used as a preselecting tool for experimental studies.

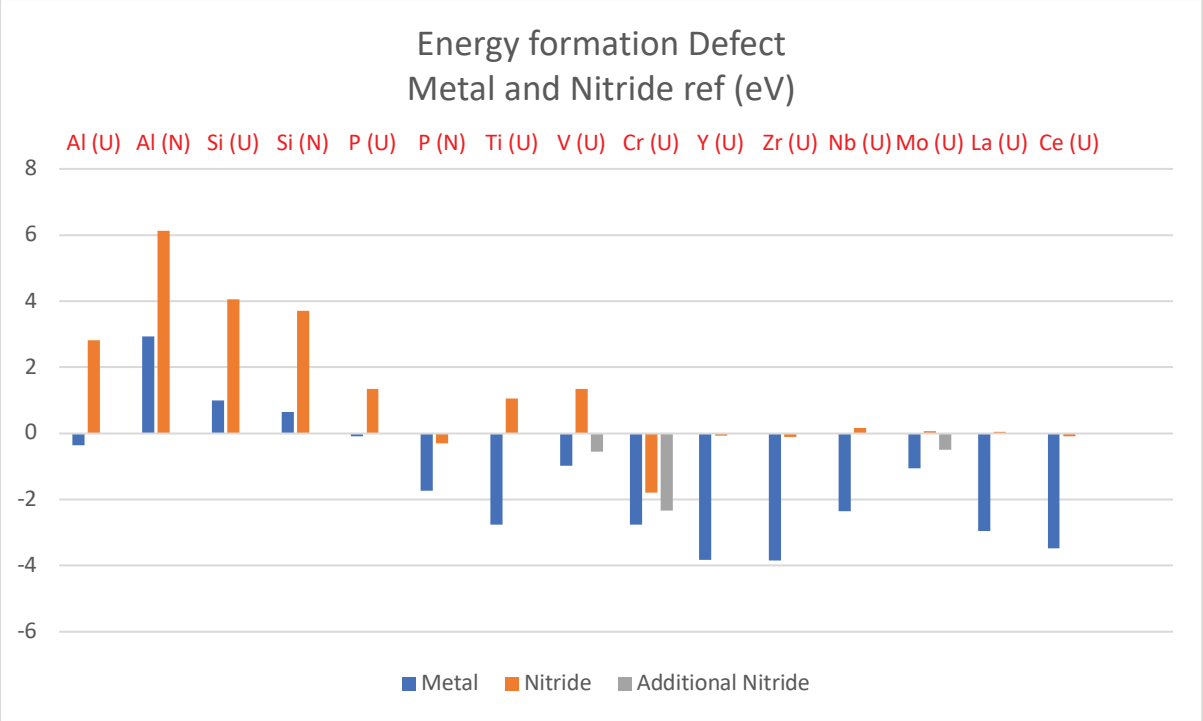

Fig. 2. Incorporation energy formation as reference from metals and nitrides

Considering the obtained results, it is possible to design composite materials with engineered microstructure by combining the insoluble in UN materials to protect the grains and soluble compounds to increase the corrosion resistance of the bulk. This concept is explained by **Figure 3.**

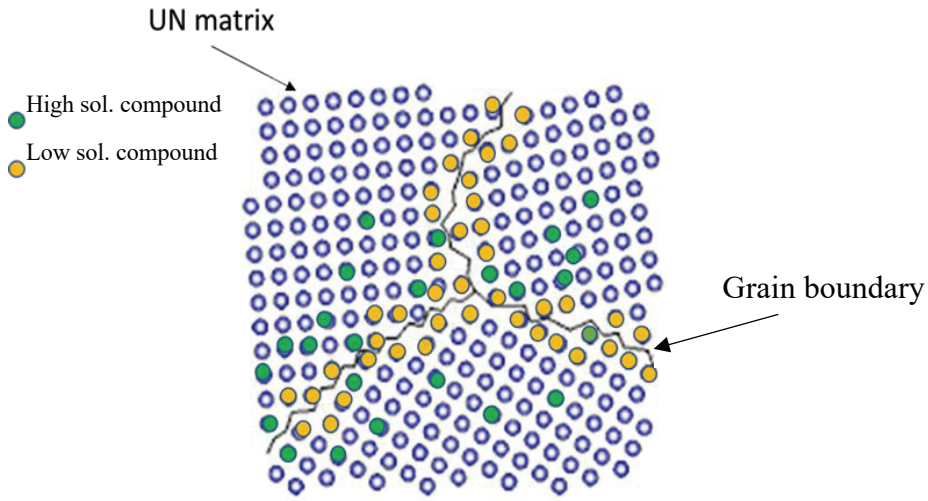

Fig. 3. Illustration of the microstructure resulting from the use of low and high solubility phases in UN matrix.

From **Figure 2** it is evident that chromium metal as well as chromium nitrides (CrN and Cr_2N) have negative values for the defect incorporation energies and, therefore, are good candidates for testing the concept of doped grains experimentally. The value for the defect incorporation energy of AlN, on the other hand, is positive, suggesting that no interaction should take place

between UN and AlN. For that reason, AlN, Cr and CrN were selected as dopants for experimental investigation. In the next section the fabrication of UN composites is presented, taking in consideration the interaction trends presented in this section. Four different systems were sintered being (i) low solubility, addition of AlN; (ii) high solubility from metal Cr and (iii) nitride CrN phase and a (iv) compound containing both low (AlN) and high (CrN) solubility to demonstrate the capability to produce a highly tailored microstructure by combining different incorporation trends.

2.2 Pellet fabrication and characterization

Composite samples were manufactured to validate the design proposed by the modeling calculations. The additives were chosen to demonstrate different modeling trends for interaction behaviour between the additives and the fuel UN matrix, namely: insolubility, limited solubility, and considerable solubility. The additive phases that were predicted to be insoluble in the UN matrix were added in the form of nanopowder (< 100nm). The purpose was to test the capability of the insoluble phase to coat the grains of UN and to work functionally to prevent it from coming into contact with the oxidising agent. Introducing the additive in the form of nanopowder would allow the material to easier distribute itself along the grain boundaries. Matrix-soluble additives were added in the form of micropowders (< 5μm). These materials were expected to form the solid solution with the UN matrix. The solid solution can operate to protect the bulk of the material from oxidation by self-passivation.

The UN powder used in this study was synthesised by the hydriding-nitriding method from natural uranium metal (acquired from the Institutt for Energiteknikk, Norway) following the procedure and the heating profile described in previously published work [31]. The resulting UN powders were transferred into an argon filled glovebox for handling. The XRD analysis on the as fabricated powder was performed using a Siemens D5000 diffractometer with Cu k-alpha target at 40 mA current and 35 kV voltage using an air-tight sample holder (Bruker, A100B138). The Rietveld refinement of the X-ray diffraction pattern on the produced UN powder was performed using Maud software [32] and the Crystallography Open Database [33]. The measured value of the lattice parameter is 4.8889 ± 0.0003 Å, corresponding to a face-centered cubic uranium mononitride [34]. Based on the obtained value of the lattice parameter the concentration of carbon impurities could be estimated to be around 300 ppm using the results of the study performed by Muromura and Tagawa [35]. Elemental analysis was performed to determine the powder oxygen and nitrogen concentrations by the inert gas fusion method using a LECO TC-136. Nitrogen and oxygen were measured to 5.4 wt% and 1600 ppm, respectively. Theoretical value for nitrogen concentration in UN is 5.56 wt% [36].

The AlN nanopowder was obtained from Sigma-Aldrich Sweden AB (98% purity), CrN (99.99% purity) and Cr (99.95% purity) powders were provided by Nanografi. The XRD analysis of the as received CrN powder confirmed the additional presence of a Cr_2N phase, with Rietveld analysis indicating a composition of 75 wt% Cr_2N and 25 wt% CrN. For simplicity, this powder will still be referred to as CrN for the remainder of the text.

The powders were mixed to obtain the following compositions in the produced pellets: UN-10AlN, UN-20AlN, UN-10Cr, UN-20Cr, UN-10CrN, UN-20CrN, UN-5AlN-5CrN, UN-10AlN-10CrN, where the numeric indicator refers to the volume percent of the secondary phase(s). The composite pellets were produced using different mixing techniques. For the first batch of pellets the composite powders were mixed mechanically inside of a glass vial with

small grinding balls. Subsequent batches were ground together in a mortar and pestle. For the pellets containing both AlN and CrN, these powders were premixed together before adding UN powder and continuing to mix. This second routine was identified as more suitable to produce a homogenous microstructure and subsequent samples were therefore produced using this route. The composite powders were transferred into graphite (9.3 mm inner diameter) sintering dies lined on the inside with graphite paper. The composite pellets were sintered using the SPS technique (Dr. Sinter, 530-ET, Stockholm University, Department of Materials and Environmental chemistry), located inside of an Ar-filled glovebox (maintained with less than 0.1 ppm O_2 and less than 0.1 ppm H_2O). Approximately 3 g of composite powders were used for each pellet. Sintering was performed in vacuum (the sintering chamber was depressurised to 2 Pa). The sintering parameters including the applied uniaxial pressure, maximum sintering temperature, holding time at the maximum temperature, as well as the densities of the sintered pellets and final oxygen composition of the sintered pellets are presented in **Table 2**. The composition of the pellets in the table is given in volume percent. The pellets that have been sintered from the premixed powders are identified by the superscript.

Table 2: Sintering parameters used to produce composite pellets.

Pellet	***Sintering temperature °C***	***Holding time, min***	***Uniaxial pressure, MPa***	***Pellet density, %TD***	***O_2, wt%***
UN	1650	3	45	97	0.3
UN-10AlN	1650	3	45	97	1.02
UN-10AlN^{premix}	1650	3	45	97	0.66
UN-20AlN^{premix}	1650	3	45	98	1.57
UN-10Cr^{premix}	1450	5	70	93	0.39
UN-20Cr^{premix}	1450	5	70	96	0.43
UN-10CrN	1450	5	70	96	0.38
UN-20CrN^{premix}	1550	5	70	99	0.22
UN-5AlN-5CrN	1550	5	70	96	0.66
UN-5AlN-5CrN^{premix}	1550	5	70	98	0.43
UN-10AlN- 10CrN^{premix}	1550	5	70	99	1.01

The density of the sintered composite pellets was measured by the Archimedes method in chloroform at the ambient temperature (T=22°C). The density of chloroform at this temperature is 1.48 g/cm^3. The amount of open porosity was measured by submerging the pellet in chloroform and pulling high vacuum (0.05 bar, just above the chloroform vapor pressure).

Phase volume fractions of the composite pellets were calculated by performing the quantitative image analysis of the micrographs using ImageJ software [37]. For each pellet composition 5 micrographs of varying magnification were analysed using the software. The area occupied by each phase on the micrograph was selected and the average value for the area fraction was obtained. The volume fraction of the corresponding phase was taken to be the measured area fraction. From the volume fraction of each phase and the theoretical densities of the individual phases (14.33 g/cm^3 for UN [34], 3.26 g/cm^3 for AlN [38], 7.19 g/cm^3 for Cr [39] and 12.7 g/cm^3 for U_2CrN_3 [40]) the density of the composite pellets was obtained by the rule of mixtures. Sintered composite pellets were cut into small pieces using a diamond saw to provide small amounts of sintered material for elemental analysis. Concentrations of oxygen and nitrogen in the sintered pellets were measured by inert fusion using a LECO TC-136, with three replicates for each material.

Transversal sections of pellets were mounted in bakelite, ground using silicon carbide paper, and polished with diamond suspension and cloth sheets. Microstructural characterization was performed by scanning electron microscopy (SEM) and energy-dispersive x-ray spectrometry (EDS) using Philips XL-30 ESEM microscope (KTH, Department of Chemistry) and JEOL JSM-7000F microscopes (Department of Materials and Environmental Chemistry, Stockholm University). Larger pieces of the sintered pellets were crushed into powder and the XRD analysis was performed on the sintered material at Studsvik Nuclear AB using a Panalytical, X-Pert^3 Power diffractometer and the Bruker sample holder. The phase composition of each pellet was determined by Rietveld analysis of the corresponding XRD pattern using a HighScore Plus software.

3. Results and discussion

3.1 UN-AlN

The resulting microstructure of the composite UN-AlN pellet is presented in **Figure 4**. It can be observed that the AlN phase (dark contrast in backscattering mode) is fairly evenly distributed over the entire sample. As was suggested by the modeling, the AlN phase demonstrated itself insoluble in the UN matrix. The EDS analysis indicated the segregation of an unreacted AlN phase being dispersed principally along the grain boundaries of the UN matrix. **Figure 5** presents high magnification images of samples produced by different mixing techniques. It is apparent that the mixture of powders prior to sintering had a significant effect on the resulting microstructure. Nanopowder, for example, has a strong tendency to cluster forming large agglomerates (**Figure 5a**). Despite this trend the results demonstrate that these agglomerates are easily broken apart by mechanical premixing of the powders (**Figure 5b** and **5c)**. Elemental analysis performed on the sintered UN-AlN pellets demonstrated a higher level of oxygen (~8000 ppm). This was not observed for pure UN pellets sintered from the same batch and same condition as a base line. This points out that the main source of O_2 is in the AlN nanopowder: a considerable amount of O_2 may have been physiosorbed in the surface. This increased level of oxygen is reflected in the XRD analysis that identified the presence of UN, AlN as well as UO_2 phase as shown in **Figure 6**. The oxygen in the system could be present in the form of uranium oxide. Small amounts of oxygen can be dissolved in the UN matrix. The solubility of oxygen in the UN has been reported to be around 5 at% [11]. The XRD analysis of the sintered composite UN-AlN pellets identified the presence of UO_2 phase in the amount of 9 wt%.

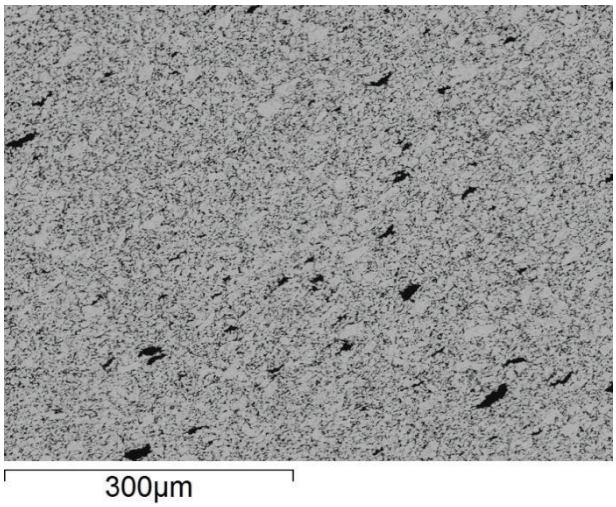

Fig. 4. Scanning electron image of the sintered composite pellet UN-20AlN^{premix}.

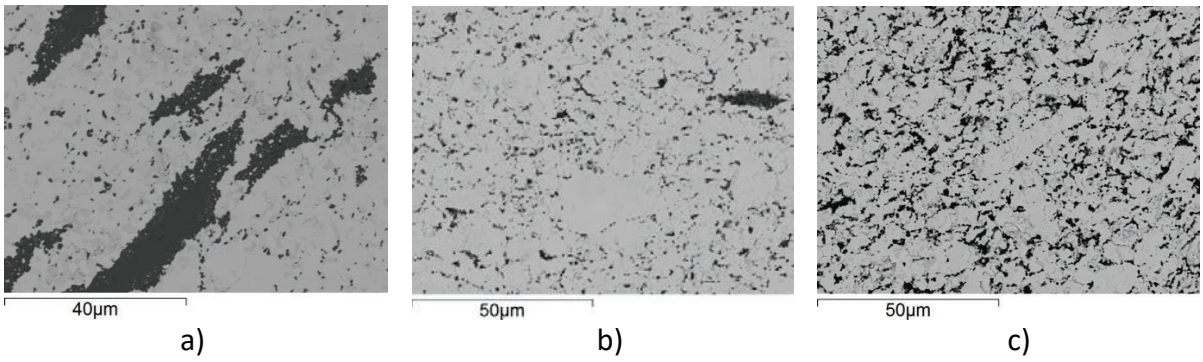

Fig. 5. Scanning electron images of sintered pellets: a) UN-10AlN, b) UN-10AlN^{premix}, c) UN-20AlN^{premix}.

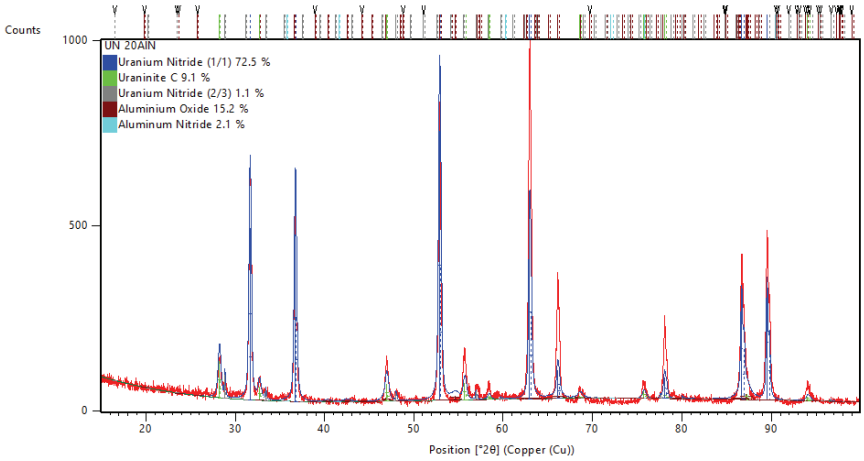

Fig. 6. XRD pattern of the as-sintered UN-20AlN^{premix} composite pellet

The absence of interaction between the AlN phase and the UN matrix is highlighted in the high magnification SEM image shown in **Figure 7**. On this image it can be seen that small particles of UN powder are dispersed within the AlN agglomerate, which demonstrates thorough mixing

of raw powders and is evidence of the absence of solubility, as neither phase is able to dissolve even such small particle sizes. On this scale it is also clear that the AlN inclusions are located along the grain boundaries of UN and a fine dispersion of the nanopowder can produce significant grain coating, thereby permitting the creation of a potentially protective layer without the need for significant addition of material.

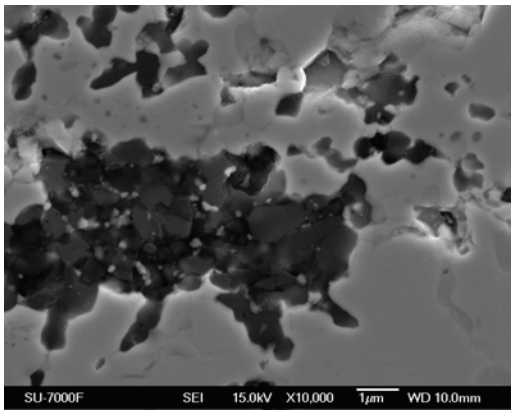

Fig. 7. Scanning electron image of sintered composite pellet UN-20AlN^{premix}

3.2 UN-Cr

The resulting microstructure for the UN composite with Cr-metal is presented in **Figure 8** for UN-10Cr^{premix} mixture. To guide the phase identification EDS was performed and a summary is presented in **Figure 9**. On the backscatter electron analysis, three distinct phases become distinguishable. The matrix, brighter in contrast, is composed of uranium and nitrogen elements. The black phase, always localized at grain boundaries, presents the composition of Cr-metal. The intermediate grey phase is observed to be occurring in the interface of Cr-metal and the matrix, and demonstrates a composition of uranium, chromium and nitrogen.

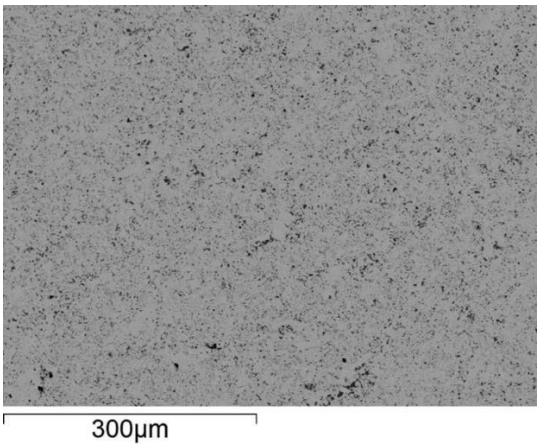

Fig. 8. Scanning electron images of the sintered UN-10Cr^{premix} pellet

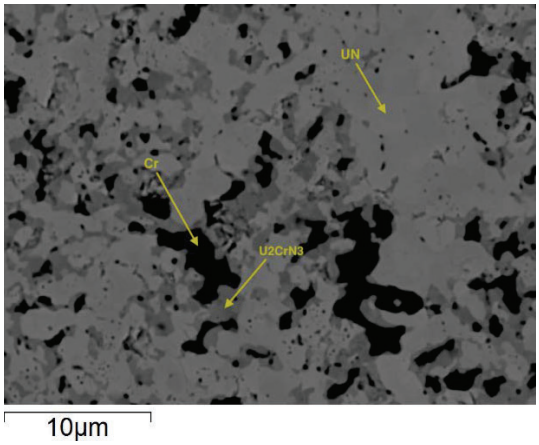

Phase	*N*	*Cr*	*U*
UN	79.05		20.95
U_2CrN_3	76.22	7.76	16.02
Cr		100	

Fig. 9. Micrograph and corresponding EDS analysis of the UN-10Cr^{premix} pellet (in atomic percent)

The proportion of uranium to chromium atoms in this intermediate grey phase was determined to be approximately 2:1 respectively. This proportion is in agreement with the ternary phase U_2CrN_3 [40]. In previous work by Herman et al., when the fabrication process of the compounds was performed through the sol-gel method, the formation of this phase was not observed [13]. However, based on the existing ternary phase diagram of the uranium-chromium-nitrogen system it is predicted to form in the temperature range between 1200°C and 1600°C [17]. This ternary phase, although described with a different crystallographic space group, can be viewed as a distorted version of UN, as can be demonstrated in **Figure 10**. The ternary U_2CrN_3 phase was previously investigated by Zachariasen et al. [41]. This phase has an orthorhombic crystal structure and belongs to space group Immm [40]. If compared with the crystal structure of UN, the similarities between the two could be detected. The unit cell of the U_2CrN_3 phase consists of two UN unit cells in *c*-direction. The U-N and Cr-N bond lengths in the ternary phase are almost the same as the bond lengths in UN and CrN. When a chromium atom replaces the uranium atom in the lattice of the face-centered cubic UN, the bond length decreases from 2.45 Å for UN to 2.07 Å for CrN causing the distortion in the original lattice [41]. The distortion in the lattice caused by Cr replacement in uranium site seems to limit the amount of solution to 33 at%, forcing the Cr to only occupy the 2nd nearest neighbours (NN). The orthorhombic structure is generally formed in the same way from a cubic lattice by stretching the bonds. The density of the ternary phase is reported to be 12.7 g/cc [40]. The uranium density of this compound is 10.61 g/cc, which is higher than the uranium density of UO_2 (9.66 g/cc), making the ternary phase a potential candidate for the ATF concept. The occurrence of this phase, being basically a solid solution with limited solution up to 33 at% demonstrated again agreement with the modeling result for the incorporation of Cr in UN. It is worth to mention that on the EDS analysis level of nitrogen is high, both for UN and U_2CrN_3 phases. That could be due to fluorescence in nitrogen caused by very energetic X-rays from uranium atoms [42]. The XRD pattern of the sintered composite pellet is shown in **Figure 11**. The amount of the phases was quantified using Rietveld analysis. Based on the results of the analysis the majority of the composite pellet consists of the unreacted UN, followed by the ternary U_2CrN_3 phase. The presence of metallic chromium could not be detected with the XRD analysis probably due to the low scattering factor this metal has in comparison with the phase containing uranium.

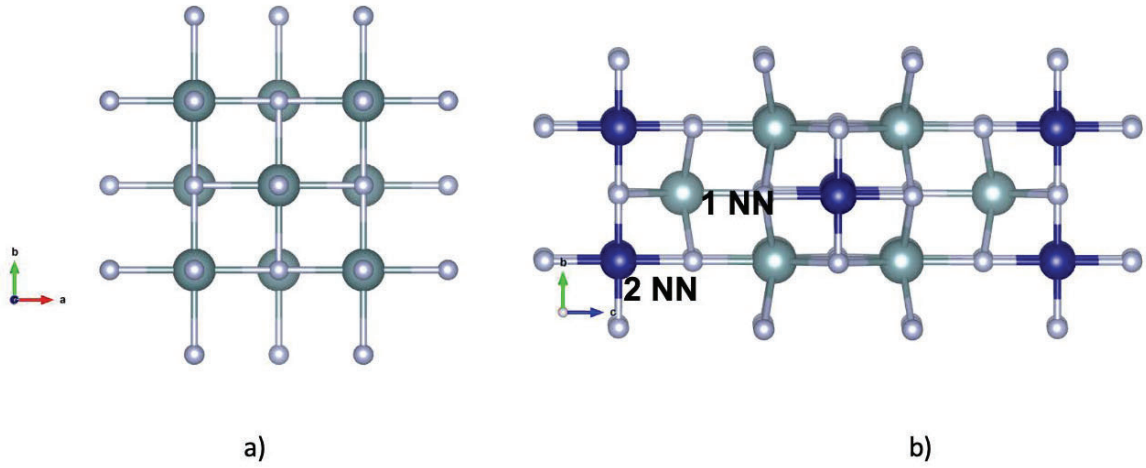

Fig. 10. Demonstration of the unit cell (a) UN and (b) U_2CrN_3

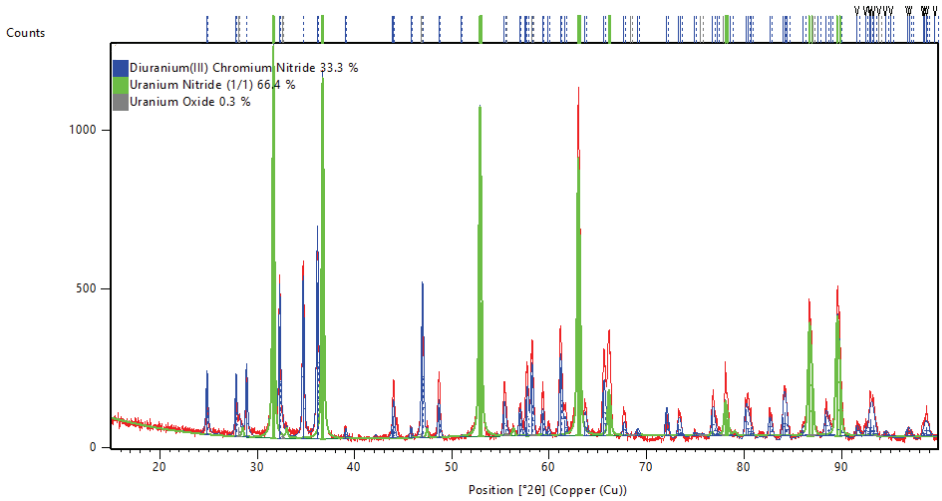

Fig. 11. XRD pattern of the as-sintered UN-20Cr^{premix} composite pellet

Theoretical densities of the UN-Cr composite pellets were calculated by quantitative image analysis using ImageJ software, as described in the methodology section. In **Figure 12**, one of the micrographs used in this calculation is shown, demonstrating how the phase selection by threshold was performed in this study.

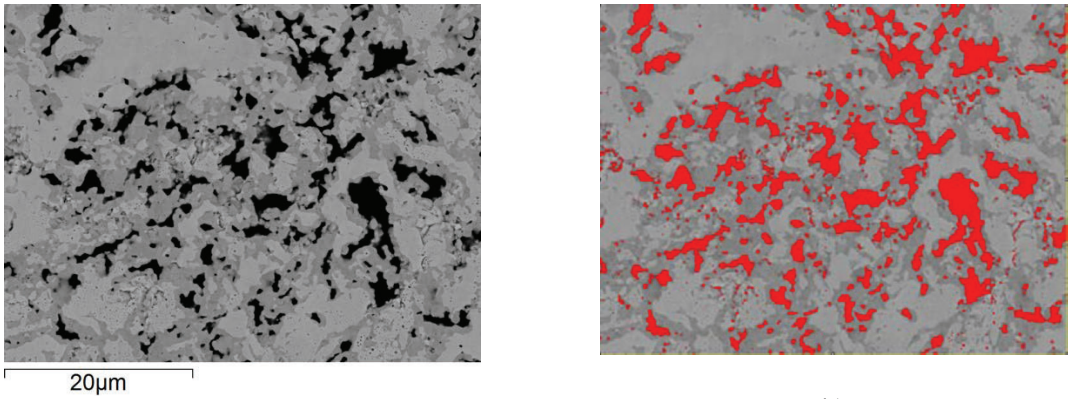

Fig. 12. Scanning electron images of UN-20Cr^{premix}: a) original, b) being analysed by ImageJ.

The actual densities of the pellets (measured by the Archimedes method) were compared to the theoretical densities, calculated by the image analysis method. Even though the sintering parameters for both pellets were identical, the densities of them were slightly different. The UN-10Cr^{premix} composite pellet exhibited lower density, 93%TD with 3.64 % open porosity. The density of the UN-20Cr^{premix} was measured to be 96%TD with 0.48% open porosity. This difference could be due to metallic chromium softening during sintering and assisting with densification.

The image analysis of the micrographs was also used to calculate the total solubility of Cr-metal in the matrix of UN. The volume fraction of the ternary phase (U_2CrN_3) in the pellets containing 10 and 20 vol % of Cr is 30% and 42% respectively. These results correspond to the amount of chromium that formed the ternary U_2CrN_3 phase in the UN matrix being 33% by weight in both pellets. This number indicates that the solubility of chromium in UN is limited. The majority of the chromium added remained in the separate phase. From the micrograph shown in **Figure 12** it could be observed that the ternary phase formed around the chromium inclusions. This indicates that chromium atoms diffused from the chromium rich regions into the uranium nitride. As was shown in the modeling calculation section the incorporation of Cr-metal into the matrix of UN is facilitated by the formation of uranium vacancies. The number of vacancies in the UN is increased dramatically during sintering. Chromium atoms move into the vacant positions in the UN lattice forming the ternary U_2CrN_3 phase. The amount of this phase is limited to the number of uranium vacancies.

3.3 UN-CrN

The microstructure of the composite UN-CrN pellet is shown in **Figure 13**. The EDS analysis and the XRD confirmed the presence of the ternary U_2CrN_3 phase similar to what has been observed for Cr-metal addition. As was suggested by the modeling calculations the formation of the solid solution between UN and CrN is also energetically favourable.

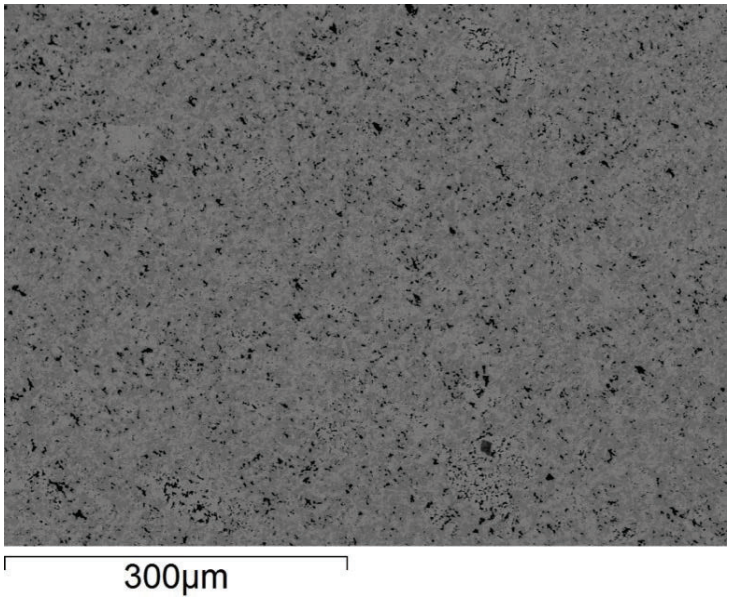

Fig. 13. Scanning electron images of UN-20CrN^{premix} composite pellet

The same qualitative image analysis of the pellet microstructure was performed providing the volume fraction of the ternary phase within the pellets, being around 52 vol% and 36 vol% for the UN-20CrN^{premix} and UN-10CrN respectively. The calculated weight fraction of Cr being present in the ternary phase is approximately 50 wt% in the UN-20CrN^{premix} and 40 wt% in the UN-10CrN. The difference in the amounts of chromium being present in the metallic form and in the ternary phase could be attributed to different mixing techniques but also to different sintering temperatures.

If compared to the composite pellets with Cr-metal as a starting material, it is evident that the doped fraction formed in the UN matrix increases if chromium enters the system in the form of the nitride, as demonstrated in **Figure 14**. The presence of nitrogen in the CrN phase changes the mechanism of formation of the ternary compound. The solubility of Cr in the UN for the UN-Cr composites was limited by the number of uranium vacancies in the UN lattice. In the UN-CrN system the formation of the solid solution is favoured thermodynamically, accompanied by the reduction in the total Gibbs energy of the system. Thermodynamically, the reactions between Cr_2N, CrN and UN are suggested to be as follows [40]:

$$0.667\ UN + 0.333\ Cr_2N \rightarrow 0.333\ U_2CrN_3 + 0.333\ Cr, \quad E_{rxn} = -21.06\ kJ/mol \qquad (3)$$

$$0.667\ UN + 0.333\ CrN \rightarrow 0.333\ U_2CrN_3, \quad E_{rxn} = -25.42\ kJ/mol \qquad (4)$$

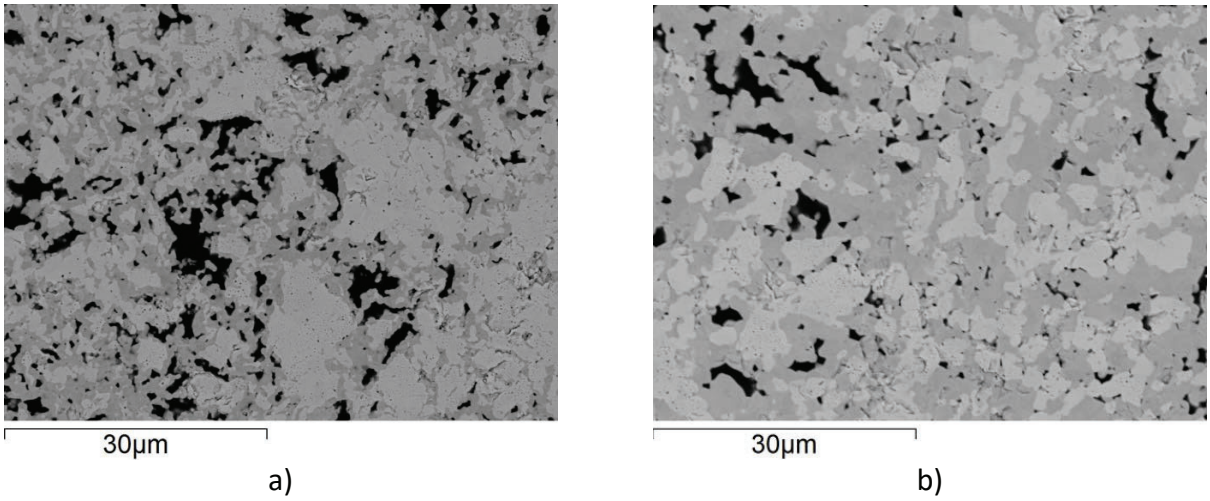

Fig. 14. Scanning electron images of sintered composite pellets: a) UN-20Cr^{premix}, b) UN-20CrN^{premix}.

The presence of the Cr_2N in the starting material resulted in the inclusions of Cr-metal. The shape of the metallic chromium phase in **Figure 15** suggests that the phase softened during sintering similar to what was observed for Cr-metal addition.

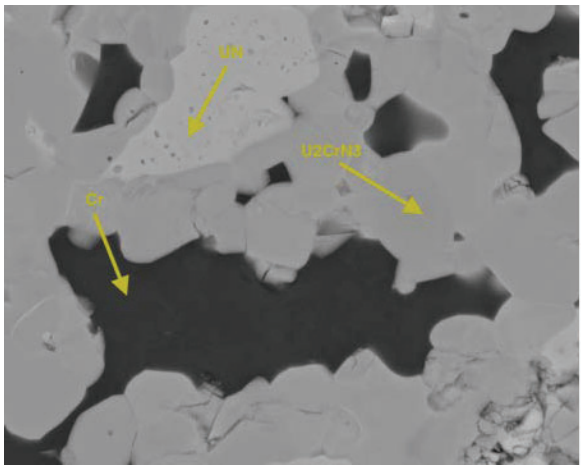

Fig. 15. Scanning electron images of sintered composite pellet UN-20CrN^{premix}.

In agreement with the modeling results these nitride composites can be used to obtain extensive solution in the UN matrix providing a high fraction of produced doped grains.

3.4 UN-CrN-AlN

The microstructure of the composite pellet containing AlN and CrN with UN is shown in **Figure 16**. Similar to the composite pellets containing only CrN or only AlN, the microstructure of the composite pellet UN-10AlN-10CrN^{premix} demonstrates the presence of the metallic chromium phase, the ternary U_2CrN_3, as well as the unreacted AlN and UN (**Figure 17**). The contrast of the image in **Figure 17** allows to differentiate between the AlN and the

metallic Cr, the AlN being slightly darker in colour than chromium. This microstructure demonstrates two trends predicted by modeling: the solubility of CrN in UN and the complete insolubility of the AlN and highlights the possibility to combine both to produce composite with a tailored microstructure.

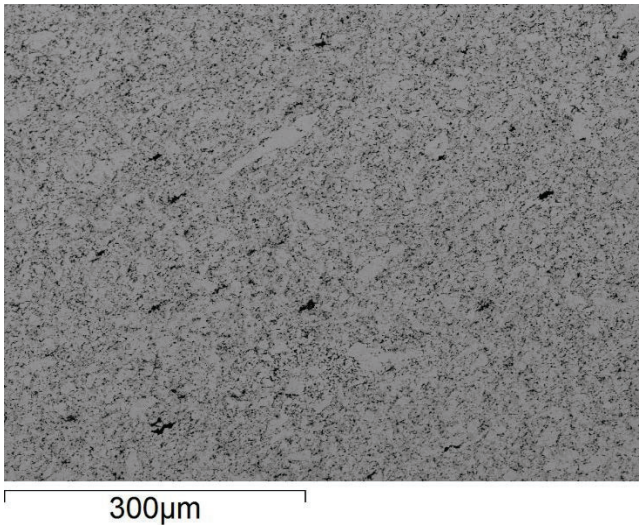

Fig. 16. Scanning electron images of sintered composite pellet UN-10AlN-10CrN^{premix}.

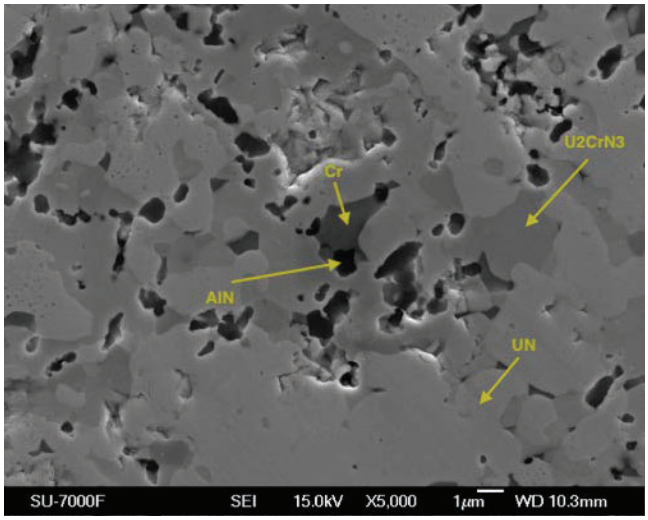

Fig. 17. Scanning electron images of sintered composite pellet UN-10AlN-10CrN^{premix}

The element mapping presented in **Figure 18** assisted further with the identification of the phases. The yellow map shows the distribution of chromium. Two trends are visible on the map. The bright yellow areas correspond to Cr-metal, formed in the reaction between Cr_2N and UN (Eq. 3). The less saturated parts of the map correspond to the ternary U_2CrN_3 phase.

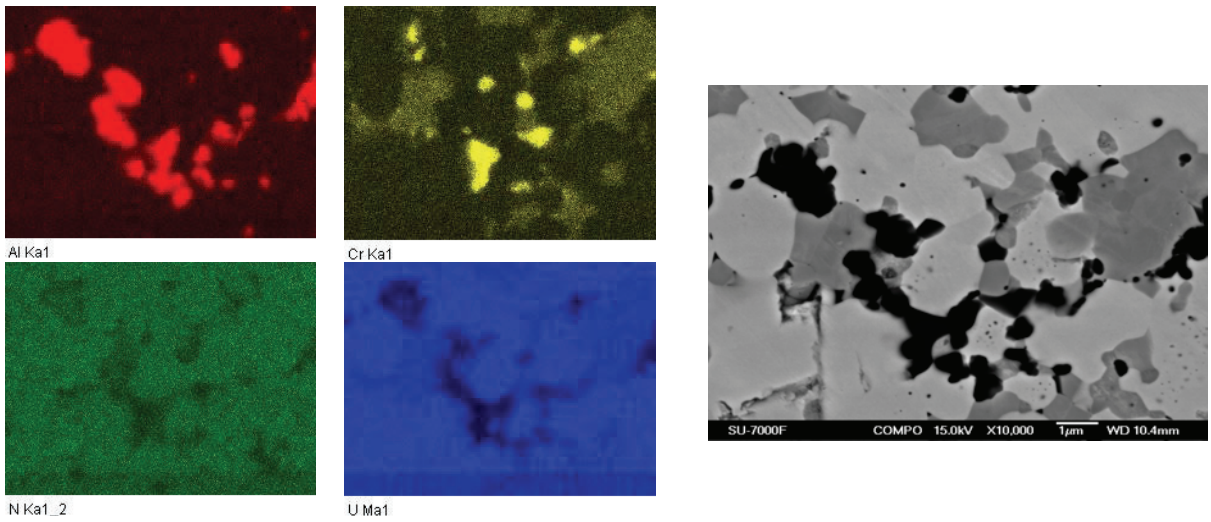

Fig. 18. Element mapping of the composite pellet UN-10AlN-10CrN^{premix}

The XRD pattern of the composite pellet UN-5AlN-5CrN is presented in **Figure 19**. The main phase after sintering is uranium nitride. The AlN phase in the sintered pellet is unchanged, further confirming the lack of interaction between this phase and the UN matrix. The presence of the diuranium(III) chromium nitride (U_2CrN_3) in the amount of 10.5 wt% confirms the solubility of chromium in the UN matrix. The oxide phase is present in the amount of 2.9 wt%, similar to the UN-AlN composites suggesting that the nanopowder surface is the main source of oxygen.

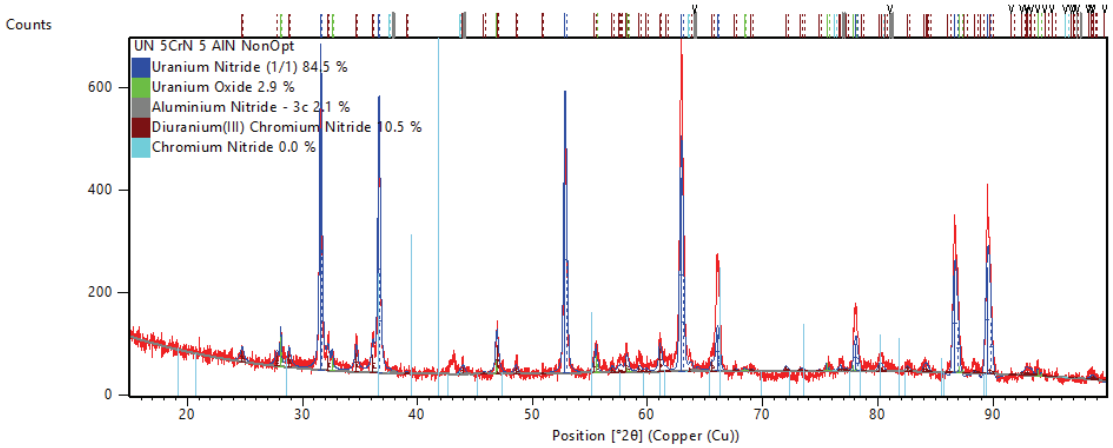

Fig. 19. XRD pattern of the as-sintered UN-5AlN-5CrN composite pellet

The interaction between the phases in the composite pellet UN-10AlN-10CrN^{premix} is shown in **Figure 20**. The interface between the UN matrix and the ternary U_2CrN_3 is smooth. The morphology of both phases appears similar. AlN exhibits different behaviour. The phase is brittle and is easily removed during sample preparation, as shown in **Figure 20 b**. It appears

that AlN introduces stress to UN matrix, where in some areas of the sample intragranular cracking in the UN matrix was observed.

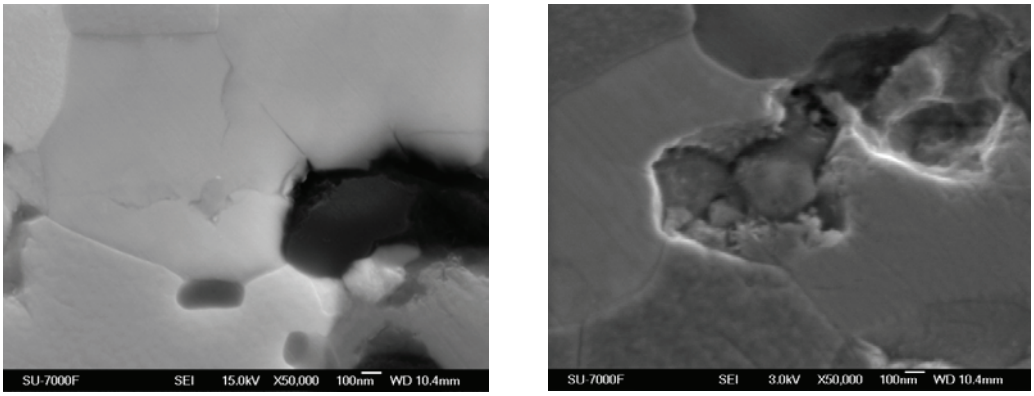

a) b)

Fig. 20. Scanning electron images of sintered composite pellet UN-10AlN-10CrN^{premix}

The resulting microstructure observed for the UN-CrN-AlN composites showed consistency with the design microstructure proposed in **Figure 3**. This highlights the efficiency of using modeling results to guide composite fabrication and reinforces the fact that the fabrication route adopted in this work is suitable to produce such tailored microstructure.

4. Conclusions

In this study we presented a methodology of fabrication of UN composites with engineered microstructure. The dopants were added into the UN matrix in order to improve the corrosion resistance of UN fuel by interacting with the UN matrix in two ways: to shield the grains of UN from coming into contact with the oxidising agent (coated grains) and to lower the rate of oxygen diffusion through the bulk (doped grains). The modeling calculations were conducted to screen the potential additive candidates and to predict the possible interactions between these additives and the UN matrix. The results based on first principles calculation predicted that elements from the electronic configuration group 3*p* (e.g., Al, Si, P) will demonstrate limited solubility in U site when added to the UN, when entered either in the form of nitride or the pure compound. The elements from the 3*d* group (e.g., Cr, V, Ti), on the other hand, were predicted to demonstrate considerable solubility with UN. From this group Cr was the only one identified as the material that will interact with the UN matrix to form solid solution, if added as metal and as a nitride phase. However, it was possible to conclude that the amount of solid solution formed when Cr-metal was added is limited by the number of uranium vacancies present in the lattice of UN. If Cr entered the system in the form of CrN or Cr_2N, the amount of the solid solution formed was predicted to be higher.

In order to evaluate the results of the modeling calculation Al and Cr were selected for the experimental investigation. Composite pellets containing AlN, CrN and Cr were sintered using the Spark Plasma Sintering. The metallographic analysis of the composite pellets confirmed the possibility to obtain an engineered microstructure. No interaction between the AlN and the UN was observed in the UN-AlN composite pellets. The unreacted AlN phase was distributed along the grain boundaries of UN, creating the coated grain effect. This experimental result

confirmed that it would be possible to produce a protective coating around the grains of UN by adding small amounts of the corrosion resistant additive. The presence of the ternary U_2CrN_3 phase was encountered in the composite pellets containing chromium, which confirms the modeling prediction of the interaction between Cr and UN. The ternary phase is a distorted version of UN formed by chromium atoms replacing the uranium atoms in the UN lattice and can be considered a solid solution (maximum Cr solubility 33 at%). This phase has not been observed experimentally in previous studies where chromium was added into the UN fuel matrix, although the existence of this phase has been predicted by the phase diagram. It is evident that the manufacturing parameters used for the fabrication of the composite materials play an important role in the resulting microstructure of the composite pellets. The amount of solid solution in the samples differed depending on whether the additive material was introduced into the system in the form of CrN or Cr-metal. The amount of the solid solution in the samples produced from Cr-metal was limited by the number of uranium vacancies formed in UN at elevated temperature. The fraction of the doped grains increased in the composite pellets produced from CrN. The formation of the ternary phase in the UN-CrN system is favoured thermodynamically. Different mechanisms of formation of the solid solution in the two systems allow to have a combination of doped grains of UN (with CrN as additive) and partially doped grains (with Cr-metal as additive). The U_2CrN_3 phase has a higher uranium density than UO_2, which makes it an interesting ATF fuel candidate. Therefore, more studies need to be done to investigate the properties and characteristics of the ternary U_2CrN_3 compound, as well as its oxidation behaviour under various oxidising environments.

Experimental results obtained in this study demonstrate that design microstructures of UN composite materials could be fabricated to create coated grains by addition of insoluble compounds as well as doped and partially doped grains by addition of soluble elements. The modeling calculations presented here can be successfully applied for screening of the potential candidates for composite materials and for predicting their interaction with the UN matrix. Using this tool prior to experimental research will allow to better design and perform experiments, choosing only the best additive candidates considering the main goal to be achieved.

REFERENCES

[1] E. O. Speidel and D. L. Keller, ‘FABRICATION AND PROPERTIES OF HOT-PRESSED URANIUM MONONITRIDE’, Battelle Memorial Inst., Columbus, Ohio, BMI-1633; EURAEC-706, May 1963. doi: https://doi.org/10.2172/4674236.

[2] G. J. Youinou and R. S. Sen, ‘Impact of Accident-Tolerant Fuels and Claddings on the Overall Fuel Cycle: A Preliminary Systems Analysis’, *Nucl. Technol.*, vol. 188, no. 2, pp. 123–138, Nov. 2014, doi: 10.13182/NT14-22.

[3] J. Zakova and J. Wallenius, ‘Fuel residence time in BWRs with nitride fuels’, *Ann. Nucl. Energy Oxf.*, vol. 47, pp. 182–191, 2012, doi: 10.1016/j.anucene.2012.03.033.

[4] S. J. Zinkle, K. A. Terrani, J. C. Gehin, L. J. Ott, and L. L. Snead, ‘Accident tolerant fuels for LWRs: A perspective’, *J. Nucl. Mater.*, vol. 448, no. 1, pp. 374–379, May 2014, doi: 10.1016/j.jnucmat.2013.12.005.

[5] Y. Yamamoto, B. A. Pint, K. A. Terrani, K. G. Field, Y. Yang, and L. L. Snead, ‘Development and property evaluation of nuclear grade wrought FeCrAl fuel cladding for light water reactors’, *J. Nucl. Mater.*, vol. 467, pp. 703–716, Dec. 2015, doi: 10.1016/j.jnucmat.2015.10.019.

[6] S. Dryepondt, K. A. Unocic, D. T. Hoelzer, C. P. Massey, and B. A. Pint, ‘Development of low-Cr ODS FeCrAl alloys for accident-tolerant fuel cladding’, *J. Nucl. Mater.*, vol. 501, pp. 59–71, Apr. 2018, doi: 10.1016/j.jnucmat.2017.12.035.

[7] J. E. Antill and B. L. Mya, ‘KINETICS OF THE OXIDATION OF UN AND U(C0) IN CARBON DIOXIDE, STEAM AND WATER AT. ELEVATED TEMPERATURES’, p. 7.

[8] K. Johnson, V. Ström, J. Wallenius, and D. A. Lopes, ‘Oxidation of accident tolerant fuel candidates’, *J. Nucl. Sci. Technol.*, vol. 54, no. 3, pp. 280–286, Mar. 2017, doi: 10.1080/00223131.2016.1262297.

[9] A. P. Shivprasad, A. C. Telles, and J. T. White, ‘Report on waterproofing of UN studies’, LA-UR-19-28422, 1565797, Sep. 2019. doi: 10.2172/1565797.

[10] D. A. Lopes, S. Uygur, and K. Johnson, ‘Degradation of UN and UN–U3Si2 pellets in steam environment’, *J. Nucl. Sci. Technol.*, vol. 54, no. 4, pp. 405–413, Apr. 2017, doi: 10.1080/00223131.2016.1274689.

[11] B. J. Jaques *et al.*, ‘Synthesis and sintering of UN-UO2 fuel composites’, *J. Nucl. Mater.*, vol. 466, pp. 745–754, Nov. 2015, doi: 10.1016/j.jnucmat.2015.06.029.

[12] J. K. Watkins, D. P. Butt, and B. J. Jaques, ‘Microstructural degradation of UN and UN-UO2 composites in hydrothermal oxidation conditions’, *J. Nucl. Mater.*, vol. 518, pp. 30–40, May 2019, doi: 10.1016/j.jnucmat.2019.02.027.

[13] A. Herman and C. Ekberg, ‘A Uranium Nitride Doped with Chromium, Nickel or Aluminum as an Accident Tolerant Fuel’, *Res. Rev. J. Mater. Sci.*, vol. 05, Jan. 2017, doi: 10.4172/2321-6212.1000196.

[14] T. J. Davies and P. E. Evans, ‘The preparation and examination of mixtures of aluminium nitride (AlN) and uranium mononitride (UN)’, *J. Nucl. Mater.*, vol. 13, no. 2, pp. 152–168, Jan. 1964, doi: 10.1016/0022-3115(64)90037-6.
[15] Y. Mishchenko, *Composite UN-UO2 fuels*. 2018.
[16] D. Costa, M. Hedberg, S. Middleburgh, J. Wallenius, P. Olsson, and D. Lopes, ‘UN microspheres embedded in UO2 matrix: An innovative accident tolerant fuel’, *J. Nucl. Mater.*, vol. 540C, Jul. 2020, doi: 10.1016/j.jnucmat.2020.152355.
[17] H. Holleck, ‘Ternary phase equilibria in the systems actinide--transition metal--carbon and actinide--transition metal--nitrogen’, International Atomic Energy Agency, Vienna, CONF-741030-P2, Jan. 1975. Accessed: Nov. 02, 2020. [Online]. Available: https://www.osti.gov/biblio/4177518.
[18] H. Holleck, E. Smallos, and F. Thümmler, ‘Zur Mischkristallbildung in den quasibinären Systemen von UN und den Mononitriden der IV A-Gruppe TiN, ZrN und HfN’, *Monatshefte Für Chem. Chem. Mon.*, vol. 99, no. 3, pp. 985–989, May 1968, doi: 10.1007/BF00913744.
[19] H. Holleck, E. Smailos, and F. Thümmler, ‘Zur mischkristallbildung von un mit den nitriden der seltenen erden CeN und NdN’, *J. Nucl. Mater.*, vol. 28, no. 1, pp. 105–109, Oct. 1968, doi: 10.1016/0022-3115(68)90061-5.
[20] H. Holleck, E. Smailos, and F. Thümmler, ‘Zur mischphasenbildung der mononitride in den systemen U- (Y, La, Pr)-N’, *J. Nucl. Mater.*, vol. 32, no. 2, pp. 281–289, Sep. 1969, doi: 10.1016/0022-3115(69)90077-4.
[21] G. Kresse and J. Furthmüller, ‘Efficiency of ab-initio total energy calculations for metals and semiconductors using a plane-wave basis set’, *Comput. Mater. Sci.*, vol. 6, no. 1, pp. 15–50, Jul. 1996, doi: 10.1016/0927-0256(96)00008-0.
[22] G. Kresse and J. Furthmüller, ‘Efficient iterative schemes for ab initio total-energy calculations using a plane-wave basis set’, *Phys. Rev. B*, vol. 54, no. 16, pp. 11169–11186, Oct. 1996, doi: 10.1103/PhysRevB.54.11169.
[23] J. P. Perdew, K. Burke, and M. Ernzerhof, ‘Generalized Gradient Approximation Made Simple’, *Phys. Rev. Lett.*, vol. 77, no. 18, pp. 3865–3868, Oct. 1996, doi: 10.1103/PhysRevLett.77.3865.
[24] P. E. Blöchl, ‘Projector augmented-wave method’, *Phys. Rev. B*, vol. 50, no. 24, pp. 17953–17979, Dec. 1994, doi: 10.1103/PhysRevB.50.17953.
[25] G. Kresse and D. Joubert, ‘From ultrasoft pseudopotentials to the projector augmented-wave method’, *Phys. Rev. B*, vol. 59, no. 3, pp. 1758–1775, Jan. 1999, doi: 10.1103/PhysRevB.59.1758.
[26] S. L. Dudarev, G. A. Botton, S. Y. Savrasov, C. J. Humphreys, and A. P. Sutton, ‘Electron-energy-loss spectra and the structural stability of nickel oxide: An LSDA+U study’, *Phys. Rev. B*, vol. 57, no. 3, pp. 1505–1509, Jan. 1998, doi: 10.1103/PhysRevB.57.1505.
[27] A. Jain *et al.*, ‘Formation enthalpies by mixing GGA and GGA $+$ U calculations’, *Phys. Rev. B*, vol. 84, no. 4, p. 045115, Jul. 2011, doi: 10.1103/PhysRevB.84.045115.
[28] O. Kubaschewski, C. B. Alcock, P. J. Spencer, and O. Kubaschewski, *Materials thermochemistry*. Oxford; New York: Pergamon Press, 1993.
[29] P. Burlet, J. Rossat-Mignod, R. Troć, and Z. Henkie, ‘Non-colinear magnetic structure of U3P4 and U3As4’, *Solid State Commun.*, vol. 39, no. 6, pp. 745–749, Aug. 1981, doi: 10.1016/0038-1098(81)90449-X.
[30] J. S. Olsen, L. Gerward, U. Benedict, S. Dabos, and O. Vogt, ‘High-pressure phases of uranium monophosphide studied by synchrotron x-ray diffraction’, *Phys. Rev. B*, vol. 37, no. 15, pp. 8713–8718, 1988, doi: 10.1103/PhysRevB.37.8713.

[31] P. Malkki, M. Jolkkonen, T. Hollmer, and J. Wallenius, ‘Manufacture of fully dense uranium nitride pellets using hydride derived powders with spark plasma sintering’, *J. Nucl. Mater.*, vol. 452, no. 1, pp. 548–551, Sep. 2014, doi: 10.1016/j.jnucmat.2014.06.012.
[32] L. Lutterotti, M. Bortolotti, G. Ischia, I. Lonardelli, and H.-R. Wenk, ‘Rietveld Texture Analysis from Diffraction Images’, *Z. Krist. Suppl.*, vol. 2007, Nov. 2007, doi: 10.1524/zksu.2007.2007.suppl_26.125.
[33] ‘Crystallography Open Database’. http://www.crystallography.net/cod/ (accessed Jul. 09, 2020).
[34] R. E. Rundle, N. C. Baenziger, A. S. Wilson, and R. A. McDonald, ‘The Structures of the Carbides, Nitrides and Oxides of Uranium [1]’, *J. Am. Chem. Soc.*, vol. 70, no. 1, pp. 99–105, Jan. 1948, doi: 10.1021/ja01181a029.
[35] T. Muromura and H. Tagawa, ‘Lattice parameter of uranium mononitride’, *J. Nucl. Mater.*, vol. 79, no. 1, pp. 264–266, 1979.
[36] R. M. Dell, V. J. Wheeler, and E. J. McIver, ‘Oxidation of uranium mononitride and uranium monocarbide’, *Trans. Faraday Soc.*, vol. 62, no. 0, pp. 3591–3606, 1966, doi: 10.1039/TF9666203591.
[37] S. M. Hartig, ‘Basic Image Analysis and Manipulation in ImageJ’, *Curr. Protoc. Mol. Biol.*, vol. 102, no. 1, p. 14.15.1-14.15.12, 2013, doi: https://doi.org/10.1002/0471142727.mb1415s102.
[38] K. M. Taylor and C. Lenie, ‘Some Properties of Aluminum Nitride’, *J. Electrochem. Soc.*, vol. 107, no. 4, p. 308, 1960, doi: 10.1149/1.2427686.
[39] H.-J. Lunk, ‘Discovery, properties and applications of chromium and its compounds’, *ChemTexts*, vol. 1, Mar. 2015, doi: 10.1007/s40828-015-0007-z.
[40] ‘Materials Project’. https://materialsproject.org/#apps/interfacereactions (accessed Aug. 19, 2020).
[41] R. Benz and W. H. Zachariasen, ‘Crystal structures of Th2CrN3, Th2MnN3, U2CrN3 and U2MnN3’, *J. Nucl. Mater.*, vol. 37, no. 1, pp. 109–113, Oct. 1970, doi: 10.1016/0022-3115(70)90187-X.
[42] D. E. Newbury* and N. W. M. Ritchie, ‘Is Scanning Electron Microscopy/Energy Dispersive X-ray Spectrometry (SEM/EDS) Quantitative?’, *Scanning*, vol. 35, no. 3, pp. 141–168, 2013, doi: https://doi.org/10.1002/sca.21041.
26/01/2021 12:22:00

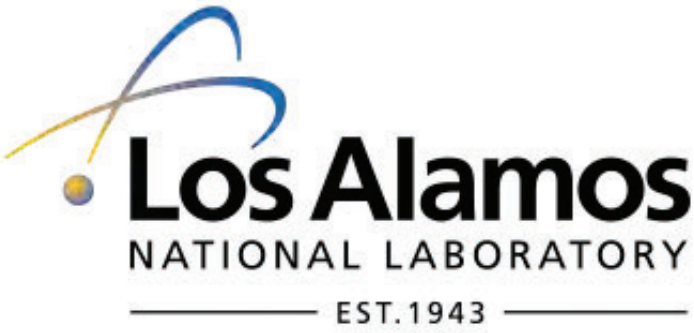

Empirical potential development for Uranium Mononitride (UN)

Vancho Kocevski, Michael W. D. Cooper, and David A. Andersson

Los Alamos National Laboratory, Los Alamos, NM 87545, USA

January 29, 2021

Contents

1 Executive Summary

Atomic-scale modeling of thermophysical and defect properties of uranium mononitride (UN) play an important role in establishing a better understanding and improved models of UN fuel performance. Having an accurate interatomic potential is crucial for generating reliable data at finite temperatures using molecular dynamic simulations. We report a new interatomic potential for UN, based on a combination of many-body and pairwise interactions. The potential was fitted to experimental thermal expansion and single crystal elastic constants, as well as Frenkel, Schottky, anti-Schottky, and antisite pair reaction energies from density functional theory (DFT) calculations. Using the potential we successfully reproduced experimental lattice parameters, thermal expansion, single crystal elastic constants, and temperature dependent heat capacity. The potential also performs reasonably well in reproducing the energy for stoichiometric defect reactions and defect migration barriers calculated using DFT. Furthermore, the potential predicted that a U split interstitial is more stable than a regular interstitial, which was later confirmed by DFT calculations. However, the potential underestimates the energy difference between the regular and split interstitial, and a more complex potential form might be needed to overcome this issue. The potential was also used to represent the behavior of UN bulk modulus at different temperatures. Finally, we demonstrate that the interatomic potential performs as well as or better than literature interatomic potentials for a number of defect and thermophysical properties of UN.

2 Introduction

The increasing demand for energy requires finding a reliable source that at the same time is carbon free, thus not contributing to global warming. Nuclear energy has been seen as one of the main options, in addition to renewable sources, such as solar, wind and hydroelectric. However, the Fukushima Daiichi accident emphasized a desire for light water reactors (LWR) with more coping time, instigating the Accident Tolerant Fuel (ATF) initiative. Uranium mononitride (UN) has been proposed as a candidate fuel for Generation IV (GEN-IV) nuclear reactors [1], as well as a possible new fuel for LWRs, replacing UO_2. UN is an attractive fuel because it has a higher fissile density than UO_2 allowing for higher burnups, a higher thermal conductivity giving larger safety margins and has been shown to be a better candidate to burn long-lived minor actinides [2–4]. However, compared to UO_2 there are insufficient studies of the changes in UN under reactor conditions. Understanding the behavior of UN during burnup, at operational temperatures, and at increased temperatures, such as those that can be caused by accidents, and its compatibility with water are crucial to assess its performance and license for use as fuel in LWRs.

Atomic-scale simulations have been shown to play an important role in reproducing and predicting the behavior of different fuels, generating reliable data for modeling microstructural changes throughout the lifetime of the fuel [5–7]. Density functional theory (DFT) provides a rigorous representation of the atomic interactions, thus allowing for accurate modeling of nuclear fuels, but the calculations are computationally demanding, limiting the size of the model systems to a few hundreds of atoms, and the simulation time to a few picoseconds. Classical Molecular Dynamics (MD) simulations overcome the system size restrictions and some of the time limitations that DFT calculations have, allowing for simulation of the finite temperature behavior of grain boundaries, dislocations, atom diffusion and irradiation behavior of fuels. However, the accuracy of the MD simulations is dependent on the quality of existing interatomic potentials. In the case of UN, there have been three MD interatomic potentials reported in the literature, one using a Morse-type potential function added to the Busing–Ida type potential [8], while the other two use a complex Angular-Dependent Potential (ADP) form [9, 10]. All three potentials report a reasonable agreement with the experimental lattice parameter and single crystal elastic constants, while Kuksin et. al. [10] report that their potential is less accurate for the DFT calculated U and N migration barriers and defect formation energies. Having a good representation of the defects in UN is crucial for studying its behavior during reactor operation and under radiation, where the formation and kinetics of defects are of critical importance for a range of fuel performance metrics.

Here we use a simple form for a UN MD interatomic potential by combining a pairwise Buckingham potential with a many-body embedded atom model (EAM) potential. We employ an empirical fitting procedure, where the potential parameters are adjusted iteratively over a series of fitting runs to improve the match of calculated v.s. experimental/DFT values. During the

fitting process we focused on reproducing the experimental lattice parameters as a function of temperature and single crystal elastic constants, as well as the DFT calculated defect formation energies, ensuring dynamic stability of the perfect UN lattice and UN with point defects. The fitted potential is afterwards evaluated for its performance in reproducing the experimental temperature dependent specific heat capacity, as well as the DFT calculated migration barriers for U and N. Also, the potential is utilized to predict the temperature dependent UN bulk modulus. Furthermore, we compare the fitted potential with the Tseplyaev and Kuksin literature potential in their ability to reproduce the experimental thermal expansion, elastic constants, and the DFT calculated defect formation energies, as well as U and N migration barriers.

3 Methods

3.1 Potential Form

For the UN interatomic potential we are using a simple form, a many-bodied EAM [11] potential with a pairwise Buckingham term [12], a combination previously used for UC [13]. Both compounds, UC and UN, have the same crystal structure and very similar bonding, such that we expect that a potential form that works well for UC should also work well for UN. Note that because UN is electronically a metal, the net charge of the atom species is considered to be zero. Beeler et al. used the more advanced MEAM potential form to model the U-Si system due to the emphasis on U_3Si_2 [14], which has a complicated crystal structure. We deemed that a simpler EAM form may be more suitable for UN due to its simple rock salt crystal structure. This had the additional benefit of reducing the number of parameters that need to be fitted. The potential energy, E_i, of an atom i with respect to all other atoms j is written as:

$$E_i = -\left[\sum_{i\neq j}\rho_{\alpha\beta}(r_{ij})\right]^{n_\alpha} + \frac{1}{2}\sum_{i\neq j}\phi_{\alpha\beta}(r_{ij}),\ n_\alpha \neq 1, \tag{3.1}$$

where α and β are used to label the species of atoms i and j, respectively. The first term in Eq. (3.1) is the EAM part, where a sum of pairwise functions, $\rho_{\alpha\beta}(r_{ij})$, between atom i and its surrounding atoms is passed through an embedding function. The power n_α establishes this embedding function to be non-linear, introducing a many-body dependence. $\rho_{\alpha\beta}(r_{ij})$ is defined as:

$$\rho_{\alpha\beta}(r_{ij}) = F_{\alpha\beta} r_{ij}^2 \exp\left(-B_{\alpha\beta}(r_{ij} - r_{\alpha\beta}^0)^2\right),\ \alpha \neq \beta, \tag{3.2}$$

where $F_{\alpha\beta}$, $B_{\alpha\beta}$ and $r_{\alpha\beta}^0$ are empirical parameters dependent on the species of the atom being embedded (α) and the species responsible for the density (β). We are using the Finnis-Sinclair form of EAM [15], embedding only the functions of different species ($\alpha \neq \beta$), i.e., N in U and U in N, while if $\alpha = \beta$, $\rho_{ij} = 0$. Note that our initial tests showed that embedding the functions of the same species, i.e., U in U and N in N would only marginally improve the accuracy of the potential. However, this would increase the number of parameters that need to be fitted, which would require more fitting data to ensure that the potential is not overfitted, thus greatly increasing the fitting time.

The $\phi_{\alpha\beta}(r_{ij})$ from the second term in Eq. (3.1) defines the pairwise interaction between the atoms i and j, having the Buckingham potential form:

$$\phi_{\alpha\beta}(r_{ij}) = A_{\alpha\beta}\exp\left(\frac{-r_{ij}}{\rho_{\alpha\beta}}\right) - \frac{C_{\alpha\beta}}{r_{ij}^6},\ \text{with } C_{\alpha\beta} = 0, \tag{3.3}$$

where $\rho_{\alpha\beta}$ and $A_{\alpha\beta}$ are empirical parameters that describe the repulsive component of the Buckingham potential between two atoms of species α and β. The Buckingham potential was used to represent all interactions: U-U, N-N and U-N.

3.2 Calculations

3.2.1 Static Calculations

Geometry optimization calculations were performed using the Large-scale Atomic/Molecular Massively Parallel Simulator (LAMMPS) [16], with a constant pressure set to 0 Pa. For the fitting procedure we used the DFT calculated U and N Frenkel energies (UFP and NFP), Schottky and anti-Schottky energies (SD and ASD), and the antisite pair formation energies (APD), as well as the volume change for individual U and N vacancy and interstitial defects. The defect formation energies and the volume change were calculated using a $2 \times 2 \times 2$ supercell of the UN conventional cell (64 atoms), the same supercell size as in our reference DFT calculations, as detailed below. Note that all defect formation energies are calculated from point defects. To ensure that pure UN, and the point defects are dynamically stable, we calculated their phonons at the Γ point using the method implemented in the general utility lattice program (GULP) [17].

The elastic constants of UN at 300 K were calculated by first running a constant volume optimization of the simulation cell with the 300 K volume taken as an average from an MD simulation (see Section 3.2.2), then deforming the simulation cell, and measuring the change in the stress tensor. We note that such an approach using statics is not best suited for calculating the elastic constants at finite temperatures, but it was chosen as a reasonable balance between accuracy and simulation time as a result of the need to perform several MD runs at each iteration of the fitting run. In future work, we will determine elastic constants directly from an MD simulation.

We calculated the migration barriers for U and N diffusion in UN using the climbing-image nudge elastic band (NEB) method as implemented in LAMMPS [18–21]. For the NEB calculations we used a $5 \times 5 \times 5$ supercell of the UN conventional cell, having 35 replicas, with a spring constant for the parallel nudging force between replicas of 1.0 eV/Å^2, and energy and force tolerance of 10^{-8} eV and 0.01 eV/Å, respectively. We considered three pathways for the diffusion of U and N: vacancy (vac), interstitial (int), and intersitialcy (icy) mechanisms.

We performed DFT calculations to obtain the reference defect formation energies. The DFT calculations were done using the Vienna Ab initio Simulation Package (VASP) [22–25]. The electron exchange correlation was modeled using the generalized gradient approximation (GGA) of Perdew, Burke and Ernzernhof (PBE) [26] and projector augmented wave (PAW) potentials [27, 28]. We used a $2 \times 2 \times 2$ supercell of the UN conventional cell, introducing U and N vacancies, interstitials, and antisites, considering a ferromagnetic ordering of the U atoms. The UN supercells with and without defects were fully relaxed using a cut-off energy of 520 eV for expanding the electronic wave functions, and a $5 \times 5 \times 5$ **k**-point mesh. Convergence criteria of 0.001 eV/Å^{-1} and 10^{-6} eV were adopted for the forces and total energy, respectively. The

formation energies, ΔE_f, for the UFP, NFP, SD, ASD and APD were calculated using:

$$\begin{aligned}
\Delta E_f(\text{UFP}) &= E_{\text{U}}^{\text{int}} + E_{\text{U}}^{\text{vac}} - 2E_{\text{pure}}, \\
\Delta E_f(\text{NFP}) &= E_{\text{N}}^{\text{int}} + E_{\text{N}}^{\text{vac}} - 2E_{\text{pure}}, \\
\Delta E_f(\text{SD}) &= E_{\text{U}}^{\text{vac}} + E_{\text{N}}^{\text{vac}} + E_{\text{pc}} - 2E_{\text{pure}}, \\
\Delta E_f(\text{ASD}) &= E_{\text{U}}^{\text{int}} + E_{\text{N}}^{\text{int}} - E_{\text{pc}} - 2E_{\text{pure}}, \\
\Delta E_f(\text{APD}) &= E_{\text{UinN}}^{\text{ant}} + E_{\text{NinU}}^{\text{ant}} - 2E_{\text{pure}},
\end{aligned} \tag{3.4}$$

where E_{pc} is the total energy of the UN primitive cell, $E_{\text{U}}^{\text{int}}$, $E_{\text{U}}^{\text{vac}}$, $E_{\text{N}}^{\text{int}}$, $E_{\text{N}}^{\text{vac}}$, $E_{\text{UinN}}^{\text{ant}}$, $E_{\text{NinU}}^{\text{ant}}$, and E_{pure} are the total energies of the supercells with U interstitial, U vacancy, N interstitial, N vacancy, U in N antisite, and N in U antisite, and the pure UN supercell, respectively.

3.2.2 Molecular Dynamic Simulations

MD simulations were carried out using LAMMPS in the NPT ensemble with Nosé-Hoover thermostat and barostat relaxation times of 0.1 ps and 0.5 ps, respectively, with a fixed timestep of 2 fs. For the fitting procedure we performed MD simulations at three different temperatures, 300 K, 1500 K and 2800 K, using a $3 \times 3 \times 3$ supercell of the UN conventional cell (216 atoms), for 10 ps. The temperature specific lattice parameter was calculated as the cube root of the volume of the cell, while the volume is averaged over the last 2 ps, ensuring that the system has reached equilibrium. The average lattice parameter at 300 K was used for calculating the elastic constants, as discussed previously.

The thermal expansion of UN was evaluated by running an MD simulations using a $3 \times 3 \times 3$ supercell of the UN conventional cell for 10 ps over a range of temperatures from 300 to 2500 K, with a step of 100 K, and the volume sampled every time step before being averaged over the last 2 ps, thereby ensuring enough time for the system to reach equilibrium. The mean linear thermal expansion coefficient, α_L was estimated from the thermal expansion data using the equation, as defined in Ref [2]:

$$\alpha_L = \frac{a - a_0}{a_0(T - T_0)}, \tag{3.5}$$

where a is the lattice parameter at temperature T, and a_0 is the lattice parameter at the reference temperature, T_0, in our case 300 K. The thermal expansion coefficient, α, is defined by the line, $\alpha = b + a * T$, that has the best correlation with α_L at the studied temperatures. For comparison purposes, we are going to use the value of α calculated at 300 K using a linear fit of α_L.

The temperature dependence of the specific heat capacity was calculated using constant pressure MD simulations, where a $20 \times 20 \times 20$ supercell of the UN conventional cell was heated between 300 and 2600 K at 25 K intervals with a fixed timestep of 2 fs and at zero pressure. At each temperature the system was held for 7 ps with the enthalpy, $H(T)$, averaged over the final 2 ps. The derivative of enthalpy, H, with respect to temperature, T, is used to calculate specific heat capacity, c_P:

$$c_P = \frac{1}{n}\left(\frac{\partial H}{\partial T}\right)_P, \tag{3.6}$$

performing a linear fit to 7 points; the H at the T of interest and H at the three neighboring lower and higher temperatures.

The temperature dependent bulk modulus, B, was determined by exerting isotropic compressive and tensile strains on the equilibrated system, respectively decreasing and increasing the average volume at 0 Pa at each temperature by 1 % and 2 %. B was calculated as the derivative of pressure (P) with volume (V):

$$B = -V\frac{\mathrm{d}P}{\mathrm{d}V}. \tag{3.7}$$

using a linear fit to 5 points. The volumes and pressures were taken from a constant pressure MD run of a $10 \times 10 \times 10$ supercell of the UN conventional cell, which was heated at temperatures between 300 and 2500 K at 100 K intervals, with a fixed timestep of 2 fs. At each temperature the system was held for 10 ps, while the V and P values at the last 2 ps were used for calculating the averages of V and P.

3.3 Fitting Procedure

Interatomic potential parameters for Eq. (3.1)–Eq. (3.3) have been determined by fitting to both experimental and DFT data. The primary fitting targets were the UN lattice parameters, elastic constants, and the defect formation energies, giving them priority by increasing their weighting in the merit function. Additionally, the DFT defect volumes, the experimental U_2N_3 [29] and UN_2 lattice parameters [30], and DFT calculated UN_2 elastic constants [31] were included in the fitting procedure, but were given at most $1/10$ of the weight for the primary targets. The properties of UN are weighted more than those of U_2N_3 and UN_2 because of the larger technological importance of UN as a nuclear fuel. Also, our initial test showed that when the defect volumes are well represented, the defect formation energies and elastic constants were less accurate, thus we chose to give a lower priority to the defect volumes.

For a given candidate parameter set, a merit function was defined based on the difference between the desired property value (from experiment or DFT) and the predicted value (from MD or statics). This merit function was then minimized using a Nelder-Mead simplex algorithm [32] to determine the parameter set that best agreed with the desired properties. Parallel static and MD evaluation of the merit function for each iteration of the fitting run was performed, reducing the minimization time of the merit function. Note that during the fitting process a potential set was disregarded if it yielded negative phonon frequencies at the gamma point for UN.

In the initial stage of the fitting process we used only the UN lattice parameters at 300 K, 1500 K and 2800 K, and elastic constants at 300 K, as well as the U_2N_3 lattice parameters, and UN_2 lattice parameters and elastic constants. Note that the reference lattice parameters at 300 K, 1500 K and 2800 K were taken from a fit of experimental UN lattice parameters [2]. The thus obtained potential was then tested for its performance to reproduce the experimental thermal expansion, showing an excellent agreement between the MD simulated and experimental thermal expansion of UN. This gave us confidence that the potential form can be successfully used to represent UN properties, and furthermore, provided a starting point for the next step of the fitting procedure. Subsequently, we added the defect formation energies and defect volumes

to the fitting procedure to ensure that the potential performs well in reproducing not only the lattice parameters, and elastic constants, but also the defect properties, which are crucial for understanding the phenomena that govern fuel performance.

While validating the migration barrier for the U intersitialcy mechanism using what was considered to be the final potential, the energy of a U split interstitial was found to be lower than the energy of a regular interstitial by 0.17 eV. Shown in Fig. 3.1 are models of the regular and split interstitials. This prompted us to evaluate the energy difference between the U regular and split interstitial (ΔE_{sp-r}) using DFT, which showed that the split interstitial has lower energy by 1.389 eV. Therefore, we decided to refit the potential using the DFT calculated ΔE_{sp-r} as a new fitting target. Note that we gave at least 10 times higher weight to the ΔE_{sp-r} compared to the defect formation energies in attempt to reproduce the DFT calculated ΔE_{sp-r}.

Figure 3.1: Ball and stick model of: a) regular; and b) split interstitial in 2×2×2 supercell of UN. The U and N atoms are shown in gray and blue, respectively, while the U interstitial atom is shown in yellow.

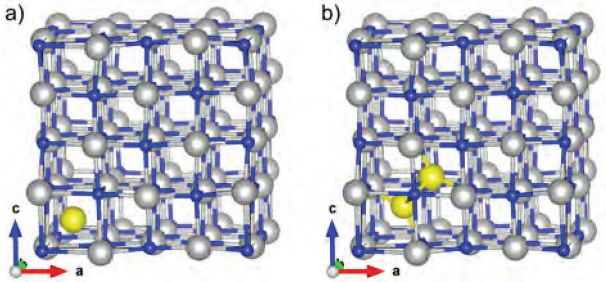

Ultimately, the final strengths and weaknesses of the potential were examined by investigating the ability of the potential to reproduce the UN temperature dependent heat capacity, and the U and N migration barriers. Also, we investigated the ability of the potential to predict the bulk modulus at different temperatures.

4 Results and Discussion

4.1 Fitting Data

The final parameter set derived by this fitting process is summarized in Table 4.1 and Table 4.2 for pairwise and many-body interactions, respectively.

Table 4.1: Parameters for the Buckingham interaction described by Eq. (3.3)

$\alpha-\beta$	$A_{\alpha\beta}$	$\rho_{\alpha\beta}$
U–U	1506.320145	0.410284265
N–N	6611.752366	0.233770951
U–N	216.8058075	0.422521856

Table 4.2: Parameters for the many-body interaction described by Eq. (3.2). The arrow depicts the atomic species being embedded in the other atomic species.

	$F_{\alpha\beta}$	$B_{\alpha\beta}$	$r^0_{\alpha\beta}$	n_α
N$\rightarrow$ U	5.2112665657	1.2918945702	1.8045415663	
U$\rightarrow$ N	3.1008714889	1.6395469102	1.3910442000	
U				0.639068598
N				0.541787851

Initially we are going to focus on how the properties calculated using the fitted potential agree with the data used for the fitting. Shown in Table 4.3 is the data used for fitting, compared with the calculated data using the final interatomic potential. The finite temperature lattice parameters of UN are in excellent agreement with the experiments, with the 300 K lattice parameter being slightly overestimated. The bulk modulus, B, and C_{12} elastic constant are slightly overestimated (error is $\sim$4 % and $\sim$17 %), while C_{11} and C_{44} elastic constants are slightly underestimated compared with the experimental values from Ref. [33] used for the fitting (error is $<$ 6 %).

In the case of the defect formation energies, the potential underestimates the NFP and SD (average error is $\sim$16 %), while UFP, ASD and APD are somewhat overestimated (average error is $\sim$40 %). Nevertheless, the potential does a great job in reproducing the order of the defect formation energies, notably the SD energy is higher than NFP, and the ASD energy is lower than UFP, as well as the difference between formation energies for these defects. Despite our best efforts, the potential predicts that the regular interstitial is slightly more stable than the split interstitial when using a $2\times2\times2$ supercell. Once a larger supercell is used, $3\times3\times3$ and $5\times5\times5$,

Table 4.3: UN data used for the fitting (experimental and DFT generated data), and data calculated using the final parameter set.

Property	Expr./DFT	New potential
300 K a (Å)	4.890[1]	4.906
1500 K a (Å)	4.944[1]	4.946
2800 K a (Å)	5.024[1]	5.024
B (GPa)	206.7[2]	215.5
C_{11} (GPa)	423.9[2]	416.5
C_{12} (GPa)	98.1[2]	115.1
C_{44} (GPa)	75.7[2]	71.0
UFP (eV)	10.108[3]	14.29
UFP split (eV)	8.719[3]	14.37
NFP (eV)	4.834[3]	4.03
SD (eV)	4.956[3]	4.14
ASD (eV)	9.985[3]	14.19
ASD split (eV)	8.596[3]	14.26
APD (eV)	12.376[3]	18.19
ΔE_{sp-r} (eV)	-1.389[3]	0.08
dV Ui (Å^3)	24.75[3]	35.27
dV Ni (Å^3)	9.94[3]	9.79
dV vU (Å^3)	-4.03[3]	-2.62
dV vN (Å^3)	-2.76[3]	4.30

[1] [2];[2] [33];[3]DFT data from this study.

ΔE_{sp-r} becomes negative, -0.17 and -0.24 eV, respectively. We would like to point out that we discovered the split interstitial late in the process after we thought we had final parameter set, and that it was not possible to fully capture the extent of the negative value with the current potential form. To overcome the issue, a more complex potential form (e.g. angular form) might need to be used, which is an attractive topic for future work. However, the simple form of the potential enables much quicker development of a new potential having other elements, such as noble gases or fission products, allowing for modeling the UN behavior after burnup.

The potential performs worse when it comes to the defect volumes, but that is expected because these properties were weighted less than the defect formation energies. In general, the potential gives a good estimate of the defect volumes, except for the N vacancy volume change, which is predicted to be positive, while DFT gives a negative volume change. As mentioned in Section 3.3, in the cases when the defect volumes were better represented, the defect formation energies and elastic constants were not. This means that getting the correct sign for the N vacancy volume change came with significant change in the other properties, especially the UFP and SD formation energies, and the C_{44} elastic constant, which would be significantly underestimated. Therefore, despite that the N vacancy volume change has an opposite sign, this property is less significant than the defect energetics for fuel performance.

Another property used in the fitting process is the UN thermal expansion. Shown in Fig. 4.1 is

the calculated UN lattice parameter v.s. T curve compared with the experimental curves reported by Kempter et. al. [34] and Benz at. al. [35]. It is noticeable that the UN lattice parameter v.s. T curve calculated using the potential follows closely the experimental curve, with the calculated lattice parameter v.s. T curve being slightly flatter. This gives rise to a smaller thermal expansion coefficient, having the form:

$$\alpha = 6.075 \cdot 10^{-6} + 5.438 \cdot 10^{-10} \cdot T \tag{4.1}$$

with the calculated thermal expansion coefficient at 300 K being $6.868 \cdot 10^{-6}$ K^{-1}, while the experimental one is $7.518 \cdot 10^{-6}$ K^{-1} [2].

Figure 4.1: UN lattice parameter v.s. T curve calculated using the potential (blue), compared with experimental curve [34, 35] (black).

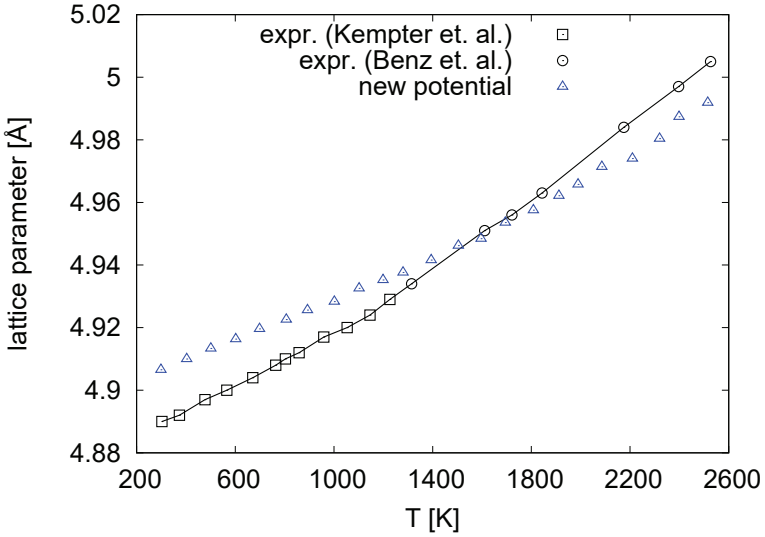

As mentioned in Section 3.3, during the fitting process we also used the U_2N_3 and UN_2 properties, but weighted them significantly lower than the UN properties. Shown in Table 4.4 are the calculated U_2N_3 and UN_2 properties, compared with the data used in the fitting, i.e., experimental lattice parameters for both compounds and DFT calculated UN_2 elastic constants. Evidently, the U_2N_3 a and b lattice parameters are significantly overestimated, while the c lattice parameter is underestimated. The potential does a slightly better job in reproducing the UN_2 lattice parameter. The C_{12} and C_{44} elastic constants of UN_2 are well reproduced, but the potential substantially underestimates the bulk modulus and C_{11} elastic constant. Having the potential giving physically meaningful values for the U_2N_3 and UN_2 properties ensures the absence of non-physical behavior of UN when simulating damage cascades or off-stoichiometric UN.

4.2 Validation of Potential

To validate the fitted potential we compare the calculated temperature dependent specific heat capacity, and U and N migration barriers with experimental data and DFT calculated migration

Table 4.4: Comparison between the U_2N_3 and UN_2 data used for the fitting (experimental and DFT), and data calculated using the fitted potentials. Note that both structures are considered to be orthorombic, $\alpha = \beta = \gamma = 90^o$.

	U_2N_3		UN_2	
Property	Expr. [29]	New potential	Expr. [30]/DFT [31]*	New potential
a (Å)	3.7	4.038	5.31	5.551
b (Å)	6.4086	6.994		
c (Å)	5.82	4.894		
B (GPa)			254*	188.6
C_{11} (GPa)			486.3*	235.6
C_{12} (GPa)			138.3*	165.1
C_{44} (GPa)			49.6*	50.6

barriers, respectively; properties that were not used during the fitting process. Furthermore, we use the potential to calculate the UN bulk modulus at different temperatures. Note that we tried to calculate the melting point of UN, but the whole system started expanding significantly beyond ∼3000 K. One should keep in mind it has been shown experimentally that UN does not melt at standard N_2 partial pressure, it actually decomposes at temperatures higher than 3035 K [36]. Reproducing the decomposition of UN is beyond the capability of the current potential form as it would require a much more complex form that can capture the divergent physics of the U metal and N_2 gas, in addition to UN.

Initially, to validate the potential we used the temperature dependent specific heat capacity, $c_P(T)$, of UN, calculated using the method discussed in Section 3.2.2. Shown in Fig. 4.2 is the calculated $c_P(T)$, compared with the measured c_P [37–40], and the $c_P(T)$ calculated using DFT [41]. The potential underestimates the experimental $c_P(T)$, which comes from the fact that in MD only the vibrational contribution to $c_P(T)$ is considered, while neglecting the electronic and magnetic contributions. Once we add the DFT determined electronic contribution for ferromagnetic (FM) UN, c_e(FM), the MD+c_e(FM) calculated $c_P(T)$ comes much closer to the experiments, especially to those reported by Takahashi et. al. [38] and Oetting et. al. [40]. It is also worth pointing out that the $c_P(T)$ from DFT and MD+c_e(FM) are very close, indicating that both our potential and DFT have similar representation of the vibrational contribution in UN. The slightly flatter MD+c_e(FM) calculated $c_P(T)$ compared to the DFT calculated $c_P(T)$ is thought to be due to the choice of UN thermal expansion; specifically, for the DFT $c_P(T)$ the experimental thermal expansion coefficient is used, and we previously showed that our potential predicts a smaller thermal expansion coefficient compared to experiments.

To understand high temperature and irradiation behavior of UN it is important to have information on self-diffusion in UN. Thus, it is beneficial for the parameterized interatomic potential to give reliable predictions of the U and N defect migration barriers. The calculated migration barriers for U and N vacancy diffusion, and N interstitial diffusion, compared with DFT evaluated migration barriers [42, 43], are detailed in Table 4.5. The calculated barrier for N vacancy migration is within the range of reported DFT values, while the barriers for N interstitial and U vacancy migration are slightly underestimated compared to the DFT values. Nevertheless, the

Figure 4.2: Comparison between the calculated temperature dependent UN specific heat capacity (c_P) (black), and the measured by Affortit [37] (green), Takahashi et. al. [38] (red), Harrington et. al. [39] (yellow), and Oerring et. al. [40] (blue), as well as the one calculated using DFT by Szpunar et. al. [41] (violet). The orange line represents the MD calculated c_P with an added electronic contribution for ferromagnetic UN, C_e(FM), calculated using DFT [41].

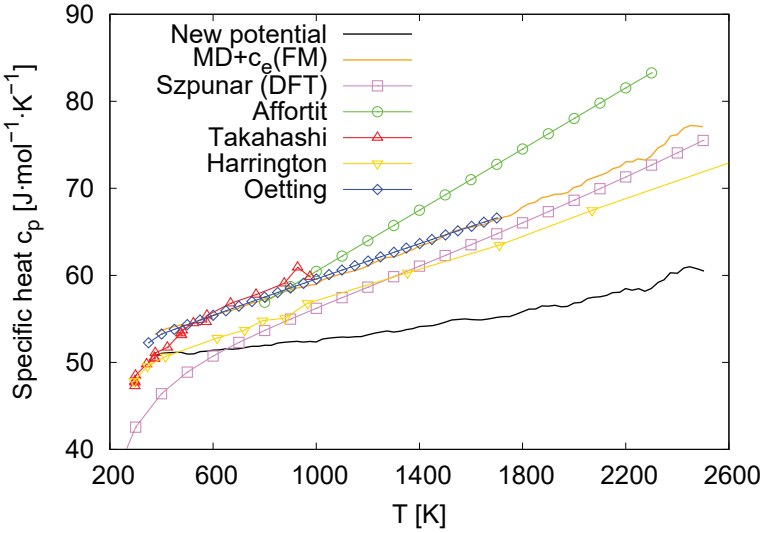

potential predicts the same ordering of the migration barriers, with U vacancy migration having the largest barrier, and N interstitial migration the lowest. Additionally, the difference between the calculated N interstitial and N vacancy migration barrier is similar to the DFT difference reported by Lopes et. al. [42], as well as the difference between the U vacancy and N vacancy is similar to the DFT difference reported by Fonseca et. al. [43]. We should also point out that all migration pathways were directly between the initial and final configuration without any significant rerouting via other defects.

Table 4.5: N and U migration barrier, in eV, compared to DFT results.

Atom	DFT [42]	DFT [43]	New potential
N vac.	2.578	2.780	2.524
N int.	2.021	1.636	2.012
N icy.			1.649
U vac.		3.466	3.363
U int.			0.280
U icy.			0.219

So far we showed a good agreement between our potential and the data used for parametrizing the potential. Also, we demonstrated the predictive capability of the potential by reproducing the DFT calculated defect migration barriers, and showed that deviation in the calculated and experimental temperature dependent specific heat comes from classical MD not including the electronic contribution. Subsequently, it is important to use the potential for calculating properties

for which experimental data does not exists, such as the temperature dependent bulk modulus. The temperature dependent bulk modulus, calculated as described in Section 3.2.2, is shown in Fig. 4.3. Interestingly, the bulk modulus shows a roughly second-order polynomial dependence on the temperature, indicating an inversely proportional relation to the lattice parameter, which increases with temperature. The polynomial dependence can be described by:

$$B = B_0 + aT + bT^2, \tag{4.2}$$

with $B_0 = 218.38$, $a = -0.0157$ and $b = -6.32 \cdot 10^{-6}$. The UN bulk modulus changes less with increasing temperature compared to the UO_2 bulk modulus [44, 45]. This difference likely comes from the different thermal expansions of UN and UO_2, with UN having smaller thermal expansion coefficient than UO_2, and thus flatter change in the bulk modulus with temperature. Additionally, Hayes et. al. [46] provided a model for the temperature dependence of the bulk modulus, derived by correlating room temperature bulk modulus data with UN porosity. However, the proposed model gives substantially flatter dependence of the bulk modulus on the temperature compared to our potential. Considering the difference in UN and UO_2 thermal expansion, the difference in the temperature dependent bulk modulus predicted by the potential seems more reasonable than the almost flat temperature dependent bulk modulus suggested by Hayes at. al.

Figure 4.3: Temperature dependent UN bulk modulus (black), compared with experimental (blue) [44] and MD calculated UO_2 bulk modulus (red) [45], and bulk modulus from the model by Hayes et. al. [46] (yellow).

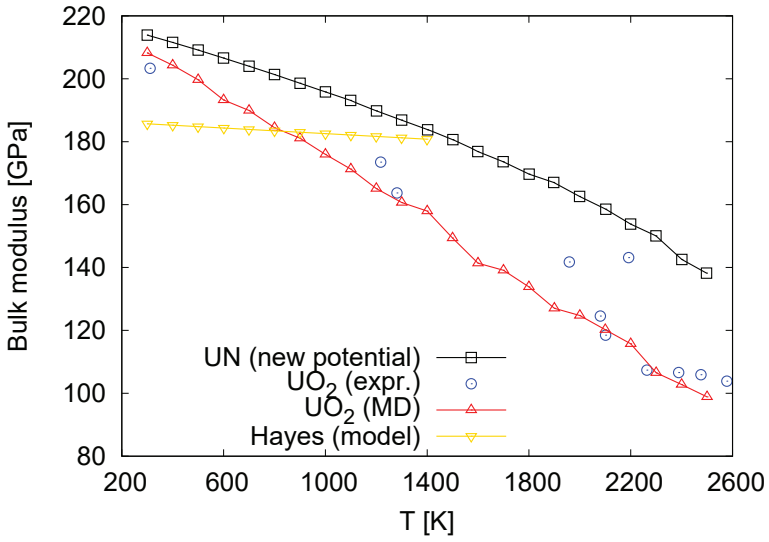

4.3 Comparison with Literature Potentials

In this section we are going to compare the performance of our potential and two literature potentials: Tseplyaev [9] and Kuksin [10] UN interatomic potentials. As mentioned previously,

Tseplyaev [9] and Kuksin [10] potentials use the more complex ADP form, while our potential has a simpler centro-symmetric form. For comparison purposes, we applied these two potentials for the calculation of thermal expansion, elastic constants, defect formation energies, and migration barriers, using the same methodology as in the calculations with the new potential. Shown in Table 4.6 are the elastic constants and the UN lattice parameter calculated using our potential and the two literature potentials, compared with experimental results. Evidently, our potential performs better than both literature potentials when it comes to reproducing the experimental lattice parameter and elastic constants, with the Kuksin potential performing the best for the C_{44} elastic constant.

Table 4.6: UN lattice parameter and elastic constants at 300 K, calculated using our potential and the two literature potentials, compared with experiment.

Property	Expr. [33]	Expr. [47]	Expr. [48]	New potential	Tseplyaev	Kuksin
a (Å)	4.890			4.906	4.820	4.854
B (GPa)	206.7	190	200	215.5	295.30	255.83
C_{11} (GPa)	423.9	391	420	416.5	601.40	491.69
C_{12} (GPa)	98.1	90	90	115.1	142.25	137.90
C_{44} (GPa)	75.7	80	79	71.0	54.97	78.26

Comparison between the UN lattice parameter *vs* T calculated using our potential, the two literature potentials, and the experiment is shown in Fig. 4.4. The Tseplyaev potential gives very good agreement with the thermal expansion coefficient of UN; however, the predicted lattice parameters are much smaller (>0.7 Å difference) compared to the experiment. The Kuksin potential also underestimates the UN lattice parameters, and it gives a smaller thermal expansion coefficient compared to the experimental one. The underestimation of the lattice parameter by the literature potentials is not unexpected because both potentials are fitted on GGA generated forces, and GGA underestimates the UN lattice parameter. The thermal expansion coefficient calculated using our potential is in better agreement with the experimental one, and our potential gives a better agreement with the experimental lattice parameter v.s. T.

The calculated defect formation energies using the literature potentials, and our potential, compared with DFT data are shown in Table 4.7. The defect formation energies calculated with Tseplyaev potential are in very good agreement with the DFT calculated defect formation energies, except for the APD energy, which is underestimated. The Kuksin potential underestimates the defect formation energies, but it is still in better agreement with DFT compared to our potential. Both Tseplyaev and Kuksin potentials predict that the U split interstitial to be much more stable than the regular interstitial. As indicated previously, both literature potentials are fitted on DFT generated forces, and more importantly use a complex angular dependent form for their potentials, which can explain why these potentials reproduce the DFT predicted stability of the U split interstitial. Even though our potential performs the worst among the three potentials when it comes to the defect formation energies, it reproduces the SD–NFP and UFP–ASD differences in formation energies, and most importantly gives reasonable values for the SD and NFP formation energies, the defects that have the lowest formation energies and thus will most likely to form in the UN.

Figure 4.4: UN lattice parameter v.s. T curve calculated using our potential (blue) and the two literature potentials, Tseplyaev (yellow) and Kuksin (red), compared with experimental thermal expansion [34, 35] (black). The thermal expansion coefficients α in 10^{-6} K^{-1}, are given in parenthesis.

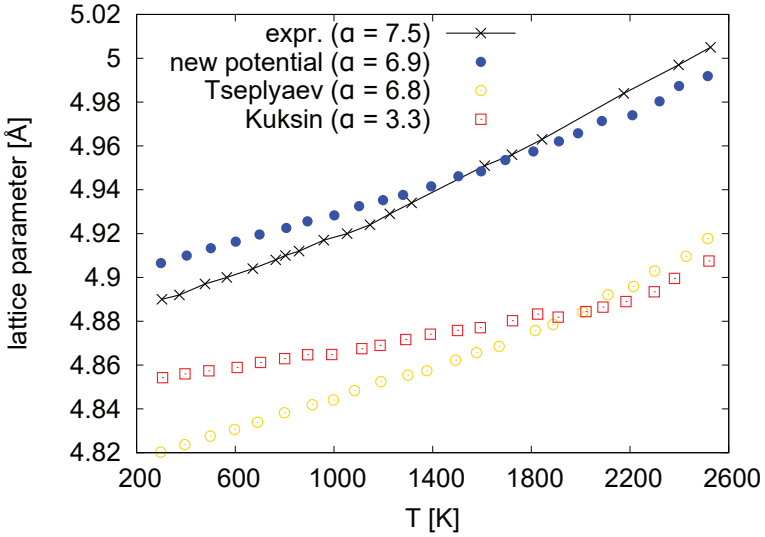

Table 4.7: Comparison between the defect formation energies, in eV, for a 2×2×2 supercell calculated using DFT, our potential and the two literature potentials.

Defect (eV)	DFT	New potential	Tseplyaev	Kuksin
UFP	10.11	14.29	9.69	8.35
UFP split	8.72	14.29	7.53	6.73
NFP	4.83	4.03	4.41	4.01
SD	4.96	4.14	4.45	4.42
ASD	9.99	14.19	9.65	7.95
ASD split	8.60	14.19	7.49	6.33
APD	12.38	18.20	8.56	9.65
ΔE_{sp-r}	-1.39	0.08	-2.16	-1.62

As discussed previously, the migration barriers for U and N are important for simulating the proper self-diffusion behavior of UN, and the irradiation response of the materials. Shown in Table 4.8 are the calculated migration barriers for vacancy migration of U and N, and interstitial migration of N, using our potential, and the two literature potentials, compared with the DFT calculated migration barriers [42, 43]. Note that we did not calculate the N intersitialcy and U interstitial and intersitialcy migration barriers because we do not have DFT values to compare with. The N interstitial and vacancy migration barrier calculated using the Tseplyaev potential are reversed compared to the DFT calculated ones, where the intersitial migration has lower barrier than vacancy migration. On the other hand, the Kuksin potential gives the correct order of the N interstitial and vacancy migration barriers, with the values being slightly lower than the

DFT calculated ones. Our potential slightly underestimates the migration barriers, but it is in better agreement with the DFT calculated migration barriers compared to the Kuksin potential. We also point out that our potential shows that U migrates directly towards a vacancy, while with the other two potentials U first goes to an interstitial site and then to a vacancy. We believe that the accurate representation of the configurational and energetic space for point defect migration, positions our potential well for application to the simulation of phenomena that are governed by point defect kinetics (e.g. irradiation effects).

Table 4.8: Comparison between the N and U migration barrier, in eV, calculated using DFT, our potential and the two literature potentials.

Atom	DFT [42]	DFT [43]	New potential	Tseplyaev	Kuksin
N int.	2.021	1.636	2.012	2.974	1.883
N vac.	2.578	2.780	2.524	2.353	2.343
U vac.		3.466	3.363	3.641	3.873

5 Conclusions

Understanding of the fuel performance and irradiation behavior of UN can greatly benefit from MD simulations, but a rigorous interatomic potential is required for accurate modeling. We report the use of the embedded atom method in conjunction with Buckingham pairwise interactions as the form of a new UN interatomic potential. The potential reproduces very well the more important properties used for the fitting process, while there is significant difference in the properties that were given lesser importance during the fitting: the defect volumes, and U_2N_3 and UN_2 properties. Moreover, the potential predicted the existence of a more stable U split interstitial, compared to the regular interstitial that we later confirmed using DFT. However, the potential underestimates the energy difference between the U split and regular interstitials, which we attribute to the lack of angular terms in the potential form used. For validation of the potential we used the temperature dependent specific heat capacity, and the U and N migration barriers. The temperature dependent specific heat capacity calculated using the potential is somewhat underestimated, which we demonstrate that it comes from the neglected electronic contribution. Also, the potential reproduces well the energy difference between the DFT calculated U and N migration barriers, although it slightly underestimates the U and N vacancy migration barriers. Finally, the potential was used to predict the temperature dependent UN bulk modulus, showing an inverse linear relation with temperature.

We also compared our potential with two literature interatomic potentials, namely the Tseplyaev and Kuksin potentials. Our potential is better at reproducing the experimental UN lattice parameters, elastic constants, and thermal expansion compared to the two considered literature potentials. Moreover, the U and N migration barriers calculated with our potential are in much better agreement with DFT migration barriers compared to the literature potentials. However, our potential performs slightly worse compared to the two literature potentials when it comes to defect formation energies, even though it gives the same order of the defect formation energies as DFT.

Acknowledgements

Los Alamos National Laboratory, an affirmative action/equal opportunity employer, is operated by Triad National Security LLC, for the National Nuclear Security Administration of the U.S. Department of Energy under Contract No. 89233218CNA000001. The work is supported by Westinghouse Electric Company LLC.

References

[1] P. D. Wilson, The nuclear fuel cycle : from ore to wastes, Oxford University Press, Oxford New York, 1996.

[2] S. Hayes, J. Thomas, K. Peddicord, Material property correlations for uranium mononitride, Journal of Nuclear Materials 171 (2-3) (1990) 262–270. doi:10.1016/0022-3115(90)90374-v.

[3] J. Zakova, J. Wallenius, Fuel residence time in BWRs with nitride fuels, Annals of Nuclear Energy 47 (2012) 182–191. doi:10.1016/j.anucene.2012.03.033.

[4] P. Malkki, The manufacturing of uranium nitride for possible use in light water reactors, Engineering Sciences, KTH Royal Institute of Technology, Stockholm, 2015.

[5] L. V. Brutzel, J.-M. Delaye, D. Ghaleb, M. Rarivomanantsoa, Molecular dynamics studies of displacement cascades in the uranium dioxide matrix, Philosophical Magazine 83 (36) (2003) 4083–4101. doi:10.1080/14786430310001616081.

[6] E. A. Marquis, J. M. Hyde, D. W. Saxey, S. Lozano-Perez, V. de Castro, D. Hudson, C. A. Williams, S. Humphry-Baker, G. D. Smith, Nuclear reactor materials at the atomic scale, Materials Today 12 (11) (2009) 30–37. doi:10.1016/s1369-7021(09)70296-2.

[7] G. Martin, S. Maillard, L. V. Brutzel, P. Garcia, B. Dorado, C. Valot, A molecular dynamics study of radiation induced diffusion in uranium dioxide, Journal of Nuclear Materials 385 (2) (2009) 351–357. doi:10.1016/j.jnucmat.2008.12.010.

[8] K. Kurosaki, K. Yano, K. Yamada, M. Uno, S. Yamanaka, A molecular dynamics study of the heat capacity of uranium mononitride, Journal of Alloys and Compounds 297 (1-2) (2000) 1–4. doi:10.1016/s0925-8388(99)00561-7.

[9] V. Tseplyaev, S. Starikov, The atomistic simulation of pressure-induced phase transition in uranium mononitride, Journal of Nuclear Materials 480 (2016) 7–14. doi:10.1016/j.jnucmat.2016.07.048.

[10] A. Kuksin, S. Starikov, D. Smirnova, V. Tseplyaev, The diffusion of point defects in uranium mononitride: Combination of dft and atomistic simulation with novel potential, Journal of Alloys and Compounds 658 (2016) 385–394. doi:10.1016/j.jallcom.2015.10.223.

[11] M. S. Daw, M. I. Baskes, Embedded-atom method: Derivation and application to impurities, surfaces, and other defects in metals, Physical Review B 29 (12) (1984) 6443–6453. doi:10.1103/physrevb.29.6443.

[12] R. A. Buckingham, The classical equation of state of gaseous helium, neon and argon, Proceedings of the Royal Society of London. Series A. Mathematical and Physical Sciences 168 (933) (1938) 264–283. doi:10.1098/rspa.1938.0173.

[13] A. Chartier, L. V. Brutzel, Modeling of point defects and rare gas incorporation in uranium mono-carbide, Nuclear Instruments and Methods in Physics Research Section B: Beam Interactions with Materials and Atoms 255 (1) (2007) 146–150. doi:10.1016/j.nimb.2006.11.017.

[14] B. Beeler, M. Baskes, D. Andersson, M. W. Cooper, Y. Zhang, A modified embedded-atom method interatomic potential for uranium-silicide, Journal of Nuclear Materials 495 (2017) 267–276. doi:10.1016/j.jnucmat.2017.08.025.

[15] M. W. Finnis, J. E. Sinclair, A simple empirical n-body potential for transition metals, Philosophical Magazine A 50 (1) (1984) 45. doi:https://doi.org/10.1080/01418618408244210.

[16] S. Plimpton, Fast parallel algorithms for short-range molecular dynamics, Journal of Computational Physics 117 (1) (1995) 1–19. doi:10.1006/jcph.1995.1039.

[17] J. D. Gale, Gulp: A computer program for the symmetry-adapted simulation of solids, Journal of the Chemical Society, Faraday Transactions 93 (4) (1997) 629–637. doi:10.1039/a606455h.

[18] G. Henkelman, H. Jónsson, Improved tangent estimate in the nudged elastic band method for finding minimum energy paths and saddle points, The Journal of Chemical Physics 113 (22) (2000) 9978–9985. doi:10.1063/1.1323224.

[19] G. Henkelman, B. P. Uberuaga, H. Jónsson, A climbing image nudged elastic band method for finding saddle points and minimum energy paths, The Journal of Chemical Physics 113 (22) (2000) 9901–9904. doi:10.1063/1.1329672.

[20] A. Nakano, A space–time-ensemble parallel nudged elastic band algorithm for molecular kinetics simulation, Computer Physics Communications 178 (4) (2008) 280–289. doi:10.1016/j.cpc.2007.09.011.

[21] E. Maras, O. Trushin, A. Stukowski, T. Ala-Nissila, H. Jónsson, Global transition path search for dislocation formation in ge on si(001), Computer Physics Communications 205 (2016) 13–21. doi:10.1016/j.cpc.2016.04.001.

[22] G. Kresse, J. Hafner, Ab initio molecular dynamics for liquid metals, Physical Review B 47 (1) (1993) 558–561. doi:10.1103/physrevb.47.558.

[23] G. Kresse, J. Hafner, Ab initio molecular-dynamics simulation of the liquid-metal-amorphous-semiconductor transition in germanium, Physical Review B 49 (20) (1994) 14251–14269. doi:10.1103/physrevb.49.14251.

[24] G. Kresse, J. Furthmüller, Efficiency of ab-initio total energy calculations for metals and semiconductors using a plane-wave basis set, Computational Materials Science 6 (1) (1996) 15–50. doi:10.1016/0927-0256(96)00008-0.

[25] G. Kresse, J. Furthmüller, Efficient iterative schemes forab initiototal-energy calculations using a plane-wave basis set, Physical Review B 54 (16) (1996) 11169–11186. doi:10.1103/physrevb.54.11169.

[26] J. P. Perdew, K. Burke, M. Ernzerhof, Generalized gradient approximation made simple, Physical Review Letters 77 (18) (1996) 3865–3868. doi:10.1103/physrevlett.77.3865.

[27] P. E. Blöchl, Projector augmented-wave method, Physical Review B 50 (24) (1994) 17953–17979. doi:10.1103/physrevb.50.17953.

[28] G. Kresse, D. Joubert, From ultrasoft pseudopotentials to the projector augmented-wave method, Physical Review B 59 (3) (1999) 1758–1775. doi:10.1103/physrevb.59.1758.

[29] R. Benz, M. G. Bowman, Some phase equilibria in the uranium-nitrogen system, Journal of the American Chemical Society 88 (2) (1966) 264–268. doi:10.1021/ja00954a015.

[30] R. E. Rundle, N. C. Baenziger, A. S. Wilson, R. A. McDonald, The structures of the carbides, nitrides and oxides of uranium1, Journal of the American Chemical Society 70 (1) (1948) 99–105. doi:10.1021/ja01181a029.

[31] T. Zergoug, S. Abaidia, A. Nedjar, M. Y. Mokeddem, Physical properties of uranium dinitride un2 by using density functional theory (dft and dft+u), International Journal of Materials and Metallurgical Engineering 9 (1) (2015) 175. doi:10.5281/ZENODO.1099362.

[32] J. A. Nelder, R. Mead, A simplex method for function minimization, The Computer Journal 7 (4) (1965) 308–313. doi:10.1093/comjnl/7.4.308.

[33] M. D. Salleh, J. E. MacDonald, G. A. Saunders, P. D. V. Du Plessis, Hydrostatic pressure dependences of elastic constants and vibrational anharmonicity of uranium nitride, Journal of Materials Science 21 (7) (1986) 2577. doi:https://doi.org/10.1007/BF01114310.

[34] C. P. Kempter, R. O. Elliott, Thermal expansion of un, uo2, uo2·tho2, and tho2, The Journal of Chemical Physics 30 (6) (1959) 1524–1526. doi:10.1063/1.1730230.

[35] R. Benz, G. Balog, B. H. Baca, U-uo2-un2 phase diagram, High Temperature Science (1970) 221–251.

[36] S. Hayes, J. Thomas, K. Peddicord, Material property correlations for uranium mononitride, Journal of Nuclear Materials 171 (2-3) (1990) 300–318. doi:10.1016/0022-3115(90)90377-y.

[37] C. Affortit, Chaleur specifique de UC et UN, Journal of Nuclear Materials 34 (1) (1970) 105–107. doi:10.1016/0022-3115(70)90014-0.

[38] Y. Takahashi, M. Murabayashi, Y. Akimoto, T. Mukaibo, Uranium mononitride: Heat capacity and thermal conductivity from 298 to 1000 k, Journal of Nuclear Materials 38 (3) (1971) 303–308. doi:10.1016/0022-3115(71)90059-6.

[39] L. C. Harrington, Heat capacity and enthaipy of uranium mononitride from 0 to12ooc (32 to 2200f), resreport, Pratt and Whitney Aircraft Co., cNLM-4461 (Mar. 1963). doi:10.2172/4509604.
URL https://www.osti.gov/servlets/purl/4509604

[40] F. L. Oetting, J. M. Leitnaker, The chemical thermodynamic properties of nuclear materials i. uranium mononitride, The Journal of Chemical Thermodynamics 4 (2) (1972) 199–211. doi:10.1016/0021-9614(72)90057-2.

[41] B. Szpunar, J. I. Ranasinghe, L. Malakkal, J. A. Szpunar, First principles investigation of thermal transport of uranium mononitride, Journal of Physics and Chemistry of Solids 146 (2020) 109636. doi:10.1016/j.jpcs.2020.109636.

[42] D. A. Lopes, A. Claisse, P. Olsson, Ab-initio study of c and o impurities in uranium nitride, Journal of Nuclear Materials 478 (2016) 112–118. doi:10.1016/j.jnucmat.2016.06.008.

[43] L. G. Fonseca, M. Hedberg, L. Huan, P. Olsson, T. R. Vollmer, Application of SPS in the fabrication of UN and (u,th)n pellets from microspheres, Journal of Nuclear Materials 536 (2020) 152181. doi:10.1016/j.jnucmat.2020.152181.

[44] M. T. Hutchings, High-temperature studies of UO2 and ThO2 using neutron scattering techniques, Journal of the Chemical Society, Faraday Transactions 2 83 (7) (1987) 1083. doi:10.1039/f29878301083.

[45] M. W. D. Cooper, M. J. D. Rushton, R. W. Grimes, A many-body potential approach to modelling the thermomechanical properties of actinide oxides, Journal of Physics: Condensed Matter 26 (10) (2014) 105401. doi:10.1088/0953-8984/26/10/105401.

[46] S. Hayes, J. Thomas, K. Peddicord, Material property correlations for uranium mononitride, Journal of Nuclear Materials 171 (2-3) (1990) 271–288. doi:10.1016/0022-3115(90)90375-w.

[47] J. A. Jackman, T. M. Holden, W. J. L. Buyers, P. de V. DuPlessis, O. Vogt, J. Genossar, Systematic study of the lattice dynamics of the uranium rocksalt-structure compounds, Physical Review B 33 (10) (1986) 7144–7153. doi:10.1103/physrevb.33.7144.

[48] C. van Doorn, P. de V. du Plessis, Anomalies in the elastic constants of antiferromagnetic uranium mononitride, Journal of Magnetism and Magnetic Materials 5 (2) (1977) 164–166. doi:10.1016/0304-8853(77)90184-6.

Microstructural degradation of UN and UN-UO_2 composites in hydrothermal oxidation conditions

Jennifer K. Watkins[a,b], Darryl P. Butt[c], and Brian J. Jaques[a,b]

[a] Micron School of Materials Science and Engineering, Boise State University, 1910 University Dr., Boise, ID 83725, USA

[b] Center for Advanced Energy Studies, 995 University Blvd., Idaho Falls, ID 83401, USA

[c] College of Mines and Earth Sciences, University of Utah, Salt Lake City, ID 84112, USA

Corresponding author: Brian J. Jaques, brianjaques@boisestate.edu

Keywords: advanced technology fuel, uranium mononitride, hydrothermal degradation, nuclear fuel

Abstract

The degradation behavior in high pressure water of UN and UN + (5-10 w%) UO_2 monolithic pellets fabricated from UN synthesized via a hydride-dehydride-nitride thermal process was investigated. Sintered pellets (> 90% theoretical density) were subjected to hydrothermal oxidation in a water-filled static autoclave at temperatures ranging from 250-350 °C and pressures to 16.5 MPa. Phase characterization and microstructural and chemical analysis was performed on the resulting corrosion products using X-ray diffraction (XRD), scanning electron microscopy (SEM) coupled with energy dispersive spectroscopy (EDS). The results of this screening study show that grain boundary attack and spallation is the primary degradation mechanism in hydrothermal oxidation conditions. The results also suggest the corrosion rate is higher in UN and UN-UO_2 with higher starting oxygen content.

1. Introduction

1.1 Motivation for research

After the earthquake and tsunami which damaged the Fukushima Daiichi nuclear power plant complex in 2011, the Department of Energy's Office of Nuclear Energy (DOE-NE) refocused its mission of developing advanced nuclear fuels with improved performance capabilities and reduced waste generation to include the development of advanced technology fuels (ATFs) for use in light water reactors (LWRs) [1-4]. ATFs are designated as fuels that can tolerate a loss of active cooling in the reactor core for a substantially longer time than the current benchmark, uranium dioxide (UO_2)-Zircaloy fuel system. In addition, ATFs should maintain or enhance fuel performance under normal and transient operating conditions, and during potential design-basis and beyond-design-basis incidents [3, 4].

Uranium mononitride (UN) and UN composite-based nuclear fuels have been considered for LWR and advanced nuclear reactor applications due to UN's high uranium density, high melting point, high thermal conductivity, and performance under irradiation, as compared to UO_2 [5-9]. These desirable properties contribute to larger power uprates, increased fuel cycle time, and higher burn-up [5, 10, 11]. However, UN has unproven performance in accident scenarios, such as a fuel cladding breach where the fuel pellet would be exposed to water or steam coolant [12-16]. The published literature relating to UN's stability under hydrolysis is limited, contradictory, and does not include the effects of UN submerged in water at elevated temperatures [13-15, 17-19]. It has been proposed that the addition of secondary phases, such as UO_2, can prevent UN from chemically reacting when exposed to water [5, 10, 16]. The work presented in this screening study investigates how the addition of UO_2 affects UN's performance in a simulated accident condition, similar to what would be experienced with a cladding breach under normal operation. Pure UN and UN-UO_2 monolithic pellets (> 90% TD) were subjected to hydrolysis at elevated temperatures (250-350 °C) and pressures (up to 16.5 MPa) relevant to LWR operating

conditions for short durations. The evolution of the microstructural degradation as temperature increases is presented. Insight into the degradation mechanism is obtained from examination and comparisons of the corroded microstructures and phase identification in the post-corrosion materials.

2. Materials and Methods

2.1 UN Powder Synthesis

UN powder was synthesized from depleted α-uranium (99.4% purity, 50 mesh) using a hydride-dehydride-nitride thermal synthesis route [20]. The hydride-dehydride-nitride route was used to limit carbon and oxygen impurities typically resulting from the more industrial carbothermic reduction and nitridation synthesis method of uranium dioxide and carbon (as noted by Muromura *et al.* [21] and Matthews *et al.* [22]). The atomized elemental uranium metal powder was washed in a 50% nitric acid solution and rinsed in methanol to remove oxides. Approximately 15 grams of uranium were loaded into a tungsten-lined alumina crucible inside an inert atmosphere glovebox (< 0.1 ppm H_2O and O_2). The crucible was sealed in a vial, transferred into a high temperature alumina tube furnace, and quickly placed under vacuum to limit exposure to air in preparation for the hydride-dehydride-nitride process. The thermal profile for the hydride-dehydride-nitride method is described in previous work [20]. The oxygen content in the process gas was continually monitored below the detectable limits of the Neutronics Inc. Model OA1 oxygen analyzer, which was less then parts per billion. Using a glove-bag and in an argon cover gas flow, the synthesized UN powder was removed from the furnace, sealed in a vial, and then immediately transferred back to the inert atmosphere glovebox. Two batches of UN powder, referred to as Batch 1 and Batch 2, prepared for this study were characterized using scanning electron microscopy (SEM) and X-ray diffraction (XRD) (Figure 1). It is important to note that the Batch 1 UN powder used for pellet fabrication had a lower amount of impurity UO_2 than the Batch 2 powder; this will be discussed further in succeeding sections. Due to the

highly reactive nature, the fine UN powder was mixed into a silicon-based vacuum grease inside an inert atmosphere glovebox prior to XRD characterization in lab air. Combustion analysis was performed using a LECO C230 and RO400 to determine carbon and oxygen content of the starting elemental uranium metal and the synthesized UN powder.

2.2 Pellet Fabrication and Sintering

Compacts of UN and UN+ (5-10 w%) UO_2 were fabricated using the synthesized UN powders and UO_2 (99.8% purity, 50 mesh) from Bio-Analytical Industries Incorporated (Boca Raton, FL). The UN and UO_2 powder mixtures were weighed into 5 gram batches, with the proportional amounts of UO_2 for the 5- and 10 w% composites. The powders were hermetically sealed inside polypropylene containers inside an argon-backfilled glovebox (<0.1 ppm O_2, H_2O), and mixed in a tabletop mixing mill (MTI 4 Tanks Mixer). Image analysis software was used to estimate particle size. After mixing, the UN and composite powders were cold-pressed at approximately 670 MPa into green pellets of right cylindrical geometry, with either a 3.175 or 6.35 mm diameter die, to approximately 62 %TD in an inert atmosphere glovebox. A small amount of zinc stearate was used as a lubricant on the die walls and punch faces prior to pressing.

Due to the potential for the green pellets to spontaneously react in air, the pellets were placed on tungsten setter plates and sealed under polyvinylidene chloride (PVDC) film with a small amount of vacuum grease to avoid oxidation during the rapid transfer into the refractory metal sintering furnace. The pellets were sintered for five hours at 1900 °C in an Ar+100 ppm N_2 atmosphere; the complete details for sintering are explained in a previous publication [20]. After sintering, the pellets were immediately transferred to an inert atmosphere glovebox. The sintered samples were prepared for SEM and XRD characterization by grinding with 1200-grit silicon carbide grit paper approximately 1/3 of the way through the pellet to create a cross-sectional surface that was perpendicular to the two parallel faces of the right cylinder. A thermal etch at 1200 °C for 12 minutes was performed in the refractory metal furnace to examine the

grain morphology of the sintered pellets. Pellet densities were determined via the Archimedes method in de-ionized water at 21 °C [23].

2.3 Hydrothermal oxidation

In preparation for radioactive hydrothermal oxidation testing, a custom static autoclave (Parker Autoclave Engineers) was modified with a containment enclosure to house the autoclave bolt assembly seal (Figure 2) and prevent any external contamination with radioactive material. A stainless-steel sample holder was fabricated to position up to four samples simultaneously within the hot zone of the autoclave, as shown in Figure 2. Layers of stainless-steel mesh separated the pellets from each other, and the entire pellet holder was secured by another layer of stainless-steel mesh to ensure the samples would not shift during loading and testing. A pellet of each composition was loaded into the sample holder in lab air; three pellets in the Batch 1 tests, four in the Batch 2 tests, including UO_2 as a benchmark. After loading the sample holder into the autoclave, 80 mL of 18.2 MΩ·cm de-ionized water was added before the system was sealed and pressurized to approximately 4.1 MPa with UHP helium. This static autoclave configuration, while similar to the static tests performed by Nelson *et al.* [24] on silicide and nitride fuels in deionized water, did not allow for loading of the samples under inert atmosphere. The maximum starting oxygen potential was calculated to be approximately 4700 ppm. It is believed this value was lower as the autoclave enclosure was continuously pressurized with UHP He until it was sealed completely at 200 °C. The temperature was ramped at 1 °C/min to and from the dwell temperature (250 – 350 °C, resulting in a pressure of 4.1-16.5 MPa) where it was held for 30 minutes prior to cooling to room temperature. Density measurements and optical macro images were recorded for the pellets after removal from the autoclave. The pellet surfaces were examined using SEM, energy dispersive spectroscopy (EDS), and XRD.

3. Results

3.1 UN Powder Synthesis

The left inset SEM image in Figure 1 shows the as synthesized UN powder exhibiting a bimodal particle size distribution and faceted morphology, as expected from the hydride-dehydride-nitride synthesis route. The larger particles and agglomerates were broken up during the milling process resulting in a powder with an average particle size of 1.1 ± 0.5 μm (inset of Figure 3). XRD of the as-synthesized powders showed the powder as primarily UN (Inorganic Crystal Structure Database powder diffraction file (ICSD PDF) 00-032-1397) with a small fraction of UO_2. Comparison of the two synthesized batches indicates increased UO_2 (ICSD PDF 00-041-1422) content in the Batch 2 powder. A semi-quantitative analysis of the XRD intensities suggests that the UO_2/UN ratio in the Batch 2 powder was twice that of the Batch 1 powder. Figure 1 also includes the pattern for the starting UO_2 powder which suggests it is primarily UO_2 but also exhibits additional peaks labeled as unknown after comparing to peaks corresponding to U_3O_8 (ICSD 00-014-1493). It is possible a small secondary phase, U_3O_7 (ICSD 00-015-0004), may be present. This U_3O_7 phase exhibits peak overlap with the indexed UO_2 pattern but may be contributing to broadening of peaks attributed to UO_2 [25, 26]. The light element chemical analysis on the starting uranium metal indicated 300 ppm and 170 ppm of carbon and oxygen, respectively, and 275 ppm and 2550 ppm of carbon and oxygen, respectively, in the Batch 1 UN powder.

3.2 Pellet Fabrication and Sintering

After mixing and milling the UN with the UO_2 powders for five hours, SEM characterization shows a bimodal particle size distribution for all compositions (inset of Figure 3). XRD of the as synthesized UN, the milled UN, and milled compositional powders reflect only UN (ICSD PDF 00-032-1397) denoted by the inverted triangles, and UO_2 (ICSD PDF 00-041-1422) as indicated by the star shape in Figure 3. All pellets were 92 ± 1.6 %TD, based on the theoretical density of UN (14.33 g/cm^3 [27]), and a typical sintered pellet is seen in Figure 4a. The typical grain morphology of a cross-sectioned sintered pellet and fracture surface are shown in Figure 4b-c.

The distribution of the UO_2 phase in the UN matrix for a UN + 10w% UO_2 pellet is shown in Figure 4d.

3.3 Pellets post-autoclave

Figure 5 shows the corroded pellets fabricated from both the Batch 1 and Batch 2 powders. Each test, regardless of temperature, resulted in pellets that were considerably darker in color than the un-corroded pellets. The densities of the corroded pellets also remained relatively constant at approximately 90 %TD as determined via Archimedes method.

The pellets fabricated with Batch 1 UN powder (containing less starting impurity UO_2) were preferentially attacked at the edges and, as expected, the level of degradation increased with increasing temperature. Also, in certain instances, the hydrothermal test resulted in complete loss of the pellet. For example, the UN + 5 w% UO_2 pellet exposed to 300 °C completely disintegrated (Figure 5). The tests at 300 and 325 °C were repeated to replicate the results. However, both repeated tests resulted in different outcomes. At 275 °C all Batch 1 pellets were retrieved, but for Batch 2 (having a higher starting impurity UO_2 content) both UN-UO_2 composite pellets were disintegrated. The Batch 1 pellets corroded in the first 300 °C test resulted in complete loss of the 5 w% UO_2 pellet. In the Batch 2 300 °C test both the 5 w% and 10 w% UO_2 composite pellets disintegrated. Similarly, for Batch 1 in the 325 °C test the 10 w% UO_2 pellet was lost and in the 350 °C the 5 w% UO_2 pellet was totally disintegrated, but in Batch 2 tests at 325 °C and 350 °C all pellets except the pure UO_2 pellet were lost. As stated previously, the maximum calculated starting oxygen potential of the pressurized water and volume of air and He balance was roughly 4700 ppm. However, the benchmark UO_2 pellets did not show any significant degradation per visual examination and XRD. The chipping on the UO_2 pellet used in Batch 2 testing at 350 °C occurred in the green state prior to sintering (Figure 5).

It is believed the starting oxygen potential was much lower since the autoclave was continuously pressurized with UHP He until it fully sealed at 200 °C.

The powder from the disintegrated pellets was retrieved for characterization and will be referred to as “sludge” in the subsequent sections. In the Batch 2 testing, pellets that remained intact showed more significant degradation than Batch 1 pellets (Figure 5). Apart from the benchmark UO_2 pellets, no discernible UN or UN composite pellets remained above 300 °C testing. As previously stated, the “sludge” was collected and dried for SEM and XRD characterization. The benchmark UO_2 pellets performed as anticipated, showing little, if any, corrosion behavior, with results similar to those reported by Une *et al.* [28] and Taylor *et al.* [29].

Post-autoclave XRD analysis – Pellets

X-ray diffraction of corroded pellet surfaces are shown in Figure 6 with the un-corroded pellet surface patterns included for reference. The XRD patterns show the analysis for the UN, UN + 5 w% UO_2, and UN + 10 w% UO_2 pellets from left to right. After autoclave testing, the primary phase in the pure UN samples is UN after excluding peaks attributed to the sample holder. However, the corroded composite UN-UO_2 pellets exhibit peaks corresponding to UN_2 (noted by the diamond markers), and what may be α-U_2N_3 (ICSD PDF 00-015-0426) as denoted by the chevron markers and droplines. Some overlap in the primary peaks for these two phases exists (29.0, 33.6, and 48.3° 2θ values). The XRD patterns show a decrease in the full width half maximum (FWHM) of the first two UO_2 peaks shown in Figure 6. This observation, most evident in the 275 and 300 °C patterns of the 5 and 10 w% samples, suggests that the UO_2 crystallites increased in size during the hydrothermal oxidation process. An oxynitride layer resulting from dissolved oxygen and/or nitrogen into the UO_2 and UN_2 lattices is most likely contributing to the peak broadening due to distortion of the lattice [30].

3.5 Post-autoclave XRD analysis – Sludge

As previously mentioned, the material collected from pellets that disintegrated during testing was dried and characterized via SEM and XRD. The XRD patterns in Figure 7 show that the retrieved powder remains primarily UN. However, as autoclave temperatures are increased, peaks attributed to UO_2 and UN_2 phases become more prominent. There is also indication of a slight amount of α-U_2N_3 denoted by the chevron marker and seen in the 300 – 350 °C tests, most notably at 2θ values 28.9, 33.6, 48.4 and 57.2°. The UO_2 phase in the sludge also shows a clear increase in the FWHM (almost an order of magnitude larger) as temperature is increased. This increase in the FWHM can be attributed to peak overlap due to the presence of the other phases as noted above and/or broadening due to lattice distortion from dissolved oxygen and nitrogen. This is easily seen at 2θ values 28.3, 32.7, and 47.0°. This increase in the FWHM is most evident in the “sludge” from the 350 °C test (Figure 7).

3.6 Post-autoclave morphology – Pellets

Microstructural characterization was performed on the corroded pellets using backscattered electron (BSE) SEM imaging. Each of the pellets that remained intact after exposure showed similar macroscopic features; the edges of the right cylinder were preferentially degraded as seen in Figures 8 and 9. The typical corroded surface microstructure for pure UN pellets is shown in the top row of Figure 8 for pellets corroded at 250 °C, 275 °C, and 300 °C, respectively. As expected, the level of degradation increases with exposure temperature. Figure 8 also illustrates how the degradation process firstly attacks grain boundaries, providing grain boundary expansion and spallation. The bottom images are from the same pellet but from the corroded edges, showing heavier attack.

The composite UN-UO_2 pellets show similar behavior to the UN, with grain boundary attack and spallation beginning at the corners of the right cylinder. In addition, the attack increases with autoclave temperature. The UN-UO_2 pellets also exhibit an additional noteworthy aspect; Figure 9 shows the top surfaces of the UN + 5 w% UO_2 and UN + 10 w% UO_2 pellets corroded at 250

°C, where light and dark phases are observed. The dark phase was identified as an oxide with EDS, as shown in Figure 10. These micrographs combined with EDS chemical analysis suggest that the oxide may be nucleating on the grains and propagating across the surface of the grains. The chemical analysis (Figure 10) of the micrograph of the UN + 5 w% UO_2 pellet surface (Figure 9) highlights that the lighter phase is distinctly nitrogen-rich, while the darker regions are oxygen-rich.

3.6 Post-autoclave morphology – Sludge

Backscattered electron SEM micrographs showing the typical morphology of the spalled material from the autoclave tests at 275 – 350 °C are seen in Figure 11. The grains are faceted and show clear separation at the grain boundaries. The individual grains in the sludge from the 275 – 300 °C tests show less granular deterioration than those collected at 325 – 350 °C, which show heavier attack.

4. Discussion

4.1 Post-autoclave: Pellets

The effect of diameter (2.85 vs. 5.65 mm) was not an intent of this study. It is interesting to note however, tests from the Batch 1 pellets were replicated at 325 °C with pellets fabricated using the larger 6.35 mm die and different results were obtained. The pure UN pellet was lost in one test and the UN + 10 w% UO_2 pellet in the other (Figure 5). This suggests the hydrothermal oxidation behavior of the tested pellets is stochastic in nature. Further studies are needed to verify that there is no size effect. As stated, the pressure within the autoclave does rise with temperature, reaching a maximum of approximately 16.5 MPa during the 350 °C tests. Although the effects of pressure were not studied explicitly, it is believed that this pressure change has little effect on the overall hydrothermal oxidation behavior. In the 325 and 350 °C tests for the Batch 1 pellets intact pellets were retrieved, whereas no pellets (with the exception of the

benchmark UO_2) were retrieved from the Batch 2 tests, and both tests experienced similar pressure changes (Figure 5). Although significant effort was made to reduce exposure of the starting UN powder to atmosphere, subsequent processing and handling of the reactive synthesized UN powder resulted in a pickup of oxygen. The aforementioned light element analysis, indicated 2500 ppm oxygen in the starting Batch 1 powder, which is within previously published specification limits for UN irradiation tests and development of UN fuel for the SNAP-50 program [27, 31]. It is believed that the actual oxygen concentration value is lower than reported, as the external lab which performed the light element chemical analysis indicated the tests were completed in lab air. As previously noted, the pellets fabricated from the Batch 2 powder did not perform as well as those in Batch 1 tests, especially the UN-UO_2 composites. Only the test at 250 °C for the Batch 2 pellets resulted in intact pellets for all three compositions. For Batch 2 pellets, tests above 250 °C resulted in degraded UN pellets and complete loss of the UN-UO_2 pellets, with the UN pellets also completely disintegrating above 300 °C. This is believed to be due to the increased starting oxygen impurity content in the Batch 2 powder.

As previously noted, the primary phase in the pure UN samples post-autoclave is UN (Figure 6). This result varies from work published by Bugl and Bauer which shows UN_2 as a corrosion product [19]. It is also contrary to results published by Sunder and Miller [17], and Rao *et al.* [14], who indicate that UN quickly converts to UO_2 (the final phase) upon exposure to water, or U_3O_8 for UN samples which had no starting UO_2 phase in them. Earlier work shows that the addition of UO_2 likely stabilizes a hyper-stoichiometric nitride phase [20]. The presence of this hyper-stoichiometric nitride phase is also in contrast to literature which states only an α-U_2N_3 phase or oxynitride phase would be present [13, 14]. However, work by Jolkkonen *et al.* [15] also indicated UN as the primary phase remaining after hydrolysis of UN in superheated steam along with UO_2 containing dissolved nitrogen and possibly an oxynitride phase. XRD analysis of the corroded pellets suggests that, in addition to UN_2, some α-U_2N_3 may be present. However,

some peak overlap occurs at 2θ values of 28.9 and 33.6° (Figure 6). A density functional study by Wang *et al.* [30] states that uranium oxynitrides possess similar XRD patterns as compared to UN_2, and it is likely that the presence of an oxynitride layer is contributing to the intensity of the peaks identified as UN_2. Studies by Dell *et al.* [13] and Sugihara and Imoto [18] on the hydrolysis of UN, following reactions (1) and (2), suggested that liberated nitrogen that does not form ammonia may dissolve into the UO_2 lattice to form an oxynitride or α-U_2N_3. As the hydrolysis proceeds, U_2N_3 can form UO_2 according to reaction (3) [13, 18], this was also reported by Jolkkonen *et al.* [15].

(1)	$UN + 2H_2O \rightarrow UO_2 + NH_3 + \frac{1}{2}H_2$	ΔG_{rxn} = -307.99 kJ/mol
(2)	$3UN + 2H_2O \rightarrow UO_2 + U_2N_3 + 2H_2$	ΔG_{rxn} = -571.59 kJ/mol
(3)	$U_2N_3 + 4H_2O \rightarrow 2UO_2 + \frac{8}{3}NH_3 + \frac{1}{6}N_2$	ΔG_{rxn} = -1158.61 kJ/mol

It has also been reported that oxygen solubility in pure UN can be as high as 7 at% and results in a slight lattice expansion per XRD [32-34]. This lattice expansion (caused by dissolved oxygen) could explain the slight shift in the UN peaks (near 2θ values of 31.6 and 36.7°) (Figure 6). Dell *et al.* [13] suggests that a surface film on UN, either a bcc-nitride or oxynitride, acts as a protective layer during the hydrolysis of UN. However, Dell also mentions that as the reaction propagates along grain boundaries, corresponding to an increase in the available surface area, the particles eventually breakdown along grain boundaries [13]. This mechanism would result in a volume expansion from the differences in the larger lattice parameters of UO_2, U_2N_3, and any oxynitride phase, as compared to UN [30]. This explains the results seen in both the pure UN and UN-UO_2 corroded pellets, where spallation of material along grain boundaries is seen

(Figures 8 and 9), a result also noted in the work by Jolkkonen *et al.* [15]. Sugihara and Imoto [18] also state that along with an oxynitride phase, a hyper-stoichiometric $UN_{1.7}$ would be formed during hydrolysis of UN according to reaction (4).

(4) $$UN + 2H_2O \rightarrow UO_2(N) + UN_{1.7} + H_2$$

As reported by Jolkkonen *et al.* [15] and according to the above listed reactions (1)-(4), the formation of ammonia and hydrogen would be expected, however the gaseous reaction products, as well as the pH of the waste liquid, was not studied explicitly in this work. The composite UN-UO_2 corroded pellets do reflect a hyper-stoichiometric (UN_2) phase in the 275-350 °C tests, denoted by the black diamonds on the XRD patterns shown in Figure 6. Rao *et al.* [14] and Lopes *et al.* [16] noted that a U_2N_3 layer is also seen between UN and UO_2 layers during hydrolysis. Work by Matzke [27] on the oxidation of UN suggests that a hyper-stoichiometric U_2N_{3-x} layer forms between the unreacted UN and UO_{2+x} surface layer and is dense and resistant to oxygen permeability. Rao *et al.* [14] also notes that samples containing a higher initial amount of UO_2 result in a higher concentration of reacted U_2N_3 and that oxygen has to diffuse through a layer of UN/U_2N_3 reacting with UN at the interface. This suggests that strain caused by a change in volume from product formation, leading to breakup of the sample, would be higher in samples having an initial amount of UO_2. This result is seen in the corroded UN-UO_2 composite pellets in this work (Figure 5). Variances between tests replicated for Batch 1 at 300 and 325 °C are indicative of the stochastic nature of the corrosion process. Results from XRD, SEM, and the darkened appearance of the post-exposure pellets also confirm that oxidation is occurring (Figure 5-Figure 10). Similar to results by Matzke [27] on the oxidation of UN single crystals, the preferential attack at the grain boundaries from oxygen diffusion and the resulting stresses leading to cleavage would contribute to an increased surface exposure. This

leads to propagation of the reactions and ultimately pellet instability. It is possible that the corroded UN samples show less degradation than the corroded UN-UO_2 composite samples because the reactions begin at the surface of the pellet and proceed to the core. In contrast, reactions in the UN-UO_2 samples occur throughout the bulk of the pellet, as described by Rao's oxidation study [14] and Lopes' UN degradation work [16]. It is also possible that the formation of a UN_2 or oxynitride layer, explained previously based on the work by Dell *et al.* [13], is responsible for the less severe degradation of the pure UN samples as compared to the UN-UO_2 samples.

4.2 Post-autoclave: Sludge

As discussed previously, literature indicates a hyper-stoichiometric nitride layer likely exists between the UN and UO_2. It is likely that a thin layer of this nitride or oxynitride is present in the sludge. While the spalled material is still primarily UN, the other phases present (UO_2, UN_2, and possibly α-U_2N_3) support the results in previously published literature of Dell *et al.*[13], Rao *et al.* [14], Sugihara and Imoto [18], Jolkkonen *et al.* [15], Lopes *et al.* [16], and Bugl and Bauer [19]. The resulting lattice strain from the dissolution of nitrogen, or oxygen, into the UO_2 or UN lattices, would contribute to the peak broadening seen in the XRD patterns of Figure 7. It can be seen from the relative peak intensities that the amount of secondary phases increases in the sludge with increasing autoclave temperature, more so than in the corroded pellets themselves. The increase in the amount of these secondary phases is explained by the fact that the sludge material comes primarily from the full disintegration of the UN-UO_2 composite pellets (Figure 5) and would consist primarily of spalled matter. According to Rao *et al.* [14], samples with a larger initial amount of UO_2 result in a higher concentration of reacted U_2N_3. Following reactions (3) and (4) discussed earlier, a higher concentration of the UO_2 and hyper-stoichiometric UN phases would be expected in the corroded material [18]. This increase in secondary phases, identified by XRD in the sludge (Figure 7) correlates to the increase in degradation seen in the

BSE SEM images of the material from the autoclave tests at 325-350 °C (Figure 11). The differences between the hydrothermal oxidation test results of Batch 1 and Batch 2 pellets can also be attributed to the increased amount of impurity UO_2 or residual dissolved oxygen in the starting UN powder used for fabrication. Higher oxygen impurity results in elevated loss of the Batch 2 pellets due to an increased formation of secondary phases.

As seen in Figure 8-9, and 11, the principal degradation mechanism is grain boundary attack, leading to subsequent spallation of the pellets into single grains. At temperatures of 275-300 °C, the pellet surfaces show grain boundary relief. As temperatures increase, separation at the grain boundaries is seen (Figure 8-9). As noted above, the hydrolysis reactions propagate along grain boundaries leading to strain from the differences in cell volume of the formation products [13-16, 27]. Differences in the resulting spalled grains from tests performed at a lower temperature versus those at higher temperatures suggest a sequence to the disintegration. As seen in Figure 11, at 275 °C the spalled material appears to be whole grains, indicating a clear separation at the grain boundaries, whereas in the 350 °C test, the sludge material is significantly more degraded and shows heavier attack. This sequencing to the degradation mechanism and resulting morphology can be explained by the repeated strain caused by changes in cell volume as the reaction products form, as discussed earlier [13, 15-18, 30].

5. Conclusions

This screening study was performed to test pellets of UN and UN-UO_2 composites under short duration, static hydrothermal oxidation conditions. The effects of the addition of a secondary phase on the microstructural degradation behavior and phase formation were assessed. Examination of the corroded microstructures shows a sequence to the breakdown of the monolithic pellets. At lower temperatures the corroded pellets exhibit clear grain boundary relief and separation. Spallation of single grains is evident as test temperatures increase from 250-350 °C. This spalled material also shows increased degradation at higher temperatures. It

is postulated that as the UN reacts with the water, the propagation of reactants forming secondary phases, starting at the grain boundaries and proceeding through the bulk, increases with temperature. Hyper-stoichiometric UN, uranium oxynitride, α-U_2N_3, and UO_2 phases along the grain boundaries result in a volume expansion due to increased lattice parameters as compared to UN. In the UN-UO_2 composites, an oxide layer appears to nucleate on the grains and propagate across the surface of the grains, presumably U_2N_3 forming UO_2 during the hydrolysis. This propagation behavior was not observed in the pure UN pellets. It is proposed that as the formation of reaction products proceeds (reaction layer and phase segregation at the grain boundaries), the expansion of the intermediate layer ultimately leads to a failure of the pellet structure. It is theorized that an increased oxygen impurity content in the starting powders enhanced the microstructural degradation behavior in samples exposed to elevated temperature and high-pressure conditions for short periods. This introductory study on the degradation mechanism (grain boundary attack) in UN and UN-UO_2 composite samples exposed to hydrothermal oxidation conditions can inform on future corrosion studies in UN and other high uranium density fuels. The role of oxygen impurities in increased degradation should be specifically investigated on advanced technology fuels. Further work to more closely match UN test conditions to typical water reactor chemistries must be completed to demonstrate improvements in accident tolerance.

Acknowledgements

This project was partially supported by the Department of Energy Nuclear Energy University Program (DOE-NEUP) grant #00120690. Additional support was provided by an Integrated University Program Graduate Fellowship.

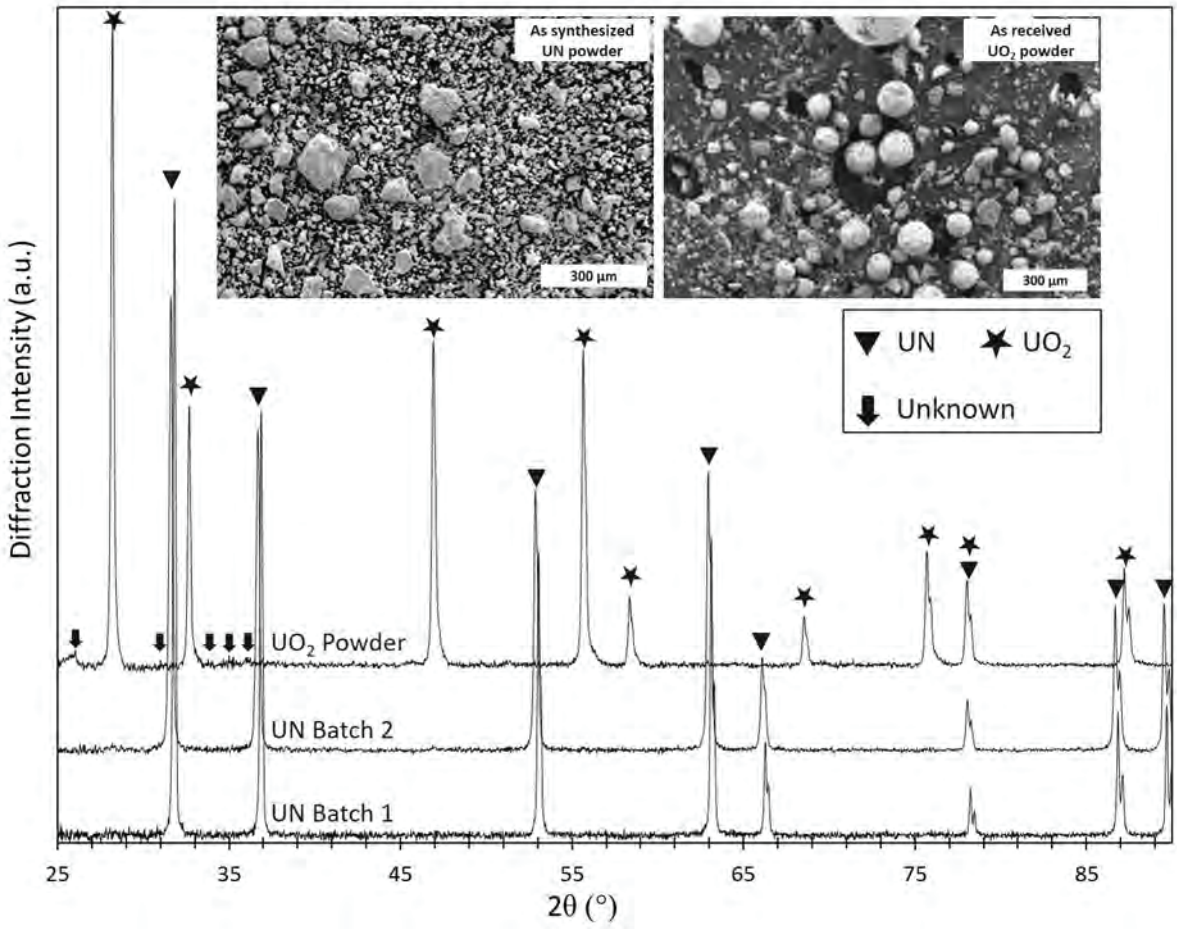

Figure 1: XRD of the two separate batches of UN powders (Batch 1 having a lower starting impurity UO_2 content than that of Batch 2). Powders were synthesized using a hydride-dehydride-nitride route, and as-received UO_2 powder. Left inset shows the morphology of the as synthesized UN powder and right inset is the morphology of the as-received UO_2 powder.

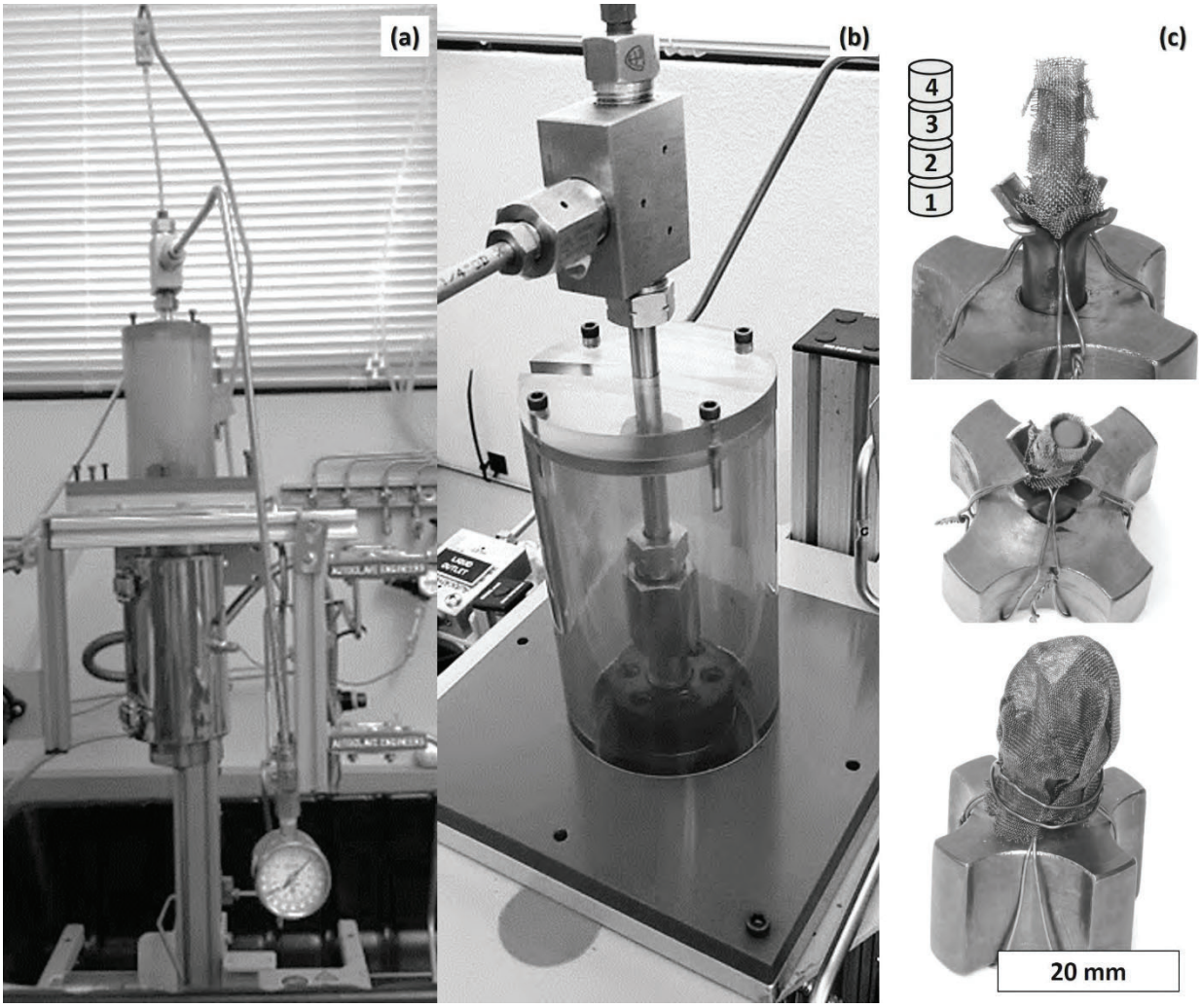

Figure 2: (a) Static autoclave used for hydrothermal oxidation testing showing the location of the heater/hot zone, (b) the custom fabricated containment enclosure for the autoclave bolt assembly, and (c) Side view of sample holder (top image), top view of the custom Autoclave sample holder showing the stainless-steel mesh for positioning up to four pellets in the hot zone of the autoclave (middle image). Once the pellets are inserted, the sample holder is encased with stainless steel (bottom image) to retain corrosion products.

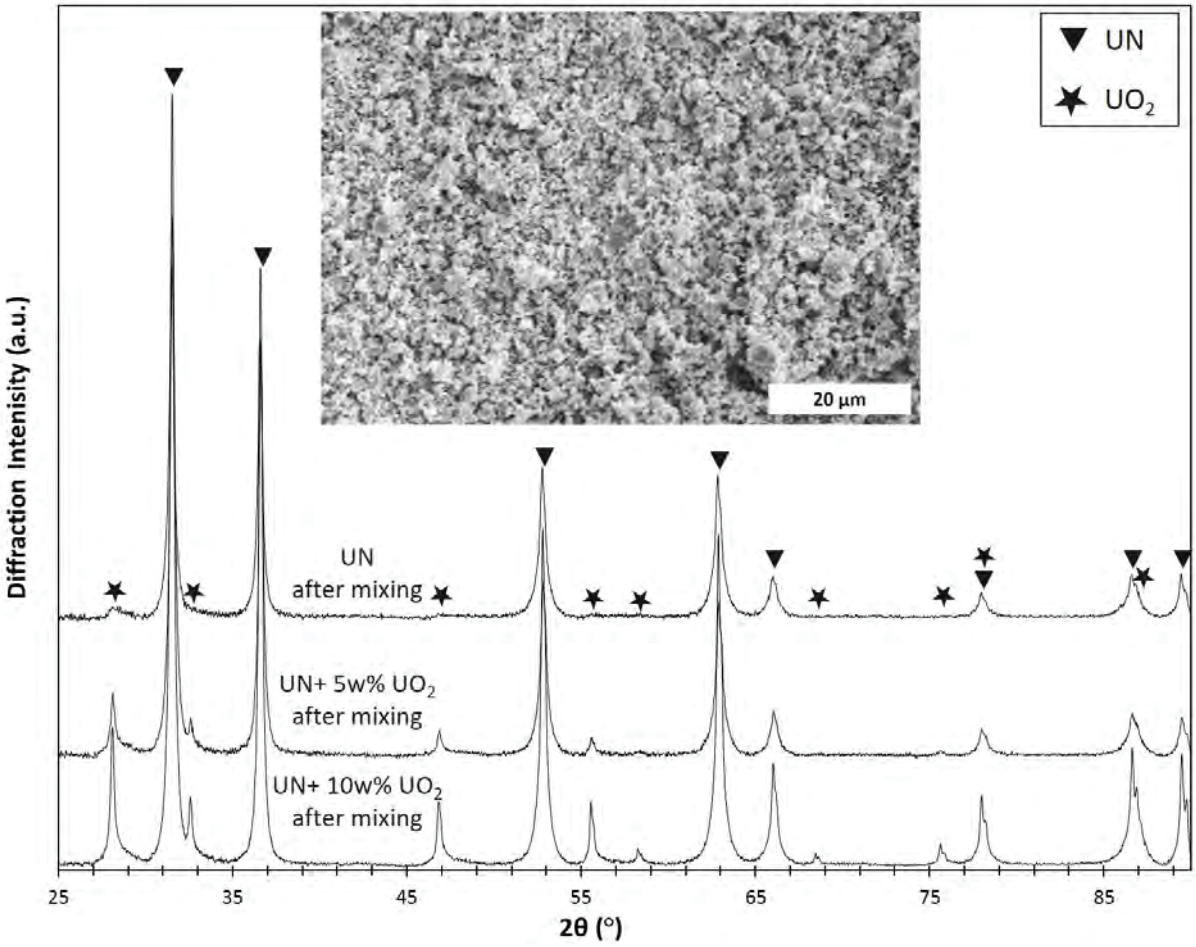

Figure 3: XRD patterns of the mixed UN and UN-UO_2 composite powders prior to pressing into pellets. The inset is an SEM micrograph showing the typical morphology of the mixed powders.

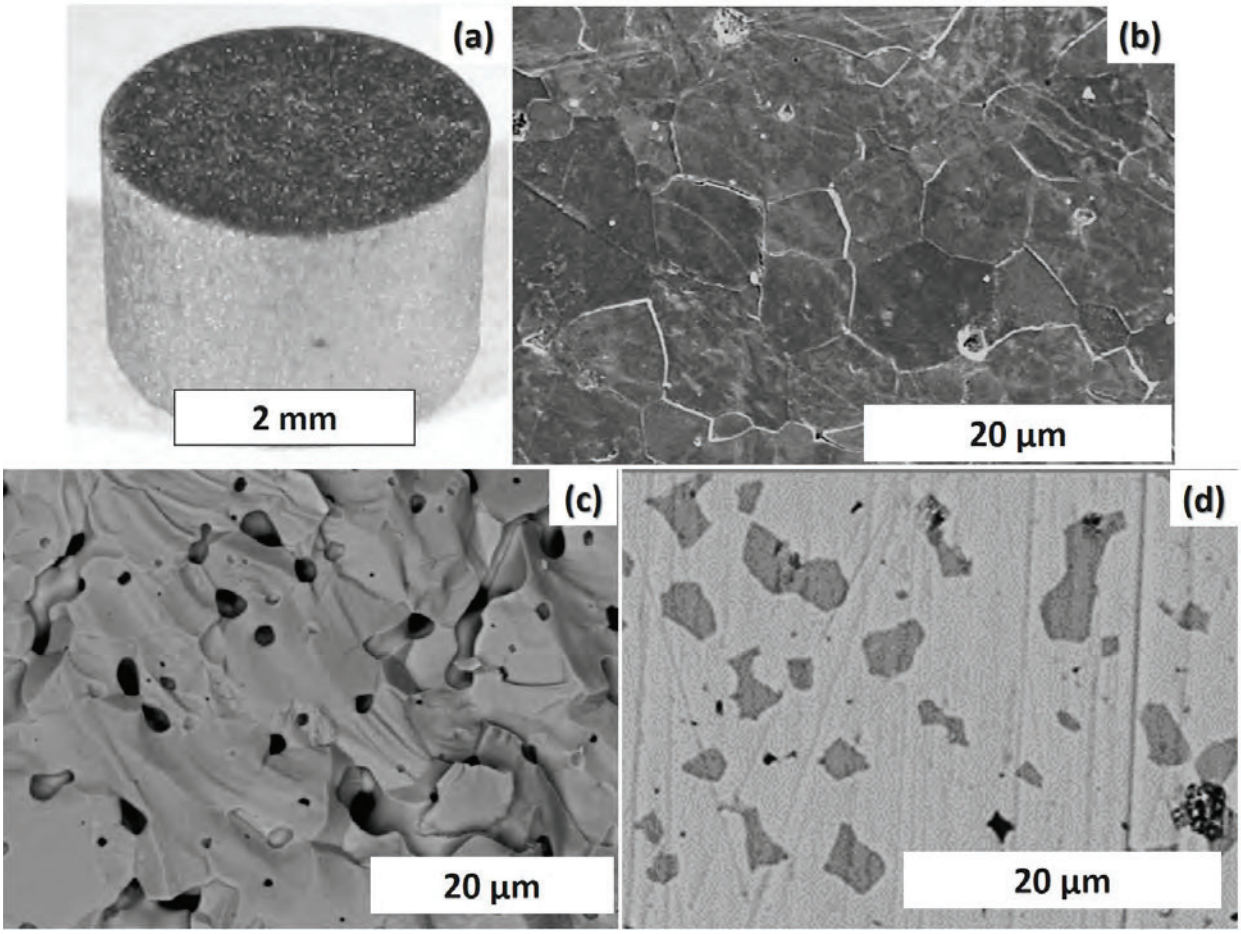

Figure 4: Images of a typical sintered pellet showing (a) right cylindrical geometry, (b) the grain structure of UN + 5 w% UO_2 pellet surface after polishing and thermal etching, (c) the fracture surface of UN + 10 w% UO_2 pellet, and (d) the typical UO_2 distribution in the UN matrix of a UN + 10 w% UO_2 pellet.

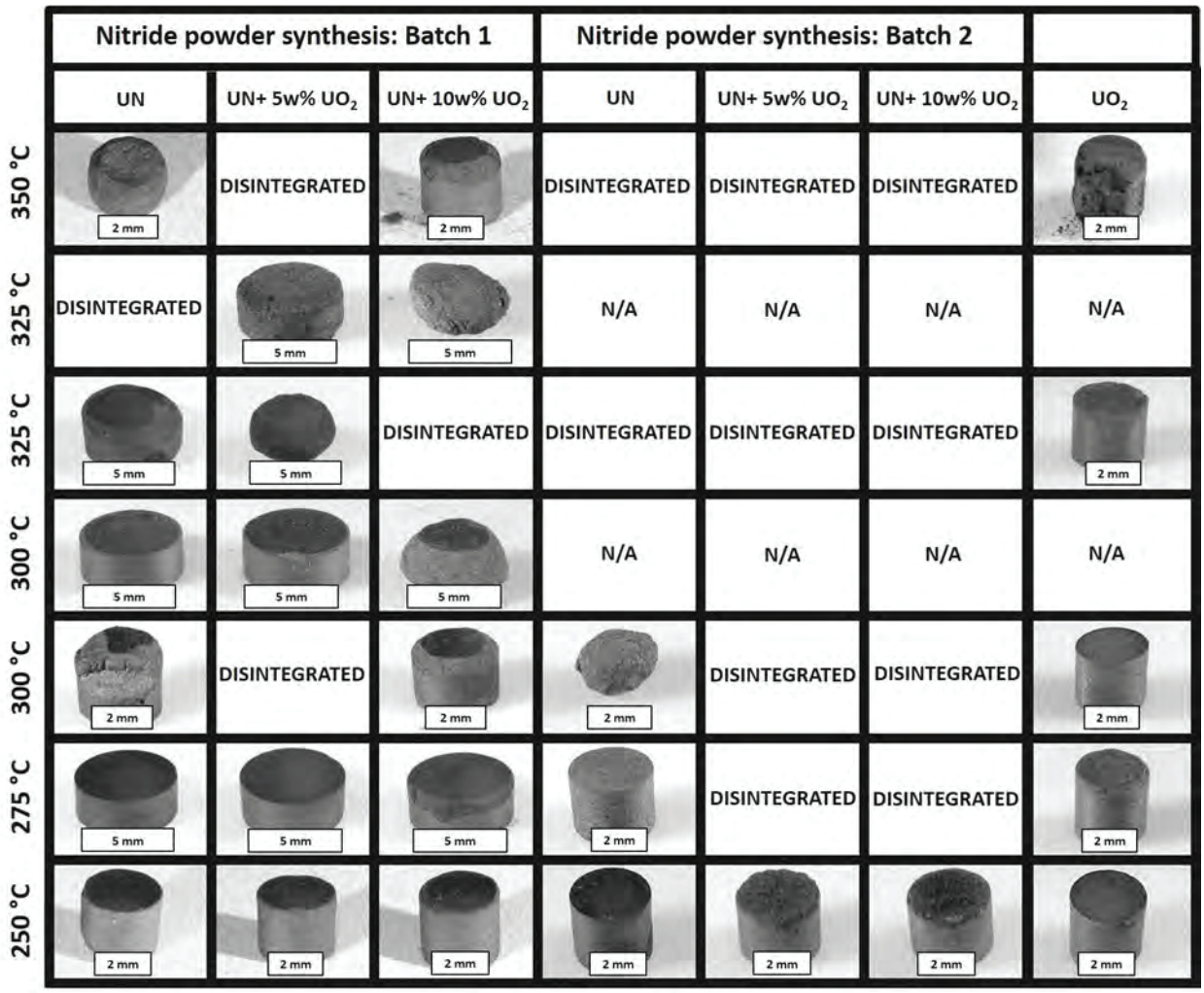

Figure 5: Images showing the relative hydrothermal oxidation behavior of pellets fabricated from the two batches of UN powder tested at 250-350 °C. The experiments with pellets fabricated from the Batch 2 powder include UO_2 pellets as a benchmark. In all cases, the right cylindrical pellets were preferentially attacked at the edges and the extent of degradation increased with increasing temperature, with some pellets completely disintegrating.

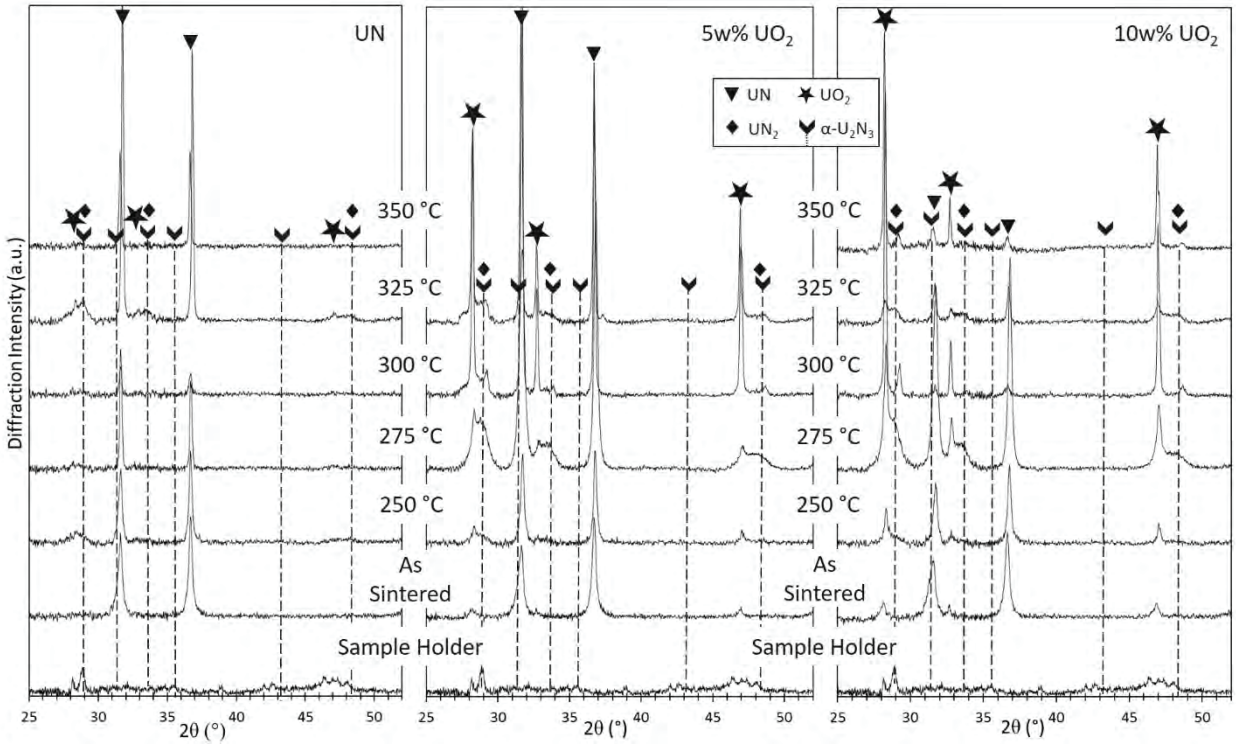

Figure 6: Comparison of XRD patterns of the as-sintered and corroded UN and UN+UO_2 composite pellets. After autoclave testing the primary phase in the pure UN samples is UN, whereas the 5 and 10 w% samples indicate a UN_2 phase or oxynitride phase (2θ values 29.0, 33.6, 48.3°) and possibly α-U_2N_3 (2θ values 28.9, 33.6, and 48.4°) as denoted by the chevron markers and droplines, most evident in the 275-325 °C data.

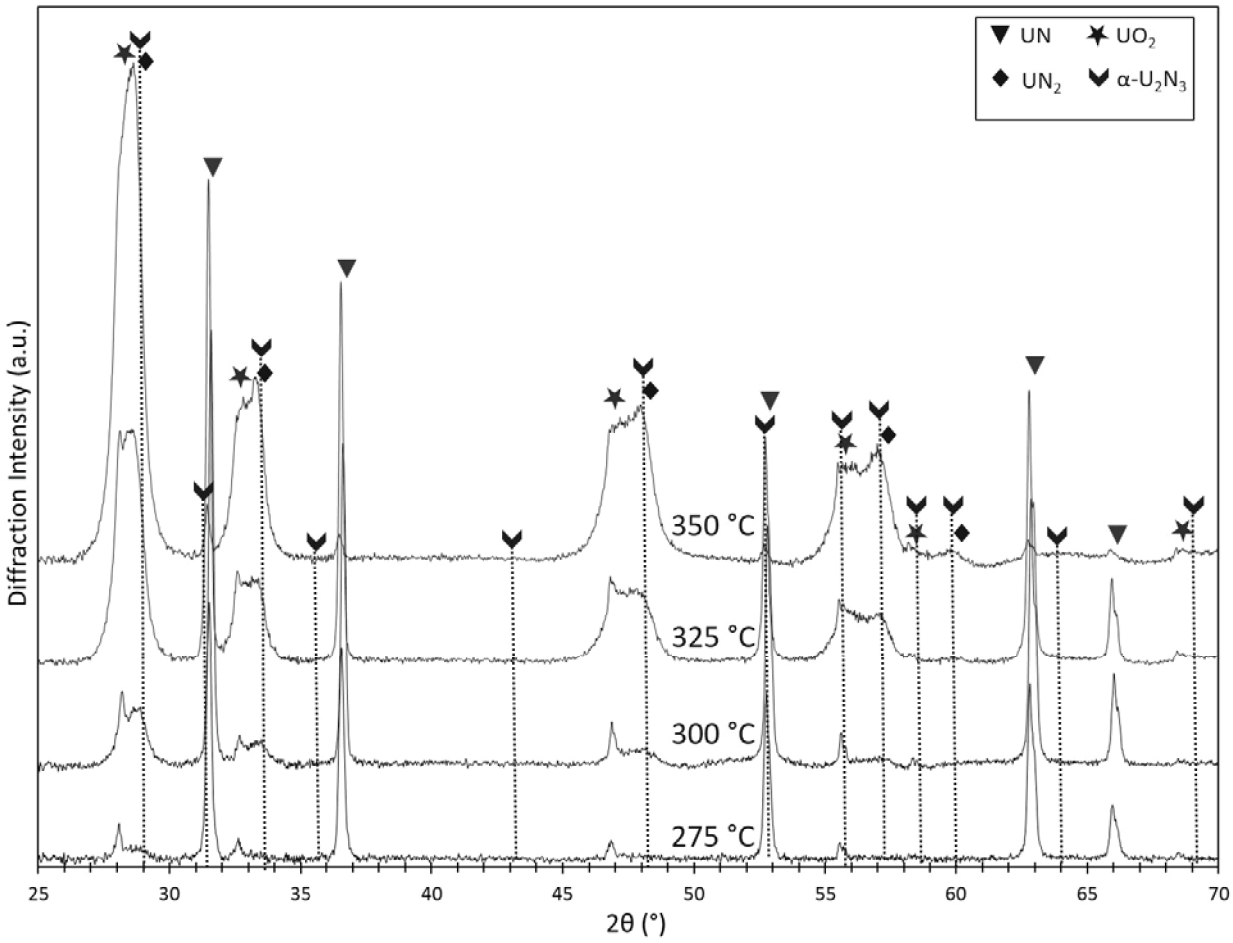

Figure 7: Comparison of XRD patterns from the recovered "sludge" showing the primary phase remains UN. However, as autoclave temperatures increase, phases of UN_2, possibly an oxynitride, UO_2, and peaks attributed to α-U_2N_3 become more prominent.

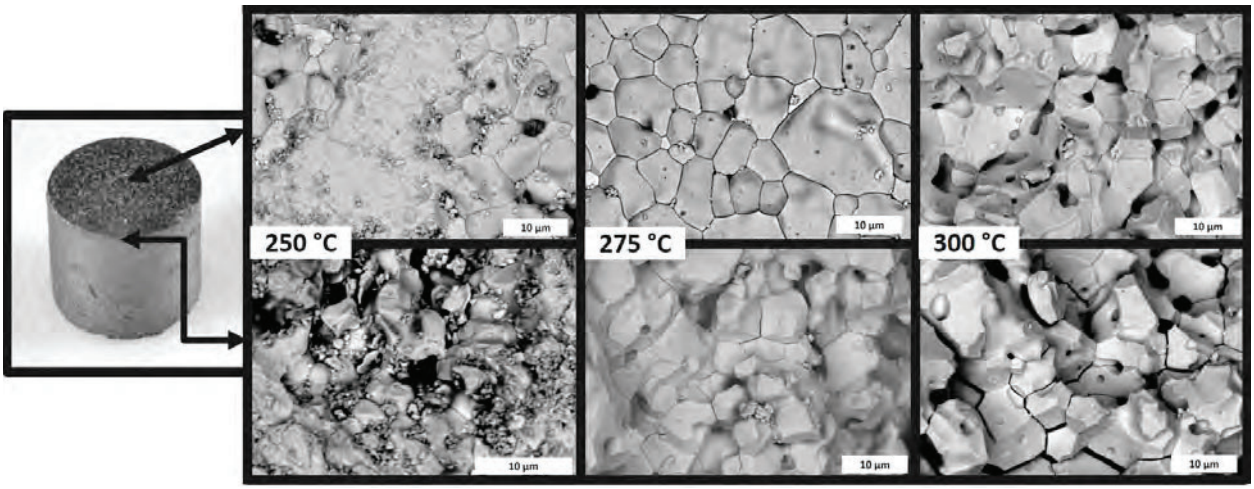

Figure 8: Backscatter electron micrographs of the corroded UN pellets at 250 °C, 275 °C, and 300 °C. The top images were taken from the less corroded, central, region of the pellet surface and the bottom images were taken from the more heavily corroded outer edges of the pellets (seen in the photograph on the left). Preferential edge and grain boundary attack is evident.

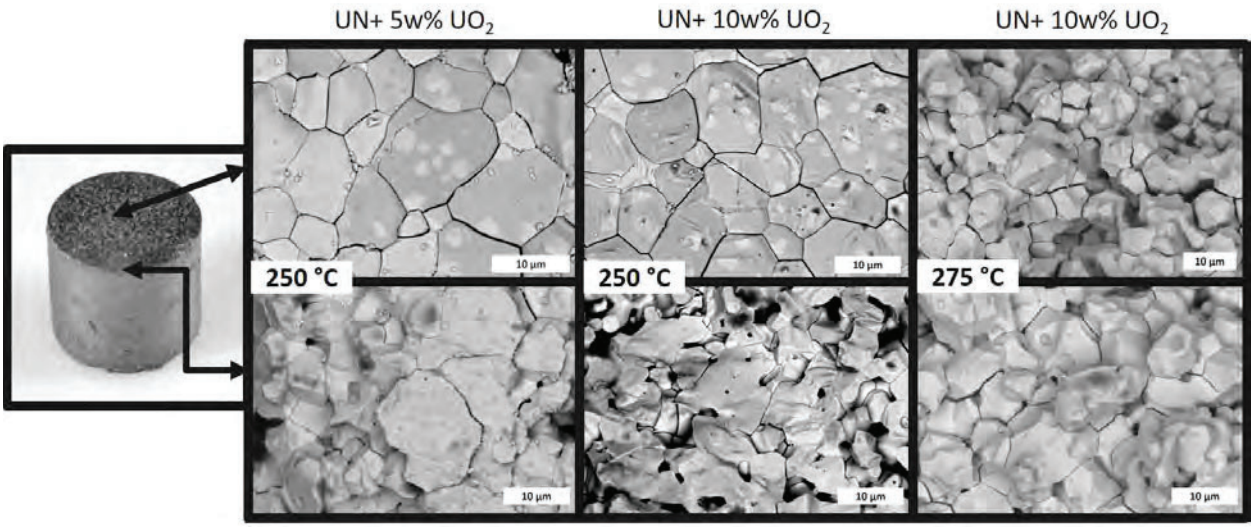

Figure 9: Backscatter SEM micrographs of the UN + 5 w% UO_2 and UN + 10 w% UO_2 composite pellets corroded at 250 °C and the UN + 10 w% UO_2 pellet corroded at 275 °C. The top images were taken from the less corroded, central, region of the pellets and the bottom images were taken from the more heavily corroded outer edges of the pellets (seen in the photograph on the left). Preferential edge and grain boundary attack is evident. The pellets corroded at 250 °C also show clear light and dark phases present across the surfaces. The dark phase was identified as an oxide phase via EDS (Figure 10).

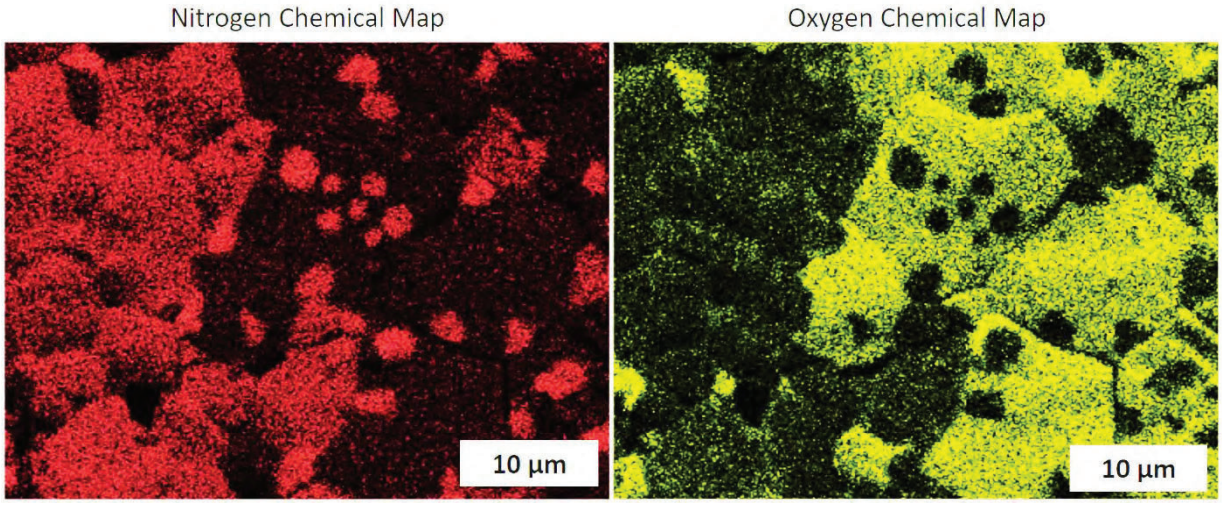

Figure 10: Chemical analysis via EDS of the UN + 5 w% UO_2 pellet surface corroded at 250 °C (seen in Figure 9) showing distinct nitrogen and oxygen-rich regions.

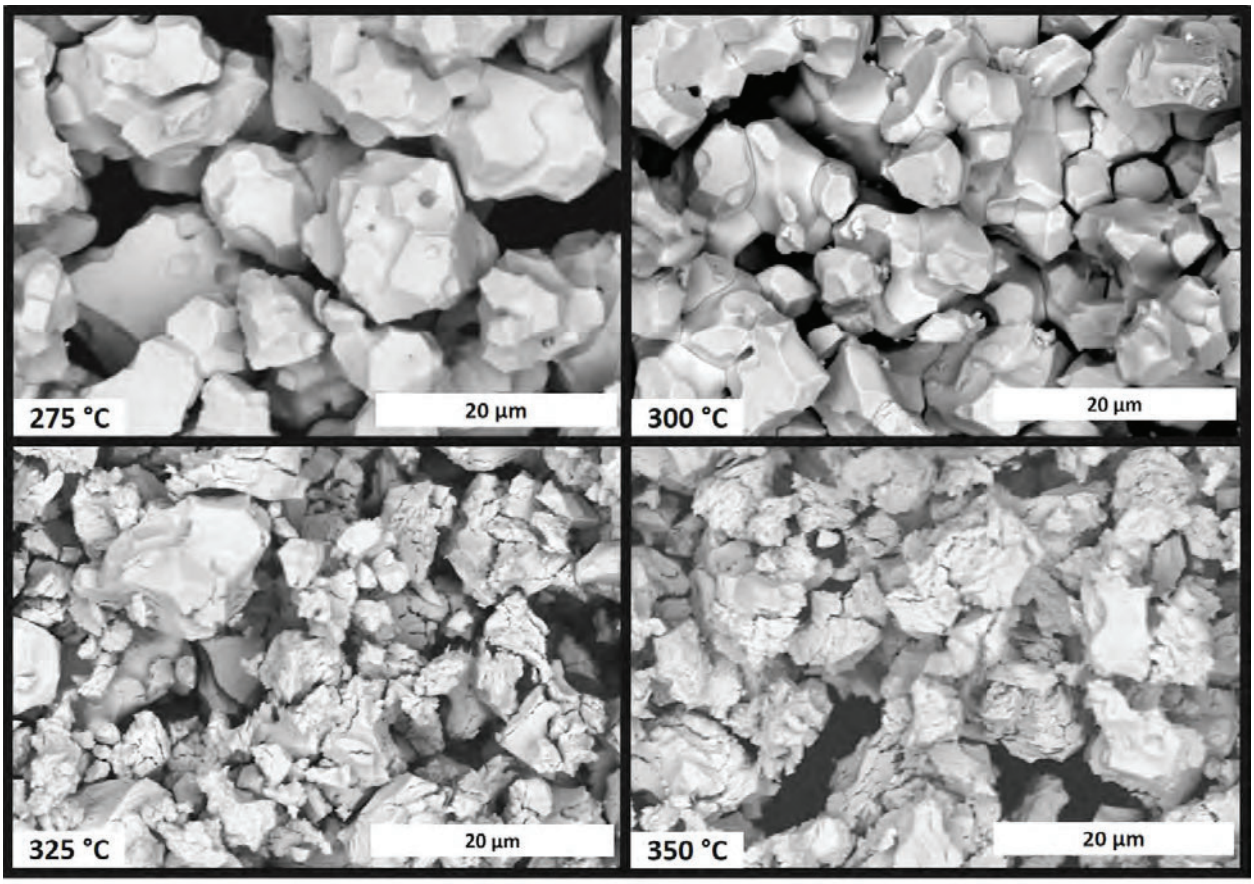

Figure 11: Backscattered electron micrographs of the recovered “sludge” from hydrothermal oxidation experiments from 275-350 °C showing large, distinct grains at 275 °C. However, as the temperature is increased, the grain size of the recovered sludge is reduced, and significant grain degradation is observed at 350 °C.

Data Availability Statement

The raw data required to reproduce these findings are available to download from Mendeley Data. The processed data required to reproduce these findings are available to download from Mendeley Data.

[1] S. Bragg-Sitton, Development of advanced accident-tolerant fuels for commercial LWRs, Nuclear News 57(3) (2014) 83.
[2] S.J. Zinkle, K.A. Terrani, J.C. Gehin, L.J. Ott, L.L. Snead, Accident tolerant fuels for LWRs: A perspective, Journal of Nuclear Materials 448(1) (2014) 374-379.
[3] F. Goldner, Development strategy for advanced LWR fuels with enhanced accident tolerance, Enhanced Accident Tolerant LWR Fuels National Metrics Workshop, Germantown, MD, 2012.
[4] D. Wachs, N. Woolstenhulme, Advanced fuel cycle technology: Special session in honor of Dr. Michael Lineberry, Transactions of the American Nuclear Society 110(INL/JOU-14-33095) (2014).
[5] N.R. Brown, A. Aronson, M. Todosow, R. Brito, K.J. McClellan, Neutronic performance of uranium nitride composite fuels in a PWR, Nuclear Engineering and Design 275 (2014) 393-407.
[6] S.L. Hayes, J.K. Thomas, K.L. Peddicord, Material property correlations for uranium mononitride: 1. physical properties, Journal of Nuclear Materials 171(2-3) (1990) 262-270.
[7] L.H. Ortega, B.J. Blamer, J.A. Evans, S.M. McDeavitt, Development of an accident-tolerant fuel composite from uranium mononitride (UN) and uranium sesquisilicide (U_3Si_2) with increased uranium loading, Journal of Nuclear Materials 471 (2016) 116-121.
[8] R.B. Matthews, Irradiation performance of nitride fuels, Los Alamos National Lab., NM (United States), 1993.
[9] H. Zimmermann, Fission gas behavior in oxide fuel elements of fast breeder reactors, Nuclear Technology 28(1) (1976) 127-133.
[10] J. Zakova, J. Wallenius, Fuel residence time in BWRs with nitride fuels, Annals of Nuclear Energy 47 (2012) 182-191.
[11] G.J. Youinou, R.S. Sen, Impact of accident-tolerant fuels and claddings on the overall fuel cycle: A preliminary systems analysis, Nuclear Technology 188(2) (2014) 123-138.
[12] J. Antill, B. Myatt, Kinetics of the oxidation of UN and U (CO) in carbon dioxide, steam and water at elevated temperatures, Corrosion Science 6(1) (1966) 17-23.
[13] R.M. Dell, V.J. Wheeler, N.J. Bridger, Hydrolysis of uranium mononitride, Transactions of the Faraday Society 63 (1967) 1286-1294.
[14] G.R. Rao, S. Mukerjee, V. Vaidya, V. Venugopal, D. Sood, Oxidation and hydrolysis kinetic studies on UN, Journal of Nuclear Materials 185(2) (1991) 231-241.
[15] M. Jolkkonen, P. Malkki, K. Johnson, J. Wallenius, Uranium nitride fuels in superheated steam, Journal of Nuclear Science and Technology 54(5) (2017) 513-519.
[16] D.A. Lopes, S. Uygur, K. Johnson, Degradation of UN and UN–U_3Si_2 pellets in steam environment, Journal of Nuclear Science and Technology 54(4) (2017) 405-413.
[17] S. Sunder, N. Miller, XPS and XRD studies of corrosion of uranium nitride by water, Journal of Alloys and Compounds 271 (1998) 568-572.
[18] S. Sugihara, S. Imoto, Hydrolysis of uranium nitrides, Journal of Nuclear Science and Technology 6(5) (1969) 237-242.
[19] J. Bugl, A.A. Bauer, Corrosion and oxidation characteristics of uranium mononitride, Battelle Memorial Institute, Columbus, OH, 1964.
[20] B.J. Jaques, J. Watkins, J.R. Croteau, G.A. Alanko, B. Tyburska-Püschel, M. Meyer, P. Xu, E.J. Lahoda, D.P. Butt, Synthesis and sintering of UN-UO_2 fuel composites, Journal of Nuclear Materials 466 (2015) 745-754.
[21] T. Muromura, H. Tagawa, Lattice parameter of uranium mononitride, Journal of Nuclear Materials 79(1) (1979) 264-266.
[22] R. Matthews, K. Chidester, C. Hoth, R. Mason, R. Petty, Fabrication and testing of uranium nitride fuel for space power reactors, Journal of Nuclear Materials 151(3) (1988) 345.
[23] ASTM, Standard Test Methods for Density of Compacted or Sintered Powder Metallurgy (PM) Products Using Archimedes' Principle, B962, ASTM International, West Conschohocken, PA, 2017.

[24] A.T. Nelson, A. Migdisov, E.S. Wood, C.J. Grote, U_3Si_2 behavior in H_2O environments: Part II, pressurized water with controlled redox chemistry, Journal of Nuclear Materials 500 (2018) 81-91.
[25] P.E. Blackburn, J. Weissbart, E.A. Gulbransen, Oxidation of Uranium Dioxide, The Journal of Physical Chemistry 62(8) (1958) 902-908.
[26] L. Desgranges, H. Palancher, M. Gamaléri, J.-S. Micha, V. Optasanu, L. Raceanu, T. Montesin, N. Creton, Influence of the U_3O_7 domain structure on cracking during the oxidation of UO_2, Journal of Nuclear Materials 402(2-3) (2010) 167-172.
[27] H. Matzke, Science of advanced LMFBR fuels, (1986).
[28] K. Une, S. Kashibe, K. Nogita, Corrosion behavior of unirradiated oxide fuel pellets in high temperature water, Journal of Nuclear Materials 227(1) (1995) 32-39.
[29] P. Taylor, D.D. Wood, D.G. Owen, Microstructures of corrosion films on UO_2 fuel oxidized in air-steam mixtures at 225°C, Journal of Nuclear Materials 223(3) (1995) 316-320.
[30] X. Wang, Z. Long, H. Huang, R. Bin, Y. Hu, L. Luo, K.-Z. Liu, P.-C. Zhang, Insight on the oxidation resistance of UO_xN_y layers: A density functional study, Computational Materials Science 123 (2016) 224-231.
[31] M. DeCrescente, M. Freed, S. Caplow, Uranium nitride fuel development, SNAP-50, Pratt and Whitney Aircraft, Middletown, Conn.(USA). Connecticut Advanced Nuclear Engineering Lab., 1965.
[32] Y. Arai, M. Morihira, T. Ohmichi, The effect of oxygen impurity on the characteristics of uranium and uranium-plutonium mixed nitride fuels, Journal of Nuclear Materials 202(1-2) (1993) 70-78.
[33] G. Jain, C. Ganguly, Experimental evaluation of oxygen solubility in UN, PuN and (U, Pu) N, Journal of Nuclear Materials 202(3) (1993) 245-251.
[34] N.A. Javed, Oxygen solubility in uranium mononitride phase, Journal of the Less Common Metals 29(2) (1972) 155-159.

Scale up of CTRN UN Production

Nuclear Technology Research and Development

Prepared for
Westinghouse Electric Company
Joshua White, Timothy Coons, John Dunwoody, Darrin Byler
Los Alamos National Laboratory
May 28, 2020

SUMMARY

This report details the carbothermic reduction and nitridation (CTRN) of uranium dioxide to form uranium mononitride along with sintering studies to fabricate dense pellets. The first part of this report will summarize different methods that have been employed at LANL or in the literature to fabricate phase pure and chemically pure UN. The following section details the CTRN method along with process optimizations to date that have been evaluated at LANL. Furnace schedules and a detailed explanation of the various steps involved throughout the entirety of the CTRN process are provided along with discussions on 15N incorporation and process recovery/recycling. Sintering of UN is evaluated in the following section, which details the literature knowledge on sintering parameters compared to LANL experimental efforts to sinter dense (>94% of the theoretical density) pellets. Efforts towards decreasing the required sintering temperatures to be more amenable to commercial process lines is included along with initial efforts understanding the role of impurities on sintering. Considerations are taken to identify commercial scale up issues and evaluating, when possible, the ability to utilize existing infrastructure. Finally, this document is expected to evolve as discussions between LANL and Westinghouse are included, with subsequent sections to be added at a later date discussing impacts to reactor application, LANL scale-up, LTA/LTR scale, and pilot plant levels of fabrication.

CONTENTS

FIGURES

TABLES

SCALE UP OF CTRN UN PRODUCTION

1. INTRODUCTION

Uranium mononitride exhibits a number of characteristics that are favorable for use in reactors owing to the high uranium density, good thermal conductivity, good chemical stability, high decomposition temperature, and chemical compatibility with fission products. Because of these attributes, it is being considered as a drop in replacement for use in light water reactors, lead fast reactors, and microreactors applications. There are many outstanding challenges for the use of UN in commercial reactors, one of which is the commercial scale up and production of full sized pellets.

Carbothermic reduction and nitridation (CTRN) has been shown to be a viable fabrication technique to produce high purity UN powder feedstocks, albeit at R&D scales. This process uses UO_2 and graphite as the source materials which reduces the UO_2 through a number of high temperature processes to yield high purity UN. The process at the R&D scale is typically done within inert glove box lines to minimize exposure of the UN powder (or intermediary steps) to prevent decomposition back to the oxide phase, which is likely to add cost and cycle time to the fabrication process. Considerations are therefore evaluated to utilize existing furnace lines as well as impacts to deviations in CTRN process development implemented at LANL. Methods to efficiently utilize enriched $^{15}N_2(g)$ are considered, but have not been demonstrated at the laboratory scale to date.

After UN powder is produced, pelletization and sintering are required. The process to fabricate UN pellets follows a similar metallurgical route as UO_2; however, experiments have shown decreased sinterability of oxygen exposed UN powder, which will be an issue in air handled oxide production lines. Similarly, the susceptibility of milled UN powder to rapid oxidation when exposed to air will require different handling methodologies compared to standard oxide pellet lines. Rates of oxidation in glove box lines are considered in this document as well as potential routes to mitigate detrimental oxidation of the UN powder. Sintering kinetics and furnace schedules for high density (~95%) UN are presented, with considerations for adapting the current oxide processing lines as well as the high temperature furnace schedules that are utilized at LANL through optimization of furnace temperatures and atmospheres.

This document is considered to be a ‘living document’ that will be added to and edited to provide the most recent information related to UN scale up.

2. Uranium Nitride Fabrication Routes

Uranium nitride synthesis routes demonstrated in the literature include CTRN of the uranium oxide [1], direct nitriding of the metal [2], [3], and ammonolysis of uranium tetrafluoride [4], [5]. A summary of the different processing routes is shown in Table 1 along with a brief overview of each method in the following subsections. However, the remainder of this document will focus on CTRN. Follow-on reports will conclude on-going efforts with the fluoride to nitride chemical processing route.

Table 1: Summary of UN production methods

	CTRN	Hydride	Ammonolysis
U Precursor	UO_2	U metal/hydride	UF_4 or UF_6
Possible contaminants	C, O	H	F
Major drawbacks	C & O contamination, processing time	Proliferation, pyrophoricity	HF byproduct during fabrication

2.1 Carbothermic Reduction and Nitridation

In the carbothermic reduction route, UO_2 is mixed with graphite powder and heated to reduce the oxide and form UC. The UC is then heated under a H_2-N_2 atmosphere to convert the UC to UN [6]. A schematic of this process is shown in Figure 1, which will be discussed in greater detail below.

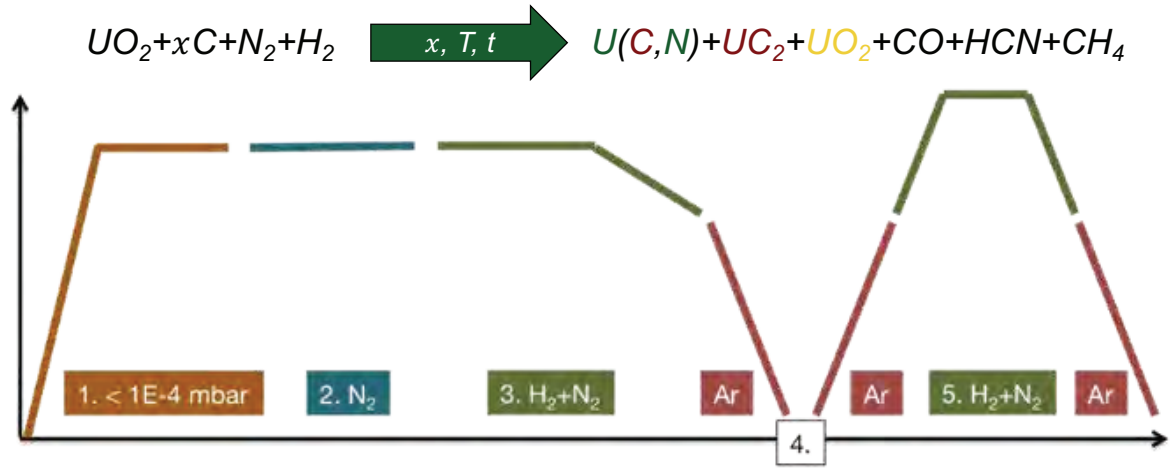

Figure 1: Schematic diagram of CTRN process to produce UN from UO_2 and graphite.

2.2 Uranium Metal Direct Nitridation

In the hydriding and nitriding route, high purity uranium metal is hydrided. The subsequent uranium hydride is then decomposed and nitrided in a purified nitrogen atmosphere. The resulting U_2N_3 is then decomposed to UN at high temperatures [2]. Much of the hydriding/dehydriding processes are conducted at lower temperatures (200-400°C) where UH_3 formation is favorable followed by off-gassing of H_2(g) above ~450°C and subsequent nitriding steps at elevated temperatures. An example of this process in its entirety is reported by Jaques et al. in [3]. Noteworthy is that both the UH_3 and U metal powders formed

through this process are extremely oxygen sensitive and pyrophoric at room temperature given the small particle sizes achieved using this processing route. This can however be beneficial from a sintering perspective as the small particle sizes have yielded higher densities at lower sintering temperatures [7], which will be discussed in Section 4. Finally, it should be considered that the starting material is metallic U, which raises concerns over proliferation control and will also require a route to produce metallic feedstocks from fluoride gas or reduction of the oxide powder to a metallic state.

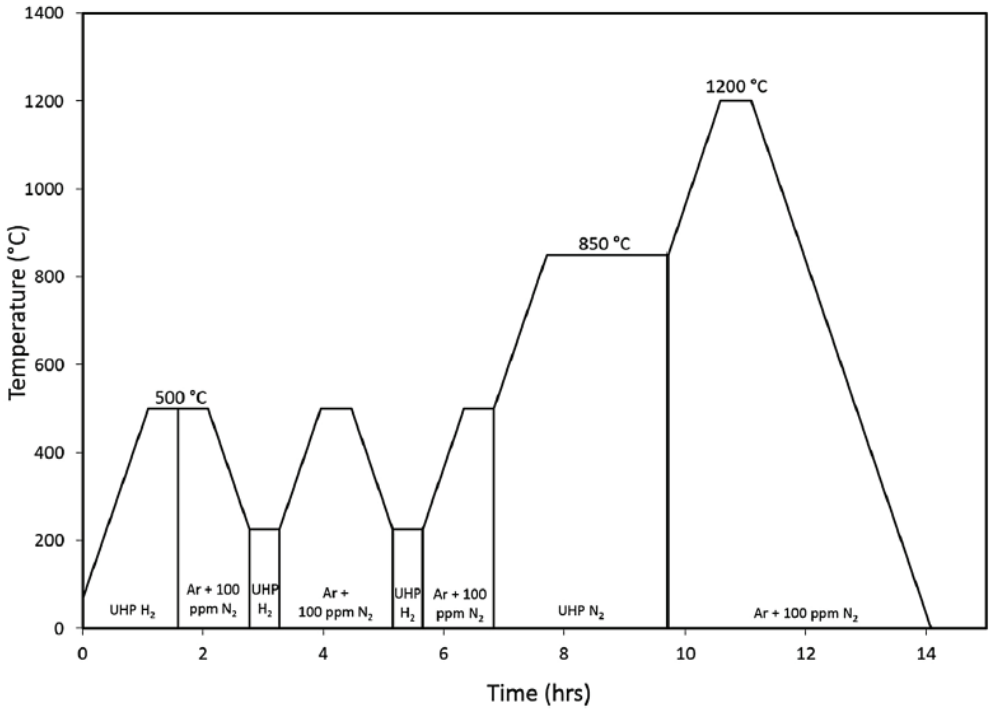

Figure 2: Hydride-dehydride to direct nitridation of U metal profile from [3].

2.3 Ammonolysis of Uranium Fluoride

A synthetic route using uranium fluorides and ammonia gas was published by Funk and Bohland, with UF_4 reacting with NH_3 at higher temperatures to form higher uranium nitrides [4]. This route was also used by Berthold and Hein who proposed the intermediate phases of U(NH)F and $U(NH_2)F_2$ [8]. Yoshihara et al. explored the reaction of UF_4 with Si and N_2 to obtain the sesquinitride (U_2N_3) [9]. More recently, Yeamans et al. published an exploration of the oxidative ammonolysis of uranium fluorides [5], [10]. The reaction of tetravalent ammonium uranium fluorides in an ammonia atmosphere at 800 °C was used to produce hexavalent UN_2, which was subsequently decomposed to UN. The reactions in Yeamans' work were performed in quartz tubes, which are vulnerable to attack by the corrosive fluorine species produced during the reaction. This could lead to a source of oxygen and thus UO_2 in the final product.

Starting with UF_4 and heating under ammonia gas, a process known as oxidative ammonolysis, UN_2 can be produced at lower processing temperatures in industry at the front end of fuel fabrication lines. This could also by pass the oxidation of UF_6 and subsequent costly CTRN steps that are currently proposed for UN fabrication at the commercial scale. UN_2 can be readily decomposed to UN at elevated temperatures (1400 °C). Demonstrations of this have been shown at LANL [11], although consistency between batches is still on-going and improving the thermodynamic and kinetic understanding of the reaction is still required.

3. LANL Carbothermic Reduction and Nitridation

Significant work has been completed to understand the impact of as-synthesized UN material quality as a function of cycle time. The CTRN process consists of two steps. In the first step, carbon and uranium oxide react to form an intermediate carbide phase. In the second step, the intermediate carbide phase reacts with nitrogen to complete the conversion to uranium nitride. A cleaning process is used to remove excess carbon and oxygen from the system. In the cleaning process, hydrogen is diffused into the material and reacts with the excess carbon from the CTRN process.

For the initial step of the CTRN process, in which the uranium oxide reacts with carbon, the two solids require intimate contact for the reaction to take place. Because of the limited carbon sources, the primary mechanism uses a solid-state reaction rather than a gas phase reaction. This limitation also dictates batch processing rather than continuous processing for the CTRN process. The cleanup process lends itself to a continuous or semi-continuous process because the mechanism involves a gas phase reaction between hydrogen and carbon. This section will detail the current CTRN process and the limitations identified with scale up will be reserved for Section 5.

3.1 Uranium Nitride Processing

The start of CTRN begins by mixing UO_2 and graphite using a high energy SPEX mill. The current process adds an excess of C to efficienctly remove the O atoms, but requires cleanup steps to remove unreacted C. Once the material is sufficiently milled and distributed, a disc is pressed to compact the mixture. A pressure of 50 MPa is typically used to form the disc. The disc is placed in a molybdenum crucible with molybdenum foil underneath to prevent any reactions between the disc and the crucible. This assembly is placed in a high temperature vacuum furnace and heated using the thermal cycle in Figure 3. The thermal cycle has several segments to complete the CTRN process in one continuous furnace run and eliminate unnecessary thermal cycling and associated delays. The first portion of the CTRN cycle is the carbo-thermic reduction (CTR) process to covert UO_2 to UC where the vacuum assists in the removal of gaseous reactant products (e.g. $CO_x(g)$). In the CTR segment, the parts are held isothermally under vacuum for 6 hours to facilitate the conversion. Introduction of $N_2(g)/H_2(g)$ facilitates reaction of the carbide to form the nitride phase. This reaction is diffusion limited and dominates the remaining cycle time. The nitridation process employs several techniques to promote the diffusion of nitrogen into the compact. These mechanisms include: over pressure of flowing nitrogen, breathing techniques (evacuate and backfill), and chemical milling. Chemical milling implies the nitride is traversing the UN and U_2N_3 phase boundary by adjusting the temperature in the furnace. This phase transformation entails a large volume expansion, thus breaking apart the compact *in situ* and promoting the exposure of non-nitrided material and excess carbon embedded at grain boundaries to help clean the as-fabricated material. During the final cool down, argon is used to maintain the mononitride phase, and suppress the formation of the U_2N_3 phase. The current cycle time for the CTRN process is around 48 hrs.

Once the CTRN cycle is complete, the compact is removed from the furnace. At this stage, uranium nitride is formed, but a significant amount of impurities is dispersed throughout the compact. Typical impurity levels post CTRN range from 10,000 - 40,000 ppm of carbon and <500 ppm of oxygen. In order to reduce the carbon and further remove oxygen impurities, a cleanup process is employed. The compact is crushed and sieved to increase the exposed surface area for the next thermal cycle, which is detailed in Figure 4. The breathing technique (evacuation and backfill) is used in the cleanup process to promote the diffusion of hydrogen in the powder bed. Current cycle times for the cleanup process range between 36-48 hrs to reach desired impurity levels. Typical post-processing includes sieving to achieve a desired particle size.

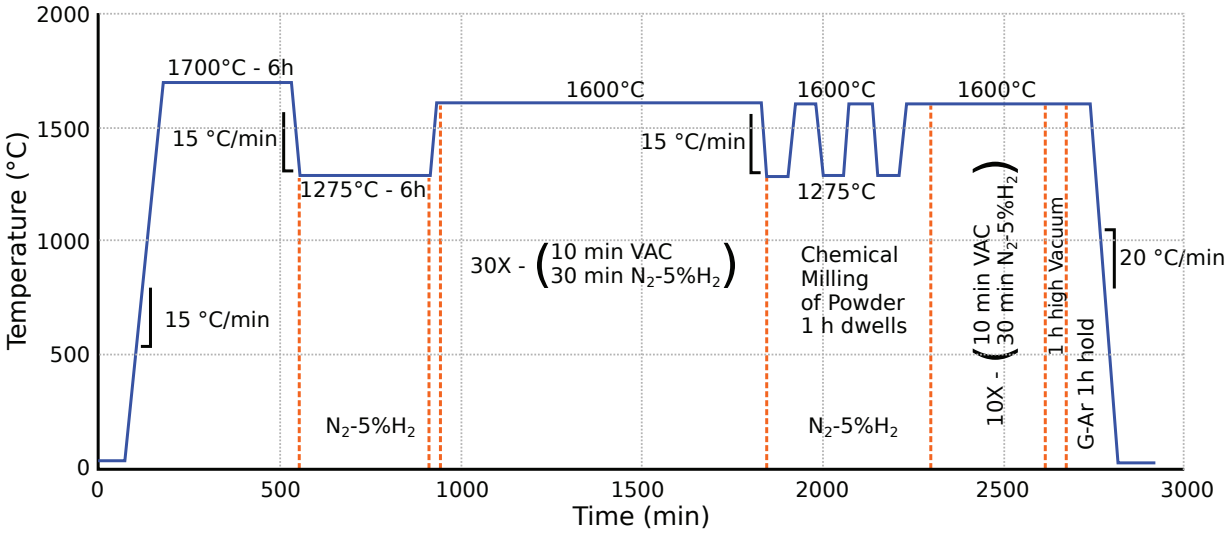

Figure 3: Currently optimized thermal cycle used for the CTRN process.

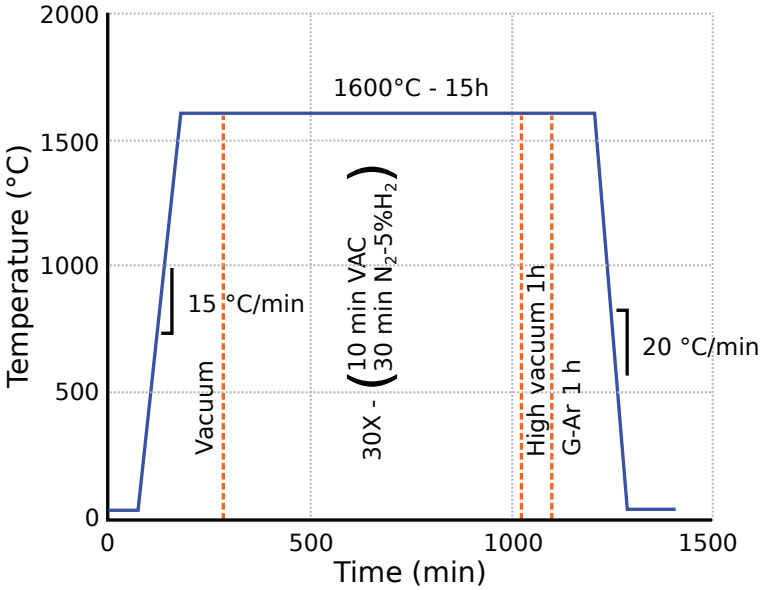

Figure 4: Cleanup cycle to decrease carbon levels in UN.

3.2 Characterization

Current characterization techniques used to evaluate the as-fabricated material at LANL are x-ray powder diffraction (XRD), combustion infrared detection, and inert gas fusion. XRD provides information about the phases of the as-fabricated UN while combustion infrared detection and inert gas fusion quantify the C and O levels, respectively. Diffraction methods provide a phase fraction accuracy of ~2% while the analytical methods can detect impurities to ~100 wppm.

3.3 Process optimization and limitations

Current overall cycle time from UO_2 feedstock to final product is about 1-2 weeks. Several experiments have been performed to reduce cycle time while maintaining product quality. The process variables that have been investigated include elimination of the initial reduction of the UO_2 feedstock, reducing thermal

cycle times and temperatures, and reducing the initial concentration of carbon. Process changes resulting from these investigations have reduced the overall cycle time from 3-4 weeks to 1-2 weeks. There is opportunity to further reduce the overall cycle time by optimizing the thermal cycle, load size, C loading, cleanup cycles, as well as by evaluating next generation equipment (e.g. fluidized beds), etc. These optimization parameters are on-going research topics with a goal to decrease overall required times and temperatures while maintaining the purity of the produced nitrides.

Changes implemented to reduce the cycle time have resulted in an increase in product variation. One observation is related to the elimination of the UO_2 feedstock reduction step. The reduction step would treat the incoming feedstock by heating the material to convert the feedstock from UO_{2+x} to $UO_{2.00}$ and also remove any surface adsorbed water from storage of the material. A potential improvement to make the CTRN process more consistent is to incorporate a low temperature hold to remove any impurities in the starting UO_2 feedstock and set the stoichiometry of the powder. The continued focus of this effort will be creating a robust cycle and reducing the overall cycle time while maintaining quality.

3.4 Reprocessing UN

As the process increases in scale, the potential for defects increases as a result of under optimized process variables or process interruptions. Similarly, there are multiple processing steps along the way where it would be desirable to recover material (e.g. grinding). The potential to rework this material needs to be investigated and evaluated for economic viability. Potential defects from the process include having nonconforming residual carbon or intermediate phases. The defective materials are amenable to rework because of the ability to convert the material back into an oxide state using a calcining furnace with an oxidizing atmosphere. The calcining process is depicted in a flow chart in Figure 5. Converting the material back into an oxide allows the material to reenter the conversion process as recycled feedstock. Using the current fabrication process as a baseline, this method encompasses a significant amount of potential process defects to be reworked. However, this rework process is not the only method that can be employed to recover defective material and these additional methods should be evaluated to determine the impact in a production setting.

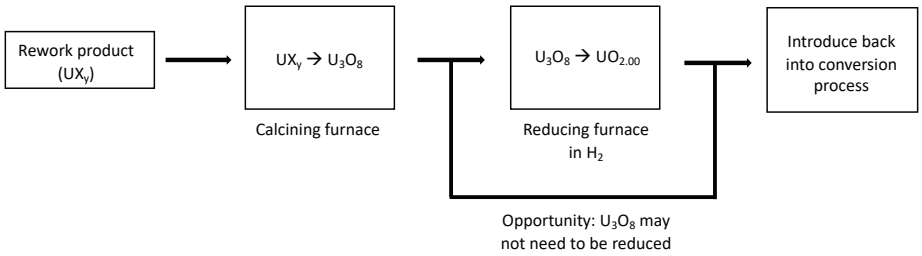

Figure 5: Recycle process to take defective process loss material and reconvert into an oxide feedstock for further processing.

3.5 Enriched ^{15}N processing and utilization

The discussion of nitrides as a fuel form eventually returns to the discussion of substituting ^{15}N for naturally occurring ^{14}N. In the absence of this substitution, the high neutron capture cross-section of ^{14}N results in $^{14}N(n,p)^{14}C$ reactions, greatly impacting neutron economics and generating a long-lived, highly radiotoxic isotope [12]. However, enrichment and purchase of ^{15}N will have an economic impact on any facility considering this substitution. An academic exercise conducted in 2017 looking at current fabrication process gas use and commercially available ^{15}N yielded an estimated cost of approximately

$16.26K/g UN produced for the $^{15}N_2$ gas consumed. Process refinement coupled with increased product yield have dropped the cost, based on 2017 prices, to roughly $1.54K/g UN.

The above estimates were based on standard and revised base CTRN fabrication routes using a flow through gas production method. Reducing the price per gram of ^{15}N enriched UN is suspected to trend with commercial interest and subsequent industrial scale up of enriched $N_2(g)$ processing plants as will process refinement to the CTRN process including efficient use and recycling of the enriched $N_2(g)$. Both of these scenarios have significant developmental hurdles, but could be part of a concerted effort to increase the purity for a scaled-up fabrication effort.

The current CTRN process relies on an atmosphere exchange principal that discards unused $^{15}N_2(g)$ along with gaseous by-products from the conversion process detailed above. Opportunities exist in 1) fine tuning the duration and number of vacuum/gas cycles, 2) capturing and scrubbing the active vacuum exhaust, and 3) recirculating or recapturing the overpressure exhaust, each of which will have broader impacts to a CTRN processing line. Fine tuning the cycle parameters would reduce overall consumption, however, it is anticipated that recovering and recycling would have the greatest impact. Recovering or recycling the overpressure exhaust would most likely be the easiest to accomplish, requiring only a pressure vessel, a pump, and an assortment of control valves. Additionally, studies could be conducted on the chemical milling stage to determine if natural nitrogen could still be used at this stage. However, this would require experimental determination of $^{14}N/^{15}N$ substitution during the U_2N_3 to UN temperature cycling. Recovering and scrubbing vacuum exhaust would be mechanically feasible, however, extensive development on the scrubbing technique(s) would be required. Any scrubbing process would have to preferentially capture or convert nitrogen gas over the other gaseous conversion byproducts, which would require extensive characterization. Conversely, these byproducts could conceivably be scrubbed in media that renders them as solid or liquid while letting the nitrogen pass through as a gas.

The second scenario would require considerable research and development efforts. Our current focus is on the CTRN fabrication route. However, several alternative fabrication routes have been investigated and reported in [12], [13]. Without going into detail over a preferred alternative route, it should be noted that the above referenced economic calculations were based on commercially available $^{15}N_2$ gas. Other ^{15}N containing substrates may be both more economical to procure and easier to recover in alternative processing routes. Regardless, it appears that for nitrides to be seriously considered as a nuclear fuel form from an economic viewpoint, among other considerations, ^{15}N enrichment still requires development of an economical technology.

4. Sintering and Pelleting of UN

A number of studies have evaluated the sinterability of UN powders. In general, there are many factors that contribute to the sintering behavior of a given material which includes: particle size of the feedstock, surface impurities, dwell temperature and time, sintering atmosphere, heating and cooling rate, pressing pressure, binders, among others. The contribution of these factors has been investigated by a number of authors in the literature as well as a concerted effort under the current FOA. The results of this are presented below with commentary on the ability to scale these processes to commercial fabrication lines reserved to the following section.

4.1 Literature summary

A number of authors have investigated the sintering of uranium nitride to understand the impact that process variables have on achieving specific densities and grain sizes to support the specific nuclear application.

Tennery et al. demonstrated the effect of sintering temperature and atmosphere, which is shown in Figure 6 [14]. The results showed that nitrided U metal powders sintered to a maximum temperature of 2100 °C using N_2 and Ar atmospheres had densities greater than 92%. The introduction of Ar (or vacuum) improves the sintering of UN, which is proposed to arise from the introduction of defects within the UN fluorite crystal structure that subsequently improve the diffusivity of the cations leading to improved densification [14]. However, the authors also noted the appearance of U-metal in the A' specimen (see Figure 6(a)) suggesting the onset of UN decomposition under non-nitrogen bearing environments between the temperature range of 2000°C and 2100°C. It is noted that the oxygen levels of the pellets in Tennery's study were <800 ppm which they proposed to be below the solubility limit of O in UN. Grain sizes ranged from 6-10 µm for the low-density specimens to a maximum of 20-40 µm for the highest density samples. Similar results to Tennery et al. have also been observed for powders produced using CTRN of UO_2 by Matthews et al. [1]. It is noted that the densities that were achieved for similar sintering temperatures were improved by 1-2% by increasing the milling energy considerably with a vibratory ball mill and extending the dwell time to 24 h compared to the 2 h holds employed by Tennery et al. However, the longer sintering time also greatly increased the grain sizes to >45 µm.

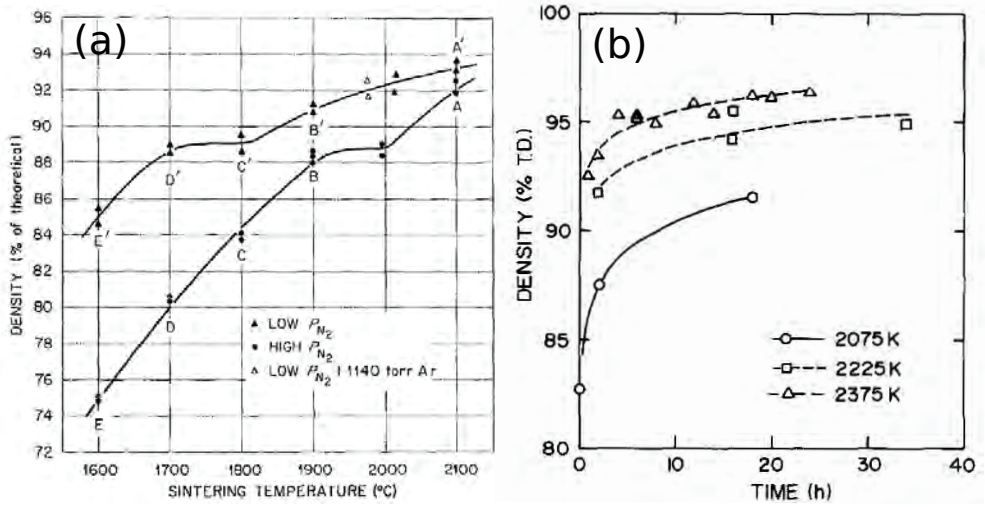

Figure 6: Results from Tennery et al. where UN is sintered as a function of temperature while varying the atmosphere [14] in (a) along with results from Matthews et al. where the isothermal holds were varied [1].

Metrorka et al. investigated the sintering behavior of UN derived from a hydride-dehydride route at temperatures ranging from 1700°C to 2500°C using standard isostatic pressing and sintering [15]. Under these conditions, the UN pellets achieved densities as high as 98% while holding for 6 h at 2500°C. However, it is noted that the grain sizes were also significantly larger, shown in Figure 7, where grains as large as 90 µm were observed. On the other hand, McLaren et al. implemented lower sintering temperatures, in the range of 1700°C, by using longer milling times and a hydride-dehydride UN which decreased the particle size to 0.5 µm to 1 µm and achieved densities as high as 94% of the theoretical density [7]. However, a maximum in the achievable density with milling time was observed in McClaren's work, likely being limited by impurity introduction from the milling media or from over-milling the powders, which decreases flowability leading to decreased green compaction [6]. It is also noted that there was some variability between powder lots in the McLaren et al. study, which is suspected to have arisen from O impurities in these small particle size distributions ultimately affecting the sinterability of the UN powders. However, these impurities were not discussed in the manuscript. The effect of pressing pressure on densification of UN has been studied by two authors [7], [15]. Although improvements to the green density were observed, as expected, there were only minor improvements to the final sintered density on the order of 1-2% increases with increased pressing pressure.

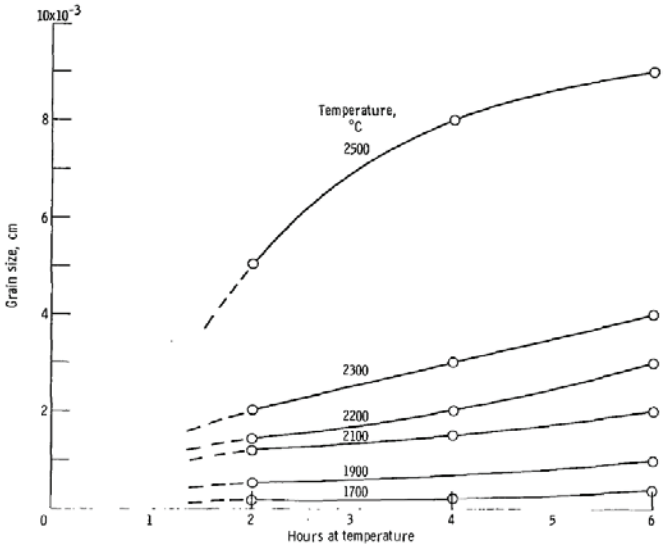

Figure 7: Grain size dependence of UN pellets sintered as a function of temperature and time from Metroka [15].

4.2 Sintering studies at LANL

Sintering studies on UN have primarily focused on the impact of sintering temperature and atmosphere during the various stages of the sintering schedule. The sintering temperature was varied from 1650°C to a maximum temperature of 2200°C. Temperatures above 1900°C were utilized in a N_2/H_2 atmosphere to minimize decomposition of UN, although on-going studies into the thermodynamics of U(l)-UN_{1-x} are ongoing to evaluate defect control in this elevated temperature range. Sintering studies were also conducted using N_2/H_2, Ar, Ar/H_2, and vacuum as the sintering atmospheres while keeping the dwell temperature constant at 1800 °C. Pressing pressures were also varied from 100 MPa to 300 MPa. Ethylene bis-stearamide was used as a binder at 0.25wt% for all pellets. Similarly, the powders were all milled with a high energy ball mill.

A summary of the results from sintering studies where the temperature was varied is shown in Figure 8, which is also compared against the relevant literature values described above. As is expected, the density of the UN pellets increases with increasing temperature and is generally in good agreement with the literature results of [1], [14], [15]. Some general trends are observed: 1) at low temperature without nitrogen, densities are on the order of 88-90% and 2) going to higher temperatures under a N_2(g) environment yielded pellets ~95%, which is consistent with Matroka's sintering studies [15].

It is noted that 2200°C is well above the normal operating temperatures utilized in commercial nuclear fuel productions. To this end, a number of 1800°C sintering runs were evaluated to decrease the maximum required sintering temperature. From this iterative process, a low temperature sintering route that employed a vacuum step at 1800°C, shown in Figure 9 (b), was able to yield UN pellets around 93.5%. It is unclear if some amount of the UN decomposes during the vacuum furnace schedule. However, this is compensated for by the addition of a N_2(g) purge towards the end of the profile to reset the stoichiometry of the UN. Furthermore, cooling to room temperature requires the furnace to be purged with Ar to prevent the destructive formation of U_2N_3, which occurs around 1400°C. Sintering studies were also conducted at 1900°C using a similar profile shown in Figure 9 (b), where the maximum dwell under vacuum was increased. Samples in this study decomposed/reacted with the W foil. As such, it is not recommended to sinter above 1800°C in a vacuum or inert atmosphere to avoid detrimental decompositions of UN.

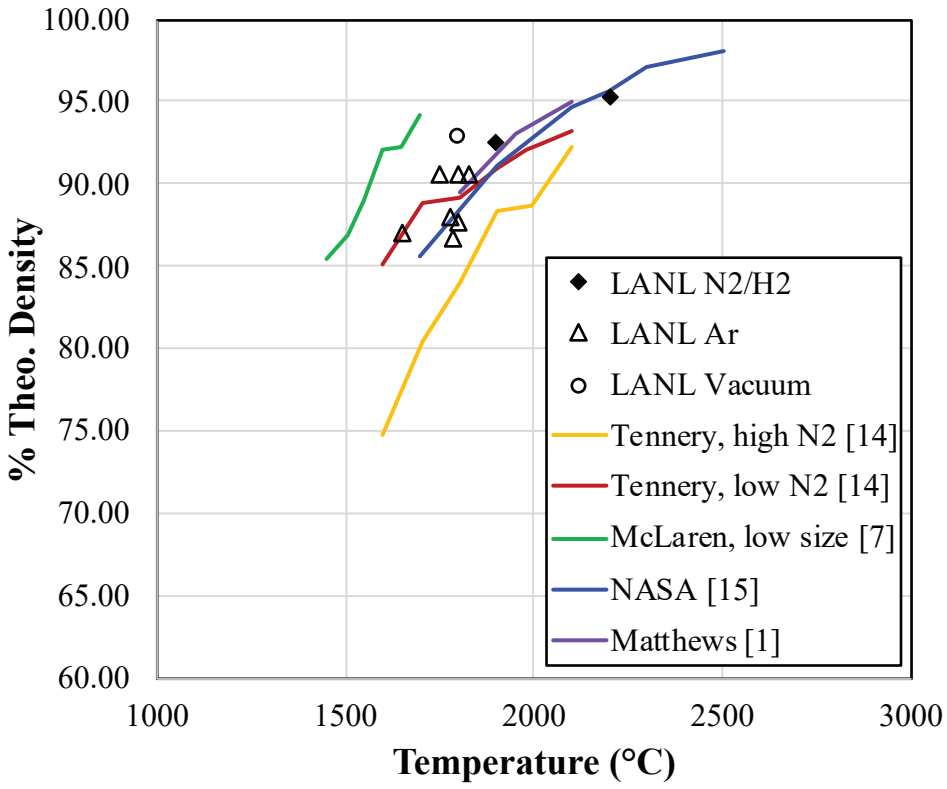

Figure 8: Results of the sintering studies at LANL compared to literature results from [1], [7], [14], [15].

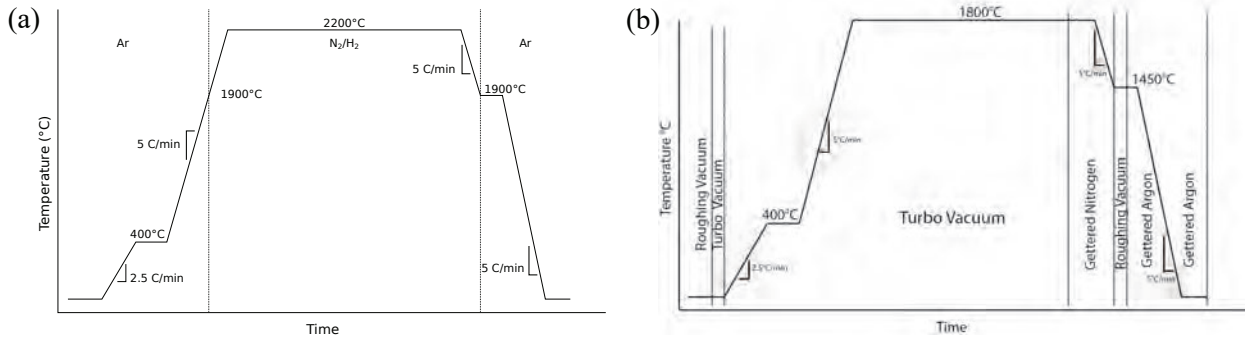

Figure 9: Furnace profiles that were successful in achieving >93% dense UN pellets.

It is noted that the results to date do not compare well with McLaren's data [7], who was able to densify UN pellets to 93-94% at temperatures <1700°C. This is expected given that McLaren utilized UN with particle sizes on the order of 0.5 µm, while the UN powder in this study was milled and sieved to <45 µm. An image of the particle sizes in the UN feedstock is given in Figure 10, which shows particles generally greater than 1 µm. Therefore, it is not surprising that the results in the present study would not agree well with McLaren's data.

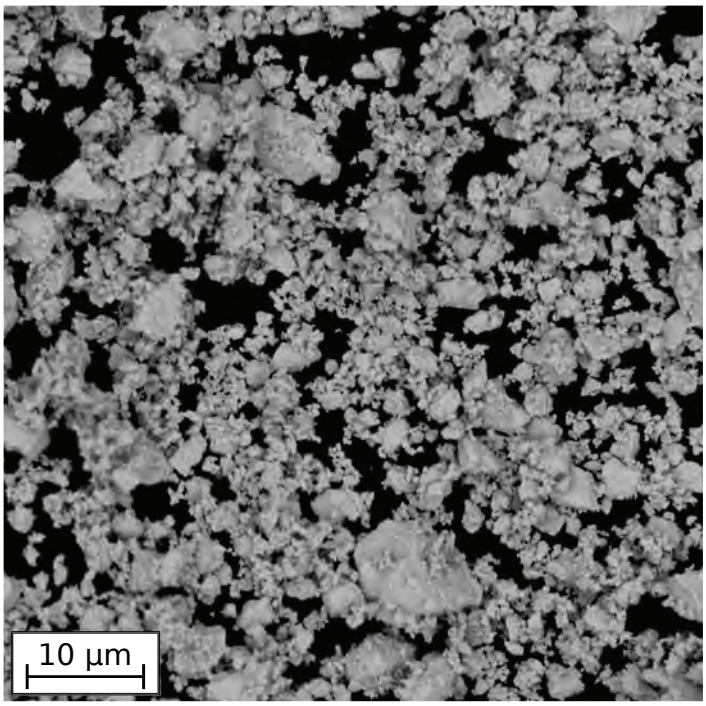

Figure 10: Particle morphology after milling and sieving to -325.

The effect of pellet pressing pressure is shown in Figure 11. Although not shown in the Figure, multiple runs were preformed yielding pressures between 100 and 300 MPa. Prior to sintering, the green densities varied between 69-71% of the theoretical density of UN from lowest pressure to highest pressure, respectively. However, these differences were largely negligible after sintering where the final densities converge within 0.5% for a given sintering profile.

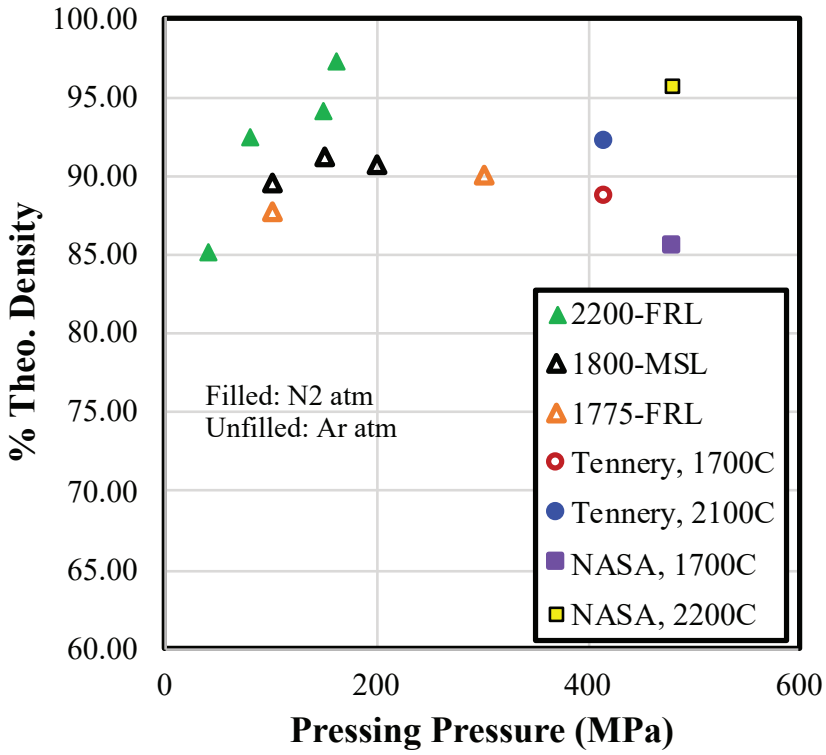

Figure 11: Pellets densities that were pressed at different pressures and compared to literature values from [14].

4.3 Grain size of sintered UN pellets

To date, only a handful of pellets have been cross-sectioned for microstructural investigations. Some representative microstructures for two temperatures that yielded reasonable densities are shown in Figure 12 (a-b). The microstructure of a UN pellet that has been sintered at 1800°C for 96 h in Ar is shown in Figure 12 (a), which has a grain size of around 20 µm. Black regions are expected to be porosity, which when quantified confirm the anticipated density of ~94%. Grain sizes for the 2200°C specimens sintered in 4%N_2/H_2 for 8 h produce grain sizes in the range of 18 µm. The porosity of the 2200°C sintered sample is difficult to quantify as there is more grain pullout as a result of the polishing procedure. Microstructures for the vacuum sintered sample at 1800°C have not been analyzed yet, but this is planned at a future date.

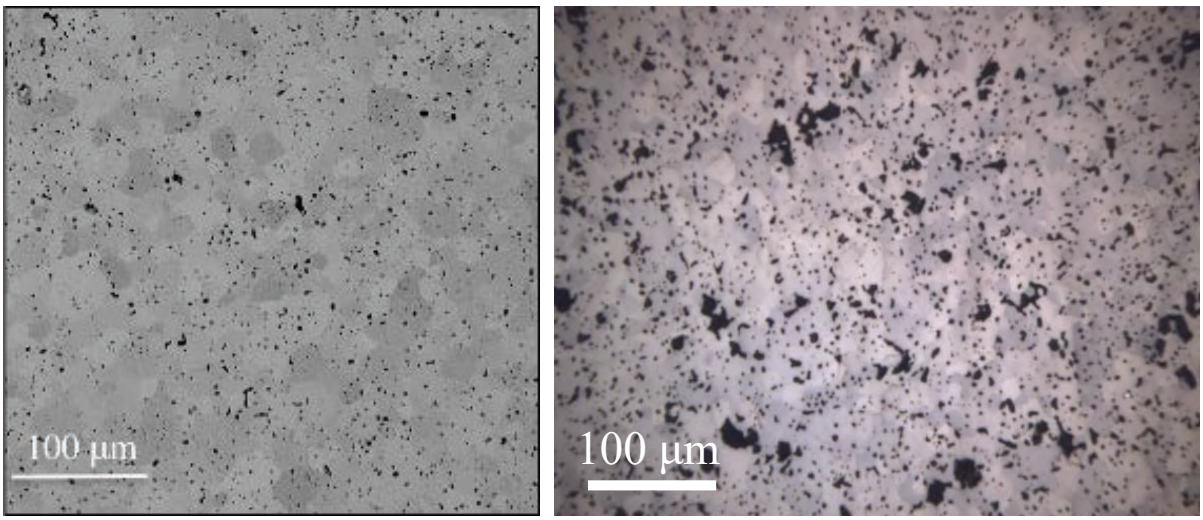

Figure 12: Microstructures of UN pellets sintered at 1800°C for 96 h in Ar (a) and 2200°C for 8 h in N_2/H_2.

4.4 Ageing of UN powder

Milled UN powders that are typical of powders prepared for sintering were exposed to an inert (<30 ppm O_2) Ar atmosphere. Phase determination of the powders as a function of time in the glove box was achieved with XRD, which is shown in Figure 13. Peaks representing crystalline UO_2 are shown to increase in intensity as a function of time. Both the UN and UO_2 peaks are broader than the instrumental peak width resolution. UN peak broadening is suspected to result from the milling procedure that causes residual stress (dislocations) on the crystalline lattice. UO_2 on the other hand doesn't likely have residual stresses, but are likely nanocrystalline in size given they were formed at room temperature; however, additional studies would be required to confirm.

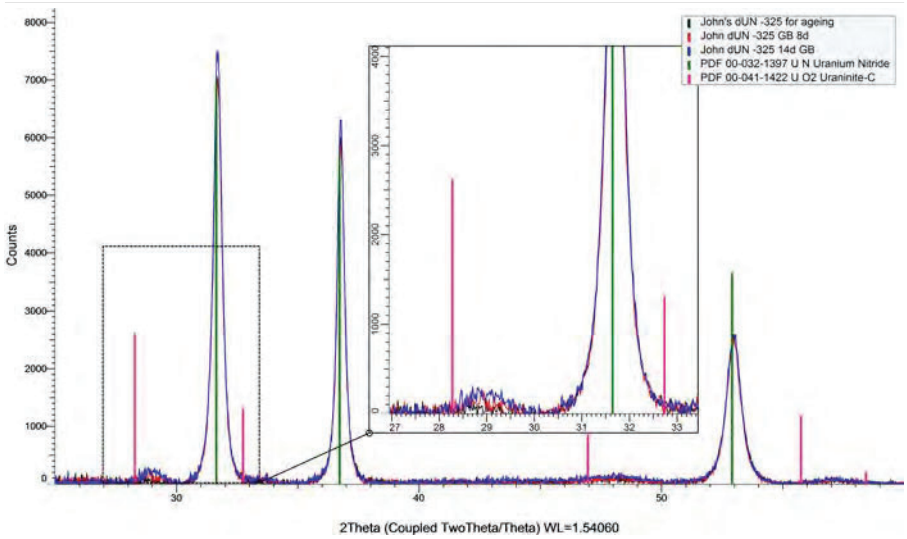

Figure 13: XRD pattern of UN powder that was milled and sieved and oxidized in a <30ppm O glove box line.

Quantification of the O content in the glove box exposed UN powders was achieved using the inert gas fusion technique (LECO836 OHN), see Figure 14. Similar to the XRD results shown above, the oxygen content increases with exposure time in the glove box. It is noted that after ~3 weeks, the oxygen content is around 6000 wppm O, or 6.5 vol% UO_2. This is well above the anticipated solubility of O within UN of ~2000 ppm [14]. The oxygen content has also not stabilized at a constant value after 3 weeks, but will likely stabilize after 1-2 weeks if a parabolic law if fit to the data. On-going studies is evaluating the ageing potential in a glove box environment as a function of UN particle size as well as particle size stability in ambient air.

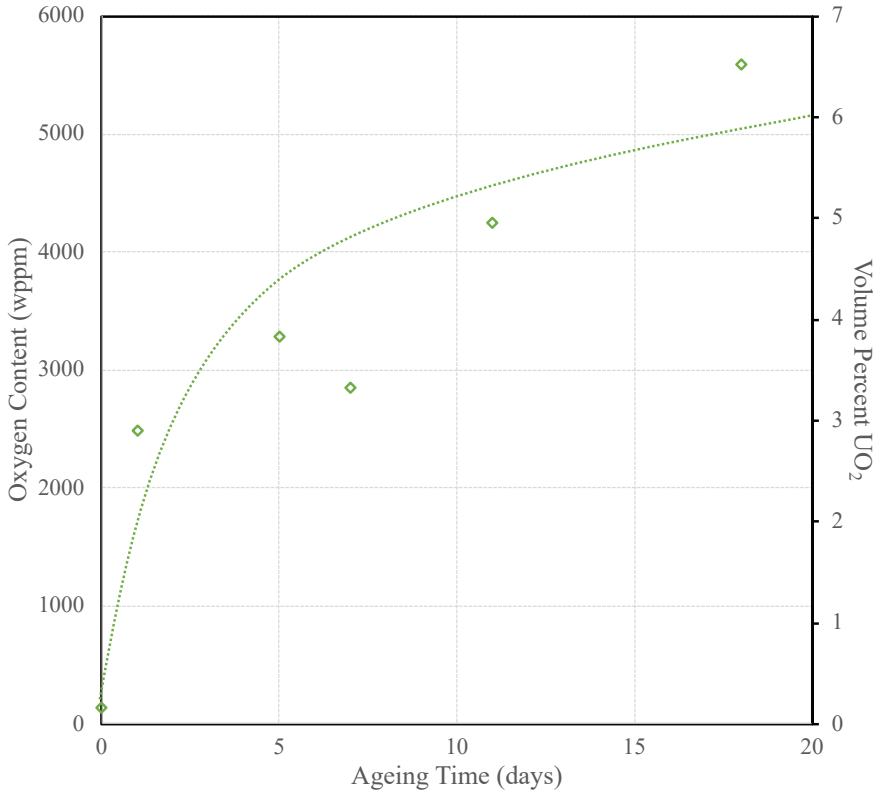

Figure 14: Oxygen content in the UN powder for sintering that was aged in a <30ppm O glove box environment for ~20 days.

4.5 Impacts to sintering from impurities

The two primary impurities left over from the CTRN process are C and O. These impurities result either from incomplete reactions during the CTRN conversion or from oxidation during handling of the powders in between furnace cycles (e.g. during the processing steps for cleanup). Similarly, UN powder that is left in an oxygen containing environment will oxidize on the surface introducing O, which is highly dependent on the surface area/particle size distribution and morphology of the UN powder. Glove box line purity effects on UN sintering is still an on-going study, but present results suggest that as-processed powders yield the highest densities, presented above. Powders that have been allowed to rest in a high purity glove box line (~30 wppm) have decreased density relative to freshly milled powders and achieve densities on the order of 85-89% dense. The mechanism for this is largely suspected to be tied to grain boundary pinning mechanisms from oxide particles that precipitate on the surface of the UN particles. Of note is that the solubility limit of O in UN is anticipated to be around 1500-2500 ppm [14] and as high as 4400 ppm at 1600°C [16], which is likely the upper limit for acceptable oxygen contamination in UN

powder/pellets. Likewise, furnace atmospheres should be oxygen free to minimize oxidation during sintering, which has also been shown to yield low density pellets.

The U-C-N system is expected to be more forgiving as the UC-UN system is completely miscible [17]. However, unreacted graphite particles or the formation of UC_2 could lead to similar detrimental sintering effects as the oxide impurities. Studies at LANL on the impact of C impurities on sintering are limited and will require more effort to evaluate the impact this has on densification of UN powders. Comparisons between low C (<500 ppm) and standard CTRN C levels ~4000 ppm have yielded the same densities when sintered in the same furnace run.

5. Identified Issues with Nitride Scaleup and Handling

This section will discuss the integration of the current LANL CTRN processing and sintering with the Westinghouse fuel processing plant. Process flow charts will be used to identify gaps and issues for a scaled CTRN process.

5.1 CTRN Scale Up

Using the flow chart as an initial starting point, several issues, challenges and assumptions are identified. The first assumption relates to the ability to modify the current production line and repurpose the current sintering furnace into a CTR process. The current process at LANL uses vacuum to promote the reaction between carbon and UO_{2+x} during the CTR section. Converting the current atmospheric continuous furnace to a vacuum furnace would be cost prohibitive so additional development to determine the feasibility of running the CTR section at atmospheric pressure will need to be conducted. A second challenge is material handling post-CTR processing. As a result of the conversion from an oxide to a carbide, the material is extremely sensitive to moisture and exposure to air, which will need to be minimized. Current processing at LANL uses inert glove boxes; while this would be undesirable for a production setting, a controlled atmosphere setup, or methods to mitigate exposure, is needed. Additionally, this controlled atmosphere needs to interface with the next processing setup and needs to continue until the material is in pellet form.

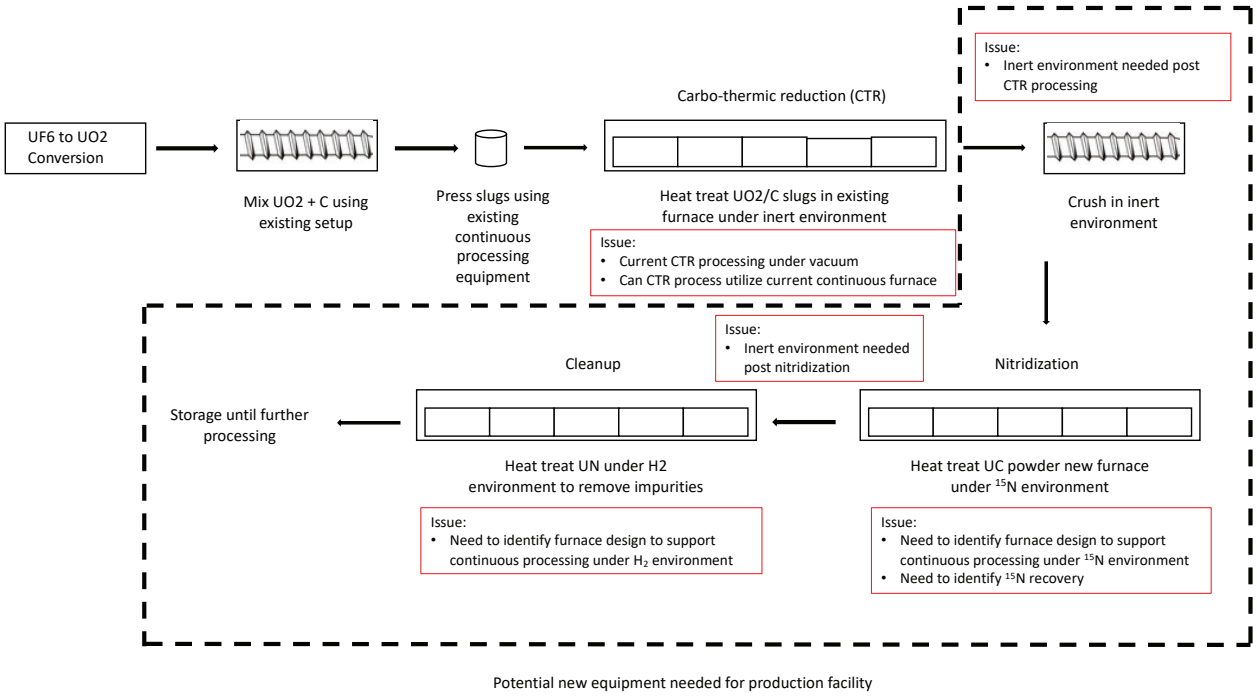

Figure 15: Flow chart and identified concerns for CTRN scale up. The dashed line area signifies new required capabilities that should be considered for commercialization.

A third challenge is the use of $^{15}N_2$ for the nitridation of the material and the appropriate furnace style to accommodate such processing as well as maintaining desirable process hand-offs. The current process at LANL uses flowing nitrogen gas to backfill the chamber and flow under a positive pressure in excess gas. This process needs to be cognizant of the expense associated with $^{15}N_2$ and an appropriate style of furnace

needs to be investigated to minimize the $^{15}N_2$ gas loss throughout the processing. Additionally, recovery of the $^{15}N_2$ gas needs to be employed to make this fabrication process economically viable.

Finally, the CTRN process uses excess carbon to drive the complete conversion of the feedstock material to UN and as a result of this a cleanup process is needed to remove the excess carbon from the as-fabricated material. The current process at LANL uses H_2/N_2 as the reactant gas to reduce the residual carbon. The process is diffusion limited and is a significant portion of the overall thermal cycle. The challenge for this process will be to incorporate an appropriate furnace schedule to limit the impact between process hand-offs. LANL is exploring new technology to shorten processing times but these investigations need to be continued to determine the right process cycle.

These are just a few observations and this discussion needs a broader view to capture all of the processing challenges to scaling UN fabrication.

5.2 Sintering Scale Up

A schematic representation of UN sintering is shown in Figure 16 where 4 primary steps are involved: 1) reduce the UN powder, post CTRN, to a sinterable particle size distribution, 2) press pellets into a green compact and load into sintering trays, 3) sinter pellets in controlled atmosphere furnace, and 4) centerless grind to dimensional tolerances and final QA.

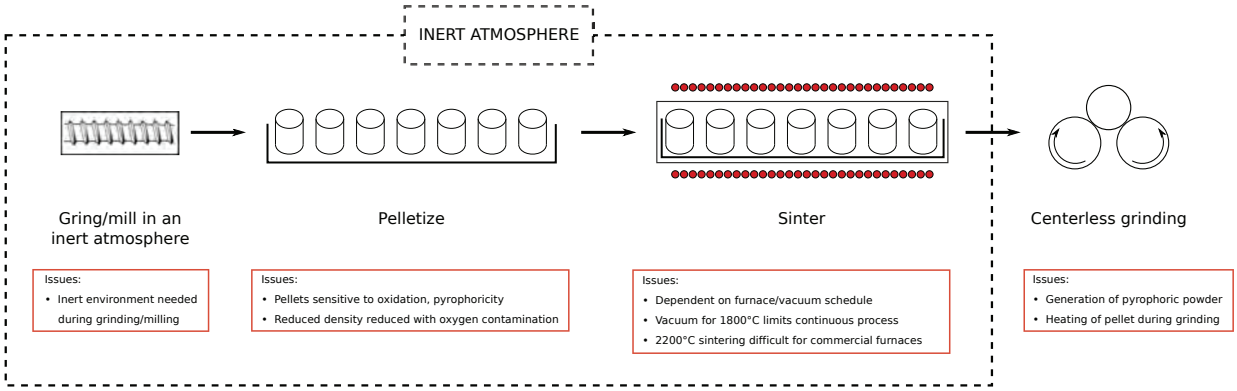

Figure 16: Identified issues for scaling up sintering of UN pellets in a commercial setting relative to typical R&D processing conditions.

As mentioned previously, the UN powder post-CTRN is too coarse to be able to sinter directly and will require a milling step to provide a particle size distribution that is amenable to sintering. Studies at LANL have shown that long high energy ball milling aids in sintering, which yields high surface area powders. The high surface energy leads to increased oxidation potential, which under an air environment will energetically oxidize even at room temperature to form oxides of uranium. An example XRD pattern of this is shown in Figure 17 where freshly milled UN powder that was sieved to sub-325 mesh oxidized on the bench top outside of a glove box environment. Because of this, all milling activities and follow-on activities through sintering should be conducted in an oxygen-free environment to minimize ageing of powders and to mitigate hazards on the commercial scale. One potential solution to address the pyrophoricity has been partially demonstrated on the U_3Si_2 system where high volume fractions (30-40 vol%) of organic binders are melted and coat the powders to minimize oxidation [18]. This method allowed powders to be exposed to air and yielded pellets ~87% dense. Work would need to be conducted to improve binder mixing/distributions, which will help prevent large pores that develop from binder inhomogeneity within the green pellets.

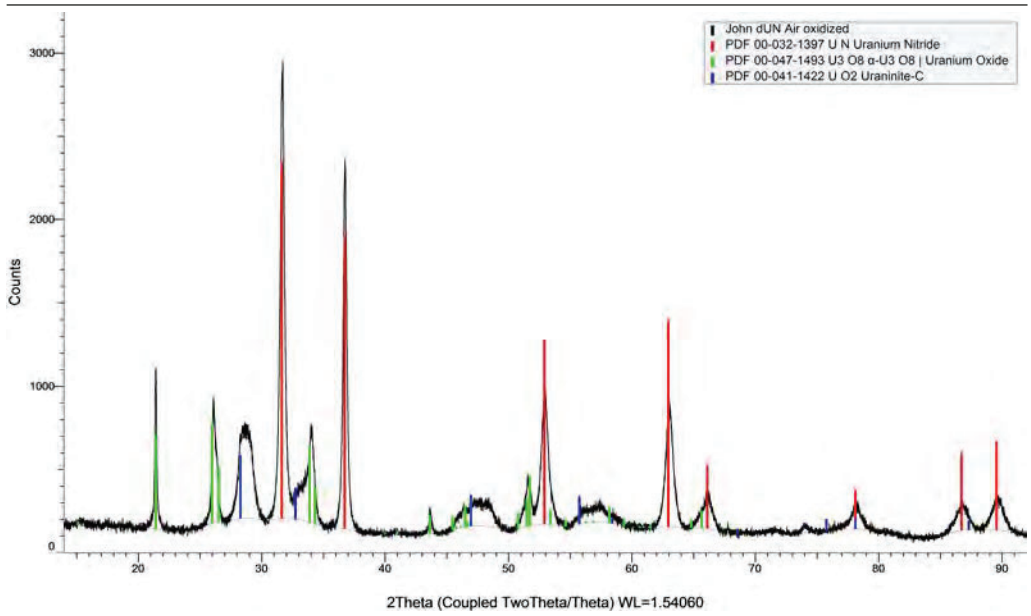

Figure 17: XRD pattern of UN powder that was milled and sieved for sintering and then exposed to air.

In Section 4, routes were identified that yield densities greater than 93%. As shown above, the sintering atmospheres and temperatures can be controlled during the furnace schedule. Sintering pellets using temperatures above 1900°C is expected to require considerable investment on a commercial scale as the normal oxide lines operate closer to 1730°C. Sintering profiles that yielded acceptable densities at lower temperatures were only demonstrated using a vacuum environment followed by subsequent re-nitridation steps to reset the stoichiometry of the mononitride. This process also requires tight temperature process control as UN has been shown to decompose to U metal above this temperature, reacting with the refractory foils. Technical challenges are expected to be encountered when incorporating a continuous processing line that involves both vacuum and changing ambient pressure atmospheres to reset stoichiometries and prevent the destructive U_2N_3 formation on cooldown.

Sintered pellets are anticipated to require grinding stages post sintering for dimensional requirements within the rods. Wet grinding and polishing have been done at LANL with minimal hazards, where the resulting removed material settles to the bottom of the liquid medium. Dry grinding in air is not recommended as the small particulates that are generated along with the heat induced by grinding will lead to sparks and/or ignition of the powder. To this end, dry grinding would be possible if conducted in an inert environment. In both cases, the removed material could be recycled by cleaning or calcining in oxygen to UO_2/U_3O_8, as is shown in Figure 5. A similar treatment could be envisioned for pellets that do not meet QA requirements for insertion into rods.

6. References

[1] R. B. Matthews, K. M. Chidester, C. W. Hoth, R. E. Mason, and R. L. Petty, "Fabrication and testing of uranium nitride fuel for space power reactors," *J. Nucl. Mater.*, vol. 151, no. 3, p. 345, 1988.

[2] P. E. Evans and T. J. Davies, "Uranium nitrides," *J. Nucl. Mater.*, vol. 10, no. 1, pp. 43–55, 1963.

[3] B. J. Jaques *et al.*, "Synthesis and sintering of UN-UO2 fuel composites," *J. Nucl. Mater.*, vol. 466, pp. 745–754, 2015.

[4] H. Funk, H., Bohland, "Zur Darstellung von Metallnitriden aus Ammoniumfluorometallaten und Ammoniak," *Zeitschrift fur Anorg. und Allg. Chemie. Band*, vol. 282, no. 1938, pp. 155–162, 1939.

[5] C. B. Yeamans *et al.*, "Oxidative ammonolysis of uranium(IV) fluorides to uranium(VI) nitride," *J. Nucl. Mater.*, vol. 374, no. 1–2, pp. 75–78, 2008.

[6] R. B. Matthews and P. E. Hart, "Nuclear fuel pellets fabricated from gel-derived microspheres," *J. Nucl. Mater.*, vol. 92, no. 2–3, pp. 207–216, 1980.

[7] J. R. McLaren and P. W. M. Atkinson, "The sintering of uranium mononitride," *J. Nucl. Mater.*, vol. 17, no. 2, pp. 142–148, 1965.

[8] H. G. Berthold, Von H.J., Hein, "Uber die Hochtemperaturammonolyse von UF4," *Angew Chemie*, vol. 81, no. 22, p. 910, 1969.

[9] T. Mitamura, M. Kanno, and T. Mukaibo, "Preparation of uranium carbide from uranium tetrafluoride," *J. Nucl. Sci. Technol.*, vol. 6, no. 1, pp. 6–11, 1969.

[10] G. W. C. Silva, C. B. Yeamans, L. Ma, G. S. Cerefice, K. R. Czerwinski, and A. P. Sattelberger, "Microscopic characterization of uranium nitrides synthesized by oxidative ammonolysis of uranium tetrafluoride," *Chem. Mater.*, vol. 20, no. 9, pp. 3076–3084, 2008.

[11] N. R. Wozniak, J. T. White, B. P. Nolen, and J. R. Wermer, "Assessment of Feedstock Synthesis Routes for High Density Fuels."

[12] Y. Arai, *Nitride fuel*, vol. 3. Elsevier Inc., 2012.

[13] B. J. Jaques, "THE SYNTHESIS AND SINTERING OF NITRIDES OF URANIUM AND DYSPROSIUM," Boise State University, 2008.

[14] V. J. TENNERY, T. G. GODFREY, and R. A. POTTER, "Sintering of UN as a Function of Temperature and N2 Pressure," *J. Am. Ceram. Soc.*, vol. 54, no. 7, pp. 327–331, 1971.

[15] R. Metroka, "Fabrication of Uranium Mononitride Compacts," no. NASA Technical Note, pp. 1–31, 1970.

[16] N. A. Javed, "Oxygen solubility in uranium mononitride phase," *J. Less-Common Met.*, vol. 29, no. 2, pp. 155–159, 1972.

[17] G. Ondracek and G. Petzow, "Thermochemische und technologische untersuchungen im system uranmononitrid-kohlenstoff," *J. Nucl. Mater.*, vol. 25, no. 2, pp. 132–143, 1968.

[18] J. T. White and S. S. Parker, "Development of Strategies to Relax Handling Constraints for High Density Fuels," Los Alamos, 2017.

Steam Oxidation of Uranium Mononitride in Pure and Reducing Steam Atmospheres to 1200 ℃

Elizabeth S Sooby [1,‡], Brian A Brigham [1], Geronimo Robles [1,2], Joshua T. White [2], Scarlett Widgeon Paisner[2], Erofili Kardoulaki[2], Brandon Williams[3]

[1] Extreme Environments Materials Laboratory, Department of Physics and Astronomy, University of Texas at San Antonio, San Antonio, TX, USA
[2] Fuels Research Laboratory, Materials Science and Technology Division, Los Alamos National Laboratory, Los Alamos, NM, USA
[3] Radiochemistry Program, Department of Chemistry and Biochemistry, University of Nevada, Las Vegas, NV, USA

ABSTRACT

Uranium mononitride (UN) has been proposed as a long-term, accident tolerant, light water reactor (LWR) fuel candidate. Though little is reported on the hydrolytic reaction of UN, it has been shown that UN powders display an onset of oxidation below 200 ºC with monolithic samples displaying an onset between 200-300 ºC with the highest reported onsets for pure UN at approximately 400 ºC observed during isothermal exposures of monoliths. What is often unreported or is at least inconsistent among these previous studies is the dependence of the response to water corrosion of UN on the fabrication method, density, and levels of light element contamination. The present study addresses the lack of kinetic data for high purity UN, assesses the sensitivity of the dynamic response of UN to the density of the monolithic sample exposed to flowing steam, as well as observes the variation in the oxidation kinetic response of UN to the presence of a common fabrication contaminant, carbon. In addition, the mass spectrometry performed on the evolved gas during the reaction with steam informs the reactions thermochemistry for UN with flowing steam during a thermal ramp and during an isothermal exposure at 500 ºC. It is concluded here that high-density samples, (≥94% theoretical density), have a significantly delayed onset of reaction with steam compared to values previously reported, the kinetic reaction is retarded in a reducing steam atmosphere (steam + 100 ppm H_2), and the reaction products are predominantly ammonia and UO_2 at temperatures less than 700 ºC, above which UO_{2+x} ($0.2 \geq x \geq 0.0$) begins to form and ammonia dissociates.

1. Introduction

High uranium density fuels (HDFs), (U-alloys, UN, UC, UB_2, U_3Si, and U_3Si_2) have seen implementation or proposal for implementation in research reactors, space reactors, kernels of particle fuel forms, and to a lesser extent as drop-in-replacements for UO_2 in the current fleet of light water reactors (LWRs). The low melt point and poor thermal stability to higher temperatures of uranium alloys and U_3Si preclude their use in LWRs, though recently much attention has been given to the potential for development of U_3Si_2, UB_2, and UN for use in the current fleet. These fuels are attractive for LWR implementation due to their high melt points compared to metallic uranium alloys and compounds, enhanced thermal conductivity compared to UO_2, and increased uranium atom density compared to UO_2. A summary of these properties can be found in Table 1. Motivated initially from the perspective of accident tolerance and a higher technical readiness when compared to UN and UB_2, uranium silicide compounds (U_3Si_2 and U_3Si_5) were investigated as drop-in-replacements for UO_2 or as composite fuel constituents (U_3Si_2, UN-U_3Si_2 and UN-U_3Si_5)[1-5]. It was quickly realized that the uranium silicide compounds exhibited little resistance to oxidation in O_2 and H_2O atmospheres at T>300 °C [6-15], proving to not provide any accident

‡ Corresponding Author: Elizabeth.Sooby@UTSA.edu

tolerance beyond the increased thermal properties, which were proposed to lead to less stored energy in the core during off-normal events involving temperature excursions [16-18].

In light of the poor performance of U_3Si_2, several investigations have assessed the effectiveness of alloying additions and composite structures to mitigate the reaction of high uranium density fuels when exposed to water, at temperature and thermal conditions characteristic of a cladding breach or rupture [19-26]. Recent reviews reporting the performance of both pure and alloyed high uranium density fuels highlight the opportunities and challenges to this approach to mitigate oxidation [27, 28]. In summary, with the exception of the addition of UB_2 as a composite phase, no addition has shown promise of mitigating the water reaction while maintaining a high enough uranium atom density to be considered a viable replacement of UO_2.

Therefore, the current focus of near-term accident tolerant fuels (ATF) has been placed on the irradiation testing and performance assessments of coated cladding and doped-UO_2 [20, 22, 29-31], though uranium silicide pellets have undergone successful lead test rod irradiations and show promise of an improved burn-up structure when compared to UO_2-based fuel forms [32, 33]. While improved cladding technologies address an ATF goal to reduce oxidation during a loss of coolant accident (LOCA) [34, 35] and doped-UO_2 will lead to increased fission product retention and enhanced fresh fuel thermal properties [29, 36, 37], neither support increased cycle lengths due to the high burn-up structure of UO_2 leading to fuel fragmentation, relocation, and dispersal (FFRD) during an off-normal event [38]. The long-term ATF fuel development efforts focus on maturing a fuel form that supports longer cycle lengths and reduces the potential for FFRD [38]. Furthermore, there are only two foreseeable avenues to increase cycle lengths while limiting FFRD: increase the fuel enrichment or deploy a uranium bearing compound with a higher uranium atom density. Therefore, attention needs to be paid to high uranium density compounds and composite structures if enrichment is to remain capped at 5% [39].

Receiving less attention as a drop-in-replacement of UO_2, uranium mononitride (UN) presents a higher thermal conductivity when compared to UO_2, the highest uranium atom density of all HDFs with liquidous temperature high enough for LWR implementation, but is significantly less studied with respect to dynamic response to coolant exposure. However, there are a number of studies which present the degradation mechanisms of UN to hydrothermal corrosion. A recent review article on UN and UN-composite oxidation performance summarized that UN powders displayed an onset of oxidation below 200 ºC with monolithic samples displaying an onset between 200-300 ºC with the highest reported onsets for pure UN at approximately 400 ºC and observed during isothermal exposures of monoliths [28, 40, 41].

Oxide spallation during UN exposure to H_2O results in mechanical failure of the fuel. In a study performed by Watkins, *et al*, monolithic UN samples and UN+UO_2 composites were autoclave tested at temperatures up to 300 °C [42]. The microstructure was observed following exposure, and the failure mechanism proceeded via grain boundary attack, resulting in boundary expansion and spallation. It was noted that fuel performance during oxidant exposure was improved by minimizing both pore density and oxide contamination originating during fabrication [41-43]. Additional research efforts have identified contaminant species, particularly UO_2, accelerates UN degradation in steam [44]. What is often unreported or inconsistent among these previous studies is the dependence of the response on the fabrication method, density, and levels of light element contamination.

Though the leading motivation for the current investigation is to provide data on the dynamic and kinetic response of UN samples fabricated with varied purity and density levels to high purity and reducing steam atmospheres, the authors also present a preliminary thermodynamic argument to inform the analysis of mass spectroscopy measurements of volatile oxidation products formed during the hydrothermal oxidation of UN reported here. While ammonia is the main gaseous product proposed by the available literature on UN hydrolysis [28, 40, 45], computational thermodynamics based on the available thermodynamic functions actually predicts the predominant evolution of nitrogen from the sample which then recombines with freed

hydrogen from the water reaction. In support of this hypothesis, the "Reaction Equations" module within HSC was used to first calculate the change in Gibbs free energy (ΔG) for a number of proposed reactions [46]. The values are derived mathematically using an internal database of thermodynamic values. It is generally agreed that one of the two primary hydrolysis reactions of UN proceed by Equation (1) (with $\Delta G_{rxn}^{600°C}$ = -366.866 kJ) below and product gases are $NH_3(g)$ and $H_2(g)$ [41, 42, 44]

$$2UN + 4H_2O(g) \rightarrow 2UO_2 + 2NH_3(g) + H_2(g) \quad (1)$$

However, a discrepancy has been noted within the HSC software. At 600 °C it can be noted that the Gibbs free energy of Equation 2 is approximately 250 kJ more favorable ($\Delta G_{rxn}^{600°C}$ = -621.399 kJ).

$$2UN + 4H_2O(g) \rightarrow 2UO_2 + 4H_2(g) + N_2(g) \quad (2)$$

While this reaction equation does not produce the gases observed in previous experimental studies, it can be proposed that the gas formation proceeds through the more favorable thermodynamic route of Equation 3 ($\Delta G_{rxn}^{600°C}$ = -2435.191 kJ) once the reaction described by (2) has progressed.

$$2UN+4H_2O(g) + ¼N_2(g) \leftrightarrow 5/2NH_3(g) + 2UO_2 + ¼ H_2(g) \quad (3)$$

This hypothesis can be supported from previous literature that notes there is a dependence on the rate of hydrolysis linked to $N_2(g)$ flow from the sample [41, 44]. The secondary hydrolysis equation of UN is detailed in the remaining reaction equations below [41, 42, 45]:

$$3UN + 2H_2O(g) \rightarrow UO_2 + U_2N_3 + 2H_2(g) \quad (4)$$

$$U_2N_3 + 4H_2O(g) \rightarrow 2UO_2 + 8/3\ NH_3(g) + 1/6\ N_2(g) \quad (5)$$

It can be assumed that both Equation 1 and 4 ($\Delta G_{rxn}^{600°C}$ = -401.234 kJ) are occurring simultaneously on the surface and along the grain boundaries of UN in high temperature steam environments. Any exposed uranium sesquinitride (U_2N_3) is hydrolyzed further to UO_2 by Equation 5 ($\Delta G_{rxn}^{600°C}$ = -2016.848 kJ). This leads to a scenario where a layer of U_2N_3 is located between the surface UO_2 and remaining bulk UN [45]. Figure 1 plots the equilibrium conditions for 1 mol of UN exposed to increasing amounts of H_2O gas, as predicted by ThermoCalc software employing the TAF-ID database [47]. The figure represents the reactants and products (plotted on the y-axis) for 1 mol UN exposed to increasing amounts of H_2O (x-axis). The software does not allow products to react with one another; hence, the free $H_2(g)$ and $N_2(g)$ and low amount of predicted NH_3 formation. Note that U_2N_3 formation is only predicted in a steam starved condition, with oxidant at less than 1 mol H_2O (g). Not included in this figure is any information about the formation of UO_{2+x}, though it has been concluded by previous investigations that in pure $H_2O(g)$, UO_2 is the terminal oxide phase and U_3O_8 has yet to be observed, though it will form hyperstoichiometric UO_2 [48]. As an abundance of steam is supplied to the sample in the current study, it is foreseeable that the oxide product will be hyperstoichiometric, UO_{2+x}.

2. Materials and Methods

2.1. Materials

Three UN sample types, all pellet geometries (right-round cylinders), were tested in the current study: high-density (>94% Th.D.), low-density (87-93% Th.D.), and high carbon containing. The UN powder used for sample fabrication was produced by the CTR-N method, where different

impurity levels of C and O can be targeted [49]. Two UN powder lots with carbon impurities at 100 wppm (used for the high- and low-density samples) and 4000 wppm (high C samples, each displaying higher density than the low-density pellets reported) levels were used to fabricate the pellets. Pellets were formed via traditional powder metallurgical methods. Impurity levels for O and C were determined using the inert gas fusion technique and combustion infrared method on both powder and sintered pellets. UN powder was high energy ball milled using Si_3N_4 jars and grinding media to size reduce the powders through a 325 mesh sieve. After milling, the powders were compressed using punch and die sets at 150 MPa prior to loading into a W-mesh element furnace connected to the glove box. Sintering was achieved at 2200°C under a N_2/H_2 atmosphere. Heating and cooling of the pellets was under an Ar atmosphere to prevent the destructive conversion to U_2N_3. All powder processing and sintering was conducted within a high purity Ar glove box line maintained below 30 ppm O_2 and < 0.1 ppm H_2O. Density values for the high-density (HD) and low-density (LD) samples were determined using the immersion density method. Geometric densities were used for all high carbon (HC) containing samples, and the LD and HD geometric densities were verified prior to testing. Immersion density measurements in Fluorinert solution were carried out on selected samples, and was found to be within 1.3 % of those found by geometric density measurements.

The average grain size of a representative pellet of each type was determined via ASTM E-112. Pellets were cross sectioned axially on an Allied HighTech TechCut 4 low speed saw, inside the glovebox, to expose the grain structure from edge to centerline. Mechanical grinding was completed on SiC discs to 1200 grit then diamond suspension polished to a 0.5-µm finish on Tech-cloth discs. Additional polishing with 0.04-µm silica colloidal suspension was used to enhance grain boundary visibility. Images across the pellet were collected on a Hitachi FlexSEM 1000 in backscattered electron (BSE) mode and are presented in Figure 2 and display uniform grain size distribution. Images were imported into ImageJ software and analyzed. The number of grain boundaries intersected by a line were counted and compared to the total length of the line.

2.2. *Steam Oxidation Testing*

The dynamic response of UN samples to high temperature steam atmospheres was measured at both the University of Texas at San Antonio (UTSA) and Los Alamos National Laboratory (LANL) with Netzsch F3 449 Jupiter simultaneous thermal analyzers (STA) (Netzsch; Selb, DE) each paired with a water vapor generator. Samples were tested under steam atmospheres (27-48 mol%), with and without H_2 (up to 100 ppm), for both thermal ramp and isotherm testing. All testing details including atmospheres and locations are summarized in Table 2. UN samples were tested using alumina (Al_2O_3) fixturing, employing an Al_2O_3 platform and Al_2O_3 working tube in either a SiC element water vapor furnace. A high temperature (T_{max}=1600°C) steam furnace (UTSA), adapted for steam testing using a custom Netzsch water vapor adapter, introduces steam, H_2, and all purge gasses at the bottom of the furnace, resulting in a well-mixed gas flow around the pellet. The dynamic flow of steam around the pellet and platform is in contrast to the flow conditions of previous studies in a conventional Netzsch water vapor furnace (LANL) [50, 51], where steam is introduced at the top of the furnace with the direction of steam flow down onto the sample. The impact of flow dynamics on the response of UN to steam was not observed as both configurations were employed in this study and consistent results.

Argon (Ar) was used as the carrier and down-blending gas for all experiments conducted under the current investigation. Specifically, ultra-high purity (UHP) Ar that was thermally scrubbed for O_2 contaminants by a titanium (Ti) charge held at 600 ºC. The authors refer to the O_2 scrubbed Ar as “gettered-Ar,” which was measured to have a partial pressure of oxygen (pO_2) less than 10^{-15} part per million (ppm). A 2100 RapidOx (Cambridge Sensotec, St. Ives, UK) with O_2 sensors located at the inlet and outlet of the furnace was used to monitor the STA for possible atmospheric contamination during testing.

Steam was produced by a Netzsch water vapor generator and introduced to the furnace via a heated (200°C) stainless steel transfer line. Additional flange collar (200°C) and exhaust head (300°C) heaters were utilized to prevent condensation. At UTSA for ramp testing, samples were exposed to gettered-Ar during ramp to 250 ºC and allowed to equilibrate for 20 minutes before steam or reducing steam (steam + H_2 100 ppm) was introduced during a thermal ramp at 10°C min^{-1} from 250 to 1200 ºC. Isothermal testing was also conducted at 400 and 500°C. During isothermal testing, the system was ramped to the test temperature under a gettered-Ar atmosphere allowing the instrument to equilibrate for 20 minutes before steam or reducing steam was introduced during 6-hr isotherms at the test temperature. At LANL, the thermal ramp tested samples were exposed to gettered-Ar to 200ºC before steam was introduced during a thermal ramp at 10°C min^{-1} from 200 to ~1000ºC.

Control of the H_2 ratio to steam was achieved through mixing 1% H_2 (balance Ar) with gettered Ar via G-series Mass Flow Controllers (MFCs; MKS Instruments, Andover, MA, US) that were programmed with a paired 946 Vacuum Controller unit (MKS Instruments). Flow of getter Ar and H_2 was set to ensure UN samples were exposed to 100 ppm H_2 during testing. Gases were combined at a Swagelok Union T connection with the mixed gases being split at a second Union T connection to the STA and a MFC regulated exhaust to ensure constant pressure (8 psi) throughout testing runs.

Mass change was normalized to initial exposed surface area for each individual sample. The mass loss rate (mg cm^{-2} min^{-1}) for isotherm testing was determined using the Netzsch Proteus software (v. 8.0) mass gain tool. Breakaway oxidation temperatures (exothermic transition) for ramp testing was calculated by the c-DTA (calculated-Differential Thermal Analysis) tool as demonstrated by Sooby-Wood et al. [8]. This onset temperature is located where the extrapolated baseline and tangent line to the exothermic peak of the reaction is identified (Figure 3). The thermocouple used for testing was calibrated with melt point standards (bismuth, zinc, aluminum, and silver), provided by Netzsch (part number 6.223.5-91.3). Post-testing, samples were removed, weighed with an Ohaus benchtop balance (Parsippany, NJ, US) and placed under Ar atmosphere in MBRAUN UNILAB pro SP glovebox (Garching, DE) for XRD characterization analysis.

To assess the volatile reaction products formed on ramp and during isothermal exposures, a coupled Netzsch Aëolos 403 Quadrupole Mass Spectrometer (QMS) measured all gaseous products at the exhaust of the STA for a subset of both isotherm and ramp runs at UTSA. These runs were conducted in a water vapor furnace as depicted in Table 2. The QMS is connected via a heated transfer line to assure all volatile products up to 300°C are measured. Data was collected from 1-100 atomic mass units (amu) (step width 1 amu) with setting time and integration time of 50 and 20 milliseconds, respectively, resulting in ~60 scan min^{-1}. Quadrupole mass spectrometry data collected during the thermal ramp was normalized to produce information relevant to the total abundance of the anticipated reaction products, NH_3(g), N_2(g), and H_2(g). A baseline signal for the thermal ramp was recorded for an identical thermal profile but with no sample present. The ion currents collected for each mass species during the baseline measurement were subtracted from the sample data collected during thermal ramp. Whenever the difference between the sample run and the baseline run was less than zero, the value was replaced with zero as there was no appreciable signal to noise variation. To determine total species abundance of ammonia the radical NH (m/z=15), which is known to speciate during the measurement ionization process in a quantifiable amount, was used to avoid obfuscation from other molecules (specifically the water radical, OH to m/z=16 and 17). The m/z = 15 signal was then divided by the fractional value of m/z = 15 present in the mass spectrum for ammonia (approximately 0.0419) as reported by NIST for mass spectrometry conducted with an ionization current of 70eV [52]. Similar corrections were made for N_2 (m/z=28 is 0.8696 of the total N_2 spectra) and H_2 (m/z=2 is 0.9804 of the total H_2 spectra).

2.3. Post oxidation characterization

X-ray diffraction (XRD) was the primary post-oxidation characterization technique employed in the present study. Since the investigation was sample limited, the investigators prioritized a complete understanding of the predominant oxidation products formed, rather than the microstructural evolution during steam oxidation of the samples tested. A sample from each set, high- and low-density as well as high C, was ground in a glovebox, maintained at less than 0.1 ppm O_2 and H_2O, using an agate mortar and pestle to provide XRD patterns for the as fabricated samples. NIST standard reference material 660c- LaB_6 was incorporated into the sample preparation for XRD measurements. Compared to the certified particle size distribution of 90% < 23.78 µm for LaB_6, it was determined that the product powder required longer comminution to minimize particle size difference effects. First, the oxidation product formed during steam or steam+H_2 exposure, including any remaining bulk sample that was note reduced to power in addition to the powder formed, was homogenized using an agate mortar and pestle in the glove box. Approximately 60 mg of UN product was separated onto a new, static-free weigh boat using a Mettler-Toledo balance calibrated to ±0.0001g. An amount of LaB_6 between 5 and 10 wt% (3-8 mg LaB_6) was added to the weigh boat. The LaB_6 and UN product were mixed for at least 10 minutes with minimal force and until the powder was one homogenous color. After homogenization, powder samples were loaded onto a zero-background sample holder and sealed with a polymer, environmental dome. A Bruker D2 Phaser (Billerica, MA, USA) equipped with a LYNXEYE XE-T Detector and copper anode was used to obtain the XRD patterns for each sample. Data for each was collected from 10 to 110 2θ over a 0.004 step size and dwell time of 2 seconds.

3. Results and Discussion

3.1. Thermal ramp testing

Thermal ramp exposure of UN pellets to steam from 250 to 1200°C followed by 2-hr isotherms at 1000 °C+ resulted in each sample reaching near or beyond terminal oxidation, as indicated in Figure 4, where a theoretical terminal mass gain of 7.1% represents conversion to UO_2 with all nitrogen bearing species volatilizing. Conversion to UO_2 (and in many cases UO_{2+x}) was observed for all tested samples regardless of steam atmosphere, sample type, or the presence/absence of H_2(g). Furthermore, all samples produced a powder product following hydrolysis as a result of volumetric expansion during the formation of UO_2. However, the exact kinetic response varied, depending on sample type and steam exposure, specifically the rate at which the sample reached terminal oxidation. More rapid kinetics are observed in the lower density samples as well as the samples exposed to higher steam concentrations, with clear indication that density is the dominant of those two variables due to the increased surface area of the higher porosity samples. A clear comparison of the low-density, high-density, and high-carbon oxidation dynamics on ramp in 32% steam is displayed in Figure 5.

The three pellet types displayed intuitive differences in their oxidation behavior, especially for c-DTA onset temperature and time until terminal oxidation as depicted in Figures 4 and 5. Across both testing at UTSA and LANL the lowest-density and high-C pellets demonstrated both lower c-DTA onset and terminal oxidation temperatures relative to high-density pellets as depicted in Table 3.

Previously reported mass gain and/or hydrolysis byproduct formation temperatures is sparse with tested samples including powders, pellets, and single crystals, and therefore existing literature data cannot be meaningfully compared to the results presented here due to varied and sometimes unreported sample densities, purities, and testing conditions (steam atmosphere,

sample exposure pathway, etc.) [53-55]. In this study, low-density pellets demonstrated lower c-DTA onset temperatures than both high-density and high-carbon pellets under identical steam atmospheres (32% steam at UTSA/27% steam at LANL), since increased porosity results in increased surface area for oxidation to occur [26]. Appreciable carbon impurities are largely not desired as UC corrosion is more rapid then UN and may cause additional issues of creep, radiation swelling, emission of gaseous fission products under irradiation [56]. Consequently, pellets with C impurities up to 4000 wppm (2787 $\pm$ 178 wppm after sintering) had lower c-DTA onset temperatures than the high-density UN pellets, indicating that soluble amounts of C likely degrade the oxidation performance of UN.

Varied steam partial pressures could play a role in the oxidation kinetics, if the system is not steam saturated; therefore, high-density pellets were tested in three different pure steam atmospheres. The thermograms for the high-density samples in varied steam partial pressures is displayed in Figure 6. Break away mass gain onset temperatures, determined by c-DTA (calculated-differential thermal analysis) [8], were similar(614-640 °C ± 5°C) for high-density pellets run under 32-48 mol% steam. As depicted in Figure 6, total mass gain of 6.7-7.1% for high-density samples was observed under each steam atmospheres (Table 3). Since no condensation was observed in the furnace tube under 32% atmospheres, this testing condition was used for all further testing conditions to reduce noise in the data. While the onsets of these conditions are comparable, it should be noted that the kinetics of isothermal exposures could vary due to the slower rise to terminal oxidation of the 32% steam atmosphere.

3.2. Reducing steam exposure

High and low-density pellets were exposed to 32 mol% reducing steam atmospheres (100 ppm H_2 mixed with the flowing steam) during ramp testing had no apparent impact on the high-density pellet tests relative to 32% steam only atmospheres, as displayed in Figure 7A but retarded mass gain for low-density pellet tests, as displayed in Figure 7B. The low-density pellet reducing steam test displayed a higher end of onset (716°C) temperature relative to the low-density pellet pure steam test (842°C, respectively). Conversely, the high-density pellet steam and reducing tests had similar c-DTA onset temperatures (range of 640-650°C+/- 6°C) and end of onset temperatures (range of 995-1004°C+/- 12°C) that were indicative of delayed oxidation relative to the low-density tests (with or without H_2), further supporting a conclusion that pellet density is the dominant variable governing oxidation kinetics in appreciable steam atmospheres.

Thermal ramp testing of high-density pellets under 32% steam atmospheres (with or without H_2) displayed significantly higher c-DTA onset and delayed terminal oxidation relative to low-density pellets (Table 3). Hydrogen containing steam environments are more typical of steam produced during a LOCA for an LWR, as it exhibits a reducing water chemistry and thus lower oxidation potential [57]. Interestingly, hydrogen was seen to exacerbate U_3Si_2 degradation due to the formation of a stable hydride phase which results in a significant volume expansion of the pellet [58-60]; however, increased degradation and earlier onsets of reaction were not observed for UN in this study.

3.3. Isothermal testing

Isothermal exposures were conducted to determine the kinetics of UN oxidation, which can be used to develop a kinetic theory for this fuel form during steam exposure. The current study was sample-limited, and as such the investigation observed the response of UN four isothermal conditions, 400 and 500 °C in 32% pure and reducing steam (steam + 100 ppm H_2). The 6-hr isotherm data is presented in Figure 8, where each condition resulted in near linear oxidation kinetics with only the low-density sample reaching a terminal oxidation at 500 °C in 32% steam without hydrogen. The 500°C tests were conducted with high-density pellets while the 400°C tests

were conducted with a combination of high- and low-density pellets due to sample availability. At both 400 and 500°C, testing under reduced steam (100 ppm H_2) atmospheres retarded UN oxidation. Mass gain rates were greater at the 500°C testing conditions relative to 400°C testing condition. Additionally, at 500°C (and during ramp for all pellet "types") several rapid mass losses (0.1-2.0 mg) occurred throughout the isotherm as powder fell off the platform during spallation of UO_2. However, at 400°C no mass loss events occurred, with or without H_2, indicating less energetic oxidation reaction.

Post-testing analysis supported reduced oxidization kinetics under reducing steam as both UN samples tested under steam atmospheres were completely pulverized while a small pellet encased in powder (UO_2) was recovered from the reducing steam tests. Of further note, at 400°C the low-density pellet tested under reducing steam gained mass more quickly than the steam only test for the first hr of the isotherm but overall gained significantly more mass through the course of the 6 hr isotherm, demonstrating the benefit of extended isotherm testing particularly when testing samples with a higher exposed surface area. It is anticipated that if the oxidation experiment was held for a longer dwell time, all samples would reach terminal oxidation. Similar to ramp testing, the density of the UN sample tested was the dominant variable in isotherm tests. The mass gain rate observed was four times lower for a high-density pellet relative to a low-density pellet in otherwise identical testing conditions. Decreased temperature (500 to 400°C) and reducing steam (vs. pure steam) displayed reduced oxidation kinetics with a mass gain rate ~1.5 and two times lower, respectively. Higher porosity samples have both greater surface area exposed to oxidizing atmosphere and greater mechanical fragmentation due to internal volume expansion, exposing new surface area and shortening diffusing pathways for the oxidant [41] driving increased oxidation kinetic rates under all testing conditions.

3.4. Post Oxidation Characterization

The x-ray diffraction (XRD) data collected for the UN samples following ramp exposure are presented in Figure 9. As can be seen from the post-ramp XRD data, all samples form a combination of UO_2 and UO_{2+x} as indicated by the shift to high angle. The stoichiometry appears to be less than $UO_{2.2}$, though further characterization and analysis, which is beyond the scope of the present study, would be necessary to determine the exact stoichiometry of these samples. Though these reached terminal oxidation at different rates depending on steam and sample condition, each ramp sample experienced a 2 hr isotherm at 1000-1200°C, which resulted in each sample having observably the same oxidation state following exposure.

Post-oxidation characterization via XRD was performed for the products formed during isotherm exposures, and the patterns collected are displayed in Figure 10 (high-density) and Figure 11 (low-density). As anticipated from the TGA results, most isothermal exposures performed here resulted in products containing both UO_2 and unoxidized UN. U_2N_3 was not observed in the collected XRD patterns, which indicates that it was not formed in appreciable abundance; XRD is not the ideal characterization tool to identify chemical species that are present in less than ~3% of the total sample. Previous work by Watkins *et al* identified thin layers of U_2N_3 surrounding grains of unoxidized UN [42], and the present study also supports that there is very little U_2N_3 present at any point during the hydrothermal oxidation process though it plays key role in the thermochemistry of the reaction. Notable observations gleaned from the collected XRD patterns include little conversion from UN to UO_2 present in the high-density 400°C sample, where conversely appreciable UO_2 is present in the 500 °C and 500 °C +100 ppm H_2 reaction products. In the low-density reaction products, appreciable UO_2 and UO_{2+x} are observed in the 400 °C isotherm, where little UO_2 is observed in 400 °C+100 ppm H_2 product, agreeing with the TGA results for these exposures. Lastly the 500 °C isothermal exposure of a low-density UN sample resulted in a mostly UO_2 reaction product.

3.5. Volatile Oxidation Products Formed

XRD patterns provide information on the presence of solid phase reaction products, and the exhaust of the STA was monitored for volatile reaction products formed *in situ* during hydrothermal exposure.

The corrected quadrupole mass spectrometer (QMS) data for thermal ramp of low-density UN samples is presented in Figure 12. The production of $NH_3(g)$ occurs first during thermal ramp exposure with appreciable production observable starting at 450 °C. Production of $N_2(g)$ and $H_2(g)$ follows at 550 °C. The presence of $NH_3(g)$ in the system peaks at 600 °C, whereas $N_2(g)$ and $H_2(g)$ peak at 700 °C. Ammonia can dissociate without a catalyst at temperatures as low as 450 °C [61]. Catalyzed decomposition can occur at even lower temperatures [62]. Ammonia decomposition is a primary method for producing hydrogen gas, and catalyzed decomposition utilizes metals such as iron or nickel. Uranium dioxide, the compound produced alongside ammonia in this reaction, is reported to act as a catalyst for ammonia decomposition at 700 °C [63].

The data presented here confirms that UO_2 and $NH_3(g)$ are the primary reaction products observed at temperatures less than 700°C, and above this temperature $NH_3(g)$ begins to dissociate, producing $N_2(g)$ and $H_2(g)$. Whether directly formed during the primary reaction or indirectly formed in a secondary reaction, the tenfold abundance of $NH_3(g)$ compared to $N_2(g)$ supports the reaction pathway described by Equations 4 and 5, which together detail the progression of the reaction beginning with U_2N_3 formation and followed by U_2N_3 oxidation to UO_2. This pathway implies the formation of a larger quantity of $H_2(g)$ than was observed; however, this is likely due to the innate challenges of making accurate quantitative measurements of hydrogen using QMS, namely a comparatively low pumping efficiency (lower acquisition rate) for this low mass species [50, 64].

To better elucidate the reaction process, isothermal data is plotted in Figure 13. For this thermal profile, steam is introduced to the sample at 53 minutes, when the increase in the hydrogen and ammonia signals is indicated. Note the logarithmic scale on the y-axis, indicating an abundance of $NH_3(g)$ more than ten times greater than that of $H_2(g)$ and $N_2(g)$. While this does not directly support any of the reaction pathways proposed, as each would require appreciable nitrogen to be produced in addition to $NH_3(g)$ and $H_2(g)$, it does support the literature observations that $NH_3(g)$ is the dominant product formed during hydrothermal corrosion of UN at T<600°C. Furthermore, the production of $H_2(g)$ and $N_2(g)$ in the ramp data is likely due to the dissociation of $NH_3(g)$, unless the thermochemical behavior of UN in steam changes at higher temperatures to preferentially form these volatiles.

4. Conclusion

The present study has shown that high-density UN has an onset of reaction in flowing steam at T >600 °C. Further, it is concluded here that high-density samples, (≥94% theoretical density), have a significantly delayed onset of reaction with steam compared to values previously reported (T <400 °C reported previously). The oxidation of UN during a thermal ramp is highly sensitive to the density of the sample, with the lowest density sample tested here displaying onsets of reaction T<400°C (87% dense with a calculated onset of 390 °C). The oxidation product identified following oxidation is primarily UO_2, with some hyperstoichiometric UO_2 present following a two-hour isothermal hold at 1200 °C. The kinetics of oxidation during ramp and isothermal exposures (400-500 °C) were shown to be less rapid when the steam atmosphere was slightly reducing, (100 ppm H_2 in steam). In addition, the mass spectrometry performed on the evolved gas during the reaction with steam informed the thermochemistry for UN when exposed to flowing steam during a thermal ramp and an isothermal exposure at 500 ºC. The reaction products are predominantly $NH_3(g)$ and

UO_2 at temperatures less than 700 ºC, above which UO_{2+x} ($0.2 \geq x \geq 0.0$) begins to form and ammonia dissociates.

5. Acknowledgments

Thanks is due to Mr. Zachary Acosta for his preliminary work in assessing the thermodynamics of the UN reaction with steam. This work was supported by the U.S. Department of Energy, Office of Nuclear Energy. This work is also part of a collaboration led by Westinghouse Electric Company comprising several national laboratories, vendors, and universities awarded in response to the DE-NE0008824 funding opportunity. Accordingly, the U.S. Government retains and the publisher, by accepting the article for publication, acknowledges that the U.S. Government retains a nonexclusive, paid-up, irrevocable, worldwide license to publish or reproduce the published form of this manuscript or allow others to do so, for U.S. Government purposes. Additional funding for student and faculty support was provided by the NNSA MSIPP CONNECT program, Grant Number DE-NA0003948.

6. References Cited

1. Wagner, A.R., et al., *Fabrication of Stoichiometric U_3Si_2 Fuel Pellets.* MethodsX, 2019.
2. Wilson, T.L., et al., *Uranium nitride-silicide advanced nuclear fuel: higher efficiency and greater safety.* Advances in Applie Ceramics, 2018. **117**: p. 76-81.
3. Ortega, L.H., et al., *Development of an accident-tolerant fuel composite from uranium mononitride (UN) and uranium sesquisilicide (U3Si2) with increased uranium loading.* Journal of Nuclear Materials, 2016. **471**: p. 116-121.
4. Harp, J.M., P.A. Lessing, and R.E. Hoggan, *Uranium Silicide pellet fabrication by powder metallurgy for accident tolerant fuel evaluation and irradiation.* Journal of Nuclear Materials, 2015. **466**: p. 728-738.
5. Nelson, A.T., et al., *Overview of Properties and Performance of Uranium-Silicide Compounds for Light Water Reactor Applications* Transactions of the American Nuclear Society, 2014. **110**.
6. Sooby Wood, E., et al., *U3Si2 behavior in H2O: Part I, flowing steam and the effect of hydrogen.* Journal of Nuclear Materials, 2018. **501**: p. 404-412.
7. Nelson, A.T., et al., *U3Si2 behavior in H2O environments: Part II, pressurized water with controlled redox chemistry.* Journal of Nuclear Materials, 2018. **500**: p. 81-89.
8. Sooby Wood, E., J.T. White, and A.T. Nelson, *Oxidation behavior of U-Si compounds in air from 25 to 1000 C.* Journal of Nuclear Materials, 2017. **484**: p. 245-257.
9. Harrison, R.W., et al., *On the Oxidation Mechanism of U3Si2 Accident Tolerant Nuclear Fuel.* Corrosion Science, 2020: p. 108822.
10. Yang, J.H., et al., *Oxidation and Phase Separation of U_3Si_2 Nuclear Fuel in High-temperature Steam Environments.* Journal of Nuclear Materials, 2020: p. 152517.
11. Gong, B., et al., *Spark plasma sintering (SPS) densified U_3Si_2 pellets: Microstructure control and enhanced mechanical and oxidation properties.* Journal of Alloys and Compounds, 2020: p. 154022.
12. Yan, T., et al., *Initial oxidation of U_3Si_2 studied by in-situ XPS analysis.* Journal of Nuclear Materials, 2019. **520**: p. 1-5.
13. Jossou, E., et al., *Oxidation behaviour of U_3Si_2: an experimental and first principles investigation.* Physical Chemistry Chemical Physics, 2018. **20**(7): p. 4708-4720.
14. Uygur, S., *Degradation mechanisms of UN and UN–10U_3Si_2 pellets of varying microstructure by comparative steam oxidation experiments*, in *TRITA-FYS*. 2016. p. 48.

15. Sweet, R.T., et al., *Performance of U_3Si_2 in an LWR following a cladding breach during normal operation.* Journal of Nuclear Materials, 2020. **539**: p. 152263.
16. Goddard, D.T., et al., *Progress in the development of high density fuels for enhanced accident tolerance.* TOPFUEL REACTOR FUEL PERFORMANCE, 2018.
17. Lyons, P. and B. Crowell. *Development of light water reactor fuels with enhanced accident tolerance*. in *Report to Congress, United States Department of Energy*. 2015. Washington, DC.
18. Goldner, F. *Development strategy for advanced LWR fuels with enhanced accident tolerance*. in *Enhanced Accident Tolerant LWR Fuels National Metrics Workshop*. 2012. Germantown, MD.
19. Mohamad, A., et al., *3Y-TZP Toughened and Oxidation-resistant U3Si2 Composites for Accident Tolerant Fuels.* Journal of Nuclear Materials, 2021. **544**: p. 152691.
20. Mohamad, A., et al., *Aluminum-doped U_3Si_2 composite fuels with enhanced oxidation resistance.* Journal of Alloys and Compounds, 2020: p. 157319.
21. Turner, J. and T. Abram, *Steam performance of UB_2/U_3Si_2 composite fuel pellets, compared to U_3Si_2 reference behaviour.* Journal of Nuclear Materials, 2020. **529**: p. 151919.
22. Gong, B., et al., *Cr Doped U_3Si_2 Composite Fuels under Steam Corrosion.* Corrosion Science, 2020: p. 109001.
23. Turner, J., S. Middleburgh, and T. Abram, *A high density composite fuel with integrated burnable absorber: U3Si2-UB2.* Journal of Nuclear Materials, 2020. **529**: p. 151891.
24. Sooby Wood, E., et al., *High Temperature Steam Oxidation Dynamics of U3Si2 with Alloying Additions: Al, Cr, and Y.* Journal of Nuclear Materials, 2020. **533**: p. 152072.
25. Sooby Wood, E., J.T. White, and A.T. Nelson, *The effect of aluminum additions on the oxidation resistance of U3Si2.* Journal of Nuclear Materials, 2017. **489**: p. 84-90.
26. Lopes, D.A., S. Uygur, and K. Johnson, *Degradation of UN and UN–U_3Si_2 pellets in steam environment.* Journal of Nuclear Science and Technology, 2017. **54**(4): p. 405-413.
27. Gonzales, A., et al., *Challenges and opportunities to alloyed and composite fuel architectures to mitigate high uranium density fuel oxidation: uranium silicide.* Journal of Nuclear Materials, 2021. **533**: p. 153026.
28. Watkins, J.K., et al., *Challenges and Opportunities to Alloyed and Composite Fuel Architectures to Mitigate High Uranium Density Fuel Oxidation: Uranium Mononitride.* Journal of Nuclear Materials, 2021. **553**(153048).
29. Arborelius, J., et al., *Advanced doped UO2 pellets in LWR applications.* Journal of Nuclear Science and Technology, 2006. **43**(9): p. 967-976.
30. Youinou, G.J. and R.S. Sen, *Impact of accidnet-tolerant fuels and claddings on the overall fuesl cycle: A preliminary systems analysis.* Nuclear Technology, 2014. **188**(2): p. 123-138.
31. Carmack, J., *Update on U.S. Accident Tolerant Fuel Program Nuclear Regulatory Commission Briefing*. 2016.
32. Cappia, F. and J.M. Harp, *Postirradiation examinations of low burnup U_3Si_2 fuel for light water reactor applications.* Journal of Nuclear Materials, 2019. **518**: p. 62-79.
33. Shah, H., et al., *Westinghouse-Exelon EnCore® Fuel Lead Test Rod (LTR) Program including Coated cladding Development and Advanced Pellets.* Top Fuel Proceedings, 2018: p. 1-9.
34. Tang, C., et al., *Protective coatings on zirconium-based alloys as accident tolerant fuel (ATF) claddings.* Corrosion Review, 2017. **35**(3): p. 141-165.
35. Gamble, K.A., et al., *ATF material model development and validation for priority fuel concepts*. 2019, Idaho National Lab.(INL), Idaho Falls, ID (United States).
36. Killeen, J.C., *Fission gas release and swelling in UO2 doped with Cr2O3.* Journal of Nuclear Materials, 1980. **88**(2-3): p. 177-184.
37. Tsuji, T., et al., *Oxygen potential, electrical conductivity and defect structure of titanium-doped uranium dioxide.* Journal of Nuclear Materials, 1989. **168**(1-2): p. 151-156.

38. Raynaud, P.A.C., *Fuel Fragmentation, Relocation and Dispersal during the Loss-of-Coolant Accident*. 2012, U.S.NRC.
39. *Very High Burn-ups in Light Water Reactors* OECD-Nuclear Energy Agency Report, 2006. **ISBN 92-64-02303-8**
40. Dell, R.M., V.J. Wheeler, and N.J. Bridger, *Hydrolysis of uranium mononitride.* Transactions of the Faraday Society, 1967. **63**(533P): p. 1286-1294.
41. Jolkkonen, M., et al., *Uranium nitride fuels in superheated steam.* Journal of Nuclear Science and Technology, 2017. **54**(5): p. 513-519.
42. Watkins, J.K., D.P. Butt, and B.J. Jaques, *Microstructural degradation of UN and UN-UO_2 composites in hydrothermal oxidation conditions.* Journal of Nuclear Materials, 2019. **518**: p. 30-40.
43. Lopes, D.A., S. Uygur, and K. Johnson, *Degradation of UN and UN-U3Si2 pellets in steam environment.* Journal of Nuclear Science and Technology, 2017. **54**(4): p. 405-413.
44. Rao, G.A.R., et al., *Oxidation and hydrolysis kinetic studies on UN.* Journal of Nuclear Materials, 1991. **185**(2): p. 231-241.
45. Sugihara, S. and S. Imoto, *Hydrolysis of uranium nitrides.* Journal of Nuclear Science and Technology-Tokyo, 1969. **6**(5): p. 237.
46. Outotec, *HSC Chemistry 9, Version 9.6.1*. 2019: Espoo, Finland.
47. Guéneau, C. and e. al, *TAF-ID.* Calphad, 2021. **72**.
48. Olander, D., *Oxidation of UO2 by High-Pressure Steam.* Nuclear Technology, 1986. **74**(2): p. 215-217.
49. Arai, Y., *3.02 - Nitride Fuel A2 - Konings, Rudy J.M*, in *Comprehensive Nuclear Materials*. 2012, Elsevier: Oxford. p. 41-54.
50. Kane, K., et al., *Air oxidation of yttrium hydride as a high temperature moderator for thermal neutron spectrum fission reactors.* Journal of Nuclear Materials, 2021. **Submitted**
51. Wood, E.S., K. Terrani, and A. Nelson, *Sensitivity of measured steam oxidation kinetics to atmospheric control and impurities.* Journal of Nuclear Materials, 2016. **477**: p. 228-233.
52. Mallard, P.J.L.a.W.G., *NIST Mass Spectrometry Data Center*, N.S.R.D.N. 69, Editor. 2014.
53. Sugihara, S. and S. Imoto, *Hydrolysis of Uranium Nitrides.* Journal of Nuclear Science and Technology, 1969. **6**(5): p. 237-242.
54. Dell, R.M., V.J. Wheeler, and N.J. Bridger, *Hydrolysis of uranium mononitride.* Transactions of the Faraday Society, 1967. **63**(0): p. 1286-1294.
55. Kulyukhin, S.A., et al., *Gas-Phase Volume Oxidation of Uranium Mononitride.* Radiochemistry, 2019. **61**(2): p. 146-155.
56. Rogozkin, B.D., N.M. Stepennova, and A.A. Proshkin, *Mononitride Fuel for Fast Reactors.* Atomic Energy, 2003. **95**(3): p. 624-636.
57. Sooby Wood, E., J. Vandegrift, and B.J. Jaques, *Steam Oxidation in Accident Conditions*, in *Reference Module in Materials Science and Materials Engineering*, R. Stoller and B.A. Pint, Editors. 2020.
58. Wood, E.S., et al., *U_3Si_2 behavior in H_2O: Part I, flowing steam and the effect of hydrogen.* Journal of Nuclear Materials, 2018. **501**: p. 404-412.
59. Middleburg, S.C., et al., *Solution of hydrogen in accident tolerant fuel candidate material: U3Si2.* Journal of Nuclear Materials, 2018. **501**(234-237).
60. Mašková, S., K. Miliyanchuk, and L. Havela, *Hydrogen absorption in U_3Si_2 and its impact on electronic properties.* Journal of Nuclear Materials, 2017. **487**: p. 418-423.
61. White, A. and W. Melville, *THE DECOMPOSITION OF AMMONIA AT HIGH TEMPERATURES.* Journal of the American Ceramic Society, 1905. **27**(4): p. 373-386.

62. Ojelade, O.A. and S.F. Zaman, *Decomposition for Hydrogen Production: A Thermodynamic Study.* Chemical Papers, 2021. **75**(57-65).
63. Valdivieso, F., et al., *Reduction of Uranium Oxide U3O8 into Uranium Dioxide UO2 by Ammonia.* Solid State Ionics, 2001. **141-142**(117-122).
64. Parkison, A.J. and A.T. Nelson, *Hydrogen measurement during steam oxidation using coupled thermogravimetric analysis and quadrupole mass spectrometry.* Measurement, 2016. **82**: p. 391-402.
65. Mcclellan, K.J., *FY2014 Ceramic Fuels Development Annual Highlights*. 2014, Los Alamos National Lab.(LANL), Los Alamos, NM (United States).
66. Kim, Y.S., *3.14 - Uranium Intermetallic Fuels (U–Al, U–Si, U–Mo)*, in *Comprehensive Nuclear Materials*, R.J.M. Konings, Editor. 2012, Elsevier: Oxford. p. 391-422.
67. White, J.T., et al., *Thermophysical Properties of U3si2 to 1773K.* Journal of Nuclear Materials, 2015. **464**: p. 275-280.
68. White, J.T. and D.D. Byler, *Report on the basic chemistry, microstructure and physical properties of high uranium density boride compounds*. 2015, Los Alamos National Laboratory: Los Alamos, NM.
69. De Coninck, R., W. Van Lierde, and A. Gijs, *Uranium carbide: Thermal diffusivity, thermal conductivity and spectral emissivity at high temperatures.* Journal of Nuclear Materials, 1975. **57**(1): p. 69-76.
70. Fink, J.K., *Thermophysical properties of uranium dioxide.* Journal of Nuclear Materials, 2000. **279**(1): p. 1-18.
71. Hayes, S.L., J.K. Thomas, and K.L. Peddicord, *Material property correlations for uranium mononitride: III. Transport properties.* Journal of Nuclear Materials, 1990. **171**(2): p. 289-299.
72. Okamoto, H., *B-U (Boron-Uranium)*, in *Binary Alloy Phase Diagrams*, T.B. Massalski, Editor. 1990, ASM International. p. 551-552.
73. Nunez, U.C., et al., *Melting point determination of uranium nitride and uranium plutonium nitride: A laser heating study.* Journal of Nuclear Materials, 2014. **449**(1-3): p. 1-8.
74. Burns, D. and S. Johnson, *Nuclear Thermal Propulsion Reactor Materials*, in *Nuclear Materials*. 2020, IntechOpen.

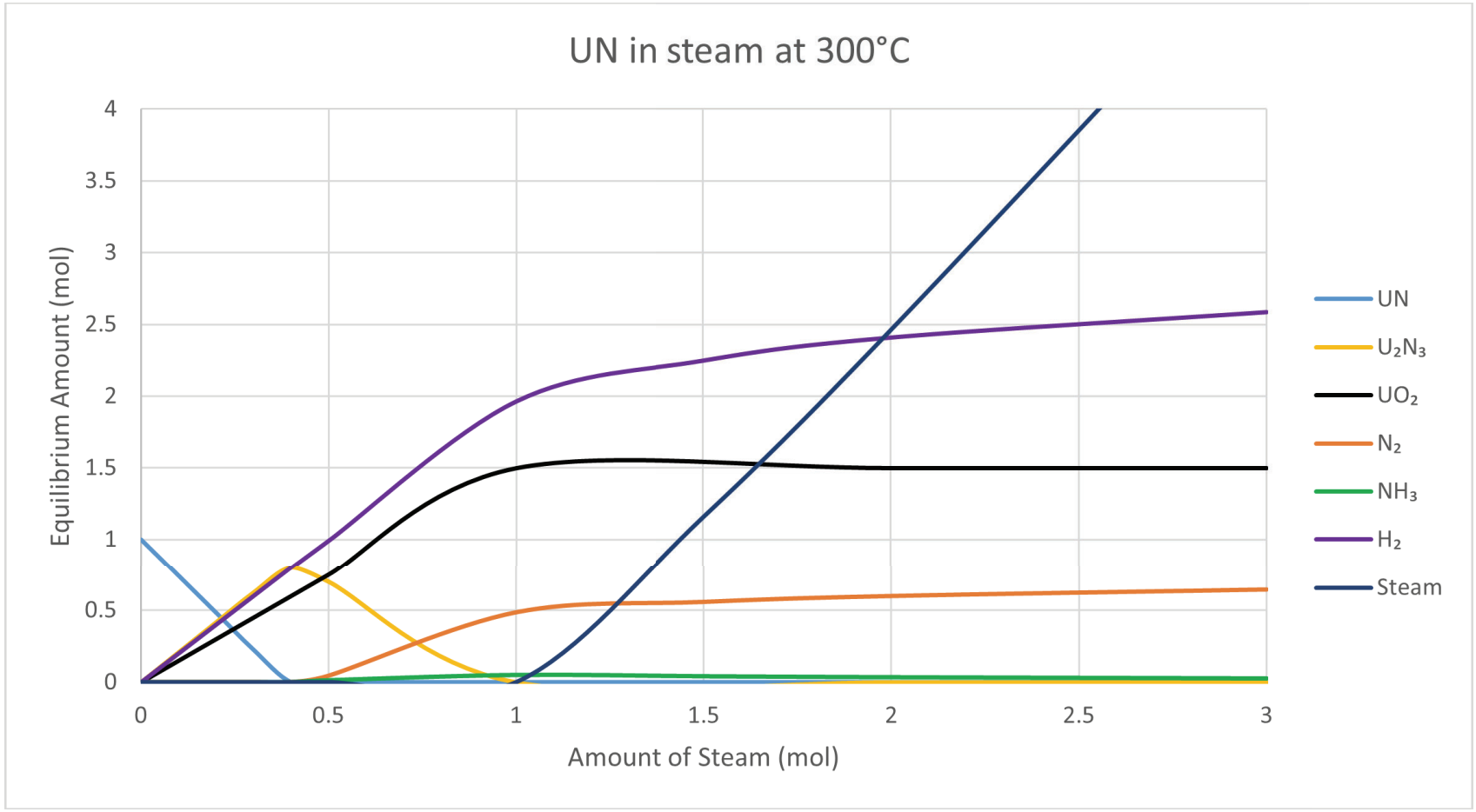

Figure 1: Equilibrium calculations made using ThermoCalc software and employing the TAF-ID database. The figure represents the reactants and products (plotted on the y-axis) for 1 mol UN exposed to increasing amounts of $H_2O(g)$ (x-axis). The software does not allow products to react with one another, which could explain the free $H_2(g)$ and $N_2(g)$ and low amount of predicted $NH_3(g)$ formation.

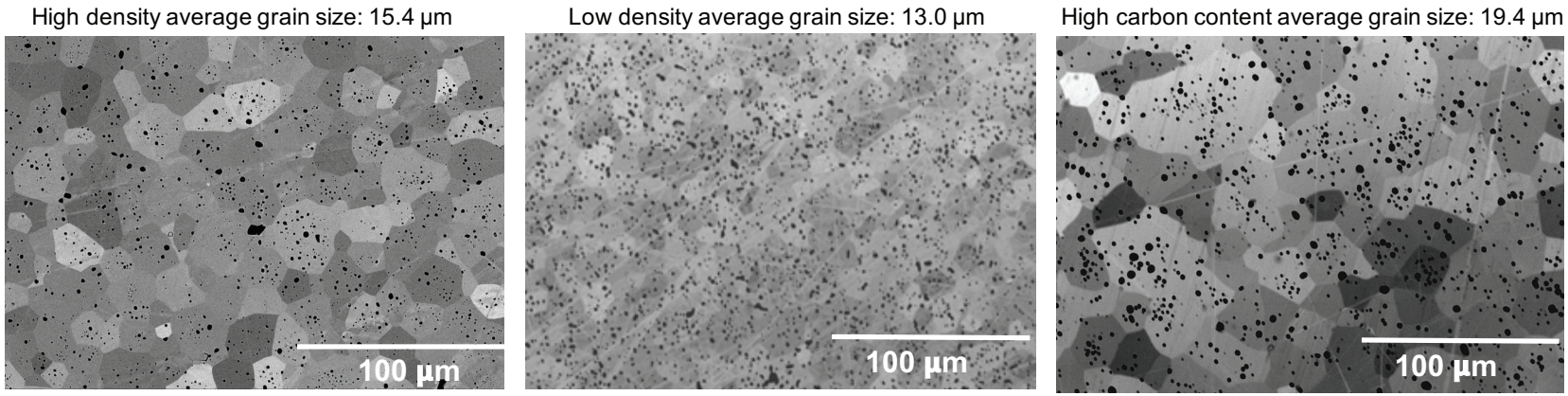

Figure 2: Characteristic micrographs of the three sample types tested in the present study. The high-density(left), with a geometric density of 94.5%, has an average grain size of 15.4 μm; the low-density sample (middle), with a geometric density of 92.0%, has an average grain size of 13μm; and finally, the high carbon sample (right), with a geometric density of 94.1%, has an average grain size of 19.4 μm.

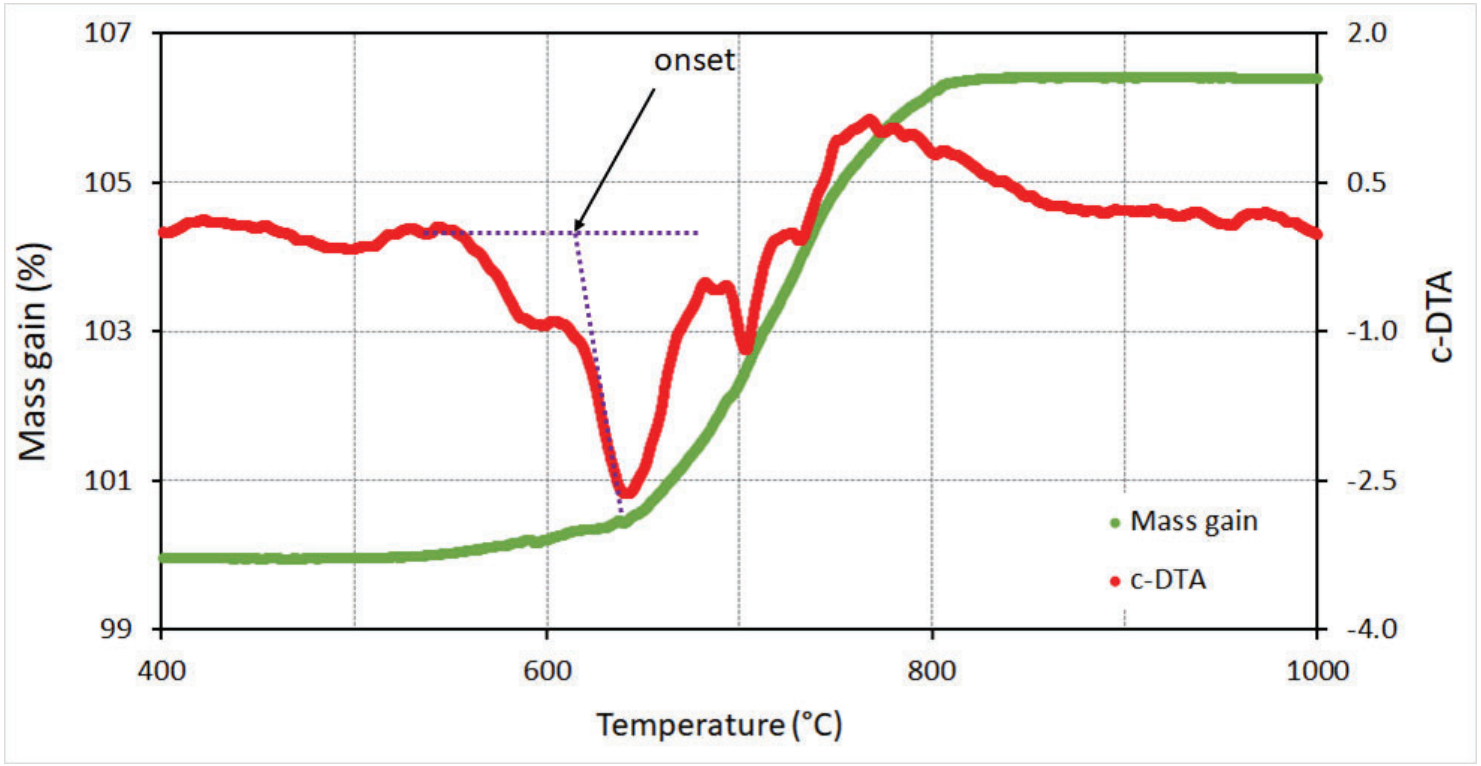

Figure 3: Example of c-DTA calculation for run #1 demonstrating how the onset for breakaway oxidation is calculated.

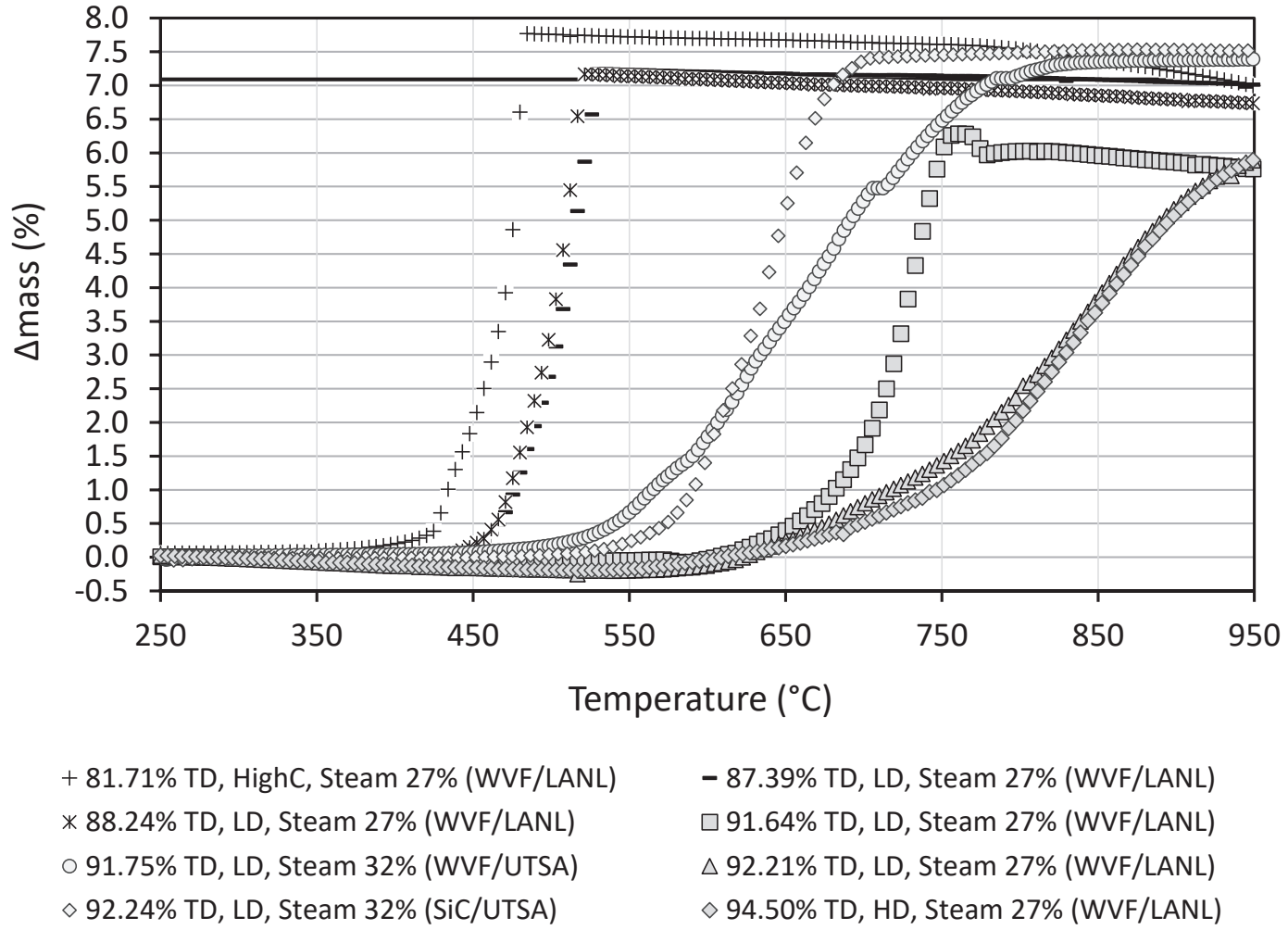

Figure 4: Thermal ramp data for all UN pellets tested at both LANL and UTSA in 27-32% steam. The solid line at 7.09% represents the theoretical terminal oxidation state for conversion to UO_2 in addition to volatile nitrogen species. 91.75% LD sample experienced spalling events at ~706 and 785°C, where 3.9 and 8.0 mg of UO_2 fell off the platform, respectively. Plotting data (circles) were normalized to improve clarity. (TD- Theoretical Density; LD- low density; HD-high density; WVF= conventional water vapor furnace; and SiC- high temperature water vapor adapted SiC element furnace).

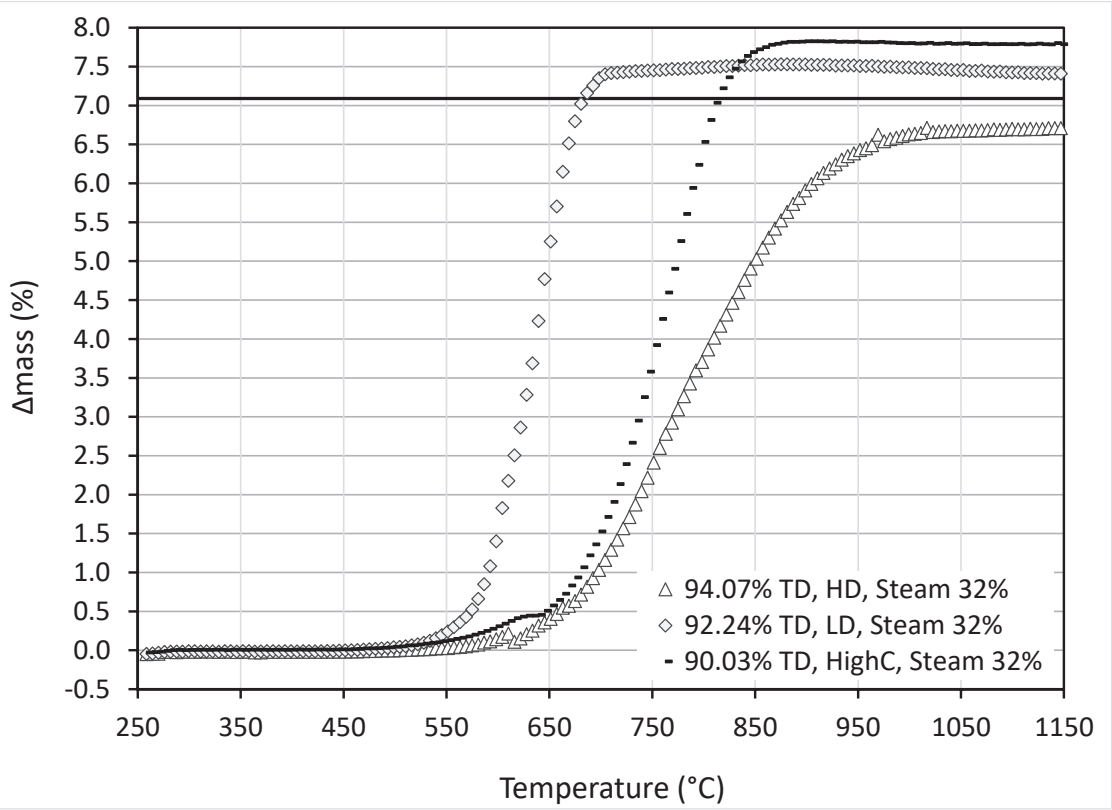

Figure 5: Mass gain demonstrated for varied sample types including high-density (HD), low-density (LD), and high carbon (highC) UN pellets at 32% steam atmosphere. The solid line at 7.09% represents the theoretical terminal oxidation state for conversion to UO_2 in addition to volatile nitrogen species. 94.07% HD sample experienced a spalling event at ~989°C, where 4.2 mg of UO_2 fell off the platform. Plotting data (triangles) were normalized to account for this event to improve clarity. (TD- Theoretical Density; LD- low density; HD-high density).

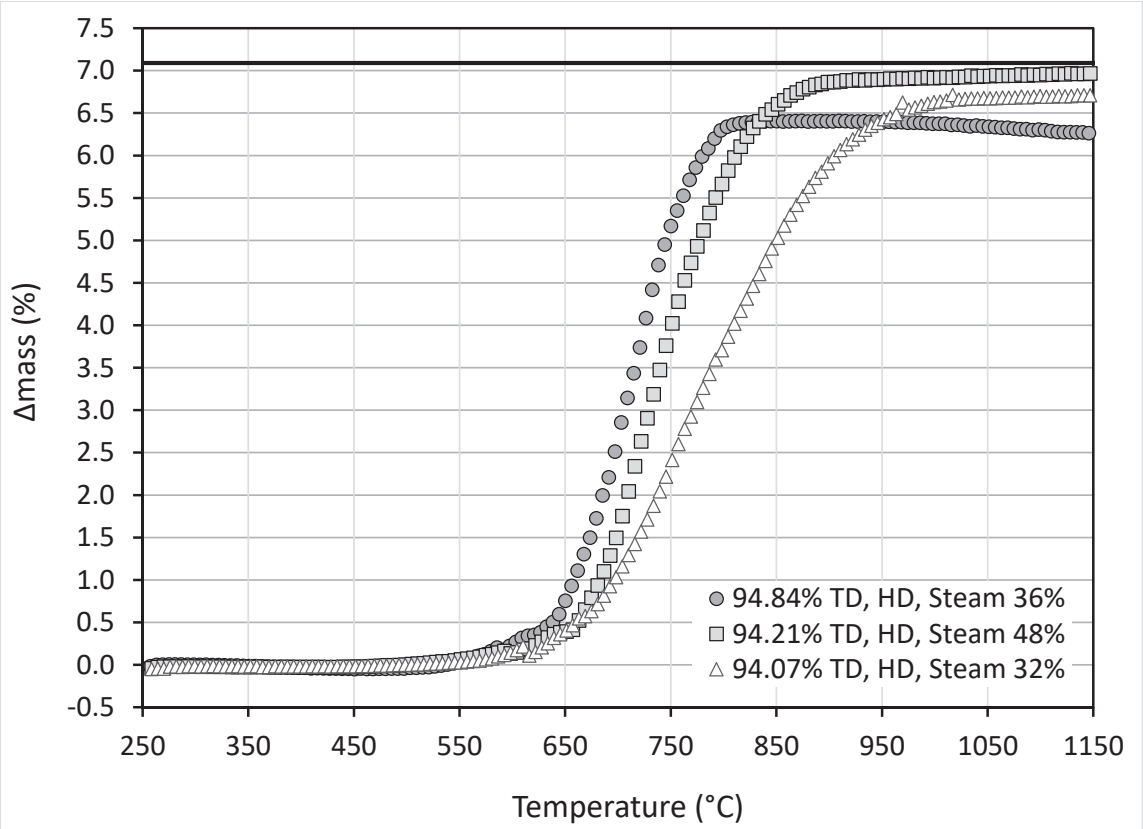

Figure 6: Mass gain demonstrated for similar density UN samples at three varied steam atmospheres. c-DTA onset temperatures were similar for each sample. The solid line at 7.09% represents the theoretical terminal oxidation state for conversion to UO_2 in addition to volatile nitrogen species. 94.07% HD sample experienced a spalling event at ~989°C, where 4.2 mg of UO_2 fell off the platform. Plotting data (triangles) were normalized to account for this event to improve clarity. (TD- Theoretical Density; HD-high density).

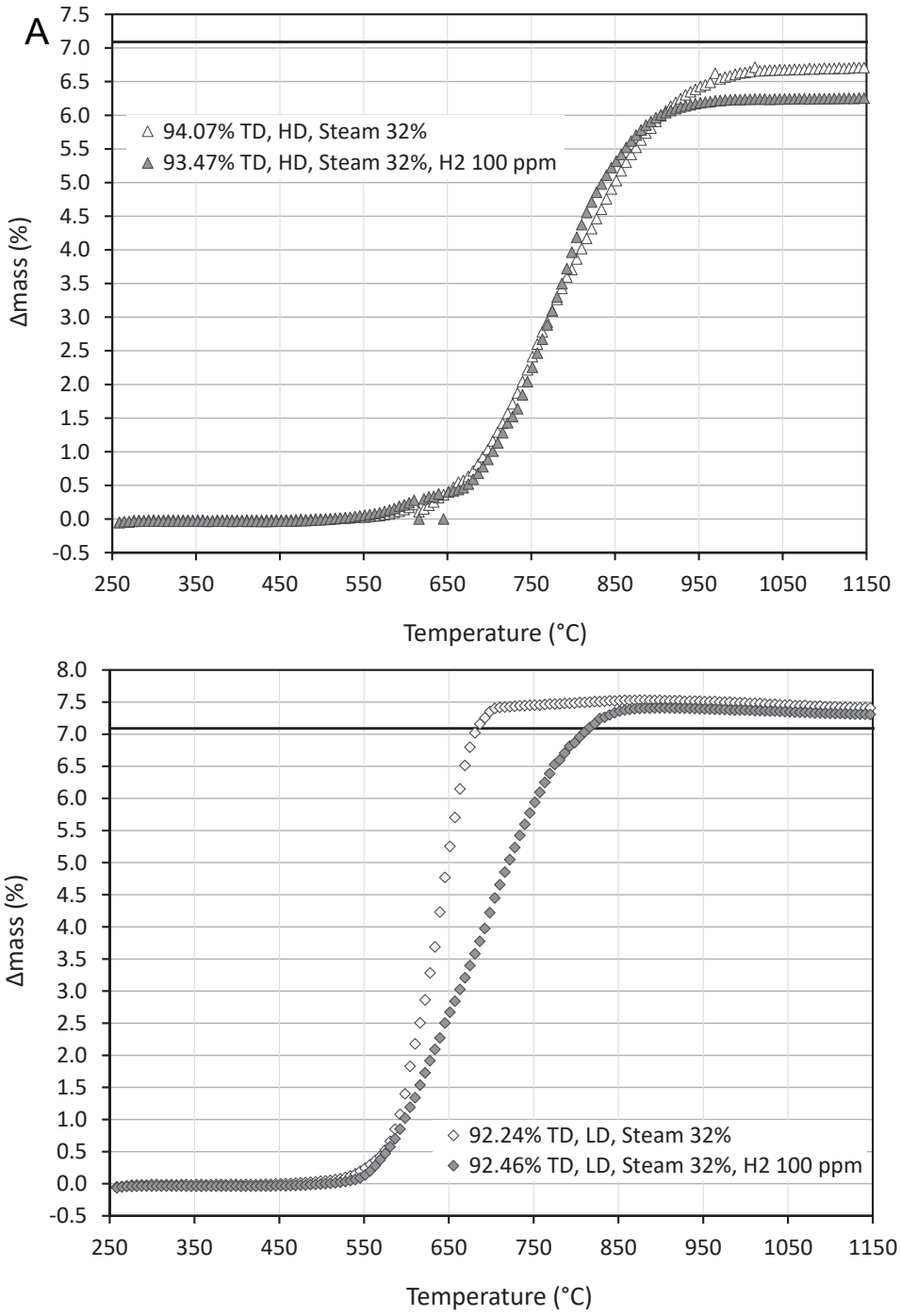

Figure 7: The effect of reducing steam is demonstrated with both (A) high-density (HD) and (B) low-density (LD) UN pellets during temperature ramp. Reducing steam extended time until terminal oxidation for the LD pellet relative to steam atmosphere. The solid line at 7.09% represents the theoretical terminal oxidation state for conversion to UO_2 in addition to volatile nitrogen species. 92.46% LD sample experienced spalling events at ~776 and 796°C, where 1.6 and 0.4 mg of UO_2 fell off the platform, respectively. 93.47% LD sample also experienced a spalling event at ~642°C, where 0.1 mg of UO_2 fell off the platform, respectively. Plotting data (filled-in diamonds and triangles) were normalized to improve clarity.

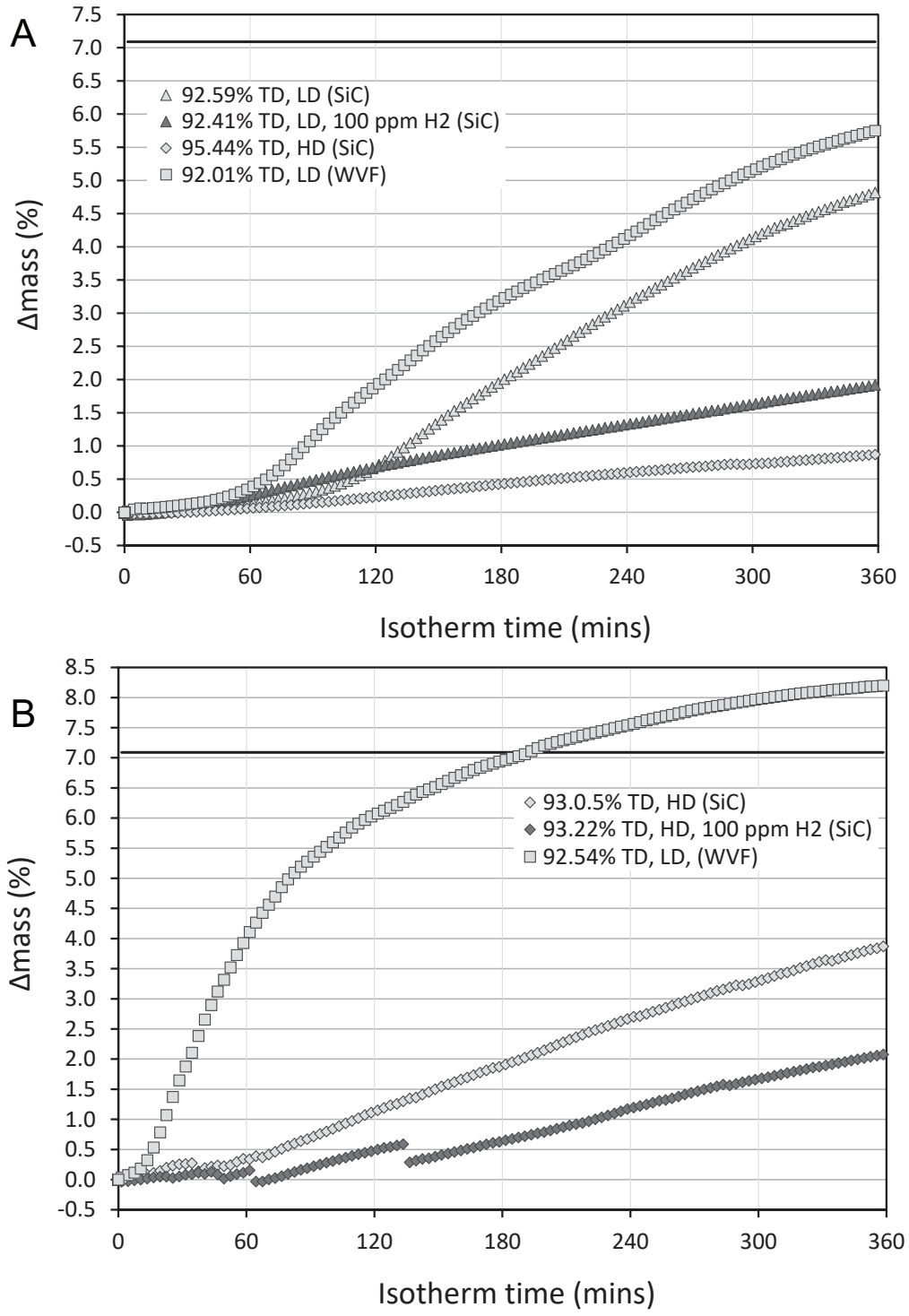

Figure 8: Thermogravimetric data for isothermal exposures of UN at both (A) 400°C and (B) 500°C for UN pellets during 6-hr isotherm tests. Reducing steam reduced mass gain for both cases. Spalling events were evident for the 500°C testing condition. The solid line at 7.09% represents the theoretical terminal oxidation state for conversion to UO_2 in addition to volatile nitrogen species. (TD- Theoretical Density; LD- low density; HD-high density).

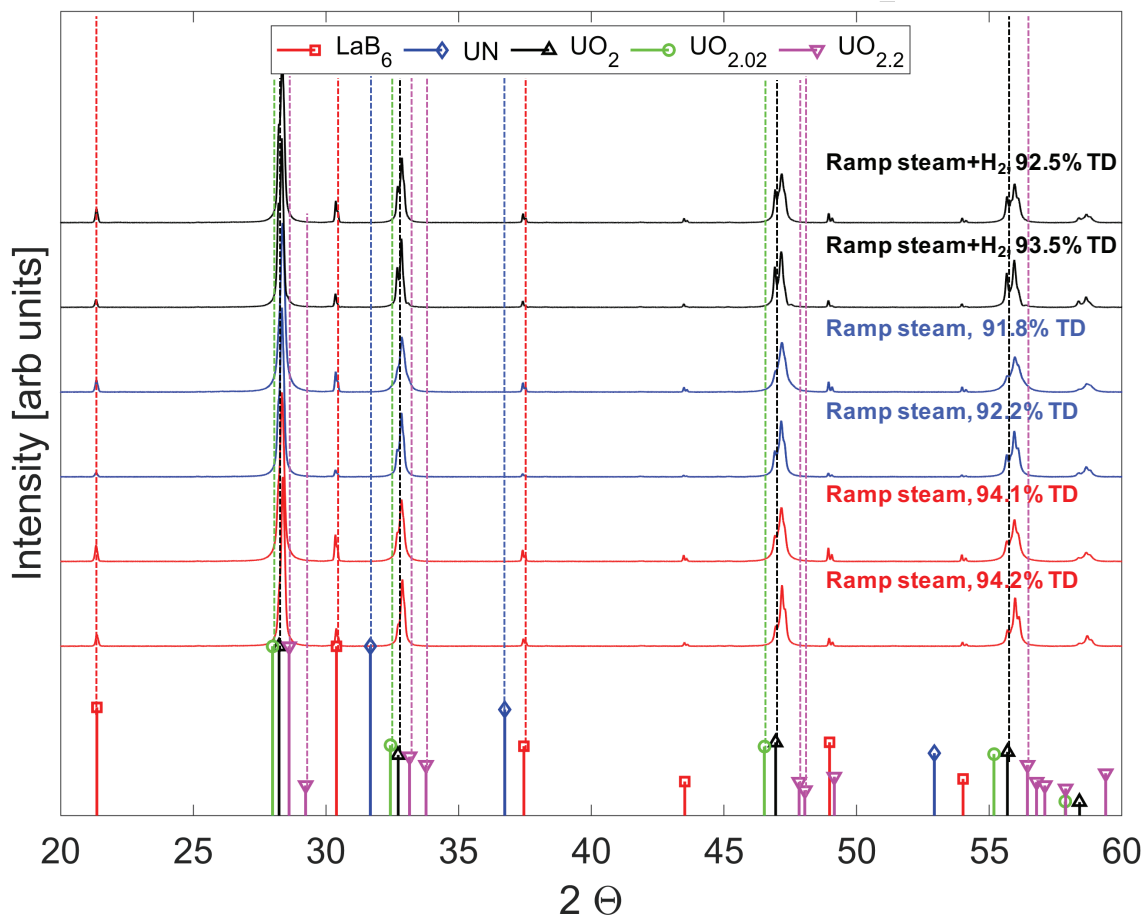

Figure 9: X-ray diffraction patterns for all UN pellets exposed to thermal ramp conditions compared to the accepted diffraction patterns for UO_2 (PDF 01-071-6416), UN (03-065-0329), and two UO_{2+x} stoichiometries ($UO_{2.2}$ PDF 00-047-1879 and $UO_{2.02}$ PDF 01-070-9082). A LaB_6 internal standard was used to enhance the analysis and comparison of the samples.

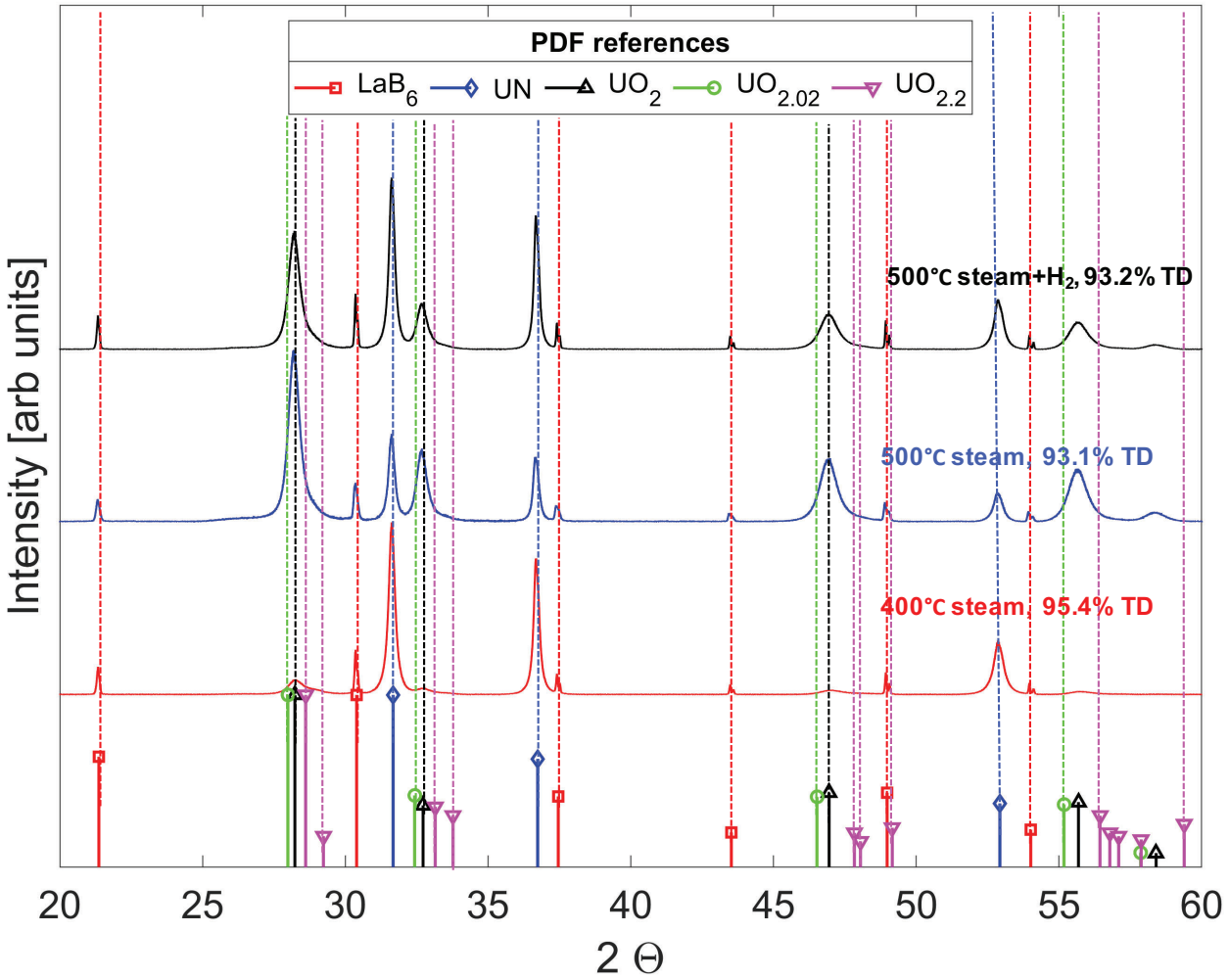

Figure 10: X-ray diffraction patterns for high-density UN pellets exposed to 6 hour isothermal steam conditions compared to the accepted diffraction patterns for UO_2 (PDF 01-071-6416), UN (03-065-0329), and two UO_{2+x} stoichiometries ($UO_{2.2}$ PDF 00-047-1879 and $UO_{2.02}$ PDF 01-070-9082) . A LaB_6 internal standard was used to enhance the analysis and comparison of the samples.

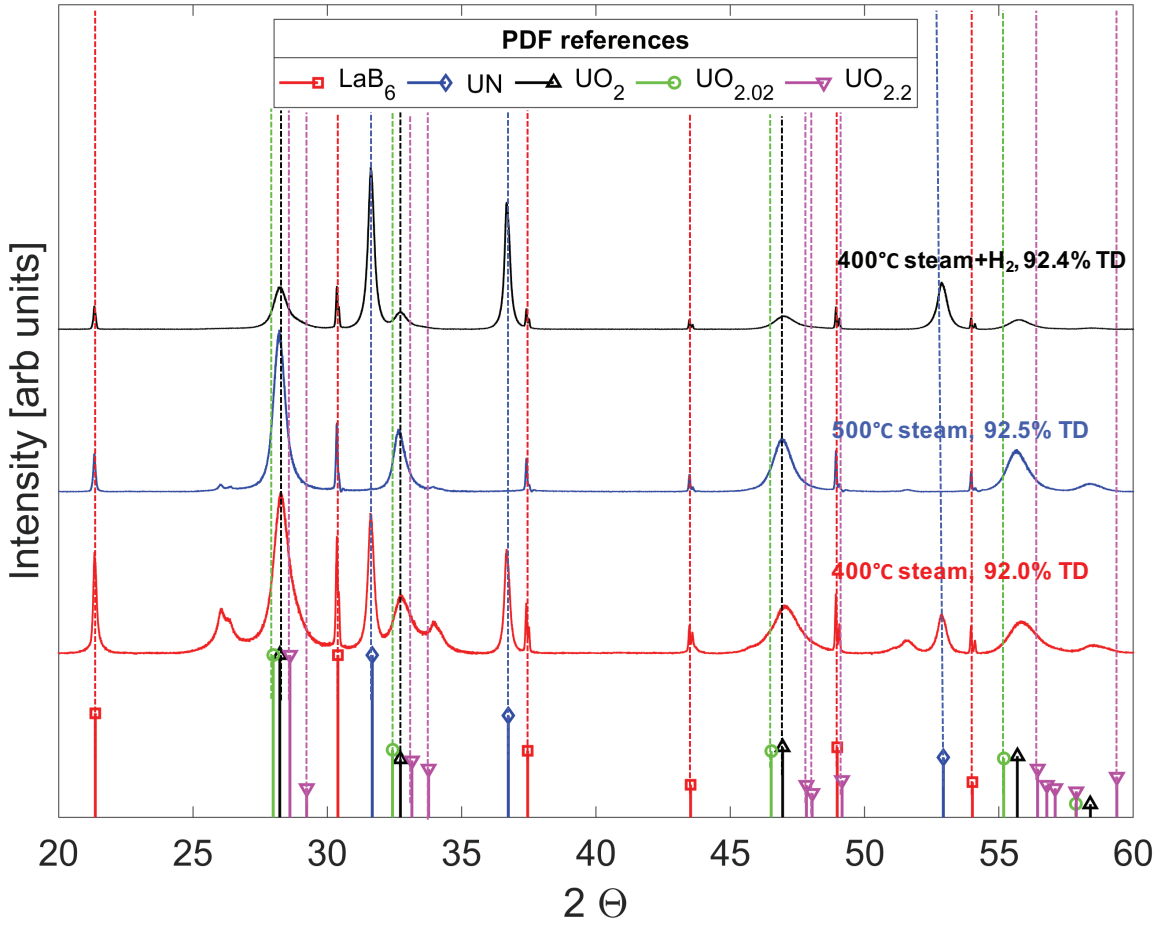

Figure 11: X-ray diffraction patterns for low density UN pellets exposed to 6 hour isothermal steam conditions compared to the accepted diffraction patterns for UO_2 (PDF 01-071-6416), UN (03-065-0329), and two UO_{2+x} stoichiometries ($UO_{2.2}$ PDF 00-047-1879 and $UO_{2.02}$ PDF 01-070-9082). A LaB_6 internal standard was used to enhance the analysis and comparison of the samples.

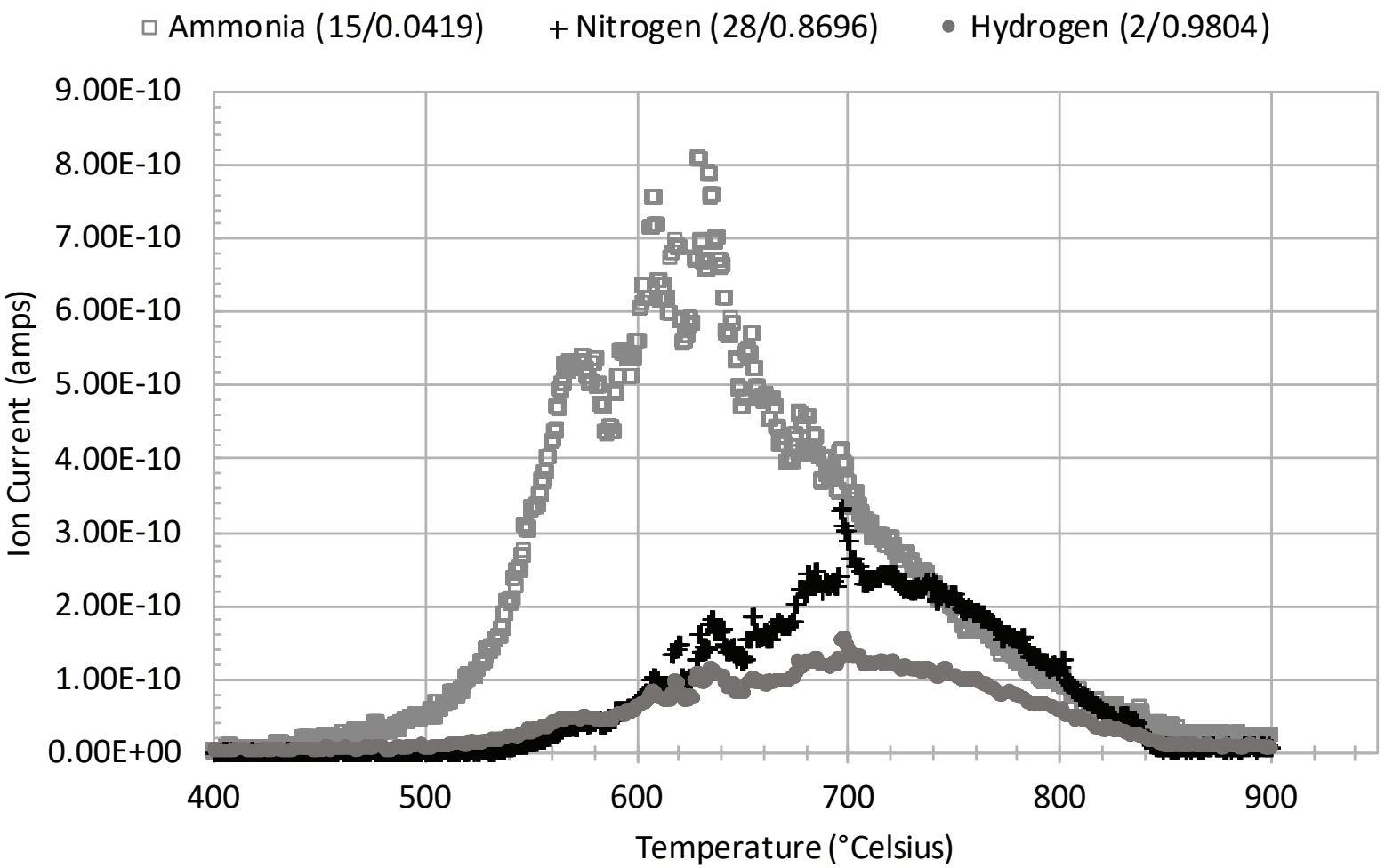

Figure 12: Corrected quadrupole mass spec. data for a low-density UN sample exposed to thermal ramp conditions to 1200°C in 32% steam, showing a higher ammonia abundance during the initial stages of oxidation with an increasing hydrogen and nitrogen signal in the later stages, with a peak in hydrogen and nitrogen production at 700°C.

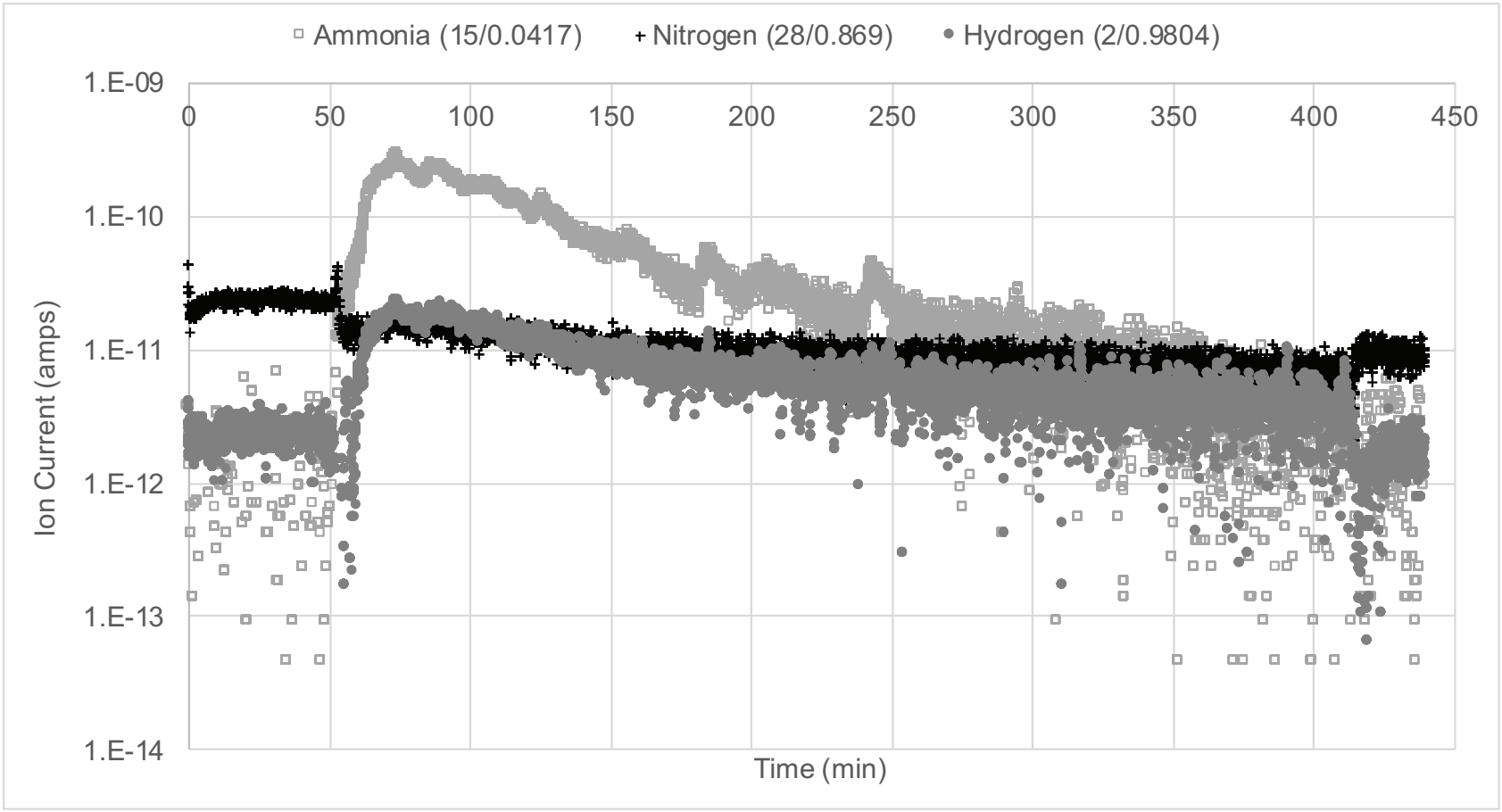

Figure 13: Quadrupole mass spectrometry data acquired during the 500 °C isothermal exposure of a UN pellet to steam. The steam is introduced to the sample around 53 minutes, when the increase in the hydrogen and ammonia signals is indicated. Note the logarithmic scale on the y-axis, indicating a >10 fold abundance of ammonia than hydrogen, and nearly no nitrogen measured above the baseline.

1
2 Table 1: Materials properties of select high uranium density fuels compared to UO_2 as reproduced from[28]

Material Properties	*UO_2*	*U_3Si_2*	*UB_2*	*UN*
Uranium density (g-U/cm^3)[30, 65, 66]	9.7	11.3	11.7	13.5
Thermal conductivity (W/m·K at 300°C)[67-71]	6.5 (95% TD)	14.7 (98% TD)	16.6 (80% TD)	16.6 (95% TD)
Melting temperature (°C)[30, 72-74]	2840	1665	2385	2847

1

2

Table 2. Summary of UN testing

Run #	Run type	Sample type	Theoretical Density (%)	Temp. (°C)	Isotherm time (hr)	Steam mol. fraction (%)	H_2 conc. (ppm)
1	Ramp	HD	94.84	1200	2	35.8	-
2	Ramp	HD	94.21	1200	2	47.9	-
3	Ramp	HD	94.07	1200	2	31.7	-
4	Ramp	LD	92.24	1200	2	31.7	-
5	Ramp	HighC	90.93	1200	2	31.7	-
6	Ramp	LD	92.46	1200	2	31.7	100
7	Ramp	HD	93.47	1200	2	31.7	100
8[a]	Ramp	HighC	93.95	1200	2	31.7	100
9	Isotherm	HD	93.05	500	6	31.7	-
10	Isotherm	HD	93.22	500	6	31.7	100
11	Isotherm	HD	95.44	400	6	31.7	-
12	Isotherm	LD	92.41	400	6	31.7	100
13	Isotherm	LD	92.59	400	6	31.7	-
14[b]	Isotherm	LD	92.54	1100	2	31.7	-
15[b]	Isotherm	LD	92.01	500	6	31.7	-
16[b]	Ramp	LD	91.75	400	6	31.7	-
17[c]	Ramp	LD	92.21	967	2	26.7	-
18[c]	Ramp	HighC	81.71	1000	2	26.7	-
19[c]	Ramp	LD	91.65	1000	2	26.7	-
20[c]	Ramp	LD	87.39	1000	2	26.7	-
21[c]	Ramp	LD	88.24	1000	2	26.7	-
22[c]	Ramp	HD	94.70	1000	1	26.7	-

[a]Run was cancelled at 650°C during ramp due to large spalling events

[b]Run with water vapor furnace with exhaust analyzed by quadrupole mass spectrometer

[c]Run at LANL with water vapor furnace

Table 3. Temperature onsets for UN ramp testing

Run #	Sample type	Theoretical Density (%)	Run summary	Initial mass gain temp. (°C)	c-DTA onset temp. (°C)	End of onset temp. (°C)	Time at end of onset (min)	Δmass at end of onset (%)
1	HD	94.84	36% steam	423	614	809	57	6.71
2	HD	94.21	48% steam	439	626	910	67	6.94
3	HD	94.07	32% steam	427	640	1004	78	6.71
4	LD	92.24	32% steam	360	578	716	48	7.42
5	HighC	90.93	32% steam	440	597	903	67	7.83
6	LD	92.46	32% steam + H_2	396	549	883	65	7.40
7	HD	93.47	32% steam + H_2	440	650	995	77	6.39
8[a]	HighC	93.95	32% steam + H_2	450	597	-	-	-
16[b]	LD	91.75	32% steam	378	550	842	60	7.34
17[c]	LD	92.21	27% steam	609	630	971	90	5.99
18[c]	HighC	81.71	27% steam	347	433	482	41	7.75
19[c]	LD	91.65	27% steam	579	705	789	72	6.04
20[c]	LD	87.39	27% steam	390	472	519	45	7.25
21[c]	LD	88.24	27% steam	409	475	518	46	7.17
22[c]	HD	94.70	27% steam	562	749	987	106	6.19

[a]Run was cancelled at 650°C during ramp due to large spalling events

[b]Run with water vapor furnace with exhaust analyzed by quadrupole mass spectrometer

[c]Run at LANL with water vapor furnace

Table 4. Isotherm mass gain summary

#	Sample type	Theoretical Density (%)	Run summary	Slope fragments	Slope (mg cm^{-2} min^{-1})	Slope Error (mg cm^{-2} min^{-1})	Δmass (%)
9	HD	93.05	32% steam at 500°C	8	1.1×10^{-1}	1.9×10^{-3}	3.88
10	HD	93.22	32% steam + H_2 at 500°C	5	7.7×10^{-2}	3.8×10^{-4}	2.07
11	HD	95.44	32% steam at 400°C	3	2.6×10^{-2}	1.0×10^{-4}	0.87
12	LD	92.41	32% steam + H_2 at 400°C	1	4.8×10^{-2}	2.3×10^{-5}	1.93
13	LD	92.59	32% steam at 400°C	1	1.4×10^{-1}	1.5×10^{-4}	4.83
14[a, b]	LD	92.54	32% steam at 500°C	1	ln 8.7 X 10^{-1}	1.6×10^{-3}	8.20
15[b]	LD	92.01	32% steam at 400°C	1	1.6×10^{-1}	1.2×10^{-4}	5.76

[a]curve fit with logarithmic instead of linear model

[b]Run with water vapor furnace with exhaust analyzed by quadrupole mass spectrometer

1
2

Steam Oxidation Performance of Uranium Mononitride during Thermal Ramp and Isothermal Conditions

Elizabeth S. Sooby,* Brian A. Brigham, Geronimo Robles, Zachary Acosta, and Joshua T. White

**Extreme Environments Materials Laboratory, Department of Physics and Astronomy, University of Texas at San Antonio, One UTSA Circle, San Antonio, TX, 78249, Elizabeth.soobywood@utsa.edu*

dx.doi.org/10.13182/T124-35144

INTRODUCTION

In an effort to advance the current light water reactor fuel technology, to provide both enhanced fuel economy and safety margins, researchers have looked to the implementation of high uranium density fuel compounds to replace conventional UO_2 [1-7]. The high uranium density fuels being considered (UN, UB_2, U_3Si_2 and their composites) provide the desired increased fuel economy and enhanced thermal conductivity, however an identified limitation of each of these compounds, hindering the qualification efforts of these fuels, is the reaction with pressurized water and/or steam [8-11]. Several efforts are ongoing to increase the oxidation resistance of high uranium density fuels, and while many alloying and composite architectures have been considered [12-15], modifications to fabrication techniques have also been shown to increase oxidation performance [16-18].

Uranium mononitride in particular has the highest uranium density of the high uranium density compounds considered, (13.5 g-U/cm^3), in addition to a high melt point (2762 °C). Experimental work on the hydrothermal oxidation performance of UN is limited. Unlike U_3Si_2, onsets of reaction and the thermodynamics of oxidation for UN have yet to be fully elucidated. The work presented here are the preliminary results of a set of steam oxidation experiments aimed to:

- identify the onset of steam oxidation reaction in high purity, high density UN,
- measure the volatile oxidation products produced during steam exposure, and
- assess the impact of a reducing steam (H_2O(g) + ppm levels of H_2) on the reaction dynamics.

BACKGROUND

The objectives of the presented work are to not only determine the kinetics of UN steam oxidation but also to measure and quantify the gaseous byproducts produced during steam exposure, to further inform the thermodynamics of UN hydrothermal corrosion, and to better understand the degradation mechanisms of this high uranium density fuel to water corrosion. Though little data is available on the dynamic behavior of UN exposed to thermal ramp conditions, there are a number of studies which present the degradation mechanisms of UN to hydrothermal corrosion. Based on the work by Watkins *et al.,* the failure mechanisms of UN exhibited during steam oxidation proceeds primarily through grain boundary attack, resulting in boundary expansion and spallation [19]. Oxide spallation results in premature mechanical failure of the fuel. In the aforementioned experiments, UN pellets were thermally ramped to 350 °C under ultra-high purity (UHP) argon and exposed to steam atmospheres at temperature, with results confirmed by backscattered SEM imaging. It was noted that fuel performance was improved by minimizing both pore density and oxide contamination from fabrication [19-21]. Furthermore, work performed by Rao *et al*. investigated the kinetics of UN hydrolysis in microspheres. Results found that there were two main kinetic regimes dependent on UO_2 contamination [22]. In cases where UO_2 contamination was below 10%, UO_2 growth proceeded via fast surface nucleation. If UO_2 content was greater than 10%, growth proceeded through fast bulk nucleation at the UO_2 site. The same study also found that the rate controlling process was the diffusion of nitrogen out of the microsphere without a proposed mechanism as to why [22].

In support of the presented investigation, the authors present a preliminary thermodynamic assessment in which HSC Chemistry 9 software is utilized and informed by previous studies to obtain a thermodynamic assessment of the progression of the water reaction with UN. The "Reaction Equations" module within HSC calculates several values in the Gibbs free energy equation [23]. The values are derived mathematically using an internal database of thermodynamic values. It is generally agreed that one of the two primary hydrolysis reactions of UN proceed by Equation (1) (with $\Delta G_{rxn}^{600°C} = 366.866$ kJ) below and product gases are NH_3(g) and H_2(g) [19, 21, 22]

$$2UN + 4H_2O(g) \leftrightarrow 2UO_2 + 2NH_3(g) + H_2(g) \quad (1)$$

However, a discrepancy has been noted within the HSC software. At 600 °C it can be noted that the Gibbs free energy of Equation 2 is approximately 500 kJ more favorable when normalized per mole of UN ($\Delta G_{rxn}^{600°C} = -621.399$ kJ).

$$2UN + 4H_2O(g) \leftrightarrow 2UO_2 + 4H_2(g) + N_2(g) \quad (2)$$

While this reaction equation does not produce the gases observed in previous experimental studies, it can be proposed that the gas formation proceeds through the more favorable thermodynamic route of Equation 3 ($\Delta G_{rxn}^{600°C} = -2435.191$ kJ) once the reaction described by (2) has progressed.

$2UN+4H_2O(g) + ¼N_2(g) \leftrightarrow 5/2NH_3(g) + 2UO_2 + ¼ H_2(g)$ (3)

This hypothesis can be supported from previous literature that notes there is a dependence on the rate of hydrolysis linked to $N_2(g)$ flow from the sample [21, 22]. The secondary hydrolysis equation of UN is detailed in the remaining reaction equations below [19, 21, 24]

$3UN + 2H_2O(g) \leftrightarrow UO_2 + U_2N_3 + 2H_2(g)$ (4)

$U_2N_3 + 4H_2O(g) \leftrightarrow 2UO_2 + 8/3\ NH_3(g) + 1/6\ N_2(g)$ (5)

It can be assumed that both Equation 1 and 4 ($\Delta G_{rxn}^{600°C}$ = -401.234 kJ) are occurring simultaneously on the surface of UN in high temperature steam environments. Any exposed uranium sesquinitride is hydrolyzed further to UO_2 by Equation 5 ($\Delta G_{rxn}^{600°C}$ = -2016.848 kJ). This leads to a scenario where a layer of U_2N_3 is located between the surface UO_2 and remaining bulk UN [24].

The study presented here will use a variety of experimental techniques, including thermogravimetric analysis, mass spectrometry, electron microscopy and x-ray diffraction, to further probe the reaction between UN and steam.

EXPERIMENTAL METHODS

UN samples tested here were produced by the CTR-N method [25] and compacted to cylindrical geometries using traditional powder metallurgy. Two UN powder lots were used with 100wppm and 4000wppm C impurities to fabricate the pellets. All powder processing and sintering was conducted within a high purity Ar glove box line maintained below 30ppm O2. Sintering of the compacts as performed in a W-mesh element furnace to a maximum temperature of 2200°C. Density values were determined using the immersion density method. Impurity levels for O and C were determined using the inert gas fusion technique and combustion infrared method on both powder and sintered pellets. The samples measured 90-94.2% theoretical density with diameters measuring 3.5-5.0 mm. A micrograph acquired on a Hitachi FlexSEM 1000 using a backscatter electron detector is displayed in Fig. 1. Using ImageJ, a simple grain intercept technique determined an average grain size of 15 µm.

Oxidation kinetics (e.g., Δmass, onset temperatures) of UN samples exposed to 75% flowing steam were quantified using a Netzsch F3 449 Jupiter simultaneous thermal analyzer (STA; Selb, Germany) paired with Netzsch 403 D Aëolos quadrupole mass spectrometer (QMS) at the furnace exhaust. UN samples were tested on an alumina platform within the STA water vapor furnace. The carrier and purge gas used for these experiments was UHP Ar which is further purified, or gettered for O_2 contamination, to sub ppm O_2 levels. Steam was generated by the Netzsch-supplied water vapor generator and introduced to the furnace via a heated (200°C), stainless steel, transfer line. Additional heaters (200°C) are utilized at the furnace inlet and collar to prevent condensation. A 2100 RapidOx (St. Ives, UK) paired with O_2 inlet and outlet sensors was used to monitor the system for O_2 contamination prior to and during oxidation testing. Onset temperatures were determined using Netzsch Proteus Software (v 8.0, 2019).

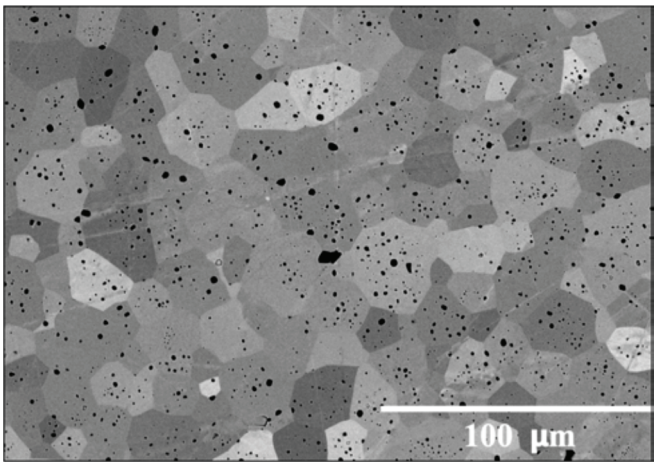

Fig. 1. Backscatter electron micrograph of characteristic UN sample received from LANL and tested in the presented study.

Oxidation kinetics (e.g., Δmass, onset temperatures) of UN samples exposed to 75% flowing steam were quantified using a Netzsch F3 449 Jupiter simultaneous thermal analyzer (STA; Selb, Germany) paired with Netzsch 403 D Aëolos quadrupole mass spectrometer (QMS) at the furnace exhaust. UN samples were tested on an alumina platform within the STA water vapor furnace. The carrier and purge gas used for these experiments was UHP Ar which is further purified, or gettered for O_2 contamination, to sub ppm O_2 levels. Steam was generated by the Netzsch-supplied water vapor generator and introduced to the furnace via a heated (200°C), stainless steel, transfer line. Additional heaters (200°C) are utilized at the furnace inlet and collar to prevent condensation. A 2100 RapidOx (St. Ives, UK) paired with O_2 inlet and outlet sensors was used to monitor the system for O_2 contamination prior to and during oxidation testing. Onset temperatures were determined using Netzsch Proteus Software (v 8.0, 2019).

During thermal ramp exposures, the furnace is brought to the test temperature under a flowing Ar atmosphere to 250 °C and held isothermally for 20 min under inert gas to allow the system to thermally stabilize. Following this 20 min hold, steam is introduced to the system during a ramp (10°C/min) from 250 °C to 1200 °C followed by a 2 hr isotherm. The molar percentage of steam in the system is engineered to be 75% for all runs presented. Following steam exposure,

samples were cooled under a flowing Ar atmosphere and reaction product material transferred to an inert, Ar atmosphere glove box (MBraun Uni-Lab Pro, pO_2 and pH_2O <0.1 ppm). Additional testing conditions to be presented at the annual meeting, but not presented in this extended abstract, include isothermal exposures at 100 °C increments from 300-1000 °C . Also, in future testing, volatile corrosion products expected from UN steam oxidation including, NH_3 (g), H_2(g), and N_2 (g), will be quantified to ascertain oxidation behavior using the QMS.

A Hitachi FlexSEM scanning electron microscope (SEM) was utilized to characterize UN samples both pre- and post- oxidation testing. Additionally, a Bruker D2 Phaser x-ray diffractometer was employed after each exposure to collect the diffraction patterns of the oxidation products formed during testing.

RESULTS

Consecutive thermal ramp exposures of UN in flowing steam have produced onsets of reaction at T>525 °C, shown in the characteristic thermogram in Fig. 2. The onset temperature measured is higher than those reported in previous investigations, where initial reaction to steam was observed at T<500 °C [26, 27]. The delay in onset is currently attributed to the high density and high purity.

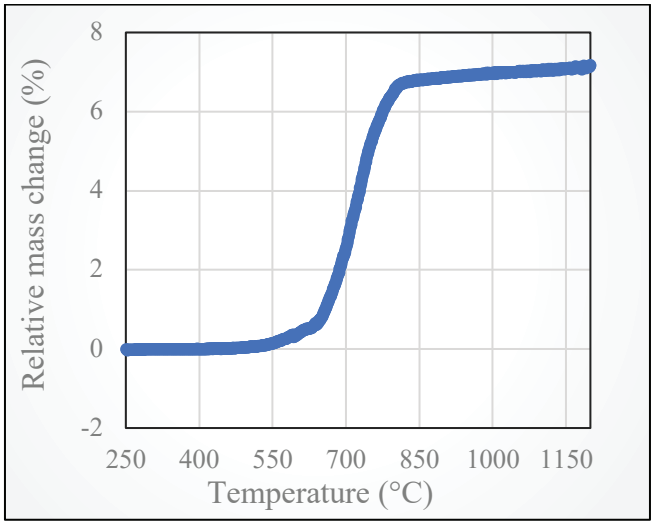

Fig. 2. Thermograph of UN sample exposed to 75% steam during a thermal ramp from 250-1200 °C at 10°C/min. Thermogram displays an onset of oxidation at T>525°C

Preliminary x-ray diffraction characterization of the post-oxidized reaction products indicate that the primary solid product is UO_2, though a shift in the peak locations to lower angle indicate that the product is likely off stoichiometric, UO_{2+x}. Further characterization of arrested sample exposures is necessary to determine the stoichiometry of the reaction products. Additionally, QMS analysis during steam exposure will enhance the interpretation of the reaction between UN and high temperature steam.

ACKNOWLEDGEMENTS

This material is based upon work supported by the Department of Energy under Award Number DE-NE0008824.

r This report was prepared as an account of work sponsored by an agency of the United States Government. Neither the United States Government nor any agency thereof, nor any of their employees, makes any warranty, express or implied, or assumes any legal liability or responsibility for the accuracy, completeness, or usefulness of any information, apparatus, product, or process disclosed, or represents that its use would not infringe privately owned rights. Reference herein to any specific commercial product, process, or service by trade name, trademark, manufacturer, or otherwise does not necessarily constitute or imply its endorsement, recommendation, or favoring by the United States Government or any agency thereof. The views and opinions of authors expressed herein do not necessarily state or reflect those of the United States Government or any agency thereof.

REFERENCES

1. GAMBLE, K.A., et al., *r n n n r r r C n* . 2019, Idaho National Lab.(INL), Idaho Falls, ID (United States).
2. HARP, J.M., P.A. LESSING, and R.E. HOGGAN, Uranium Silicide Pellet Fabrication by Powder Metallurgy for Accident Tolerant Fuel Evaluation and Irradiation. *rn r r* , **466**, 728-738, (2015).
3. JOHNSON, K.D., et al., Fabrication and Microstructural Analysis of Un-U3si2 Composites for Accident Tolerant Fuel Applications. *rn r r* , **477**, 18-23, (2016).
4. WILSON, T.L., et al., Uranium Nitride-Silicide Advanced Nuclear Fuel: Higher Efficiency and Greater Safety. *n n C r* , **117**, 76-81, (2018).
5. WOOD, E.S., et al., *n n r n*, in *n n r C r* . 2020, Elsevier. p. 371-418.
6. ZHOU, W. and W. ZHOU, Enhanced Thermal Conductivity Accident Tolerant Fuels for Improved Reactor Safety – a Comprehensive Review. *nn r n r* , **119**, 66-86, (2018).
7. ZINKLE, S.J., et al., Accident Tolerant Fuels for Lwrs: A Perspective. *rn r r* , **448**, , 374-379, (2014).
8. SWEET, R.T., et al., Performance of U_3Si_2 in an LWR Following a Cladding Breach During Normal

Operation. *rn r r* , **539**, 152263, (2020).
9. JOSSOU, E., et al., DFT+ U Study of the Adsorption and Dissociation of Water on Clean, Defective, and Oxygen-Covered U_3Si_2 {001},{110}, and {111} Surfaces. *rn C r C*, **123**, , 19453-19467, (2019).
10. SOOBY WOOD, E., et al., U3Si2 Behavior in H2o: Part I, Flowing Steam and the Effect of Hydrogen. *rn r r* , **501**, 404-412, (2018).
11. NELSON, A.T., et al., U3Si2 Behavior in H2O Environments: Part II, Pressurized Water with Controlled Redox Chemistry. *rn r r* , **500**, 81-89, (2018).
12. LI, N., et al., Oxide Morphology of a Fecral Alloy, Kanthal Apmt, Following Extended Aging in Air at 300-600°C. *r n r r n n* , **49**, , (2018).
13. SOOBY WOOD, E., et al., High Temperature Steam Oxidation Dynamics of U3Si2 with Alloying Additions: Al, Cr, and Y. *rn r r* , **533**, 152072 (2020).
14. SOOBY WOOD, E., J.T. WHITE, and A.T. NELSON, The Effect of Aluminum Additions on the Oxidation Resistance of U3Si2. *rn r r* , **489**, 84-90, (2017).
15. SOOBY WOOD, E., J.T. WHITE, and A.T. NELSON, The Synthesis and Air Oxidation Behavior of U-Si-Al and U-Si-B Compositions. *r n n r n r* , **TopFuel2016**, (2016).
16. GONG, B., et al., Cr Doped U3Si2 Composite Fuels under Steam Corrosion. *C rr n n* , 109001, (2020).
17. GONG, B., et al., U_3Si_2 and UO_2 Composites Densified by Spark Plasma Sintering for Accident-Tolerant Fuels. *rn r r* , **534**, 152147, (2020).
18. GONG, B., et al., Spark Plasma Sintering (SPS) Densified U_3Si_2 Pellets: Microstructure Control and Enhanced Mechanical and Oxidation Properties. *rn n C n* , 154022, (2020).
19. WATKINS, J.K., D.P. BUTT, and B.J. JAQUES, Microstructural Degradation of UN and UN-UO_2 Composites in Hydrothermal Oxidation Conditions. *rn r r* , **518**, 30-40, (2019).
20. LOPES, D.A., S. UYGUR, and K. JOHNSON, Degradation of UN and UN-U3Si2 Pellets in Steam Environment. *rn r n n n* , **54**, , 405-413, (2017).
21. JOLKKONEN, M., et al., Uranium Nitride Fuels in Superheated Steam. *rn r n n n* , **54**, , 513-519, (2017).
22. RAO, G.A.R., et al., Oxidation and Hydrolysis Kinetic Studies on UN. *rn r r* , **185**, , 231-241, (1991).
23. OUTOTEC, *C r r n 6* . 2019: Espoo, Finland.
24. SUGIHARA, S. and S. IMOTO, Hydrolysis of Uranium Nitrides. *rn r n n n* , **6**, , 237, (1969).
25. ARAI, Y., *0 r n n* , in *C r n r r* . 2012, Elsevier: Oxford. p. 41-54.
26. DELL, R.M., V.J. WHEELER, and N.J. BRIDGER, Hydrolysis of Uranium Mononitride. *r n n r* , **63**, , 1286-1294, (1967).
27. DELL, R.M., V.J. WHEELER, and E.J. MCIVER, Oxidation of Uranium Mononitride and Uranium Monocarbide. *r n n r* , **62**, , 3591 (1966).

Uranium nitride (UN) pellets with controllable microstructure and phases – fabrication by spark plasma sintering and their thermal-mechanical and oxidation properties

Kun Yang[1], Erofili Kardoulaki,[2] Dong Zhao,[1] Bowen Gong,[1] Andre Broussard,[1] Kathryn Metzger,[3]

Joshua T. White,[2] Michael R. Sivack,[3] Kenneth J. Mcclellan,[2] Edward J. Lahoda[3] and Jie Lian[1]

[1]Department of Mechanical, Aerospace and Nuclear Engineering, Rensselaer Polytechnic Institute

[2]Los Alamos National Laboratory

[3]Westinghouse Electric Company

* Corresponding author, Email: lianj@rpi.edu; Office: 518-276-6081; Fax: 518-276-6025

Abstract

Dense UN pellets with controlled microstructures and tailored grain size from large-grained to a few microns are synthesized by spark plasma sintering (SPS) combined with high energy ball milling. The impacts of the sintering conditions on fuel microstructure, grain size, physical density, and phase behavior are systematically investigated, and the thermal-mechanical properties and oxidation behavior of the SPS densified UN pellets are characterized. Higher sintering temperatures and longer ball milling durations and thus finer starting UN powders promote sintering and densification, and dense UN pellets above 95% theoretical density can be achieved by SPS at 1600 ^{o}C for 10 mins. UN phase purity is maintained in the SPS-densified pellets sintered at a lower temperature and short duration. A phase heterogeneity with secondary UO_2 or uranium sesquinitride U_2N_3 occurs for the UN pellets sintered at higher temperatures using finer UN powders. The hardness and fracture toughness of the SPS-densified UN pellets increase with smaller grain sizes and higher densities to 7.9 Gpa and 3.5 MPa $m^{1/2}$, respectively. Both small

(1-2 μm) and large grain-sized (30-50 μm) UN pellets exhibit good thermal conductivity, which is higher for the UN pellets with greater density. Dynamic oxidation testing by a TGA-DSC thermal analyzer in air shows that the onset temperature for oxidation varies with microstructure and phase heterogeneity of the SPS densified UN pellets. Particularly, the smaller-grained (micron-sized) UN pellets containing uranium oxides and U_2N_3 display lower weight gain and significantly-reduced oxidation kinetics, and full oxidation completes at a temperature above 900 ºC when tested with a ramp rate of 10 ºC/min.

1. Introduction

Uranium mononitride (UN) is a candidate fuel form for light water reactors with enhanced accident tolerance due to its high thermal conductivity and high fissile element density. The uranium density of UN is 13.55 g/cm^3 [1], significantly higher than UO_2 (9.75 g/cm^3) [2]. UN also has excellent thermal conductivity (e.g., 20.6 W/m-K for UN *vs.* 3.5 W/m-K for UO_2 at room temperature) [3-6]. Because of higher uranium density, light water reactors could be uprated up to 15% by adopting the UN fuel with smaller fuel assemblies compared to conventional UO_2 fuels [7]. UN has also been a candidate fuel form for liquid-metal-fast reactors. Specifically, the linear heat generation rate in the fuel elements of fast reactors can be as high as 42 kW/m [8] for the lead cooled fast reactor and 54 kW/m [9] for the sodium cooled fast reactor. The high thermal conductivity of UN can enable lower fuel temperatures and thus, large thermal safety margins under transient conditions [10,11]. UN is also favorable for the spent fuel reprocessing due to its ease of dissolution in nitric acid (HNO_3), making this fuel compatible with the Purex process [12].

However, the application of uranium mononitride (UN) for light water reactors is constrained by its intrinsic problems including reactivity of ^{14}N, oxidation and corrosion of UN with water and steam and thus loss of its structural integrity. The high neutron capture cross section of ^{14}N would

deteriorate the neutron economy and produce the radioactive ^{14}C isotope through neutron absorptions by ^{14}N [13,14]. The cross section thermal absorption can be significantly reduced by using enriched nitrogen, ^{15}N, which has a lower absorption cross section [15]. Despite the neutronic advantage that UN provides over UO_2, it is known that UN can react exothermically with water, consequently resulting in fuel pellet pulverization, washout and relocation, a major concern in water cooled nuclear reactor applications [11,16]. UN pellets can readily oxidize in super-heated steam, and complete degradation can occur within 1 hour in 0.5 bar steam at 500 ^{o}C [17]. The onset oxidation temperature of UN pellets in atmosphere was previously reported as 320 ^{o}C, significantly lower than these of other accident tolerance fuels (ATFs). For example, the onset temperature for oxidation of U_3Si_2 is typically 384 ^{o}C [18]. Therefore, the development of oxidation and corrosion resistance of UN is critical for its realization as the leading ATF concept and a high burnup fuel option. The key questions needed to be addressed for its practical application include: (1) how to further increase the onset temperature of oxidation and (2) how to reduce the kinetics of oxidation and corrosion kinetics and increase the coping time of fuels under accident conditions.

The manufacturing of nitride fuel pellets remains an issue as it is challenging to densify nitride fuel pellets with densities over 90% using conventional sintering methods [19]. Sintering temperatures as high as 2300 ^{o}C are typically required to achieve a sintered density above 95% theoretical density (TD), e.g., by hot isostatic sintering [4,7]. In addition, UN tends to dissociate and decompose to metallic uranium at high temperatures, which can be further oxidized to uranium oxides. Different routes including liquid phase sintering have been used in order to decrease the sintering temperature and achieve high densities (e.g., 90% TD when sintered at 1700 ^{o}C) [20]. Recent efforts focusing on the sintering behavior of UN using SPS have demonstrated a reproducible technique for densifying UN pellets as high as 99% TD at 1650 ^{o}C, a dramatic

reduction in sintering temperatures [12,21]. In addition to densified pellets, UN compacts of various densities, porosities and geometry maybe needed for various types of reactor designs with different temperature and burnup requirements, which also poses the requirement of microstructure controls during fuel fabrication and consolidation. For example, sufficient residual porosity in nuclear fuel matrix might be needed in order to accommodate fission products and reduce swelling at higher burn ups [19]. Large grain-sized microstructures and highly densified UN pellet with evenly-distributed, less porosity are desirable in the fuel to strengthen the fuel structure and delay the fission gas release [4,22]. Therefore, it is necessary to investigate and understand the sintering characteristics of UN pellets and identify the control on the microstructure, phase stability as well as the thermo-mechanical performance.

In this study, we densify UN pellets using SPS combined with high energy ball milling (HEBM) to control the microstructure, physical density and grain sizes from 1-2 μm to very large grain structure (up to 50-60 μm). The effects of different sintering conditions (temperature, duration and ball milling conditions) on sintering characteristics of the UN pellets are investigated. Thermal-mechanical properties of the sintered UN pellets such as thermal diffusivity/conductivity, micro-hardness and fracture toughness are measured and compared with literature values. SPS densified UN pellets are simultaneously mechanically strong and tough as compared with their counterparts sintered by conventional sintering. Of particular importance, the oxidation resistance of the as-sintered UN pellets can be tailored by altering the microstructure and physical density. The onset oxidation temperature can be up to 434 ^{o}C for the pellets sintered at relatively lower sintering temperature (1550 ^{o}C). Small grain-sized UN pellets show significantly-improved oxidation resistance with reduced oxidation kinetics and less weight gain compared to larger grain sized UN counterparts. These results show the immense potentials of using microstructure control to improve the key characteristics and fuel properties of UN fuels.

2. Materials and Methods

2.1 Powder preparation and sparking plasma sintering

High purity UN powders with low impurity (i.e. oxygen and carbon) levels were produced through a carbothermic reduction and nitridization approach. The as-received UN powders were subsequently refined into smaller particle sizes to enhance their sinterability by HEBM. The HEBM process is used as a pre-processing method to effectively facilitate the synthesis of materials that are traditionally difficult to sinter, e.g., for tungsten or molybdenum [19]. The HEBM process was conducted in a tungsten carbide (WC) ball milling jar equipped with a fully-sealed WC cap (Pulverisette 7, Idar-Oberstein, Germany). The UN powders were pre-loaded in a glove box with a controlled moisture and oxygen level lower than 2 ppm to prevent the oxidation of UN powders and possible phase degradation to UO_2 during powder handling and sintering. After the UN powders are densified into dense compacts, limited oxidation can only occur on the surface of the dense pellets in air [22]. During the HEBM process, 5 grams of as-received high purity UN powders and two 8-mm diameter WC milling balls were loaded in the ball milling jar and the ball milling speed was maintained at 500 rpm with 15 minutes for each cycle. A 10 minute idle time was carried out between two ball milling cycles. The particle size of the UN starting powders can be controlled by tailoring the ball milling cycles. The UN particle sizes post 4 cycle- and 44 cycle-ball milling are ~60 μm and ~10 μm as shown in Figure 1a and Figure 2a. The milled powders typically show a feature of a granule morphology. Longer ball milling cycles to 80 cycles and 100 cycles were also applied to further refine the particle size of the UN feedstock, greatly improving the sinterability and thus density of the SPS-densified UN pellets.

The consolidation of the dense UN pellets was conducted inside an environmentally-controlled glovebox interfaced with a Fuji 211x SPS apparatus (Fuji, Dr. Sinter SPS 211-LX, Saitama, Japan). The graphite die with an inner diameter of 10-mm was loaded with 1.2 grams of

ball milled-UN powders (Figure 1b). A graphite foil was wrapped at the inner wall of the die, which acted as an insulating layer between the powders and the graphite die. The graphite foil was first coated by a boron nitride spray prior to loading UN powders to prevent the possible diffusion and reaction between graphite and UN during the sintering. Carbon atoms could replace nitrogen atoms in the uranium nitride structure in a substitutional solid solution, and might accelerate the reaction between the fuel and cladding materials during the reactor operation, leading to cladding embrittlement [15,22]. Two foil disks coated by BN were placed on both the bottom and top of the graphite die to assure easy removal of the punch after sintering and mitigate the possible reaction. A piece of graphite felt was wrapped around the die to reduce heat losses at elevated temperatures. During SPS sintering, the temperature was monitored and controlled by a pyrometer focused on a pre-drilled hole on the graphite die. The SPS sintering was conducted with a heating rate of 200 ^{o}C/min until reaching the target temperature and held isothermally up to 10 minutes. Hydrostatic pressurization was applied from a pre-loading of 10 MPa before heating up and gradually increased to 50 MPa during SPS sintering. The pressure was released after the completion of sintering followed by free cooling to room temperature. During sintering and cooling, the SPS chamber was purged with high purity argon with a flow rate of 1 L/min. The dense pellets were ground and polished using silicon carbide papers and diamond paste. The density of the sintered pellets obtained with different HEBM and SPS sintering conditions was measured via an Archimedes immersion method with anhydrous ethanol as the measuring media. The as-measured theoretical density is shown in Table 1 assuming the fully dense UN pellet with a theoretical density of 14.3 g/cm^3 [19].

2.2. Microstructural characterization of the sintered pellets

X-ray Diffraction (XRD) patterns of the sintered UN pellet were acquired using a Panalytical X'Pert XRD system (Westborough, MA, USA) with a Cu Kα radiation source, the

wavelength of which is 1.5406 Å. The scanning range is 10^o to 90^o with a scanning step of 0.05^o and a scanning rate of 2 s/step. The microstructure and elemental analysis of the as-sintered UN pellets were characterized through a SEM equipped with an energy dispersive X- ray spectrometer (EDS) (Oxford, UK) using a Versa Dual-beam system). The average grain size was measured using the rectangular intercept method according to the American society for testing and materials (ASTM) E112-196 standard (1992) [23].

2.3 Thermal mechanical properties measurements and dynamic oxidation testing

Thermal diffusivity of the as-sintered UN pellets was measured with a laser flash apparatus (LFA-457, NETZCH, Bavaria, Germany). Prior to the measurement, the UN pellets were coated with sprayed graphite paste on both sides. After loading the sample, the chamber of the LFA was evacuated three times and filled with ultra-high purity argon at a flow rate of 100 ml/min, maintained throughout the measurement. Thermal diffusivity was measured three times in the range of 300 K to 800 K with an interval of 100 K. The corresponding heating rate is 5 ^oC/min during the measurement and a Cape-Lehman model with pulse correction based on non-linear regression was used to evaluate the thermal diffusivity. Corresponding thermal conductivity, κ (w/m-K), was calculated using Equation (1), where ρ is the density of the sample pellet, α is the measured thermal diffusivity ($mm^2 \cdot s^{-1}$), and c_p is the specific heat capacity [24]. The temperature dependent density is calculated with equation 2 mentioned in Ref. (24) based on the density determined at the reference temperature T_0 (e.g., room temperature) and the calculated mean value of the coefficient of thermal expansion of UN [25].

$$\kappa = \alpha \rho c_p \quad (1)$$

$$\rho = \frac{\rho_0}{[1+\alpha_p(T-T_0)]^3} \quad (2)$$

At each temperature, the specific heat capacity c_p was corrected by considering the phase impurities through a Neumann-Kopp rule by the rule of mixtures of the constituent compounds [26]. The thermal conductivity of fully-dense pellets was further derived by normalizing all of the data points to 100% TD based on equation (3) [27], where P is the measured porosity, the k and $k_{measured}$ stand for the corrected thermal conductivities for a fully-dense specimen and the measured thermal conductivity of the specimen with minor porosity, respectively.

$$k_{measured} = (1-P)^{1.5} \quad (3)$$

The mechanical properties of the as-sintered samples were measured using a microhardness tester (a LECO M-400 micro-hardness tester) using a diamond-shaped indenter to create indentation on the specimen's surface. Each indentation was performed at room temperature (25 ^{o}C) with a load of 1 kgF (~9.8 N) for 15 seconds. More than 10 indentations were generated for every specimen. The indentations were examined according to the standard ASTM C1327 [28]. Hardness and fracture toughness were derived by evaluating the SEM images taken at each indentation. Specifically, hardness (GPa) was calculated using Eq. (4), where P is the load applied and α is the mean of the indentation's diagonal lengths (μm).

$$H = 1.854\frac{P}{\alpha^2} \quad (4)$$

Fracture toughness was subsequently derived using Eq. (5), where σ is a parameter associated with indenter geometry, E is Young's modulus based on the previous report [21], H is the hardness derived from Eq. (4), P is the applied load, and C is the mean crack length.

$$K_{IC} = \sigma(\frac{E}{H})^{0.5}(\frac{P}{C^{1.5}}) \quad (5)$$

The dynamic oxidation testing was conducted using a simultaneous DSC/TGA system (SDT650, TA instrument, DE, USA), which is a thermal analyzer that measures the mass change and heat flow when the temperature of the specimen changes with a weight sensitivity of 0.1 µg. In the current work, the thermogravimetric analyzer was used to monitor the oxidation behavior of the UN pellets and to determine the onset temperature and weight gain during oxidation. A piece of pellet of~20 mg was loaded into an aluminum oxide crucible. The sample was heated up to 1000 ºC with a heating rate of 10 ºC/min in air, during which heat flow and mass change were simultaneously monitored and recorded. The chamber was then gradually cooled down to room temperature once the maximum temperature of 1000 ºC was reached. The onset temperature of the oxidation was taken as the transition point of the heat flow curve described in literature [29]. Time of completion for the oxidation was defined as the time from the oxidation onset to the full oxidation of the pellet when the weight did not change anymore. The sample pellet post oxidation treatment was then characterized by XRD to identify the final oxidation product.

3. Results and discussion

3.1 Microstructure control of the SPS densified UN pellets

The microstructure and surface morphology of the UN pellets can be controlled by varying the sintering temperature and the starting powder size, as demonstrated in Figures 1-4. The microstructure of the sintered pellets was observed using SEM on the polished and fractured surfaces as shown in Figure 1c and 1d (4 cycle-ball milled UN powders), Figure 2a-e (44 cycle-ball milled UN powders), and Figure 3a-d (80 cycle- and 100 cycle-ball milled UN powders). The ball-milled UN powders observed by SEM show an agglomerated morphology with average

particle sizes of 60 μm and 10.5 μm for the powders ball milled for 4 cycles and 44 cycles (Figure 1a and 2a), respectively. The actual powder particle sizes should be smaller than the sizes observed due to the severe particle agglomeration. A loose microstructure with an open porous structure can be observed for the pellets sintered at 1400 ºC with 4 cycles of UN powders, indicating that this temperature is not sufficient to fully densify the pellets, consistent with a previous work by Johnson (2018) [19]. By increasing the sintering temperature to 1700 ºC, high densities can be achieved as shown in Figure 1d. The grain sizes in general are within the range of 15-30 μm and 10-60 μm for the pellets consolidated at 1400 ºC and 1700 ºC, respectively. The large variation in the grain sizes can be attributed to grain coarsening which occurs at the end of the sintering process [19]. For comparison, the grain sizes of the UN pellets using the powders milled for 44 cycles are smaller, as shown in Figure 2. The corresponding grain sizes are within 2-20 μm for the UN pellet consolidated at 1400 ºC, which increases to ~35 μm for the pellets sintered at 1700 ºC. It is obvious that both starting UN powder sizes and sintering temperatures impact the grain structure of the SPS densified UN pellets. The grain size of the sintered UN pellets can be further reduced by ball-milling the UN powders for 80 and 100 cycles. Table 1 summarizes the average grain sizes of the UN pellets sintered at different temperatures from UN powders after 4, 44, 80 and 100 cycle-ball milling. In general, ball milling leads to refinement of the initial particle size of the UN feedstock and reduces the grain size of the sintered bodies. High temperature sintering promotes densification and grain coarsening. The as-sintered UN pellets with the corresponding powders ball milled for 80 cycles and 100 cycles can be seen in Figure 3. The pellets can be significantly densified by sintering at 1550 ºC for 10 minutes with 80 cycle-ball milled UN powders, as shown in Figure 3b. The corresponding grain size for these pellets is 6 μm. Dense UN pellets with a sub-micron grain size (~0.6 μm) can be successfully achieved through consolidating the 100 cycle-ball milled UN powders at 1550ºC for 10 minutes (Fig. 3c). The grain size increases to ~6 μm for

the pellet when sintered at 1650 ºC for 10 minutes (Figure 3d). The average grain size of the 1600 ºC-sintered pellet with 44 cycle-ball milled powders is 28 μm, significantly larger than that of the UN pellet sintered at the same temperature with a starting powder particle size around 6 μm [7], which can be attributed to the lower uniaxial pressure applied herein (50 MPa) compared to 70 MPa. Highly densified UN pellets (96.5% TD) with grain sizes of several tens of microns to a few-micron sized can be readily achieved by SPS by controlling HEBM durations and sintering conditions.

Figure 2f summarizes the impact of sintering variables (temperature and duration) and HEBM milling time on the physical density of the sintered UN pellets by SPS. For the pellet sintered at 1300 ºC using 44 cycle-ball milled powders, the physical density is low (only 76% TD), consistent with the highly porous feature showing UN particles loosely packed together. The physical density of the sintered pellets increases significantly by increasing the sintering temperature from 1300 ºC to 1700 ºC. The polished surfaces shows that highly densified pellets without manifest porous structures only achieved by increasing the sintering temperature above 1500 ºC (see insets in Figure 2c-e). The open porosity was almost eliminated at 1600 ºC and a highly densified pellet with theoretical density of 95% was obtained. In contrast, high density UN pellets can only be achieved at temperatures above 1900 ºC, or even higher, via conventional isostatic hot pressing or extrusion methods as demonstrated in Figure 2f [4]. Therefore, compared to isostatic hot-pressing, SPS can achieve significantly higher densities at lower temperatures within short sintering durations [4,10,30,31].

In addition, consolidation using smaller-sized starting powders also results in a greater physical density. For the pellet consolidated with 100 cycle-ball milled UN powders at 1600 ºC, the physical density is above 97% TD (Figure 2f). This is consistent with the previous research in which pellet density and grain size increased with longer ball milling durations [4]. The

corresponding SEM images of both fractured and polished surfaces of the UN pellets sintered with 80 cycle- and 100 cycle-ball milled powders (see Figures 3b-3d) clearly show highly densified microstructures without open porosity. The rapid densification process can be accelerated through prolonging the thermal hold time from 2 to 10 minutes (see Figures 3a and 3b). A similar trend can be found for UN pellets sintered by hot-pressing or SPS [4,19].

However, physical density of the SPS densified pellets decreases at sintering temperatures above 1700 ^{o}C, as shown in Figure 2f. The reduced physical density for the pellet sintered at 1700 ^{o}C can also be evidenced by the observation of fine pores inside the UN grains accompanied by the formation of fine grains, which can be detected as uranium oxides, as shown in Figure 4. Elemental analysis by EDS shows oxygen from the fine particles as denoted by the elemental line scanning and spot elemental analysis (see Figure 4b). As a comparison, the UN grains only display a small amount of oxygen (~2.5 at%). These results suggest the formation of a possible impurity oxide phase during SPS sintering above 1700 ^{o}C since the starting UN powders contained less than 1000 ppm oxygen. In addition to the intrinsic oxygen in the starting UN powders, surface oxidation could also occur on the fractured surface before microstructure characterization by SEM. A further possibility of the fine particle observation might be attributed to a possible phase decomposition of UN at high temperature [32], leading to the formation of metallic uranium and release of nitrogen, particularly in a low nitrogen environment as the SPS sintering condition herein. The metallic uranium decomposed from UN can be further oxidized to UO_2 during high temperature sintering or during surface oxidation. The phase decomposition of UN pellets was previously reported in literature, and the formation of free metallic uranium and UO_2 is a concern for the chemical compatibility of UN pellets with cladding and liquid metal, a topic to be investigated [12,33

3.2 Phase behavior of the SPS densified UN pellets

The phase stability and heterogeneity can also be controlled by tailoring the UN powder size and SPS consolidating conditions. The corresponding XRD profiles were acquired and the quantitative analysis was performed by Rietveld XRD peak refinement by MDI Jade 6.5. The refinement was conducted for multiple rounds (duplicate for 10-30 times) until the weighted residual error of refinement (R_{wp}^2) reached 10% and expected residual error (R_{exp}^2) reached 5%, are shown in Fig. 5a-c and Table 2. A minor crystalline phase of UO_2 can be found for the UN pellets consolidated with 44 cycles ball-milled UN powders at 1600 ºC, which can be attributed to the gradual phase degradation at elevated temperatures followed by the enhancement of UO_2 crystallinity, consistent with previous research conducted by Malkki (2015) [15]. The amount of the minor phase UO_2 increases from 3.1 wt% to 7.5 wt% as the sintering temperature increases from 1400 to 1600 ºC, significantly above the initial oxygen level (less than 1000 ppm) in the high purity UN powders. These results suggest that additional oxidation may occur during UN powder processing and SPS sintering. In addition to the formation of the secondary phase of UO_2, a minor crystalline phase of U_2N_3 was also observed in the pellets consolidated with finer UN powders ball-milled for 80 cycles. This can be attributed to the partial decomposition of the UN powders to uranium oxide during the SPS sintering process. The U_2N_3 might also originate from an $U(ON)_{2-x}$ type oxynitride phase [10]. The corresponding amounts of U_2N_3 are estimated as 1.1 wt% and 0.6 wt% for the samples consolidated at 1550 ºC and 1600 ºC, respectively. The crystalline phases became much more complicated by consolidating the sample pellets with 100 cycle-ball milled UN powders as indicated in Figure 5c. Besides the U_2N_3 and UO_2 secondary phases, other uranium oxide phases including UO_3 and $UO_{2.34}$ can also be observed for the UN pellets consolidated at different temperatures (1525 ºC and 1650 ºC) with 100 cycle-ball milled powders. The semi-quantitative phase compositions derived from XRD peak refinement are summarized in Table 2, which shows the U_2N_3 phase increasing with sintering temperature. The highest amount of U_2N_3

(23.1 wt%) can be achieved for the pellet sintered at 1650 ºC using 100 cycle-ball milled powders. The finer UN powders after 100 cycle-ball milling could be more sensitive to the oxidation during the powder handling and phase decomposition during sintering processes. The as-sintered UN pellets exhibit a slightly higher lattice constant compared to that of pure UN powders (4.889 Å). The corresponding lattice constants shown in Figure 5d generally increase for the pellets sintered at higher temperatures, suggesting a lattice expansion occurred during the SPS consolidation. This is in consistent to a previous research by Hayes (1990), who demonstrated a linear increase in the lattice parameter with temperature [25]. The lattice expansion is typically a result of tensile strain on the structural lattice of materials due to a mismatch expansion coefficient of the fuel pellet itself and graphite dies and thus resultant thermal strain upon cooling and temperature variation [34]. Both the microstructure and crystalline phases can be controlled by tailoring the starting powder sizes and sintering conditions.

Table 1 Summary of the grain sizes and lattice constants of the as-sintered UN pellets

4 cycle ball milling	grain size (μm)	Lattice constant (Å)
1400 ºC-50 mpa-10 min	15-30	4.895
1700 ºC-50 mpa-10 min	10-60	4.932
44 cycles	grain size (μm)	
1300 ºC-50 mpa-10 min	0.5-15	4.894
1400 ºC-50 mpa-10 min	2.5-20	4.899
1500 ºC-50 mpa-10 min	25	4.904
1600 ºC-50 mpa-10 min	28	4.911
1700 ºC-50 mpa-10 min	32	4.915
80 cycle ball milling	grain size (μm)	
1550 ºC-50 mpa-10 min	8	4.903
1600 ºC-50 mpa-10 min	10	4.906
100 cycle ball milling	grain size (μm)	
1550 ºC-50 mpa-10 min	0.6	4.907
1650 ºC-50 mpa-10 min	6	4.915

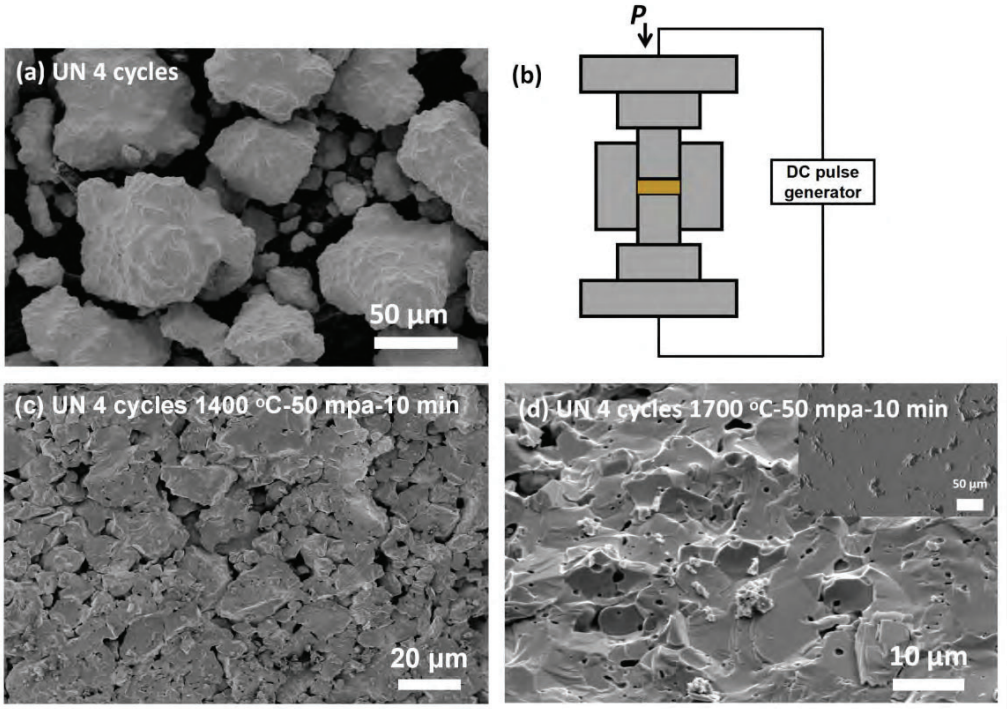

Figure 1. SEM images of as-milled powders (a), and the fractured surfaces and the polished surfaces of the UN pellets consolidated with 4 cycle-ball milled UN powders at 1400 (c) and 1700 °C (d) , and the setup of the SPS consolidation (b).

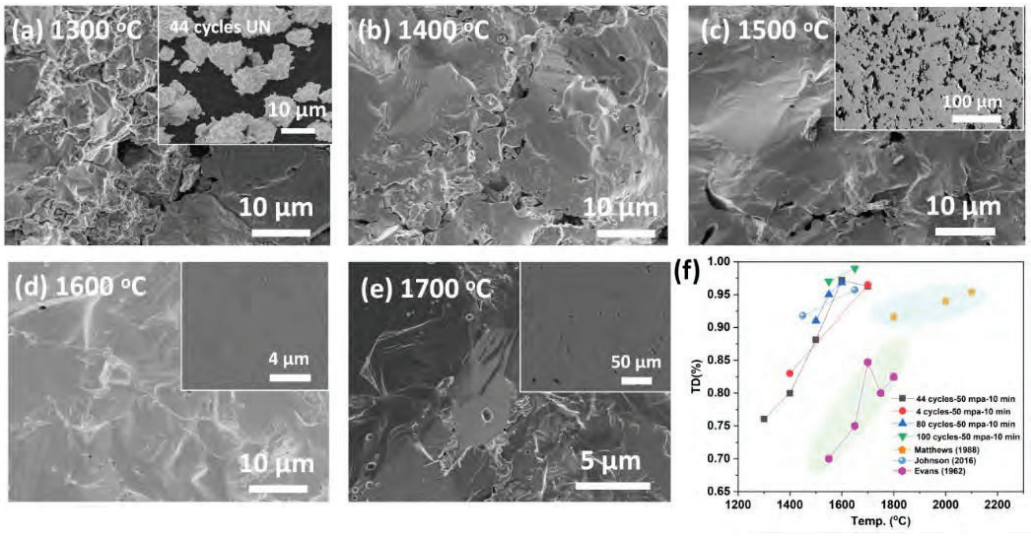

Figure 2. SEM images (a-e) of the polished (insets in Fig. 2c-2e) and fractured surfaces of the UN pellets consolidated with 44 cycle-ball milled UN powders (inset in Fig. 2a) under various temperatures at 50 MPa for 10 mins; and (f) physical densities of the SPS-densified UN pellets at different sintering and HEBM conditions.

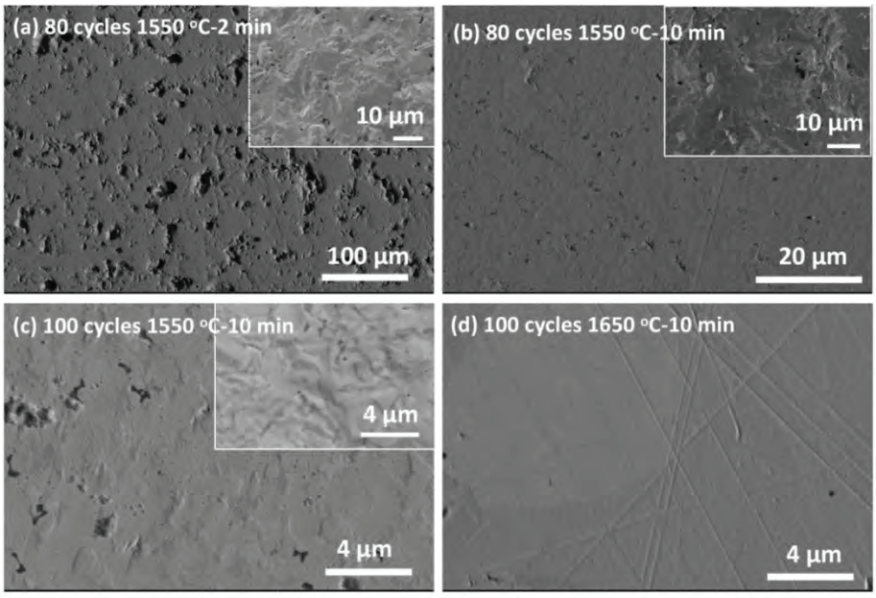

Figure 3. SEM images of the polished and fractured (insets in Fig. 3a-3c) surfaces of the UN pellets consolidated with 80 cycle and 100 cycle-ball milled UN powders (at 50 MPa).

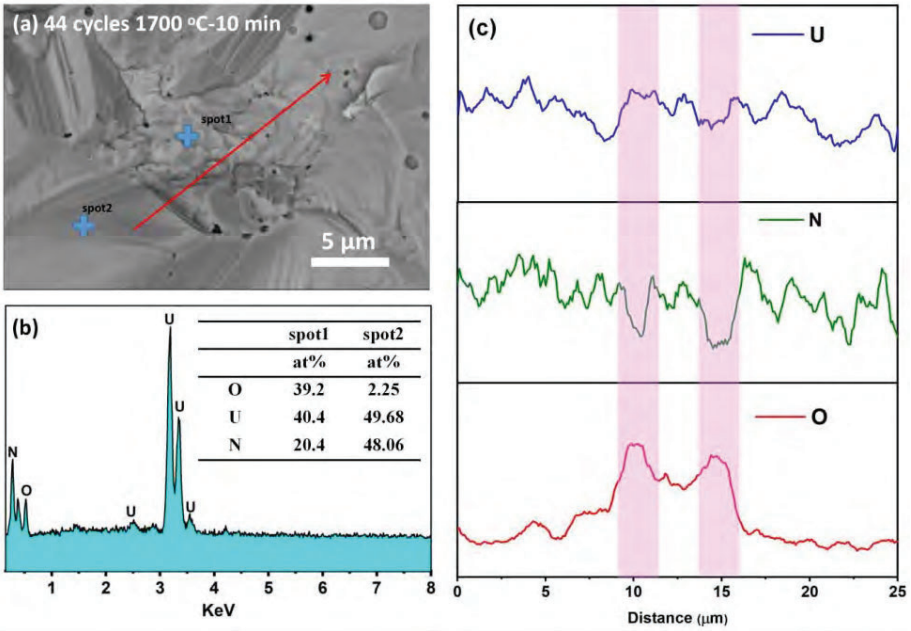

Figure 4. SEM image (a), EDS elemental analysis (b) and an elemental line scanning (c) across the grain boundary of the UN pellet sintered under 1700 °C with 44 cycle-ball milled UN powders.

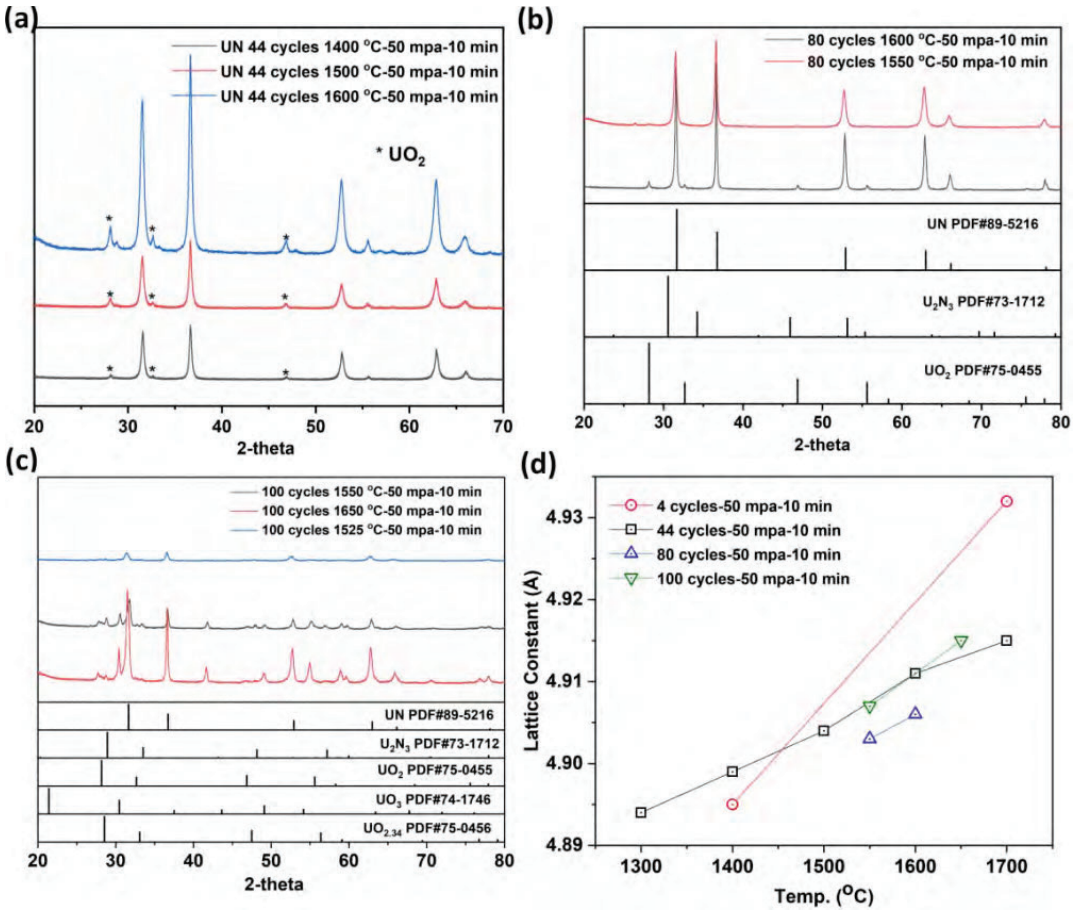

Figure 5. XRD profiles (a-c) of the as-sintered UN pellets and calculated lattice parameter(d) for the UN pellets sintered at different SPS sintering and ball milling conditions (44, 80 and 100 cycles).

Table 2 Semi-quantitative analysis and phase content (wt%) based on Riteveld refinement of XRD patterns

44 cycles	**UN**	**UO_2**	**$UO_{2.34}$**	**U_2N_3**	**UO_3**
1400 °C-50 mpa-10 min	96.9±2.3	3.1±0.6	0	0	0
1500 °C-50 mpa-10 min	96.2±1.9	3.8±0.2	0	0	0
1600 °C-50 mpa-10 min	92.5±2.1	7.5±0.5	0	0	0
80 cycles	**UN**	**UO_2**	**$UO_{2.34}$**	**U_2N_3**	**UO_3**
1550 °C-50 mpa-10 min	95.4±2.2	3.5±0.2	0	1.1±0.1	0

1600 °C-50 mpa-10 min	92.7±1.8	6.7±0.2	0	0.6±0.1	0
100 cycles	**UN**	**UO_2**	**$UO_{2.34}$**	**U_2N_3**	**UO_3**
1525 °C-50 mpa-5 min	95.1±2.4	4.1±0.4	0.6±0.1	1.8±0.1	12.7±1.2
1550 °C-50 mpa-10 min	85.4±2.2	5.3±1.1	0	1.0±0.1	8.3±0.5
1650 °C-50 mpa-10 min	62.4±1.4	4.1±0.4	0.8±0.1	23.1±2.1	9.6±0.5

3.3 Thermal and mechanical properties of the UN pellets and microstructure impact

The mechanical properties of the as-sintered UN pellets were measured by a Vicker's hardness tester. The micron hardness gradually increases for the UN pellets consolidated with 44 cycle-ball milled UN powders under varied temperatures from 1300 °C to 1700 °C, consistent with the increase in the physical density shown in Figure 2f. The highest Vicker's hardness is 6.78 GPa for the pellet consolidated under 1700 °C, while the lowest one is 1.65 GPa for the sample consolidated at 1300 °C. On the other hand, the Vicker's hardness is higher for the sample consolidated with finer UN powders and thus the pellet with smaller grain sizes as shown in Figure 6c. This can be explained by the Hall-Petch effect, as detailed in equation (5), where H is the hardness of the materials, H_0 is the single crystal hardness, k_H is a parameter describing the stress intensity, and D is the grain size [35]. From the equation, it is clear that hardness is negatively correlated to the grain size. The pile-up of dislocations at grain boundaries impedes the movement of dislocations and thus increases the strength and hardness of materials [36]. The lowest Vicker's hardness can be observed for the pellet consolidated with 4 cycle-ball milled UN powders with larger grain sizes. The highest one of 7.89 GPa is observed for the pellet consolidated with 100 cycle-ball milled UN powders with the smallest grain size and highest density (99% TD). This is significantly higher than the value (~4.46 GPa) for the UN pellet consolidated under 1650 °C via hot pressing, while slightly lower than that of

the UN pellet sintered at 1800 ºC (~8.34 GPa), possibly due to the high porosity for the hot-pressed UN pellet (82.5% TD) [32]. Transgranular fracture dominates the UN pellets consolidated by SPS for both smaller (100 cycle-ball milled powders) and larger grain sizes (44 cycle-ball milled powders), as evidenced by the cracks propagating across the grain boundaries shown in Figures 6 and 7. In addition, the fracture toughness of the SPS densified UN pellets is within the range of 2.5-3.5 MPa $m^{1/2}$, representing three-fold enhancement as compared with UO_2 (around 1 MPa $m^{1/2}$) and also comparable to the SPS-densified U_3Si_2 pellets as demonstrated in Figure 6d. In addition, the fracture toughness of smaller grain-sized UN pellets (100 cycle-ball milled powders) is slightly higher than that of larger grain-sized UN pellets. These results suggest that the SPS-densified UN pellets have good resistance against crack propagation.

The thermal diffusivity of the as-sintered pellets was measured by a laser flash analyzer from room temperature to 550 ºC, and their thermal conductivity was subsequently calculated, as shown in Figure 8. A slight reduction in the thermal conductivity above 500 ºC can be a result of slight oxidation of the UN pellets during LFA measurements when above the onset temperature for oxidation as inferred from the dynamic oxidation testing to be discussed later. The thermal conductivity evaluated at full density considering the impact of porosity is shown in Figure 8. The thermal conductivity is significantly higher for the pellets sintered at elevated temperatures (1500-1600 ºC) compared to the sample consolidated at 1400 ºC, consistent with grain size enlargement and increase in densification. Another observation is that larger grain-sized pellets (from 4 and 44 cycle-ball milled UN powders) have significantly higher thermal conductivity than smaller grain-sized UN pellets (manufactured from 80 cycle-ball milled UN). Previous research conducted by Yang [44] studied the relationship between grain size and thermal conductivity of nanocrystalline yttria-stabilized zirconia and found that the thermal conductivity of the smaller crystalline specimen is significantly lower than the coarse-grained

specimen. Nan [45] and Dong [30] also derived relationships between the grain size and thermal conductivity and obtained similar grain size-dependent correlation, confirming thermal conductivity reduction with smaller grain sizes. The highest thermal conductivity of 16 W/m-K and 20.8 W/m-K are measured at 25 °C and 425 °C for the UN pellets consolidated at 1550 °C with 44 cycle-ball milled UN powders (Figure 8c). The SPS-densified UN pellets show higher thermal conductivity than other accident tolerant fuels such as U_3Si_2 (7-16 W/m-K) (see Figure 8c), but inferior to UB_2 (34 W/m-K at 25 °C and 23 W/m-K at 425 °C, respectively) [39,46]. The high thermal conductivity of the densified UN pellets can enable lower fuel temperatures and a large thermal safety margin for a transient operation. In addition, the thermal conductivity for the sample consolidated at 1600 °C is slightly reduced, which can be attributed to the severe phase degradation to the low thermal conductivity phase of UO_2 (7.5 wt%) as confirmed by the XRD profile in Figure 5a.

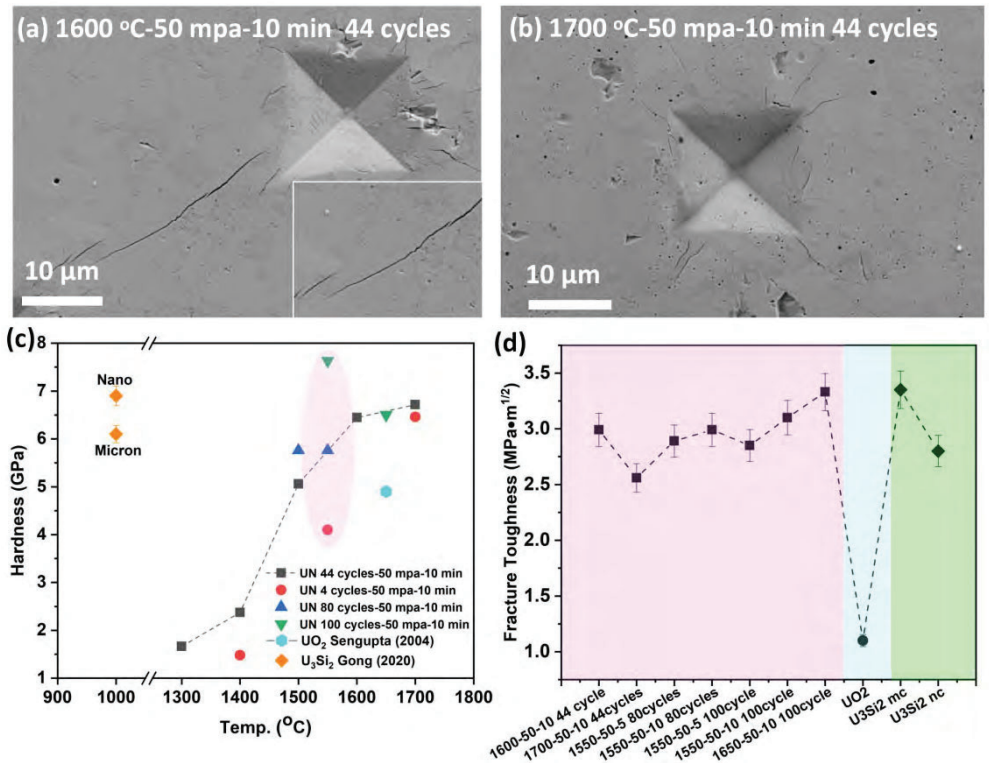

Figure 6. SEM images (a and b) showing micro-indentation on the surfaces of UN pellets consolidated with 44 cycle-ball milled UN powders under 1600 and 1700 °C; and micro hardness (c) and fracture

toughness(d) of the UN pellets sintered under different conditions as compared to reference data on U_3Si_2[18] and UO_2[40]

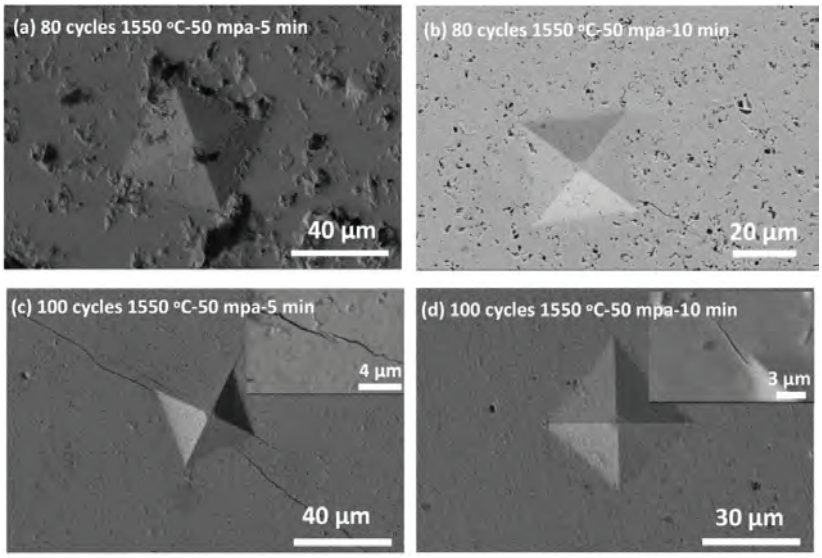

Figure 7. SEM images (a-d) showing micro indentation on the polished surfaces of the UN pellets consolidated with 80 or 100 cycle-ball milled UN powders.

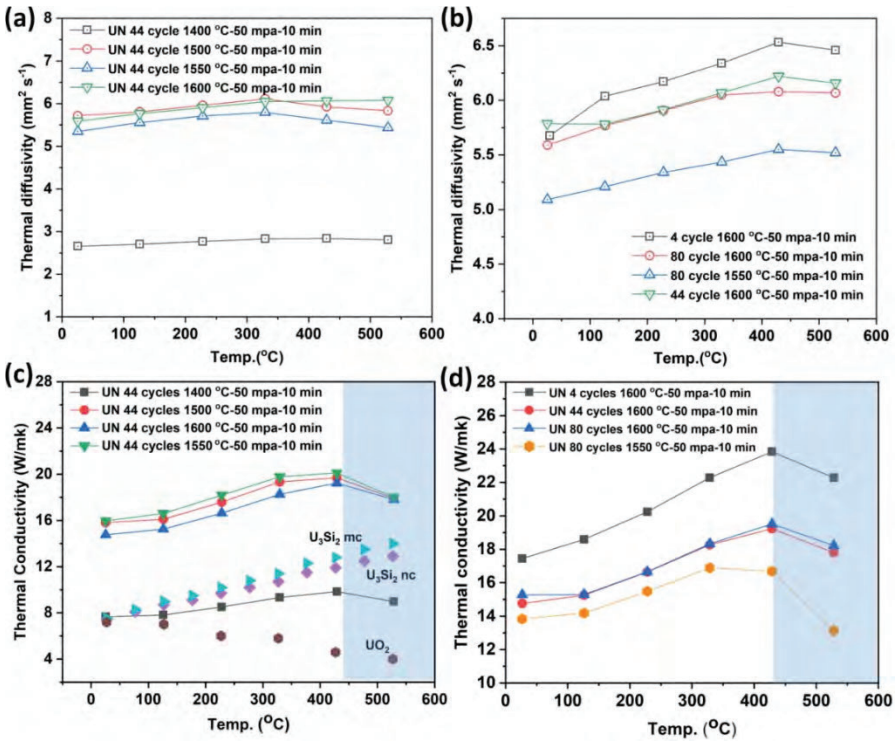

Figure 8. Thermal diffusivity (a,b) and calculated thermal conductivity (c,d) of the as-sintered UN pellets with different microstructures as sintered at different temperatures and ball milling

durations.

3.4 Dynamic oxidation behavior of the SPS consolidated UN pellets

The dynamic oxidation behavior of the SPS densified UN pellets along with heat flow and weight gain were measured by a dynamic TGA tests with a ramp of 10 ºC/min up to 1000 ºC as shown in Figure 9. The onset temperature for oxidation, oxidation rate and the terminal oxidation are determined and summarized in Table 3. The oxidation rate (wt%/min) is calculated from the weight gain percentile divided by the total oxidation time. Comparing the UN pellets fabricated under various temperatures, pellets with higher densities typically display greater onset temperatures for oxidation, probably due to the slow oxygen diffusion in dense fuel pellets [16,35,47]. The effect of porosity on the oxidation kinetics of sintered UN pellets has been previously studied by Johnson (2016) [48] reporting that eliminating the open porosity can considerably delay the onset temperature and reduce the oxidation rate. The onset temperature for the UN pellets consolidated with 80 cycle-ball milled powders are within the range of 323 ± 10 to 410 ± 11 ºC corresponding to sintering temperature between 1500 ºC (92% TD) to 1600 ºC (98.2% TD). These are generally higher than the values (260 ºC) and (320 ºC) reported by Costa (2021) [16] and Johnson (2016) [48] for the UN pellets with theoretical density of 83.8% and 92%. Johnson (2016) [48] also repored that the onset temperature increased from 320 ºC to 440 ºC when the physical density of the SPS-densified pellets (sintered at1650 ºC and 134 MPa) increased from 92% to 99.8%.

The measured weight gain corresponding to the oxidation of UN is 12.17 wt% for the UN pellet fabricated at 1500 ºC, slightly higher that the weight gain (11.4 wt%) reported by Johnson (2016) [48]. The weight gain gradually reduces for the pellets sintered at higher temperatures from 1500 ºC to 1600 ºC, which might be attributed to a slight phase degradation of UN during SPS sintering and the existence of secondary uranium oxide phases (see Figure 5 and Table 2).

A previous study [49] reported that the oxidation of UN began around 200 ºC with a slow absorption of oxygen. At higher temperatures, the intensive incorporation of oxygen accompanied by the loss of nitrogen leads to the formation of an intermediate uranium oxynitride. When all the UN transforms to the final product U_3O_8 as evidenced by the XRD shown in Fig. 9c, the full weight is 11.4 wt% assuming nitrogen is released [50]. A slight weight reduction can be observed in the TGA curve after the completion of full oxidation, which might be attributed to the release of trapped nitrogen from an intermediate oxynitride [16,50,51].

In addition to physical density as controlled by different sintering temperatures, the grain structure also has profoundly impacted the oxidation behavior of the densified UN pellets as manipulated by different ball milling durations. The onset temperatures for the UN pellet sintered with finer UN powders (44 cycles or 80 cycles) despite the lower sintering temperatures are higher than these of the UN pellets consolidated with 4 cycle-ball milled powders. Similar results are also reported in which the finer-grained U_3Si_2 pellets exhibit higher oxidation resistance with significantly reduced oxidation kinetics [46]. The onset temperature of 434 ºC can be observed for the 44 cycles UN pellet sintered at 1600 ºC (the blue curve in Fig. 9b).

The UN pellets sintered with 100 cycle-ball milled UN powders displays slightly higher onset temperatures than the pellets sintered with 80 cycle- or 44 cycle-ball milled powders, but significantly reduced oxidation kinetics as evaluated by the weight gain percentage per unit time (0.088 wt%/min) as compared to other samples (Table 3). The oxidation of the dense UN pellet sintered with 100 cycle–ball milled powders completes beyond 900 ºC at a ramping rate of 10 ºC/min, significantly higher than the completion temperature of other UN pellets. For example, the oxidation completes quickly for the pellets sintered with 4 cycle-ball milled powders with the oxidation completion point around 600 ºC and the oxidation rate is almost triple (as high as 0.248 wt%/min). The enhanced oxidation resistance for smaller grain-sized

UN pellets might be attributed to the strain effect that could retard the oxidation in dense UN post SPS consolidation. The strain effect on the oxidation behavior is also consistent with a previous observation for air oxidation of Si, in which a small amount of strain will alter oxidation resistance significantly [52].

The significantly-reduced oxidation kinetics for the pellets with increased ball milling durations from 4 cycles to 100 cycles can also be evidenced from the heat flow. Specifically, a plateau heat flow can be identified for the pellets sintered with both 80 cycle- and 100 cycle-ball milled powders, indicating a slow heat release as a result of mild oxidation reaction. The lower oxygen pickup (7.2 wt%) for the UN pellet consolidated with 100 cycle-ball milled powders might be attributed to the phase heterogeneity in which partial oxidation and decomposition occur during SPS sintering with finer UN starting powders with the existence of both UO_x and U_2N_3 as demonstrated in the XRD profile in Figure 5c. These results highlight a correlation among processing conditions, microstructure control and phase heterogeneity that can affect the oxidation kinetics of the UN pellets to improve its oxidation resistance of the UN fuel as the leading ATF candidate and a new form for advanced reactor systems. Further autoclave and steam oxidation tests are ongoing to further investigate the impact of the microstructure control and phase heterogeneity on the oxidation and corrosion resistance of the SPS-densified UN pellets.

Table 3 Summary of the dynamic oxidation tests of the SPS densified pellets sintered at different conditions as measured by a TGA-DSC thermal analyzer. The ramping rate is 10 ^{o}C/min.

	Onset temperature (^{o}C)	Weght gain (%)	Oxidation completion point (^{o}C)	Oxidation rate (wt%/min)
1500 ^{o}C-50 mpa-10min 80 cycles	327.5	12.2	657.7	0.211

1600 ºC-50 mpa-10min 80 cycles	356.7	11.3	699.5	0.184
1550 ºC-50 mpa-10min 80 cycles	405.4	11.3	646.4	0.2
1700 ºC-50 mpa-10min 4 cycles	419.5	12.9	596.7	0.248
1550 ºC-50 mpa-10min 100 cycles	425.7	7.2	914.4	0.088
1600 ºC-50 mpa-10min 44 cycles	452.3	10.8	674.4	0.183

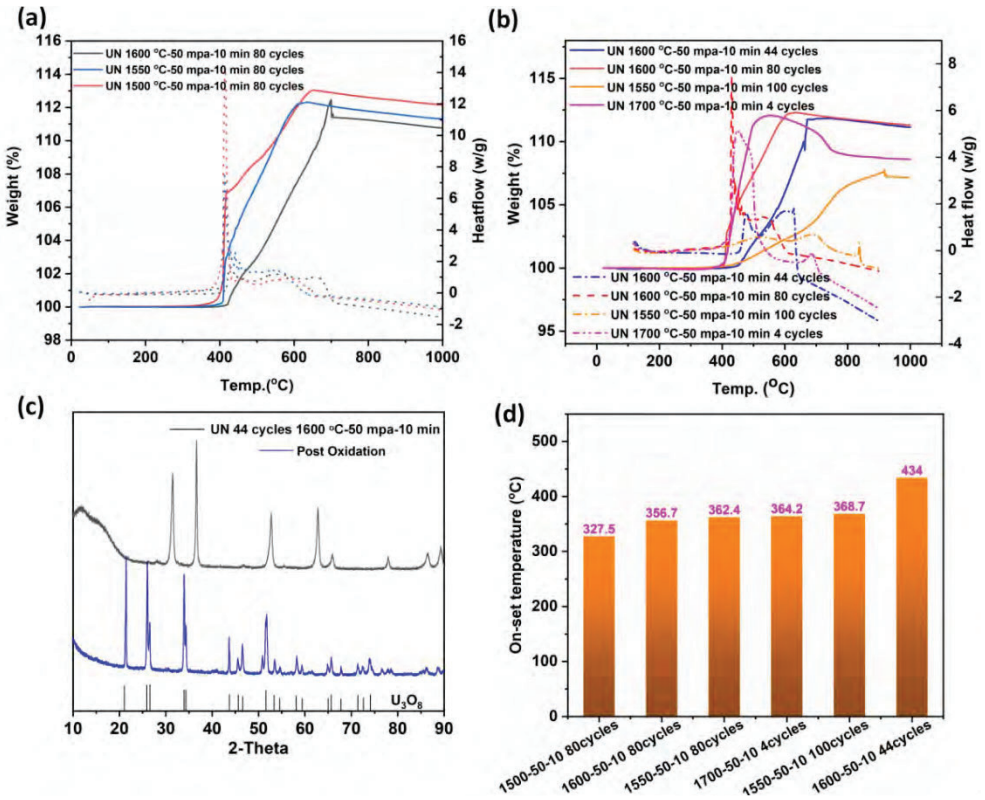

Figure 9. Dynamic oxidation tests (a, b) by a thermo-gravimetric analyzer with a temperature ramping (10 ºC/min) in air showing different oxidation behaviors of the SPS densified UN pellets with various microstructure and phase heterogeneity; (c) a XRD diffraction of the UN pellet post oxidation testing showing U_3O_8 as the final oxidation product; and (d) a bar chart represents the anti-oxidation capacity of the as-sintered UN pellets.

4. Summary

In summary, dense UN pellets can be fabricated by SPS with controllable microstructures and phase heterogeneity by controlling the particle sizes of the starting powders and synthesis

conditions. The corresponding thermal-mechanical properties and oxidation behavior are characterized on the SPS densified UN pellets by SEM, XRD, thermal diffusivity measurements, micro-hardness testing and TGA analysis. The correlation among sintering parameters, microstructure control, phase behavior and thermal mechanical properties is investigated. Longer ball milling durations and elevated sintering temperatures promote densification and grain growth, and dense pellets with controlled grain structures tailored from several tens of microns to submicron can be obtained. Phase heterogeneity and phase degradation including the formation of uranium oxides and U_2N_3 can be found during SPS sintering when reducing the size of the starting UN powders and increasing the sintering temperature. SPS densified UN pellets exhibit high thermal conductivities, and the continuously-increasing thermal conductivity with temperature suggests a dominant effect of electron transport for heat conduction. The SPS-densified UN pellets possess simultaneously-high hardness (4.46-7.89 GPa) and fracture toughness about 3.5 MPa $m^{1/2}$, significantly better than UO_2 and comparable to the SPS-densified U_3Si_2 pellets. The hardness and fracture toughness increase by increasing the pellet density as well as reducing the grain size. The oxidation resistance of the SPS-densified UN pellets is generally enhanced by reducing the grain size for the pellets sintered with UN powders ball milled at longer durations. The oxidation kinetics can be greatly reduced for the pellets with finer grain structures and existence of uranium oxides and U_2N_3 phases, highlighting important impacts of microstructure control and phase evolution on the oxidation resistance of UN fuel pellets.

Acknowledgement

This work was supported by the US Department of Energy's (DOE's) Office of Nuclear Energy under a Nuclear Engineer University Program (award number: DE-NE0008947) and by Westinghouse Electric Company under the DOE ATF program supported by the Department of Energy under Award Number DE-NE0008824. This report was prepared as an account of

work sponsored by an agency of the United States Government. Neither the United States Government nor any agency thereof, nor any of their employees, makes any warranty, express or implied, or assumes any legal liability or responsibility for the accuracy, completeness, or usefulness of any information, apparatus, product, or process disclosed, or represents that its use would not infringe privately owned rights. Reference herein to any specific commercial product, process, or service by trade name, trademark, manufacturer, or otherwise does not necessarily constitute or imply its endorsement, recommendation, or favoring by the United States Government or any agency thereof. The views and opinions of authors expressed herein do not necessarily state or reflect those of the United States Government or any agency thereof.

References cited:

[1] Uno M., Nishi T., Takano M. Thermodynamic and thermophysical properties of the actinide nitrides. Comprehensive Nuclear Materials, Oxford, 61-85 (2012).

[2]Szpunar B., Szpunar J.A. Thermal conductivity of uranium nitride and carbide. International Journal of Nuclear Energy, 178360(2014)1-7.

[3]Ross S.B., El-genk M.S. Thermal conductivity correlation for uranium nitride fuel between 10 and 1923K. Journal of Nuclear Materials, 151(1988)313-317.

[4]Matthew R.B., Chidester K.M., Hoth C.W., Mason R.E., Petty R.L. Fabrication and testing of uranium nitride fuel for space power reactors. Journal of Nuclear Materials, 151(1988)334-344.

[5]Costa D.R., Hedberg M., Middleburgh S.C., Wallenius J., Olsson P., Lopes D.A. UN Microspheres embedded in UO_2 matrix: an innovative accident tolerant fuel. Journal of Nuclear Materials, 540(2020)1-8.

[6]Ross S.B., El-genk M.S. Uranium nitride fuel swelling correlation. Journal of Nuclear Materials, 170(1990)169-177.

[7]Kim G.H., Ahn J.S., Ahn S.J. Grain growth and densification of uranium mononitride during

spark plasma sintering. Ceramic International, 47(2021)7258-7262.

[8]Dragunov Y.G., Lemekhov V.V., Smirnov V.S., Chernetsov N.G. Technical solutions and development stages for the BREST-OD-300 Reactor unit. Atomic Energy, 113(2012)70-77.

[9]Oshkanov N.N., Saraev O.M., Bakanov M.V., Govorov P.P., Potapov O.A., Ashurko M., Poplavskii V.M., Vasilev B.A., Kamanin Y.L., Ershov V.N. 30 years of experience in operating the BN-600 sodium cooled fast reactor. Atomic Energy, 108(2010)234-239.

[10]Yang J.H., Kim D.J., Kim K.S., Koo Y.H. UO_2-UN composites with enhanced uranium density and thermal conductivity. Journal of Nuclear Materials, 465(2015)509-515.

[11]Ortega L.H., Blamer B.J., Evans J.A., McDeavitt S.M. Development of an accident-tolerant fuel composite from uranium mononitride (UN) and uranium sesquisilicide (U_3Si_2) with increased uranium loading. Journal of Nuclear Materials, 471(2016)116-121.

[12]Malkki P., Jolkkonen M., Hollmer T., Wallenius J. Manufacture of fully dense uranium nitride pellets using hydride derived powders with spark plasma sintering. Journal of Nuclear Materials, 452(2014)548-551.

[13]Brown N.R., Aronson A., Todosow M., Brito R., McClellan K.J. Neutronic performance of uranium nitride composite fuels in a PWR. Nuclear Engineering and Design, 275(2014)393-407.

[14]Pukari M. Experimental and theoretical studies of nitride fuels. Royal Institute of Technology, Swiss. Ph.D dissertation. (2013)

[15]Malkki P. The manufacturing of uranium nitride for possible use in light water reactors. Royal Institute of Technology, Swiss. Thesis. (2015)

[16]Costa D.R., Hedberg M., Middleburgh S.C., Wallenius J., Olsson P., Lopes D.A. Oxidation of UN/U_2N_3-UO_2 composites: an evaluation of UO_2 as a oxidation barrier for the nitride phases. Journal of Nuclear Materials, 544(2021)1-10.

[17]Jolkkonen M., Malkki P., Johnson K., Wallenius J. Uranium nitride fuels in superheated

steam. Journal of Nuclear Science and technology, 54(2017)513-519.

[18]Gong B.W., Yao T.K., Lei P.H., Harp J., Nelson A.T., Lian J. Spark plasma sintering (SPS) densified U_3Si_2 pellets: microstructure control and enhanced mechanical and oxidation properties. Journal of Alloys and Compounds, 825(2020)1-10.

[19]Johnson K.D., Lopes D.A. Grain growth in uranium nitride prepared by spark plasma sintering. Journal of Nuclear Materials, 503(2018)75-80.

[20]Lessing P. Oxidation Protection of uranium nitride fuel using liquid phase sintering. Idaho Falls, ID: Idaho National Lab, (INL/EXT-12-24974) (2012).

[21]Muta H., Kurosaki K., Uno M., Yamanaka S. Thermal and mechanical properties of uranium nitride prepared by SPS technique. Proceedings of the symposium on spark plasma synthesis and sintering. 43(2008)6429-6434.

[22]Metroka R.R. Fabrication of uranium mononitride compacts. Lewis Research Center, NASA TN D-5876.

[23]ASTM E112-E196. Standard test methods for determining average grain size. ASM International, West Conshohocken, (2004).

[24] Cape, J. and Lehman, G. (1963) Temperature and Finite Pulse-Time Effects in the Flash Method for Measuring Thermal Diffusivity. Journal of Applied Physics, 34, 1909-1913.

[25] Hayes S.L., Thomas J.K., Peddicord K.L. Material property correlations for uranium mononitride I. Physical properties. Journal of Nuclear Materials, 171(1990)262-270.

[26] Barin I. Thermochemical data of pure substance. VCH, Weinheim, 1995.

[27] Rice R.W. Porosity of ceramics: properties and applications, CRC press, Boca Raton, FL., 1998.

[28] ASTM C1327. Standard test method for Vickers indentation hardness of advanced ceramics. 2019

[29] Wood E.S., White J., Nelson A. Oxidation behavior of U-Si compounds in air from 25 to

1000 ºC. Journal of Nuclear Materials, 484(2017)245-257.

[30] McLaren J.R., Atkinson P.W.M. The sintering of uranium mononitride. Journal of Nuclear Materials, 17(1965)142-148.

[31] Dong H.C., Wen B., Melnik R. Relative importance of grain boundaries and size effects in thermal conductivity of nanocrystalline materials. Scientific Reports, 4(2014)1-5.

[32] Tennery V.J., Godfrey T.G., Potter R.A. Synthesis, Characterization and fabrication of UN. Oak ridge National Lab, Tennessee, ORNL-4608 (1970).

[33] Evans P.E., Davies T.J. Uranium nitrides. Journal of Nuclear Materials, 1(1963)43-55.

[34] Santara B., Giri P.K., Imakita K., Fujii M. Microscopic origin of lattice contraction and expansion in undoped rutile TiO2 nanostructures. Journal of Physics D: Applied physics, 47(2014)215302.

[35] Gong B.W., Yao T.K., Lei P.H., Cai L., Metzger K.E., Lahoda E.J., Boylan F.A., Mohamad A., Harp J., Nelson A.T., Lian J. U_3Si_2 and UO_2 composites densified by spark plasma sintering for accident tolerant fuel. Journal of Nuclear Materials, 534(2020)1-8.

[36] Scattergood R., Koch C. A modified model for Hall-Petch behavior in nano-crystalline materials. Scripta Metallurgy Material, 27(1992)1195-1200.

[37] Sengupta A.K., Basak C.B., Jarvis T., Bhagat R.K., Pandey V.D., Majumdar S. Effect of titania addition on hot hardness of UO_2. Journal of Nuclear Materials, 325(2004)141-147.

[38] Frazer D., Maiorov B., Carvajal-Nunez U., Evans J., Kardoulaki E., Dunwoody J., Saleh T.A., White J.T. High temperature mechanical properties of fluorite crystal structured materials (CeO2, ThO2, and UO2) and advanced accident tolerant fuels (U3Si2, UN and UB2). Journal of Nuclear Materials, 153035(2021).

[39] Kardoulaki E., White J.T., Byler D.D., Frazer D.M., Shivprasad A.P., Saleh T.A., Gong B., Yao T.K., Lian J., McClellan K.J. Thermophysical and mechanical property assessment of UB2 and UB4 sintered via spark plasma sintering. Journal of Alloys and Compounds,

818(2020)153216.

[40] Mussler B., Swain M.V., Claussen N. Dependence of fracture toughness of alumina on grain size and test technique. Journal of American Ceramic Society, 65(1982)566-572.

[41] Oguma M. Microstructure effects on fracture strength of UO2 fuel pellets.Journal of Nuclear Science and Technology, 19(1982)1005-1014.

[42] Adachi T., Osaki M., Araki W., Kwon S.C. Fracture toughness of nano and micron spherical silica-particle-filled epoxy composites. Acta Materialia, 56(2008)2101-2109.

[43] Tzeng S.H., Tsai J.L. Size effect on fracture behaviors of epoxy composites with micron and nano alumina particles. Key Engineering Materials, 334-335(2007)777-780.

[44] Yang H.S., Bai G.R., Thompson L.J., Eastman J.A. Interfacial thermal resistance in nanocrystalline yttria stabilized zirconia. Acta Materialia, 50(2002)2309-2317.

[45] Nan C.W. Determining the kapitza resistance and the thermal conductivity of polycrystals: A simple model. Physical Review B, 57(1998)8265-8268.

[46] Gong B.W., Frazer D., Yao T.K., Hosemann P., Tonks M., Lian J. Nano and micro Indentation testing of sintered UO_2 fuel pellets with controlled microstructure and stoichiometry. Journal of Nuclear Materials, 516(2019)169-177.

[47] Johnson K.D., Strom V., Wallenius J., Lopes D.A. Oxidation of accident tolerant fuel candidates. Journal of Nuclear Science and Technology, 54(2017)280-286.

[48] Johnson K.D., Wallenius J., Jolkkonen M., Claisse A. Spark Plasma sintering and porosity studies of uranium nitride. Journal of Nuclear Materials, 473(2016)13-17.

[49] Paljevic M., Despotovic Z. Oxidation of uranium mononitride. Journal of Nuclear Materials, 57(1975)253-257.

[50] Rao G.A.R., Mukerjee S.K., Vaidya V.N., Venugopal V., Sood D.D. Oxidation and hydrolysis kinetic studies on UN. Journal of Nuclear Materials, 185(1991)231-241.

[51] Dell R.M., Wheeler V.J., McIver E.J. Oxidation of uranium mononitride and uranium

monocarbide. Transaction of the Faraday Society, 62(1966)3591-3606.

[52] Gokce B., Aspnes D.E., Gundogdu K. Effect of strain on bond specific reaction kinetics during the oxidation of H-terminated (111) Si. Applied Physics Letter, 98(2011)121912.

Appendix 12 - UO2 Fuel

Report: Planned Dopants

Dylan Windsor & Dr. Haixuan Xu
University of Tennessee, Knoxville-Dept. of Materials Science and Engineering

Summary:

The dopants currently being considered for inclusion in Uranium Dioxide (UO_2) are Cerium (Ce), Lanthanum (La), Yttrium (Y), Niobium (Nb), Chromium (Cr), Magnesium (Mg), and Bismuth (Bi). This list was compiled based on the consideration of several factors perceived to have significant impacts on the suitability of a given dopant in the UO_2 system. The considered parameters included charge effects in similar oxide environments, ionic radii, solubility and phases in the UO_2 system, neutron cross-section, and finally whether or not the dopant in question is a fission product of UO_2.

Table 1: Here is a summary table of the dopants remaining on the list after all criterion were applied. Notice that Bi and Mg do not have information for quite a few of the criteria used; however, these two were still on the list since they have ionic radii that are within ~15 pm of U. The information on the solubility limits of several of these dopants was not available or was limited (as in the case of Nb).

Dopant	Ionic Radii (pm)[1]	Charge (+)[1]	Solubility (at.%)	Phase	Lattice Const.
Ce	115	3	<30%	Fluorite	Decrease[10]
La	117.2	3	9-10%[12]	Fluorite	Decrease
Y	104	3	<15%[11]	Fluorite	Decrease
Nb	78	5	---	Fluorite	Decrease
Cr	75.5, 63.0	3, 5	~0.45%[5]	Fluorite	Decrease[5]
Mg	86	2	---	---	---
Bi	117	3	---	---	---

General Fluorite Structure of UO_2:

The phase of UO_2 being considered is the fluorite structure, wherein Uranium cations with a +4 formal charge occupy face-centered cubic lattice cites while Oxygen anions with a -2 charge occupy tetrahedral interstitial sites. Several materials with this structure have shown capability to host a substantial amount of dopant before transformation into other competing phases. The primary mode of integration into the structure for cation dopants is substitution, which leads to changes in the lattice constant. Thus, dopants being considered are those which may reasonably change the electronic structure of the UO_2 fluorite phase to favor electronic conduction without changing the phase of the parent structure.

Criterion I: Ionic Charge and Radii

Compilation of the initial list of dopants was performed by comparing ionic radii and charge state of ions of most of the elements on the periodic table. For this, the Shannon ionic radii and associated charge state were compared, finding the most suitable dopants from tabulated data[1]. Dopants whose Shannon ionic radii which were within several picometers of the ionic radii of Uranium (U) in the UO_2 system and a charge state within +2 or +5 compared to U were kept on the list as possible dopants. This criterion also allows initial evaluation of ionic mismatch in the doped UO_2 system. Combining with the charge compensating defects, oxygen vacancy in this case, a significant local stress may be introduced in the host material. Similarly, too large a size difference between a given dopant ion and the uranium

would cause high stresses, therefore introducing phase instability into the UO_2 matrix. The initial list of possible suitable dopants obtained in this way was then rigorously checked against solubility information found in the literature, and for those dopants whose solubility and phase information could be found in the UO_2 system, the solubility and phase were used to either remove or keep possible dopants.

Criterion II: Solubility and Phase

The solubility/phase criterion was applied by checking the literature using the ICSD database and Phase Equilibria Diagrams (PED) online database. Data found in the literature was assessed further by comparing the solubility[3,4,5,6,8] and phase transition[4,6] in the fluorite lattice structure to remove more dopants from the list. The solubility of most dopants given in the literature and phase diagrams found show a limit of approximately 10% (though notable exceptions were Gd and Er at 40% and 62.5%, respectively) before stresses resulting in phase changes occurred in the fluorite structure. Those dopants which were documented to cause a phase change in the $U_{1-x}M_xO_{2\pm n}$ (where M is an arbitrary dopant) system were rejected as suitable dopants. It should also be noted that those dopants for which no information on solubility or phase transitions could be found were kept on the list. The list of dopants for consideration by this time had been reduced to Ce, La, Y, Nb, Cd, Gd, Cr, Mg, Bi, Er, and Yb.

Criterion III: Fission Product and Neutron Absorption

Finally, the neutron cross-section and fission production in UO_2 were considered. These criteria were applied by finding available literature information on neutron cross-section and stability of fission products of UO_2 under radiation conditions[2]. This search revealed that of the list of dopants Cd, Gd, Er, and Yb were strong neutron absorbers. In addition, it was found that Nb, Cd, La, Y, and Ce were fission products which form in the UO_2 system; however, except for Cd, each of these fission products formed a solid solution with the UO_2.[2] As such, the dopants Cd, Gd, Er and Yb were removed from the list of suitable dopants.

Table A.1[9]: The following table outlines the data used to eliminate the final group of possible dopants, leaving only those highlighted in green as the list of suitable dopants for consideration. The data shows the absorption for fission neutrons in addition to the incoherent (Incoh.) and coherent (Coh.) scattering cross-sections (Scat. X.), and the incoherent and coherent scattering length (Scat. L.). Note the high absorption cross section (Abs. X.) for Cd, Gd, and Yb, this is the reason for their removal from the list of suitable dopants. These data were compiled from the Neutron scattering lengths and cross sections website from the National Institute of Standards and Technology (NIST).

Isotope	Natural Abundance/half -life	Coh. Scat. L	Incoh. Scat. L.	Coh. Scat. X	Incoh. Scat. X.	Tot Scat. X	Abs. X for 2200m/s n^o
----	----	fm	fm	barn	barn	barn	barn
Ce	----	4.84	----	2.94	0.001	2.94	0.63
136	0.19	5.8	0	4.23	0	4.23	7.3(1.5)
138	0.25	6.7	0	5.64	0	5.64	1.1
140	88.48	4.84	0	2.94	0	2.94	0.57
142	11.08	4.75	0	2.84	0	2.84	0.95
La	----	8.24	----	8.53	1.13	9.66	8.97

138	0.09	8.(2.)	----	8.(4.)	0.5	8.5(4.0)	57.(6.)
139	99.91	8.24	3	8.53	1.13	9.66	8.93
Y	100	7.75	1.1	7.55	0.15	7.7	1.28
Nb	100	7.054	-0.139	6.253	0.0024	6.255	1.15
Cd	----	4.87-0.7i	----	3.04	3.46	6.5	2520.(50.)
106	1.25	5.(2.)	0	3.1	0	3.1(2.5)	1
108	0.89	5.4	0	3.7	0	3.7	1.1
110	12.51	5.9	0	4.4	0	4.4	11
111	12.81	6.5	----	5.3	0.3	5.6	24
112	24.13	6.4	0	5.1	0	5.1	2.2
113	12.22	-8.0-5.73i	----	12.1	0.3	12.4	20600.(400.)
114	28.72	7.5	0	7.1	0	7.1	0.34
116	7.47	6.3	0	5	0	5	0.075
Gd	----	6.5-13.82i	----	29.3	151.(2.)	180.(2.)	49700.(125.)
152	0.2	10.(3.)	0	13.(8.)	0	13.(8.)	735.(20.)
154	2.1	10.(3.)	0	13.(8.)	0	13.(8.)	85.(12.)
155	14.8	6.0-17.0i	(+/-)5.(5.)-13.16i	40.8	25.(6.)	66.(6.)	61100.(400.)
156	20.6	6.3	0	5	0	5	1.5(1.2)
157	15.7	-1.14-7.9i	(+/-)5.(5.)-55.8i	650.(4.)	394.(7.)	1044.(8.)	259000.(700.)
158	24.8	9.(2.)	0	10.(5.)	0	10.(5.)	2.2
160	21.8	9.15	0	10.52	0	10.52	0.77
Cr	----	3.635	----	1.66	1.83	3.49	3.05
50	4.25	-4.5	0	2.54	0	2.54	15.8
52	83.79	4.92	0	3.042	0	3.042	0.76
53	9.5	-4.2	6.87	2.22	5.93	8.15	18.1(1.5)
54	2.36	4.55	0	2.6	0	2.6	0.36
Mg	----	5.375	----	3.631	0.08	3.71	0.063
24	78.9	5.66	0	4.03	0	4.03	0.05
25	10	3.62	1.48	1.65	0.28	1.93	0.19
26	11.01	4.89	0	3	0	3	0.0382
Bi	100	8.532	----	9.148	0.0084	9.156	0.0338
Er	----	7.79	----	7.63	1.1	8.7	159.(4.)
162	0.14	8.8	0	9.7	0	9.7	19.(2.)
164	1.56	8.2	0	8.4	0	8.4	13.(2.)
166	33.4	10.6	0	14.1	0	14.1	19.6(1.5)
167	22.9	3	1	1.1	0.13	1.2	659.(16.)
168	27.1	7.4	0	6.9	0	6.9	2.74

170	14.9	9.6	0	11.6	0	11.6(1.2)	5.8
Yb	----	12.43	----	19.4	4	23.4	34.8
168	0.14	-4.07-0.62i	0	2.13	0	2.13	2230.(40.)
170	3.06	6.77	0	5.8	0	5.8	11.4(1.0)
171	14.3	9.66	-5.59	11.7	3.9	15.6	48.6(2.5)
172	21.9	9.43	0	11.2	0	11.2	0.8
173	16.1	9.56	-5.3	11.5	3.5	15	17.1(1.3)
174	31.8	19.3	0	46.8	0	46.8	69.4(5.0)
176	12.7	8.72	0	9.6	0	9.6	2.85

Plan Moving forward:

Furthermore, the list of dopants was arranged in a way so as to test those dopants for which the most information had been gathered would be tested first. The current plan of action is to test La and Y first, followed shortly by Ce. Based on calculations of the electronic structure for these dopants, multiple dopants may be tested simultaneously to observe the impact on the electronic structure.

References:

[1]Barsoum, M. W. (1997). *Fundamentals of ceramics*. New York: McGraw-Hill.

[2]R.W Grimes and C.R.A. Catlow, *The Stability of Fission Products in Uranium Dioxide*, Phil. Trans. R. Soc. Lond. A (1991) **335**, 609-634

[3]T. Cardinaels et al./ Journal of Nuclear Materials 424 (2012) 289-300

[4]C. Keller, Uranoxid-Oxide der Seltenen Erden, J. Inorg. Nucl. Chem. 1969, Vol. 31. Pp. 965 to 980

[5]A. Leenaaers et al./Journal of Nuclear Materials 317 (2003) 62-68

[6]T.A. Olds et. al./ Journal of Nuclear Materials 530 (2020) 151959

[7]S.C. Middleburgh et al./ Journal of Nuclear Materials 427 (2012) 359-363

[8]A. Baena et al./ Journal of Nuclear Materials 461 (2015) 271-281

[9]National Institute of Standards and Technology, *Neutron Scattering Lengths and Cross Sections*, Neutron News, Vol.3, No. 3, 1992, pp. 29-37

[10]S.-H. Kang et al. / Journal of Physics and Chemistry of Solids 63 (2002) 773-780

[11]Phase Equlibria Diagrams Online Database (NIST Standard Reference Database 31), The American Ceramic Society and the National Institute of Standards and Technology, 2020, Figure Number 353

[12]Phase Equlibria Diagrams Online Database (NIST Standard Reference Database 31), The American Ceramic Society and the National Institute of Standards and Technology, 2020, Figure Number 6848

Report: Computational Methodology

Dylan Windsor & Haixuan Xu
University of Tennessee, Knoxville-Dept. of Materials Science and Engineering

Summary:

There are currently three levels of density functional theory (DFT) in consideration, used in previous works, to study the properties of uranium dioxide (UO_2) in addition to doped UO_2 systems: DFT+U, hybrid functionals of DFT (henceforth, simply "hybrid"), and DFT+DMFT. The question addressed herein concerns which level of DFT is required to accurately describe the properties of interest in UO_2 systems, while providing the greatest efficiency for computational resources under the current time and resource constraints. First, it is important to note that standard DFT functionals, such as Local Density Approximation (LDA) and Generalized Gradient Approximation (GGA), are well known to be insufficient to describe electronic properties of systems which contain highly correlated electrons, failing even to calculate the insulating behavior of UO_2[1-7]. These drawbacks make standard forms of DFT functionals inadmissible for use in the current work, and as such, are not considered further. Contrariwise, DFT+U has been used in many studies of the UO_2 systems to great effect, reproducing both structural and electrical properties to an appreciable accuracy in comparison to experiment[1-7], through a user supplied Hubbard-U parameter that provides an energy penalty on the correlated electron orbitals. This however, introduces metastable state solutions by causing electrons to become localized to certain bands during electronic relaxation, which may not be escaped easily[1-2, 5-6], and avoided only through methods such as occupation matrix control, stepwise increases in Hubbard-U parameter, etc[1-2, 6]. Alternatively, hybrid functionals, such as HSE or PBE0, may be used to even more accurately approximate material properties by mixing the Hartree-Fock (HF) exact exchange with standard DFT functionals. Thus, hybrid functionals remain relatively computationally efficient while increasing the accuracy of calculations, with the drawback of still needing a user specified variable to explicitly define the amount of mixing between the standard DFT functional and the more accurate HF exact exchange[6, 8-13, 14]. The final method under consideration is DFT+DMFT, where DFT is augmented through use of dynamic mean-field theory (DMFT) to allow for the solution of local many-body electron problems[5-6, 14-16]. Through the inclusion of local many-body electron interactions, strongly correlated systems of electrons may be treated even more precisely and accurately than in hybrid or DFT+U; however, the computational cost of this accuracy is considerably greater than hybrid functionals, insofar as to make DFT+DMFT infeasible on systems larger than 10s of atoms[6]. After assessing and comparing each of these methods, we posit that a combination of hybrid and DFT+U used in conjunction would provide the most time and resource efficiency, while sacrificing the least accuracy.

DFT+U:

The DFT+U level of theory achieves greater accuracy, especially in materials with correlated electrons, than standard DFT functionals by including a Hubbard-like Coulomb interaction (U) parameter in the total energy of the electrons:

$$E_{DFT+U} = E_{DFT} + E_{Hub} - E_{dc} \quad (1)^2$$

where E_{DFT} is the energy contribution from the standard DFT functional, E_{Hub} is the energy from the Hubbard-like Coulomb interaction, and E_{dc} is the double counting term (energy removed from E_{DFT}, being replaced by E_{Hub}). The E_{Hub} term is a Coulomb type interaction accounted for in the orbitals where the highly correlated electrons are found, providing a more accurate representation of the interaction energy between electrons in those orbitals, which does not include the erroneous self-interaction present in E_{DFT}[1-2, 5-6]. E_{dc}, the double-counting term, attempts to remove the part of E_{DFT}, which is now being accounted for with E_{Hub}, by applying an energy penalty to fractionally occupied bands[2]. The energy penalty results in metastable states, or local minima, that can be very difficult to escape, due to the magnitude of the energy penalty.

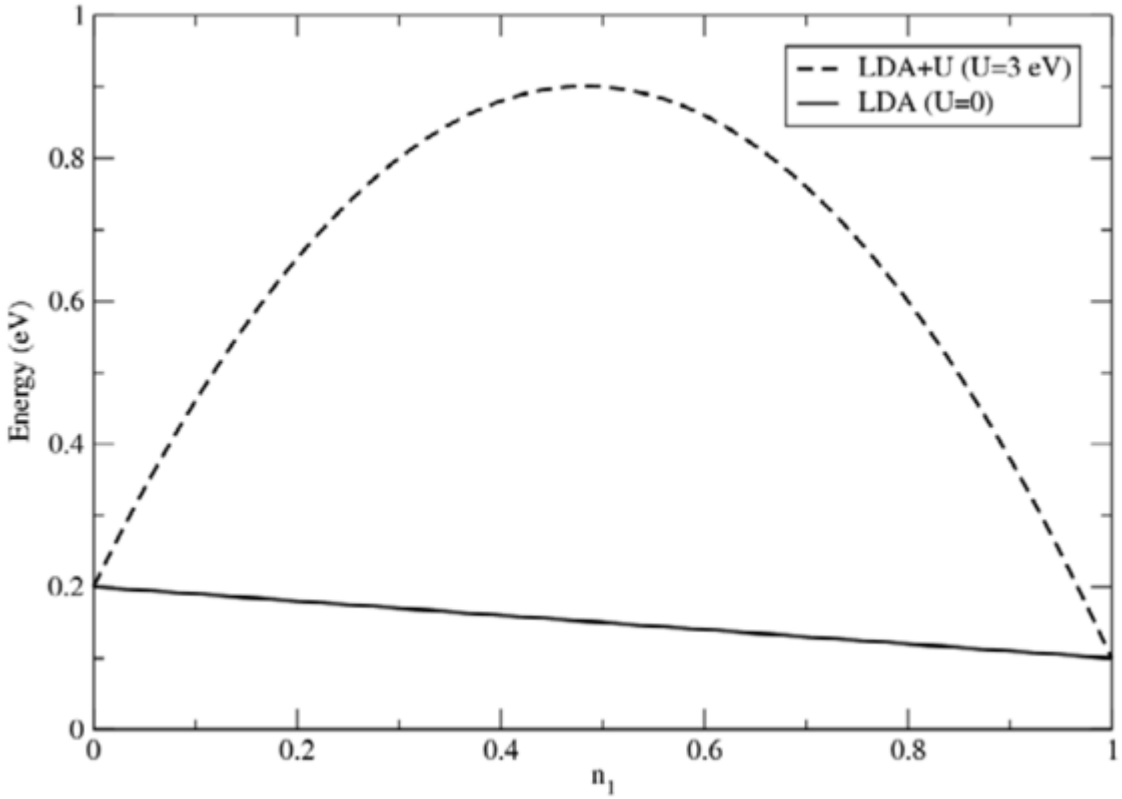

Figure 1[2]: Herein, a two-state system with a single electron is considered, where n_1 is the occupation number for the band considered. Note, when using the LDA+U functional and energy penalty is applied to fractional occupations, and it is this energy penalty that results in the creation of additional metastable states.

Furthermore, calculations may become stuck in these local minima and never reach the ground state[1-2]. To further complicate matters, the value of "U" is user defined, many electrical properties of the material depend on this value quite strongly, and different properties depend on it in varying degrees, meaning a single value of U may not obtain all desired properties[5-6]. However, it is prudent to note, structural properties, including bulk modulus and lattice parameters, exhibit a much smaller dependence on the U-parameter value than electronic or magnetic properties[1-2, 5-6].

i	j	Matrix	$E-E_{\min}$ (eV)	Gap (eV)
−3	−2	[1100000]		No convergence
−3	−1	[1010000]	0.00	2.8
−3	0	[1001000]	1.87	Metallic
−3	1	[1000100]	0.71	1.6
−3	2	[1000010]	1.63	Metallic
−3	3	[1000001]	3.45	0.1
−2	−1	[0110000]		No convergence
−2	0	[0101000]	1.65	0.9
−2	1	[0100100]		No convergence
−2	2	[0100010]	2.62	0.2
−2	3	[0100001]		No convergence
−1	0	[0011000]	1.87	Metallic
−1	1	[0010100]	0.71	1.6
−1	2	[0010010]	1.63	Metallic
−1	3	[0010001]	0.00	2.8
0	1	[0001100]	1.87	Metallic
0	2	[0001010]	0.10	2.0
0	3	[0001001]	1.87	Metallic
1	2	[0000110]	1.63	Metallic
1	3	[0000101]	0.00	2.8
2	3	[0000011]	2.32	Metallic

Table 1: This work performed by [1], shows the careful exploration of the existing metastable states of UO_2. The metastable states range from simply having slightly higher cohesive energy, to being incorrectly described as metallic. These states were explored using the occupation matrix control scheme, and it is shown in [1] that these states can be avoided by use of one of several methods (see text).

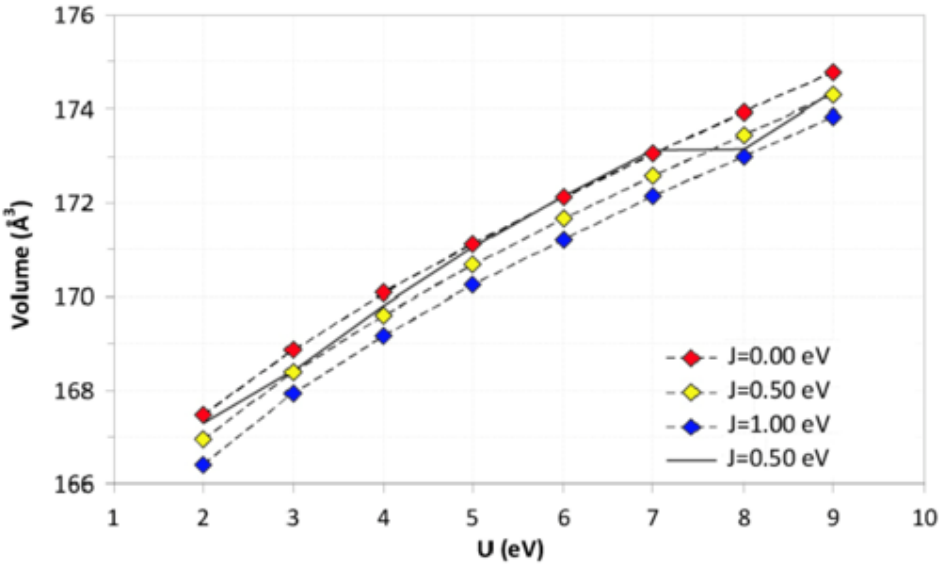

Figure 2: This figure is taken from [2]. The colored curves are for highlighting the OCM method, while solid black is initializing a calculation from random orbitals. As shown here, the choice of U parameter doesn't seem to strongly influence the lattice constant.

There are several ways to set the value of U, two of the most popular being U-ramping and setting U empirically to match desired properties (property matching)[5]. In the case of UO_2, the widely accepted values of U are ~3.9 to 3.96 eV, as calculated from x-ray photoemission spectra[17, 18], although other values are used as well, extending the range from around 3.5 to 4.0 eV. Ramping the U-parameter, by contrast, is used far less often to set the value of U itself, and is instead used alongside two other methods to avoid metastable states: i.) occupation matrix control, (OMC) wherein the occupation matrix is set to nearly the ground state occupation matrix using progressively more accurate guesses; ii.) U-ramping, where incrementally (usually 0.1 eV) larger values of U, starting from 0 eV, are used from the previous calculations wavefunctions to converge the system slowly to the ground state; iii.) quasi-annealing (QA), in which a "fake" fluctuation is applied to the background potential to explore the potential energy surface[2-3]. It has been shown by Dorado *et al*. that even the metastable state closest to the ground state occurs at a difference of +12 meV, with 20 other metastable electronic configurations possible as well (Table 1). Some of these metastable states possess energies even up to 3.45 eV above the ground state or with a metallic band structure, making them an important hurdle in the calculation of electronic properties that, when improperly handled, can result in significant error[3]. For UO_2, this is much less a danger due to the significant body of previous works performed specifically to

explore and avoid these metastable states, and to find the U values for which the experimental values of properties are reproduced[1-5, 9, 14].

Table 2. UO_2 bulk properties (cell parameters, cohesive energy E_{coh}, bulk modulus B, and bandgap Δ), calculated with different approximations beyond DFT, including DFT + U with different functionals, hybrid functionals (PBE0, HSE, EECE), and SIC.

Authors	Approx.	Basis	(a, b, c) (Å)	E_{coh} (eV)	B (GPa)	Δ (eV)
Dudarev [84]	LSDA + U	LMTO/ASA	(5.36, 5.36, 5.36)			1.1
Dudarev [85]	LSDA + U	LMTO/ASA	(5.37, 5.37, 5.37)	22.2	173	1.3
Yun [86]	PBE + U	PAW	(5.44, 5.44, 5.44)	20.3	209	1.8
Iwasawa [87]	PBE + U	PAW	(5.52, 5.52, 5.47)		190	1.8
Prodan [32]	PBE0	GAUSSIANS	(5.45, 5.45, 5.45)		219	3.1
	HSE		(5.46, 5.46, 5.46)		222	2.4
Gupta [88]	PW91 + U	PAW	(5.52, 5.52, 5.52)	21.7	209	1.8
Geng [89]	LSDA + U	PAW	(5.44, 5.44, 5.44)	32.8	208	1.5
	PBE + U		(5.55, 5.55, 5.55)	28.8	181	1.6
Nerikar [90]	PW91 + U	PAW	(5.49, 5.49, 5.49)			1.9
Gryaznov [91]	LSDA + U	PAW	(5.46, 5.46, 5.42)	26.0	196	1.8
	PBE + U		(5.57, 5.57, 5.51)	23.0	180	1.9
	PW91 + U		(5.56, 5.56, 5.51)	23.1	183	1.9
Yu [92]	GGA + U	PAW	(5.54, 5.54, 5.49)	21.2		1.2
Dorado [34]	PBE + U	PAW	(5.57, 5.57, 5.49)		187	2.3
Jollet [35]	EECE	PAW	(5.51, 5.51, 5.51)		199	2.0
Petit [93]	SIC	LMTO/ASA	(5.47, 5.47, 5.47)		219	2.6
Devey [94]	GGA + U	PAW	(5.54, 5.54, 5.54)		197	2.6
Sanati [95]	LSDA + U	PAW	(5.45, 5.45, 5.45)		221	
	PBE + U		(5.55, 5.55, 5.55)		192	
Thompson [96]	PW91 + U	PAW	(5.54, 5.54, 5.54)		188	2.8
Tian [97]	PBE + U	PAW	(5.55, 5.55, 5.55)	21.8	192	2.2
Dorado [82]	LSDA + U	PAW	(5.41, 5.41, 5.41)	24.8	222	2.3

(Table 2 is reproduced from [2])

However, in the case of several of the dopants being considered in this study, namely, Bi, Cr, and Nb, it has been difficult to find a U-parameter applied to the correlated electrons for the doped species in the UO_2 environment. This means there would be error associated with choosing a U-parameter for these materials, since U depends on crystal structure, chemical environment, and is also often chosen for the property of interest[1-5, 9]. Furthermore, assuming a correct U-parameter could be chosen and vetted against experiment, the issue of ensuring each calculation converges to the global minimum would involve OCM[2], U-ramping[2], or QA[2], each of which expand the time required to obtain the properties of interest. It is the authors belief that learning and executing the required techniques within VASP would require more time than per system than would hybrid calculations.

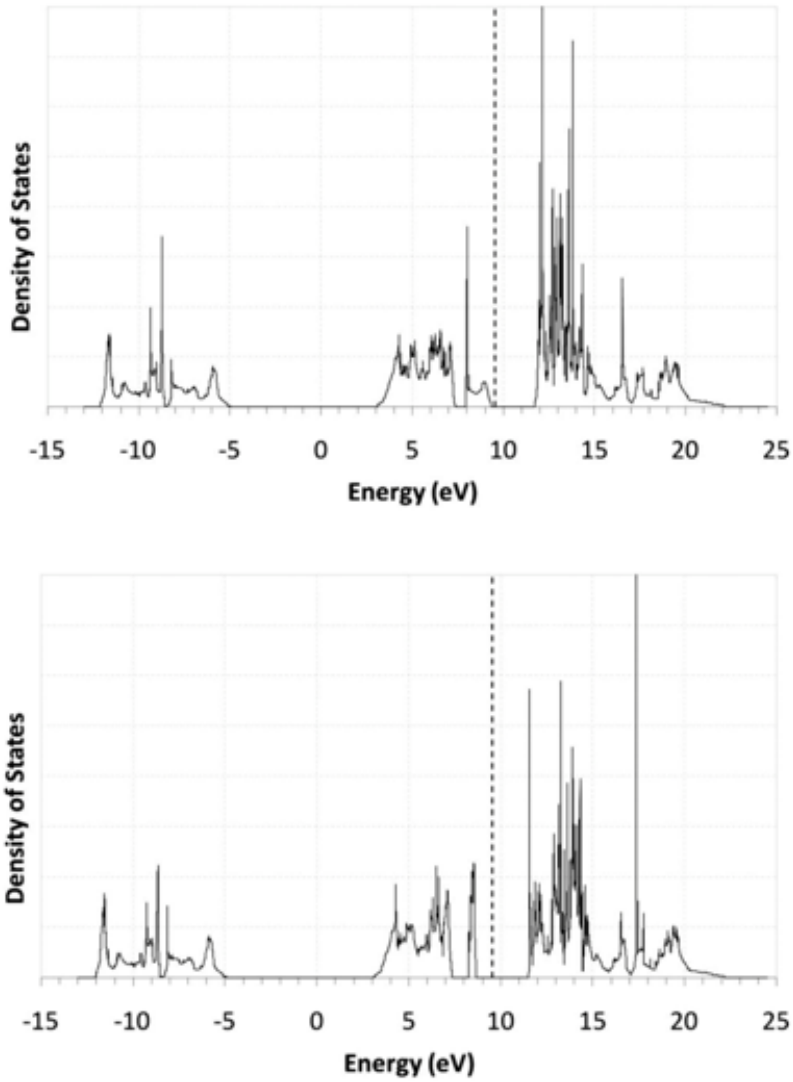

Figure 3[1]: The total density of states (DOS) of the ground state (above) and the first metastable state (below) of UO_2, as calculated in [1] using the OCM method. It should be noted here, the danger of metastable states and not carefully choosing the U parameter accordingly, since the metastable states can have significantly different electronic structures.

This stems from the nature of the study, by looking for a particular property in a variety of unknown systems the OCM process, for example, would need to be repeated for every system. On the other hand, if the study were focused on a single system, there would only be need to perform the OCM process once to explore the properties of the system, since the occupation of the orbitals in the system would be unchanged or would start from the same place.

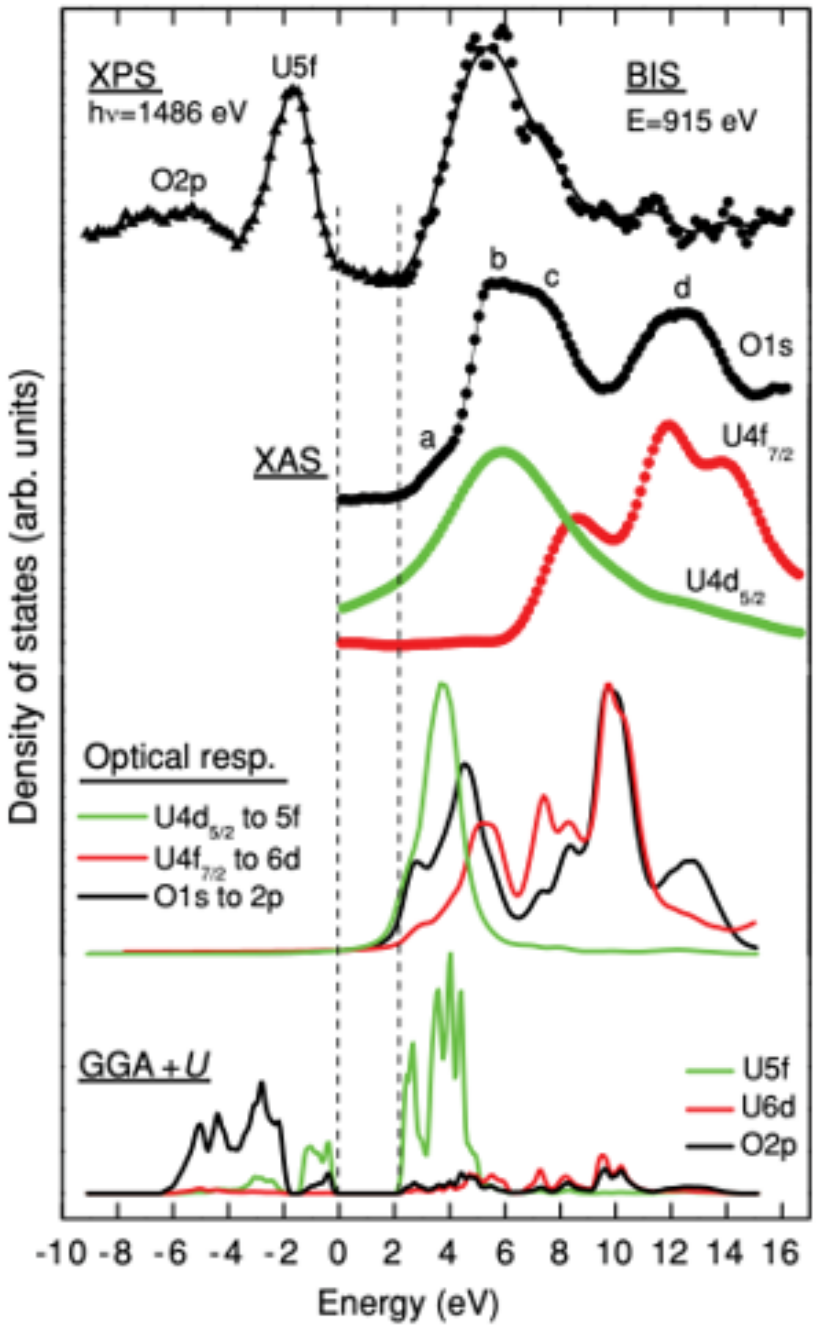

Figure 4[7]: Shown here is a comparison of GGA+U to experimental data of various kinds. Upper panel: XPS, BIS, and XAS are shown, where XPS and BIS are aligned on the valence band maximum and conduction band minimum with a band gap of 2.1 eV. XAS spectra of O 1s, U $4d_{5/2}$, and U $4f_{7/2}$ are aligned with the conduction band minimum (first two shown in TFY mode, and last in TEY mode). Features a and b originate from hybridization of O 2p and U 5f, while c and d result from hybridization of O 2p and U 6d. The middle panel shows the optical responses, and the bottom shows GGA+U calculated partial DOS using U_{eff} = 4.261 eV applied to U 5f orbitals. This illustrates the closeness that can be achieved to experimental data using DFT+U; however, it should be noted that [7] made no mention of ensuring the results were for the ground

state and not a metastable state. Additionally, there have been several recent studies of using DFT+U on defect system as well to some success.

Hybrid:

There are currently two hybrid functionals under consideration for the current work, PBE0 and HSE, both of which are implemented in VASP, and have been used to study the UO_2 system. The hybrid functional PBE0 has been shown to achieve high levels of accuracy reproducing properties of actinide oxide materials. However, there is a large computational cost associated with performing calculations using PBE0, due to the inclusion of the Hartree-Fock (HF) exact exchange component that provides the improved accuracy.

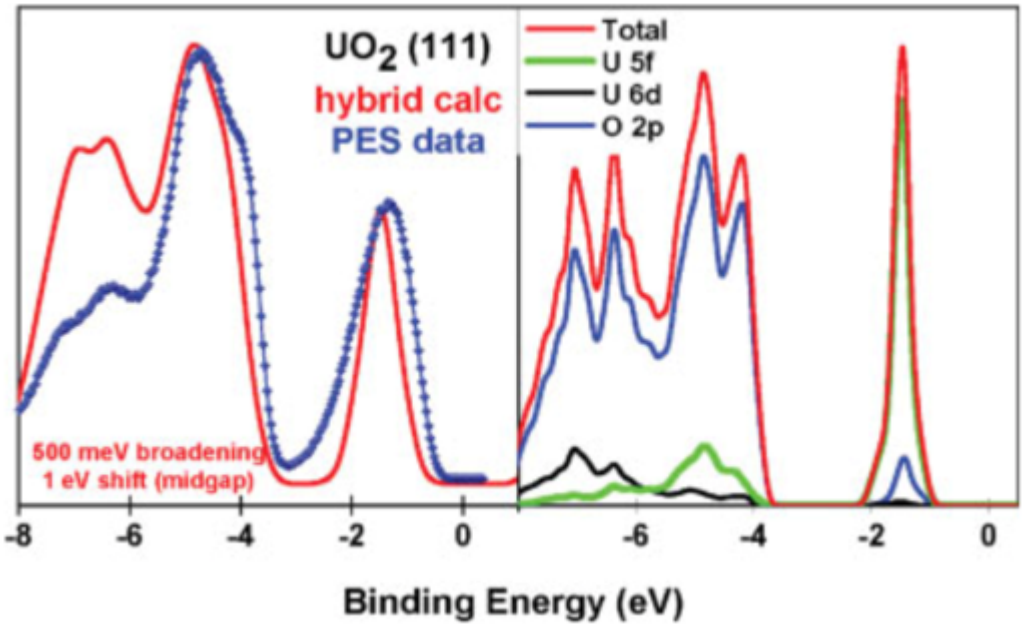

Figure 5[13]: In this figure, from [13], experimental PES DOS data is compared to a hybrid functional calculation of the DOS. This shows very good agreement between the methods.

The HSE functional realizes higher computational efficiency compared to PBE0 by substituting a screened Coulomb potential for the full one, which is split using the error function. The parts of the exact exchange are split into the short- and long-range portions of the HF, where the long-range HF is replaced by the long-range portion of the GGA functional. This leads to the energy calculation:

$$E_{xc}^{screened} = aE_x^{HF,SR}(\omega) + (1-a)E_x^{GGA,SR}(\omega) + E_x^{GGA,LR}(\omega) + E_c^{GGA} \quad (2),[11]$$

where the parameters a and ω are responsible for mixing, $E_{xc}^{screened}$ is the total energy of the calculation, the superscripts HF and GGA refer to energy components from the exact exchange and standard DFT GGA, respectively, and the superscripts LR and SR refer to long-range or short-range. The mixing parameter ω is internally set to 0.15 $Bohr^{-1}$ based on the initial

realization of the functional, while a is set by the user, usually 0.25, based on arguments from perturbation theory. Amazingly, GGA and screened Coulomb substitution has been shown not to depreciate the agreement of HSE results with experimental studies, and in a test against benchmarked semiconductor materials yielded an absolute mean error of 0.26eV, agreeing quantitatively with the benchmark calculations using quantum Monte Carlo.

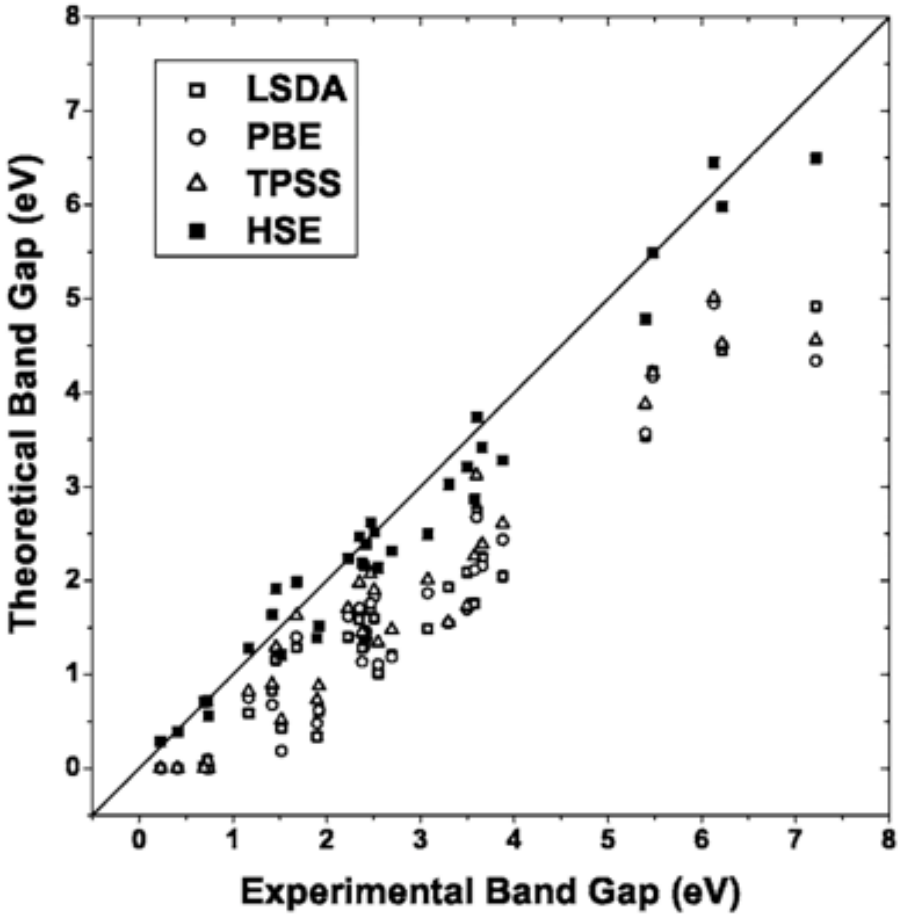

Figure 6[8]: Shown here is a comparison of the local spin-density approximation (LSDA), PBE generalized gradient approximation (GGA), TPSS (a meta-GGA), and the HSE hybrid functional to experimental data for benchmark semiconductors. It is shown here that HSE agrees very well with experiment and is superior to the other functionals used.

In addition to the computational efficiency improvements over PBE0, HSE improves upon older hybrid functionals, such as B3LYP and PBEh, by correctly handling metallic systems as well. Finally, in a study of silicon phases and defects, the HSE functional was shown to agree very well with both experimental and benchmark Diffusion Monte Carlo (DMC) results on diffusion energy barriers, defect formation energies, and cohesive energy of crystalline materials[8]. Thus, based on improved computational efficiency over PBE0 without suffering significant accuracy loss, as well as improvements to allow the handling of metallic systems, the HSE functional would work very well in the current work, given the inclusion of dopants may change the electronic structure of the UO_2. **Finally, given the good quantitative picture of the electronic structure given by HSE, and its computational efficiency advantages over previous**

renditions of hybrid, the authors believe HSE would best suit the careful study of the band structures of even doped systems of UO_2.

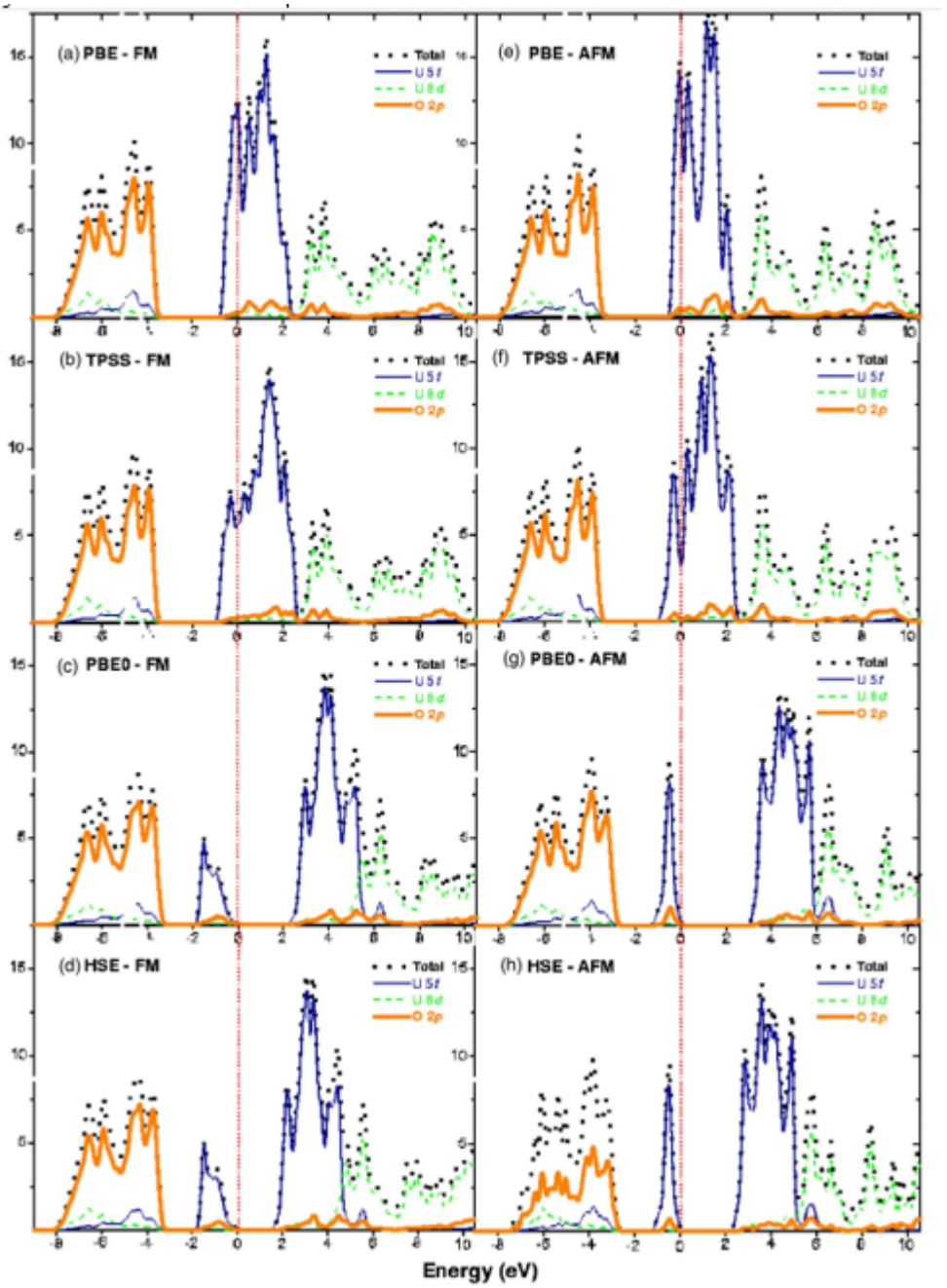

Figure 7[11]: Shown on the left are comparisons of the ferromagnetic (FM) and antiferromagnetic (AFM) states of bulk UO_2 as calculated by several different functionals for comparison. PBE and TPSS are pure DFT functionals, which are compared based on calculated partial and total DOS data with hybrid functionals PBE0 and HSE. Note the significant improvements to the DOS structure from HSE and PBE0.

DFT+DMFT:

The final method under consideration is DFT+DMFT, wherein the static mean-field theory, DFT, is supplemented with dynamic mean-field theory. In DMFT, the local many-body electron problem is solved instead of the one-electron problem posed in DFT, meaning that interactions between electrons are more accurately accounted for and properties based entirely on electron-electron interactions would lend themselves to study. As such, DMFT allows study of solid systems and their properties at finite temperature, in addition to considerations of properties at 0 K[15]. This makes DFT+DMFT the most accurate method currently being considered for use in the current work; however, the cost of this accuracy is a computational tax on resources greater than that of even PBE0, being suitable for only 10s of atoms in very small supercells[6, 16]. Furthermore, it is noted by Amadon[16] that previous to use of DMFT, the computational cost was so prohibitive that no calculations were performed on actinides at all, and while these advances have improved computational efficiency enough to make it feasible there are still several hurdles to overcome when using DFT+DFMT[16]. First, a self-consistent DFT+U calculation, or several, must be carried out using the U-ramping method and constrained random phase approximation (cRPA) to calculate both the Coulomb and Hund's interactions, the separate components of the U-parameter. Second, these parameters are used with the wavefunctions and eigenvalues obtained therein, weighted with the correlated Wannier orbitals, to calculate the noninteracting polarizability. The noninteracting polarizability is used with the cRPA method to calculate the new U parameter for DFT+U, a process that is repeated until the value for U has converged. These Wannier functions are also used here to calculate the lattice Green's function, from which the local electron interactions are calculated, which is the DMFT part of the process. The self-energy in this method is computed afterword (not using DMFT), using a continuous-time quantum Monte Carlo (CTQMC) solver, and is fed back into the lattice Green's function until the self-energy has converged[16]. As such, the spin-orbit coupling and other local effects are accurately described using this method, and it is one of the few methods capable of describing paramagnetic structures very accurately as well[16]. Finally, based on the above discussions and figures below, while DFT+DMFT is certainly a navigable theory for simulating small UO_2 systems very accurately, it is not feasible to simulate supercells greater than a few 10s of atoms. Since the edge of DFT+DMFT's limitation is only 10s of atoms it would be practically infeasible to use in the current work where defects included as the systems are doped would further increase the computational cost.

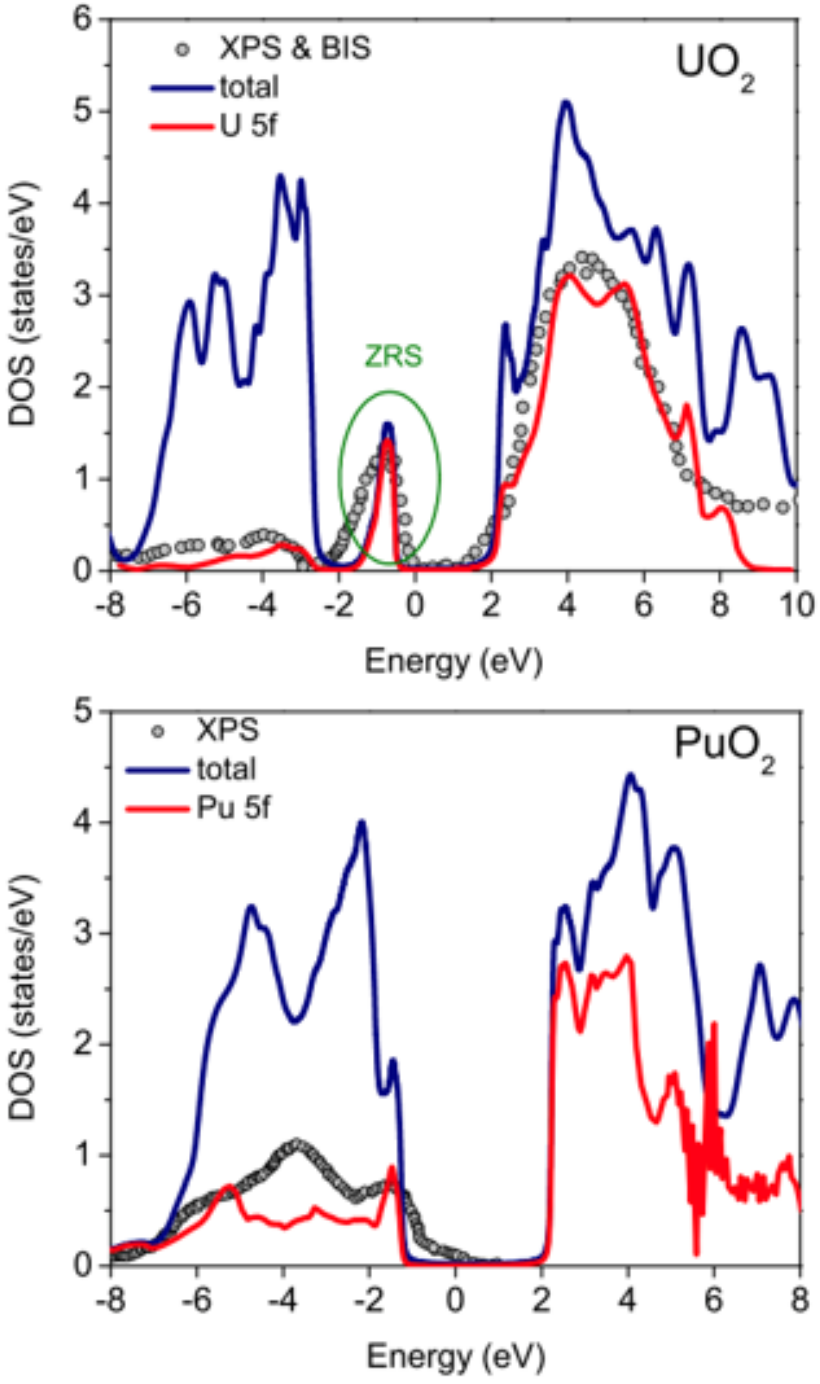

Figure 8[16]: Herein, the DFT+DMFT spectral functions are compared to the experimental spectra. The U experimental photoemission spectrum was gathered at 398K, and the DFT+DMFT results shown here show good agreement[16] with experiment.

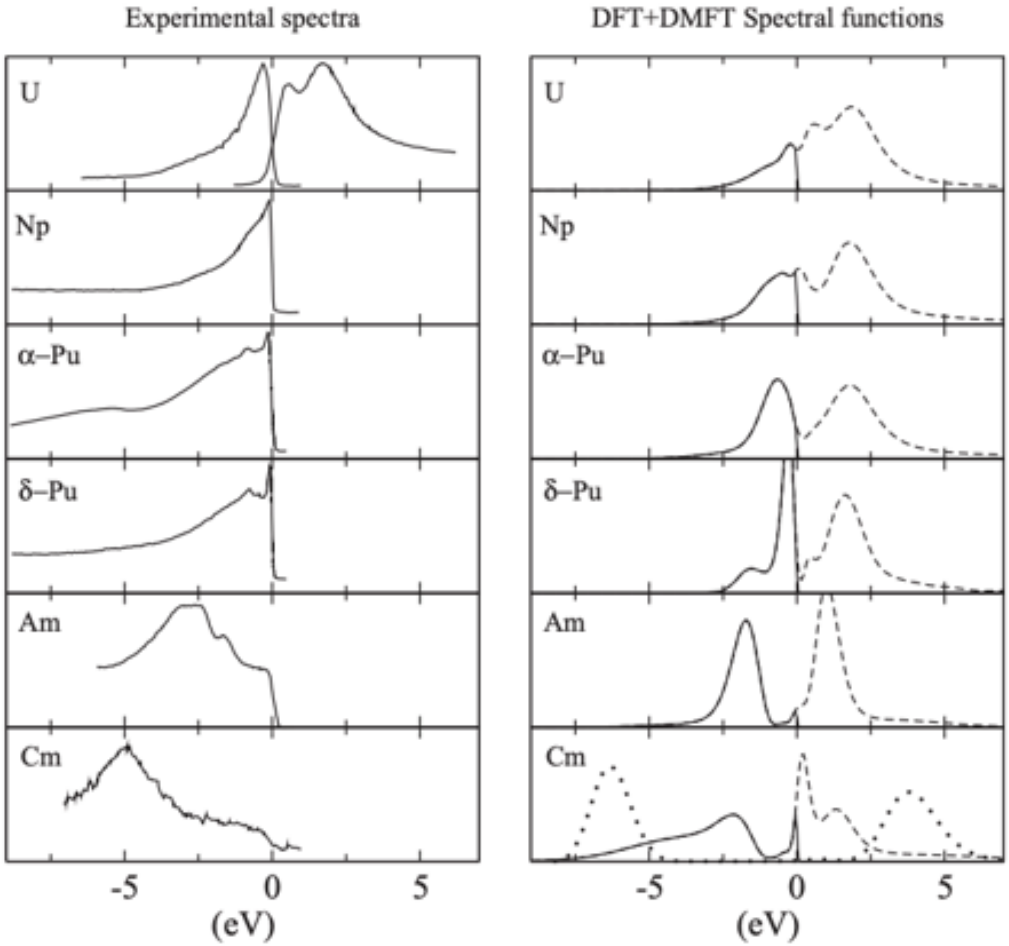

Figure 9[14]: To the left, the partial and total DOS of UO_2 as calculated by DFT+DMFT in [14] is shown against XPS and BIS experimental data. The agreement here between the U 5f DOS and XPS/BIS data is very good, showing the accuracy of the DFT+DMFT.

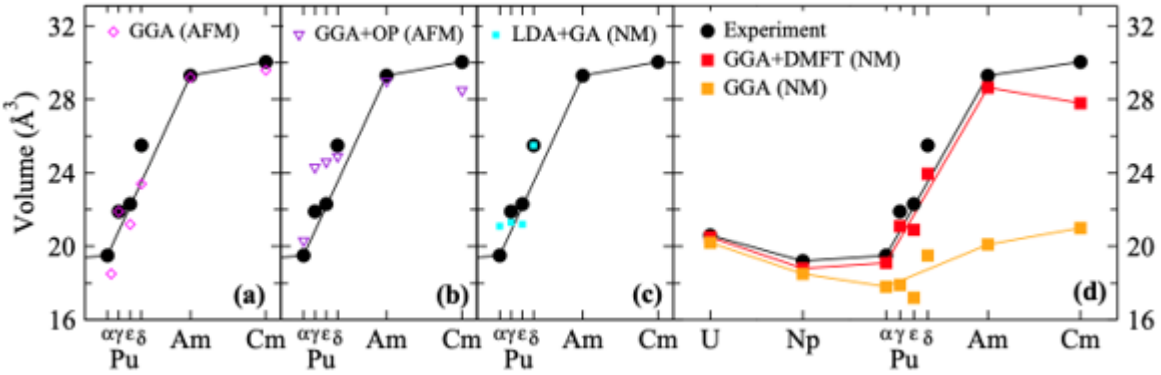

Figure 10[16]: Above (from [16]), experiment, GGA+DMFT, and GGA calculated volumes of cells are compared for several of the actinides in the rightmost window. Note that for U, there is little requirement for the use of DMFT for structural parameters, since there is little difference within the calculated volumes. In later actinides where spin-orbit coupling becomes a more dominant effect, there standard DFT (such as GGA) is not sufficient.

Comparison and Conclusion:

In comparing the three methods above, the accuracy is highest in DFT+DMFT, followed by hybrid, and last is DFT+U, while the computational efficiency trend is the opposite. However, the accuracy required can be easily assessed by comparison with experimental data.

Property	a=b	c	E_coh	Gap
Method	(Å)	(Å)	(eV)	(eV)
Experimental	5.47	5.47	21.9[12]	2.0-2.5[2,3,13,18]
PBE+U				
Yun 2005[5]	5.44	5.44	20.3	1.8
Geng 2007[3]	5.55	5.55	28.8	1.6
Gryaanov 2009[4]	5.57	5.51	23	1.9
Dorado 2009[1]	5.57	5.49		2.3
Tian 2012[5]	5.55	5.55	21.8	2.2
Hybrid (Prodan 2006)[11]				
PBE0	5.45	5.45		3.1
HSE	5.46	5.46		2.4
DFT+DMFT[14]				
Yin				2.2

Table 1: Data taken from various studies (based on the table in [5]) is shown here. Note the higher degree of accuracy in later studies using DFT+U, when metastable states were more carefully considered, as in Tian and Dorado. The cohesive energy, as well as band gap agree with the experimental data, but the lattice parameters have less accuracy here. (It should be noted that the authors have obtain better agreement with experiment for the current work). The hybrid functionals maintain good agreement with experimental data in both structural parameters and band gap. Finally, as expected, the DFT+DMFT method obtained high accuracy for the value of the band gap.

Note from the discussions above, that to accurately replicate experimental data concerning the electronic structure of UO_2, DFT+U sufficiently reproduces the structural data and lattice parameters of the UO_2 system when compared to experiment and the other two methods in question[1-2, 5, 16]. Finally, while DFT+U is capable of reproducing the band gap and Mott insulating behavior correctly, and in agreement with experimental, hybrid, and DFT+DMFT benchmark values[2, 5], it can only reproduce the DOS (and therefore band structure itself) qualitatively, and does not necessarily agree with the structure reported by hybrid and DFT+DMFT[11, 7, 14, 16].

Since DFT+U seems to reproduce structural parameters in addition to an accurate value for the band gap, this level of theory should be relegated to use for finding the structural parameters and to quickly look at an approximate DOS when needed. This way, the section of the work involving structural energy minimization will have the greatest computational efficiency without sacrificing accuracy.

When looking at the reproduction of an accurate DOS, figures 5, 7, and 9 should be compared. Note the accuracy of the DFT+DMFT technique and hybrid are comparable to one another and both reproduce good agreement with experiment when calculating DOS and band structure[10, 11]. As such, with the extra computational burden of DFT+DMFT and the limited time constraints for the current work, it seems pragmatic to use hybrid, since it will provide the needed boost in accuracy over DFT+U, allowing for a quantitative picture of the electronic structure, without the large computational burden of DFT+DMFT.

Summary Main Points:

i.) DFT+U agrees with benchmark methods and experiment for structural parameters, cohesive energies, and band gap values, and provides the greatest computational efficiency of the methods in question. As such, DFT+U will be used for structural relaxations, but not electronic structure study (i.e. DOS and Band structure calculations)

ii.) Hybrid agrees with benchmark methods and experiment for structural parameters and electronic structure, providing the needed accuracy in both areas, but less computationally efficient than DFT+U. Therefore, hybrid will be used for DOS, partial DOS, and band structure calculations.

iii.) DFT+DMFT is itself considered a benchmark method for looking at structural parameters and electronic structures; however, its computational cost is so prohibitive that it is impractical for the current work.

Issues:

During acquisition and set up of resources purchased for the project, a member of the Advanced Computing Facility (ACF) staff, working in the area where the resources are housed, contracted COVID-19. As a result, access to the area where the resources are has been denied to staff in charge of setting up the resources, causing a significant delay in the project workflow, and putting the calculations significantly behind schedule.

References:

[1]Dorado *et. al.* / PHYSICAL REVIEW B 79, 235125 (2009) DOI: 10.1103/PhysRevB.79.235125

[2]Dorado *et. al.* / J. Phys.: Condens. Matter **25** (2013) 333201 DOI: 10.1088/0953-8984/25/33/333201

[3]Geng, H.Y ., Y . Chen, Y . Kaneta, M. Kinoshita (2007), *Physical Review B*, 75, 054111

[4]Gryaznov et. al. / Phys. Chem. Chem. Phys., 2009, 11, 7241–7247 DOI: 10.1039/b907233k

[5]M. Bertolus , M. Krack , M. Freyss , R. Devanathan, "Ch. 14: Assessment of current atomic scale modelling methods for the investigation of nuclear fuels under irradiation: Example of uranium dioxide," NEA/NSC/R(2015)5

[6]M. Freyss, "Ch.12 : Density Functional Theory" NEA/NSC/R(2015)5

[7]S.-W. YU et al. / PHYSICAL REVIEW B 83, 165102 (2011) DOI: 10.1103/PhysRevB.83.165102

[8]Heyd *et al.* / J. Chem. Phys. **123**, 174101 (2005) DOI: 10.1063/1.2085170

[9]Krukau *et al.* / J. Chem. Phys. **125**, 224106 (2006) DOI: 10.1063/1.2404663

[10]Peralta *et al*. / Physical Review B **74**, 073101 (2006) DOI: 10.1103/PhysRevB.74.073101

[11]PRODAN, SCUSERIA, AND MARTIN / PHYSICAL REVIEW B 73, 045104 (2006) DOI: 10.1103/PhysRevB.73.045104

[12]PRODAN, SCUSERIA, AND MARTIN / PHYSICAL REVIEW B **76**, 033101 (2007) DOI: 10.1103/PhysRevB.76.033101

[13]Roy et al. • Vol. 29, No. 13 • Journal of Computational Chemistry DOI 10.1002/jcc.21036

[14]Yin, Q., A. Kutepov, K. Haule, G. Kotliar, S.Y. Savrasov, W.E. Pickett (2011), *Physical Review B*, 84, 195111

[15]A. Georges *et. al.*: Dynamical mean-field theory of… / Rev. Mod. Phys., Vol. 68, No. 1, January 1996

[16]Bernard Amadon / Physical Review B **94**, 115148 (2016) DOI: 10.1103/PhysRevB.94.115148

[17]Kotani A. and Yamazaki T (1992) Systematic analysis of core photoemission spectra for actinide di-oxides and rare earth sesqui-oxides Prog. Theor. Phys. Suppl. **108** 117

[18]Vydrov *et al.* / J. Chem. Phys. **125**, 074106 (2006) DOI: 10.1063/1.2244560

Additional References

Baer, Y., J. Schoenes (1980), *Solid State Communications*, 33, 885

Bates,J.,C.Hinman,T.Kawada(1967),*JournalofAmericanCeramicSociety*,50,652

Batista *et al*. / Physical Review B **74**, 121102(R) (2006) DOI: 10.1103/PhysRevB.74.121102

Brothers *et al.* / J. Chem. Phys. **129**, 011102 (2008) DOI: 10.1063/2955460

Kelly,P.J.,M.Brooks(1987),*JournaloftheAmericanChemicalSociety*,FaradayTrans.2 83, 1189

Killeen,J.(1980),*JournalofNuclearMaterials*,88,185

Myers, H., T. Jonsson, R. Westin (1964), *Solid State Communications*, 2, 321

Yamazaki T. and Kotani A. (1991) Systematic analysis of 4f core photoemission spectra in actinide oxides J. Phys. Soc. Japan **60** 49

Report: Results of Dopant Studies

Dylan Windsor & Haixuan Xu
University of Tennessee, Knoxville-Dept. of Materials Science and Engineering

Summary:

Many dopants were considered to improve the conductivity of Uranium Dioxide (UO_2) in its antiferromagnetic (AFM) ground state: Cerium (Ce), Lanthanum (La), Yttrium (Y), and Niobium (Nb) were targets for cationic substitution, while different concentrations of Nitrogen (N) were investigated for anionic substitution. As discussed in previous deliverables, the concentrations chosen for substitutions of both types were limited to "safe" concentrations that could be theoretically replicated based on thermochemical determinations and phase diagrams from the literature. In addition, it was determined (see deliverable 2) the level of theory required to quantitatively determine the density of states of these doped systems was hybrid Density Functional Theory (DFT), while an appropriate qualitative calculation requires only a DFT+U level of theory. Based on the aforementioned, DFT+U was used to perform calculations on a specific concentration of each cationic dopant and over varying concentrations of the anionic dopant, N.

Table S1: Herein, all of the data for the study is summarized for each of the dopant cases considered in the current study and compared with UO_2. Each dopant case caused the band gap to be reduced to varying degrees, with the greatest reduction in the band gap being Ce and Nb for cationic dopants, and 25 at. % Nitrogen doped (8xN) for anionic dopants. However, there are no completely metallic systems contained herein using DFT+U.

System	Cation (at. %)	Anion (at. %)	Band Gap (eV)	Band Gap Reduction (%)	E-fermi (eV)	Lattice Parameter Difference (%)	Lattice Parameter (Å)	Gap (UO2)-Gap (System)
UO2	0	0	2.33	0.00	8.113	0.00	5.47719	0.00
Single Neutral Ce	6.25	0	0.81	65.19	8.081	-0.13	5.47013	1.52
Single Neutral La	6.25	0	1.50	35.45	8.220	-0.02	5.47599	0.83
Neutral La Defect Complex	12.5	0	1.33	42.92	8.647	0.40	5.49898	1.00
Single Neutral Nb	6.25	0	0.62	73.43	9.352	-0.51	5.44940	1.71
Neutral Y Defect Complex	12.5	0	1.77	23.99	7.634	-0.26	5.46283	0.56
1xN UON	0	3.125	1.52	34.94	8.380	-0.12	5.47088	0.81
2xN UON	0	6.25	1.51	35.19	8.390	-0.28	5.46181	0.82
4xN UON	0	12.5	1.28	45.02	8.583	-0.57	5.44607	1.05
8xN UON-SQS	0	25	1.28	45.15	8.766	-1.09	5.41757	1.05
8xN UON	0	25	0.96	58.80	9.034	-1.09	5.41757	1.37
16xN UON	0	50	1.22	47.77	9.105	-2.00	5.36755	1.11

Methodology:

The Vienna ab-initio Simulation Package (VASP)[1-5] was used to carry out all simulations for the current study. Each relaxation calculation was performed with a fluorite structure supercell containing 48 atoms (16 U sites and 32 O sites) of size $\sqrt{2}$x$\sqrt{2}$x2 using a 2x2x2 Monkhorst-Pack (k-point) grid. For the density of states (DOS) calculations, a 6x6x6 k-point grid was used alongside a tetrahedron method with Blöchl corrections[6] for Brillouin zone integration to generate a precise and accurate DOS plot with 1500 points taken over a 16eV window of energy, where the features of interest for this study are found. Finally, those calculation parameters used in both types of calculations are an energy cutoff of 550eV, a +U parameter of 3.5eV applied to U, and the PBEsol functional.

Each relaxation calculation was carried out by freezing atomic positions or cell volume in alternating cycles, such that VASP was able to relax both the volume and atomic positions of each doped system while the shape of the supercell remained constant. Relaxations using this method preserve the fluorite $\sqrt{2}$x$\sqrt{2}$x2 supercell structure, while allowing symmetry with the cell to be broken during relaxation. The structures converged to a state where the force was below 5E-03 eV/Å on each atom and the energy difference between iterations was under 1E-06 eV. Highly accurate DOS plots generated from the charge density of a subsequent fully self-consistent calculation are those contained herein.

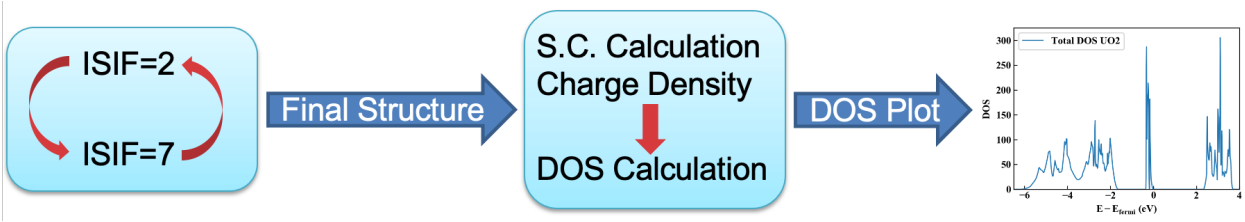

Figure M1: A graphic representation of the calculation methodology, where ISIF is the tag that controls the relaxation degrees of freedom in VASP, and S.C. stands for "self-consistent."

Results:

(i.) **Justification of Using DFT+U:**

As shown in Fig. R1, the DFT+U DOS result from this study is in good qualitative agreement with the HSE hybrid functional result for the AFM state of Prodan et. al. [7], giving credence to the aforementioned methodology and ensuing DOS. In addition, the hybrid results from Prodan et. al. for the AFM state gives a band gap of 2.2-2.4 eV, which is also in good quantitative agreement with the calculated band gap of 2.33 eV from Fig. R1.

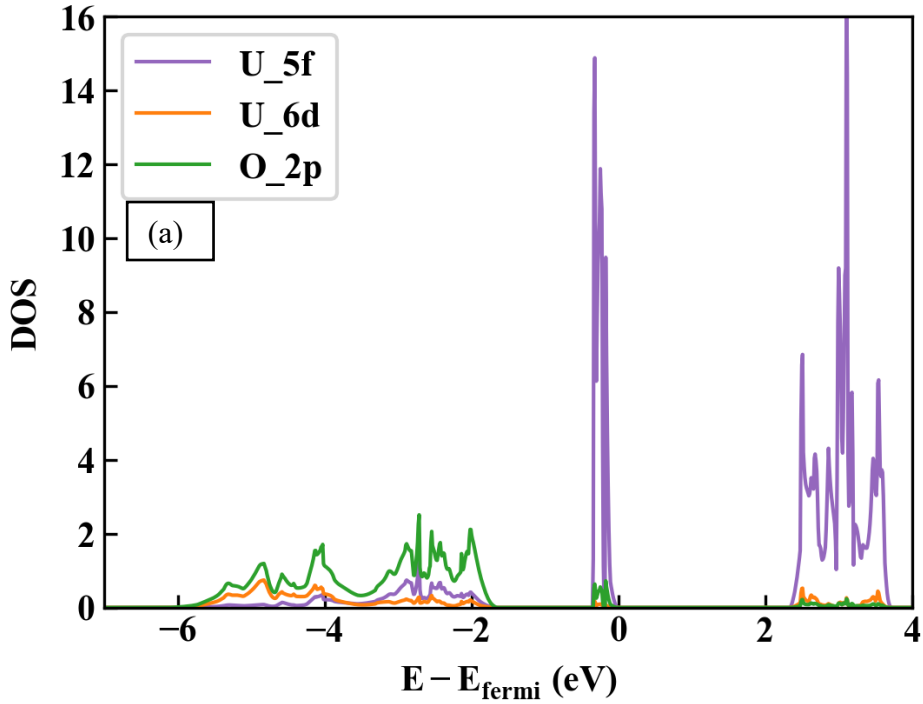

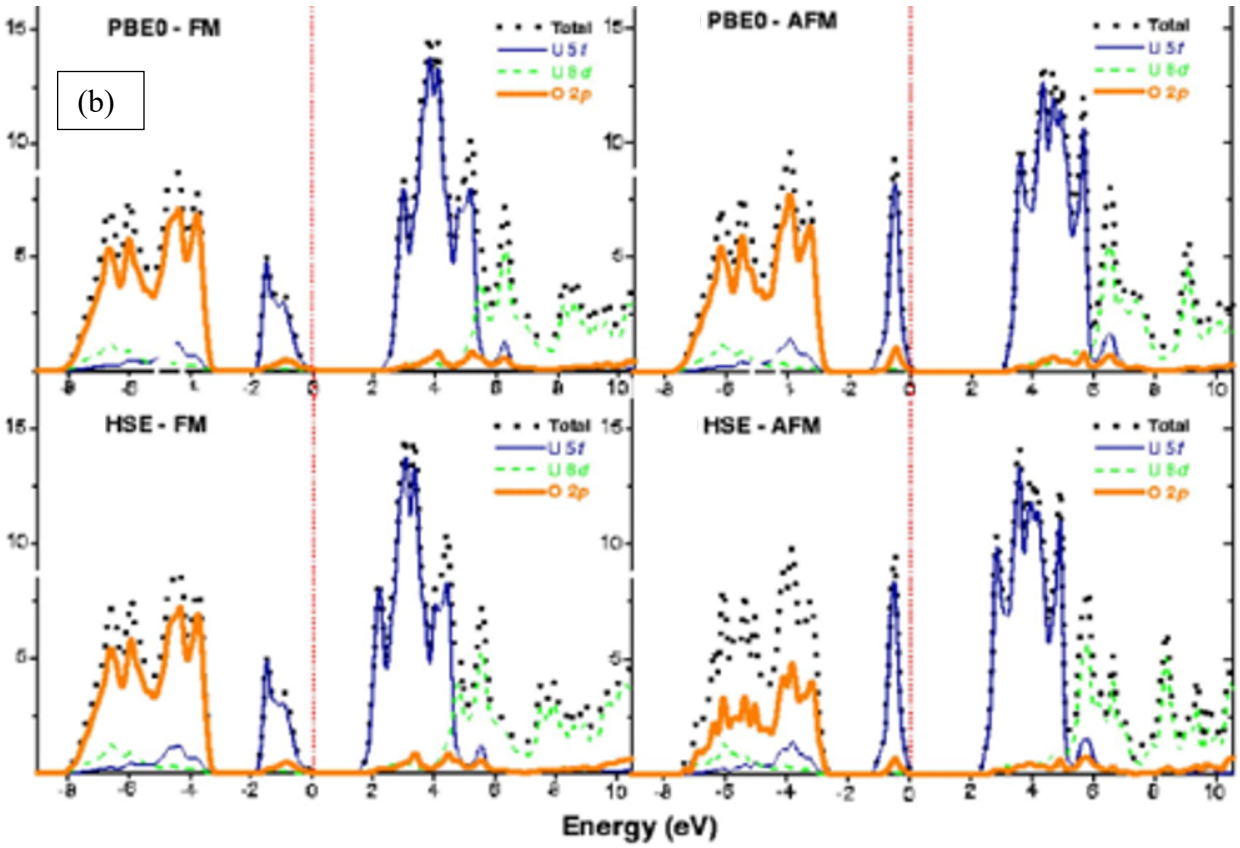

Fig. R1: For justification of current results, the partial DOS of UO_2 (Fig. R1(a)) was generated in the same way as each of the doped systems and compared to the hybrid functional HSE and PBE0 results of Prodan et. al. [7] (Fig. R1(b)) for the antiferromagnetic (AFM) state.

(ii.) **Cation Doping:**

Each of the cationic dopants under consideration were placed into the uranium sublattice by replacing a single U atom with the given dopant, resulting in an atomic % concentration of 6.25, or a given dopant was placed into the lattice as a defect complex (2 U replacements and 1 V_O). In this way the effects each dopant had on UO_2 were investigated separately. It should also be noted here that those calculations for a defect complex were initially used, but due to time constraints were discontinued. This is justified by the kind of study being presented, wherein many cases are screened to get a sense of the qualitative effects of each dopant with the goal of moving to a more accurate technique, like hybrid functionals, in the most promising cases.

Table R1: The cationic dopants most capable of reducing the band gap seem to be both Ce and Nb, though each of the cationic dopants did reduce the band gap somewhat, as expected.

System	Cation (at. %)	Band Gap (eV)	Band Gap Reduction (%)	E-fermi (eV)	Lattice Parameter Difference (%)	Lattice Parameter (Å)	Gap (UO2)-Gap (System)
UO2	0	2.33	0.00	8.113	0.00	5.47719	0.00
Single Neutral Ce	6.25	0.81	65.19	8.081	-0.13	5.47013	1.52
Single Neutral La	6.25	1.50	35.45	8.220	-0.02	5.47599	0.83
Neutral La Defect Complex	12.5	1.33	42.92	8.647	0.40	5.49898	1.00
Single Neutral Nb	6.25	0.62	73.43	9.352	-0.51	5.44940	1.71
Neutral Y Defect Complex	12.5	1.77	23.99	7.634	-0.26	5.46283	0.56

Since, the La neutral defect complex reduces the band gap by 8% more than its single replacement counterpart, the single replacement case for Y was deemed of less relative importance due to the small band gap reduction of the neutral Y defect complex. Even though the defect complexes do reduce the band gap more than the single substitutions, based on the above data, this does not indicate that the doped material will naturally have a greater reduction in the band gap than shown, since in the defect complexes the concentration of the dopant is higher. This is further corroborated by the lack of any key changes between the DOS of a single La substitution and an La defect complex (Fig. R3 and R4). In each case, the La d- and f-states contribute to the leading edge (higher energy side) of the band gap, and only slightly to the tailing edge (lower energy side). This is only minorly modified by the presence of an oxygen vacancy in the defect complex case, where p-states of oxygen now appear to hybridize with the contribution of the dopant at the leading and tailing edge of the band gap (see Fig. R4 and R6). Contrarily, the best candidates for cationic doping, Ce and Nb, reduced the band gap by >60% based on considerably different effects than the other dopants being considered. Both Ce and Nb cause additional bands to be added near the center of the band gap, and the orbitals of the dopant in each case contribute to the leading edge of the band gap as well (see Fig. R2 and R5). However, the Nb d-states are more effective for reducing band gap than the Ce f-states, even causing the Fermi energy to be elevated significantly from the original UO_2 system. These factors make Nb the most promising candidate moving forward, and highest priority for HSE calculations on single cationic dopants, followed closely by Ce.

Cationic Conclusions:

- There is very little change between single substitution cases and defect complex cases.
- The greatest band gap reductions occurs in Nb and Ce, where the d- and f-states contribute to the center of the band gap.
- La and Y contributed primarily to the leading edge of the band gap, and as a result do not reduce the band gap by as much.

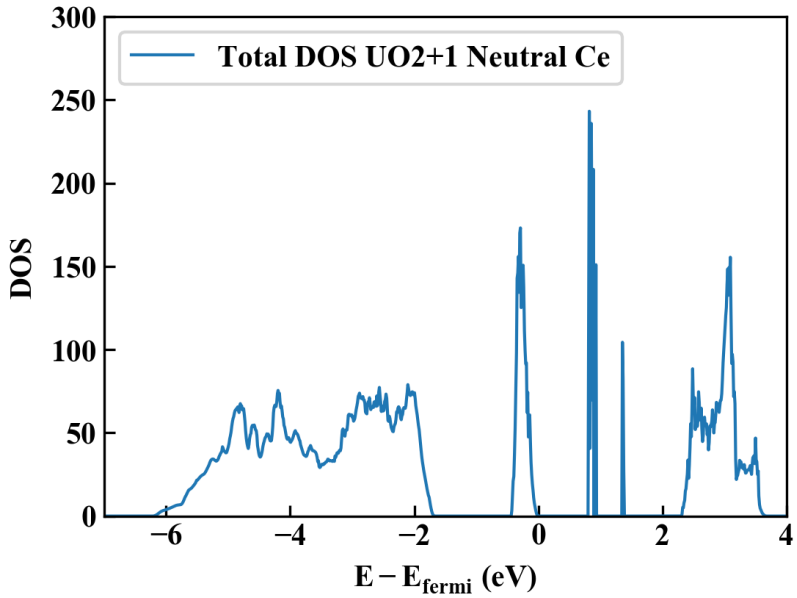

Fig. R2: A single Ce substitution on the U sublattice results in a 6.25 at. % Ce, decreasing the lattice parameter of the fluorite structure by -0.13%. The band gap, as calculated from the total DOS (left) has been reduced by nearly 65% to 0.81 eV. This results from the apparent contribution of Ce 5d and 4f valence states to form vacant states in center of the band gap, as shown in the site-projected partial DOS (below).

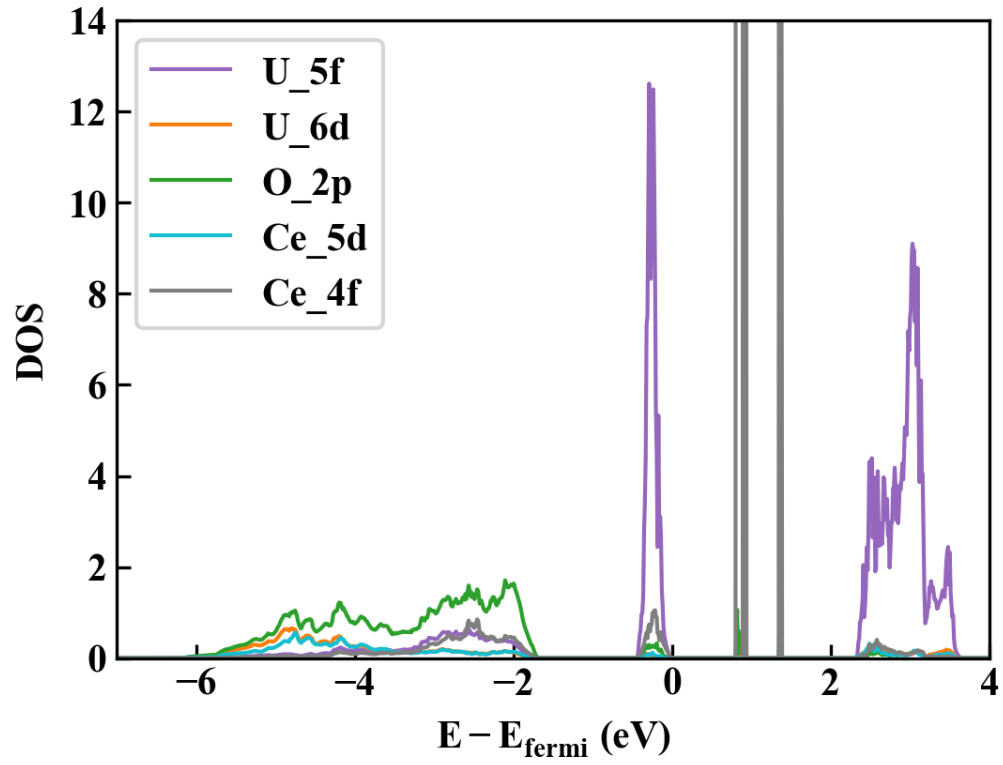

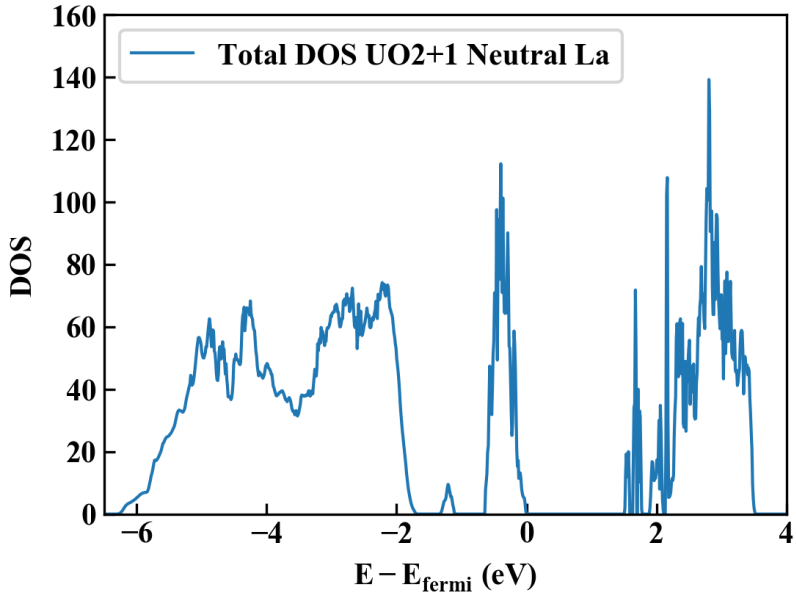

Fig. R3: A single La substitution decreases the lattice parameter of UO_2 by -0.02%, and the band gap by nearly 35% to 1.50 eV. Based on the site-projected partial DOS below, it appears the band gap reduction occurs by addition of states at the leading edge of the band gap by La 5d and 4f electrons.

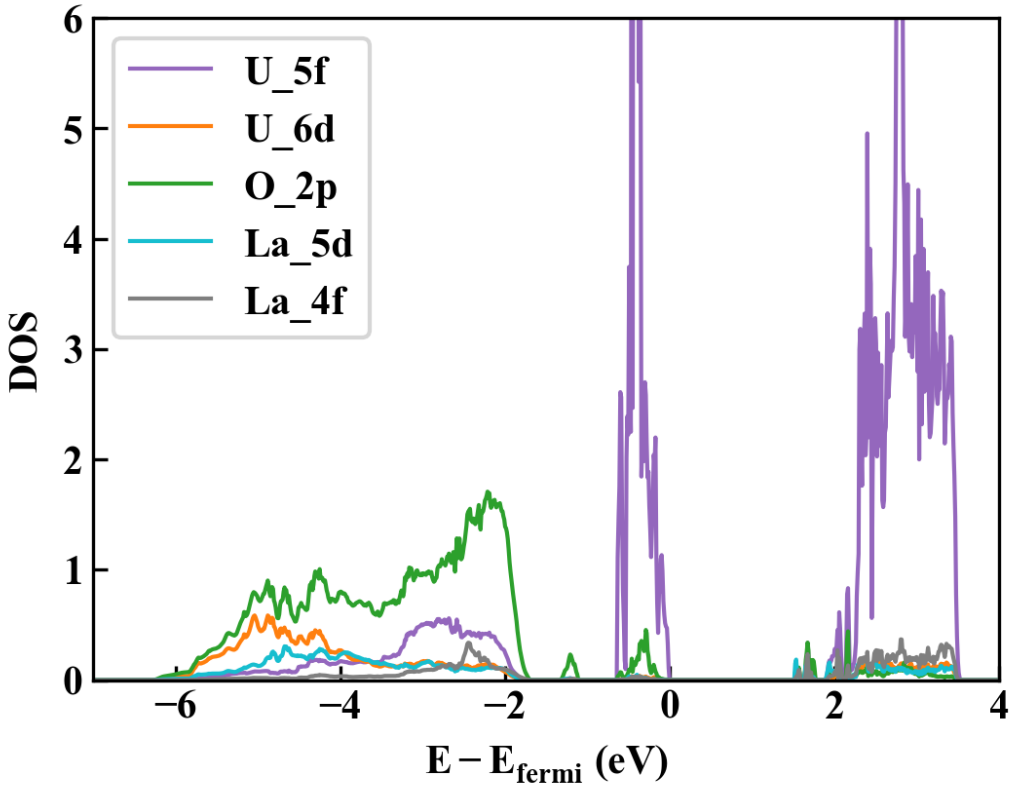

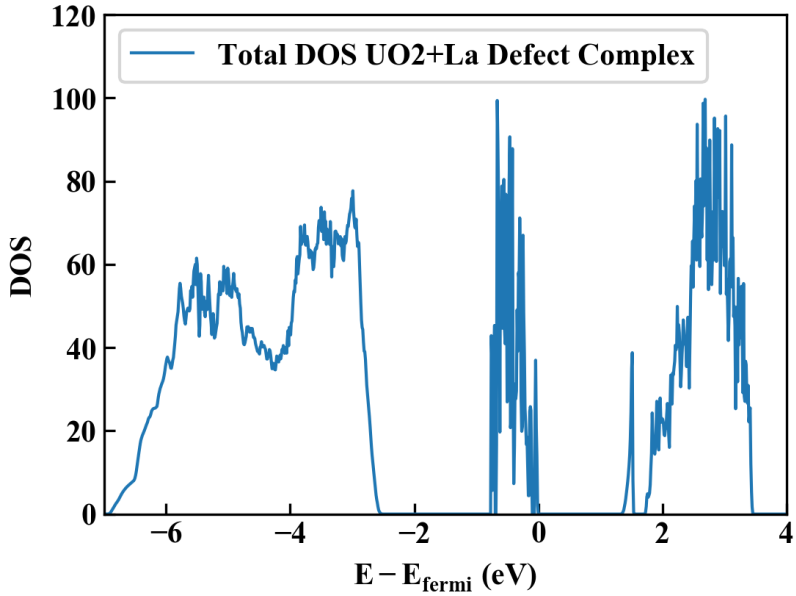

Fig. R4: The 2 $La_U^{'}$ + $V_O^{\bullet\bullet}$ defect complex (12.5 at. % La and 3.125 at. % O) increases the lattice parameter of UO_2 by -0.40%, but still decreases the band gap to 1.33 eV. The site-projected partial DOS below suggests the band gap reduction results from similar effects in both this and the single replacement case. Although here it seems the oxygen orbitals are modified by the presence of a vacancy.

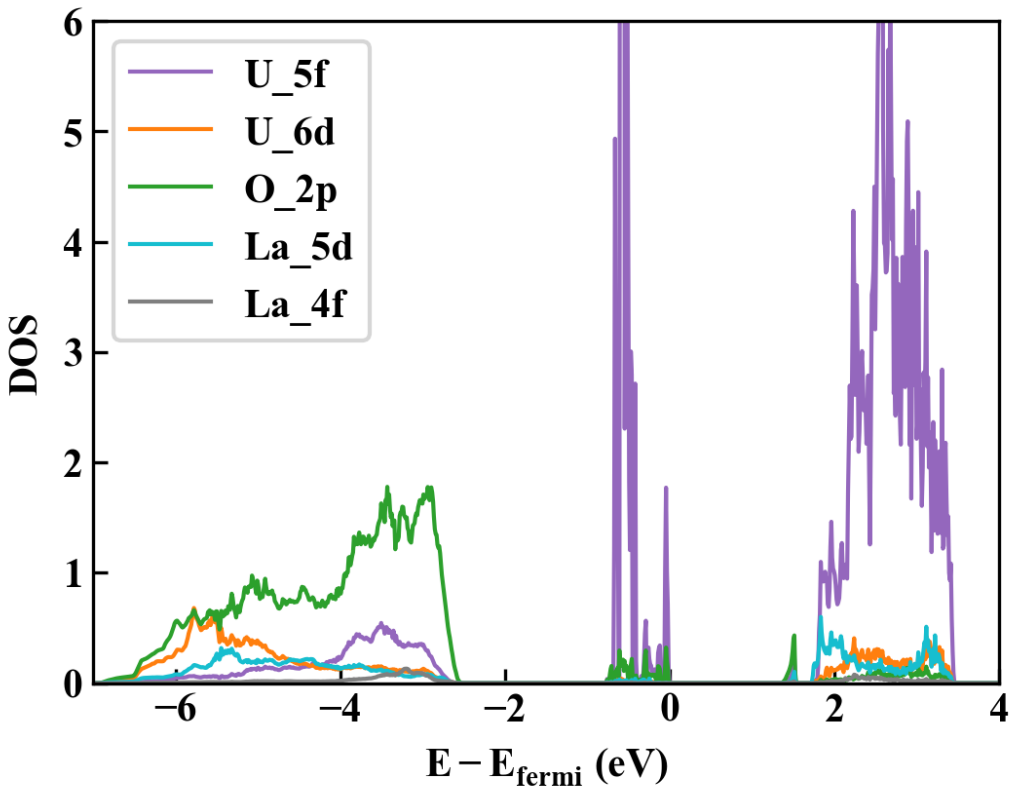

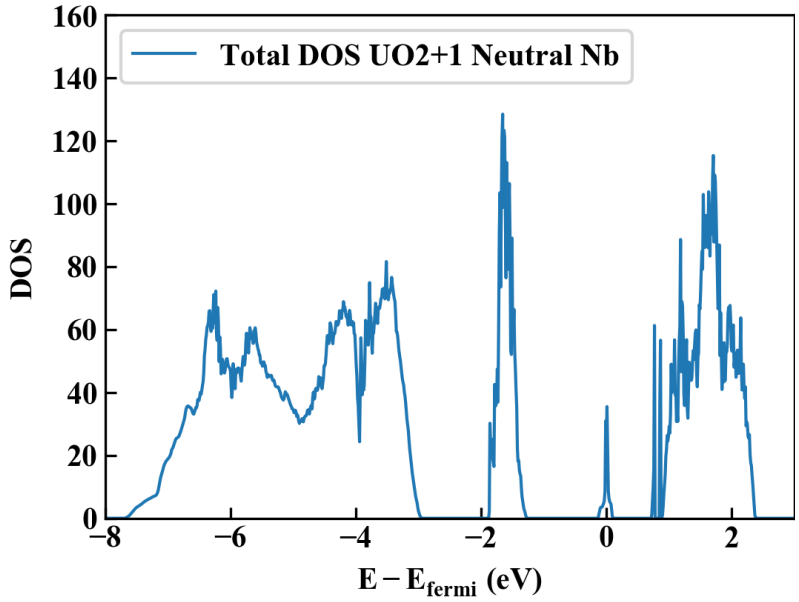

Fig. R5: A 6.25 at. % (single substitution) of Nb doped into the cell decreases the lattice parameter and band gap by -0.51% and 73%, respectively. This band gap reduction, based on the site-projected partial DOS, occurs as a result of Nb 4d states adding to the center and leading edge of the band gap. In addition, the fermi energy has shifted to the states added by doping with Nb.

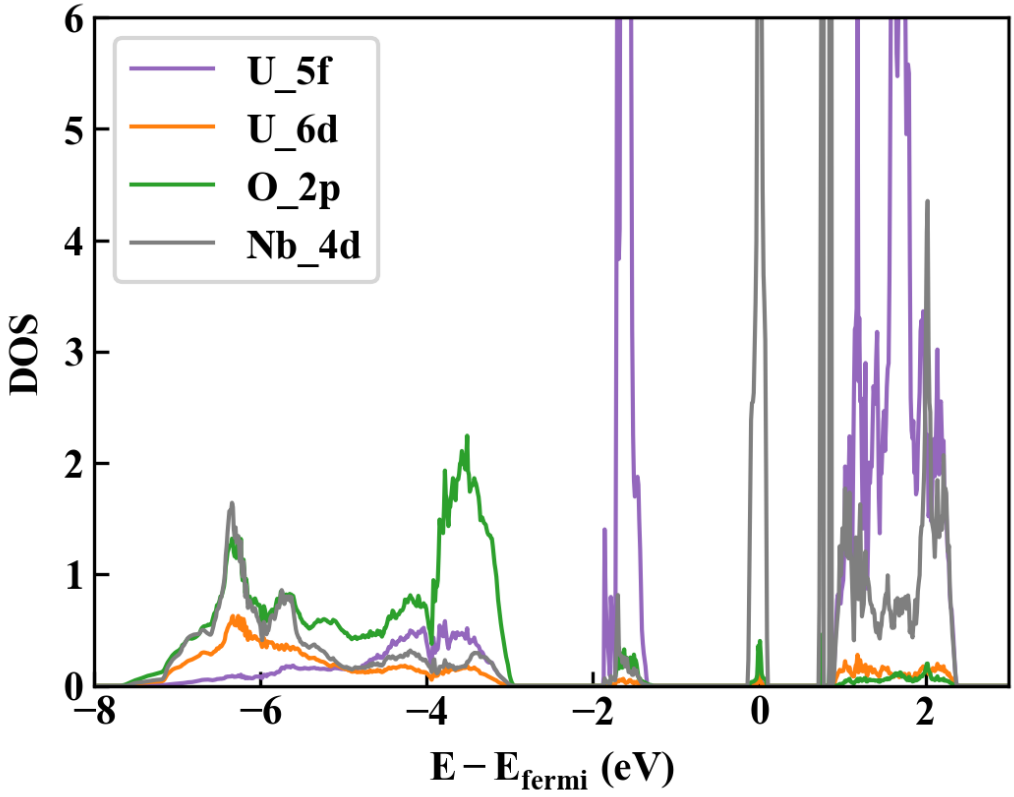

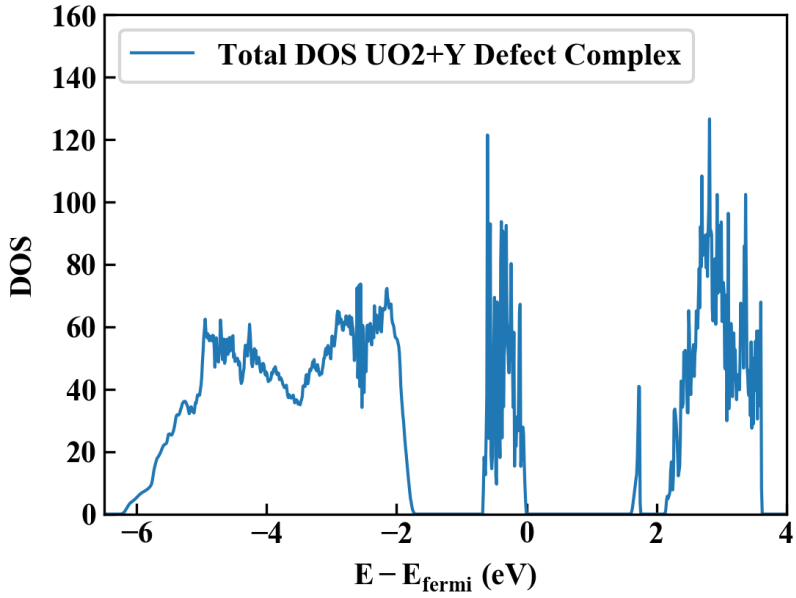

Fig. R6: The introduction of 12.5 at. % Y and 3.125 at. % O (2 $Y_U^{'}$ + $V_O^{\bullet\bullet}$ defect complex) decreases the lattice parameter of UO_2 by -0.40% and the band gap by 24%. The result is a band gap of 1.77 eV, resulting from the addition of Y 4d states to the leading edge of the band gap, according to site-projected partial DOS below. There are also contributions from the oxygen vacancy overlapping with the Y 4d states.

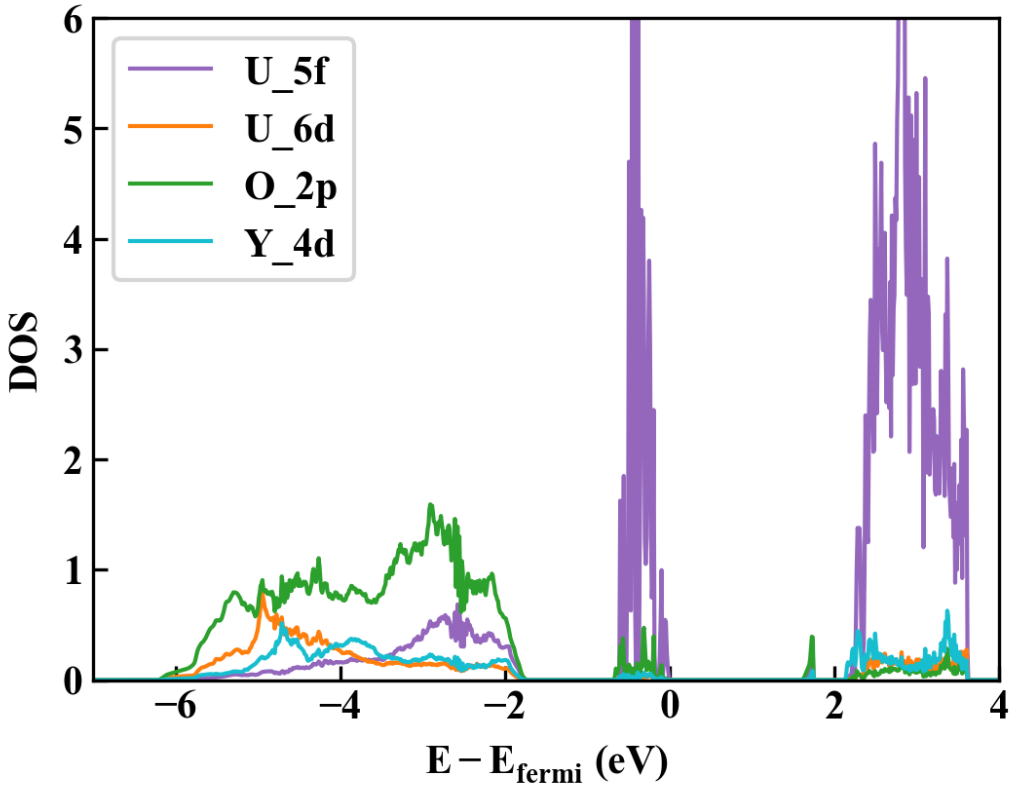

(iii.) **Anion Doping:**

Based on literature found supporting the stability for many compositions of a $UO_{(2-x)}N_x$ system, N concentrations ranging from 3% (single O sublattice substitution) to 50% (16 O sublattice substitutions) were used to explore the effects of anionic doping in UO_2. Nitrogen was chosen for the first anionic doping case since the UN system has a metallic band structure, though further anionic doping cases were not fully investigated due to time constraints. As such, N remains the only anionic dopant with complete results over a compositional range, although the effects of chemical environment on the N substitutions couldn't be fully explored.

Table R2: The compositional effects of N are shown above, where an increase in concentration is met by a steady decrease in the lattice parameter, and a variable decrease in the band gap. It seems based on the above results that a concentration of 25 at. % N is the most promising candidate for band gap reduction. Here, SQS (special quasi-random structure) is a structure generated by fitting the 2- and 3-body radial distribution functions to those of a completely random system at the specified concentrations.

System	Anion (at. %)	Band Gap (eV)	Band Gap Reduction (%)	E-fermi (eV)	Lattice Parameter Difference (%)	Lattice Parameter (Å)	Gap (UO2)-Gap (System)
UO2	0	2.33	0.00	8.113	0.00	5.47719	0.00
1xN UON	3.125	1.52	34.94	8.380	-0.12	5.47088	0.81
2xN UON	6.25	1.51	35.19	8.390	-0.28	5.46181	0.82
4xN UON	12.5	1.28	45.02	8.583	-0.57	5.44607	1.05
8xN UON-SQS	25	1.28	45.15	8.766	-1.09	5.41757	1.05
8xN UON	25	0.96	58.80	9.034	-1.09	5.41757	1.37
16xN UON	50	1.22	47.77	9.105	-2.00	5.36755	1.11

Based on Table R2, increasing the concentration of N results in a steady decrease in lattice parameter and band gap, accompanied by an increase in the Fermi energy level. However, both the increase in the Fermi energy level and decrease in band gap do not occur in a linear fashion. Rather, both effects have a kind of saturation behavior, after which the efficacy of increasing the N concentration is significantly reduced. In fact, it seems there may be an increase in the band gap by increasing the concentration of N beyond 25 at. %. These effects seem correlated to the changes in the DOS that result from the increasing number of N p-states added primarily to the leading and tailing edges of the band gap (Fig. R7-R12). Additionally, it seems that as the concentration of N increases in the system there arises an increasing density of p-states in the range of -2 to 0 eV, achieving the greatest density in the DOS of the 25 at. % (8xN) system, in direct correlation with large a band gap reduction in the system. Both this effect and the Fermi energy increase observed with increasing N concentration seem to saturate in the 8xN system, and little change is observed in band gap reduction upon further increase in N substitutions.

Anionic Conclusions:

- As N concentration increases, there is a significant increase in the density of N p-states between -2 and 0 eV.
- The densest the p-states become is at 25 at. % N, where the band gap reduction is greatest.
- The greatest reduction in the band gap seems correlated to these states.

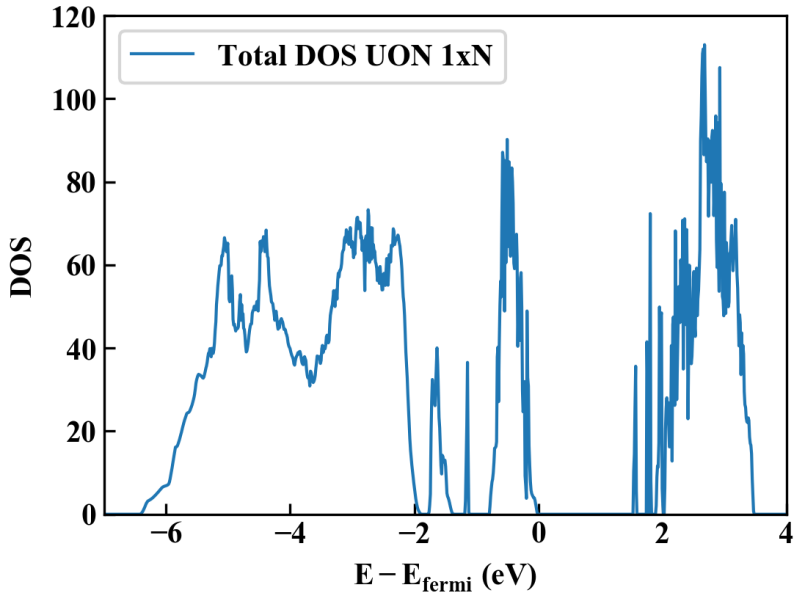

Fig. R7: A single substitution (3.13 at. %) of N decreases the lattice parameter and band gap by -0.12% and 35%, respectively. The site-projected partial DOS, below suggests the band gap reduction occurs as a result of added states at the leading and tailing ends of the band gap.

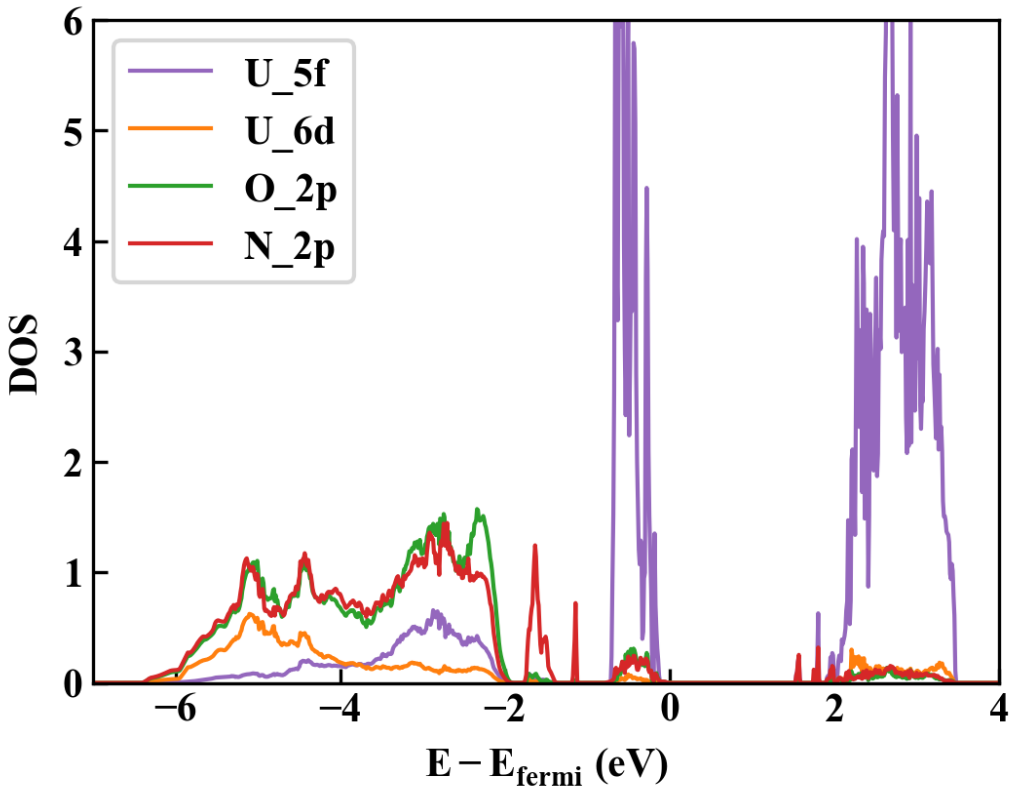

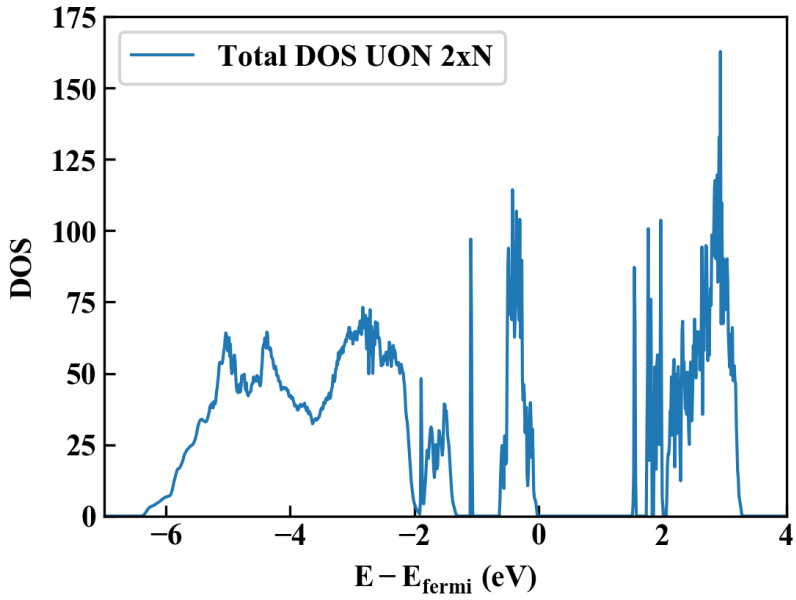

Fig. R8: A 6.25 at. % (2 substitutions) of N doped into the cell decreases the lattice parameter of UO_2 by –0.28%, and the band gap by nearly 35% to 1.51 eV. The p-states of N add again to the leading and tailing edges of the band gap, resulting in the band gap reduction.

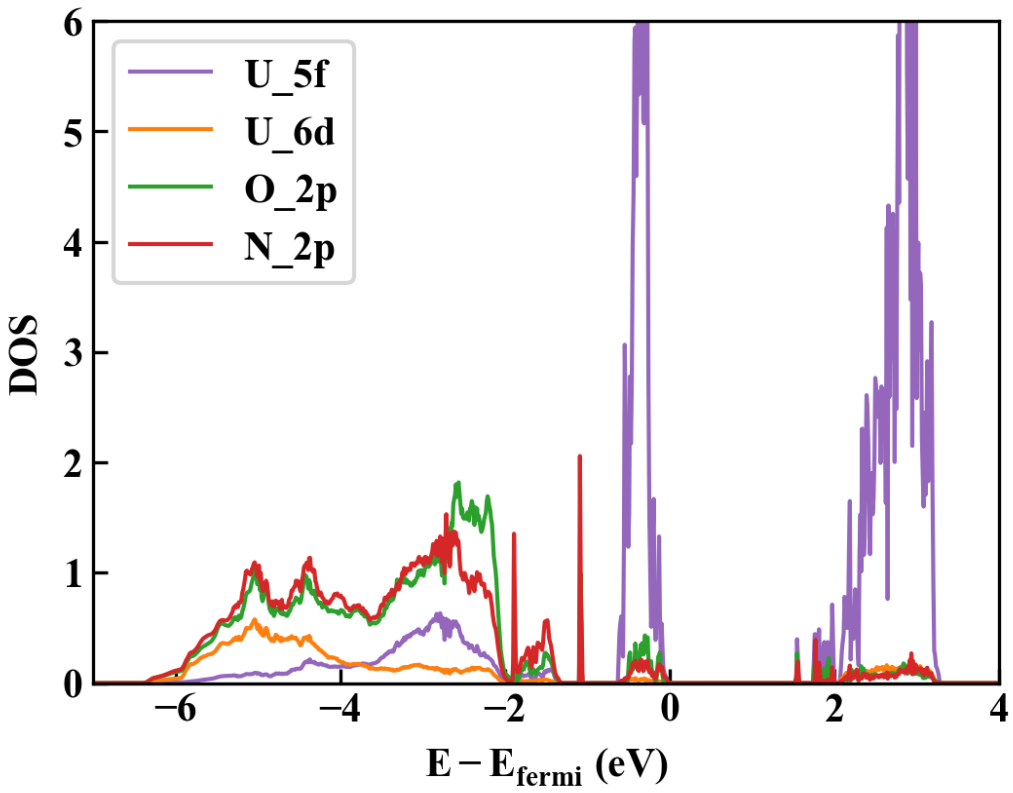

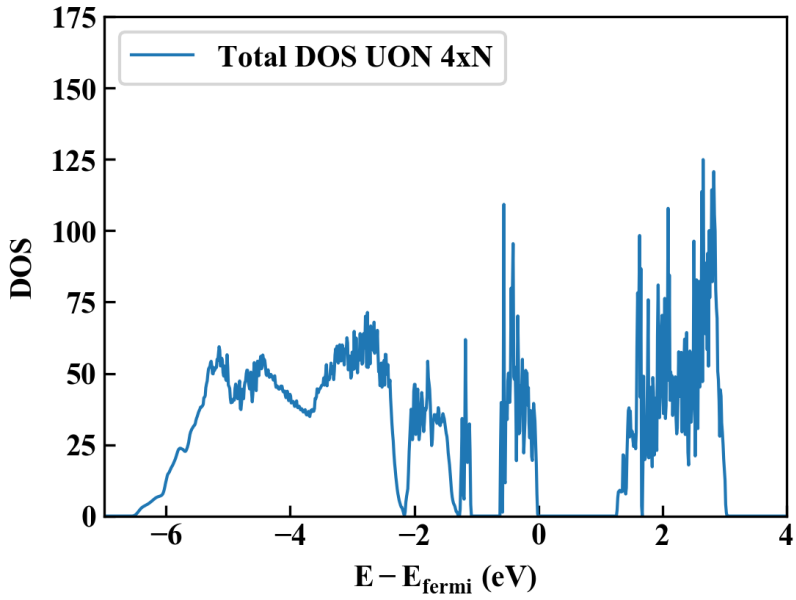

Fig. R9: A 12.5 at. % (4 substitution) of N decreases the lattice parameter and band gap by -0.57% and 45%, respectively. The band gap reduction occurs here as a result of N p-states hybridizing with preexisting states at the leading and tailing edges of the band gap.

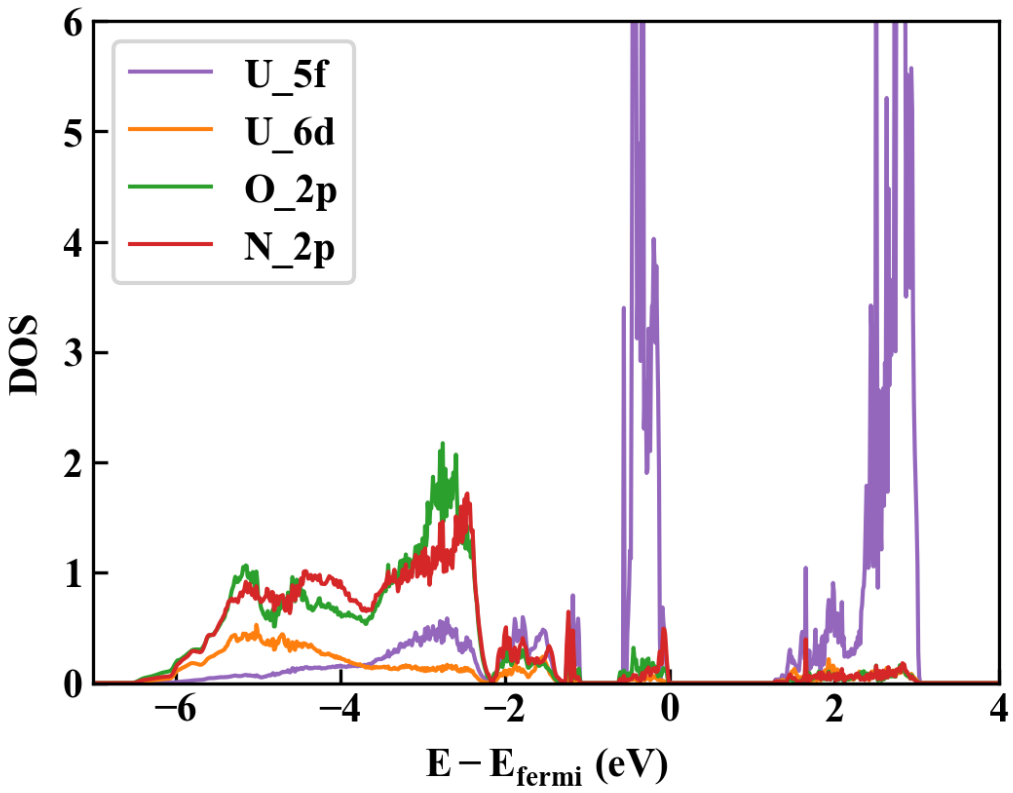

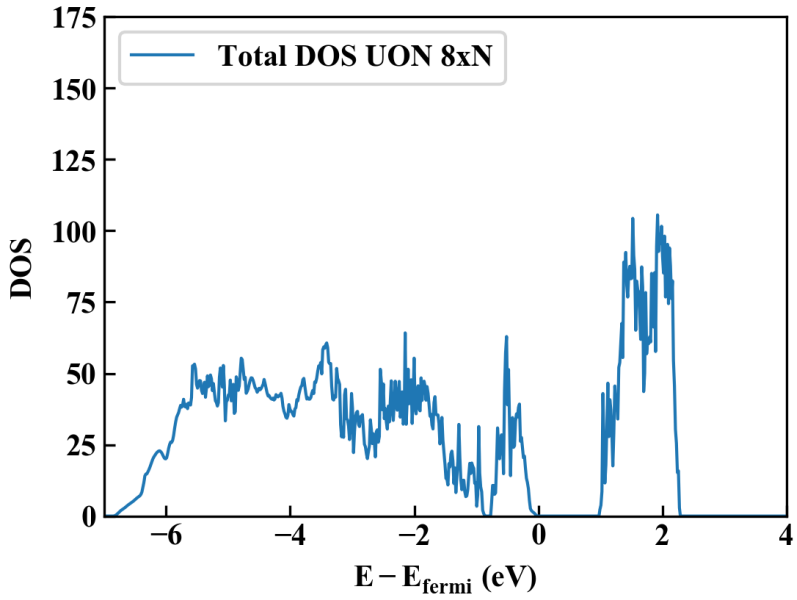

Fig. R10: At a concentration of 25 at. % N (8 substitutions) the lattice parameter and band gap decrease by -1.09% and 58.8%, respectively. Here the band gap reduction appears to follow from p-state hybridization at the leading and tailing edges of the band gap, but there are additional states concentrated near the Fermi energy, which seem to result from the higher concentration of N.

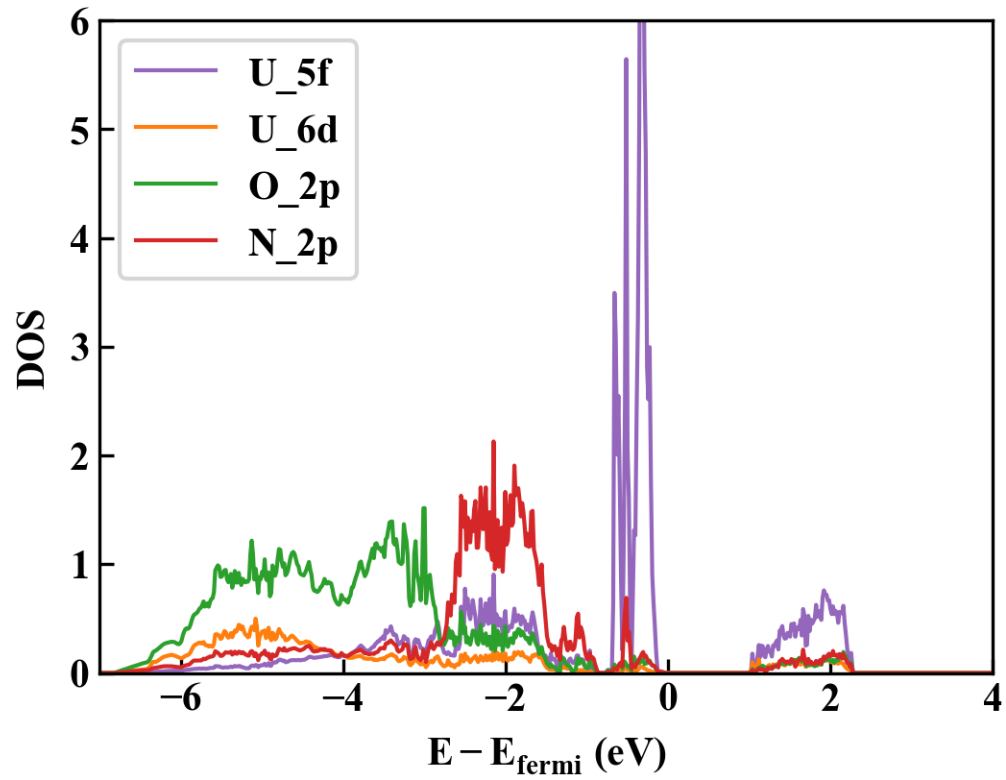

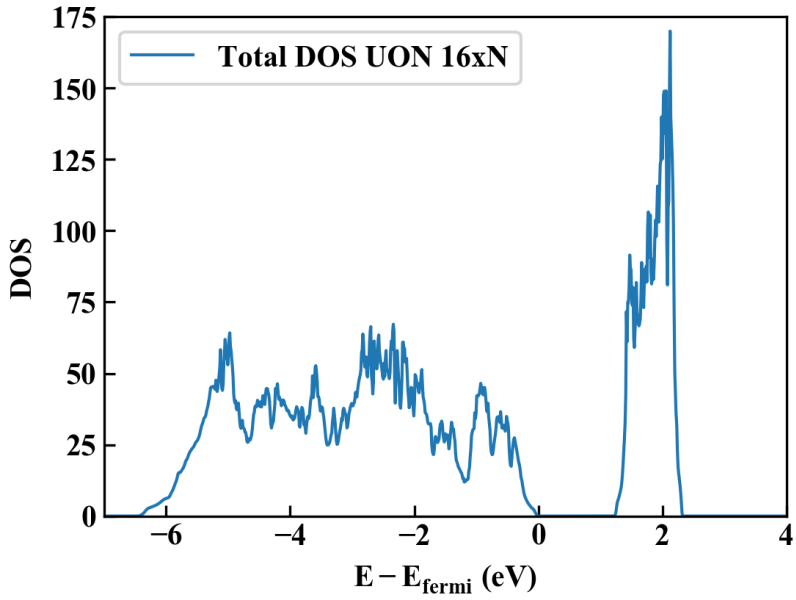

Fig. R11: At 50 at. % (16 substitutions) of doped N the lattice parameter and band gap decrease by -2.00% and 47.7%, respectively. In this case, the additional N p-states contributed mainly the leading edge of the band gap, though states were also added to the tailing edge of the band gap.

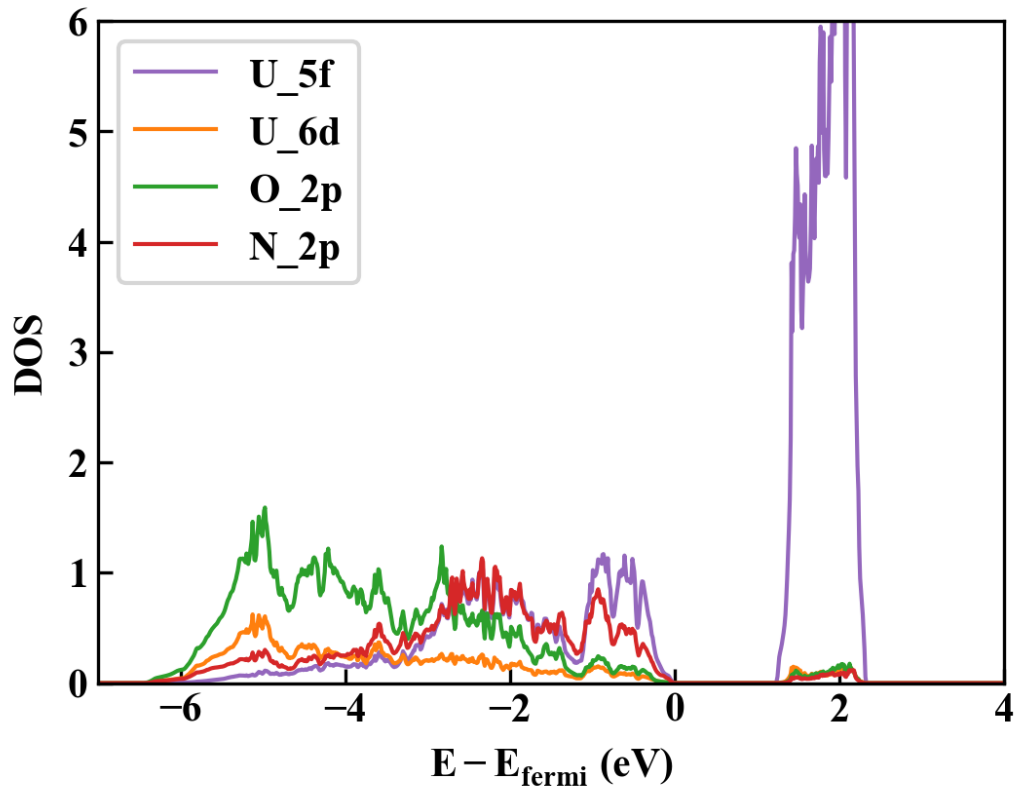

(iii.) **Exploring SQS at 25 at.% N:**

The initial SQS[8-9] results for the 8xN system seem to suggest the chemical environment of the doped N atoms does have a nontrivial effect on the band gap reduction in the system, though details of this interaction were not completely investigated due to time constraints. Despite this loss of efficacy in SQS 8xN, the aforementioned trend of increasing density in p-states between -2 and 0 eV in the 8xN system holds, preserving the qualitative features of the DOS when comparing the 8xN and SQS-8xN

systems (Fig. R10 and R12). Based on these analyses, it seems the 25 at. % concentration of N is the most promising candidate for anionic doping, and further work screening for anionic dopants should begin from 25 at. % anionic substitutions for comparison.

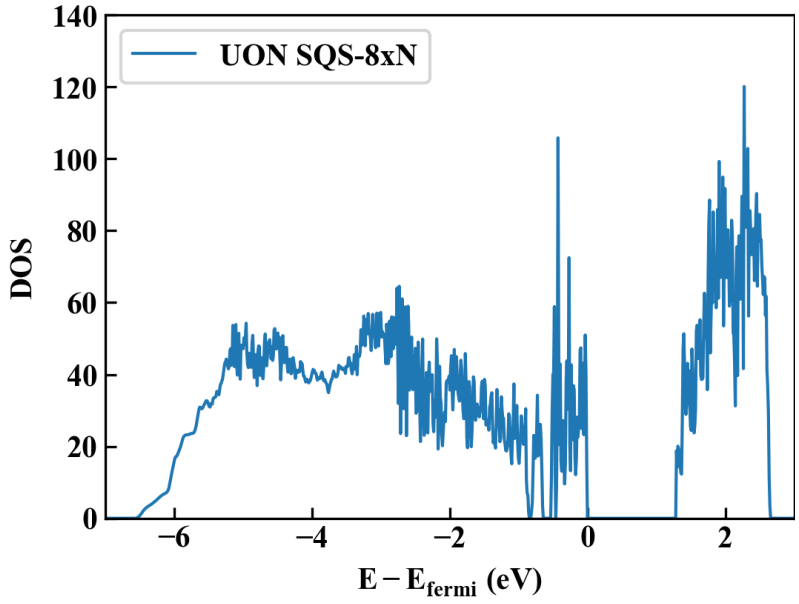

Fig. R12: Here an SQS of the 15 at. % N composition was tested, resulting in a lattice parameter decrease of -1.09%. However, the band gap reduction is only 45%. The band gap reduction appears to result from additional N p-states at the leading and tailing edges the band gap. Additionally, there is a large concentration of N p-states just below the Fermi energy.

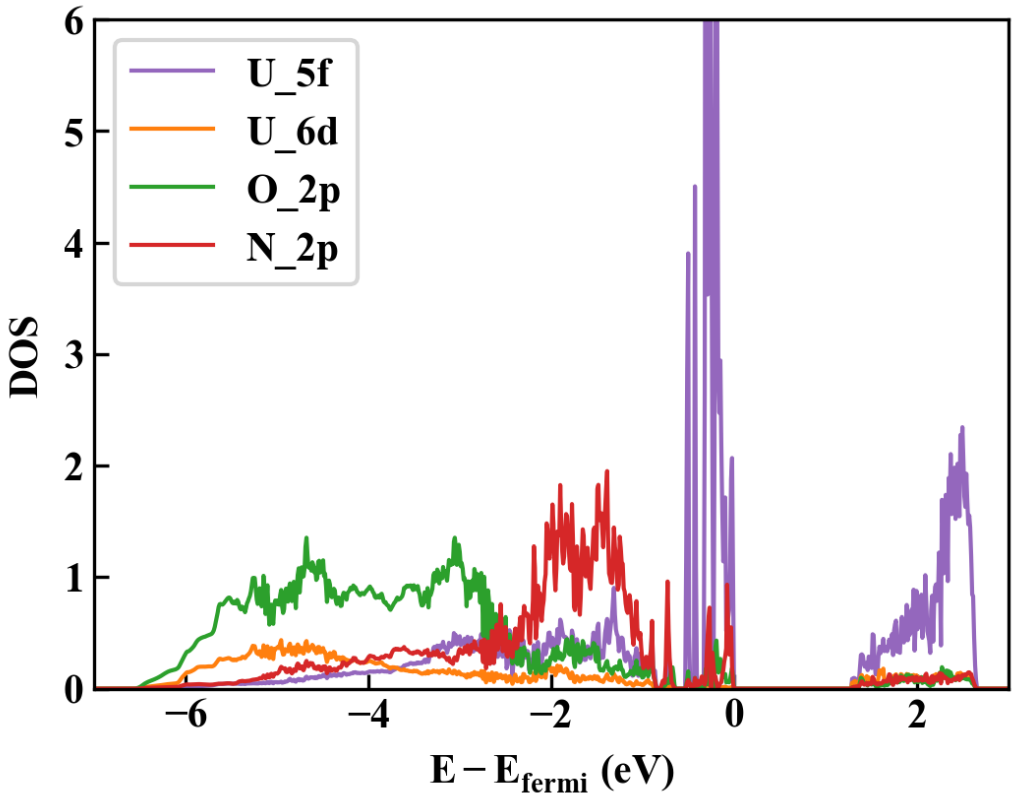

Conclusions:

The study of the band gap reduction effect for the cationic dopants Ce, La, Nb, and Y, and the compositional range of the anionic dopant N have resulted varying success. Neither of the cationic dopants La or Y reach a band gap reduction far above ~40% and tend to see the greatest contribution to band gap reduction by addition of states to the leading edge of the band gap. In contrast, both of Nb and Ce achieve a band gap reduction of >60%, which is primarily due to the addition of states to the center of the band gap, and a significant increase in the Fermi energy in the case of Nb. In exploring the compositional effects of N doping, the band gap reduction effect appeared to increase with increasing concentration up to 25 at. %, then saturated thereafter. An increase in the Fermi energy and in N p-state contributions just below the Fermi energy were observed to accompany this behavior, again followed by a saturation and diminishing effect upon further increases in N concentration. Finally, those dopants with the greatest promise for increasing the thermal conductivity of the fluorite UO_2 fuel are Ce, Nb, and ~25 at. % N. Furthermore, since DFT+U is known to underestimate the effects of highly correlated electron systems relative to hybrid functionals, such as PBE0 and HSE, it is possible the band gap will be further reduced upon hybrid DFT treatment of the systems.

Moving forward, hybrid functional treatment and compositional effects in the most promising cases, in addition to further screening of anionic dopants, and a thorough investigation of the impact of local chemical environment would be in order. Hybrid treatments providing a much clearer quantitative picture of both the DOS and Band structure would allow for a more complete analysis of the band gap reduction effects in doped and codoped systems, and a more accurate assessment of the resulting improvements to thermal conductivity. Further screening of anionic dopants could quickly reveal any other systems which provide promising band gap reduction effects. Finally, it appears, based on initial SQS results, that the impact of local chemical environment may be nontrivial in this system, and certainly worthy of an estimation for the magnitude of the effect on the system.

References:

[1]G. Kresse and J. Hafner. Ab initio molecular dynamics for liquid metals. Phys. Rev. B, 47:558, 1993.

[2]G. Kresse and J. Hafner. Ab initio molecular-dynamics simulation of the liquid-metal-amorphous-semiconductor transition in germanium. Phys. Rev. B, 49:14251, 1994.

[3]G. Kresse and J. Furthmüller. Efficiency of ab-initio total energy calculations for metals and semiconductors using a plane-wave basis set. Comput. Mat. Sci., 6:15, 1996.

[4]G. Kresse and J. Furthmüller. Efficient iterative schemes for ab initio total-energy calculations using a plane-wave basis set. Phys. Rev. B, 54:11169, 1996.

[5]P. E. Blöchl, *Phys. Rev. B* 1994, **50**, 17953– 17979

[6]P. E. Blöchl, O. Jepsen, O. K. Andersen, *Phys. Rev. B* 1994, **49**, 16223– 16233

[7]PRODAN, SCUSERIA, AND MARTIN / PHYSICAL REVIEW B 73, 045104 (2006) DOI: 10.1103/PhysRevB.73.045104

[8]A. van de Walle, The Alloy Theoretic Automated Toolkit, 2001, http://cms.northwestern.edu/atat/.

[9]A. Zugner et. al. “Special Quasirandom Structures,” Phys. Rev. Lett. 65, 3 353-356 (1990) DOI: 10.1103/PhysRebLett.65.353